Universidad de Huelva

Departamento de Química “Profesor José Carlos Vílchez Martín”

New Bimetallic Monovalent Aluminium and Gallium Systems with Alkali Metals and Rhodium for Small Molecule and C–H Activation

Memoria para optar al grado de doctora
presentada por:

Hellen Skarleth Videa Dubón

Fecha de lectura: 17 de junio de 2025

Bajo la dirección del doctor:

Antonio Jesús Martínez Martínez

Huelva, 2025

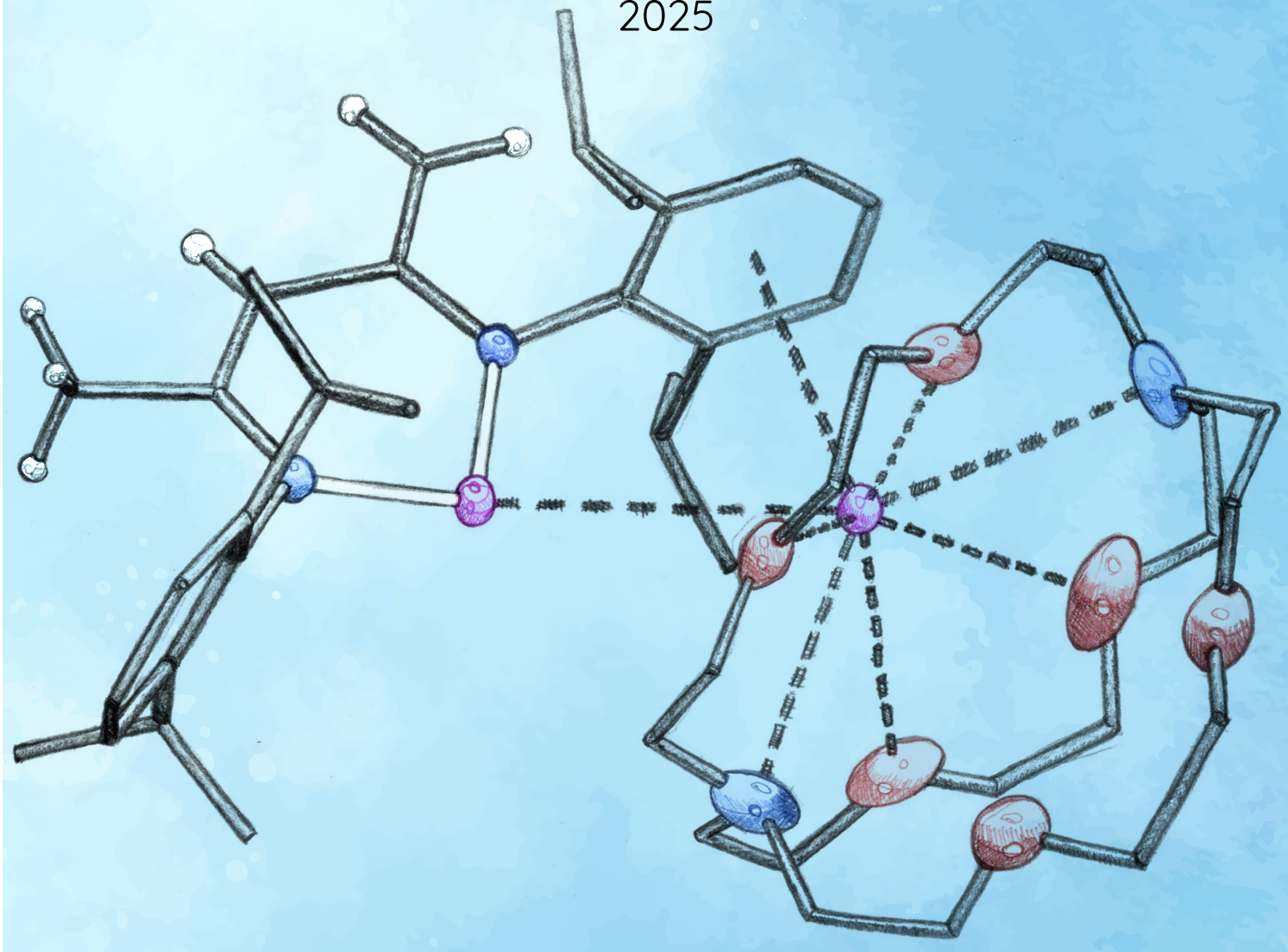
CC BY NC ND

Universidad de Huelva

New Bimetallic Monovalent Aluminium and Gallium Systems with Alkali Metals and Rhodium for Small Molecule and C–H Activation

Hellen Skarleth Videa Dubón

Doctoral Thesis
2025





NEW BIMETALLIC MONOVALENT ALUMINIUM AND GALLIUM SYSTEMS WITH ALKALI METALS AND RHODIUM FOR SMALL MOLECULE AND C–H ACTIVATION

Programa de Doctorado:

Ciencia y Tecnología Industrial y Ambiental

Hellen Skarleth Videa Dubón

Tesis Doctoral 2025

NEW BIMETALLIC MONOVALENT ALUMINIUM AND GALLIUM SYSTEMS WITH ALKALI METALS AND RHODIUM FOR SMALL MOLECULE AND C–H ACTIVATION

por

Hellen Skarleth Videa Dubón

Trabajo presentado para aspirar al

Título de Doctora en Ciencias Químicas

Huelva, marzo 2025

Fdo: Hellen Skarleth Videa Dubón

El Director:

Fdo. Dr. Antonio J. Martínez Martínez

“El hecho de que dé consejos no significa que sea más inteligente que tú, solo que he cometido más errores”

“El maestro ha fallado más veces de las que la aprendiz lo ha intentado”

Index

Abbreviations and Symbols ..... ***III***

Resumen ..... ***IX***

Summary ..... ***XXIII***

CHAPTER I

Synthesis, Characterisation and Reactivity of Electron-Rich Anionic Aluminium(I) Species: From Aggregation Control to H_2 Activation

1.1 Introduction **3**

1.1.1 Neutral Aluminium(I) Species: Aluminylenes 4

1.1.2 Nucleophilic Aluminium(I) Anions: Aluminyls 6

1.2 Objectives **11**

1.3 Results and Discussion **13**

1.3.1 Synthesis of Alkali Metals Aluminyls 13

1.3.2 Nuclear Magnetic Resonance (NMR) Spectroscopy Studies 16

1.3.3 Diffusion Order SpectroscopY (DOSY) NMR Studies 23

1.3.4 Single-Crystal X-ray Structural Analysis 29

1.3.5 Reactivity Studies: Activation of H_2 at Aluminyls 35

1.3.6 Synthesis of Alkali Metal Dihydridoaluminates 48

1.3.7 Diffusion Order SpectroscopY (DOSY) NMR Studies 56

1.3.5 Crystal Structures of Aluminium Dihydrides 60

1.4 Conclusions **69**

1.5 Experimental Methods **71**

1.5.1 Materials 71

1.5.2 Synthesis and Characterisation of Alkali Metal Aluminyls 72

1.5.3 Synthesis and Characterisation of Alkali Metal Dihydridoaluminates 75

1.6 References **79**

CHAPTER II

Synthesis, Characterisation and Reactivity of Electron-Rich Anionic Gallium(I) Species: Alkali Metal Mediated C–H Activation

2.1 Introduction 85

2.1.1 Overview of Neutral Gallium(I) Chemistry: Gallylenes 85

2.1.2 Anionic Gallium(I) Species: Gallyls 87

2.2 Objectives 91

2.3 Results and Discussion 93

2.3.1 Synthesis of Alkali Metal Gallyls 93

2.3.2 Nuclear Magnetic Resonance (NMR) Spectroscopy Studies 95

2.3.3 Diffusion Order SpectroscopY (DOSY) NMR Studies 102

2.3.4 Single-Crystal X-ray Structural Analysis 107

2.3.5 Computational Studies 116

2.3.6 Small Molecule Reactivity 127

2.3.7 C−H Bond Reactivity 130

2.4 Conclusions 137

2.5 Experimental Methods 139

2.5.1 Materials 139

2.5.2 Synthesis and Characterisation of Alkali Metal Gallyls 141

2.6 References 151

CHAPTER III

Synthesis, Characterisation and Reactivity of Bimetallic Ga−Rh Species: H_2 Activation and Catalytic Hydrogenation of Olefins

3.1 Introduction 157

3.1.1 Amine and Phosphine Ligands in Rhodium Chemistry 159

3.1.2 Carbene Ligand in Rhodium Chemistry 164

3.1.3 Group 13 M(I) Carbene Analogues as Metalloligands 168

3.2 Objectives 171

3.3 Synthesis of Ga(I)–Rh(I) Species form Rh(I) Amine/Olefin Precursors 173

3.3.1 Rh(I) Amine/Olefin Complexes: Precursors for M(I) Ligand-Exchange 173

3.3.2 Heterometallic Ga(I)–Rh(I) Olefin Species 175

3.3.3 Characterisation of Rh(I) Amine/Olefin and Heterometallic Ga(I)–Rh(I) Olefin Complexes 177

3.3.4 Crystal Structures 184

3.4 H_2 Activation and Hydrogenation of Olefins by Heterobimetallic Ga(I)–Rh(I) Species 192

3.4.1 Speciation/Stability NMR Studies of cis-[2_2−Rh(NBD)][$BAr^F{}_4$] with H_2 . 192

3.4.2 Speciation/Stability NMR Studies of cis-[2_2−Rh(COD)][$BAr^F{}_4$] with H_2 . 194

3.4.3 Speciation/Stability Crystallographic Studies with H_2 200

3.4.4 Speciation/Stability Mass Spectroscopic Studies with H_2 204

3.4.5 Catalytic Hydrogenation of Olefins by the Heterometallic Ga(I)–Rh(I) Species 209

3.4.6 Computational Mechanistic Insights 214

3.4 Conclusions 219

3.5 Experimental Methods 221

3.5.1 Materials 221

3.5.2 Synthesis and Characterisation of Rhodium(I) Diamino Complexes 222

3.5.2 Synthesis and Characterisation of Heterometallic Ga(I)−Rh Olefin Complexes 226

3.6 References 233

CHAPTER II

Other Scientific Works Developed in this Doctoral Thesis

4.1 Introduction 241

4.2 Chapter 9: Solid/Gas Reactivity of Organometallic Species in Confined Spaces 243

4.3 Revealing unbound β-diketiminate anions: structural dynamics from caesium complexes 245

4.4 Reversible Redox Ligand-Centered Reactivity in 2,6-Bisiminopyridine Aluminum Systems 251

Conclusiones 267

Conclusions 273

Abbreviations and Symbols

Abbreviations and Symbols

12-cr-4	12-crown-4 or 1,4,7,10-tetraoxacyclododecane (*12-corona-4 o 1,4,7,10-tetraoxaciclododecano*)
15-cr-5	15-crown-5 or 1,4,7,10,13-Pentaoxacyclopentadecane (*15-corona-5 o 1,4,7,10,13-Pentaoxaciclopentadecano*)
18-cr-6	18-crown-6 or 1,4,7,10,13,16-Hexaoxacyclooctadecane (*18-corona-6 o 1,4,7,10,13,16-Hexaoxaciclooctadecano*)
Ar	Aromatic Group (*Grupo aromático*)
BDI	β-diketiminate (*1,3-dicetimina o β-dicetimina*)
br	Broad (*ancho*)
$BAr^F{}_4^-$	tetrakis[3,5-bis(trifluoromethyl)phenyl]borate anion (*anión tetraquis[3,5-bis(trifluorometil)fenil]borato*)
CD_2Cl_2	Deuterated dichloromethane (*Diclorometano deuterado*)
CH_2Cl_2	Dichloromethane (*Diclorometano*)
C_6D_6	Deuterated benzene (*Benceno deuterado*)
CsHMDS	Caesium bis(trimethylsilyl)amide (*Bis(trimetilsilil)amida de cesio*)
ºC	Degree Celsius (*Grados Celsius*)
Cryp	2,2,2-cryptand or 4,7,13,16,21,24-hexaoxa-1,10-diazabicyclo[8.8.8]hexacosane (*2,2,2-criptando o 4,7,13,16,21,24-hexaoxa-1,10-diazabiciclo[8.8.8]hexacosano*)
[CAT]	Catalyst (*Catalizador*)
COSY	Homonuclear *CO*rrelation *S*pectroscop*Y* (*Espectroscopia de correlación homonuclear*)
d	Doublet (*Doblete*)
DCM	Dichloromethane (*Diclorometano*)
Dipp	2,6-diisopropylphenyl group (*Grupo 2,6-di-isopropilfenilo*)
DFT	Density Functional Theory (*Teoría del funcional de la densidad*)
DOSY	*D*iffusion *O*rder Spectroscop*Y* (*Espectroscopia Ordenada por Difusión*)
ESI	Electrospray ionisation (*Ionización por electrospray*)
Eqiv	Equivalents (*Equivalentes*)

g	Grams (*Gramos*)
h	Hours (*Horas*)
Hz	Hertz (*Hercios*)
HRMS	High resolution mass spectrometry (*Espectrometría de masas de alta resolución*)
HMDS	Bis(trimethylsilyl)amide (*Bis(trimetilsilil)amida*)
HMDS(H)	Bis(trimethylsilyl)amine (*Bis(trimetilsilil)amina*)
HMBC	*H*eteronuclear *M*ultiple *B*ond *C*orrelation spectroscopy (*Espectroscopia de Enlaces Múltiples Heteronucleares*)
HSQC	*H*eteronuclear *S*ingle *Q*uantum *C*oherence spectroscopy (*Espectroscopia de Correlación Heteronuclear de un Único Cuanto*)
IPr	1,3-bis(2,6-diisopropylphenyl)imidazol-2-ylidene ligand (*Ligando 1,3-bis-(2,6-diisopropilfenil)imidazol-2-ilideno*)
J	Coupling constant (*Constante de acoplamiento*)
K	Kelvin, Degree Kelvin before (*Kelvin, antes grados Kelvin*)
KHMDS	Potassium bis(trimethylsilyl)amide (*Bis(trimetilsilil)amida de potasio*)
LiHMDS	Lithium bis(trimethylsilyl)amide (*Bis(trimetilsilil)amida de litio*)
m	Multiplet (*Multiplete*)
Me	Methyl group (*Grupo metilo*)
mg	Milligrams (*Miligramos*)
µg	Micrograms (*Microgramos*)
MHz	Megahertz (*Megahercios*)
min	Minutes (*Minutos*)
mL	Millilitres (*Mililitros*)
mmol	Millimole (*Milimol*)
NacNac	1,3-diketiminate or β-diketiminate (*1,3-dicetimina o β-dicetimina*)

NaHMDS	Sodium bis(trimethylsilyl)amide (*Bis(trimetilsilil)amida de sodio*)
NMR	Nuclear Magnetic Resonance (*Resonancia Magnética Nuclear*)
NHC	*N*-heterocyclic carbene (*Carbeno N-heterocíclico*)
Ph	Phenyl group (*Grupo fenilo*)
*i*Pr	Isopropyl group (*Grupo isopropilo*)
ppm	Parts per million (*Partes por millón*)
s	Singlet in NMR (*Singlete en RMN*)
s	Second, for time association (*Singlete con relación al tiempo*)
t	Triplet in NMR (*Triplete en RMN*)
t	Time, for time association (*Tiempo con relación al tiempo*)
tBu	tert-Butyl group (*Grupo tert-butilo*)
TMEDA	N,N,N′,N′−Tetramethyilethylenediamine (*N,N,N′,N′−Tetrametiletilendiamina*)
THF	Tetrahydrofuran (*Tetrahidrofurano*)
Tol	Toluene (*Tolueno*)
v br	very broad (*muy ancho*)
δ	Chemical shift in ppm (*Desplazamiento químico en ppm*)
η^x	Hapticity: the coordination of a ligand to a metal centre via an uninterrupted and contiguous series of atoms (*Hapticidad: átomos contiguos de un ligando que están coordinados a un átomo central*)
κ^x	Denticity: the number of donor groups in a given ligand that bind to the central metal atom in a coordination complex) (*Denticidad: número de átomos en un solo ligando que se unen al metal central en un complejo de coordinación*)

Resumen

Resumen

El estudio de metales es bajo estado de oxidación no es un área nueva en química sintética, especialmente para los metales de transición. Sin embargo, en estas últimas décadas, el estudio de metales del bloque p en bajo estado de oxidación ha sufrido un gran auge debido a que han demostrado ser capaces de realizar transformaciones de gran interés químico y sintético. Son especialmente relevante los ejemplos descritos de metales monovalentes del Grupo 13, donde el aluminio(I) y el galio(I), han adquirido una gran relevancia gracias a su comportamiento análogo a los carbenos, que les permite realizar transformaciones que antes se creían exclusivas de los metales de transición. Ampliando así los conceptos fundamentales de la reactividad conocida de los elementos del bloque p, dado que estas especies ricas electrónicamente de Al(I) y Ga(I) han mostrado una gran habilidad para romper enlaces fuertes (p. ej., H–H, C–H, C–C) y mediar en procesos catalíticos. Estos hallazgos ponen de manifiesto un cambio radical en la química moderna, donde los elementos del bloque p pueden emular e incluso competir con la reactividad clásicamente asociada a los metales de transición, gracias a los avances en el diseño inteligente de nuevos ligandos y a efectos cooperativos metal–metal que estos pueden establecer.

Es por ello, que esta *Tesis Doctoral* se ha centrado en la síntesis, caracterización y aprovechamiento de la reactividad de nuevos complejos de Al(I) y Ga(I), los cuales exhiben diversas interacciones metal–metal. Para ello se ha realizado un estudio sistemático tanto de sus estructuras en estado sólido, como un análisis del modo en que estas especies promueven o ceden electrones, y los equilibrios que presentan en disolución, poniendo de manifiesto comportamientos fluxionales, sugiriendo que estas agregaciones son dinámicas.

La *Tesis* consta de tres *Capítulos* interconectados, donde cada uno aborda un aspecto de especies de aluminio y galio en bajo estado de oxidación, que presentan diferentes estados de agregación con distintos metales alcalinos y hasta las interacciones cooperativas con metales de transición (en concreto, el rodio) mediante sutiles modificaciones. Prestando especial atención a la activación de sustratos inertes, como el dihidrógeno (H_2), y al estudio de la activación de enlaces C–H en condiciones suaves, con el fin de trazar paralelismos y, a la vez, superar las capacidades típicas de los catalizadores basados en metales de transición del bloque d.

Capítulo I

Síntesis, Caracterización y Reactividad de Especies Aniónicas de Aluminio(I) Ricas en Electrones: Control de Agregación y Activación de H_2

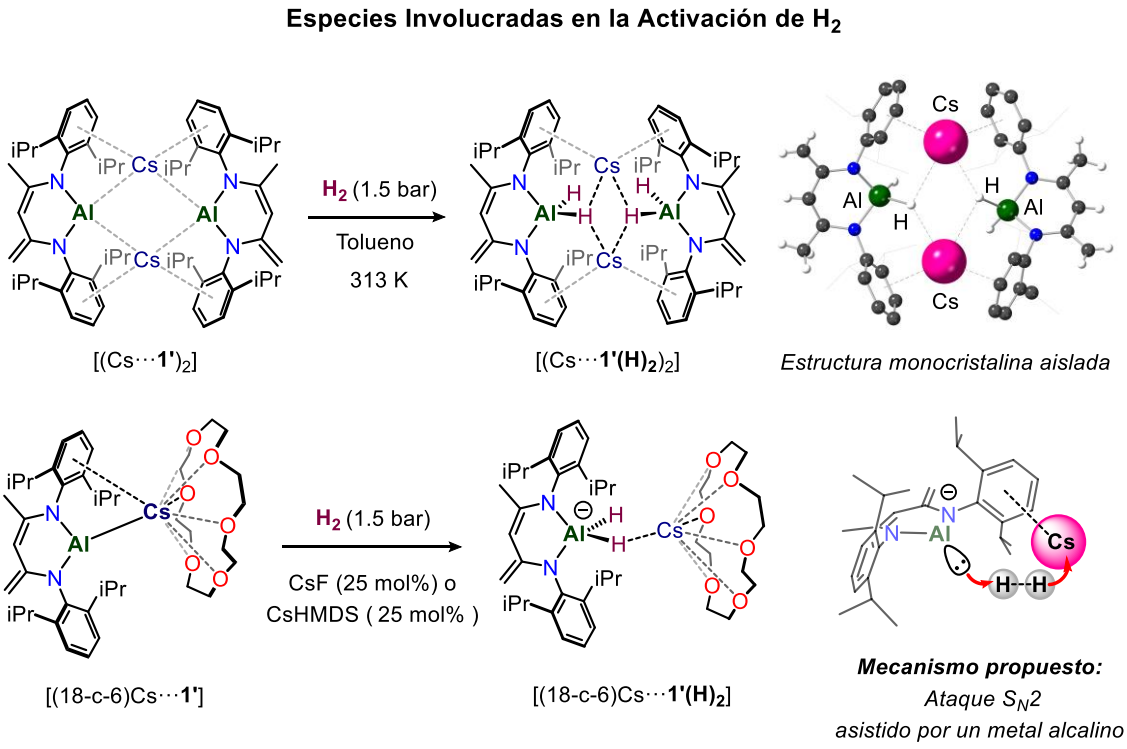
El *Capítulo I* se centra en el desarrollo sintético, caracterización y reactividad de especies aniónicas de aluminio(I) (aluminilos) y dihidridoaluminatos (Al(III)–H), soportadas en ligandos β-dicetiminato. Parte de este trabajo se basa en el innovador trabajo descrito por Schnöckel, quién en la década de 1990 describió complejos neutros de Al(I), comúnmente conocidos como aluminilenos, representando la primera demostración de aluminio en una configuración de baja valencia (R_2Al:), análoga a un carbeno (R_2C:). Posteriormente, otros derivados neutros de Al(I) han sido descritos, estabilizados por una variedad de ligandos, mostrando una notable reactividad con enlaces Si–H, O–H y P–H en diversos sustratos.

En 2018, la química de los metales del Grupo 13 experimentó un avance significativo cuando los grupos de Aldridge y Goicoechea publicaron el primer complejo de aluminilo aniónico, $[Al(I)]^-$, estabilizado por un ligando derivado de xanteno de tipo tripodal y un contraión de potasio (K^+). Este hallazgo revolucionó la concepción tradicional del aluminio como elemento electrofílico, demostrando un comportamiento de "umpolung", en el que el aluminilo actúa como un potente nucleófilo, facilitando la activación de enlaces H–H, C–H e incluso C–C. Inspirado por este descubrimiento, el *Capítulo I* detalla el diseño y aislamiento de nuevos sistemas de aluminilo aniónico soportados en estructuras β-dicetiminato. La introducción estratégica de grupos metilo en la parte trasera del ligando β-dicetiminato nos permitió la formación de un entorno quelante dianiónico, capaz de estabilizar especies electrónicamente ricas de $[Al(I)]^-$.

Por ende, para la síntesis y aislamiento de una nueva serie de especies aniónicas de aluminio en bajo estado de oxidación (aluminilo), se empleó una base suave derivada de la hexametildisilazida con diferentes metales alcalinos, AM(HMDS). Esto permite una modulación de los cationes alcalinos (Li^+ a Cs^+), que junto con la incorporación de ligandos dadores (éteres corona, criptandos) proporcionan una estrategia controlada para aislar diversos estados de agregación en disolución y en estado sólido. Abarcando desde pares diméricos hasta pares iónicos monoméricos y, en última instancia, especies de aluminilo completamente separadas (o "*naked*"). Los análisis detallados por RMN, difracción de rayos X y

cálculos computacionales revelaron la compleja interacción metal–metal $Al^{-}\cdots AM^{+}$, cuya naturaleza influye en su reactividad.

Dentro de las posibles transformaciones que pueden llevar a cabo por estas especies, destaca la capacidad de ciertos sistemas de aluminilo diméricos para activar H_2 en condiciones suaves, siendo un ejemplo paradigmático de reactividad dado que son reacciones típicamente asociadas a metales de transición y anómalas dentro de la química del bloque p. Por el contrario, los centros monoméricos o "*naked*" de $Al(I)]^{-}$ permanecen inactivos a menos que se introduzcan cationes alcalinos "libres", en particular Cs^{+}, en el sistema, Esquema 1. Estas observaciones ponen de manifiesto una sinergia bimetálica, en la que el centro nucleofílico $[Al(I)]^{-}$ y el catión alcalino AM^{+} cooperan para reducir las barreras de activación en procesos de escisión de enlaces, especialmente en moléculas pequeñas como el H_2, reflejando estrategias catalíticas similares en metales de transición del bloque d.



Esquema 1. Interacciones metal–metal en sistemas de aluminilo y su papel en la activación de H_2 estudiadas en el *Capitulo I*.

En paralelo, los estudios computacionales mediante DFT proporcionaron información clave del mecanismo de reacción, demostrando cómo los enlaces $Al^{-}\cdots AM^{+}$ favorecen la activación de H_2 mediante un mecanismo tipo S_N2 facilitado

por la presencia del catión alcalino. El Esquema 1 ilustra estas dinámicas de enlace metal–metal en sistemas de aluminilo y su papel en la activación de H_2.

Por tanto, el *Capítulo I* pone de manifiesto que, bajo el entorno electrónico y estructural adecuado, los complejos de aluminio en bajo estado de oxidación pueden exhibir reactividad tipo metal de transición. Más allá de ampliar la caja de herramientas sintéticas para los elementos del Grupo 13, este trabajo sienta las bases para futuras aplicaciones en catálisis y activación de enlaces, donde la modulación del entorno alcalino podría desbloquear nuevas reactividades previamente consideradas exclusivas de los metales de transición.

Capítulo II

Síntesis, Caracterización y Reactividad de Especies Aniónicas de Galio(I) Ricas en Electrones: Activación C–H Mediada por Metales Alcalinos

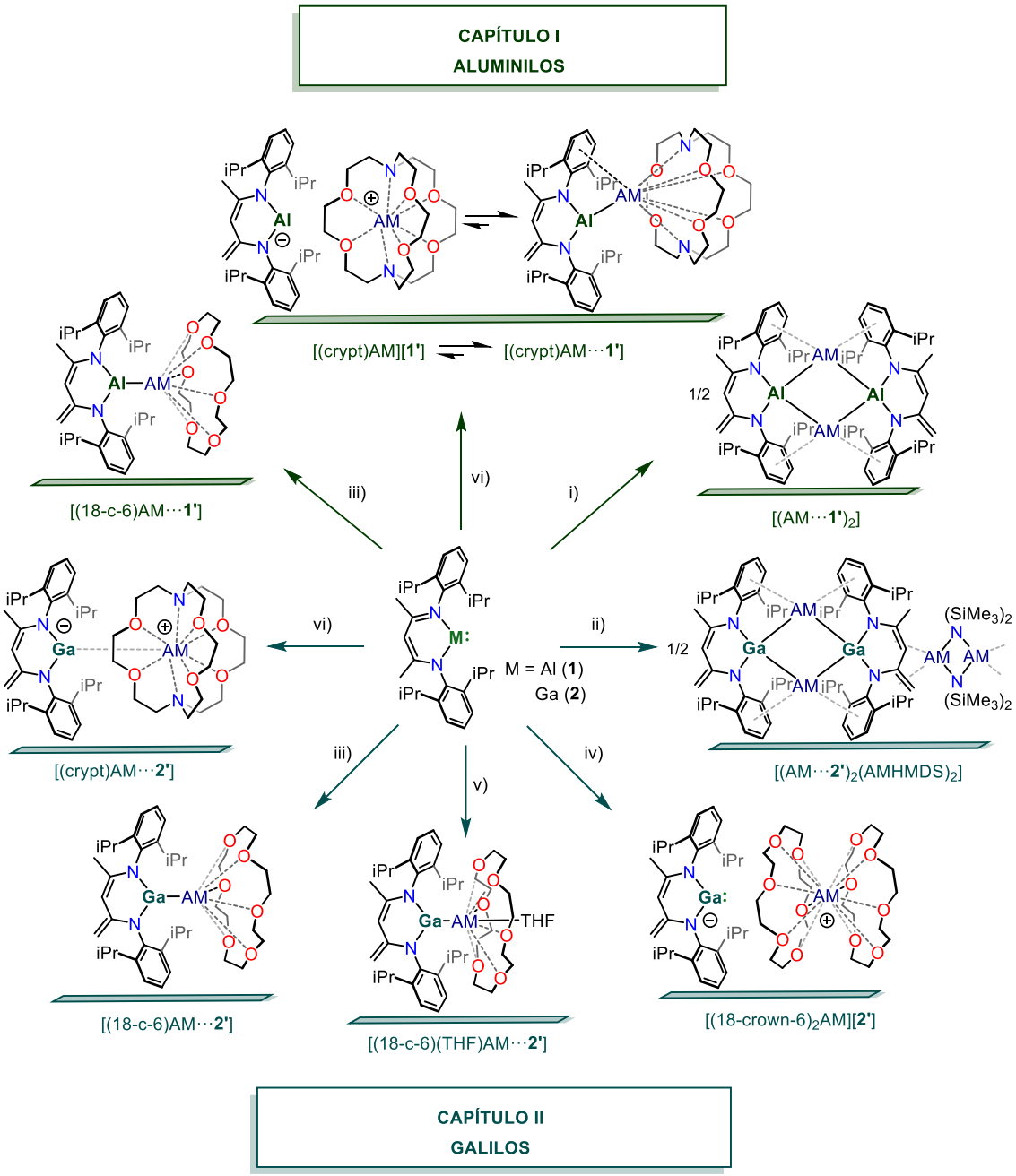
El *Capítulo II* describe especies de galio(I) (galilo), los cuales son análogos más pesados de los aluminilos presentados en el capítulo anterior. Si bien el galio comparte muchas similitudes fundamentales con el aluminio, la cantidad de sistemas Ga(I) estables descritos es significativamente menor, especialmente en lo que respecta a complejos aniónicos de tipo galilo $[Ga(I)]^-$, en cuanto a sus homólogos de aluminilo $[Al(I)]^-$. A pesar de que en 1999 Schmidbaur demostrase la viabilidad de formar estos complejos aniónicos de Ga(I), más sin embargo, la mayoría de los estudios posteriores se centraron en su validación estructural en lugar de expandir sus aplicaciones sintéticas o en explorar su reactividad.

Aprovechando el conocimiento ya adquirido con los sistemas de aluminio, en este capítulo se describe una serie de nuevos complejos aniónicos de galio monovalente estabilizados por el ligando β-dicetiminato, ampliando así la familia de análogos carbenoides del Grupo 13. Los estudios espectroscópicos (RMN, DOSY) y estructurales (difracción de rayos X) revelaron similitudes y diferencias clave con respecto a sus análogos más ligeros de aluminio. Por ejemplo, los enlaces $Ga^-\cdots AM^+$ en los sistemas de galilo exhiben un comportamiento parecido al observado en los aluminilos, no obstante, las interacciones que se establecen son mucho más robustas, favoreciendo la formación de agregados persistentes en disolución. En consecuencia, usando ligandos dadores de tipo éteres corona o criptando, junto con diferentes cationes metálicos alcalinos (Li^+ a Cs^+), se logró estabilizar estas especies aniónicas de galilo en formas de dímero o como

compuestos bimetálicos monoméricos (Esquema 2). Además, las especies diméricas de galio(I) demostraron ser especialmente robustas, siendo estabilizadas por la interacción adicional con una molécula de la base empleada en su síntesis (AM(HMDS)). En conjunto, estas modificaciones permitieron modular sistemáticamente los modos de agregación (monomérico *vs*. dimérico) de los centros Ga(I) tanto en disolución como en estado sólido.

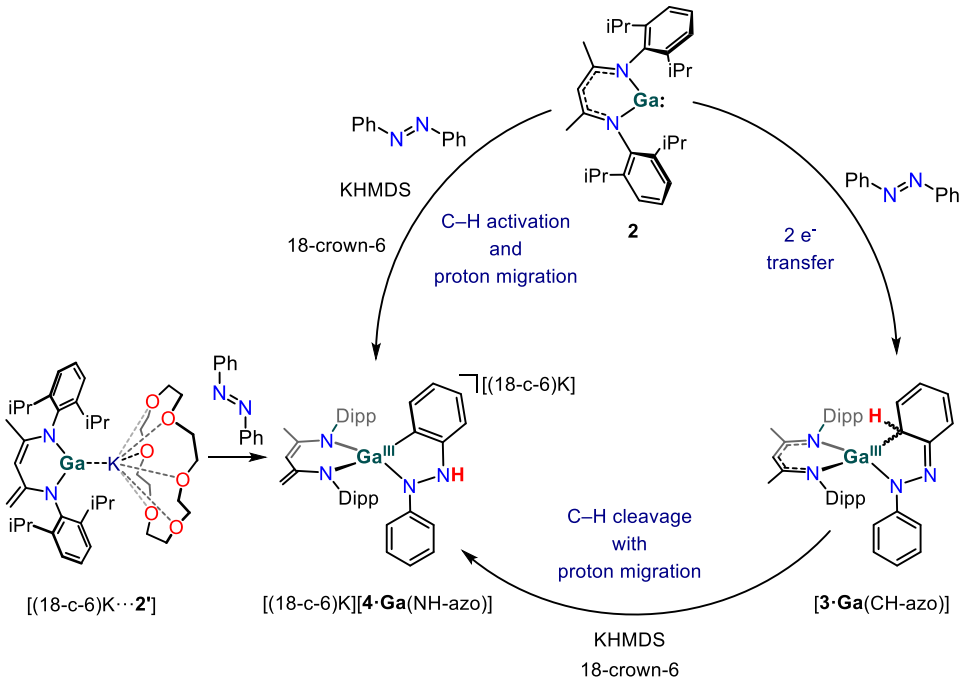
Para profundizar en la naturaleza electrónica y el enlace químico de estos nuevos sistemas de galilo, se realizaron estudios computacionales mediante teoría del funcional de la densidad (DFT). Estos cálculos revelaron que la distribución de carga sobre el esqueleto del β-dicetiminato, junto con la coordinación del metal alcalino, incrementa la estabilidad de la carga y evita procesos de nucleación Ga–Ga, minimizando posibles rutas de descomposición. Los estudios de orbitales moleculares confirmaron que la diferencia entre los orbilates HOMO–LUMO de estas especies galilo son comparables a la de los aluminilos nucleófilos, lo que respalda su potencial como especies reactivas en la activación de enlaces y aplicaciones catalíticas. Estos resultados computacionales fueron esenciales para racionalizar la divergencia en la reactividad observada entre el galio y el aluminio, proporcionando una explicación teórica de las diferencias fundamentales en su comportamiento en la activación de moléculas pequeñas.

Los estudios de reactividad de los diferentes sistemas galilo revelaron que, a diferencia de los aluminilos, no son capaces de activar dihidrógeno gas (H_2) bajo las mismas condiciones empleadas para sus homólogos que activan eficazmente esta molécula poco reactiva. Esta diferencia subraya cómo pequeñas variaciones en los niveles de energía de los orbitales, radios iónicos y la coordinación con metales alcalinos pueden influir drásticamente en los resultados de reactividad, incluso dentro del mismo grupo de la tabla periódica.



Esquema 2. Estados de agregación de sistemas aniónicos de aluminilo y galilo. Arriba: ejemplos seleccionados de aluminilos del *Capítulo I*. Abajo: ejemplos seleccionados de galilos del *Capítulo II*.

Sin embargo, los aniones galilo $[Ga(I)]^-$ exhibieron una notable selectividad en la funcionalización de enlaces C–H, como lo demuestra su reactividad con azobenceno. Esta transformación implica una transición redox de Ga(I) a Ga(III), Esquema 3. A diferencia de los aluminilos, que operan predominantemente a través de mecanismos nucleofílicos, los aniones galilo parecen favorecer rutas de transferencia de un solo electrón o la adición oxidante, demostrando un mecanismo distinto de activación de enlaces.



Esquema 3. Reactividad en la activación de enlaces C–H de sistemas galilo con metales alcalinos estudiada en el *Capítulo II*.

En conjunto, estos hallazgos amplían considerablemente el alcance de la química de galio(I), mostrando que las interacciones Ga–metal alcalino no solo pueden emplearse para la estabilización estructural, sino también para la modulación de la reactividad. La capacidad de los galilos para llevar a cabo transformaciones redox controladas, son una característica ausente en los aluminilos, y resalta su potencial en aplicaciones catalíticas. Estos resultados abren el camino para explorar aún más el papel del Ga(I) en la catálisis cooperativa de los grupos principales, brindando nuevas oportunidades más allá de las tradicionalmente exploradas para sus análogos de aluminio.

Capítulo III

Síntesis, Caracterización y Reactividad de Especies Bimetálicas Ga−Rh: Activación de H_2 e Hidrogenación Catalítica de Olefinas

En el *Capítulo III* se explora la química de coordinación y la reactividad de especies neutras de β-dicetiminato de Al(I) y Ga(I) con metales de transición, centrándose en rodio (Rh). Si bien las interacciones entre el grupo principal en estado de oxidación bajo y los metales de transición han despertado un creciente interés, la mayoría de los estudios previos se han limitado a la caracterización estructural sin abordar en profundidad su potencial catalítico. Partiendo de las similitudes electrónicas entre las especies Al(I)/Ga(I) como metaloligandos y los carbenos N-heterocíclicos (NHCs), exploramos la capacidad de estos compuestos de actuar como ligandos de tipo L hacia Rh, con el objetivo de generar sistemas heterometálicos estables y evaluar su impacto en la reactividad del metal de transición.

A pesar de los diversos intentos, la naturaleza del sistema neutro de Al(I) no logró establecer interacciones Al–Rh estables, poniendo de manifiesto limitaciones electrónicas fundamentales en su estructura para la coordinación con metales de transición. A diferencia, el sistema neutro monovalente de galio que desplazó con éxito ligandos clásicos del tipo N-dadores en precursores de Rh(I), generando una nueva familia de especies heterotrimetálicas Ga_2Rh (Figura 1). Los estudios sintéticos sistemáticos demostraron que el metaloligando Ga(I) modula la densidad electrónica en Rh(I), proporcionando una estabilización inusual para las interacciones metal–metal. La combinación de RMN, IR y difracción de rayos X de monocristal confirmó la alta estabilidad del enlace Ga–Rh. Así mismo, se intentó sintetizar un compuesto NHC–Rh con la misma distribución observada para las especies Ga_2Rh, no obstante, estos esfuerzos fueron infructuosos, resaltando la excepcional robustez del enlace Ga(I)–Rh, y reforzando aún más el papel único de Ga(I) como un metaloligando compatible con metales de transición.

Motivados por la alta estabilidad del enlace Ga(I)–Rh(I), exploramos la reactividad y especiación de estos complejos heterometálicos *cis*-$[Ga_2Rh(olefin)]^+$ en presencia de H_2 (Figura 1). Donde experimentos de monitorización in situ por RMN revelaron que estos sistemas activan H_2 de manera rápida y selectiva. Si bien, solo el derivado de COD reaccionó limpiamente con H_2, dando lugar a un complejo dihidruro de Rh(III) con simetría C_{2v} y a un intermedio Rh(III)–η^3-alilo, donde un

ligando COD parcialmente hidrogenado reemplaza un fragmento alqueno (Figura 1). La difracción de rayos X de monocristal y los estudios de RMN a temperatura variable confirmaron que el sistema Rh(III)–η^3-alilo mantiene un equilibrio dinámico, interconvirtiéndose entre las especies de Rh(III)–dihidruro y Rh–COD (Figura 1). Este comportamiento dinámico resalta el papel único del Ga(I) en la estabilización de los intermediarios clave Rh(III)–hidruro, facilitando una activación selectiva de H_2 y rutas de reorganización de enlaces distintas de los catalizadores clásicos de Rh(III).

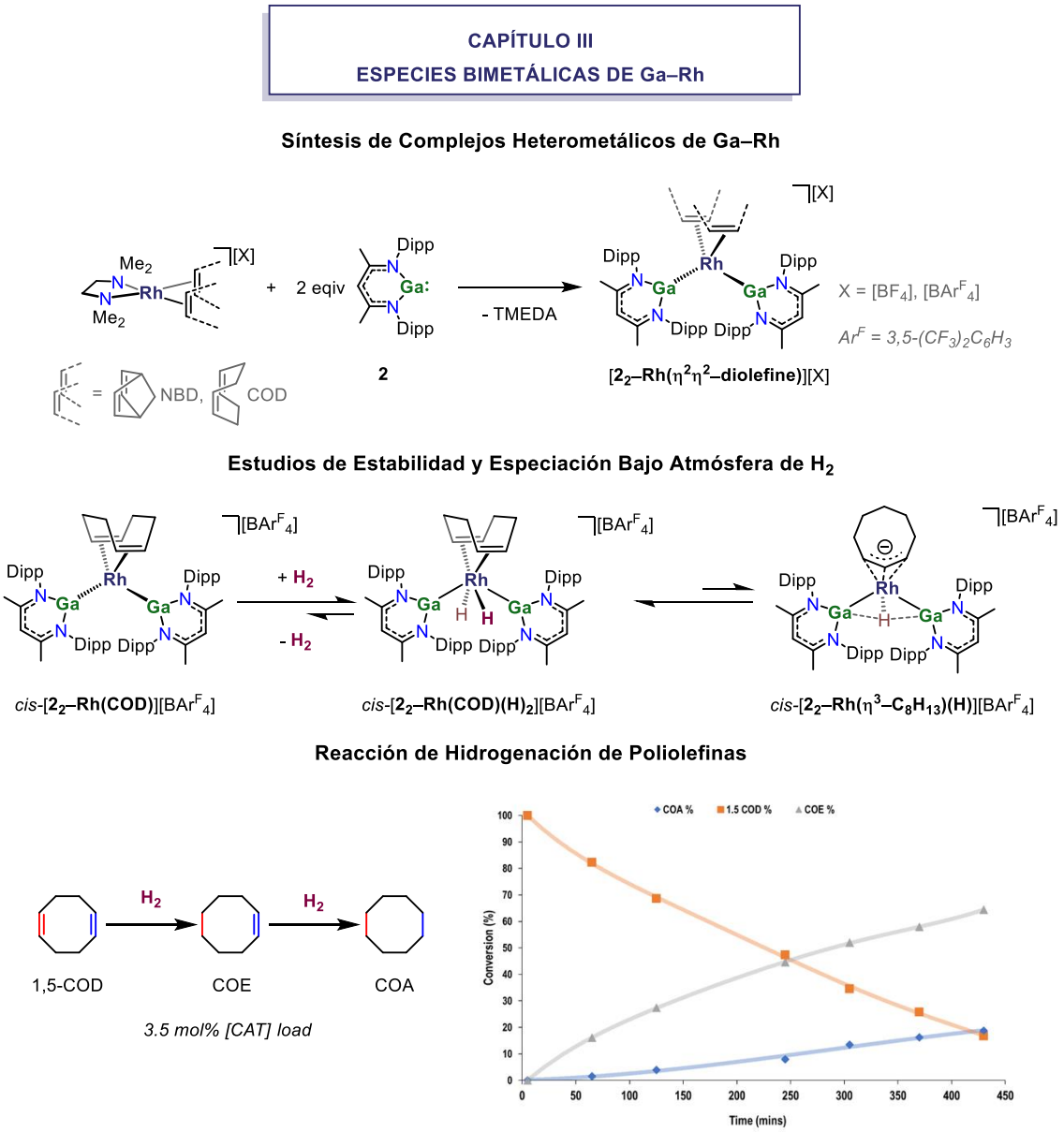


Figura 1. Interacciones metal–metal Ga(I)–Rh(I), especiación con H_2 y su papel en la hidrogenación selectiva de diolefinas abordadas en el *Capítulo III*.

A la vista de estos estudios de especiación con H_2, evaluamos el potencial catalítico de estos sistemas *cis*-Ga_2Rh en la hidrogenación de di- y poli-olefinas. Los resultados demostraron una marcada selectividad, las olefinas no conjugadas sufrieron hidrogenación parcial, favoreciendo la formación de mono-olefinas hidrogenadas (Figura 1), mientras que las olefinas conjugadas fueron completamente hidrogenadas al alcano correspondiente. Esta preferencia estereoelectrónica observada sugiere que estos sistemas *cis*-Ga_2Rh estabilizan especies intermedias de Rh(III)–dihidruro, modulando las etapas de hidrogenación secundaria hacia el alcano. Notablemente, estudios comparativos con complejos de Rh–fosfina mostraron que los metaloligandos de Ga(I) previenen reacciones secundarias no deseadas, mientras que los sistemas convencionales de Rh con ligandos P-dadores sufrieron la pérdida de selectividad durante la hidrogenación. Esto respalda la idea de que los metaloligandos de Ga(I) pueden influenciar en la reactividad de Rh(I), proporcionando un rendimiento catalítico y una selectividad superiores en comparación con los sistemas Rh tradicionales.

Para profundizar en el entendimiento de los efectos electrónicos que gobiernan los enlaces Ga–Rh, la activación de H_2 y la selectividad en la hidrogenación, se realizaron cálculos mediante teoría del funcional de la densidad (DFT). Los perfiles energéticos de Gibbs revelaron que los metaloligandos Ga(I) cumplen una doble función. En primer lugar, modulan la densidad electrónica en Rh, estabilizando así intermedios clave Rh(III)–H, y en segundo lugar, actúan como metaloligandos no inocentes, reduciendo la barrera energética para la ruptura de H_2 mediante interacciones cooperativas metal–metal. Los resultados computacionales indicaron que la hidrogenación de olefinas no conjugadas transcurre a través de un intermedio Rh(III)–dihidruro de baja energía, mientras que las olefinas conjugadas tienden a formar aductos alilo–Rh(III) altamente estables. Este hallazgo explica la selectividad observada experimentalmente, en la que las olefinas no conjugadas dan preferentemente mono-hidrogenados, mientras que los sustratos conjugados se hidrogenan completamente. Los estudios teóricos también revelaron que las interacciones Ga–Rh desempeñan un papel electrónico directo en la estabilización de los estados de transición, proporcionando una explicación del mecanismo para la alta selectividad catalítica observada.

Es por todo esto, que el *Capítulo III* representa un avance significativo en la química bimetálica Ga–Rh, estableciendo los metaloligandos Ga(I) como una alternativa viable a los carbenos NHC y las fosfinas en la química de coordinación y

catálisis de Rh. Al demostrar una reactividad selectiva en hidrogenación, revelar una red dinámica de especiación Rh(III)–hidruro, y validar los aspectos clave del mecanismo mediante DFT, abriendo la puerta a nuevas aplicaciones del Ga(I) en catálisis de metales de transición. Finalmente, los efectos cooperativos entre Ga(I) y Rh(I/III) proporcionan una nueva base para el diseño de nuevos catalizadores heterometálicos, hacienda uso de la sinergia existente entre metales de los grupos principales y los metales de transición.

Por ende, esta *Tesis Doctoral* representa un avance significativo en la química de los elementos del grupo principal en bajo estado de oxidación, mediante el desarrollo de nuevos sistemas aniónicos de Al(I) y Ga(I). Diseñando nuevos complejos bimetálicos que presentan interacciones metal–metal con metales alcalinos (Li^+, Na^+, K^+, Cs^+) y con metales de transición. Estos resultados proporcionan evidencia sólida de que las especies de Al(I) y Ga(I), tradicionalmente consideradas meras curiosidades de la química de los grupos principales, pueden actuar como potentes entidades nucleofílicas o especies con actividad redox, con un comportamiento similar al de los metales de transición.

La activación de H_2 por agregados Al(I)–metal alcalino, junto con la funcionalización C–H mediada por especies aniónicas de Ga(I), demuestra la gran versatilidad de estos compuestos en la activación de moléculas pequeñas. Un ámbito de la química que ha estado históricamente dominado por los metales de transición. Además, la síntesis y aplicación de complejos Ga–Rh demuestran que los metaloligandos de Ga(I) pueden ser una alternativa viable a los carbenos NHC clásicos, mostrando una notable estabilidad, y selectividad durante la activación de H_2 y la hidrogenación catalítica de sustratos insaturados. Este enfoque representa un modelo para desarrollar sistemas más selectivos empleando combinaciones metales de los grupos principales y aquellos de transición. Dado que los efectos cooperativos observados entre los centros de Al(I) y Ga(I) monovalentes, junto con sus combinaciones con metales alcalinos y de transición, suponen nuevas vías para el diseño de sistemas bimetálicos con propiedades electrónicas y perfiles de reactividad superiores a los sistemas homometálicos. Estableciendo así nuevas bases para futuras aplicaciones en catálisis, diseño de nuevos sistemas en la activación de moléculas pequeñas y transformaciones cooperativas empleando interacciones sinergéticas de tipo metal–metal.

Summary

Summary

Over the past decade, synthetic chemistry has seen groundbreaking advances stemming from the design of low-valent main-group compounds. In particular, monovalent Group 13 metals, most notably aluminium(I) and gallium(I), have garnered attention for their carbene-like behaviour, which facilitates transformations once believed to be the exclusive domain of transition metals. By broadening the core concepts of main-group reactivity, these electron-rich Al(I) and Ga(I) species have demonstrated the capacity to break strong bonds (e.g., H–H, C–H, C–C) and to mediate catalytic processes. Their success underscores a dramatic shift in modern chemistry, where main-group elements can mirror or even rival classical transition-metal reactivities through clever ligand architectures and metal–metal cooperative effects.

This *Doctoral Dissertation* centres on synthesising, characterising, and harnessing the reactivity of new Al(I) and Ga(I) complexes featuring a variety of metal–metal bonding interactions. A systematic approach is adopted to elucidate both their solid-state structures, with a focus on how these frameworks promote electron sharing or donation, and their solution-phase equilibria, which reveal fluxional behaviours and dynamic aggregation. Through subtle changes such as tuning the alkali-metal cations or coupling to transition metals, we uncover novel pathways for challenging bond activations.

The *Thesis* is organised into three interlinked *Chapters*, each spotlighting a particular facet of these low-valent species, spanning aggregation modes with different alkali metals to cooperative interactions with transition metals (notably rhodium). Special emphasis is placed on activating inert substrates, such as dihydrogen (H_2), and exploring the pursuit of C–H bond activation under mild conditions, thereby drawing parallels to and extending beyond the capabilities of typical d-block catalysts.

Collectively, this *Thesis* highlight how such low-valent main-group metal platforms, stabilised by an intricate network of metal–metal bonding, can mimic, complement, or even surpass conventional transition-metal reactivity. By integrating experimental insights with computational models, this work paints a comprehensive picture of how Al(I) and Ga(I) carbene surrogates, in concert with carefully chosen counterions or transition-metal centres, represent a frontier in small-molecule activation and selective catalytic transformation.

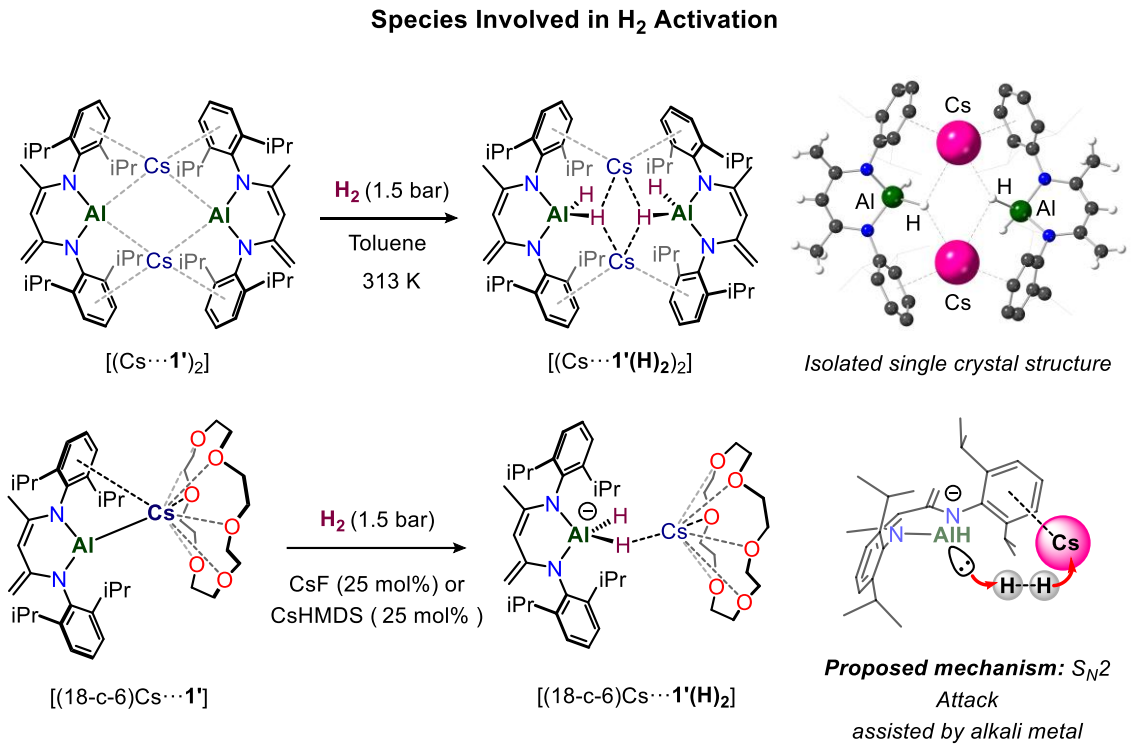
Chapter I

Synthesis, Characterisation and Reactivity of Electron-Rich Anionic Aluminium(I) Species: From Aggregation Control to H_2 Activation

Chapter I focuses on the synthetic development, characterisation, and reactivity of anionic aluminium(I) (aluminyl) and dihydridoaluminate (Al(III)–H) species supported by β-diketiminate frameworks. This work builds on pivotal milestones set in motion by Schnöckel, whose 1990s discovery of neutral Al(I) complexes, commonly referred to as aluminylenes, marked the first demonstration of aluminium in a low-valent (R_2Al:), carbene-like configuration (R_2C:). Various other neutral Al(I) derivatives soon followed, harnessing a broad array of supporting ligands and displaying remarkable reactivities with Si–H, O–H, and P–H bonds across diverse substrates.

In 2018, the field underwent a significant breakthrough when the groups of Aldridge and Goicoechea disclosed the first anionic aluminyl complex, $[Al(I)]^-$, stabilised by a tripodal xanthene-derived ligand and a potassium (K^+) counterion. That landmark compound revolutionised perceptions of aluminium's traditional electrophilicity, demonstrating "umpolung" behaviour that allowed these aluminyl species to act as potent nucleophiles and mediate the activation of H–H, C–H, and even C–C bonds. Motivated by this paradigm-shifting discovery, *Chapter I* details the design and isolation of new anionic aluminyl systems, this time supported by β-diketiminate frameworks. By strategically introducing methyl substituents into the β-diketiminate backbone, we established a dianionic ligand environment capable of anchoring electron-rich $[Al(I)]^-$ species (Scheme 1).

Using hexamethyldisilazide-based alkali-metal amide reagents, AM(HMDS), under relatively mild conditions, a range of low-valent anionic aluminyl species were synthesized. Subsequent modulation of alkali-metal cations (Li^+ to Cs^+) and donor ligands (crown ethers, cryptands) provided a controlled strategy to assemble diverse aggregation states in both solution and the solid state, extending from dimeric pairs to monomeric ion pairs, and further to fully separated (or "*naked*") aluminyl anions. NMR, X-ray crystallographic, and computational analyses shed light on the rich interplay of $Al^-\cdots AM^+$ (metal–metal) contacts that drives key transformations.



Scheme 1. Metal–metal bonding interactions in aluminyl systems and their role in H_2 activation in *Chapter I*.

Among these transformations, the ability of certain dimeric aluminyl complexes to cleave H_2 under mild conditions stands out as a prime example of transition-metal-like reactivity in main-group chemistry. By contrast, monomeric or "*naked*" $[Al(I)]^-$ centres typically remained inactive unless "free" alkali-metal cations, especially Cs^+, were introduced into the system. These observations underscore a bimetallic synergy wherein the nucleophilic $[Al(I)]^-$ centre and the coordinating AM^+ cation collaborate to lower barriers for bond-breakage steps in small molecules like H_2, closely mirroring certain d-block catalytic pathways. In tandem, DFT calculations provided mechanistic insights, highlighting how labile $Al^-\cdots AM^+$ bonding fosters an S_N2– like mode of dihydrogen cleavage facilitated by the alkali-metal cation. Scheme 1 schematically illustrates these metal–metal bonding dynamics in aluminyl systems and their role in H_2 activation.

Chapter II

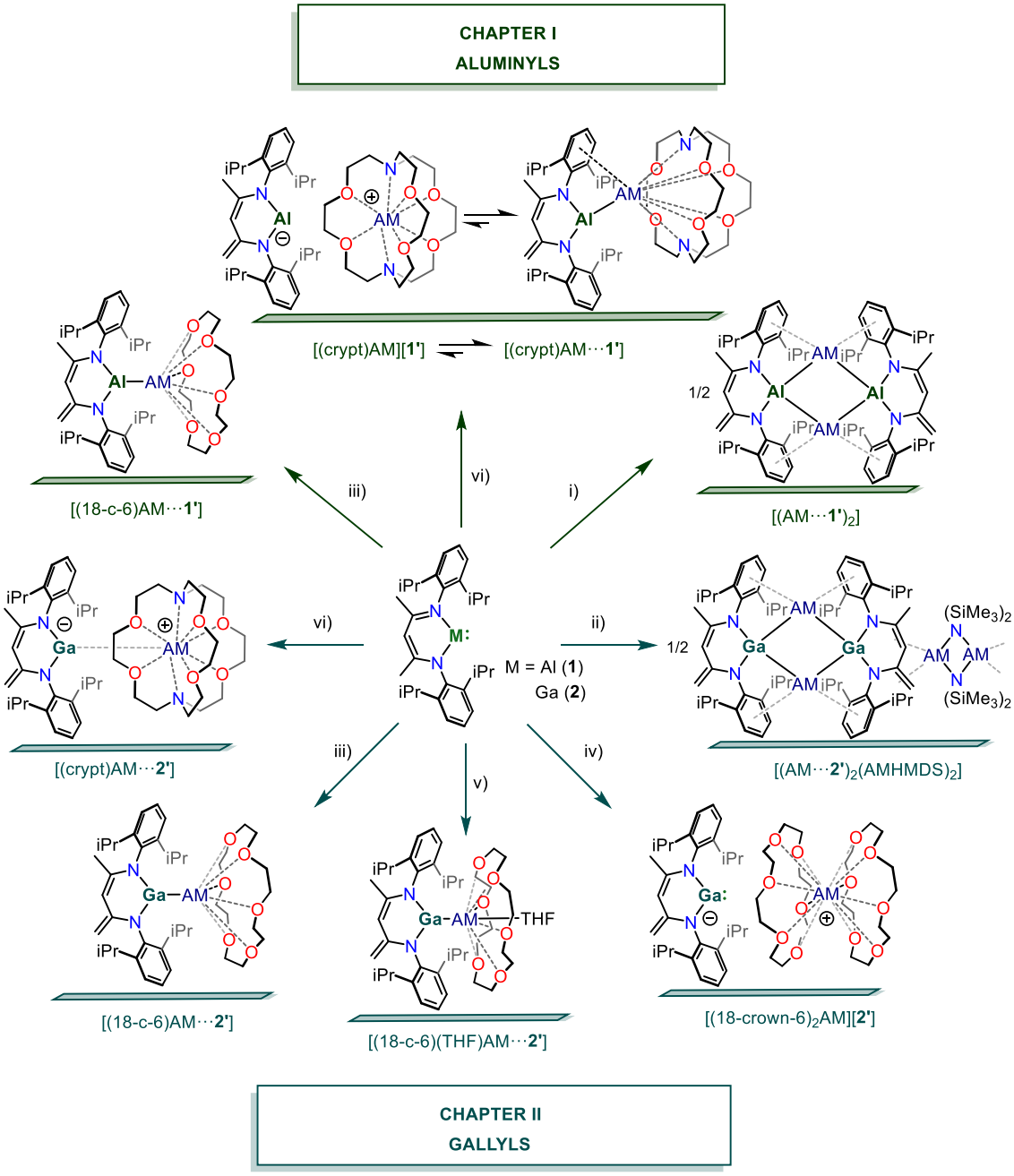
Synthesis, Characterisation and Reactivity of Electron-Rich Anionic Gallium(I) Species: Alkali Metal-Mediated C–H Activation

Chapter II shifts the focus to gallium(I) species (gallyls), heavier analogues of the previously introduced aluminyl complexes. Although gallium shares many fundamental parallels with aluminium, examples of stable Ga(I) systems, particularly anionic gallyls $[Ga(I)]^-$, have historically been limited in number. While Schmidbaur's pioneering study (1999) demonstrated that anionic Ga(I) complexes could be accessed, most subsequent efforts centred on structural validation rather than delving into synthetic expansion or reactivity exploration.

Building on that groundwork, we herein describe a series of novel anionic β-diketiminate gallium(I) complexes, thus extending the family of heavier Group 13 carbene analogues. Detailed spectroscopic (NMR, DOSY) and crystallographic (X-ray) analyses showed both commonalities with, and key divergences from, their aluminyl counterparts. For instance, gallium–alkali-metal bonding in these gallyls exhibits broad similarities to that in aluminyl complexes, the $Ga^{-}\cdots AM^{+}$ interactions are generally less labile, favouring more persistent aggregated ion pairs in solution. Employing crown ethers and 2,2,2-cryptand donors, in conjunction with various alkali-metal cations (Li^+ to Cs^+), further stabilised the gallyl anions into dimeric or heavily aggregated bimetallic frameworks (Scheme 2). In addition, these dimeric gallium(I) species exhibited notable robustness, aided by additional charge-balancing interactions with alkali-metal amides (e.g., AMHMDS). Collectively, such modifications enabled us to systematically tune the aggregation modes (monomeric *vs*. dimeric assemblies) of the Ga(I) centres in both solution and the solid state.

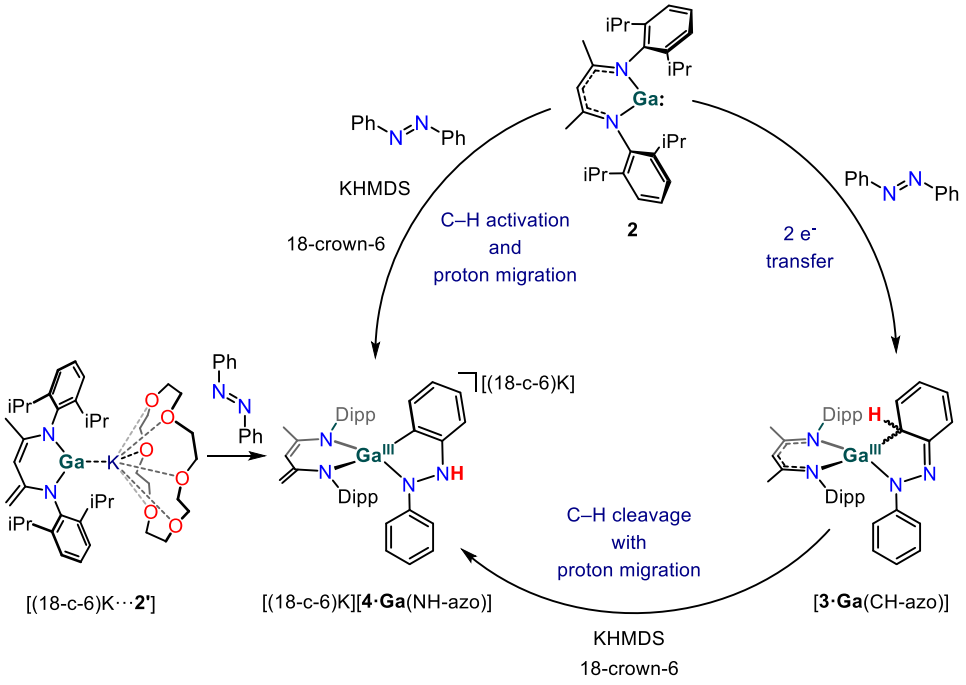
To further elucidate the electronic properties and bonding nature of these gallyl species, density functional theory (DFT) calculations were conducted. Computational studies provided key insights into how the charge distribution across the β-diketiminate ligand framework, in conjunction with alkali-metal coordination, increases charge stabilisation, thereby preventing Ga–Ga nucleation and unwanted decomposition pathways. The frontier molecular orbital (HOMO–LUMO) gaps of these gallyl species were found to be comparable to those of nucleophilic aluminyl systems, supporting their potential as reactive platforms for bond activation and catalytic applications. These computational results further clarified the distinct

reactivity differences between gallium and aluminium, providing a theoretical framework to rationalise their divergent behaviour in small-molecule activation.



Scheme 2. Aggregation states of anionic aluminyl and gallyl systems. Top: Selected aluminyl species from *Chapter I*. Bottom: Selected gallyl species from *Chapter II*.

Reactivity studies revealed that, in contrast to aluminyls, these gallyl systems did not cleave H_2 under conditions where aluminyl anions efficiently activated dihydrogen. This difference underscores how subtle variations in orbital energy levels, ionic radii, and alkali-metal coordination influence reactivity outcomes, even within the same Group 13 family. Nevertheless, the anionic gallyl species exhibited remarkable selectivity in C–H bond functionalisation, as exemplified by their reaction with azobenzene. This transformation involves a redox transition from Ga(I) to Ga(III), mirroring transition-metal-like oxidative and reductive processes (Scheme 3). Unlike aluminyls, which predominantly engage in nucleophilic reactivity, gallyl anions appear to favour single-electron transfer or oxidative addition-type pathways, demonstrating a distinct mechanism for bond activation.



Scheme 3. C–H activation reactivity of alkali-metal-stabilized gallyl systems from *Chapter II*.

Taken together, these findings significantly broaden the scope of gallium(I) chemistry, illustrating how Ga–alkali-metal interactions can be harnessed not only for structural stabilisation, but also for reactivity modulation. The ability of gallyls to undergo controlled redox transformations, a feature largely absent in aluminyl systems, underscores their potential for catalytic applications, particularly in redox-mediated bond activation reactions. These results pave the way for further

exploration of Ga(I) in main-group cooperative catalysis, offering new directions beyond those traditionally pursued for aluminium congeners.

Chapter III

Synthesis, Characterisation and Reactivity of Bimetallic Ga−Rh Species: H_2 Activation and Catalytic Hydrogenation of Olefins

Chapter III investigates the coordination chemistry and reactivity of neutral monovalent β-diketiminate Al(I) and Ga(I) species with transition metals, particularly rhodium (Rh). While low-valent main-group–transition-metal interactions have garnered increasing interest, most studies remain structural in nature, with relatively few exploring catalytic potential. Recognising the electronic parallels between Al(I)/Ga(I) species as metalloligands and classical N-heterocyclic carbene (NHC) ligands, we sought to harness their L-type coordination ability toward Rh to form stable heterobimetallic systems and examine their impact on transition-metal reactivity.

Despite its low-valent nature, the β-diketiminate Al(I) system failed to form stable Al–Rh bonding associations, highlighting fundamental limitations in its electronic structure for transition-metal coordination. In contrast, the heavier Ga(I) metalloligand congener successfully displaced classical N-ligands from Rh(I) precursors, yielding a new class of heterotrimetallic Ga_2Rh species (Figure 1). Systematic synthetic studies demonstrated that the Ga(I) metalloligand effectively modulates the electron density at Rh(I), providing an unusual stabilisation of metal–metal interactions. Comprehensive NMR, IR, and single-crystal X-ray diffraction studies confirmed the high stability of Ga–Rh bonds, in stark contrast to classical NHC–Rh or phosphine–Rh analogues, which either underwent ligand scrambling or decomposed under similar conditions. Notably, our failed attempts to prepare analogous NHC–Rh complexes underscore the exceptional robustness of Ga(I)–Rh bonding, further reinforcing the unique role of Ga(I) as a transition-metal-compatible metalloligand.

Encouraged by these findings, we explored the reactivity and speciation of these heterometallic *cis*-$[Ga_2Rh(olefin)]^+$ species in the presence of H_2 (Figure 1). In situ NMR monitoring revealed that these systems undergo rapid and selective H_2 addition. Notably, only the COD derivative reacted cleanly with H_2, yielding a stable

C_{2v}-symmetric Rh(III) dihydride complex, as well as an unprecedented allyl–Rh(III) intermediate, where a partially hydrogenated η^3-allyl COD ligand replaces one alkene moiety (Figure 1). Single-crystal X-ray diffraction and variable-temperature NMR studies confirmed that this system remains in dynamic equilibrium, interconverting between allyl–Rh, Rh(III)–dihydride, and unreacted COD precursor in the presence of H_2. This dynamic behaviour highlights the unique role of Ga(I) in stabilising critical Rh(III)–hydride intermediates, thus enabling selective H_2 activation and bond rearrangement pathways distinct from classical Rh(III) catalysts.

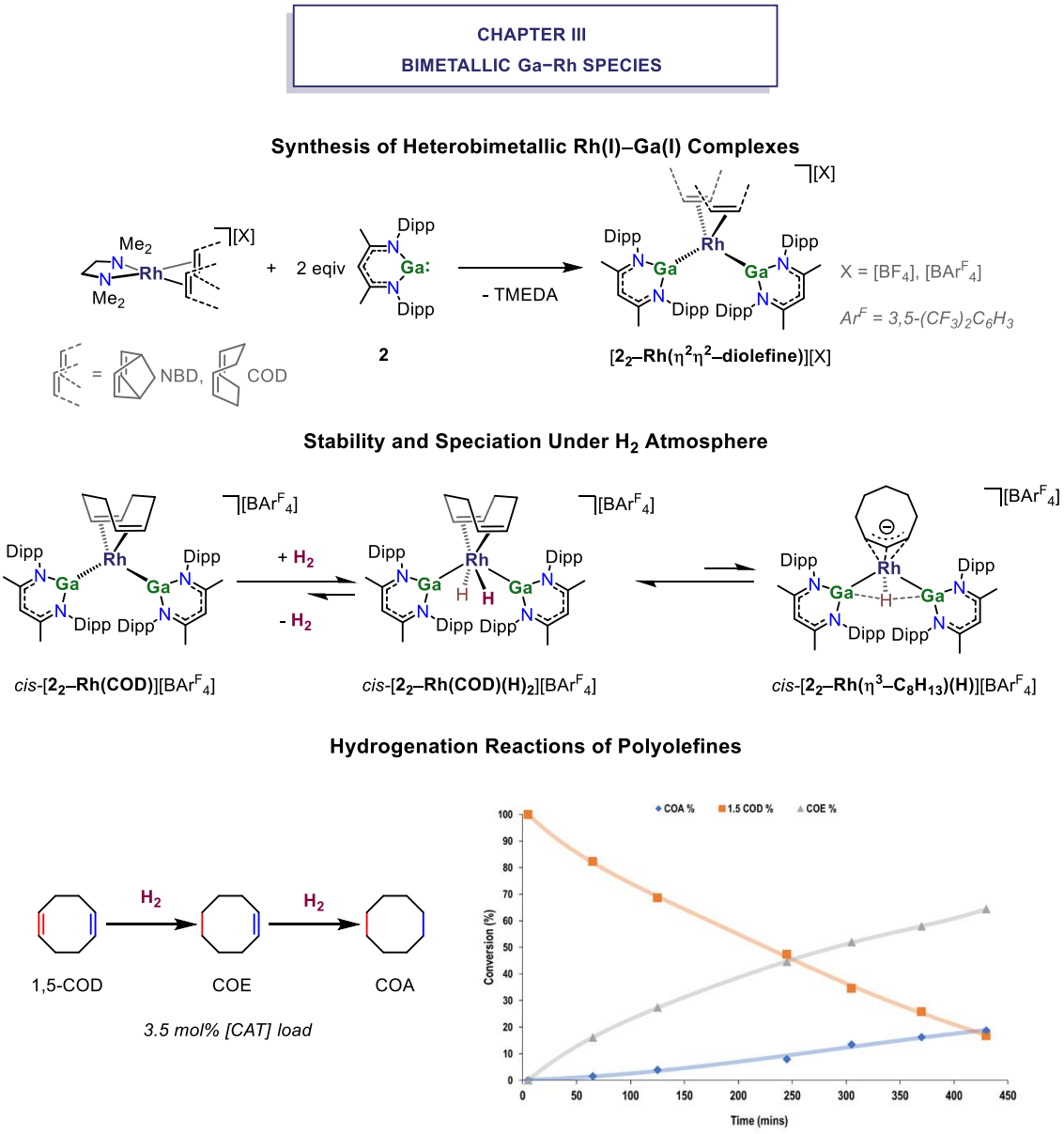


Figure 1. Ga(I)–Rh(I) metal–metal bonding interactions, speciation with H_2 and their role in selective hydrogenation of diolefins discussed in *Chapter III*.

Building on these H_2 speciation studies, we examined the catalytic potential of these *cis*-Ga_2Rh complexes in the hydrogenation of di- and polyolefins. The results demonstrated a selective pattern: non-conjugated olefins underwent partial hydrogenation, favouring the formation of mono-hydrogenated products, whereas conjugated olefins underwent complete hydrogenation. This observed stereoelectronic preference suggests that these *cis*-Ga_2Rh systems uniquely stabilise intermediate Rh(III)–dihydride species, thereby modulating secondary hydrogenation steps. Notably, comparative studies with phosphine–Rh complexes revealed that the Ga(I) metalloligands prevent undesired side reactions, whereas classical P-donor Rh systems rapidly lost ligands and lacked selectivity during hydrogenation. This strongly supports the notion that Ga(I) metalloligands can fine-tune Rh(I) reactivity, yielding superior catalytic performance and selectivity compared to conventional Rh-based systems.

To rationalise the electronic effects governing Ga–Rh bonding, H_2 activation, and hydrogenation selectivity, density functional theory (DFT) calculations were conducted. The computed Gibbs energy profiles revealed that Ga(I) metalloligands serve a dual role. Firstly, they modulate the electron density at Rh, thereby stabilising key Rh(III)–H intermediates, and secondly, they act as non-innocent metalloligands, lowering the energy barrier for H_2 cleavage through cooperative metal–metal interactions. DFT results revealed that the hydrogenation of non-conjugated alkenes proceeds via a low-energy Rh(III)–dihydride intermediate, whereas conjugated systems preferentially form highly stable allyl–Rh(III) adducts. This computational insight explains why non-conjugated olefins selectively form mono-hydrogenated products, whereas conjugated substrates proceed directly to full hydrogenation. The theoretical findings also suggest that Ga–Rh interactions play a direct electronic role in stabilising transition states, offering a rationale for the superior selectivity observed experimentally.

This *Chapter III* significantly advances bimetallic Ga–Rh chemistry, establishing Ga(I) metalloligands as a viable alternative to classical NHC or phosphine donors. By demonstrating selective hydrogenation reactivity, uncovering a dynamic Rh(III)–hydride speciation network, and validating key mechanistic features via DFT, these findings pave the way for further applications of Ga(I) in transition-metal catalysis. Ultimately, the cooperative effects between Ga(I) and Rh(I/III) centres provide a new blueprint for designing heterobimetallic catalysts, challenging conventional wisdom on main-group–transition-metal interactions.

This *Doctoral Dissertation* significantly advances the field of low-valent main-group chemistry by developing novel anionic Al(I) and Ga(I) systems, featuring diverse bimetallic metal–metal bonding interactions with alkali metals (Li^+, Na^+, K^+, Cs^+), and their association with transition metals, exemplified by the catalytically active Ga–Rh complexes described herein. These findings provide compelling evidence that Al(I) and Ga(I) species, traditionally viewed as main-group curiosities, can function as powerful nucleophilic or redox-active entities with transition-metal-like behaviour.

The successful activation of H_2 by Al(I)–alkali-metal aggregates, as well as C–H functionalisation mediated by anionic Ga(I) species, underscores the broad utility of these compounds in small-molecule activation, an area historically dominated by transition metals. Moreover, the synthesis and application of Ga–Rh complexes establish Ga(I) metalloligands as a viable alternative to classical carbene NHC ligands, demonstrating stability, selectivity, and mechanistic flexibility in H_2 activation and catalytic hydrogenation of unsaturated hydrocarbons. These Ga(I) metalloligands enable selective partial hydrogenation of non-conjugated olefins, while stabilising key Rh(III)–hydride intermediates, provides a blueprint for fine-tuning transition-metal reactivity using non-traditional main-group frameworks.

The cooperative effects observed between low-valent aluminium and gallium centres and their alkali- and transition-metal counterparts open new avenues for the rational design of bimetallic systems with tailored electronic structures and reactivity profiles. By bridging gaps in the fields of low-valent main-group and transition-metal chemistry, this work expands the fundamental understanding of Group 13 elements, laying the groundwork for future applications in catalysis, small-molecule activation, and metal–metal cooperative transformations.

CHAPTER I:

Synthesis, Characterisation and Reactivity of Electron-Rich Anionic Aluminium(I) Species: From Aggregation Control to H_2 Activation

1.1 Introduction

Aluminium, the most abundant metal in the Earth's crust, is prised for its low cost, low toxicity, and lightweight alloys, as well as for its pivotal role as a Lewis-acid catalyst in critical industrial processes such as Friedel–Crafts alkylations.[1] Typically, aluminium assumes a +3 oxidation state (e.g., $AlCl_3$) in stable, trivalent complexes that function as electrophiles in myriad organic transformations. Over the past decade, however, it has become increasingly evident that low-valent aluminium, especially in monovalent (+1) oxidation states, can orchestrate chemical reactivity once deemed exclusive to transition metals.[2] This realisation opens a new dimension in main-group chemistry, wherein aluminium can participate in small-molecule activation under the right structural and electronic conditions.

A transformative concept in main-group chemistry is the notion of carbene analogues, species isoelectronic with classical R_2C: carbenes but built around different elements, spanning Group 13 (Al, Ga, In), Group 14 (Si, Ge, Sn, Pb), and Group 15 (N, P, Sb, Bi).[3] In classical carbene chemistry, a six-electron valence shell and an unoccupied p-orbital impart both nucleophilic (lone-pair donation) and electrophilic (p-acceptor) character. Representative carbenes examples **I** and **II** are shown in Figure 1.[4] Over the past three decades, numerous heavier carbene analogues have emerged, from mere synthetic curiosities to potent reagents and widely used ligands in catalysis. Early examples of carbene analogues in Group 14 include silylenes and germylenes (species **III**) while Group 15 gave rise to phosphinidenes **IV** and nitrenes **V** among others. However, the domain of Group 13 remained comparatively underdeveloped.

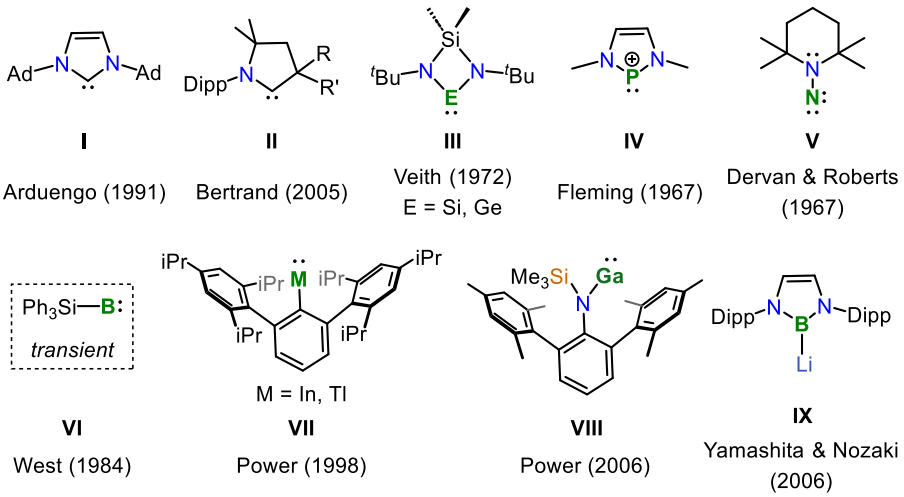


Figure 1. Selected classical carbenes and heavier carbene analogues.

Early evidence of such “carbene-like” behaviour in heavier Group 13 metals includes the transient boron(I) species **VI** (borylene) detected through indirect experiments, indium(I) and thallium(I) (indylene and tallylene) derivatives **VII**, as well as gallium(I) (gallylene) species **VIII**.[5] Notably, Yamashita and Nozaki’s demonstrated that nucleophilic boryl anions **IX** sparked the concept of “umpolung” in Group 13,[6] a principle now extended to aluminium(I) species, highlighting the nucleophilic or ambiphilic reactivity that can arise when substituents or ligands appropriately stabilise electron-rich low-valent Group 13 centres. Interestingly, many “free” or monomeric anionic Al(I) complexes exist in equilibrium with higher aggregates, leading to so-called “latent” or “masked” aluminyl forms that are effectively released upon heating or changes in solvent conditions, thereby harnessing their hidden nucleophilic reactivity.

In this landscape, the domain of aluminium(I) chemistry is now at the forefront, thanks to a surge of breakthroughs revealing aluminylenes (neutral Al(I)) and aluminyls (anionic Al(I)) capable of bond activations (C–H, C–F, H–H) reminiscent of transition metals,[3, 7], such as oxidative addition, reductive elimination, and diverse small-molecule activations at the most abundant metal.[3, 8] Thus, the central objective of this *Chapter I* is to chart the development of novel aluminium carbene analogues, particularly electron-rich anionic aluminyls, study their structural motifs, and reactivities, with special attention to the challenging transition-metal-like bond activations (e.g., H_2 activation) that underscore a unique potential for groundbreaking applicability of aluminium beyond its conventional +3 oxidation state.

1.1.1 Neutral Aluminium(I) Species: Aluminylenes

Historically, monovalent aluminium can be traced back to the 1940s, when simple AlX (X = Cl, Br, I) species hinted at partially reduced states.[9] However, the quest for organometallic aluminium(I) species began with a major breakthrough when Schnöckel realised the isolation of the tetrameric $[Al(Cp^*)]_4$ species **X** in 1991 via the reduction of AlCl with $Mg(Cp^*)_2$ ($Cp^* = C_5Me_5$, Figure 2). In the solid state, $[Al(Cp^*)]_4$ forms a tetrahedral core stabilised by bulky Cp* ligands, but dissociates into monomeric units in solution, enabling its reactivity as a ligand in transition-metal chemistry.[10] Subsequent modifications gradually shifted the equilibrium toward the free monomer, such as in Braunschweig´s example **XI**. This phenomenon already hinted at masked monovalent Al(I) centres, mirroring the concept of aluminium

carbene analogues that require high steric or electronic stabilisation. Subsequent work by Roesky gave rise to monomeric Al(I) complexes, like (^{Dipp}BDI)Al(I) **XII**, stabilised by a bulky β-diketiminate (BDI) ligand, formed by reducing a diiodide precursor with potassium metal, which acts as an aluminium analogue of N-heterocyclic carbenes.[11] This approach parallels NHC-carbene frameworks, with the BDI ligand furnishing both steric protection and partial p-donation. The choice of BDI ligands was strategic, as they are well-known to coordinate a wide range of metals across the periodic table in a variety of oxidation states.[12] Notwithstanding the success of Roesky's aluminylene **XII** provided a robust platform to develop further BDI-based monovalent aluminium(I) complexes[11] with bulky tert-butyl substituents in the ligand backbone of (^{tBu,Dipp}BDI)Al(I),[13] and bearing distinct flanking aromatic groups such as 2,6-diisopentylphenyl (Dipep) substituents in (^{Dipep}BDI)Al(I).[14]

Despite these initial successes, many of these neutral Al(I) species existed in equilibria with dimeric or oligomeric forms, sometimes requiring specialised ring or backbone ligands (e.g., bulky terphenyl amides) to suppress undesired polymerisation or disproportionation pathways. The Roesky's complex **XII**, for instance, was among the first "true" solid-state monomeric aluminylene, illustrating how a robust β-diketiminate framework could anchor a low-coordinate aluminium carbene-like centre.[11] Recent advances have also shown that some unsupported aluminium(I) systems **XIII** and **XIV** can overcome these hurdles by implementing sterically encumbered one-coordinate Al(I) centres by flanking bulky aromatic groups.[15] Though still in an early stage, these low-coordinate Al(I) species display potential for novel reactivity.

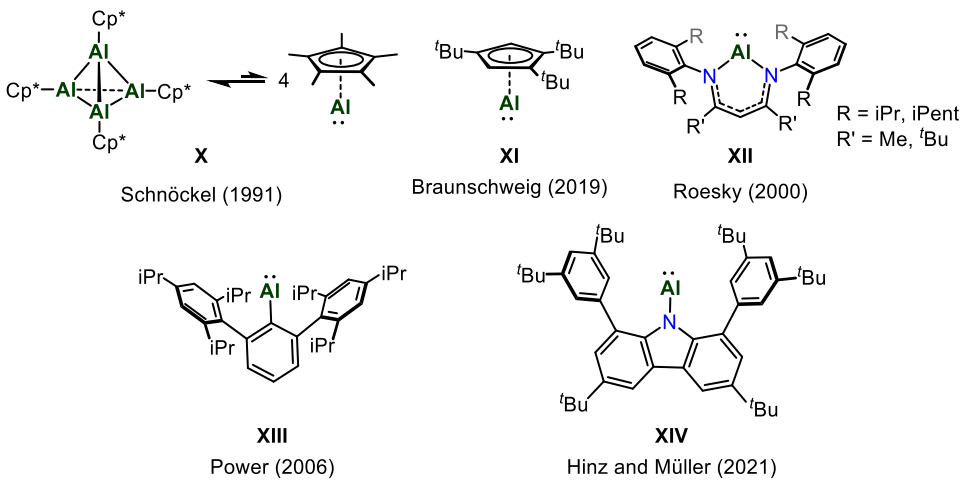


Figure 2. Selected examples of neutral aluminium(I) carbene analogues.

Though historically overshadowed by group 14 or 15 heavier main-group analogues, these aluminylenes can execute transition-metal-like transformations. For instance, the aluminylene **XII** mediates the cleavage of robust bonds such as C–H, C–F, and C–C, under mild reaction conditions, mimicking d-block catalysts.[7, 16] In combination with tungsten carbonyl complexes, it allows stepwise formation of extended carbon chains via CO and CO_2 insertions, and can reversibly cycloadd to 1,3-cyclohexadiene or to strained alkenes under CO atmosphere, forming an insertion complex under gentle heating and returning to the cycloadduct upon cooling (Figure 3).[17] It is also capable of engaging in mild-condition reversible reactions with terminal or strained alkenes in an oxidative addition/reductive elimination type of reactivity with norbornene, ethylene and allylbenzene.[18] Such reversible transformations, often unusual in s- and p-block contexts, highlight how these low-valent aluminium centres parallel d-block catalysis. As such, the broader perspective on these bond-cleavage processes by β-diketiminate aluminylene species extends beyond the typical reactivity of main-group species.[19]

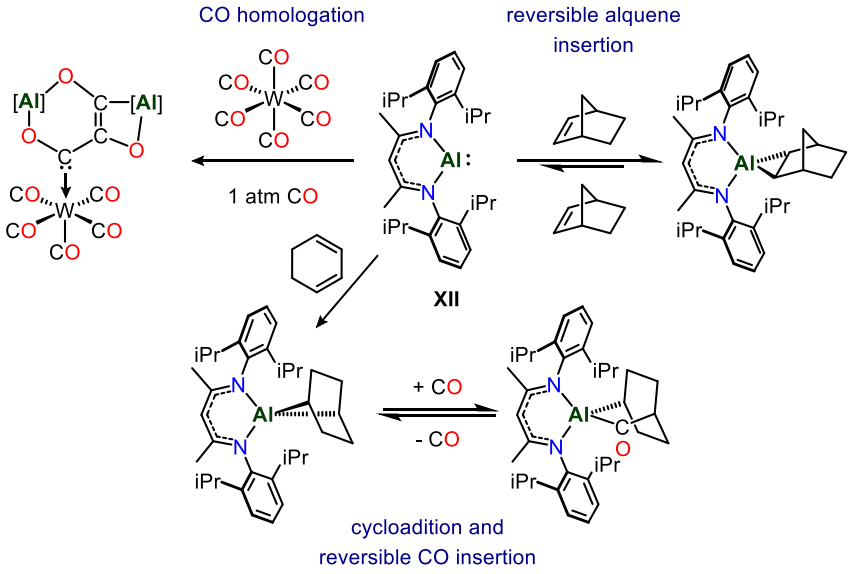


Figure 3. Representative examples of transition metal-like reactivity of (^{Dipp}BDI)Al(I) **XII**.

1.1.2 Nucleophilic Aluminium(I) Anions: Aluminyls

Although aluminium is classically recognised for its Lewis acidity, the discovery of nucleophilic anionic Al(I) species (aluminyls) has radically broadened the scope of Al(I) chemistry.[6] Analogous transformations in boron(I) were demonstrated by Yamashita and Nozaki's boryl anion **IX**,[6] (Figure 1), highlighting an umpolung phenomenon that inverts the polarity of Group 13 centres.[6] Inspired by

such breakthroughs, researchers sought to harness the same principle in gallium(I) and indium(I) systems; however, translating this concept to aluminium(I) proved more challenging.[20]

The first aluminyl example **XV**, was reported by Aldridge and Goicoechea in 2018 using a NON-xanthene-based diamido ligand, marking a paradigm shift in aluminium chemistry (Figure 4).[21] These aluminyl species feature a highly electron rich aluminium(I) carbene-like centre, enabling them to act as nucleophiles in reactions with electrophiles such as alkyl halides, metal halides, and hydrogen sources. Nonetheless, the reductive approach using halide precursors or Al–Al bond cleavage with strong reductants like KC_8 and alkali-metal naphthalenides remains essential, and sometimes challenging, to accessing stable Al(I) frameworks under mild conditions. Indeed, aluminyl **XV** ability to oxidatively cleave the H–H bond to form an Al(III) species, (NON)Al$(H)_2$, arguably represents the first main-group metal to effect direct H_2 activation.

Shortly thereafter, Coles and colleagues introduced a second anionic aluminyl complex **XVI**, stabilised by the dianionic bis(amidodimethyl)disiloxane $[O(SiMe_2NR)_2]^{2-}$.[22] A structural comparison revealed that aluminyl **XV** is three-coordinated, while the species **XVI** is strictly two-coordinate, each adopting distinct frameworks but similarly reliant on steric and electronic constraints to sustain an anionic Al(I) centre. Collectively, these pioneering results opened the door to a wide variety of gallyls systems, using five-, six- or seven-member bridging frameworks (species **XVII**–**XXI**).[23] All these examples required bulky bidentate ligands, either N,N'- or N,C-donor, to stabilise the electron-rich Al(I) centres within a cyclic framework. Moreover, more recently, these advances have culminated with the isolation of the first examples of acyclic aluminyls **XXII** in 2023,[24] followed by the disclosure of O,O'-acyclic examples **XXIII** in 2024.[25]

Among the series of aluminyls reported, the BDI-based anionic aluminyls **XXIV** stand out. While many aluminyl anions form via reductive routes involving halide or Al–Al bond reductions with strong reductants like KC_8, ligand deprotonation under basic conditions has also proven fruitful for easily accessing aluminyl species, particularly those derived from neutral β-diketiminate Al(I) species **XII**. In particular, Harder and co-workers showed that deprotonation of the BDI backbone's methyl moiety leads to a dianionic diamido ligand capable of anchoring an Al(I) centre in **XXIV**.[14, 26]

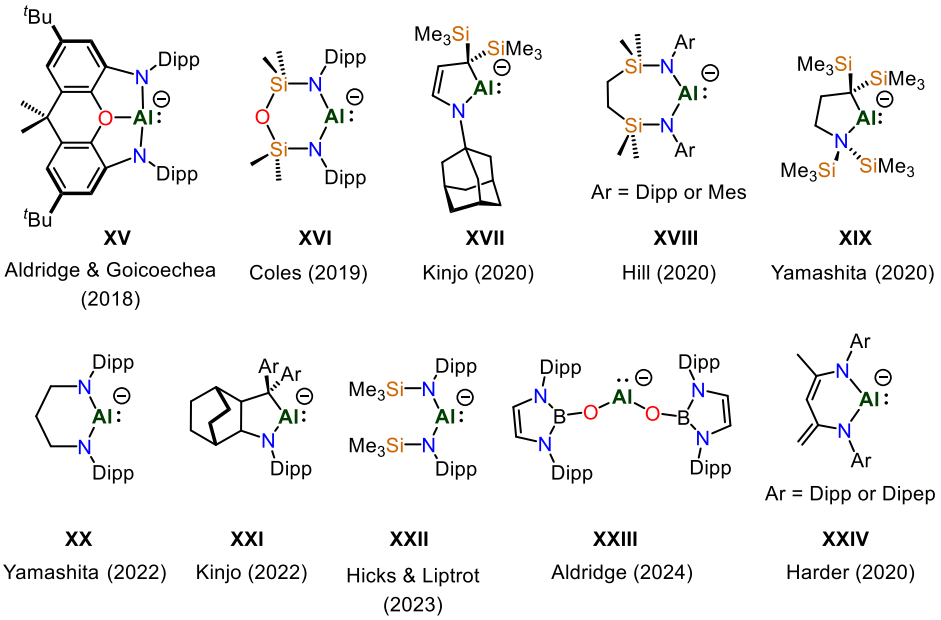


Figure 4. Known examples of anionic aluminium(I) carbene analogues.

1.1.2.1 Alkali Metal Ion Pairing and Reactivity of Aluminyls

Single-crystal X-ray analyses have unveiled diverse bimetallic interactions in these new aluminyl systems, thereby enabling a classification based on their aggregation states. The alkali metal (AM^+) cation proves crucial in guiding their geometry and reactivity. Typically, reducing a suitable aluminium precursor with an AM reagent generates contacted dimeric pairs (CDPs), wherein AM^+ bridges two Al(I) centres and often interacts with an ancillary aromatic substituent ($AM^+\cdots\pi$-arene) from the bulky ligand framework. The CDP's crystal structures can exhibit "symmetric," "slipped," or "twisted" configurations, each reflecting a different orientation of the aluminyl anions and the bridging AM^+ cation (Figure 5).[14, 21-22, 23a, 23b, 23e, 27] In solution, DOSY NMR spectroscopy proved a valuable spectroscopic technique to study their aggregation states through diffusion and hydrodynamic analyses of the resulting solution species.

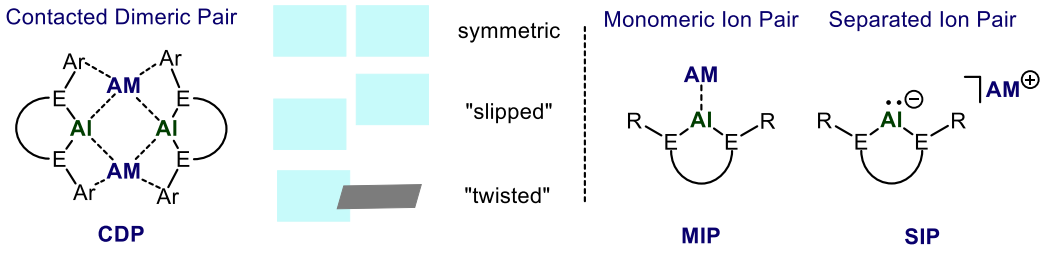
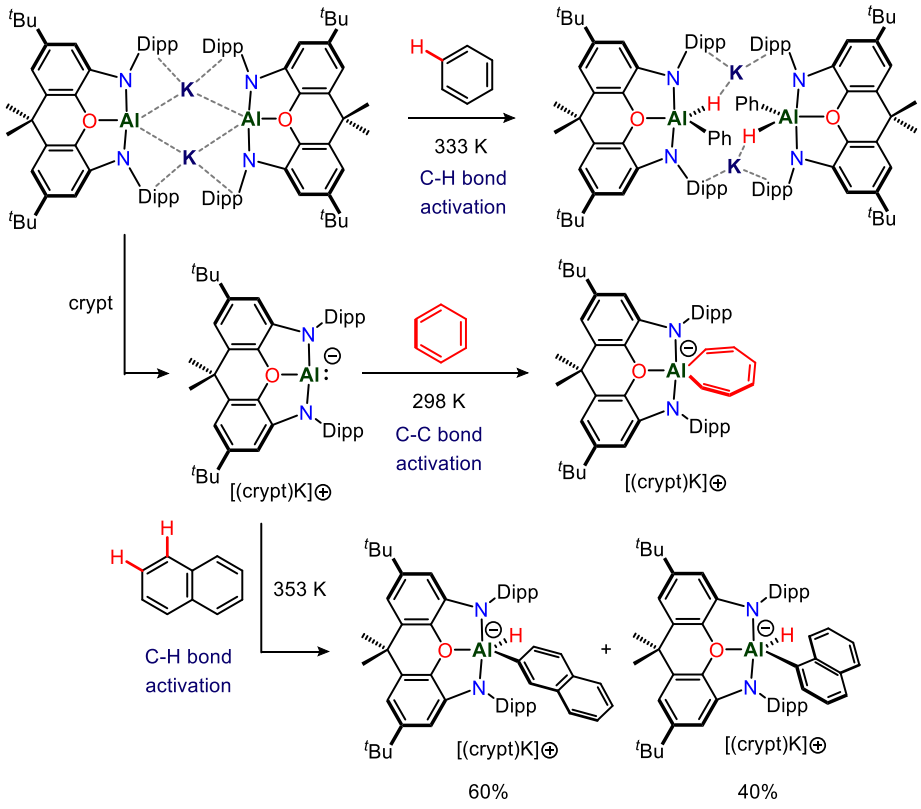


Figure 5. Structural classification of aluminyl compounds.

Conversely, by removing the stabilising $AM^{+}\cdots\pi$-arene interactions (e.g., employing supporting ligands devoid of aromatic groups) or using strong donors (THF, ethers, or polydentate amine ligands like TMEDA, crown ethers or cryptands) can yield monomeric ion pairs (MIPs). These systems feature an unsupported, highly polar Al···AM bond and are often reversible (e.g, heating a MIP can revert it to a CDP, and *vice versa*).[23e, 27b] "Naked" or separated ion pairs (SIPs) free from alkali metal interactions is typically achieved by fully encapsulating AM^{+} with cryptand or multiple crown ethers, thus, leaving freely such highly-reactive aluminyl anions. Despite the vast progress in aluminyl chemistry only "naked" SIP examples for the aluminyls **XV**–**XVIII** (Figure 4) have been reported.[21, 22b, 23b, 23d]

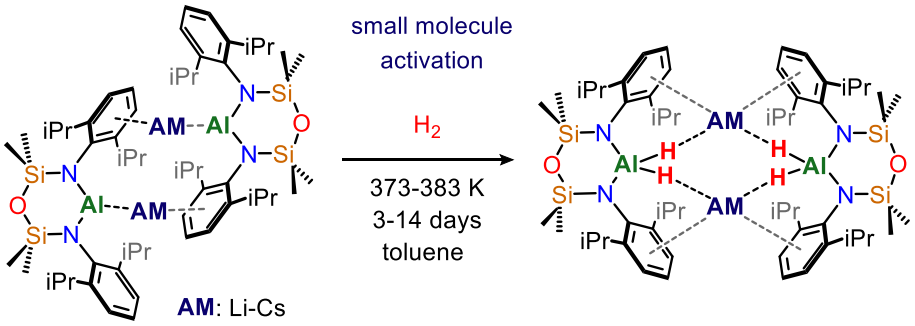
Computational analyses confirm that the Al(I) centre in aluminyls is predominantly HOMO centred featuring a directional aluminium lone pair, while the LUMO involves significant p-orbital character, endowing these anionic species frontier gaps of approximately 3.4–4.1 eV, [27a, 28] indicating that these aluminyls could engage in bond-activation pathways with ambiphilic reactivity reminiscent of classical singlet carbenes.



Scheme 1. Divergent reactivity of CDP and SIP aluminyl systems.

Interestingly, their aggregation plays a key role, with each structural class dictating markedly different reactivity. For instance, CDP aluminyls usually activate C–H bonds in aromatic substrates, such as benzene, upon heating, whereas in their SIP aggregation state can break a C–C bonds for the same aromatic molecule (Scheme 1).[29] Even though, a degree of selectivity can be achieved on C–H activation of polyaromatics, such as naphthalene, which can be activated at either the α-C–H and β-C–H bonds within a 4:6 molar ratio via SIP aluminyls. [29] Similarly, other "naked" aluminyls have displayed reactivity in E–H (N–H,[23d, 30] O–H,[30b] Si–H,[23d, 30b] P–H[30b]) oxidative additions and [2+2] or [4+2] cycloadditions involving unsaturated C≡C,[31] C=C,[29, 31-32] and C=N[23b] bonds, and even the reduction of white phosphorus from P_4 to $(P_4)^-$. [33]

More recently developments involve the use of aluminyls to activate small molecules such CO_2, N_2O, NH_3 and H_2, forming aluminium-carbonates, cis-hyponitrites, and amides or hydrides.[28a, 34] In these contexts, small molecule activation is usually achieved by dimeric aluminyls in cooperation with alkali metal AM^+ counterions at elevated temperatures (Scheme 2). Hence, despite these feats, H_2 activation often necessitates prolonged heating and carefully tuned stoichiometry, illustrating just how challenging direct hydrogen cleavage can be in main-group metal systems compared to transition-metal analogues.



Scheme 2. Activation of H_2 using dimeric alkali metal aluminyl systems.

1.2 Objectives

Motivated by the recent surge in electron-rich aluminium(I) chemistry and its parallels to transition-metal reactivity, this chapter sets out to develop and thoroughly characterise a new family of β-diketiminate-based aluminium complexes, encompassing both anionic aluminium(I) (aluminyls) and aluminium(III)–H (dihydridoaluminates) systems under mild reaction conditions. To accomplish this, we deploy controlled and convenient deprotonation routes that preserve low-valent or hydride-containing Al centres. In particular, we target a diverse range of aggregation states (dimeric, monomeric, or separated ion pairs) that allow meaningful comparisons of structure, electronic configuration, and reactivity. In parallel, we investigate how different alkali-metal cations (Li^+–Cs^+) and donor ligands (crown ethers, cryptands) influence both the solution-phase equilibria and the solid-state organisation of these electron-rich aluminium species.

A core objective is to apply such anionic low-valent aluminium(I) species to small-molecule activation, notably focusing on H_2-activation and pinpointing the role of alkali-metal interactions in controlling the efficacy of dihydrogen cleavage across various aggregation states. Special attention is paid to how alkali-metal coordination (e.g., alkali metal ion AM^+ doping) can unlock latent reactivity or stabilise key intermediates, echoing dual-metal cooperativity in traditional catalysis. Complemented by computational insights, we clarify the structural motifs responsible for mediating small-molecule activation at these anionic aluminium(I) complexes. Ultimately, by drawing on parallels among aluminyls, dihydridoaluminates, and related main-group analogues, this chapter aims to demonstrate how low-valent aluminium(I) can surpass its classical Lewis-acid role and approach transition-metal-like versatility, thereby opening new horizons for Group 13 catalysis and reactivity.

1.3 Results and Discussion

1.3.1 Synthesis of Alkali Metal Aluminyls

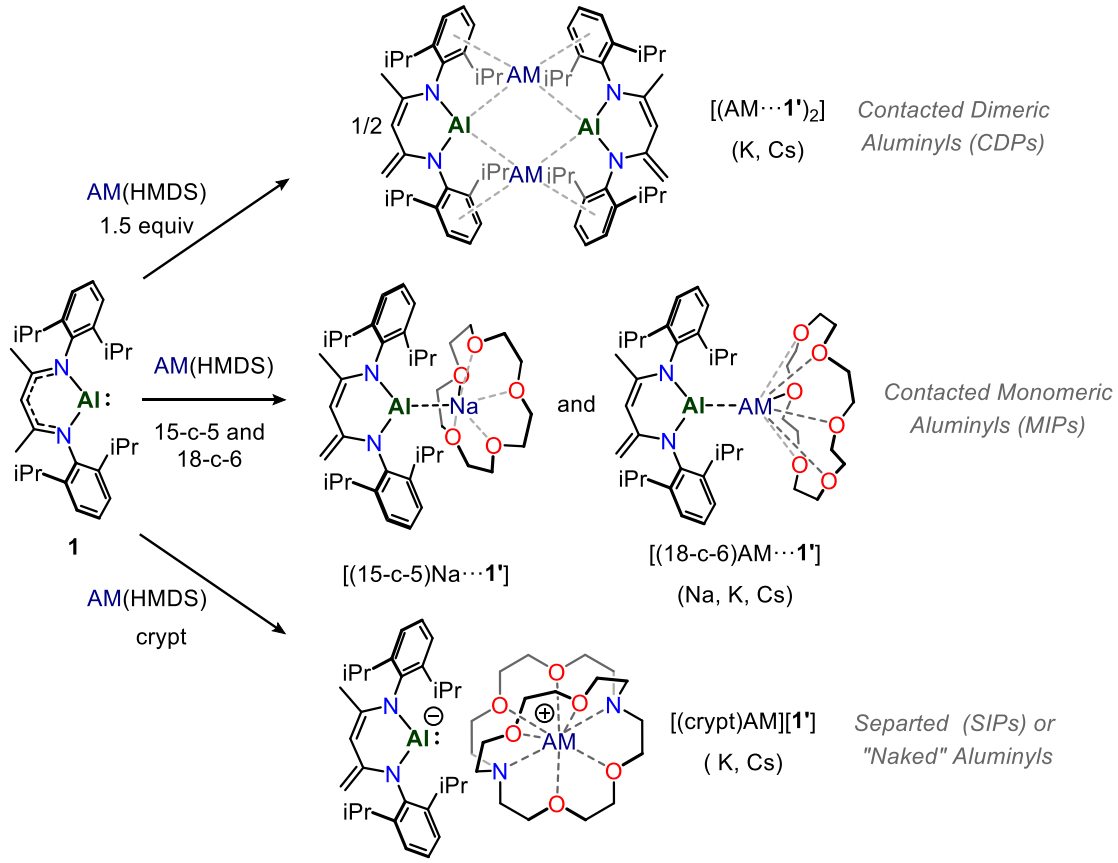
Building on the pioneering example by Aldridge and Goicoechea, who demonstrated that aluminyls can be stabilised by a xanthene-based diamido ligand (**XV**, Figure 4), we sought to develop related β-diketiminate (BDI)-supported aluminyl species. Although Harder and co-workers had shown that BDI backbones could yield dimeric aluminyls **XXIV**, our objectives were twofold: firstly, to extend these systems toward monomeric or "naked" species with strong potential for transition metal–like reactivity, and secondly, to improve their synthetic convenience, broadening the scope of available β-diketiminate-derived aluminyl complexes.

To that end, we turned to Roesky's neutral aluminylene complex **XII**, particularly (^{Dipp}BDI)Al **1**[11] with a β-diketiminate framework bearing two 2,6-diisopropylphenyl (Dipp) substituents. A key feature of this BDI ligand is the mild acidity of its backbone methyl substituents, which can be deprotonated by a sufficiently strong base, thus generating a dianionic ligand scaffold[35] capable of stabilising an electron-rich Al(I) centre. Drawing on prior demonstrations that BDI ligands can stabilise main-group metals in multiple oxidation states, such as Mg(I),[36] In(I),[37] and Ge(II),[38] we reasoned that direct deprotonation of **1** using alkali metal amides would afford distinct aluminyl ion pairs, each featuring an anionic Al(I) centre anchored by a deprotonated BDI.

Scheme 3 illustrates our fundamental approach. Treating the aluminylene **1** with alkali-metal bis(trimethylsilyl)amides (AMHMDS; M = Li, Na, K, Cs) in aromatic solvents provided a straightforward route to the aluminyl [**1'**]$^-$. In practice, the success of methyl deprotonation at the backbone of the BDI ligand depended strongly on the base strength and the subsequent Al···AM interactions. Specifically, KHMDS or CsHMDS in toluene at room temperature generated the dimeric aluminyl complexes [(AM···**1'**)$_2$] (AM = K, Cs). By contrast, reactions with LiHMDS or NaHMDS employing the same reaction conditions gave unreacted starting materials, demonstrating an essential *cation effect* in guiding Al···AM interactions with the heavier Cs^+ and K^+ *versus* the lighter Na^+ and Li^+.

Shortly after we embarked on this work, an alternative route emerged in the literature, in which alkali-metal graphite reagents (e.g., RbC_8 or CsC_8) were used to form dimeric aluminyl species [(Rb···**1'**)$_2$] and [(Cs···**1'**)$_2$] from **1** under mechanochemical (ball and milling) conditions.[27b] Although that reductive protocol

does yield the dimeric species, our base-induced deprotonation approach (Scheme 3) offers a more convenient and controlled entry to these β-diketiminate aluminyls under comparatively mild conditions, without specialised reductants. Similarly, deprotonation of **1** using the organo potassium reagent $KCH(SiMe_3)_2$ is known to yield the potassium dimeric aluminyl $[(K\cdots\mathbf{1'})_2]$;[26] but attempts to employ the heavier $CsCH(SiMe_3)_3$ under similar conditions led to intractable reaction mixtures. By contrast, CsHMDS effected clean and reproducible deprotonation to give $[(Cs\cdots\mathbf{1'})_2]$, a further illustration of the practicality of our newly developed method.



Scheme 3. Synthesis of alkali metal derivatives of the novel anionic β-diketiminate-based aluminium(I) carbene analogue $[\mathbf{1'}]^-$ (HMDS = bis(trimethylsilyl)amide).

As we have also noted, the stability and reactivity of $[\mathbf{1'}]^-$ are strongly influenced by the nature of the interactions with the alkali metal counterions. When we introduced the three-dimensional cryptand (2.2.2-cryptand, crypt) into reactions of **1** in toluene at room temperature for 5 mins with KHMDS or CsHMDS, the larger K^+ or Cs^+ cations were fully encapsulated, yielding the "naked" aluminyl $[\mathbf{1'}]^-$ paired with $[(crypt)AM]^+$ cations, as separated $[(crypt)AM][\mathbf{1'}]$ ion pairs (AM = K, Cs). These

represent the first examples known of charge separated aggregates of the "naked" aluminyl anion [**1'**]$^-$. The increased reactivity of the "naked" aluminyl [**1'**]$^-$ made its preparation and isolation challenging, and these species necessitates handling in more polar and inert aromatic solvents (e.g. fluorobenzene) to remain soluble and stable after isolation from toluene. However, no suitably stable complexes were forthcoming with lighter LiHMDS or NaHMDS, giving intractable mixtures and thus suggesting that encapsulating Li^+ or Na^+ fails to stabilise [**1'**]$^-$ effectively in these conditions. The increased stability for the heavier alkali metal aluminyls [(crypt)AM][**1'**] (AM = Cs ~ K > Na ~ Li) contrasts with that for the contacted dimeric pairs [(AM···**1'**)$_2$] (decreasing from Li to Cs).[27b] Alternatively, employing the less bulky two-dimensional crown ligands 15-crown-5 (15-c-5) and 18-crown-6 (18-c-6) caused the resulting aluminyls to adopt a contacted monomeric ion pair structure, [(crown)AM···**1'**], (AM = Na, K, Cs) in which the alkali metal is not fully entrapped and preserves a direct [**1'**]$^-$···AM^+ interactions. However, repeated attempts to form a lithium monomeric aluminyl were unsuccessful, presumably because the highly reactive nature of the [**1'**]$^-$ anion and less favourable Al···Li coordination, leading to decomposition under various conditions and presence of various ratios of crown ethers (18-crown-6, 15-crown-5, and even the smaller 12-crown-4). By contrast, employing 15-crown-5 (for Na) or 18-crown-6 (for Na, K and Cs) in toluene or benzene at room temperature for, followed by 2 hours of stirring, yielded these MIP aluminyls, [(15-c-5)Na···**1'**] and [(18-c-6)AM···**1'**] (AM = Na, K, Cs), in reasonable isolated yields upon precipitation or crystallization with *n*-hexane and subsequent drying under vacuum.

These steps underscore the sensitivity of [**1'**]$^-$ and how increasing the coordination around the alkali metal can modulate the aggregation from dimeric species to monomeric pairs. While the separated species [(crypt)AM][**1'**] required more polar aromatic solvents (e.g. fluorobenzene) to remain soluble and stable in solution, the dimeric [(AM···**1'**)$_2$] and contacted crown-stabilised aluminyls [(crown)AM···**1'**] were handled under less polar toluene or benzene solutions. Despite effectively generating these aluminyl ion pairs, we observed no immediate cleavage of C–H, C–C, or C–F bonds in toluene, benzene, or fluorobenzene under our standard conditions, in contrast to certain "contacted" aluminyls[26-27, 39] or neutral aluminylene systems,[40] known to activate aromatic rings. Hence, while deprotonation indeed furnishes an anionic Al(I) nucleophilic centre, more forcing

conditions or activated substrates appear necessary to induce bond activation in these alkali metal aggregates of [**1'**]$^-$.

Overall, this novel deprotonation strategy with alkali-metal amides stands as a key improvement in accessing β-diketiminate-based aluminyl species under mild reaction conditions over other methodologies. The following sections will outline the structural characterisation and solution behaviour of these new aluminyl complexes, as well as highlight their reactivity. Our analyses include monodimensional NMR spectroscopy (^{1}H, ^{11}B, ^{13}C, ^{19}F, ^{27}Al, ^{133}Cs), two-dimensional NMR techniques (^{1}H-^{1}H COSY, ^{1}H-^{13}C HSQC, ^{1}H-^{13}C HMBC), *D*iffusion-*O*rdered NMR *S*pectroscop*Y* (DOSY NMR) to probe aggregation in solution, single-crystal X-ray diffraction, elemental analysis, and computational modelling. Subsequently, we will describe how attempts to activate dihydrogen with these bimetallic ion pairs led to striking reactivity outcomes, underscoring their potential as transition metal-like mediators in small-molecule activation, particularly with H_2.

1.3.2 Nuclear Magnetic Resonance (NMR) Spectroscopy Studies

Having established that deprotonation of **1** with various alkali-metal bis(trimethylsilyl)amide reagents (AMHMDS; AM = Na, K, Cs) in aromatic solvents yields dimeric (CDPs), separated (SIPs), or contacted monomeric (MIPs) aggregates of the aluminyl anion [**1'**]$^-$, we next examined their solution-state properties via NMR spectroscopy. As uniformly observed for aluminyls reported to date, these newly isolated aluminyl species fail to show any observable ^{27}Al resonances, despite repeated attempts and settings, ^{27}Al NMR signals remain elusive across the entire aluminyl family. The strong quadrupolar relaxation of ^{27}Al (I = 5/2), combined with the highly electron-rich Al(I) centre, likely contributes to line-broadening beyond detection, a phenomenon widely reported for low-valent aluminium complexes.

1.3.2.1 Contacted Dimeric Aluminyls

The Dimeric aluminyl complexes [(AM···**1'**)$_2$] (AM = K, Cs) each display characteristic spectroscopic signatures indicative of partial deprotonation at one of the β-diketiminate backbone methyl substituents. In toluene-d_8, unit consistently appears as two broad singlets in the δ 3.6–3.9 and δ 2.7–2.9 ranges (Figure 6), aligning with similar resonances documented in previously characterized dimeric aluminyls (Table 1).[14, 26, 27b] Such splitting and downfield/broad signals for the

methylene CH_2=C group reflects a degree of backbone BDI conjugation within these aluminyl anions.

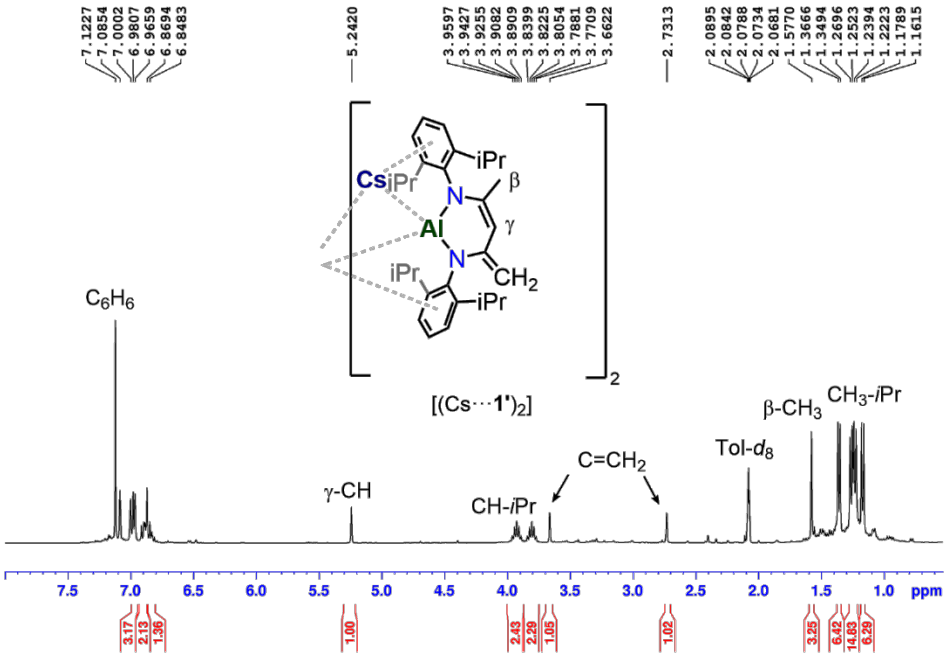


Figure 6. ^{1}H NMR (400 MHz, Tol-d_8, 298 K) of [(Cs···**1'**)$_2$].

Alongside these methylene peaks, the residual backbone methyl group resonates near δ 1.5–1.7, while the backbone γ-CH proton appears as a singlet in the δ 5.2–5.4 window, slightly more downfield than in neutral aluminylene precursor **1** (δ ~ 5.1). Two sets of septets in the δ 3.6–4.1 region integrate to the isopropyl (iPr) methine protons of each Dipp substituent, whereas the iPr methyl groups manifest themselves as doublets (δ 1.0–1.4).

Although the overall ^{1}H NMR patterns remain broadly similar for potassium *versus* caesium dimers, minor cation-induced shifts are discernible. In [(K···**1'**)$_2$], the methylene CH_2=C group resonates at δ 3.73 and 2.79, whereas in the caesium analogue [(Cs···**1'**)$_2$] they shift slightly downfield to δ 3.66 and 2.73. Similarly, the γ-CH and iPr signals differ by about 0.05–0.1 ppm between the two systems. Such small, systematic variations reflect the distinct ionic radii and coordination preferences of K^+ *versus* Cs^+, a trend often noted in related dimeric aluminyl frameworks.[14, 26, 27b]

Table 1. Selected ^{1}H and ^{133}Cs{^{1}H} NMR signals (δ, ppm) for [(AM···**1'**)$_2$] (AM = K, Cs).

Species	γ-CH ^{1}H	CH_2=C ^{1}H	β-Me ^{1}H	CH-*i*Pr ^{1}H	^{133}Cs
[(K···**1'**)$_2$]					
Harder[26] (C_6D_6)[a]	5.36	3.92	1.64	3.89	
		2.98		3.72	
This work (Tol-d_8)[b]	5.19	3.73	1.57	3.79	
		2.79		3.66	
[(Cs···**1'**)$_2$]					
Harder[27b] (C_6D_6)[a]	5.42	3.90	1.61	4.10	
		2.90		3.83	
This work (Tol-d_8)[b]	5.24	3.66	1.57	3.92	51.2
		2.73		3.82	$\nu_{1/2}$ = 889 Hz

[a] 600 MHz, C_6D_6, 298 K. [b] 400 MHz, Tol-d_8, 298 K.

In the ^{13}C NMR spectra, the methylene carbons appear near δ 77, the γ-CH carbon at δ 102–103, and the aromatic or aliphatic carbons at the expected positions. As anticipated earlier, ^{27}Al NMR signals are absent. For the caesium CDP aluminyl derivative [(Cs···**1'**)$_2$], the ^{133}Cs NMR experiment detects a broad peak at δ 51.2, indicating a unique Cs^+ coordination environment within this aluminyl dimer.

Overall, these NMR data verify that both potassium- and caesium-based dimeric aluminyl species, [(AM···**1'**)$_2$], remain intact in solution, each deriving from deprotonation of the BDI backbone to form [**1'**]$^-$. Their spectroscopic profiles closely mirror those of analogous dimeric aluminyl compounds already reported,[26, 27b] yet highlight the relative ease of our deprotonation route (Section 1.3.1) to access these β-diketiminate-supported aluminyl dimers, compared to older protocols that depended on stronger reductants (alkali metal graphite derivatives of the type (AM)C_8) or organo alkali metal reagents.

1.3.2.2 Contacted Monomeric Aluminyls

We next examined the monomeric ion pairs (MIPs), in which the alkali metal engages in direct Al···AM interactions with the electron-rich aluminyl centre. Although deprotonation routes generated dimeric aluminyl aggregates, [(AM···**1'**)$_2$], and "naked" ion pairs, [(crypt)AM][**1'**], with larger alkali metals K and Cs, attempts to isolate lithium monomeric aluminyl [(crown)Li···**1'**] were unsuccessful, reflecting both the high reactivity of [**1'**]$^-$ and less favourable Li···Al coordination in these conditions.

Nonetheless, Na^+, K^+, and Cs^+ proved accessible under carefully chosen donor ligands (15-crown-5 or 18-crown-6) to yield the new contacted monomeric ion pairs [(crown)AM···**1'**] (Scheme 3). Here, we detail their NMR features in toluene-d_8 (Tol-d_8), with selected resonance data summarised in Table 2.

All monomeric ion pairs [(crown)AM···**1'**] (AM = Na, K, Cs), exhibit the γ-CH proton of the β-diketiminate backbone consistently resonating at δ 5.3–5.4 as a singlet (Table 2). The newly formed methylene (CH_2=C) fragment of the dianionic BDI framework, consistently appears as a pair of small doublets or broad singlets (J ~ 1.8–2.0 Hz) in the δ 3.6–3.8 and δ 2.7–2.9 range. These signals are reminiscent of the resonances observed for the potassium and caesium dimeric aluminyls, [(AM···**1'**)$_2$], but are shifted slightly, often more downfield, owing to differences in the Al···alkali metal interactions and their distinct structural geometries.

At δ 1.7–1.8, a singlet integrates for the unreacted methyl substituent of the BDI backbone. The isopropyl-CH moieties of the Dipp aromatic rings appear as two septets in the δ 4.2–3.9 region (each integrating relatively to two protons, J ~ 6.5–7.0 Hz), whereas the iPr methyl groups result with overlapping doublets near δ 1.5–1.3. No resonances attributable to unreacted neutral aluminylene **1** remain, indicating complete deprotonation to the [**1'**]$^-$ anion under these conditions.

In the case of the Na^+, K^+ and Cs^+ MIPs, [(18-c-6)Na···**1'**], [(18-c-6)K···**1'**] and [(18-c-6)Cs···**1'**], an additional ^{1}H singlet arises around δ 2.9–3.1, corresponding to the 18-crown-6 ring-ether environment. For the Na^+ MIP aluminyl, [(15-c-5)Na···**1'**], a similar crown-ether resonance is observed near δ 2.8. These signals reflect crown coordination to the alkali metals AM^+ and are slightly deshielded compared to free crown ethers, consistent with crown···alkali metal binding.

In ^{13}C NMR, the newly formed methylene (CH_2=C) carbon resonates at δ 75–77, consistent with partial conjugation in the deprotonated BDI skeleton. The γ-CH carbon typically appears at δ ~ 102, while the ring carbons in the Dipp substituents remain near the expected chemical shifts for iPr-substituted phenyl frameworks. The donor crown ethers are also readily identified, displaying intense aliphatic peaks around δ 68–70.

As for the dimeric aluminyls, [(AM···**1'**)$_2$] (AM = K, Cs), and essentially all aluminyl species reported in the literature, no ^{27}Al resonance is observed here. This "NMR silence" has become a defining trait of aluminyl chemistry and likely stems from rapid relaxation or broadening caused by the highly electron rich aluminyl

environment. When the caesium-based crown MIP, [(18-c-6)Cs···**1'**], is examined by ^{133}Cs NMR, a broad resonance appears at δ 19.6, distinctly upfield from that of free CsHMDS (δ 119.2).[41] The δ(^{133}Cs) reflects a prominent Al···Cs interaction between the negatively charged aluminyl anion [**1'**]$^-$ and Cs$^+$ in the contacted ion pair [(18-c-6)Cs···**1'**]. Similar Cs$^+$-aluminyl contacts appears in related aluminyls, although this is the first ^{133}Cs NMR characterisation of a monomeric caesium aluminyl system.[27a, 27b]

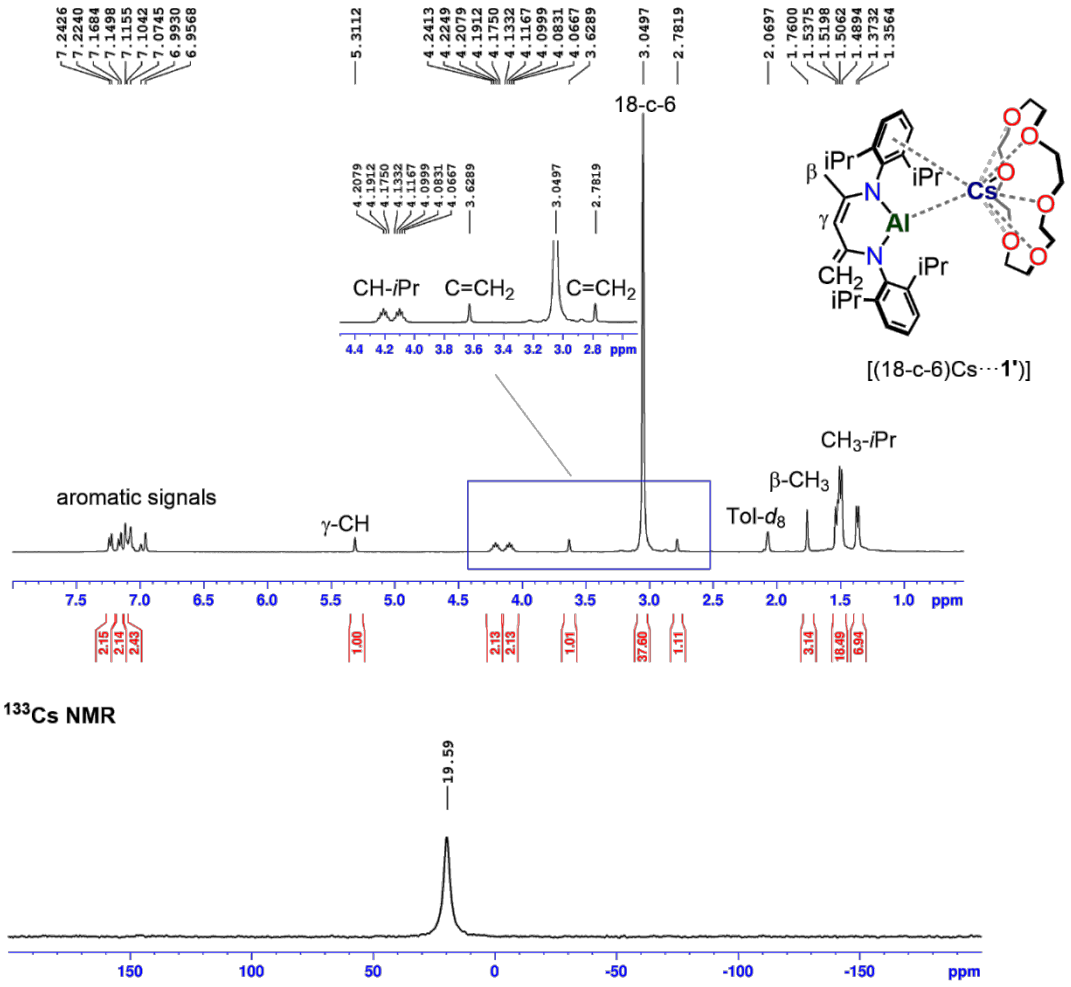


Figure 7. ^{1}H NMR (500 MHz, top) and ^{133}Cs{^{1}H} NMR (52.4 MHz, bottom) of [(18-c-6)Cs···**1'**)] in Tol-d_8 at 298 K.

Table 2. Selected ^{1}H and ^{13}C{^{1}H} NMR signals (δ, ppm) in Tol-d_8 at 298 K of [(crow)AM···**1'**] (crown = 15-crown-5, 18-crown-6; AM = Na, K, Cs).

Complex	γ-CH		CH_2=C		β-Me		crown ether		
	^{1}H	^{13}C	^{1}H	^{13}C	^{1}H	^{13}C	^{1}H	^{13}C	^{133}Cs
[(15-c-5)Na···**1'**]	5.33	102.2	3.71[a] 2.90[a]	75.9	1.76	24.2	2.87	68.5	
[(18-c-6)Na···**1'**]	5.37	102.7	3.71 2.81	76.2	1.70	24.1	2.96	69.0	
[(18-c-6)K···**1'**]	5.34	102.2	3.69[b] 2.84[b]	75.5	1.76	24.3	2.97	69.69	
[(18-c-6)Cs···**1'**]	5.31	102.2	3.62 2.78	75.0	1.76	24.2	3.04	70	19.6

[a] Doublet (J = 1.8 Hz). [b] Doublet (J = 2.0 Hz).

1.3.2.3 Separated Aluminyls

Whereas monomeric crown-stabilised ion pairs (MIPs) feature direct Al···AM interactions in the [(crown)AM···**1'**] species, fully encapsulating the alkali metal cation with a three-dimensional donor such as 2,2,2-cryptand (crypt) allows complete separation, generating "naked" or fully separated ion pairs, [(crypt)AM][**1'**] (AM = K, Cs). We successfully isolated only two novel charge-separated aluminyl species, [(crypt)K][**1'**] and [(crypt)Cs][**1'**], because charge-separation profoundly amplifies the reactivity of the "naked" aluminyl anion, making the preparation and isolation of these SIPs particularly challenging with lighter alkali metals (Na and Li).

Unlike the dimeric and contacted species, which are often stable in toluene or benzene, the separated ion pairs [(crypt)K][**1'**] and [(crypt)Cs][**1'**] proved insoluble in such lower-polarity solvents. Hence, their NMR characterisation was carried out in non-deuterated fluorobenzene (C_6H_5F), which prevents decomposition and provides sufficient solubility. Consequently, attempts at stability testing in even mildly polar donors (e.g., THF) lead to rapid decomposition reactions. Although C_6H_5F has two intense signals between δ 7.3–6.3 that partially overlap certain aromatic resonances of the aluminyl [**1'**]$^-$ anion, the key features remain clearly discernible. Selected NMR data is summarised in Table 3.

In both [(crypt)K][**1'**] and [(crypt)Cs][**1'**], a singlet at δ 5.1–5.2 integrates to the γ-CH proton of the β-diketiminate backbone, consistent with the partial double-bond character conferred by deprotonation at the adjacent methyl site (Figure 8). The

alkene CH_2=C moiety of the dianionic BDI skeleton appears as two small doublets at δ ~ 3.4 and δ ~ 2.6 (J = 1.8–2.2 Hz), each integrating for a single proton. These chemical shifts and splitting patterns match the partial backbone conjugation observed in the dimeric aluminyls [(AM···**1'**)$_2$] and contacted monomers [(crown)AM···**1'**]. In addition, two multiplets (or broadened resonances) in the δ ~ 4.2 and δ ~ 3.9 region each integrate for two protons, consistent with the iPr-CH groups. Similarly, the iPr-methyl signals appear as overlapping doublets around δ 1.4–1.1. Finally, the backbone methyl group resonates as a singlet near δ ~ 1.6. The cryptand protons exhibit three distinct resonances: a singlet at δ ~ 3.1 and two broader multiplets near δ ~ 3.0 and δ ~ 2.0. These reflect the distinct environments for the bridging CH_2 groups from the cryptand ligand, further corroborating the encapsulation of K^+ or Cs^+.

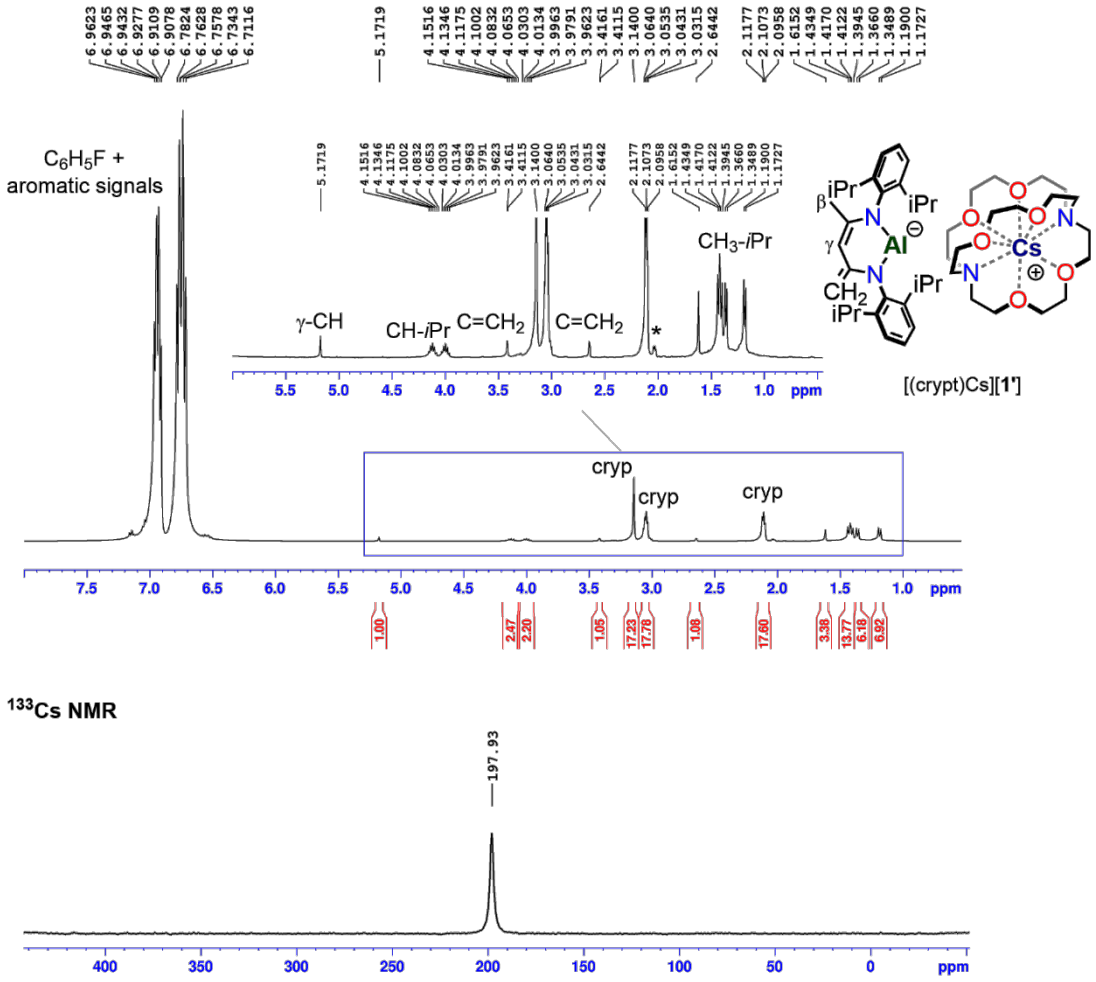


Figure 8. ^{1}H NMR (400 MHz, top) and ^{133}Cs{^{1}H} NMR (52.4 MHz, bottom) of [(crypt)Cs][**1'**] in C_6H_5F at 298 K. (*) correspond with residual traces of toluene.

Table 3. Selected ^{1}H and $^{13}C\{^{1}H\}$ NMR signals (δ, ppm) of [(crypt)AM][**1'**] (AM = K, Cs) in C_6H_5F at 298 K.

Complex	γ-CH		CH_2=C		β-Me		crypt		
	^{1}H	^{13}C	^{1}H	^{13}C	^{1}H	^{13}C	^{1}H	^{13}C	^{133}Cs
[(crypt)K][**1'**]	5.20	101.1	3.42[a]	72.6	1.64	23.6	3.09	70.0	
			2.66[a]				3.02	67.1	
							2.05	53.3	
[(crypt)Cs][**1'**]	5.17	101.1	3.41[b]	73.0	1.61	23.6	3.14	70.0	197.9
			2.64[b]				3.05	69.7	
							2.10	54.9	

[a] Doublet (J = 2.2 Hz); [b] Doublet (J = 1.8 Hz).

Overall, fully separated ion pairs [(crypt)K][**1'**] and [(crypt)Cs][**1'**] share closely analogous $^{1}H/^{13}C$ chemical shifts, verifying that the alkali metal no longer exerts strong direct interactions upon the ^{27}Al NMR silent aluminyl [**1'**]$^-$ anion. In contrast, the ^{133}Cs NMR experiment reveals a characteristic resonance for [(crypt)Cs][**1'**] at δ 197.9, considerably more downfield than, for example, the contacted pair [(18-c-6)AM···**1'**] (δ 19.6). This extreme shift underlines the more pronounced separation of Cs^+ from the aluminyl centre when entrapped by crypt in [(crypt)Cs][**1'**], contrasting with the direct Al···Cs contact in the MIP [(18-c-6)AM···**1'**] species and correlating with a more ionic and separated arrangement.

1.3.3 *D*iffusion *O*rder *S*pectroscop*Y* (DOSY) NMR Studies

NMR diffusion-ordered spectroscopy (DOSY) offers valuable insights into the solution-phase aggregation and equilibria of these newly formed aluminyl ion pairs, providing approximate molecular weights (MWs) of the species in aromatic solvents. Such analyses clarify whether the complexes persist in solution as discrete dimers, monomeric ion pairs, or a dynamic mixture of aggregated states. Additionally, DOSY results can hint at whether any partial dissociation into free [**1'**]$^-$ and separated alkali cation occurs.

1.3.3.1 General DOSY Methodology and Calibration

Because each aluminyl [**1'**]$^-$ ion-pairs sample exhibits high air- and moisture-sensitivity, we implemented our own external calibration (OEC) in-house strategy using a 15 mM mixture of 3,4-tetraphenylnaphthalene, 1-phenylnaphthalene,

adamantane, and tetramethyl silane in toluene-d_8 or fluorobenzene solvents. Plotting log(*D*) versus log(*MW*) for these reference compounds furnishes a linear calibration curve, enabling us to extract MW values for each aluminyl species by analysing the diffusion coefficients (*D*, m^2/s) of distinct resonances in their ^1H NMR spectra, typically with ± 10–20% error range in the MW estimates. Additionally, we also cross-checked these MW values with Stalke's ECC (established calibration curves),[42] which classify diffusing molecules into compact spheres (CS), dissipated spheres and ellipsoids (DSE), or expanded discs (ED), categories reflecting different hydrodynamic shapes. See Figure 9 with a selection of these sphere models for selected molecules we have successfully benchmarking in related caesium β-diketiminate solution chemistry.[43]

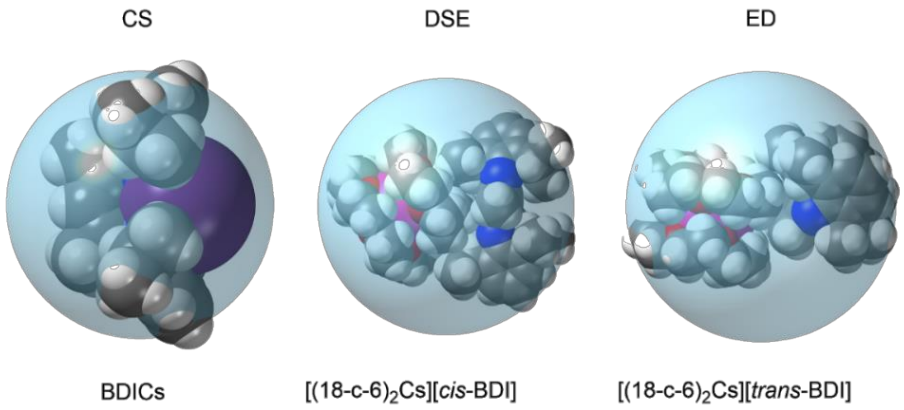


Figure 9. Stalke classification[42] of molecules according to compact spheres (CS), dissipated spheres (DSE), or expanded discs (ED), for selected caesium BDI species[43] related to the aggregation states of the aluminyl [**1'**]$^-$.

1.3.3.2 Monomer-Dimer Equilibrium in Dimeric Aluminyls

We examined the dimeric aluminyl complex [(Cs···**1'**)$_2$] by ^1H DOSY in toluene-d_8 (Tol-d_8) solution. DOSY results in solution revealed diffusion coefficients intermediate between those predicted for a monomeric ion pair aluminyl (Cs···**1'**) and a fully dimeric species [(Cs···**1'**)$_2$], suggesting the existence of an equilibrium in toluene-d_8 solution: [(Cs···**1'**)$_2$] ⇄ 2 (Cs···**1'**). This observation mirrors the behaviour previously reported by Harder in benzene for this dimeric species.[27b]

The diffusion coefficient leads to an MW (751 g/mol by OEC and 696 g/mol by ECC-DSE) that exceed the monomeric MW (577 g/mol) but fall short of the dimeric value (1153 g/mol). This indicates an ongoing monomer-dimer exchange, with the

equilibrium favouring the monomeric species due to weaker aluminium···caesium interactions. These data suggest that the Cs exhibits weaker dimerization energies and a higher propensity to dissociate into monomers in solution, compared to potassium.

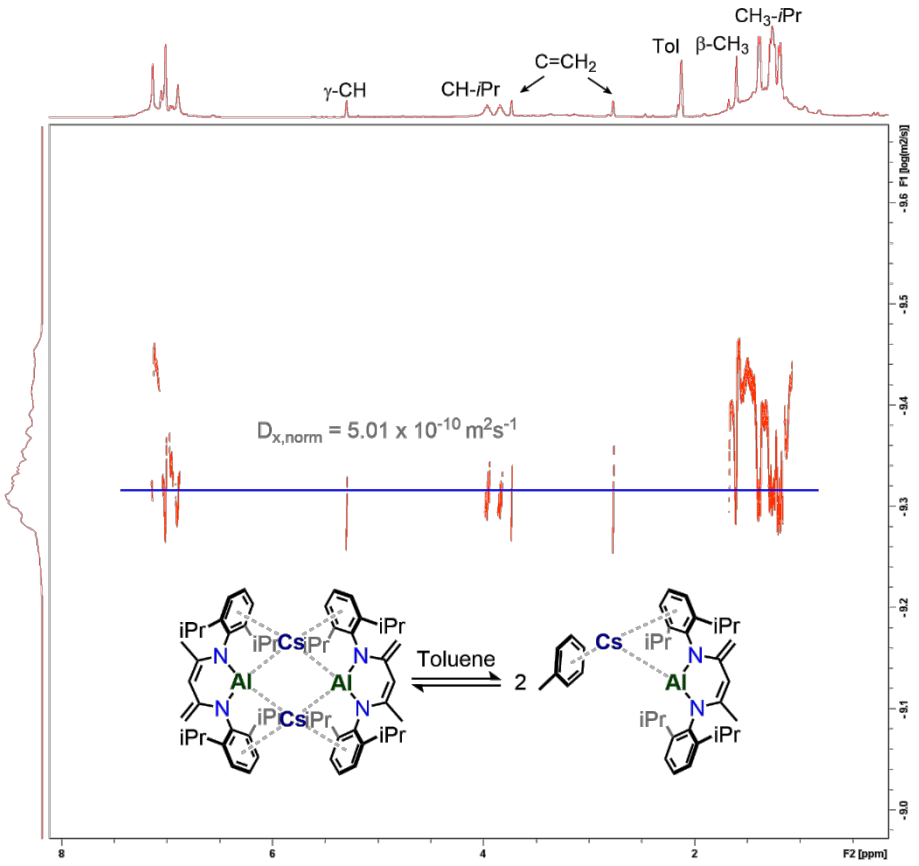


Figure 10. ^{1}H DOSY NMR (400 MHz, Tol-d_8, 298 K) showing a single set of peaks corresponding to an average monomer-dimer [(Cs···**1'**)$_2$] ⇄ 2 [(Cs···**1'**)] equilibrium in solution.

These DOSY results underscore the dynamic solution behaviour of the solvent-free dimeric aluminyl, [(Cs···**1'**)$_2$], which maintains a delicate equilibrium between monomeric and dimeric forms. Notably, the DOSY experiment highlights that their solution-phase behaviour is governed by the interplay of Al···AM interactions and the sensitivity of the aluminyl anion [**1'**]$^-$ to the size and nature of the alkali metal cation, demonstrating a greater tendency toward monomerization with larger cations like Cs^+, due to weaker Al···Cs interactions and greater ionic radius.

1.3.3.3 Contact-Separated Dynamics in Monomeric Cryptand Aluminyls

Turning to the charge-separated (or "naked") ion pairs [(crypt)AM][**1'**] (AM = K, Cs), we performed DOSY in fluorobenzene to mitigate potential decomposition. If the species were fully ionic in solution, one would expect two distinct diffusing entities [**1'**]$^-$ and [(crypt)AM]$^+$. Instead, each sample displayed a single set of diffusion coefficients across all resonances (Figure 11) implying a time-averaged diffusion constant and, thereby, an equilibrium between contacted and separated species: [(crypt)AM][**1'**] ⇄ [(crypt)AM···**1'**], where the aluminyl anion [**1'**]$^-$ can still partially contact the encapsulated K^+ or Cs^+ cation.

For [(crypt)K][**1'**], the OEC and EEC-derived MW (1209 g/mol and 892 g/mol) significantly exceeds the sum of separate [(crypt)K]$^+$ cation (416 g/mol) and aluminyl anion [**1'**]$^-$ (444 g/mol). These DOSY data suggest a fluxional interplay between partially contacted [(crypt)K···**1'**] (859 g/mol) and truly separated [(crypt)K]$^+$ and [**1'**]$^-$ in fluorobenzene solution. This is reflected in an equilibrium situation between contacted and separated species, [(crypt)K][**1'**] ⇄ [(crypt)K···**1'**], that is slightly shifted towards the contacted pair [(crypt)K···**1'**]. Also, considering the observed diffusion rates, the incorporation of additional fluorobenzene molecules into this association is conceivable.

For the [(crypt)Cs][**1'**], the situation mirrors the potassium aluminyl species, with DOSY-based MW ~ 1064–1172 g/mol versus 444 g/mol for [**1'**]$^-$ and 509 g/mol for [(crypt)Cs]$^+$ cation, with a MW of 953 g/mol for a true contacted species [(crypt)Cs···**1'**]. As above, the measured *D* values relate to MW of aggregation states that are intermediate between charge-separated and contacted monomeric pairs, thus likely averages an ensemble of partial contacting events in solution reflecting an ongoing [(crypt)Cs][**1'**] ⇄ [(crypt)Cs···**1'**] equilibrium in solution, shifted towards the contacted pair [(crypt)Cs···**1'**].

In addition, variable-temperature (VT) ^{1}H NMR data in the range 248–298 K further support a rapid exchange between separated and contacted forms, [(crypt)AM][**1'**] ⇄ [(crypt)AM···**1'**], resulting in averaged chemical shifts at all temperatures, suggesting that this is a fast dynamic process in the NMR time scale. In this context, while most of the reported charge-separated aluminyls retain their unconnected ionic structures in solution,[23b, 23d, 28b, 29] only the lighter lithium-separated derivative [Li(tmeda)$_2$][(OSiN^{Dipp})Al] seemed to co-exist with contacted species through discoordination of a tmeda ligand.[22b] Nevertheless, it is an intriguing

behaviour involving charge-separated species for the aluminyl anions [**1'**]$^-$ without losing a ligand. It provides proof of the dynamic solution nature of "naked" aluminyl anions with their counterions through labile contacted monomeric species that influence their stability and reactivity.

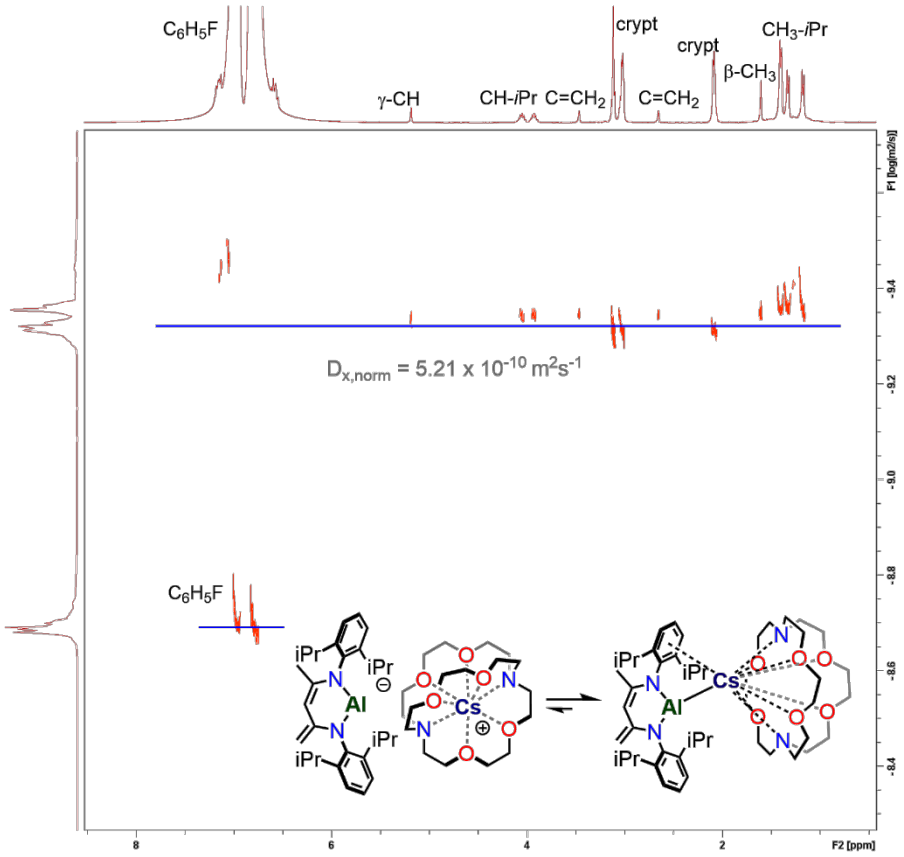


Figure 11. ^{1}H DOSY NMR (400 MHz, C_6H_5F, 298 K) showing a single set of peaks corresponding to an average [(crypt)Cs][**1'**] ⇄ [(crypt)Cs···**1'**] equilibrium in solution.

1.3.3.4 Robust Contacted Monomeric Crown Aluminyls

Lastly, we scrutinised the DOSY response of the crown-stabilised monomeric aluminyls, [(15-c-5)Na···**1'**] and [(18-c-6)AM···**1'**] (AM = Na, K, Cs) in toluene-d_8 (see Figure 12 for 18-crown-6 potassium as a selected example). In each case, DOSY data revealed only one diffusing species in solution. For [(15-c-5)Na···**1'**], the measured diffusion coefficient corresponded (via OEC) to an MW of 755 g/mol, close to the calculated 687 g/mol (9% deviation). Using the DSE estimation gave a similar 738 g/mol estimate. Likewise, [(18-c-6)Na···**1'**] displayed a diffusion coefficient matching an MW of 767 g/mol by OEC (731 g/mol calc.; 5% error) with DSE approach

giving 750 g/mol (3% difference). For [(18-c-6)K···**1'**], OEC analysis gave 914 g/mol, whereas the DSE curve indicated 878 g/mol; both differ by 15–20% from the calculated 747 g/mol. However, if the monomeric ion pair is solvated by a toluene molecule, the theoretical MW (839 g/mol) aligns within 10%. A similar scenario emerged for [(18-c-6)Cs···**1'**], with an OEC-based 1077 g/mol and the DSE approach predicted 984 g/mol *versus* the calculated 841 g/mol. Again, considering one toluene ligand narrows the discrepancy below 10–15%.

Thus, these DOSY observations confirm each crown-stabilised monomeric aluminyl appears as one discrete aggregate in solution, with no sign of free [**1'**]$^-$ or separate [(crown)AM]$^+$ cations in solution. This robust single-species diffusion pattern echoes the strong direct Al···AM bridging contact in such crown-based monomeric complexes and stands in contrast to the fluxional behaviour identified for the [(crypt)AM][**1'**] species.

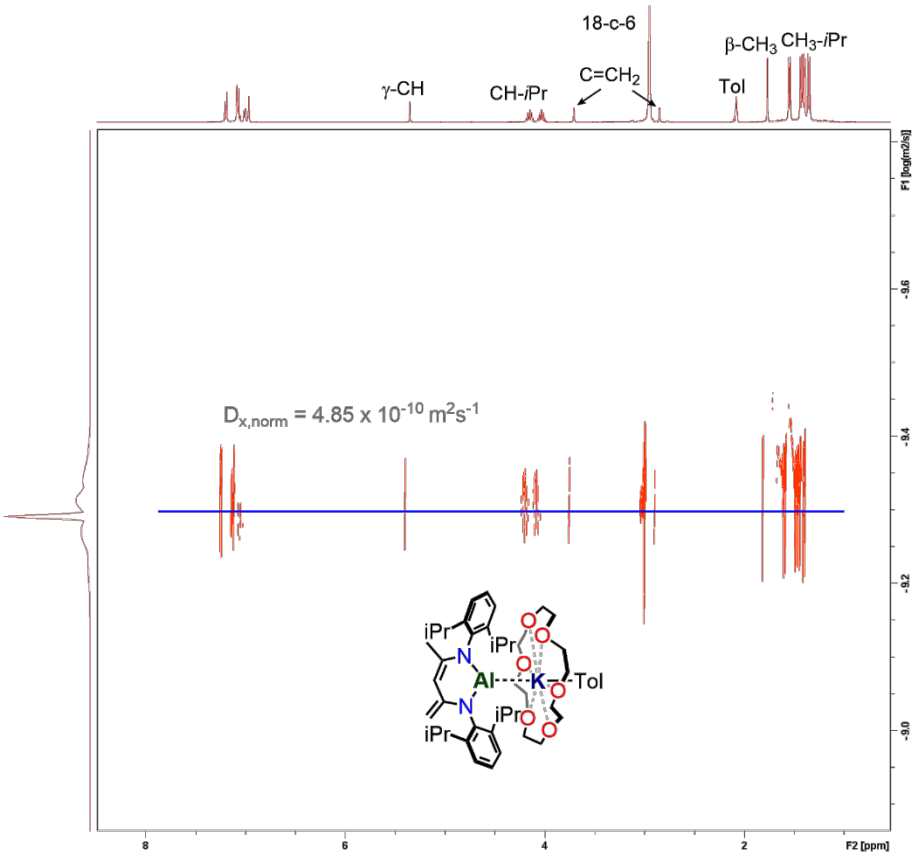


Figure 12. ^{1}H DOSY NMR 400 MHz of [(18-c-6)K···**1'**] in Tol-d_8 at 298 K.

1.3.4 Single-Crystal X-ray Structural Analysis

During our investigations on β-diketiminate-supported aluminyl systems, we succeeded in growing single crystals for several monomeric aluminyl complexes incorporating crown or cryptand donor ligands, [(crown)AM···**1'**] and of [(crypt)AM][**1'**]. These structures provide crucial insight into how the alkali metal and the negatively charged Al(I) centre organise themselves in the solid state, and how these solid-state motifs correlate with the solution behaviour presented in Sections 1.3.2 and 1.3.3. Although repeated crystallisation attempts for the dimeric complexes [(AM···**1'**)$_2$] were unsuccessful, giving oils or amorphous solids, such dimeric aluminyl structures have already been published by Harder and co-workers,[26, 27b] so we focus here on the newly obtained monomeric ion pairs, [(crown)AM···**1'**] and of [(crypt)AM][**1'**].

1.3.4.1 Contacted Monomeric Aluminyls

We obtained suitable crystals for the monomeric aluminyl complexes [(crown)AM···**1'**] bearing Na^+ or Cs^+ ions in conjunction with 15-crown-5 (Na) or 18-crown-6 (Cs). The crystals of [(15-c-5)Na···**1'**] and [(18-c-6)Cs···**1'**] were grown by layering *n*-hexane over a toluene solution, each structure crystallising in an orthorhombic system (*Pca21* and Pbca, respectively). In both systems, the BDI-ligated aluminyl anion [**1'**]$^-$ establishes a direct Al···AM bond while the crown partially sequesters the sodium or caesium cations (Figure 13).

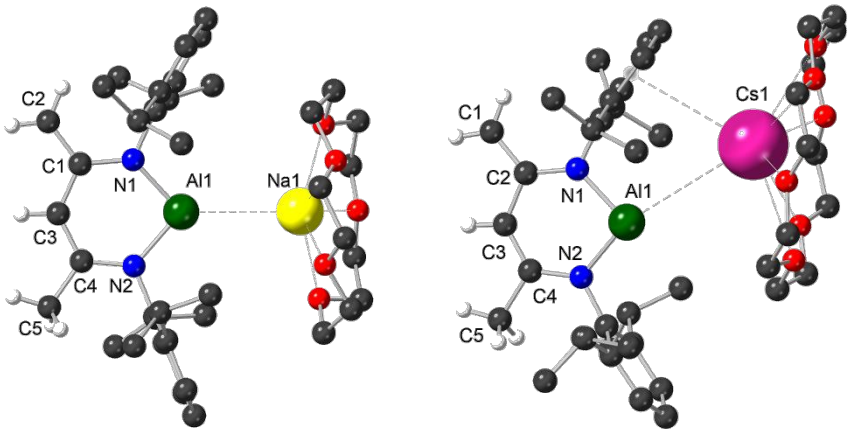


Figure 13. Molecular structure of [(15-c-5)Na···**1'**] and [(18-c-6)Cs···**1'**]. All H atoms except those from the {C1,C5}-backbone of the BDI ligand have been omitted for clarity.

Table 4. Selected bond distances (Å) and angles (°) for compounds [(18-c-6)AM···**1'**].

	Na	Cs
Al–AM	3.1350(18)	3.825(4)
N1–Al1	1.878(3)	1.873(7)
N2–Al1	1.880(3)	1.902(8)
N1–C1	1.396(4)	1.365(11)
C1–C2	1.399(5)	1.373(14)
C1–C3	1.422(5)	1.450(12)
C3–C4	1.389(5)	1.350(11)
C4–C5	1.472(5)	1.502(14)
C4–N2	1.379(4)	1.365(12)
AM–Centroid	-	3.617
N1–Al1–N2	95.79(13)	94.8(3)

Table 4 presents key bond distances and angles. In both structures, the deprotonation of a BDI methyl substituent is confirmed by the methylene CH_2=C (C1–C2) distance, near 1.37–1.40 Å (typical of partial double-bond character), while the C4–C5 remains consistent with a single-bond motif. The Al–N distances (1.87–1.90 Å) reflect a low-coordinate Al(I) environment akin to previously described aluminyl analogues.[14, 22b, 26-27]

Notably, Al···Na in [(15-c-5)Na···**1'**] measures 3.13 Å, whereas Al···Cs in [(18-c-6)Cs···**1'**] is 3.82 Å. Both length values slightly exceeding the sums of the relevant covalent radii ($\sum_{cov}$(Al,Na) = 2.87 Å; $\sum_{cov}$(Al,Cs) = 3.65 Å),[44] but still indicate a significant interaction with the heavier Cs^+ with respect to the Na^+ cation. These Al···Na and Al···Cs distances are comparable to other reported aluminyl systems (2.74–3.11 Å for Na, and 3.62–3.79 Å for Cs).[14, 22b, 26-27] In the sodium complex, the Na^+ cation is strongly coordinated by five oxygen donors of nearly planar 15-crown-5, whereas in the caesium species, the Cs^+ cation also engages in cation···π(arene) contacts (3.62 Å) with the Dipp ring, underscoring heavier alkali metals' propensity for multifaceted cation···aromatic interactions.[45]

Overall, these crystallographic data indicating Al···alkali metal distances consistent with significant interactions and the partial encapsulation of the alkali ions by crown or crypt ligands aligns well with the NMR (DOSY) observations of robust and discrete monomeric species in solution (Section 1.3.3.4), confirming that the solution-phase aggregation states inferred from DOSY and ^{1}H NMR, namely robust

monomeric pairs or limited equilibria, are indeed reflected in the solid-state bonding motifs of [(15-c-5)Na···**1'**] and [(18-c-6)Cs···**1'**].

1.3.4.2 Separated Aluminyl Pairs

Having established that "naked" aluminyl anion [**1'**]$^-$ are accessible when K^+ and Cs^+ ions are fully encapsulated by a cryptand ligand, we pursued single-crystal X-ray analyses of the potassium and caesium derivatives, [(crypt)K][**1'**] and [(crypt)Cs][**1'**]. Unlike the monomeric crown complexes [(crown)AM···**1'**], where direct Al···AM interactions persist in the solid state, these crypt-based complexes exhibit a dynamic equilibrium between separated and partially contacted geometries, consistent with our DOSY observations (Section 1.3.3.2). Key structural data are presented in Table 5.

Single crystals of [(crypt)K][**1'**] were grown from a saturated toluene solution. The crystals pack in the monoclinic P21/c space group, featuring one discrete anionic aluminyl [**1'**]$^-$ unit and one fully encapsulated [(crypt)K]$^+$ cation per asymmetric unit (Figure 14). In this structure, the K^+ cation is well fitted within the cryptand cavity (K–O ~ 2.8 Å, K–N ~ 3.0 Å), whereas the measured Al···K separation (~7.51 Å) significantly exceeds the sum of their covalent radii ($\sum_{cov}$(Al,K) = 4.98 Å).[44] Hence, no direct Al···K contact is formed, confirming a fully separated ion pair in the solid state for [(crypt)K][**1'**].

In contrast, attempts to crystallise [(crypt)Cs][**1'**] initially afforded low-quality crystals from toluene. However, dissolving the isolated solid in warm fluorobenzene, followed by addition of *n*-hexane, ultimately produced two distinct crystal types: needle-shaped crystals corresponding to the fully separated SIP [(crypt)Cs][**1'**], and block-shaped crystals identified as the newly formed "contacted" crypt species [(crypt)Cs···**1'**] (Figure 14). For the fully separated CIP form, [(crypt)Cs][**1'**], each unit cell includes two independent aluminyl [**1'**]$^-$ anions and two [(crypt)Cs]$^+$ cations. For both units, the Cs···Al distance is too large to suggest any direct interaction (5.24 Å). By contrast, in the contacted aluminyl [(crypt)Cs···**1'**] species, the Cs···Al distance (~ 4.11 Å) becomes distinctly shorter approaching the sum of their covalent radii ($\sum_{cov}$(Al,Cs) = 3.65 Å), thus, forming a monomeric contacted geometry reminiscent of the caesium crown-based [(18-c-6)Cs···**1'**] species (Figure 13).

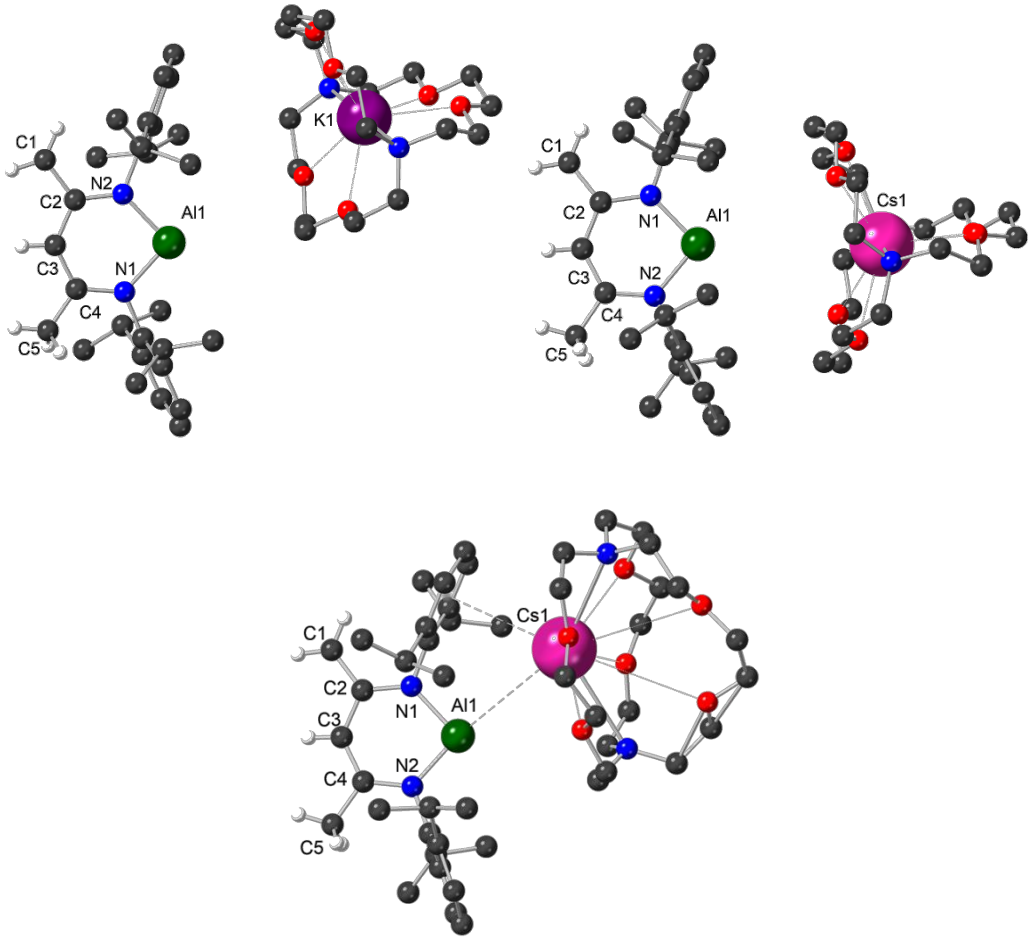
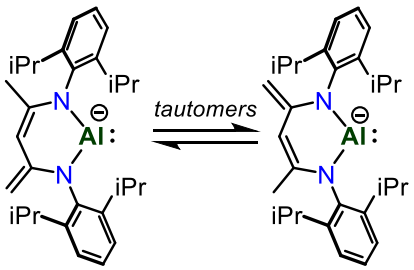


Figure 14. Molecular structure of [(crypt)K][**1'**] (top left), [(crypt)Cs][**1'**] (top right) and [(crypt)Cs··**1'**] (bottom-centre). All H atoms except those from the {C1,C5}-backbone of the BDI ligand have been omitted for clarity.

Table 5. Selected bond distances (Å) and angles (°) for [(crypt)AM][**1'**] |(AM = K, Cs).

	K	Cs (separated)	Cs (contacted)
Al1–AM	7.5164(12)	5.243(3)	4.1085(3)
N1–Al1	1.909(2)	1.889(6)	1.895(3)
N2–Al1	1.891(3)	1.909(7)	1.894(3)
N2–C2/ N1–C2	1.391(4)	1.409(10)	1.381(5)
C2–C1	1.434(4)	1.414(10)	1.411(5)
C2–C3	1.407(4)	1.398(11)	1.430(5)
C3–C4	1.402(4)	1.396(10)	1.386(5)
C4–C5	1.432(4)	1.463(13)	1.469(5)
C4–N1/ C4–N2	1.387(4)	1.381(11)	1.388(4)
AM–Centroid	-	-	3.655
N1–Al1–N2	94.11(11)	95.6(3)	94.86(13)

Both, the fully separated SIP aluminyls, [(crypt)K][**1'**] and [(crypt)Cs][**1'**], and the partially contacted form [(crypt)Cs···**1'**], present C–C bond lengths of about 1.42 Å across the entire N_2C_5-BDI-backbone, suggesting conjugation introduced by deprotonation rather than a strictly localised methylene (CH_2=C) moiety. By contrast, in crown-stabilised monomeric or solvent-free dimeric aluminyls, feature a well-defined "double-bond-like" distance (CH_2=C ~ 1.38 Å) and a complementary single bond (Me–C ~ 1.49 Å) in the BDI backbone, reflecting deprotonation at one specific methyl substituent. Here, this uniform ~ 1.44 Å metric indicates a delocalised negative charge, rather than localisation at one methyl site.



Scheme 4. Representation of the tautomeric forms of [**1'**]$^-$.

Taken together, these crypt-solvated aluminyl structures confirm two key aspects. Firstly, the BDI backbone in the separated crypt aluminyls, [(crypt)K][**1'**], [(crypt)Cs][**1'**], shows fully conjugated C_5N_2-skeleton, and secondly, these crypt aluminyls can adopt both fully "free" (separated) and partially contacted positions, as exemplified by [(crypt)Cs··**1'**], matching the DOSY evidence for a dynamic

equilibrium in solution in both K- and Cs-crypt aluminyls (Section 1.3.3.3). The ability of Cs^+ to move in or out of the cryptand cavity helps explain the single averaged diffusion coefficient in DOSY for [(crypt)Cs][**1'**], reflecting a time-averaged mixture of separated and weakly contacted forms. This solution/solid-state parallel highlights the distinctive dynamic nature of this unique β-diketiminate-supported aluminyl anion [**1'**]$^-$ when stabilised by cryptand solvated [(crypt)AM]$^+$ cations.

1.3.5 Reactivity Studies: Activation of H_2 at Aluminyls

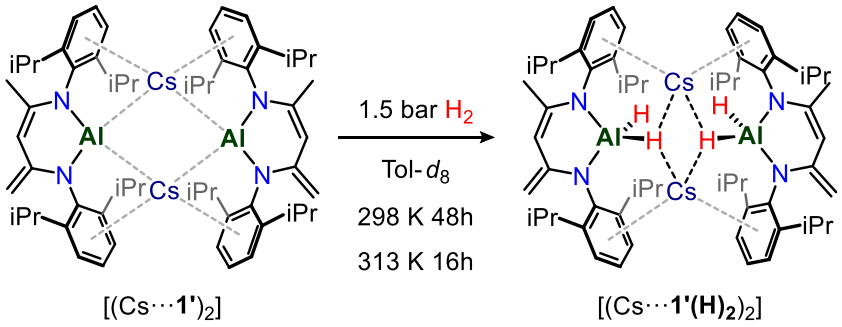
Since the seminal report of anionic aluminyls in 2018,[21] numerous parallels have been drawn between these nucleophilic main-group complexes and traditional transition-metal species, particularly with regard to small-molecule activation. In this context, the ability of certain contacted (i.e., dimeric) aluminyls to activate dihydrogen (H_2) is especially noteworthy. Pioneering examples include the xanthene-based aluminyl $[(NON^{Xanthene})Al\cdots AM]_2$[21] which slowly reacts with H_2 (5 bar) at room temperature (5 days) to form a bimetallic dihydride $[(NON^{Xanthene})Al(H)_2(K)]_2$, and the siloxide-supported aluminyl $[(OSiN^{Dipp})Al\cdots AM]_2$,[28b] which accomplishes H_2 cleavage at 393 K over several days forming $[(OSiN^{Dipp})Al(H)_2M]_2$ (1.5 bar, 393 K; $t_{1/2}$ = 1.5 (Li), 6 (Na), 12 (K) days; $t_{1/2}$ ~ 50% conversion).[21, 28b]

In contrast, the corresponding reactivity of monomeric aluminyls, particularly those that exist as separated or crown-encapsulated ion pairs, remains largely unexplored.[46] The following sections address this gap by investigating whether different aggregation states of our β-diketiminate-derived aluminyl anion [**1'**]$^-$ can facilitate oxidative addition of H_2. Notably, our studies reveal that dimeric and monomeric ion pairs display divergent capabilities in H_2 cleavage, illustrating the nuanced roles of alkali-metal coordination in promoting or inhibiting key bond-activation processes.

1.3.5.1 Reactivity of Dimeric Aluminyls with H_2

Although potassium and caesium dimeric aluminyls, $[(K\cdots\mathbf{1'})_2]$ and $[(Cs\cdots\mathbf{1'})_2]$, have been reported,[26, 27b] their specific H_2-activation profiles remained unknown. We targeted these species first, given their established monomer–dimer equilibrium in solution, which could potentially liberate highly reactive monomeric [**1'**]$^-$ fragments under mild conditions.

These experiments were conducted by monitoring the reactivity of the different isolated aluminyls with H_2 gas by *in-situ* ^{1}H NMR spectroscopy. Approximately 14 µmol of each dimeric aluminyl, $[(AM\cdots\mathbf{1'})_2]$ (AM = K, Cs), were loaded into a J. Young-valve NMR tube containing 0.5 mL of toluene-d_8. The pale-yellow solutions were subjected to three freeze–pump–thaw cycles, then exposed to 1.5 bar H_2. The reaction progress was monitored via ^{1}H NMR at room temperature (298 K) or upon mild heating (313 K), Scheme 5.



Scheme 5. Activation of H_2 using the dimeric aluminyl system [(Cs···**1'**)$_2$].

In the case of the potassium derivative, [(K···**1'**)$_2$], the reaction proceeded rapidly (within hours) but led to a complex mixture of uncharacterised products under both 298 K and 313 K conditions. No well-defined dihydride species analogous to those reported for other aluminyl systems was detected, suggesting that the potassium dimer may undergo competing pathways or decomposition during H_2 exposure. By contrast, the caesium dimer [(Cs···**1'**)$_2$] displayed more controlled and selective behaviour. Its pale-yellow solution gradually became colourless over two days at 298 K, and ^{1}H NMR analysis showed quantitative conversion to a new dihydride species, subsequently identified as [(Cs···**1'(H)$_2$**)$_2$]. Notably, raising the temperature to 313 K accelerated the reaction, achieving complete consumption of [(Cs···**1'**)$_2$] within 16 h under 1.5 bar H_2. Separate syntheses of the same dihydride confirmed that its ^{1}H NMR signatures matched those formed in situ, thus corroborating the stoichiometric oxidative addition of H_2 by the dimeric caesium aluminyl. Figure 15 illustrates a typical stacked ^{1}H NMR progression for [(Cs···**1'**)$_2$] at 313 K. The disappearance of the dimeric signals and the concurrent emergence of diagnostic peaks for the hydride ligands in [(Cs···**1'(H)$_2$**)$_2$]. are readily apparent.

This NMR data demonstrate that while both the K and Cs dimers can engage with H_2, only the caesium derivative does so cleanly to give a definitive dihydride product [(Cs···**1'(H)$_2$**)$_2$]. This difference underscores how subtle variations in alkali-metal interactions, and, by extension, the equilibrium between aggregated and partially dissociated aluminyl fragments, can dictate the outcome of H_2 activation in dimeric aluminyl systems.

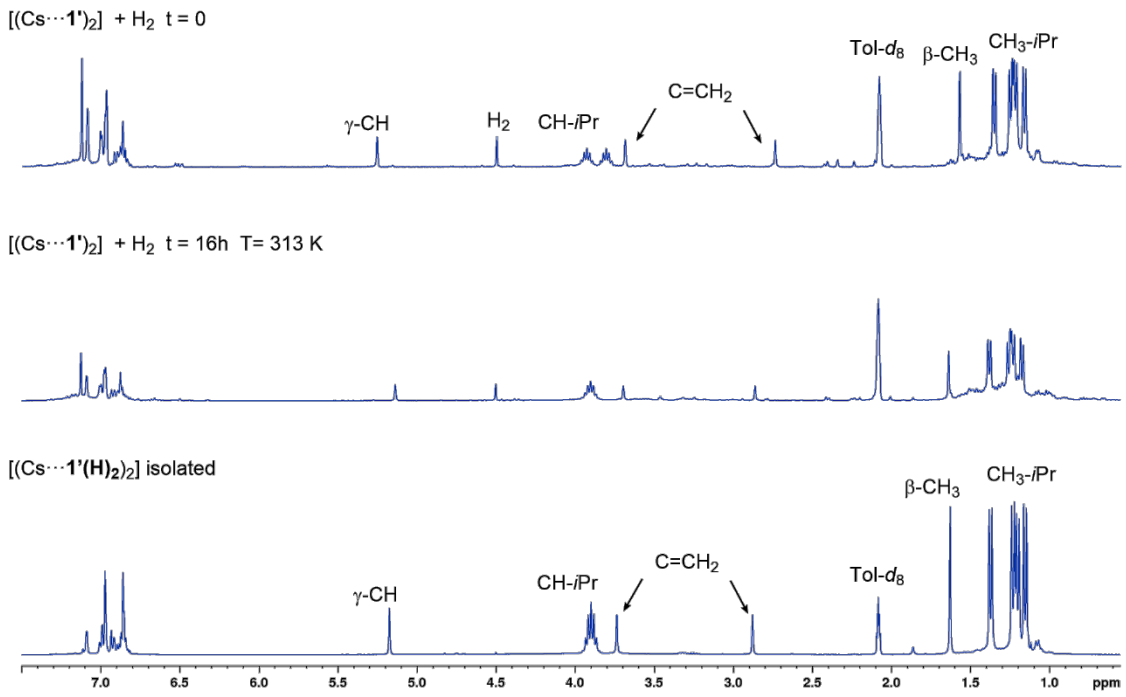


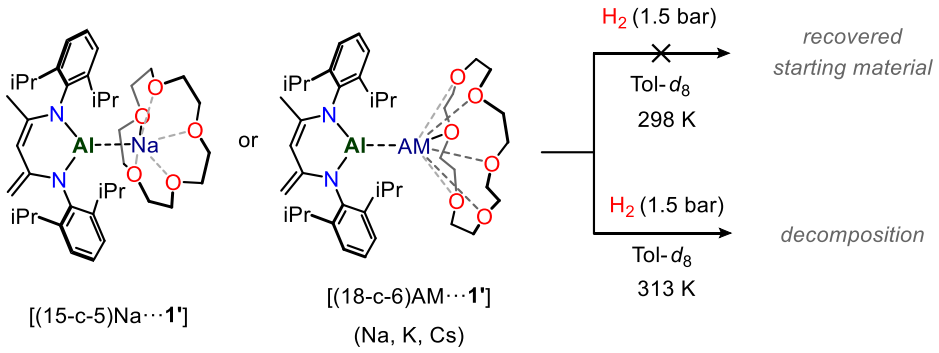
Figure 15. Stacked ^{1}H NMR (400 MHz, Tol-d_8, 298 K) spectra of H_2 activation monitoring with [(Cs···**1'**)$_2$] (top: H_2, 1.5 bar, RT, t = 0; middle: H_2, 1.5 bar, 313 K, t = 16 h; bottom: isolated [(Cs···**1'(H)$_2$**)$_2$]).

1.3.5.2 Reactivity of Monomeric Aluminyls with H_2

Building on the successful H_2 cleavage by dimeric aluminyls, we next examined whether monomeric ion pairs could display analogous reactivity. To this end, we focused on crown-encapsulated aluminyls [(15-c-5)Na···**1'**], and [(18-c-6)AM···**1'**] (AM = Na, K, Cs), each of which exists in solution as a discrete monomeric contact ion pair. Following the same protocol, 14 µmol of each was dissolved in toluene-d_8, transferred to a J. Young-valve NMR tube, degassed, and pressurised with 1.5 bar of H_2. The reaction mixtures were monitored at both 298 K and 313 K for up to seven days by ^{1}H NMR.

In stark contrast to the caesium dimer, none of the sodium- or potassium-based monomeric aluminyls, [(15-c-5)Na···**1'**], [(18-c-6)Na···**1'**] or [(18-c-6)K···**1'**], showed evidence of H_2 cleavage at room temperature for extended periods of time (Scheme 6). Monitoring the reaction under mild heating conditions (313 K) during 7 days, led to decomposition of these samples in the presence of H_2 producing complicated reaction mixtures in the ^{1}H NMR spectra. Notably, no resonances corresponding to a putative dihydride, [(crown)AM···**1'(H)$_2$**], were detected. We infer that these monomeric sodium and potassium aluminyls are either insufficiently

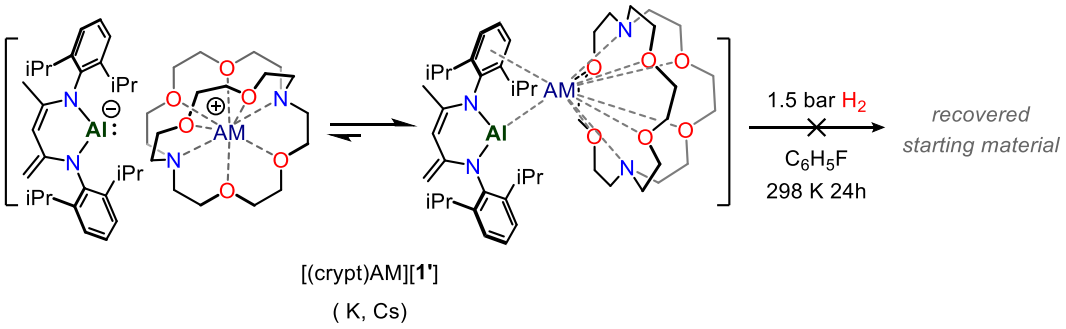
reactive toward H_2 (due to higher kinetic barriers) or prone to side reactions that preclude formation of stable dihydride complexes.



Scheme 6. Activation of H_2 using contacted monomeric aluminyl systems.

Interestingly, the caesium monomer [(18-c-6)Cs···**1'**] likewise resisted H_2 activation under identical conditions. Even after 24 h at 313 K under 1.5 bar H_2, its ^{1}H NMR spectrum showed only the signals of the starting material. This inertness contrasts sharply with the ready H_2 cleavage displayed by its dimeric analogue [(Cs···**1'**)$_2$], underscoring that a close Al···Cs bridging motif in the dimer is essential for mediating H_2 activation. Evidently, the single-site environment of the monomeric [**1'**]$^-$ centre, despite strong alkali-metal contact, is insufficient to facilitate dihydrogen oxidative addition under these conditions.

Lastly, we evaluated the "naked" ion pairs, [(crypt)K][**1'**] or [(crypt)Cs][**1'**], which lack direct Al···AM interactions in the solid state yet exhibit dynamic contact-separated equilibria in solution (Section 1.3.3.3). Approximately 14 µmol of each was transferred to a J. Young NMR tube in fluorobenzene (chosen for its solubility and stability profile toward these highly reactive species) and subsequently exposed to 1.5 bar H_2. Despite their presumed higher reactivity, neither cryptand-encapsulated potassium nor caesium aluminyl showed definitive oxidative addition to form [(crypt)AM][**1'(H)$_2$**]. At lower temperatures (298 K), no reaction was observed; at mild heating (313 K), both complexes underwent partial decomposition, evidenced by new, ill-defined signals in the ^{1}H NMR spectra and the absence of characteristic hydride peaks.



Scheme 7. Activation of H_2 using "naked" aluminyl systems.

Taken collectively, these data reveal that, unlike the dimeric caesium aluminyl, monomeric and "naked" aluminyl ion pairs of [**1'**]$^-$ do not cleanly activate H_2 under the tested conditions. Although such species can, in principle, adopt transiently contacted geometries, our observations suggest that the dual-metal cooperation or pre-organization in dimeric frameworks may be pivotal for mediating H_2 cleavage in the aluminyl context.

1.3.5.3 H_2 Activation of Monomeric Aluminyls in the Presence of CsF and CsHMDS salts

A central takeaway from our DOSY NMR studies (Section 1.3.3) is that "naked" or separated ion pairs of the aluminyl anion [**1'**]$^-$ can equilibrate with partially contacted forms in solution, a process contingent on the presence and coordination state of the alkali-metal cation. Concurrently, our initial exploration of H_2 activation by monomeric aluminyls revealed that, in most instances, they either failed to cleave H_2 or decomposed when used in isolation (Section 1.3.5.2). The standout exception was a serendipitous discovery, trace additions of caesium hexamethyldisilazide (CsHMDS) enabled [(crypt)Cs][**1'**] to activate H_2 at relatively mild conditions. This finding hinted that free or weakly complexed Cs^+ ions might act as Lewis acid co-factors or bridging cations that promote a higher aggregated "dimer-like" arrangement around the aluminium centre, thereby rendering dihydrogen cleavage feasible.

In a more systematic assessment of this phenomenon, substoichiometric amounts of CsHMDS (~ 25 mol% relative to aluminyl) were added to a solution of the cryptand-based monomeric aluminyl [(crypt)Cs][**1'**]. The reaction was performed in fluorobenzene under an inert atmosphere, with 1.5 bar of H_2 introduced at room temperature (298 K). As illustrated in Figure 16, the ^{1}H NMR spectrum after 24 h showed complete consumption of [(crypt)Cs][**1'**] and the appearance of new resonances corresponding to the dihydride product [(crypt)Cs][**1'(H)$_2$**], which matched an independently prepared reference sample (Section 1.3.6). Crucially, the same reaction without CsHMDS yielded no observable H_2 cleavage, thereby underscoring the pivotal role of free Cs^+ ions in facilitating aluminium-mediated bond activation. Although the specific mechanism remains under investigation, the data support a model wherein added CsHMDS partially dissociates, releasing solvated Cs^+ cations that interact with the aluminyl centre in a manner conducive to forming and stabilising an Al···H_2 transition state or intermediate.

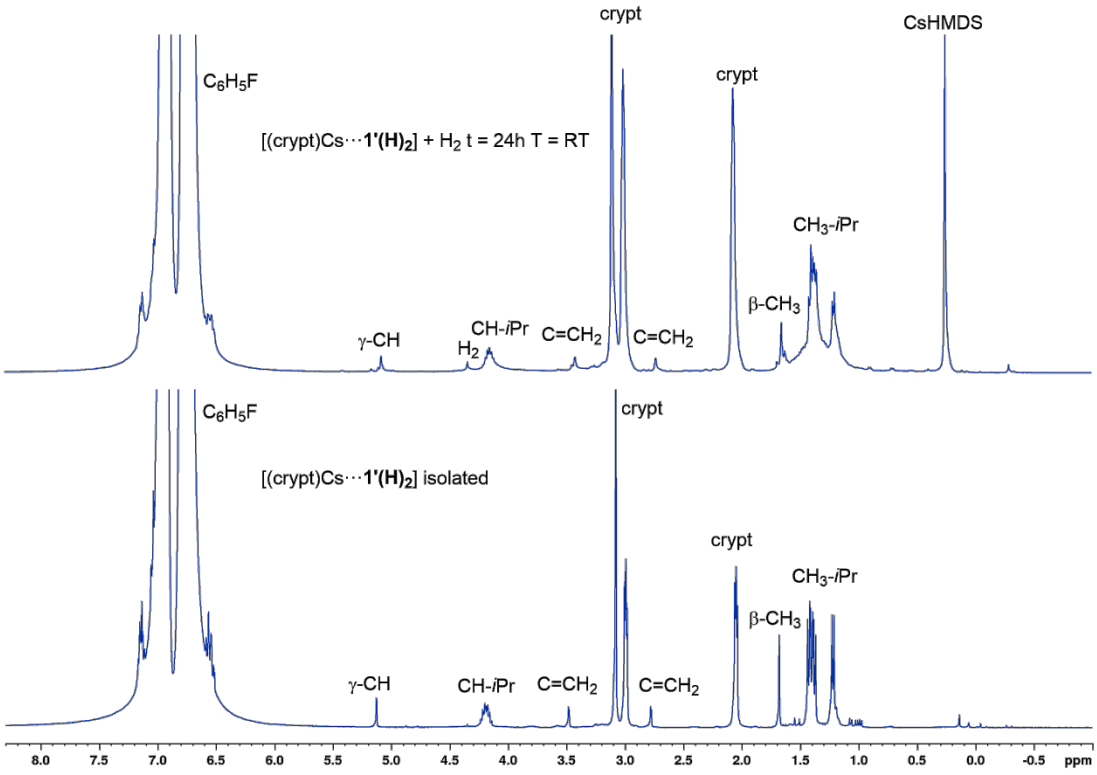
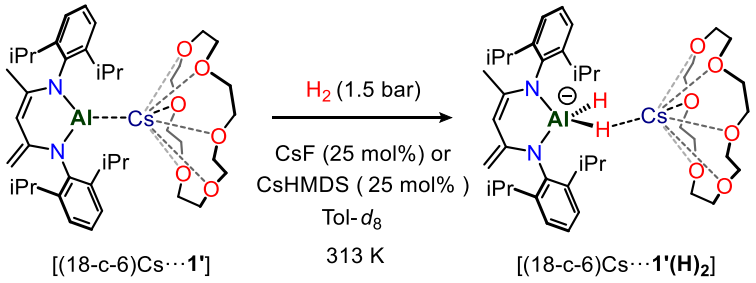


Figure 16. Stacked ^{1}H NMR (400 MHz, *C_6H_5F*, 298 K) spectra for the reaction of [(crypt)Cs···**1'**] and CsHMDS (~ 25 mol% relative to aluminyl) with H_2 (1.5 bar) in fluorobenzene at 298 K. The top trace shows the system after 24 h; bottom trace, the isolated dihydride [(crypt)Cs···**1'(H)$_2$**]).

To probe the generality of this phenomenon, we next examined whether other sources of Cs^+ ions, such as caesium fluoride (CsF), could facilitate H_2 cleavage by monomeric aluminyls, [(crypt)AM][**1'**] and [(crown)AM···**1'**]. The robust complex [(18-c-6)Cs···**1'**] already known for its inertness toward H_2 alone (Section 1.3.5.2), was chosen for these studies. In a typical experiment, 14 µmol of [(18-c-6)Cs···**1'**] was dissolved in 0.5 mL of toluene-d_8 and transferred to a J. Young-valve NMR tube. A substoichiometric amount of CsF (~ 25 mol%) was then added to this pale-yellow solution under an inert atmosphere, followed by three freeze-pump-thaw cycles. Finally, the tube was pressurised with 1.5 bar of H_2 and kept at room temperature (298 K) for 24 h. Under these mild conditions, no immediate changes were detected by ^{1}H NMR, indicating that ambient-temperature reactivity remained negligible.

However, upon heating the reaction mixture to 313 K, however, a distinct transformation began to unfold, and after approximately 19 h, complete consumption of [(18-c-6)Cs···**1'**] was observed by ^{1}H NMR. Concomitantly, new signals consistent with the dihydride complex [(18-c-6)Cs···**1'(H)$_2$**] emerged, mirroring those from an independently synthesised sample of such complex (Section 1.3.6). Figure 17 illustrates the progression of this reaction: the top trace shows the starting monomeric aluminyl in toluene-d_8, and the middle spectrum confirms the presence of H_2 (δ ~ 4.5–4.6 in toluene-d_8) alongside unperturbed [(18-c-6)Cs···**1'**] immediately after CsF addition at room temperature. The bottom trace, recorded after 19 h at 313 K, reveals the complete disappearance of the monomeric aluminyl signals from [(18-c-6)Cs···**1'**] and the emergence of a new resonance pattern corresponding to the dihydride product [(18-c-6)Cs···**1'(H)$_2$**], Scheme 8.



Scheme 8. Activation of H_2 using contacted monomeric aluminyl systems in presence of CsF or CsHMDS salts.

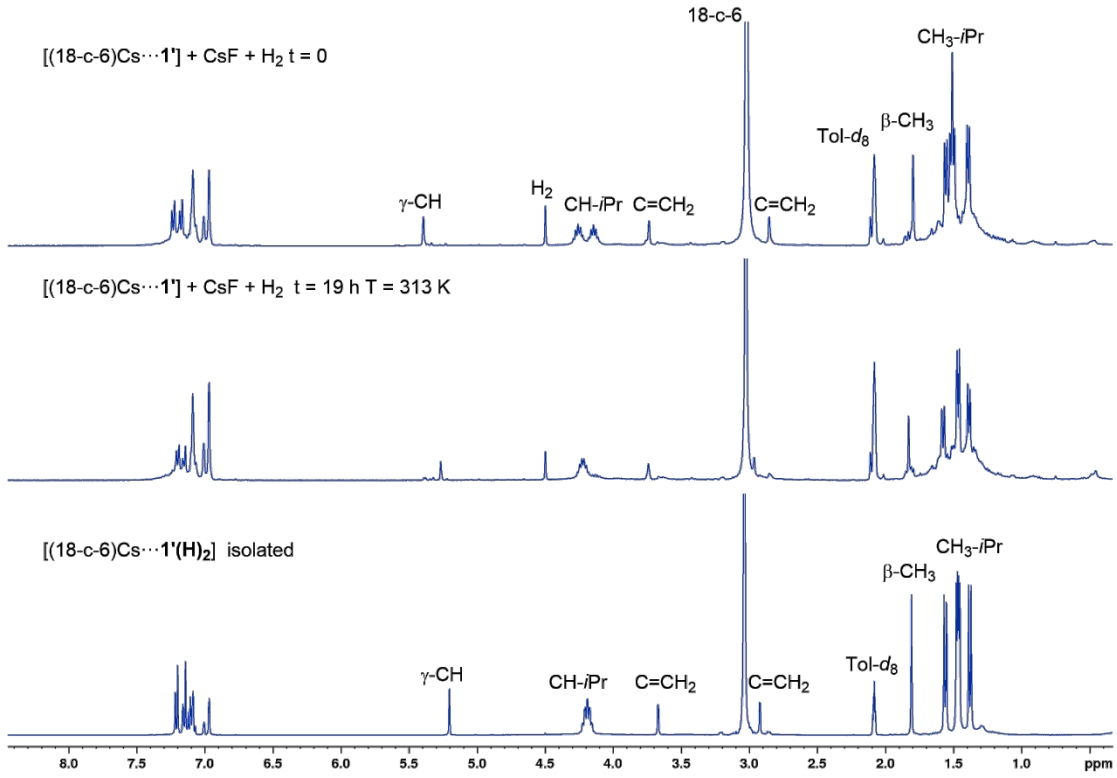


Figure 17. Stacked ^{1}H NMR (400 MHz, Tol-d_8, 298 K) spectra illustrating the reaction of [(18-c-6)Cs···**1'**] with CsF and H_2 (1.5 bar) in Tol-d_8 at 313 K. The top spectrum depicts the solution immediately after CsF addition and H_2 introduction (t =0); the middle trace the reaction after 19 h at 313 K; and the bottom spectrum, the isolated dihydride [(18-c-6)Cs···**1'(H)$_2$**]).

Importantly, while CsHMDS provides a strongly basic co-ligand ($HMDS^-$) that might intercept or transiently bind the aluminyl centre, CsF introduces only F^-, a comparatively weaker base in non-polar solvents. Despite this difference, both salts ultimately yield free Cs^+ in solution, which appears to be the common factor driving H_2 activation. Thus, even though CsHMDS and CsF are not equivalent in their basicity, both can donate Cs^+ ions that reorganise monomeric aluminyls into a more active arrangement. Mechanistically, the higher basicity of $HMDS^-$ may facilitate partial deprotonation events or alternative coordination equilibria, whereas F^- remains more inert under these conditions. Nonetheless, in both scenarios, the availability of free Cs^+ seems key to unlocking the latent reactivity of anionic aluminium(I) species toward H_2 activation.

Interestingly, similar results leading to the formation of [(18-c-6)Cs···**1'(H)$_2$**] was obtained by replacing CsF with CsHMDS during the activation of H_2 [(18-c-6)Cs···**1'**] at 313 K, Scheme 8. However, attempts to replicate this CsF

strategy using the cryptand-based aluminyl [(crypt)Cs][**1'**] did not yield a clean dihydride product. Instead, partial decomposition was observed even at room temperature, indicating that the nature of the supporting ligand and specific solvation environment of Cs^+ can critically affect reactivity pathways. Nonetheless, the overall conclusion from these Cs^+ doping experiments is that additional sources of free Cs^+, be it CsHMDS or CsF, can reorganise a monomeric (or "naked") aluminyl into a more active state capable of cleaving H_2, presumably via the formation of a transient, dimeric-like transition state.

Although the precise mechanistic details remain to be fully elucidated, a plausible scenario is that free Cs^+ solvated by crown ether or cryptand ligands migrates into the vicinity of the aluminyl anion [**1'**]$^-$ and re-establishes partial contact with the BDI framework and/or solvent molecules (toluene). This reorganised arrangement is structurally akin to a "dimeric-like" intermediate, wherein Al···H_2 coordination becomes feasible. The alkali-metal centre may help stabilize the transition state by weakly binding the incoming H_2 molecule or by polarizing the Al–H bonds as they form. Notably, the large ionic radius of Cs^+ likely lowers the barrier for such fluxional metal–ligand rearrangements, explaining the relative ease of H_2 activation once a sufficient concentration of free Cs^+ is present. This phenomenon parallels certain transition-metal systems, where cooperative cation or ligand interactions expedite bond activations that might otherwise be kinetically hindered. Hence, even small amounts of free Cs^+ can transform what is typically a stable, unreactive aluminyl into one that undergoes quantitative H_2 cleavage under relatively mild conditions.

Beyond its immediate mechanistic implications, these results demonstrate that monomeric aluminyl frameworks, which alone show minimal reactivity toward dihydrogen, can be coaxed into efficient H_2 activation upon doping with substoichiometric Cs^+ salts. Whether introduced in the form of CsHMDS or CsF, free caesium cations appear to shift the equilibrium toward a higher aggregated arrangement conducive to oxidative addition. The combination of DOSY data (showing equilibria between separated and contacted species), independent evidence of dihydride formation, and direct parallels with known dimeric aluminyls collectively underscores the pivotal role of cation speciation. In doing so, it provides another striking illustration of how fine-tuning alkali-metal coordination and solvation can unlock latent small-molecule reactivity in low-valent aluminium complexes, a principle that resonates with numerous transition-metal catalytic paradigms.

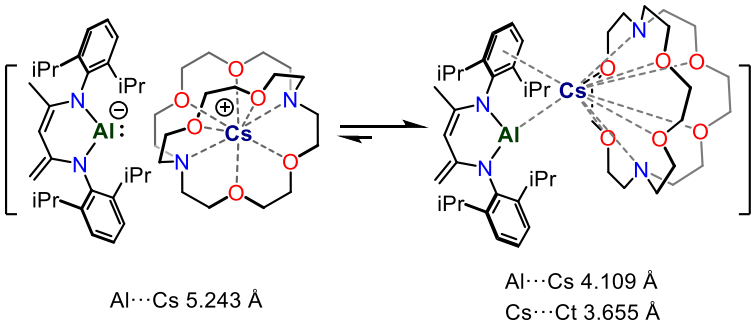
1.3.5.4 Computational Mechanistic Insights: H_2 Activation by Aluminyls and the Role of "free" Alkali Metals

Although our experimental results strongly indicate that free or partially coordinated alkali-metal Cs^+ cations are integral to H_2 activation by aluminyl complexes, [(crypt)Cs][**1'**] and [(18-c-6)Cs···**1'**] detailed mechanistic pathways remain to be fully delineated. With this in mind, we initiated a collaboration with the group of Prof. Agustí Lledós at the Universitat Autònoma de Barcelona (UAB). Their ongoing theoretical studies aim to elucidate how the presence, or absence, of solvated alkali-metal cations modifies reaction pathways for dihydrogen cleavage at the electron rich aluminyl centre rationalise why certain "naked" monomeric ion pairs fail to react unless supplemented with free Cs^+. While the calculations are still in progress, the preliminary insights below already offer a compelling framework that aligns with our experimental observations.

The central objective of the computational inquiry is twofold. First, it seeks to confirm whether the dynamic equilibria revealed by ^{1}H DOSY NMR (Section 1.3.3) for certain aluminyl ion pairs (e.g., [(crypt)Cs][**1'**]) genuinely persist in solution, or if they represent mere bench-stable or artifact states. Second, it probes how different aggregation states, monomeric ion pairs, separated "naked" anions, or dimeric assemblies, impact the energy barriers and mechanistic details of H_2 cleavage. In pursuit of these goals, the Lledós group employed density functional theory (DFT) methods to optimise and compare potential intermediates, transition states, and reaction products, introducing explicit ligand solvation of the potential "free" alkali metals AM^+ counterions, $[AM(toluene)]^+$, generated from ionisation of either CsF or CsHMDS, and varying ionic coordination.

With special focus on the caesium aluminyls who showed broad scope during H_2 activation, a foundational aspect of the project involved optimising both the "contacted" and "separated" forms of [(crypt)Cs][**1'**] (Scheme 9), drawing upon the crystallographic coordinates and the solution behaviour described in Sections 1.3.3 and 1.3.4. The results suggest that these two ionic states differ by only a small Gibbs free-energy margin (3 kcal/mol), strongly supporting the fluxional equilibria that our DOSY data implied. Notably, the calculations indicate that Cs^+ can shuttle between partial encapsulation within the cryptand and a more extended arrangement near the aluminyl centre, as seen crystallographically (see Section 1.3.4.1) confirming how large alkali-metal cations may adopt multiple binding modes within these aluminyls. Similar fluxional AM^+–ligand dynamics were also found for the potassium analogue

[(crypt)K][**1'**] akin to those labile dynamics reported in transition-metal complexes featuring weakly coordinating anions,[47] a parallel that highlights the unusual but potent role of alkali-metal speciation in main-group chemistry.



Scheme 9. Representation of the dynamic equilibrium observed for the monomeric crypt stabilised aluminyl pairs [(crypt)Cs][**1'**] ⇄ [(crypt)Cs···**1'**].

After establishing that low-energy equilibria exist among various ionic conformations for the crypt stabilised aluminyls, [(crypt)AM][**1'**] ⇄ [(crypt)AM···**1'**] (AM = Cs, K), the calculations turned to the actual cleavage of the H–H bond by these species. In line with our experimental observations, a series of model reactions were explored. When the "naked" aluminyl anion [**1'**]$^-$ was tested in silico for H_2 activation, the computed free-energy barrier was 40 kcal/mol. This result indicates that the aluminyl anion [**1'**]$^-$ can effectively activate H_2 alone without the participation of an alkali metal counterion, reflecting the bimetallic contribution during H_2 activation. This result mirrors our experimental findings, as we observed that the crypt aluminyls, that are in equilibrium between separated and contacted species, [(crypt)AM][**1'**] ⇄ [(crypt)AM···**1'**], generating freely [**1'**]$^-$ anions in solution, not activate dihydrogen.

Similarly, the computational studies result with high activation barriers (> 39–40 kcal/mol) for H_2 using the contacted crown species, [(crown)AM···**1'**] (AM = Na, K, Cs). These computational data echo our unsuccessful attempts to cleave H_2 using monomeric complexes even under thermal conditions without extra Cs^+ doping.

The crucial turning point emerged when coordinatively unsaturated alkali metal cations AM^+ were additionally introduced, as a loosely solvated alkali metal cations in toluene, $[AM(toluene)_n]^+$ within the monomeric aluminyl aggregates of [**1'**]$^-$, either directly from monomeric crypt or crown stabilised species, [(crypt)AM···**1'**] or

[(crown)AM···**1'**], or withing the monomeric species resulting from the dissociation of the dimeric aluminyls [(AM···**1'**)$_2$] ⇄ 2 [AM···**1'**].. Under these conditions, the Gibbs free-energy barriers for H_2 activation dropped significantly (< 20 kcal/mol). These lower barriers qualitatively match our experimental observations that doping a monomeric aluminyl with CsF or CsHMDS (i.e., extra Cs^+) can unlock H_2 cleavage. The calculations thus reinforce the idea that bimetallic cooperation, between Al(I) and alkali metals AM^+, is indispensable for dihydrogen activation.

Figure 18 schematically depicts a representative transition state identified in the computational studies involving the aluminyl anion [**1'**]$^-$ and a "free" Cs^+ counterion, highlighting a new type of activation mode of H_2 potentially involving a "nucleophilic S_N2-like" attack on the H–H bond by the electron rich and nucleophilic Al(I) centre (Al···$\eta^1(H_2)$) aided by the participation of a Cs^+ cation as a hydride acceptor (Al$^-$···(H···H)···Cs^+). Electronic structure analysis suggests a scenario in which the Al(I) centre donates electron density into the σ* orbital of H_2, while Cs^+ helps stabilise the resulting negative charge on the evolving hydride moiety. In essence, the transition state can be viewed as an almost linear Al–H–H–Cs four-centre arrangement, wherein partial hydride transfer to Cs^+ lowers the barrier relative to a purely anionic or monomeric environment. These findings correlate closely with our experimental evidence that purely "naked" aluminyl anions remain inert while dimeric or Cs^+-doped monomeric systems efficiently cleave H_2 under mild conditions.

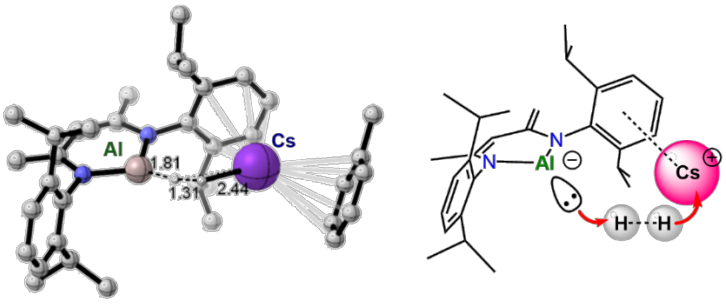


Figure 18. Conceptual depiction of a bimetallic transition state for H_2 bond cleavage involving [**1'**]$^-$ and [Cs(toluene)]$^+$. The reaction pathway indicates a cooperative approach, where the Al··· $\eta^1(H_2)$ interaction is partially stabilised by transient H_2···Cs contact.

While still preliminary, these computational insights provide a coherent model that harmonises with our experimental data:

- DOSY NMR data detected multiple solution states, in particular dynamic solvent-free dimeric species [(AM···**1'**)$_2$] resulting with monomerisation in aluminyl (AM···**1'**) species, and labile crypt monomeric aggregates [(crypt)AM···**1'**] giving free [**1'**]$^-$ anions, consistent with small, computed energy differences between contacted *versus* separated aluminyl pairs.

- H_2 reactivity indicated that extra Cs^+ doping (CsF and CsHMDS) or formation of dimeric species is critical for dihydrogen cleavage, mirroring the lowering of computed barriers for multi-metal scenarios where the involvement of extra or "free" AM^+ cations is needed for energetically accessible activation pathways.

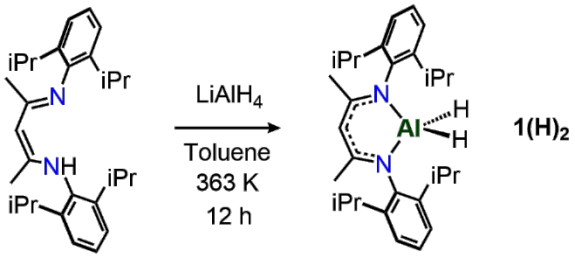
- The mechanistic studies parallel to known transition-metal hydride systems are suggested by the partial "hydride transfer" steps computed in the Al–H–H–Cs transition states.

Moving forward, the Lledós group will refine these models, incorporating explicit solvation with larger clusters of toluene and cryptand/crown ligands, and will explore alternative reaction pathways (e.g., two-step processes or interactions with other small molecules). Such additional layers of complexity could help determine whether further main-group transformations, like C–H or C–F bond activations, might be possible at the newly developed β-diketiminate-stabilised aluminyl via bimetallic modes with participation of alkali metal AM^+ counterions. Once finalised, these computational studies may enable rational design of new Al(I)-based catalysts, leveraging alkali-metal cooperation to achieve broader and more selective small-molecule activations. The synergy between experimental and computational perspectives highlights how bimetallic cooperativity, mediated by alkali-metal cations, can dramatically expand the reactivity profile of electron-rich aluminyl centres. We anticipate a more granular and quantitative understanding of the relevant transition states, which should not only explain our current H_2 reactivity findings but also suggest guidelines for tuning ligand environments to realise new catalytic processes in the main-group arena.

1.3.6 Synthesis of Alkali Metal Dihydridoaluminates

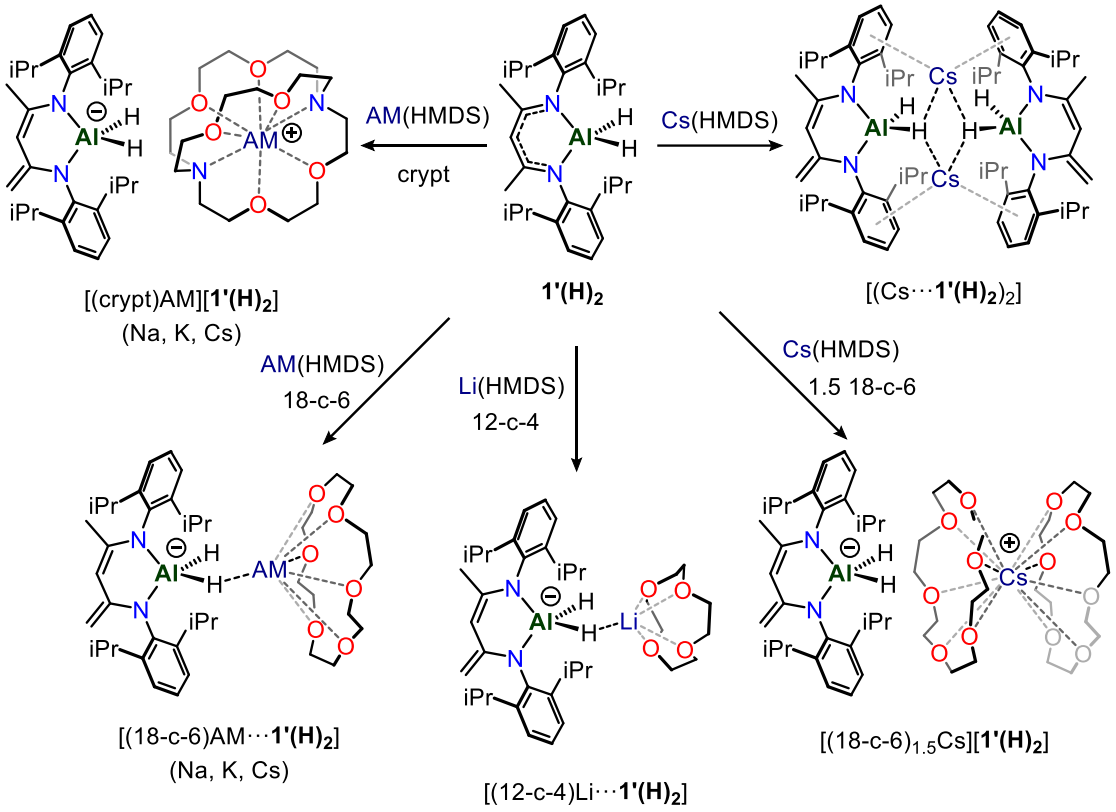
Building on the high reactivity and flexibility exhibited by our β-diketiminate-stabilised aluminyl species (Sections 1.3.1–1.3.4) and aiming to confirm their H_2, activation pathways, we synthetised a novel series of dihydridoaluminates derivatives from the same β-diketiminate ligand skeleton (^{Dipp}BDI). In addition, we reasoned that isolating such alkali-metal Al(III) dihydrides analogous to our previously developed aluminyl systems would permit systematic comparisons of aggregation, coordination state, and reactivity across a broader range of Al(III) complexes.

Our starting point was the neutral aluminium(III) dihydride (^{Dipp}BDI)Al$(H)_2$, denoted as **1(H)$_2$** (Scheme 10). Although protocols for similar complexes are known in the literature,[48] we adopted a modified synthetic procedure that improved yield and reproducibility under our laboratory conditions. A Schlenk was charged with ^{Dipp}BDI(H) and $LiAlH_4$ powder. Then, dry toluene was added, and the resulting grey suspension was stirred for 12 hours at 363 K, this procedure was done carefully given the reaction a H_2 gas production. Then, the resulting suspension was filtered via cannula and the volatiles were removed under vacuum to give a light brown crude. The product was crystallised from a concentrated solution in *n*-hexane at room temperature to give colourless block-shape crystals of **1(H)$_2$**.



Scheme 10. General synthetic protocol to obtain **1'(H)$_2$**.

Once isolated, **1(H)$_2$** was treated with alkali-metal bis(trimethylsilyl)amides (AMHMDS; AM = Li, Na, K, Cs) allowing approaches closely related to those employed for the aluminyls (Section 1.3.1). In this case, deprotonation at the BDI framework transforms **1(H)$_2$** into an anionic aluminium(III) dihydride, [**1'(H)$_2$**]$^-$, which then forms bimetallic ion pairs with Li^+, Na^+, K^+ and Cs^+ counterions. Subsequent addition of donor ligands (either crown ethers or cryptands) allows the isolation of either contacted dimeric pairs or monomeric dihydride complexes, mirroring the aggregation patterns observed among the aluminyl family.



Scheme 11. Synthesis of alkali metal derivatives of the novel anionic β-diketiminate-based aluminium(III) $[\mathbf{1'(H)_2}]^-$ complexes (HMDS = bis(trimethylsilyl)amide).

An initial, donor-free route involved reacting **1(H)₂** with CsHMDS in toluene at room temperature for 5 hours, affording an almost colourless solution. Partial removal of the solvent, followed by addition of *n*-hexane, yields a pale-yellow suspension. After cannula filtration, the resulting solid can be isolated as a contacted dimeric pair, $[(Cs\cdots\mathbf{1'(H)_2})_2]$. Only the caesium dimeric pair was obtained under these conditions: attempts to generate the lithium, sodium or potassium analogues repeatedly led to intractable mixtures upon heating or no observable reaction at room temperature. This cation selectivity is reminiscent of the heavier-metal preference observed for aluminyl dimer $[(AM\cdots\mathbf{1'})_2]$ formation (Section 1.3.1). As far as we know, this Cs dihydride dimer is unreported in the literature, underlining the novelty of this synthetic route to access highly stable aluminium hydride species which are soluble in aromatic solvents.

By contrast, introducing two-dimensional donor ligands (crown ethers) shifts the equilibrium away from dimeric aggregates, yielding monomeric ion pairs $[(crown)AM\cdots\mathbf{1'(H)_2}]$. Specifically, combining **1(H)₂** with AMHMDS (AM = Li, Na, K, or Cs) in toluene and immediately adding the appropriate crown ether (12-c-4 for Li^+,

18-c-6 for Na^+, K^+ and Cs^+) results in the precipitation of a yellowish solids. After filtering off the supernatant and washing with *n*-hexane, the monomeric crown-stabilised species can be isolated in solid form. These contacted ion pairs, now bearing Al(III)–H moieties, are analogous to the "monomeric" aluminyls previously secured under similar conditions (Section 1.3.2.2).

A further expansion of this methodology harnesses crypt to produce fully separated ion pairs, [(crypt)AM][**1'(H)$_2$**] (AM = Na, K, Cs), again via deprotonation of the BDI backbone in toluene. In these cases, K^+ or Cs^+ (and occasionally Na^+) can be fully encapsulated by the cryptand, leaving the anionic species [**1'(H)$_2$**]$^-$ "naked". In parallel to the aluminyl scenario, the Li derivative could not be isolated, presumably owing to less favourable Li^+ encapsulation or competing side reactions. The resulting crypt-stabilised dihydrides exemplify fully separated or "naked" Al(III)–H anions, again paralleling the alkali-metal–induced structural motifs observed among the aluminyl family.

These bimetallic systems were characterised by conventional techniques, such as ^{1}H, ^{11}B, ^{13}C, ^{19}F, ^{1}H-^{1}H COSY, ^{1}H-^{13}C HSQC, ^{1}H-^{13}C HMBC, ^{1}H DOSY NMR, single X-ray diffraction, elemental analysis, and infrared spectroscopy. The dihydride aluminate compounds [(Cs···**1'(H)$_2$**)$_2$], [(crown)AM···**1'(H)$_2$**] (AM = Li, Na, K, Cs), [(crypt)AM][**1'(H)$_2$**] (AM = Na, K, Cs), showed IR bands at 1685 and 1739 cm^{-1} corresponding to Al–H stretching modes.

1.3.6.1 Nuclear Magnetic Resonance (NMR) spectroscopy studies.

1.3.6.2 Contacted Dimeric Aluminium Dihydrides

In order to elucidate the structural and electronic features of this newly prepared caesium dimeric dihydride, [(Cs···**1'(H)$_2$**)$_2$], detailed NMR spectroscopy experiments were performed in toluene-d_8 at 298 K. This complex is unreported in the literature, making its NMR profiles particularly noteworthy. Overall, their ^{1}H NMR patterns closely mirror those found in dimeric aluminyl systems (see Section 1.3.2.1), yet the presence of two Al–H hydride ligands on each aluminium(III) centre yields distinct resonances that often appear broad or partially overlapping. This broadness reflects the sluggish relaxation of the hydrides on the NMR timescale, coupled with fluxional behaviour in solution, causing them to merge with nearby signals from the β-diketiminate framework. Selected ^{1}H and ^{13}C resonances for [(Cs···**1'(H)$_2$**)$_2$] is summarised in Table 6.

For the dimeric aluminium(III) dihydride, [(Cs···**1'(H)$_2$**)$_2$], the aromatic region (δ 7.2–6.9) exhibits partially overlapping signals attributable to the phenyl substituents of the BDI ligand, while the characteristic γ-CH backbone proton resonates as a singlet at δ 5.17 (Figure 19). Two overlapping septets at δ ~ 3.8, corresponding to the isopropyl methine (CH) groups of the Dipp substituents, and two more singlets (δ 3.73 and 2.87) reflect the alkene functionality (CH_2=C) within the deprotonated BDI backbone. In the aliphatic region, a distinct singlet at δ 1.62 is assigned to the methyl substituent of the BDI ring, and four sets of doublets in the δ ~ 1.4–1.1 range indicate the methyl groups of the Dipp units. Crucially, the Al–H resonances appear as a broad singlet at δ ~ 4.0, overlapping partially with the isopropyl and alkene signals and confirming the dual hydride nature of each dimeric unit.

Corroborating these ^{1}H NMR findings, ^{13}C NMR spectrum reveals alkene carbon resonating at δ 77.6 and a backbone γ-CH carbon near δ 100, in line with typical β-diketiminate environments. Attempts to observe ^{27}Al signals for this dimeric pair, [(Cs···**1'(H)$_2$**)$_2$], yielded no discernible resonances, likely owing to rapid relaxation or significant line broadening characteristic of electron-rich Al(III) centres. However, in the ^{133}Cs NMR spectrum, a broad singlet emerges at δ –7.7, suggestive of a single yet fluxional alkali-metal environment consistent with dynamic Al(III)–H···Cs interactions.

Altogether, these NMR data confirm the structural integrity and bimetallic nature of [(Cs···**1'(H)$_2$**)$_2$], while underscoring parallels with previously reported dimeric aluminyl species.[49] The pronounced overlap and breadth of the Al(III)–H hydride signal highlights the cooperative, potentially fluxional binding of Al–H···Cs motifs. This reflects not only its dimeric aggregation states but also its dynamic behaviour in solution.

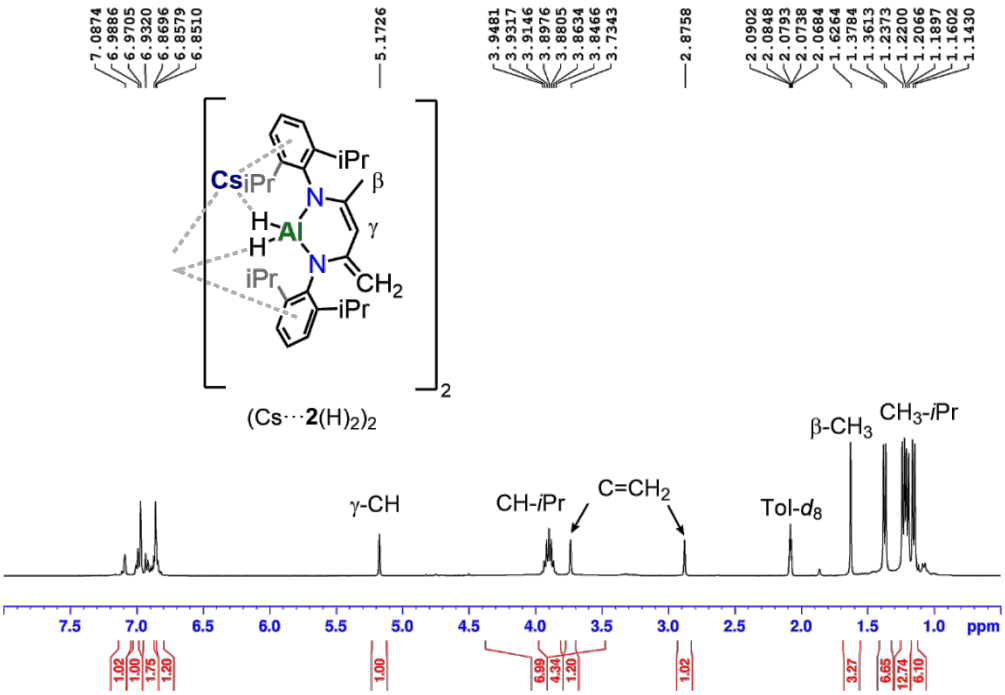


Figure 19. ^{1}H NMR (400 MHz, Tol-d_8, 298 K) of [(Cs···**1'(H)$_2$**)$_2$].

Table 6. Selected ^{1}H and ^{13}C{^{1}H} NMR signals (δ, ppm) in Tol-d_8 at 298 K of [(Cs···**1'(H)$_2$**)$_2$].

Complex	H_2	γ-CH		$C=CH_2$		β-Me		
	^{1}H	^{1}H	^{13}C	^{1}H	^{13}C	^{1}H	^{13}C	^{133}Cs
[(Cs···**1'(H)$_2$**)$_2$]	4.0	5.17	99.2	3.73 2.87	77.6	1.62	23.2	-7.7

1.3.6.3 Monomeric ion pairs (MIP) of alkali metal aluminium dihydrides

Following their synthesis, the monomeric ion pairs [(crown)AM···**1'(H)$_2$**] (where crown is 12-c-4 for Li^+, 18-c-6 for Na^+, K^+ or Cs^+) were investigated by NMR spectroscopy under various solvent conditions, dictated by the solubility of each alkali-metal dihydridoaluminates. The lithium congener, [(12-c-4)Li···**1'(H)$_2$**] was characterised in THF-d_8, potassium and caesium analogues [(18-c-6)K···**1'(H)$_2$**] and [(18-c-6)Cs···**1'(H)$_2$**] in toluene-d_8, and the sodium complex [(18-c-6)Na···**1'(H)$_2$**] in non-deuterated fluorobenzene (FB). Although these solvents introduce minor chemical-shift variations, the overarching multiplicity and chemical-shift ranges remain consistent across the series, underscoring the common structural motif of a β-diketiminate (BDI) backbone with Al(III)–H hydride units.

In general, each monomeric system exhibits a singlet in the δ 4.5–5.2 range for the BDI γ-CH group, along with two partially overlapping septuplets near δ 3.7–4.2 corresponding to the isopropyl methine CH-Dipp substituents. The alkene protons (CH_2=C) typically appear as two separate resonances (δ ~ 3.6 and 2.1), reflecting partial double-bond character in the deprotonated BDI ring. Meanwhile, the ring-ether environments of the crown ligands often manifest as singlets or narrow multiplets around δ 3.0, with slight variations depending on the metal and solvent. In the aliphatic region, a singlet near δ 1.6–1.8 corresponds to the BDI backbone methyl group, while a series of doublets between δ 1.6–1.2 marks the methyl substituents of the Dipp units. Collectively, these observations confirm a consistent monomeric dihydroaluminate framework for each alkali-metal cation under the chosen donor and solvent conditions.

Further support for these assignments comes from ^{13}C NMR spectra, which locate the alkene carbons in the δ 70–76 range and the γ-CH carbon at δ ~ 100, markers of a partially conjugated β-diketiminate skeleton. In all cases, however, ^{27}Al NMR spectra remained silent, presumably due to rapid relaxation or line broadening commonly encountered in electron-rich Al(III) complexes. By contrast, a broad ^{133}Cs resonance at δ 30.9 was observed for [(18-c-6)Cs···**1'(H)$_2$**], indicating a distinct caesium environment that differs notably from free CsHMDS (δ 119.2).[41] Taken together, these results demonstrate the formation of stable monomeric ion pairs for Li^+, Na^+, K^+, and Cs^+ under carefully selected donor ligands and solvent conditions, while also highlighting the dynamic nature of the Al(III)–H···AM^+ interaction. As illustrated in Figure 20 for the caesium congener [(18-c-6)Cs···**1'(H)$_2$**], the observed ^{1}H NMR profile closely resembles that of the analogous potassium complex [(18-c-6)K···**1'(H)$_2$**], underscoring how crown-based monomeric ion pairs can display comparable spectral features regardless of the specific alkali-metal centre involved.

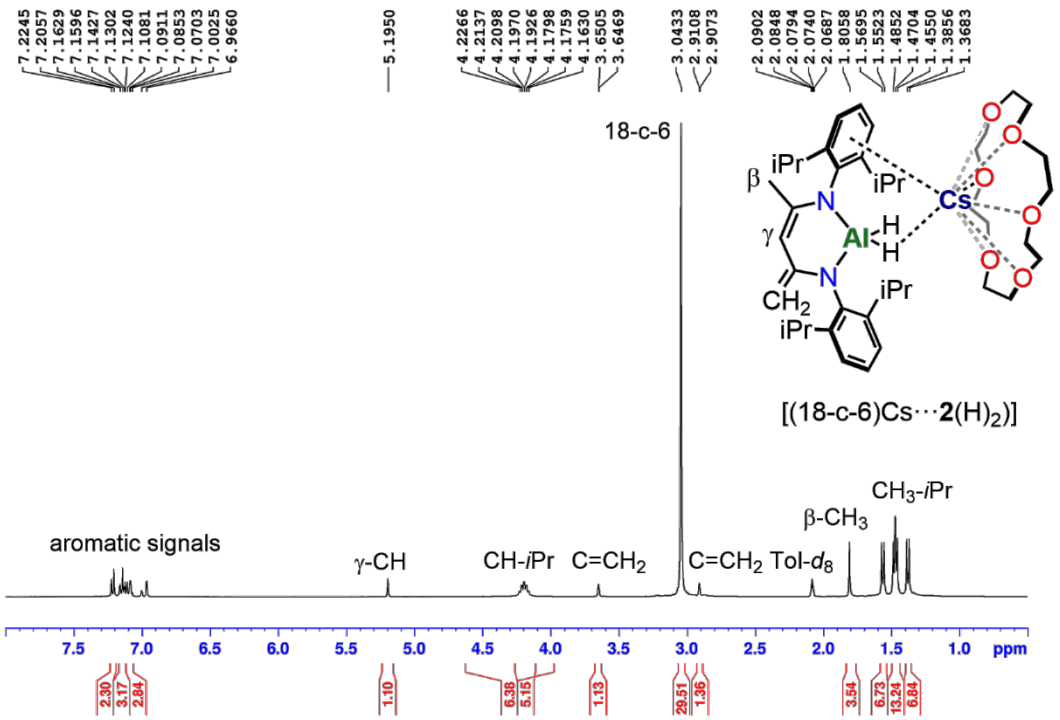


Figure 20. ^{1}H NMR (400 MHz, Tol-d_8, 298 K) of [(18-c-6)Cs···**1'(H)$_2$**)].

Table 7. Selected ^{1}H and ^{13}C{^{1}H} NMR signals (δ, ppm) at 298 K of [(crown)AM···**1'(H)$_2$**] where AM =Li, Na, K or Cs.

Complex	γ-CH		C=CH$_2$		β-Me		crown		^{7}Li or
	^{1}H	^{13}C	^{1}H	^{13}C	^{1}H	^{13}C	^{1}H	^{13}C	^{133}Cs
[(12-c-4)Li···**1'(H)$_2$**] in THF-d_8	4.57	99.3	2.87[a] 2.17[a]	73.7	1.42	24.9	3.56	69.0	-0.5
[(18-c-6)Na···**1'(H)$_2$**] in FB	5.16	98.4	3.50 2.70	73.6	1.66	23.0	3.10	67.6	
[(18-c-6)K···**1'(H)$_2$**] in Tol-d_8	5.20	99.0	3.47 2.90	75.8	1.74	23.8	2.90	69.9	
[(18-c-6)Cs···**1'(H)$_2$**] in Tol-d_8	5.10	98.4	3.64[b] 2.90[b]	75.2	1.80	24.3	3.04	69.8	30.9

[a] Doublet (J = 2.2 Hz). [b] Doublet (J = 1.4 Hz).

1.3.6.4 Separated Aluminium dihydrides

The final class of complexes, [(crypt)AM][**1'(H)$_2$**] (AM = Na, K, Cs), exhibited limited solubility in less polar solvents such as benzene or toluene. Therefore, NMR analyses were conducted in non-deuterated fluorobenzene (C_6H_5F). Despite the

intense solvent peaks in the δ 7.3–6.3 region overlapping with the aromatic resonances of the β-diketiminate (BDI) ligand and the Dipp substituents, the key signals were sufficiently distinguishable to allow confident assignments.

In general, the three complexes [(crypt)Na][**1'(H)$_2$**], [(crypt)K][**1'(H)$_2$**] and [(crypt)Cs][**1'(H)$_2$**] display nearly identical ^{1}H NMR profiles (Table 8). Their shared structural hallmark is a fully encapsulated alkali-metal cation by the crypt macrocycle, leaving the [**1'(H)$_2$**]$^-$ anion unconnected to the hydride Al–H units. The BDI backbone γ-CH proton resonates around δ 5.0–5.1 as a singlet, while the alkene segment (CH_2=C) emerges at δ 3.5 and 2.7. These alkene resonances may appear as singlets or small doublets (J = 1.5–2.0 Hz), depending on sample concentration and spectral resolution. The cryptand ligand itself shows three major resonances at δ ~ 3.0, 2.9, and 2.0 (multiplets or a mixture of singlets and multiplets), corresponding to the bridging CH_2 groups in crypt. In the aliphatic region, a singlet near δ 1.6 is assigned to the BDI backbone methyl group, with multiple doublets (δ 1.4–1.1) indicating the isopropyl methyls on the Dipp substituents.

Corroborating these ^{1}H NMR findings, the ^{13}C NMR spectra locate the alkene carbons at δ ~ 74 and the γ-CH carbon near δ ~ 99, typical of partially conjugated β-diketiminate rings. Although no ^{27}Al resonance is detected, likely due to the broadening or rapid relaxation commonly encountered in electron-rich Al(III) hydride species, ^{133}Cs NMR measurements of [(crypt)Cs][**1'(H)$_2$**] reveal a broad peak at δ 190.8, shifted significantly from the reference value δ 119.2 of free CsHMDS.[41]

Overall, these NMR results confirm that fully encapsulating the alkali metal with cryptand effectively isolates the dihydride [**1'(H)$_2$**]$^-$ anion in solution, precluding direct alkali-metal interactions and underscoring the structural and electronic parallels with the separated-ion-pair aluminyl complexes (Section 1.3.2.3).

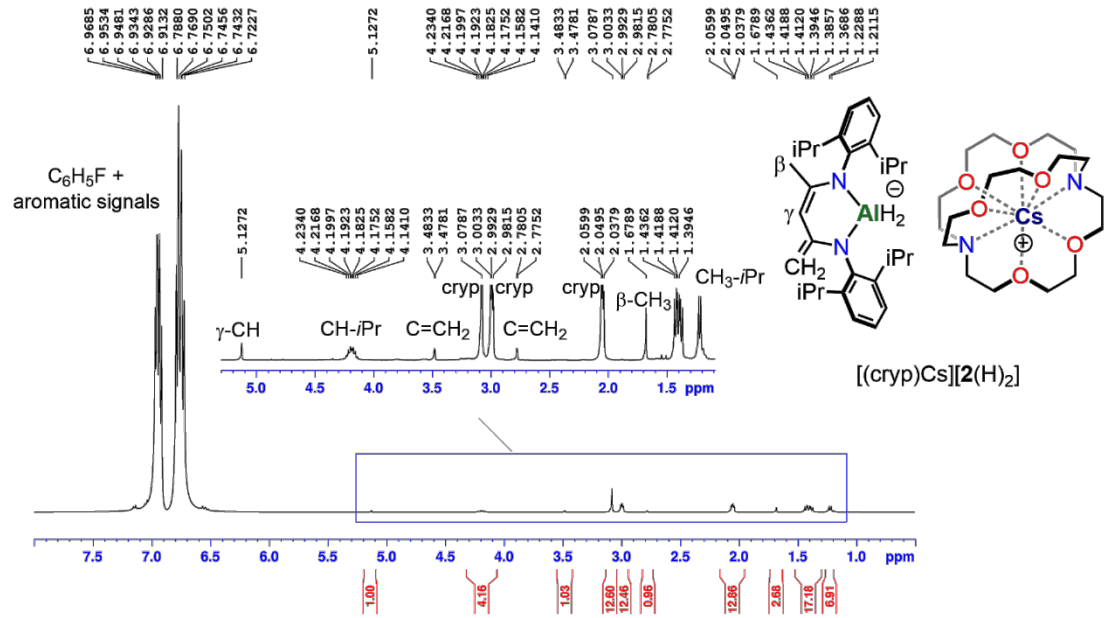


Figure 21. ^{1}H NMR (400 MHz, C_6H_5F, 298 K) of [(crypt)Cs][**1'(H)$_2$**].

Table 8. Selected ^{1}H and ^{13}C{^{1}H} NMR signals (ppm) in C_6H_5F at 298 K of [(crypt)AM][**1'(H)$_2$**] (AM = Na, K, Cs).

Complex	γ-CH		C=CH$_2$		β-Me		crypt		
	^{1}H	^{13}C	^{1}H	^{13}C	^{1}H	^{13}C	^{1}H	^{13}C	^{133}Cs
[(crypt)Na][**1'(H)$_2$**]	5.06	98.9	3.40 2.71	73.4	1.62	23.8	3.02 2.97 2.02	70.1 67.2 53.4	
[(crypt)K][**1'(H)$_2$**]	5.06	98.9	3.40 2.71	73.4	1.63	23.8	3.08 2.96 1.98	70.1 67.2 53.4	
[(crypt)Cs][**1'(H)$_2$**]	5.12	98.9	3.47[a] 2.77[a]	73.8	1.67	23.5	3.07 2.99 2.04	70.1 67.2 54.8	190.8

[a] Doublet (J = 2.1 Hz).

1.3.7 Diffusion Order SpectroscopY (DOSY) NMR studies.

Having established that DOSY NMR proved critical for elucidating the solution-phase aggregation states of aluminyl complexes (Section 1.3.3), we applied a similar approach to these newly synthetised aluminium(III) dihydride species. By analysing their diffusion coefficients (D, m^2/seg) and comparing them with theoretical molecular weights (MW, g/mol), we aimed to determine whether each dihydride species persists in solution as a discrete dimer, a monomeric ion pair, or a dynamic

mixture of aggregated states. As with the aluminyls, we employed both our own external calibration (OEC) strategy and Stalke's established calibration curves (ECC) to estimate MW from the measured diffusion coefficients,[42] taking into account hydrodynamic shapes classified as dissipated spheres and ellipsoids (DSE) or related models (Table 9 and Table 10).

Initially, we examined the contacted dimeric species, [(Cs···**1'(H)$_2$**)$_2$]. ^{1}H DOSY experiments in toluene-d_8 revealed a single diffusing entity (Figure 22), suggesting that, under these conditions, the complex does not persist as a fully dimeric assembly in solution. Instead, the measured diffusion coefficient corresponds to an MW of 783 g/mol (ECC) or 637 g/mol (OEC), values more consistent with a monomeric species (calculated MW of 579 g/mol) than with the theoretical dimeric MW of 1157 g/mol. We note that minor discrepancies likely reflect partial solvation by one or two toluene molecules. Consequently, the DOSY data indicate that [(Cs···**1'(H)$_2$**)$_2$] predominantly adopts a monomeric form (Cs···**1'(H)$_2$**) in solution, aligned with analogous result for caesium dimeric aluminyl that also favours partial dissociation in aromatic solvents, [(Cs···**1'**)$_2$] ⇄ 2 (Cs···**1'**).

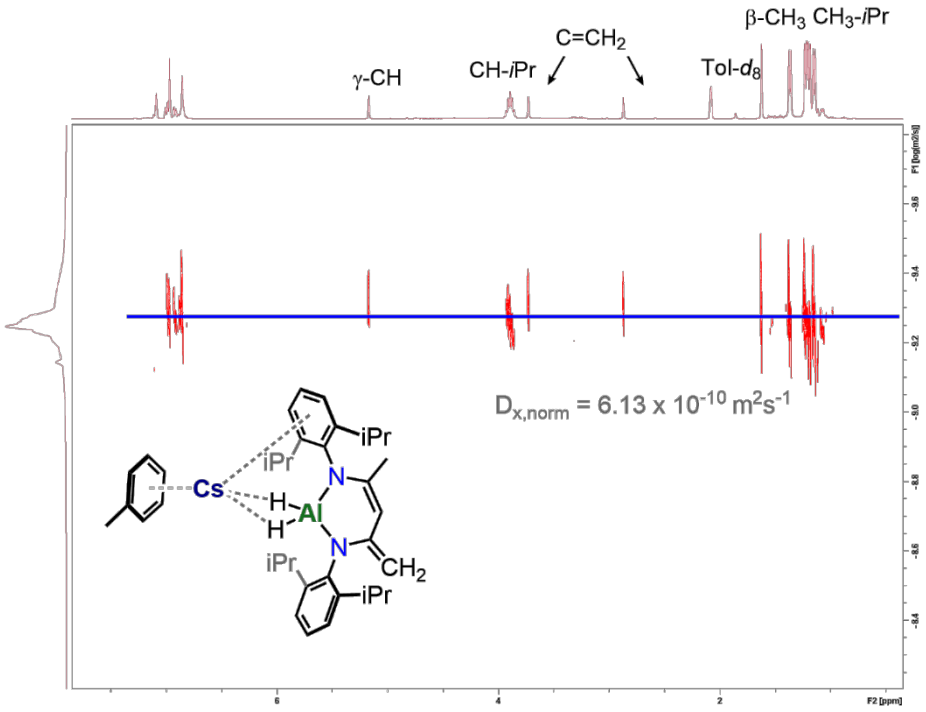


Figure 22. ^{1}H DOSY NMR 400 MHz of [(Cs···**1'(H)$_2$**)$_2$]···(Tol)$_n$ in Tol-d_8 at 298 K.

Table 9. D (m^2s^{-1}) and MW values for of [(Cs···**1'(H)$_2$**)$_2$] in Tol-d_8 at 298 K.

Species	$D_{x,norm}$ ($m^2 \cdot s^{-1}$)	MW found (g/mol)	MW calc (g/mol)	MW error (%)
Diffusing species	$6.13 \cdot 10^{-10}$	783[a]; 637[b]		
[(Cs····**1'(H)$_2$**)$_2$]			1157	48[a];82[b]
(Cs····**1'(H)$_2$**)			579	3[a];9[b]
(Cs····**1'(H)$_2$**)···Tol			671	12[a];5[b]

[a] *Values from ECC-CS*. [b] *Values from OEC (own external calibration method).*

Turning to the monomeric crown aluminium dihydride pairs, [(crown)AM···**1'(H)$_2$**], each system (12-c-4 for Li^+, 18-c-6 for Na^+, K^+ or Cs^+) was probed under its respective solvent conditions, dictated by solubility requirements. For instance, [(12-c-4)Li···**1'(H)$_2$**] in THF-d_8 show a single diffusing species, and analysing the diffusion coefficients, we derived an MW of 663 g/mol (OEC) or 644 g/mol (ECC-DSE), in excellent agreement with the calculated MW of 629 g/mol for a contacted Li monomeric pair. Similarly, the sodium congener [(18-c-6)Na···**1'(H)$_2$**], despite initial hints of multiple diffusing species in solution (recorded in fluorobenzene), exhibits diffusion coefficients converging to an MW of 850–950 g/mol, again pointing toward a single contacted entity (the theoretical MW is 732 g/mol). Minor discrepancies can stem from partial coordination by solvent or dynamic ligand exchange, but the net conclusion is that a monomeric, contacted Al(III)–H···Na^+ species predominates in solution.

Further verifying this pattern, the potassium and caesium monomeric ion pairs in toluene-d_8 also show one principal diffusing entity each. For [(18-c-6)K···**1'(H)$_2$**], DOSY yields an MW of 790–765 g/mol, aligning well (within 15% error) with the calculated 713–750 g/mol range, especially if modest solvation by toluene is considered. Analogously, the caesium monomeric salt [(18-c-6)Cs···**1'(H)$_2$**] displays MW estimates of 1222–1092 g/mol by OEC/ECC, again within an acceptable error margin relative to the theoretical of 1050 g/mol.

Finally, DOSY on the separated ion-pair systems [(crypt)AM][**1'(H)$_2$**] (AM = Na, K, Cs) in fluorobenzene (Figure 23) revealed data suggesting the coexistence of two distinct diffusing species, presumably [**1'(H)$_2$**]$^-$ and the cryptand-encapsulated cation, [(crypt)Na]$^+$, [(crypt)K]$^+$ or [(crypt)Cs]$^+$. However, close analysis of the diffusion coefficients indicates single-species MWs more consistent with a contacted arrangement in solution than with fully separated ions. For example,

[(crypt)Na][**1'(H)$_2$**] exhibits an MW near 845–939 g/mol, contrasting with the simple sum of discrete [**1'(H)$_2$**]$^-$ (446 g/mol) and [(crypt)Na]$^+$ (399 g/mol) masses. As with the other examples, dynamic solvation by fluorobenzene or partial re-coordination likely accounts for these intermediate values, and we infer that these species maintain significant cation–anion contact in solution.

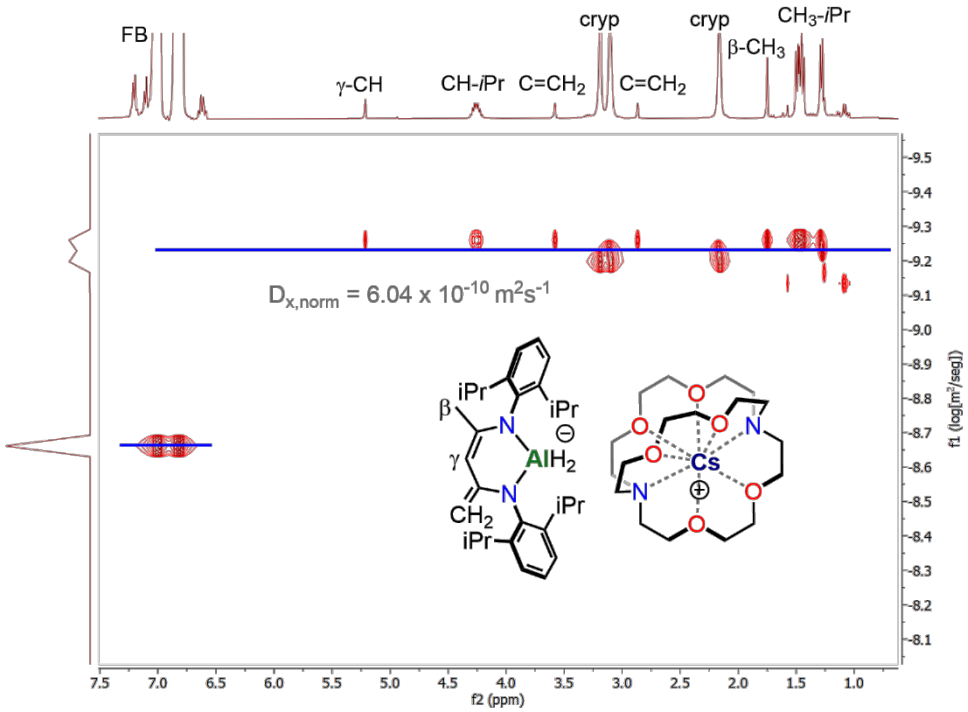


Figure 23. ^{1}H DOSY NMR 400 MHz of [(crypt)Cs][**1'(H)$_2$**] in C_6H_5F at 298 K.

Table 10. D (m^2s^{-1}) and MW values for [(crypt)AM][**1'(H)$_2$**] (AM = Na, K or Cs) in C_6H_5F at 298 K.

Species	$D_{x,norm}$ ($m^2 \cdot s^{-1}$)	MW found (g/mol)	MW calc (g/mol)	MW error (%)
Na				
Diffusing species [(crypt)Na···**1'(H)$_2$**]	$5.43 \cdot 10^{-10}$	865[a]; 939[b]	845	2[a];10[b]
K				
Diffusing species [(crypt)K···**1'(H)$_2$**]	$5.33 \cdot 10^{-10}$	826[a]; 971[b]	861	4[a];11[b]
Cs				
Diffusing species [(crypt)Cs···**1'(H)$_2$**]	$6.04 \cdot 10^{-10}$	906[a]; 811[b]	955	5[a];5[b]

[a] *Values from ECC-Merge*. [b] *Values from OEC (own external calibration method).*

In sum, the DOSY data for aluminium dihydrides corroborate the fluxional and solvent-dependent behaviours observed with aluminyls (see Section 1.3.3) revealing that "dimeric" dihydride [(Cs···**1'(H)$_2$**)$_2$] frequently exists in monomeric or partially solvated forms in solution, (Cs···**1'(H)$_2$**) while monomeric [(crown)AM···**1'(H)$_2$**] or "separated" examples [(crypt)AM][**1'(H)$_2$**] can still display contact with their respective alkali-metal cations. These findings underscore the importance of considering solution equilibria and solvation effects when interpreting structural assignments and reactivities of β-diketiminate-based Al(III) hydrides.

1.3.1 Crystal Structures of Aluminium Dihydrides

1.3.1.1 Dimeric Aluminium Dihydride Pairs

Crystallographic analysis was successfully performed on a pale-yellow needle sample of the caesium dimeric dihydride complex, [(Cs···**1'(H)$_2$**)$_2$]. These crystals grew from a concentrated toluene solution layered with *n*-hexane, an approach that selectively precipitates the target species. The resulting orthorhombic structure (space group *Pccn*) features half of the dimeric unit in the asymmetric cell; via crystallographic symmetry, the full dimer is generated, revealing two dihydridoaluminates fragments that face each other in a slightly twisted arrangement (Figure 24). Each aluminium centre bears two hydride ligands bridging toward the caesium sites, and the Cs^+ cations further stabilise the structure through weak π-aryl interactions with adjacent Dipp substituents. Collectively, these Al–H···Cs contacts, along with the BDI coordination, consolidate the dimeric motif.

Inspection of bond lengths within the β-diketiminate framework confirms the successful deprotonation of the methyl backbone group. Specifically, the C1–C2 distance (1.38 Å) is consistent with partial double-bond character (typical of C=C 1.34–1.38 Å), while the C4–C5 distance (1.48 Å) more closely resembles a single bond (Table 11). Such well-defined C–C/C=C separation contrasts with certain disordered backbones reported by Harder and co-workers, suggesting that in [(Cs···**1'(H)$_2$**)$_2$], the ligand adopt a comparatively "ordered" arrangement in the solid state. The Al–N bond lengths of 1.83–1.84 Å echo typical values for Al(III) or Al(I) within BDI-like ligands.[12, 35, 50]

Notably, the hydride positions were also localised, revealing Al–H distances of 1.59–1.73 Å. These values, though on the shorter side for Al(III)–H bonds, are consistent with bridging hydrides in high-electron-density aluminium species. Moreover, only one hydride from each Al centre interacts with each caesium cation;

the Cs···H separation (2.88 Å) suggests a stabilising electrostatic or multicentric (three-centre two-electron) bonding $(Al–H)^{-}\cdots Cs^{+}$ component, with the Al···Cs distance (4.10 Å) being larger than the sum relevant covalent radii ($\sum_{cov}$(Al,Cs) = 3.65 Å).[44]

These metrics confirm that the hydrides in [(Cs···**1'(H)$_2$**)$_2$] bridge the Al and Cs centres, resulting in an extended network of Al–H–Cs interactions. The clear distinction between C1–C2 and C4–C5 bond lengths underscores the partial double-bond character introduced by the BDI ligand's deprotonation, while the short Al–H and Cs–H distances highlight the bridging nature of the hydrides. Such structural details parallel earlier aluminyl X-ray findings (Section 1.3.4.1) and underscore how metal–hydride bridging can stabilise dimeric assemblies in electron-rich aluminium compounds.

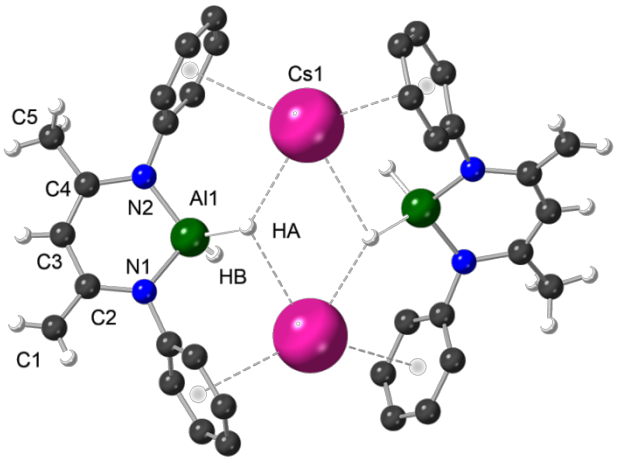


Figure 24. Molecular structure of [(Cs···**1'(H)$_2$**)$_2$]. All H atoms except the hydrides HA, HB and those from the {C1,C5}-backbone of the BDI ligand have been omitted for clarity.

Table 11. Selected bond distances (Å) and angles (°) for compounds [(Cs····**2(H)$_2$**)$_2$].

Al1–Cs	4.0993(9)	Cs–Centroid	3.218
Al1–HA	1.73(3)	Cs1–HA	2.85(3)
Al1–HB	1.59(3)	Cs1–HB	4.66(3)
N1–Al1	1.8342(19)		
N2–Al1	1.8387(18)		
N1–C1	1.382(3)		
C1–C2	1.386(3)		
C2–C3	1.451(3)		
C3–C4	1.378(3)		
C4–C5	1.485(3)		
C4–N2	1.396(3)		
N1–Al1–N2	101.44(8)		

1.3.1.2 Monomeric Aluminium Dihydride Pairs

Single-crystal X-ray analyses were also undertaken on monomeric alkali-metal dihydridoaluminates species, [(crown)AM···**1'(H)$_2$**], each stabilised by different crown ethers. Only three complexes, [(12-c-4)Li···**1'(H)$_2$**], [(18-c-6)Na···**1'(H)$_2$**] and [(18-c-6)K···**1'(H)$_2$**] yielded crystals suitable for definitive structural elucidation. These data reveal that the anion, [**1'(H)$_2$**]$^-$, adopts a similarly deprotonated β-diketiminate (BDI) skeleton across all three examples, mirroring the trend observed in their aluminyl analogues (Section 1.3.4.1). Selected metrics for these crown stabilised alkali-metal dihydrides are shown in Table 12.

In [(12-c-4)Li···**1'(H)$_2$**] (Figure 25), which crystallised in a *P2$_1$/n* monoclinic lattice, the C1–C2 bond (1.38 Å) and C4–C5 bond (1.48 Å) confirm partial double-bond and single-bond character, respectively, indicating a well-defined deprotonation of one BDI methyl groups. The aluminium centre coordinates two hydrides (Al–H 1.51–1.58 Å), and the lithium cation lies slightly out of plane with the crown ether, engaging in a contact with one hydride via an Al–H···Li interaction (1.84 Å). A similar structural motif emerges in [(18-c-6)Na···**1'(H)$_2$**] (Figure 26), crystallising in a *P2$_1$/c* network with two ion pairs per unit cell. Again, the BDI backbone features a discrete C1–C2 double-bond-like segment (1.36 Å) and a C4–C5 single bond (1.51 Å). The Na$^+$ cation also leans toward one of the hydrides, with the Na–H contact at 2.42 Å. In addition, an alternative separated version of [(18-c-6)Na···**1'(H)$_2$**], namely [(18-c-6)(THF)$_2$Na][**1'(H)$_2$**] (Figure 26), was obtained when crystallising the

same species from THF, revealing that the Na^+ centre can coordinate two additional THF ligands instead of interacting with a hydride. Consequently, the sodium is encapsulated by 18-c-6 in a "butterfly" arrangement, supplemented by two THF molecules at comparable Na–O distances (~ 2.30 Å), while the anionic dihydride unit [**1'(H)$_2$**]$^-$ core remains largely unchanged.

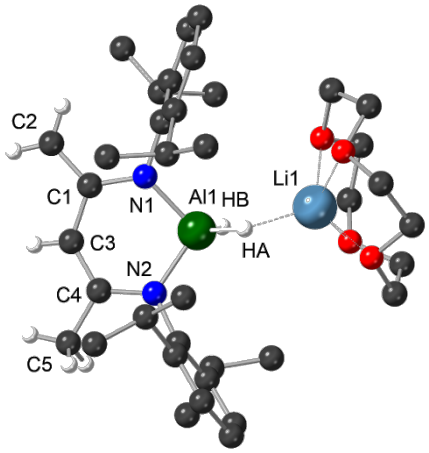


Figure 25. Molecular structure of [(12-c-4)Li···**1'(H)$_2$**]. All H atoms except the hydrides HA, HB and those from the {C1,C5}-backbone of the BDI ligand have been omitted for clarity

Although attempts to grow crystals of the corresponding K^+ and Cs^+ monomeric contacted dihydrides were less fruitful. However, the separated dihydride complex [(18-c-6)$_{1.5}$Cs][**1'(H)$_2$**] (Figure 27), confirmed a similar structural motif akin to [(18-c-6)(THF)$_2$Na][**1'(H)$_2$**]. Table 13 summarises selected metrics for [(18-c-6)$_{1.5}$Cs][**1'(H)$_2$**]. Notably, none of these monomeric contacted dihydridoaluminate structures with crown Li^+, Na^+ show π–arene or cation···aromatic interactions comparable to those seen in the dimeric species [(Cs···**1'(H)$_2$**)$_2$], implying that hydride bridging or electrostatic Al–H···Li/Al–H···Na contacts are the primary means of stabilising the cationic fragment. Taken together, these crystallographic results reinforce that the anionic [**1'(H)$_2$**]$^-$ core remains consistent across different alkali metals, while the precise cationic coordination environment, either via crown ether, additional solvent molecules, or direct hydride interaction, governs the assembly of these monomeric ion-pair dihydrides.

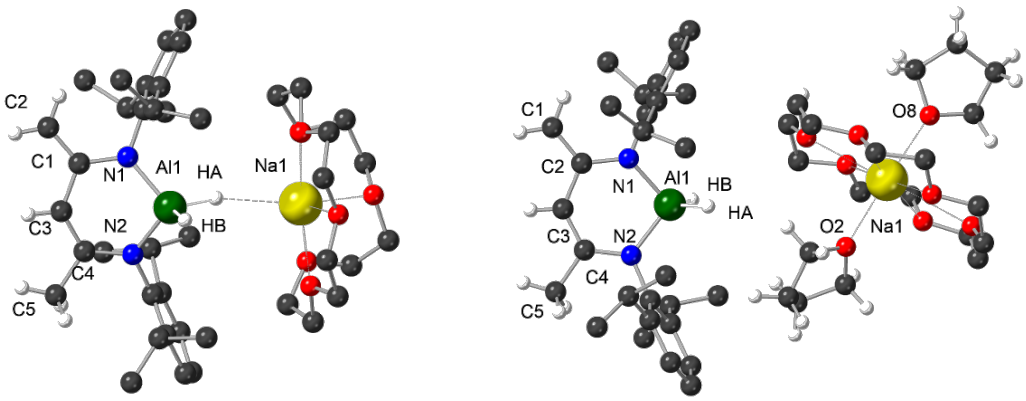


Figure 26. Molecular structure of [(18-c-6)Na···**1'(H)$_2$**], and [(18-c-6)(THF)$_2$Na][**1'(H)$_2$**]. All H atoms except the hydrides HA, HB and those from the {C1,C5}-backbone of the BDI ligand have been omitted for clarity.

Table 12. Selected bond distances (Å) and angles (º) for compounds [(12-c-4)Li···**1'(H)$_2$**], [(18-c-6)Na···**1'(H)$_2$**] and [(18-c-6)(THF)$_2$Na][**1'(H)$_2$**].

	Li	Na	Na(THF)$_2$
Al–AM	3.001(13)	3.763(2)	6.5949(19)
Al–HA	1.58(2)	1.56(4)	1.56(4)
Al–HB	1.51(2)	1.60(4)	1.52(4)
AM–HA	1.84(2)	2.42(4)	5.32(4)
AM–O2	-	-	2.314(3)
AM–O8	-	-	2.301(4)
N1–Al1	1.8524(14)	1.866(3)	1.859(3)
N2–Al1	1.8577(14)	1.861(3)	1.872(3)
N1–C1	1.389(2)	1.388(5)	1.384(4)
C1–C2	1.385(2)	1.364(6)	1.369(5)
C1–C3	1.454(2)	1.462(5)	1.458(5)
C3–C4	1.380(2)	1.359(6)	1.364(5)
C4–C5	1.489(3)	1.510(6)	1.499(5)
C4–N2	1.382(2)	1.379(5)	1.380(4)
N1–Al1–N2	100.54(6)	99.21(15)	99.70(13)

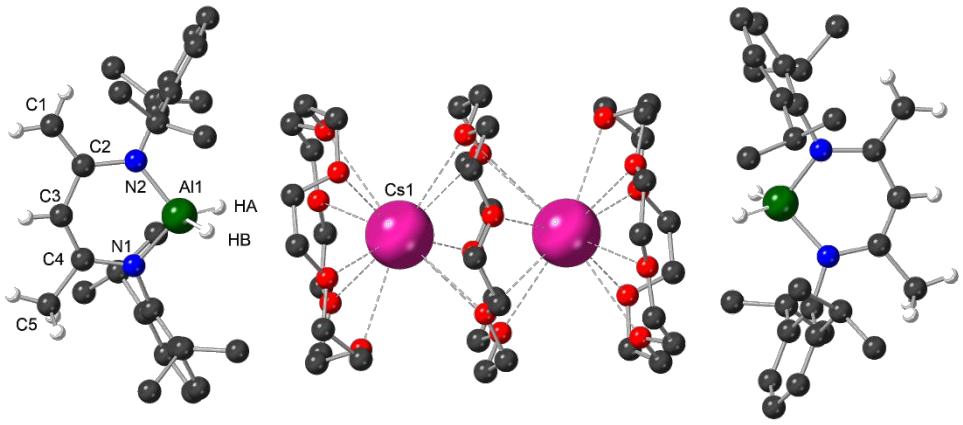


Figure 27. Molecular structure of $[(18\text{-c-}6)_{1.5}Cs][\mathbf{1'(H)_2}]$. All H atoms except the hydrides HA, HB and those from the {C1,C5}-backbone of the BDI ligand have been omitted for clarity.

Table 13. Selected bond distances (Å) and angles (°) for compound $[(18\text{-c-}6)_{1.5}Cs][\mathbf{1'(H)_2}]$.

	Cs
Al–Cs	8.7253(15)
Al–HA	1.50(6)
Al–HB	1.64(5)
Cs–HB	7.89(4)
N1–Al1	1.873(5)
N2–Al1	1.851(4)
N2–C2	1.397(6)
C1–C2	1.369(7)
C2–C3	1.451(8)
C3–C4	1.359(7)
C4–C5	1.512(8)
C4–N1	1.374(6)
N1–Al1–N2	100.14(19)

1.3.1.3 Separated ion pairs

In the final category of alkali-metal dihydridoaluminate species, single crystals of the separated species [(crypt)AM][**1'(H)$_2$**] (AM = K, Cs) were obtained by slow diffusion of *n*-hexane into a saturated solution of the isolated complexes. Both structures crystallised in a triclinic *P–1* lattice, indicating minimal symmetry within the asymmetric unit. In each case, two independent ion-pair units reside in the unit cell, and no direct contacts appear between the anionic dihydride unit [**1'(H)$_2$**]$^-$ and the cationic [(crypt)K]$^+$ and [(crypt)Cs]$^+$ counterions, underscoring the fully "separated" nature of these species in the solid state (Figure 28). Table 14 summarises selected metrics for [(crypt)K][**1'(H)$_2$**] and [(crypt)Cs][**1'(H)$_2$**], providing key metrical parameters, including Al–H, Al–AM, and relevant C–C distances within the backbone.

Despite the absence of anion···cation interactions, the BDI backbone in these separated ion pairs presents some bond-length averaging between double and single bond character. Specifically, C1−C2 and C4−C5 measure approximately 1.43 Å, an intermediate distance suggestive of the partial C=C/C–C delocalisation. This observation contrasts with the well-defined C=C and C–C bonds observed in the more "contacted" dihydride analogues, dimeric [(Cs···**1'(H)$_2$**)$_2$] and monomeric [(crown)AM···**1'(H)$_2$**] aggregates. Meanwhile, the Al–H distances (1.55–1.68 Å) are slightly longer than the 1.50–1.60 Å typically seen in contacted pairs, a discrepancy that might reflect the anion's latent ability to interact with the alkali metal ions AM$^+$. Although no such bridging is found in these crystals, the solution-phase DOSY data (Section 1.3.7) suggest that partial Al–H···AM contacts can arise dynamically when solvated in more polar media.

On the cationic side, as previously noted in cryptand-based aluminyl complexes, the K$^+$ or Cs$^+$ centre fits within the three-dimensional crypt ligand cavity, adopting a conformation consistent with full cation encapsulation. The measured AM–O (crypt) distances (2.7-3.0 Å) do not differ significantly, implying a symmetric coordination sphere around the alkali metal. Such a "locked-in" conformation stands in contrast to crown-stabilised or solvent-bound metal centres, where partial bridging to the anion or π-arene interactions are more common.

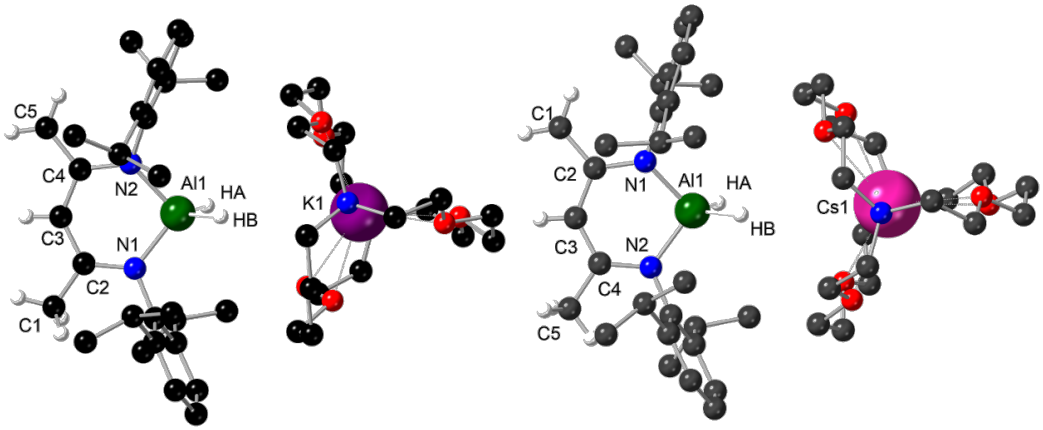


Figure 28. Molecular structure of [(crypt)AM][**1'(H)$_2$**] (AM = K or Cs). All H atoms except the hydrides HA, HB and those from the {C1,C5}-backbone of the BDI ligand have been omitted for clarity.

Table 14. Selected bond distances (Å) and angles (°) for compounds [(crypt)AM][**1'(H)$_2$**] (AM = K or Cs).

	K	Cs
Al–AM	5.3381(17)	5.570(3)
Al–HA	1.55(5)	1.624(5)
Al–HB	1.68(4)	1.626(8)
AM–HA	5.40(4)	5.680(9)
AM–HB	3.84(4)	4.044(9)
AM–O[a]	2.832	2.978
AM–N(crypt)[a]	3.0235	3.0685
N1–Al1	1.871(3)	1.858(6)
N2–Al1	1.868(4)	1.858(6)
N1–C2	1.381(6)	1.376(12)
C1–C2	1.438(6)	1.423(13)
C2–C3	1.399(7)	1.437(14)
C3–C4	1.413(6)	1.375(11)
C4–C5	1.429(7)	1.457(15)
C4–N2	1.381(6)	1.376(12)
N1–Al1–N2	99.19(17)	98.9(3)

[a] Average distance

1.4 Conclusions

In this chapter, we have expanded the realm of electron-rich aluminium chemistry by developing a family of anionic aluminium(I) (aluminyl) and aluminium(III)–H (dihydridoaluminate) complexes, each supported by a dianionic β-diketiminate scaffold. Through controlled deprotonation protocols, we accessed a wide variety of aggregation states (dimeric, monomeric, and fully separated ion pairs) and demonstrated how subtle modifications—such as changing the alkali-metal cation (Li^+–Cs^+) or introducing donor ligands (crown ethers, cryptands), can decisively influence both solid-state geometries and solution-phase equilibria. Detailed characterisation established that dimeric species partially dissociate into monomers in solution, while separated forms can regain Al···alkali metal contact dynamically.

Crucially, we showed that H_2 activation in the anionic aluminium(I) systems depends strongly on alkali-metal interactions. For instance, dimeric caesium aluminium(I) complexes readily cleave H_2 under mild conditions, yet their monomeric or "naked" anionic Al(I) counterparts generally fail unless in the presence of "free" Cs^+ (e.g., via CsF or CsHMDS). This finding underscores a cooperative mechanism wherein the nucleophilic Al(I) centre and the alkali-metal cation together lower the barrier for oxidative addition of H_2, recalling the bimetallic synergy found in certain transition-metal processes. Complementary computational studies reinforce these observations, suggesting that fluxional solvation of larger cations (particularly Cs^+) helps stabilise key transition states. By contrast, the resulting β-diketiminate-stabilised dihydridoaluminate species (Al(III)–H) derivatives mirror this structural tunability, highlighting again how aggregation and solvation define the solution landscape of electron-rich aluminium species.

These insights demonstrate that low-valent aluminium(I) complexes can exhibit transition-metal-like reactivity given the right alkali-metal coordination and electron-rich ligand environments. Beyond broadening the synthetic toolbox for Group 13 elements, this work paves new avenues for catalytic bond-activation pathways, where fine-tuning the alkali-metal environment might unleash further reactivities previously deemed exclusive to d-block metals.

1.5 Experimental Methods

Herein a representative synthesis and characterisation of Caesium species only as model compounds, further details about these and other compounds are specified in the Annexes attached to this thesis.

1.5.1 Materials

All experiments were carried out under an inert atmosphere of nitrogen gas in a glove box (MBraun, Labmaster SP) or by using standard Schlenk techniques. Benzene, *n*-hexane and toluene were dried over Na benzophenone stored under an atmosphere of nitrogen gas over K mirror. Fluorobenzene (FB) was stirred over Al_2O_3 for two hours before stirring over CaH_2 overnight, vacuum distillation, and subsequent three-fold freeze-pump-thawing. Deuterated benzene (C_6D_6) and deuterated toluene (Tol-d_8) were dried with CaH_2, distilled under low pressure (< 1 × 10^{-2} mbar) and stored under an atmosphere of nitrogen gas over a potassium mirror. Anhydrous deuterated tetrahydrofuran (THF-d_8) was purchased from Cambridge Isotopes or Merck and stored under an atmosphere of nitrogen gas over molecular sieves (3 Å). Al powder (99.97%) and NaHMDS were purchased from Alfa-Aesar, stored in a glove box, and used as received. 4,7,13,16,21,24-hexaoxa-1,10-*d*iazabicyclo[8.8.8]hexacosane (abbreviated as crypt) was purchased from Merck, distilled and stored in a glove box. 1,4,7,10,13,16-hexaoxacyclooctadecane (18-c-6), bis(trimethylsilyl)amine HMDS(H), $LiAlH_4$, *n*-BuLi and CsF were purchased from Merck and used as received. 2-((2,6-*d*iisopropylphenl)imido)-2-penten-4-one[51] **BDI**(H), (^{Dipp}BDI)Al (**1**), LiHMDS,[52], KHMDS,[52] CsHMDS,[41] and (^{Dipp}BDI)AlH_2 (**1**$(H)_2$)[48] were prepared according to reported procedures.

NMR experiments were conducted in J. Young tap NMR tubes prepared and sealed under a nitrogen atmosphere. Multinuclear NMR spectra were collected on either a Bruker AVIIIHD 400 nanobay (equipped with a 9.4 tesla magnet) or Bruker AVIII 500 (equipped with 11.7 tesla magnet and a Prodigy cryoprobe) spectrometer at 298 K unless otherwise stated. The non-deuterated solvents (fluorobenzene) were locked to an external standard sample of 10% fluorobenzene in C_6D_6. ^{7}Li and ^{133}Cs NMR data were referenced to external standard solutions of LiCl and $CsNO_3$ in D_2O (0.1 M). Assignments of NMR resonance signals in the ^{1}H and ^{13}C{^{1}H} NMR spectra were made with the help of two-dimensional NMR experiments (^{1}H,^{1}H-COSY, ^{1}H,^{13}C-HSQC, ^{1}H,^{13}C-HMBC). Chemical shifts (δ) are reported in ppm and

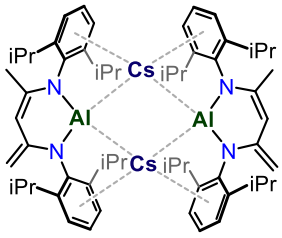
referenced to residual solvent resonances. The coupling constants (J) were expressed in hertz. The signal multiplicities are denoted as s (singlet), d (doublet), sept (septet), m (multiplet), and br (broad).

CHN elemental microanalyses were performed at the elemental analysis services of the Metropolitan University of London using a Thermo Flash 2000 Elemental Analyser by manipulating and preparing the samples under an inert atmosphere of pure and dry nitrogen gas inside a glove box before analysis. This was followed by the immediate transfer of the sample to the analyser to prevent environmental exposure. Both crystalline and bulk materials of the highly reactive and air-sensitive complexes were provided in sealed glass ampoules, ensuring complete protection from atmospheric conditions, and were analysed in several attempts. To aid the complete combustion of specific complex samples, V_2O_5 was also incorporated. Although both crystalline and bulk forms of the highly reactive, air-sensitive complexes were analysed multiple times, consistent results were challenging to obtain because of the inherent reactivity of these systems. This high reactivity, underscored by the small hydrolysis observed in both crystalline and bulk samples in solution by NMR spectroscopy, contributed to the challenges in obtaining meaningful elemental analysis data. Consequently, obtaining accurate elemental analysis data for such reactive complexes proved difficult, primarily because of sample decomposition and suboptimal combustion efficiency. Representative values of the organometallic species are presented in the characterisation data. Despite efforts to maintain the bulk purity of the compounds, some failed to meet the ± 0.4% accuracy criteria. The complications associated with CHN combustion analysis, especially for reactive organometallic species, are well-documented and understood in the literature.[53]

Infrared (IR) spectra were obtained using Nujol mulls between KBr discs inside a nitrogen glove box on a Bruker Alpha FT-IR spectrometer.

1.5.2 Synthesis and characterisation of Alkali Metal Aluminyl

1.5.2.1 Synthesis and characterisation of [(Cs···1')$_2$]



One J. Young's ampoule was charged with (^{Dipp}BDI)Al **1** (35 mg, 0.079 mmol) and CsHMDS (35 mg, 0.119 mmol). Then, dry toluene (1.5 mL) was added to give a light-yellow solution. The reaction mixture was vigorously stirred for 30 min at room temperature. After this time, the reaction mixture

was filtered via cannula to give a light-yellow solution. Then, n-hexane (5 mL) was added to give a yellow suspension. The resulting solid was filtered via cannula and dried under vacuum to give [(Cs···**1'**)$_2$] as a yellow foamy solid in a nearly quantitative yield (> 95%).

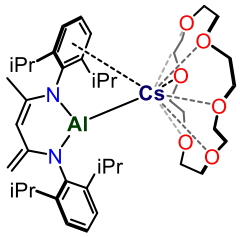
^{1}H NMR (400 MHz, Tol-d_8, 298 K): δ 7.12 (s, 2 H, Ar), 6.87 (m, 4 H, Ar), 5.325 (s, 1 H, γ-CH), 3.93 (sept, 2 H, J = 7.0 Hz, CH-^{i}Pr), 3.80 (sept, 2 H, J = 6.9 Hz, CH-^{i}Pr), 3.69 (s, 1 H, C=CH_2), 2.74 (s, 1 H, C=CH_2), 1.57 (s, 3 H, β-Me), 1.35 (d, 6 H, J = 6.9 Hz, Me-^{i}Pr), 1.24 (d, 12 H, J = 6.7 Hz, Me-^{i}Pr), 1.21 (d, 6 H, J = 6.8 Hz, Me-^{i}Pr), 1.16 (d, 6 H, J = 6.9 Hz, Me-^{i}Pr).

^{13}C{^{1}H} NMR (125.6 MHz, Tol-d_8, 298 K): δ 154.3 (*C*=CH_2), 150.0 (Ar), 149.4 (Ar), 142.1 (*C*-Me), 123.8 (Ar), 123.3 (Ar), 102.6 (γ-CH), 77.1 (C=*C*H_2), 28.1 (CH-^{i}Pr), 28.0 (CH-^{i}Pr), 25.2 (Me-^{i}Pr), 25.1 (Me-^{i}Pr), 23.6 (Me-^{i}Pr), 23.5 (β-Me).

^{133}Cs NMR (52.4 MHz, Tol-d_8, 298 K): δ 51.2 (v br).

Elemental analysis found (calc.) for $C_{29}H_{40}AlCsN_2$: C 51.27 (60.42), H 6.02 (6.99), N 3.98 (4.86).

1.5.2.2 Synthesis and characterisation of [(18-c-6)Cs···1']



One J. Young's ampoule was charged with (^{Dipp}BDI)Al **1** (39 mg, 0.088 mmol), CsHMDS (29 mg, 0.099 mmol) and 18-crown-6 (30 mg, 0.113 mmol). Then, dry toluene (1.5 mL) was added, and the resulting reaction mixture was vigorously stirred at room temperature. After 5 mins, the reaction mixture was filtered via cannula and volume of the resulting yellow solution was reduced (0.5 mL) under vacuum. Upon addition of n-hexane a yellow suspension was obtained. The solid was filtered via cannula and dried under vacuum for 2 hours to give [(18-c-6)Cs···**1'**] as a pale-yellow solid. Yield: 50 mg, 0.059 mmol, 67%. Crystals suitable for an X-ray diffraction study were obtained by slow diffusion of n-hexane (1 mL) into a solution of [(18-c-6)Cs···**1'**] in toluene (0.5 mL).

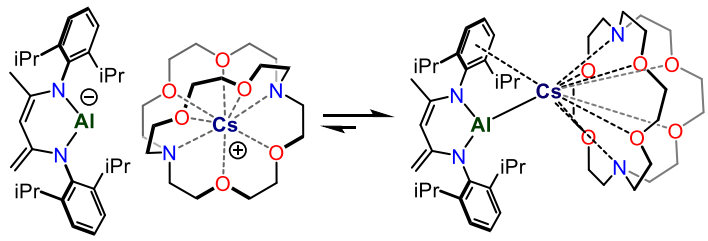
^{1}H NMR (400 MHz, Tol-d_8, 298 K): δ 7.23 (d, 2 H, J = 7.7 Hz, Ar), 7.15 (d, 2 H, J_1 = 7.4 Hz, Ar), 7.10 (m, 2 H, Ar), 5.31 (s, 1 H, γ-CH), 4.20 (sept, 2 H, J = 689 Hz, CH-^{i}Pr), 4.09 (sept, 2 H, J = 6.7 Hz, CH-^{i}Pr), 3.62 (s, 1 H, C=CH_2), 3.04 (s, 24 H, 18-crown-6), 2.78 (s, 1 H, C=CH_2), 1.76 (s, 3 H, β-Me), 1.50 (m, 18 H, Me-^{i}Pr), 1.36 (d, 6 H, J = 6.7 Hz, Me-^{i}Pr).

$^{13}C\{^{1}H\}$ NMR (125.6 MHz, Tol-d_8, 298 K): δ 155.6 (C=CH_2), 149.9 (Cq, Ar), 149.3 (Cq, Ar), 148.1 (Cq, Ar), 147.9 (Cq, Ar), 143.0 (C-Me), 124.1 (CH, Ar), 123.0 (CH, Ar), 122.6 (CH, Ar), 102.2 (γ-CH), 75.0 (C=CH_2), 70.0 (18-crown-6), 28.4 (CH-^{i}Pr), 28.3 (CH-^{i}Pr), 26.0 (Me-^{i}Pr), 26.0 (Me-^{i}Pr), 25.8 (Me-^{i}Pr), 24.5 (Me-^{i}Pr), 24.2 (β-Me).

^{133}Cs NMR (52.4 MHz, Tol-d_8, 298 K): δ 19.6 (br).

Elemental analysis found (calc.) for $C_{41}H_{64}AlCsN_2O_6$: C 59.07 (58.57), H 7.84 (7.67), N 3.05 (3.33).

1.5.2.3 Synthesis and characterisation of [(crypt)Cs][1']



One J. Young's ampoule was charged with (^{Dipp}BDI)Al **1** (30 mg, 0.067 mmol), CsHMDS (23 mg, 0.078 mmol) and crypt (26 mg, 0.069 mmol). Then, dry toluene (1.5 mL) was added, and the reaction mixture was vigorously stirred at room temperature to give a pale-orange suspension. After 5 mins, the solid was filtered via cannula and dried under vacuum for 2 h to give [(crypt)Cs][**1'**] as a pale-orange crystalline powder. Yield: 25 mg, 0.026 mmol, 40%. Suitable needle-like crystals of its separated ion pair form [(crypt)Cs][**1'**] for an X-ray diffraction study were obtained by slow diffusion of n-hexane (1 mL) into a solution of [(crypt)Cs][**1'**] in dry fluorobenzene (1 mL).

The isolated pale orange-solid was dissolved in J. Young's NMR tube in fluorobenzene, then warmed up to 40°C, and then layered with n-hexane when warm. Allowing slowly cooling down the mixture gave a mixture of two different crystals, needles, and a small crop of plates. Both crystals were studied by single X-ray diffraction crystallography. The needle-like crystals were confirmed to be the ion pair separated species [(crypt)Cs][**1'**], also obtained as a single product by crystallisation from the same solvent mixture at room temperature. On the other hand, the block-like crystals corresponded to a new contacted ion pair species [(crypt)Cs···**1'**]. Dissolving the mixture of types of crystals, the separated ion pair [(crypt)Cs][**1'**] and the mixture of contacted ion pair [(crypt)Cs···**1'**] and separated [(crypt)Cs][**1'**] species, in fluorobenzene at room temperature gave a unique set of resonances matching those observed for a solution of crystals of the separated ion pair [(crypt)Cs][**1'**] species in the same solvent. In addition, ^{1}H DOSY NMR studies in fluorobenzene indicates that both species, the contacted and separated ion par

aggregates, exist in equilibrium in fluorobenzene solution. ^{1}H VT NMR study in fluorobenzene in the range temperature 243-298K did not change the spectrum resonances.

^{1}H NMR (500 MHz, *fluorobenzene (C_6H_5F)*, 298 K): δ aromatic signals are overlapped with solvent peaks, 5.17 (s, 1 H, γ-CH), 4.11 (sept, 2 H, J = 6.9 Hz, CH-^{i}Pr), 3.99 (sept, 2 H, J = 6.8 Hz, CH-^{i}Pr), 3.41 (d, 1 H, J = 1.8 Hz, C=CH_2), 3.14 (s, 12 H, crypt), 3.05 (m, 12 H, crypt), 2.64 (d, 1 H, J = 1.9 Hz, C=CH_2), 2.10 (m, 12 H, crypt), 1.61 (s, 3 H, β-Me), 1.41 (m, 12 H, Me-^{i}Pr), 1.35 (d, 6 H, J = 6.8 Hz, Me-^{i}Pr), 1.18 (d, 6 H, J = 6.9 Hz, Me-^{i}Pr).

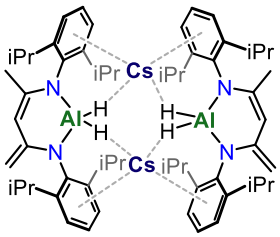
^{13}C{^{1}H} NMR (125.6 MHz, *fluorobenzene (C_6H_5F)*, 298K): *δ* 155.8 (*C*=CH_2), 148.6 (Cq, Ar), 148.0 (Cq, Ar), 147.7 (Cq, Ar), 147.4 (Cq, Ar), 142.8 (*C*-Me), 122.6 (CH, Ar), 122.1 (CH, Ar), 101.1 (γ-CH), 73.0 (C=*C*H_2), 70.0 (crypt), 67.9 (crypt), 54.9 (crypt), 27.8 (CH-^{i}Pr), 27.8 (CH-^{i}Pr), 25.4 (Me-^{i}Pr), 25.4 (Me-^{i}Pr), 25.3 (Me-^{i}Pr), 24.1 (Me-^{i}Pr), 23.6 (β-Me).

^{133}Cs NMR (52.4 MHz, *fluorobenzene (C_6H_5F)*, 298 K): *δ* 197.9 (s).

Elemental analysis found (calc.) for $C_{47}H_{76}AlCsN_4O_6$: C 54.79 (59.23), H 7.20 (8.04), N 5.19 (5.88).

1.5.3 Synthesis and characterisation of Alkali Metal Dihydridoaluminates

1.5.3.1 Synthesis and characterisation of [(Cs···1'(H)$_2$)$_2$]



One J. Young's tap ampoule was charged with (^{Dipp}BDI)AlH_2 **1(H)$_2$** (31 mg, 0.069 mmol) and CsHMDS (21 mg, 0.072 mmol). Then, toluene (2 mL) was added to give a solution which was vigorously stirred for 5 hours to give a light-yellow solution. After this time, *n*-hexane (15 ml) was added to give a pale-yellow suspension. The resulting solid was filtered via cannula and dried under vacuum for 1 hour to give [(Cs···**1'(H)$_2$**)$_2$] as a pale yellow-solid. Yield: 30 mg, 0.052 mmol, 75%. Suitable crystals (pale-yellow needles) for an X-ray diffraction study were obtained from a concentrated solution of [(Cs···**1'(H)$_2$**)$_2$] in a 1:10 mixture of toluene:*n*-hexane at room temperature after 48 hours.

^{1}H NMR (400 MHz, Tol-d_8, 298 K): *δ* 6.90-7.08 (several m, 6 H), 4.97 (s, 1 H, *γ*-CH), 3.90 (v br s, 2 H, AlH_2), 3.80 (m, 4 H, CH-^{i}Pr), 3.52 (s, 1 H, C=CH_2), 2.77 (s, 1 H, C=CH_2), 1.59 (s, 3 H, β-Me), 1.33 (d, 6 H, J = 6.8 Hz, Me-^{i}Pr), 1.19 (m, 18 H, Me-^{i}Pr).

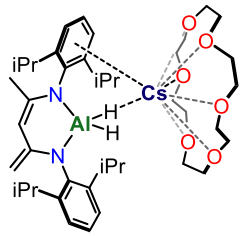
$^{13}C\{^{1}H\}$ NMR (100.6 MHz, Tol-d_8, 298 K): δ 155.8 (C=CH_2), 150.0 (Ar), 149.3 (Ar), 146.0 (Ar), 145.6 (C-Me), 124.5 (Ar), 124.0 (Ar), 99.2 (γ-CH), 77.6 (C=CH$_2$), 28.0 (CH-^{i}Pr), 27.8 (CH-^{i}Pr), 26.2 (Me-^{i}Pr), 25.6 (Me-^{i}Pr), 25.1 (Me-^{i}Pr), 24.4 (Me-^{i}Pr), 23.2 (β-Me).

^{133}Cs NMR (52.4 MHz, Tol-d_8, 298 K): δ –7.7 (v br).

IR (KBr/Nujol, cm^{-1}): ν(Al–H) 1735, 1656.

Elemental analysis found (calc.) for $C_{29}H_{42}AlCsN_2$: C 57.15 (60.20), H 6.73 (7.32), N 4.02 (4.84).

1.5.3.2 Synthesis and characterisation of [(18-c-6)$_{1.5}$Cs···1'(H)$_2$]



One J. Young's ampoule was charged with ^{Dipp}BDI)AlH$_2$ **1(H)$_2$** (53 mg, 0.118 mmol), CsHMDS (39 mg, 0.133 mmol) and 18-crown-6 (39 mg, 0.147mmol). Then, dry toluene (1.5 mL) was added, and the resulting solution was stirred at room temperature, and immediate precipitation of a pale-yellow solid was obtained. The suspension was filtered via cannula and the solid was dried under vacuum to give [(18-c-6)$_{1.5}$Cs···**1'(H)$_2$**] as a pale-yellow solid. Yield: 50 mg, 0.059 mmol, 50%. Crystals suitable for an X-ray diffraction study were obtained by slow diffusion of of n-hexane (3 mL) into a solution of [(18-c-6)$_{1.5}$Cs···**1'(H)$_2$**] in dry toluene (1 mL).

^{1}H NMR (400 MHz, Tol-d_8, 298 K): δ 7.21 (d, 2 H, J = 7.5 Hz, Ar), 7.71-7.06 (m, 4 H, *overlapped with solvent peaks)*, 5.10 (s, 1 H, γ-CH), 4.29 (v br s, 2 H, AlH$_2$), 4.19 (m, 4 H, CH-^{i}Pr), 3.64 (d, 1 H, J = 1.4 Hz, C=CH$_2$), 3.04 (s, 36 H, 18-crown-6), 2.90 (d, 1 H, J = 1.4 Hz, C=CH$_2$), 1.80 (s, 3 H, β-Me), 1.56 (d, 6 H, J = 6.9 Hz, Me-^{i}Pr), 1.33 ("t", 12 H, J = 5.9 Hz, Me-^{i}Pr), 1.37 (d, 6 H, J = 6.9 Hz, Me-^{i}Pr).

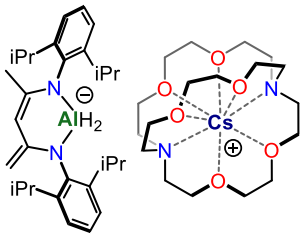
$^{13}C\{^{1}H\}$ NMR (100 MHz, Tol-d_8, 298 K): δ 156.9 (C=CH_2), 149.6 (Ar), 148.5 (Ar), 146.5 (Ar), 145.7 (Ar), 145.6 (C-Me), 124.4 (Ar), 123.6 (Ar), 123.1 (Ar), 98.4 (γ-CH), 75.2 (C=CH$_2$), 69.8 (18-crown-6), 28.1 (CH-^{i}Pr), 27.9 (CH-^{i}Pr), 26.8 (Me-^{i}Pr), 26.2 (Me-^{i}Pr), 25.8 (Me-^{i}Pr), 24.8 (Me-^{i}Pr), 24.3 (β-Me).

^{133}Cs NMR (52.4 MHz, Tol-d_8, 298 K): δ 30.9 (v br).

IR (KBr/Nujol, cm^{-1}): ν(Al–H) 1764, 1698.

Elemental analysis found (calc.) for $C_{47}H_{78}AlCsN_2O_9$: C 53.89 (57.90), H 7.38 (8.06), N 2.50 (2.87).

1.5.3.3 Synthesis and characterisation of [(crypt)Cs][1'(H)$_2$]



One J. Young's ampoule was charged with ^{Dipp}BDI)AlH$_2$ **1(H)$_2$** (50 mg, 0.112 mmol) and CsHMDS (34 mg, 0.116 mmol). Then, dry toluene (1.5 mL) was added, and the resulting mixture was stirred at room temperature for 30 mins. After this time, full deprotonation to form [Cs···**1'(H)$_2$**]$_2$ was observed by a ^{1}H NMR spectroscopy monitoring study in Tol-*d*$_8$. Then, the resulting yellow solution was cannulated and stirred in a J Young's Ampoule containing 2.2.2-cryptand (41 mg, 0.109 mmol). Instant precipitation of a pale-yellow solid was obtained. The solid was filtered via cannula, dissolved in 1.5 mL of dry fluorobenzene and layered with *n*-hexane in a J. Young's crystallisation tube. Allowing for slow diffusion at room temperature gave needle-like crystals of [(crypt)Cs][**1'(H)$_2$**] suitable for an X-ray diffraction study. Yield: 165 mg, 0.209 mmol, 57%.

^{1}H NMR (500 MHz, *fluorobenzene (C$_6$H$_5$F)*, 298 K): *δ aromatic signals are overlapped with solvent peaks*, 5.08 (s, 1 H, γ-CH), 4.12 (sept, 4 H, J = 7.4 Hz, CH-^{i}Pr), 3.44 (d, 1 H, J = 2.0 Hz, C=CH$_2$), 3.06 (s, 12 H, crypt), 2.97 (s, 12 H, crypt), 2.73 (d, 1 H, J = 2.0 Hz, C=CH$_2$), 2.03 (s, 12 H, crypt), 1.61 (s, 3 H, β-Me), 1.36 (d, 6 H, J = 6.9 Hz, Me-^{i}Pr), 1.33 (d, 6 H, J = 6.7 Hz, Me-^{i}Pr), 1.31 (d, 6 H, J = 6.7 Hz, Me-^{i}Pr), 1.15 (d, 6H, J = 6.9 Hz, Me-^{i}Pr).

^{13}C{^{1}H} NMR (125.6 MHz, *fluorobenzene (C$_6$H$_5$F)*, 298 K): *δ* 157.2 (*C*=CH$_2$), 148.5 (Ar), 148.0 (Ar), 146.0 (Ar), 145.8 (Ar), 145.5 (*C*-Me), 123.5 (Ar), 123.4 (Ar), 123.0 (Ar), 122.6 (Ar), 98.9 (*γ*-CH), 73.8 (C=*C*H$_2$), 70.1 (crypt), 67.2 (crypt), 54.8 (crypt), 27.6 (CH-^{i}Pr), 27.3 (CH-^{i}Pr), 26.1 (Me-^{i}Pr), 25.8 (Me-^{i}Pr), 25.4 (Me-^{i}Pr), 24.17 (Me-^{i}Pr), 23.5 (β-Me).

^{133}Cs NMR (52.4 MHz, *fluorobenzene (C$_6$H$_5$F)*, 298 K): *δ* 190.8 (v br).

IR (KBr/Nujol, cm^{-1}): *ν*(Al–H) 1683, 1739.

Elemental analysis found (calc.) for C$_{47}$H$_{78}$AlCsN$_4$O$_6$: C 59.58 (59.11), H 7.90 (8.23), N 5.67 (5.87).

1.6 References

[1] a) A. Hinz, F. Breher, *Angew. Chem. Int. Ed.* **2018**, *57*, 8818-8820; b) R. Sunke, S. B. Nallapati, J. S. Kumar, K. Shiva Kumar, M. Pal, *Org. Biomol. Chem.* **2017**, *15*, 4042-4057.

[2] a) P. P. Power, *Nature* **2010**, *463*, 171-177; b) C. Weetman, S. Inoue, *ChemCatChem* **2018**, *10*, 4213-4228; c) R. L. Melen, *Science* **2019**, *363*, 479-484; d) R. D. Dewhurst, M.-A. Légaré, H. Braunschweig, *Commun. Chem.* **2020**, *3*, 131.

[3] M. He, C. Hu, R. Wei, X.-F. Wang, L. L. Liu, *Chem. Soc. Rev.* **2024**, *53*, 3896-3951.

[4] a) F. E. Hahn, L. Wittenbecher, R. Boese, D. Bläser, *Chem. Eur. J.* **1999**, *5*, 1931-1935; b) V. Lavallo, Y. Canac, C. Präsang, B. Donnadieu, G. Bertrand, *Angew. Chem. Int. Ed.* **2005**, *44*, 5705-5709; c) M. Melaimi, R. Jazzar, M. Soleilhavoup, G. Bertrand, *Angew. Chem. Int. Ed.* **2017**, *56*, 10046-10068; d) M. Soleilhavoup, G. Bertrand, *Chem* **2020**, *6*, 1275-1282.

[5] a) S. T. Haubrich, P. P. Power, *J. Am. Chem. Soc.* **1998**, *120*, 2202-2203; b) M. Niemeyer, P. P. Power, *Angew. Chem. Int. Ed.* **1998**, *37*, 1277-1279; c) R. J. Wright, M. Brynda, J. C. Fettinger, A. R. Betzer, P. P. Power, *J. Am. Chem. Soc.* **2006**, *128*, 12498-12509.

[6] a) Y. Segawa, M. Yamashita, K. Nozaki, *Angew. Chem. Int. Ed.* **2007**, *46*, 6710-6713; b) H. Kisu, T. Kosai, T. Iwamoto, M. Yamashita, *Chem. Lett.* **2021**, *50*, 293-296; c) W. Lu, H. Hu, Y. Li, R. Ganguly, R. Kinjo, *J. Am. Chem. Soc.* **2016**, *138*, 6650-6661; d) D. Seebach, *Angew. Chem., Int. Ed.* **1979**, *18*, 239-258.

[7] M. Asay, C. Jones, M. Driess, *Chem. Rev.* **2011**, *111*, 354-396.

[8] a) X. Zhang, Y. Mei, L. L. Liu, *Chem. Eur. J.* **2022**, *28*, e202202102; b) H. W. Roesky, S. S. Kumar, *Chem. Commun.* **2005**, 4027-4038.

[9] W. Klemm, E. Voss, K. Geiersberger, *Z. Anorg. Allg. Chem.* **1948**, *256*, 15-24.

[10] a) C. Gemel, T. Steinke, M. Cokoja, A. Kempter, R. A. Fischer, *Eur. J. Inorg. Chem.* **2004**, *2004*, 4161-4176; b) S. González-Gallardo, T. Bollermann, R. A. Fischer, R. Murugavel, *Chem. Rev.* **2012**, *112*, 3136-3170; c) R. A. Fischer, J. Weiß, *Angew. Chem. Int. Ed.* **1999**, *38*, 2830-2850; d) A. Hofmann, T. Tröster, T. Kupfer, H. Braunschweig, *Chem. Sci.* **2019**, *10*, 3421-3428; e) H. Sitzmann, M. F. Lappert, C. Dohmeier, C. Üffing, H. Schnöckel, *J. Organomet. Chem.* **1998**, *561*, 203-208; f) C. Dohmeier, E. Baum, A. Ecker, R. Köppe, H. Schnöckel, *Organometallics* **1996**, *15*, 4702-4706.

[11] C. Cui, H. W. Roesky, H.-G. Schmidt, M. Noltemeyer, H. Hao, F. Cimpoesu, *Angew. Chem. Int. Ed.* **2000**, *39*, 4274-4276.

[12] Y.-C. Tsai, *Coord. Chem. Rev.* **2012**, *256*, 722-758.

[13] X. Li, X. Cheng, H. Song, C. Cui, *Organometallics* **2007**, *26*, 1039-1043.

[14] S. Grams, J. Mai, J. Langer, S. Harder, *Organometallics* **2022**, *41*, 2862-2867.

[15] a) X. Zhang, L. L. Liu, *Angew. Chem. Int. Ed.* **2021**, *60*, 27062-27069; b) A. Hinz, M. P. Müller, *Chem. Commun.* **2021**, *57*, 12532-12535; c) J. D. Queen, A. Lehmann, J. C. Fettinger, H. M. Tuononen, P. P. Power, *J. Am. Chem. Soc.* **2020**, *142*, 20554-20559.

[16] S. Nagendran, H. W. Roesky, *Organometallics* **2008**, *27*, 457-492.

[17] a) R. Y. Kong, M. R. Crimmin, *J. Am. Chem. Soc.* **2018**, *140*, 13614-13617; b) R. Y. Kong, M. R. Crimmin, *Chem. Commun.* **2019**, *55*, 6181-6184.

[18] a) C. Bakewell, A. J. P. White, M. R. Crimmin, *Angew. Chem. Int. Ed.* **2018**, *57*, 6638-6642; b) C. Bakewell, A. J. P. White, M. R. Crimmin, *Chem. Sci.* **2019**, *10*, 2452-2458.

[19] a) G. Linti, H. Schnöckel, *Coord. Chem. Rev.* **2000**, *206-207*, 285-319; b) C. Weetman, H. Xu, S. Inoue, in *Encyclopedia of Inorganic and Bioinorganic*

Chemistry, **2020**, pp. 1-20; c) M. N. Sudheendra Rao, H. W. Roesky, G. Anantharaman, *J. Organomet. Chem.* **2002**, *646*, 4-14.
[20] a) D. Dange, S. L. Choong, C. Schenk, A. Stasch, C. Jones, *Dalton Trans.* **2012**, *41*, 9304-9315; b) R. J. Schwamm, M. D. Anker, M. Lein, M. P. Coles, C. M. Fitchett, *Angew. Chem. Int. Ed.* **2018**, *57*, 5885-5887; c) M. D. Anker, M. Lein, M. P. Coles, *Chem. Sci.* **2019**, *10*, 1212-1218.
[21] J. Hicks, P. Vasko, J. M. Goicoechea, S. Aldridge, *Nature* **2018**, *557*, 92-95.
[22] a) M. J. Evans, M. D. Anker, C. L. McMullin, S. E. Neale, M. P. Coles, *Angew. Chem. Int. Ed.* **2021**, *133*, 22463-22466; b) M. J. Evans, M. D. Anker, M. G. Gardiner, C. L. McMullin, M. P. Coles, *Inorg. Chem.* **2021**, *60*, 18423-18431.
[23] a) R. J. Schwamm, M. P. Coles, M. S. Hill, M. F. Mahon, C. L. McMullin, N. A. Rajabi, A. S. S. Wilson, *Angew. Chem. Int. Ed.* **2020**, *59*, 3928-3932; b) R. J. Schwamm, M. S. Hill, H.-Y. Liu, M. F. Mahon, C. L. McMullin, N. A. Rajabi, *Chem. Eur. J.* **2021**, *27*, 14971-14980; c) G. Feng, K. L. Chan, Z. Lin, M. Yamashita, *J. Am. Chem. Soc.* **2022**, *144*, 22662-22668; d) K. Koshino, R. Kinjo, *J. Am. Chem. Soc.* **2020**, *142*, 9057-9062; e) C. Yan, R. Kinjo, *Angew. Chem. Int. Ed.* **2022**, *61*, e202211800; f) S. Kurumada, S. Takamori, M. Yamashita, *Nat. Chem.* **2020**, *12*, 36-39.
[24] R. A. Jackson, A. J. R. Matthews, P. Vasko, M. F. Mahon, J. Hicks, D. J. Liptrot, *Chem. Commun.* **2023**, *59*, 5277-5280.
[25] D. Sarkar, P. Vasko, A. F. Roper, A. E. Crumpton, M. M. D. Roy, L. P. Griffin, C. Bogle, S. Aldridge, *J. Am. Chem. Soc.* **2024**, *146*, 11792-11800.
[26] S. Grams, J. Eyselein, J. Langer, C. Färber, S. Harder, *Angew. Chem. Int. Ed.* **2020**, *59*, 15982-15986.
[27] a) T. X. Gentner, M. J. Evans, A. R. Kennedy, S. E. Neale, C. L. McMullin, M. P. Coles, R. E. Mulvey, *Chem. Commun.* **2022**, *58*, 1390-1393; b) S. Grams, J. Mai, J. Langer, S. Harder, *Dalton Trans.* **2022**, *51*, 12476-12483; c) R. J. Schwamm, M. D. Anker, M. Lein, M. P. Coles, *Angew. Chem. Int. Ed.* **2019**, *58*, 1489-1493.
[28] a) J. Hicks, P. Vasko, J. M. Goicoechea, S. Aldridge, *Angew. Chem. Int. Ed.* **2021**, *60*, 1702-1713; b) M. J. Evans, M. D. Anker, C. L. McMullin, S. E. Neale, M. P. Coles, *Angew. Chem. Int. Ed.* **2021**, *60*, 22289-22292.
[29] J. Hicks, P. Vasko, J. M. Goicoechea, S. Aldridge, *J. Am. Chem. Soc.* **2019**, *141*, 11000-11003.
[30] a) A. Heilmann, J. Hicks, P. Vasko, J. M. Goicoechea, S. Aldridge, *Angew. Chem. Int. Ed.* **2020**, *59*, 4897-4901; b) M. J. Evans, M. D. Anker, M. P. Coles, *Inorg. Chem.* **2021**, *60*, 4772-4778.
[31] K. Sugita, R. Nakano, M. Yamashita, *Chem. Eur. J.* **2020**, *26*, 2174-2177.
[32] M. J. Evans, S. E. Neale, M. D. Anker, C. L. McMullin, M. P. Coles, *Angew. Chem. Int. Ed.* **2022**, *61*, e202117396.
[33] a) M. M. D. Roy, A. Heilmann, M. A. Ellwanger, S. Aldridge, *Angew. Chem. Int. Ed.* **2021**, *60*, 26550-26554; b) M. S. Hill, M. F. Mahon, C. L. McMullin, S. E. Neale, K. G. Pearce, R. J. Schwamm, *Z. Anorg. Allg. Chem.* **2022**, *648*, e202200224; c) K. Koshino, R. Kinjo, *Organometallics* **2020**, *39*, 4183-4186.
[34] M. P. Coles, M. J. Evans, *Chem. Commun.* **2023**, *59*, 503-519.
[35] C. Camp, J. Arnold, *Dalton Trans.* **2016**, *45*, 14462-14498.
[36] a) S. P. Green, C. Jones, A. Stasch, *Science* **2007**, *318*, 1754-1757; b) S. J. Bonyhady, C. Jones, S. Nembenna, A. Stasch, A. J. Edwards, G. J. McIntyre, *Chem. Eur. J.* **2010**, *16*, 938-955; c) A. Stasch, C. Jones, *Dalton Trans.* **2011**, *40*, 5659-5672; d) C. Jones, *Nat. Rev. Chem.* **2017**, *1*, 0059.
[37] M. S. Hill, P. B. Hitchcock, *Chem. Commun.* **2004**, 1818-1819.
[38] S. Yao, C. van Wüllen, M. Driess, *Chem. Commun.* **2008**, 5393-5395.
[39] a) S. Grams, J. Mai, J. Langer, S. Harder, *Dalton Trans.* **2022**, *51*, 12476-12483; b) J. Hicks, P. Vasko, A. Heilmann, J. M. Goicoechea, S. Aldridge, *Angew. Chem. Int. Ed.* **2020**, *59*, 20376-20380.

[40] a) O. Kysliak, H. Görls, R. Kretschmer, *Chem. Commun.* **2020**, *56*, 7865-7868; b) T. Chu, Y. Boyko, I. Korobkov, G. I. Nikonov, *Organometallics* **2015**, *34*, 5363-5365; c) M. R. Crimmin, M. J. Butler, A. J. P. White, *Chem. Commun.* **2015**, *51*, 15994-15996.
[41] A. I. Ojeda-Amador, A. J. Martínez-Martínez, A. R. Kennedy, C. T. O'Hara, *Inorg. Chem.* **2016**, *55*, 5719-5728.
[42] a) S. Bachmann, R. Neufeld, M. Dzemski, D. Stalke, *Chem. Eur. J.* **2016**, *22*, 8462-8465; b) A.-K. Kreyenschmidt, S. Bachmann, T. Niklas, D. Stalke, *ChemistrySelect.* **2017**, *2*, 6957-6960; c) R. Neufeld, D. Stalke, *Chem. Sci.* **2015**, *6*, 3354-3364.
[43] H. Videa, A. J. Martínez-Martínez, *Dalton Trans.* **2023**, *52*, 13058-13062.
[44] B. Cordero, V. Gómez, A. E. Platero-Prats, M. Revés, J. Echeverría, E. Cremades, F. Barragán, S. Alvarez, *Dalton Trans.* **2008**, 2832-2838.
[45] T. X. Gentner, R. E. Mulvey, *Angew. Chem. Int. Ed.* **2021**, *60*, 9247-9262.
[46] N. Villegas-Escobar, A. Toro-Labbé, H. F. Schaefer III, *Chem. Eur. J.* **2021**, *27*, 17369-17378.
[47] a) J. Yin, J. Li, G.-X. Wang, Z.-B. Yin, W.-X. Zhang, Z. Xi, *J. Am. Chem. Soc.* **2019**, *141*, 4241-4247; b) D. V. Konarev, A. V. Kuzmin, S. S. Khasanov, A. F. Shestakov, D. I. Nazarov, A. Otsuka, H. Yamochi, H. Kitagawa, R. N. Lyubovskaya, *Eur. J. Inorg. Chem.* **2020**, *2020*, 2615-2623; c) D. I. Nazarov, M. G. Andronov, A. V. Kuzmin, S. S. Khasanov, E. I. Yudanova, A. F. Shestakov, A. Otsuka, H. Yamochi, H. Kitagawa, D. V. Konarev, *Dalton Trans.* **2021**, *50*, 15620-15632; d) M. Zhong, X. Cui, B. Wu, G.-X. Wang, W.-X. Zhang, J. Wei, L. Zhao, Z. Xi, *CCS Chemistry* **2021**, *4*, 532-539.
[48] C. Cui, H. W. Roesky, H. Hao, H.-G. Schmidt, M. Noltemeyer, *Angew. Chem. Int. Ed.* **2000**, *39*, 1815-1817.
[49] S. Banerjee, G. M. Ballmann, M. J. Evans, A. O'Reilly, A. R. Kennedy, J. R. Fulton, M. P. Coles, R. E. Mulvey, *Chem. Eur. J.* **2023**, *29*, e202301849.
[50] Y. Liu, J. Li, X. Ma, Z. Yang, H. W. Roesky, *Coord. Chem. Rev.* **2018**, *374*, 387-415.
[51] X. He, Y. Yao, X. Luo, J. Zhang, Y. Liu, L. Zhang, Q. Wu, *Organometallics* **2003**, *22*, 4952-4957.
[52] M. F. Lappert, M. J. Slade, A. Singh, J. L. Atwood, R. D. Rogers, R. Shakir, *J. Am. Chem. Soc.* **1983**, *105*, 302-304.
[53] a) *Organometallics* **2016**, *35*, 3255-3256; b) A. C. Aiken, P. F. DeCarlo, J. L. Jimenez, *Anal. Chem.* **2007**, *79*, 8350-8358; c) R. E. H. Kuveke, L. Barwise, Y. van Ingen, K. Vashisth, N. Roberts, S. S. Chitnis, J. L. Dutton, C. D. Martin, R. L. Melen, *ACS Cent. Sci.* **2022**, *8*, 855-863.

CHAPTER II:

Synthesis, Characterisation and Reactivity of Electron-Rich Anionic Gallium(I) Species: Alkali Metal Mediated C–H Activation

2.1 Introduction

In recent years, main-group metal complexes have attracted considerable attention, leading to notable advances in bond activation chemistry. Heavier main-group elements, in particular, have demonstrated transformations reminiscent of transition-metal systems, especially in the activation of small molecules.[1] Among these, monovalent Group 13 metals possess a lone-pair/vacant-orbital configuration, enabling them to behave as carbene analogues. Owing to their isoelectronic relationship with carbenes, such complexes often exhibit amphiphilic properties that facilitate unusual reaction pathways.[2] Despite their fascinating reactivity, isolating Group 13 metals in the +1 oxidation state remains synthetically challenging, as these metals strongly favour the +3 oxidation state. Furthermore, the presence of a lone pair in monovalent species confers substantial basicity, making Group 13 metals prone to disproportionation.[3]

2.1.1 Overview of Neutral Gallium(I) Chemistry: Gallylenes

Monomeric gallium(I) compounds (gallylenes) are generally more stable than their lighter aluminium(I) congeners (aluminylenes). Even so, the first examples of Ga(I) complexes were not reported until the 1990s, when Schmidbaur and co-workers pioneered the isolation of both cationic and anionic monovalent gallium species (**I** and **II**, Figure 1).[4] The cationic low-valent gallium complex **I** was stabilised by π-arene coordination to two mesitylene groups, along with Coulombic interactions involving chloride atoms in the $[GaCl_4]^-$ counterion.[5] The same group employed an N-heterocyclic carbene (NHC) ligand to achieve high stability for the anionic species **II**.[6]

Beyond these discrete ion-pair complexes, low-valent gallium species can also form strongly bonded tetrameric aggregates **III**,[7] which may dissociate into monomeric units under highly dilute conditions, similarly to the cyclopentadienyl low-valent aluminium(I) species reported by Schnöckel.[8] Seeking other stable, monomeric Ga(I) variants, Parkin and co-workers introduced a tris(pyrazolyl)hydroborate framework **IV**, yielding the first discrete Ga(I) complex that was neither mixed-valent nor significantly aggregated.[9]

A variety of ligands has since been developed to access stable, well-defined Ga(I) complexes, where both steric and electronic considerations are crucial for isolating these unusual low-valent species. For instance, Jones and co-workers

employed a four-membered guanidinate ligand to prepare the Ga(I) NHC analogue **V**, featuring an acute N–Ga–N bite angle and a less sterically protected gallium centre.[10] The Aldridge group also reported the neutral gallium(I) complex **VI** by combining bulky substituents with a multidentate phosphino-amide ligand based on a xanthene backbone.[11] In this complex, the gallium centre displayed only weak interactions with the oxygen and phosphorus atoms, paralleling earlier observations in amido gallium complexes from the Power and Jones groups.[12] Additionally, organogallium(I) aryl species emerged as valuable candidates for stabilizing Ga(I). Although many attempts to synthesize such complexes resulted in digallenes (RGa=GaR),[13] the Power and Nagase groups[14] and, later, the Kretschmer group[15] showed that superbulky ligands can indeed stabilize monomeric aryl-gallium(I) complexes **VII** and **VIII**.

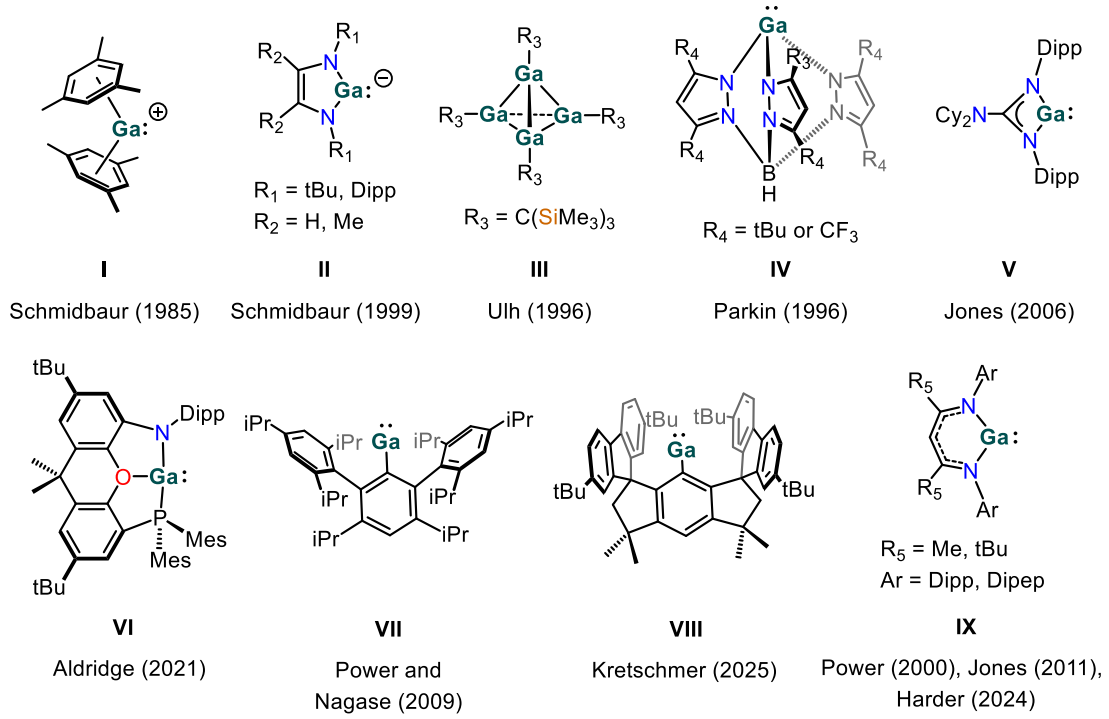


Figure 1. Selected examples of monovalent gallium(I) carbene analogues.

Among the many ligand frameworks used, β-diketiminates (BDIs) have proven especially effective at stabilizing neutral Ga(I) species **IX**, as these monoanionic, chelating ligands provide robust steric protection through carefully chosen substituents.[16] Moreover, the reactivity of BDI-supported Ga(I) species can be fine-tuned by modifying their steric and electronic profiles, and in some cases, the BDI framework itself can act as a non-innocent ligand, participating in redox

processes.[17] Overall, low-valent gallium complexes, particularly those stabilised by bulky BDI ligands, feature a lone pair of electrons and an empty p-orbital, enabling them to activate and cleave bonds in small molecules (Figure 2).[16c, 18]

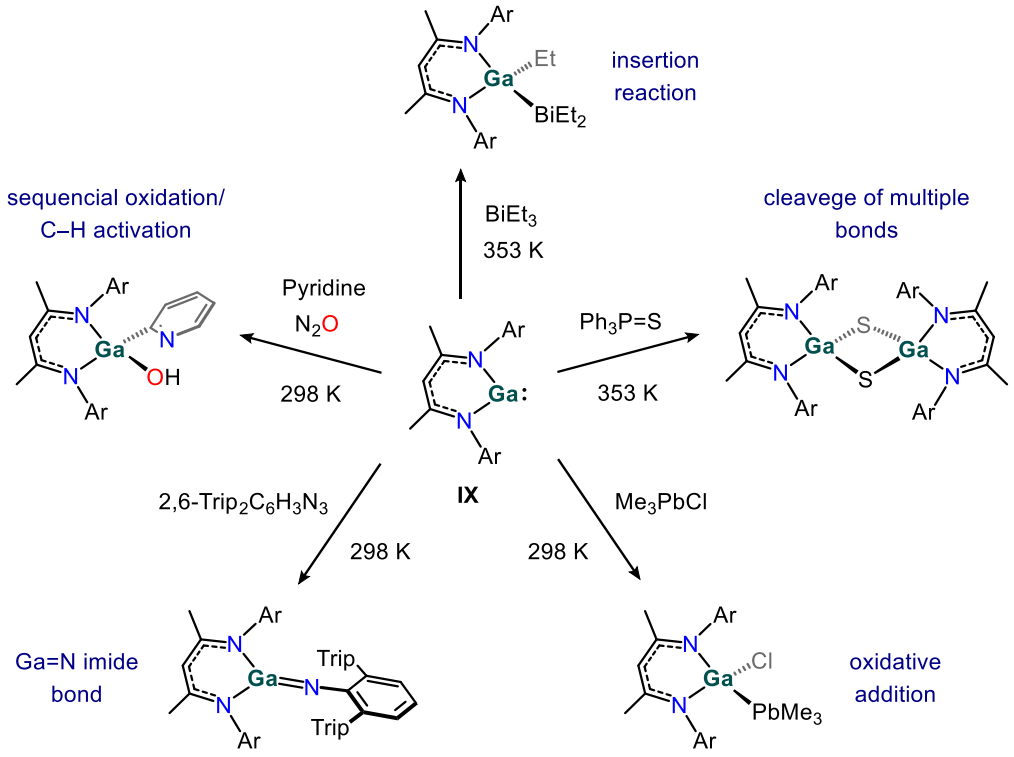
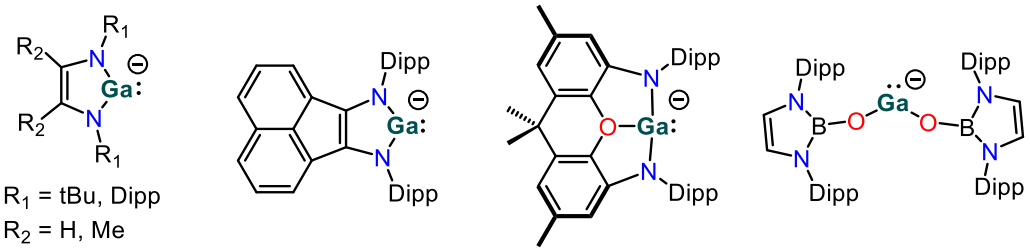


Figure 2. Overview of the reactivity of neutral gallium(I) β-diketiminate species **IX**.

2.1.2 Anionic Gallium(I) Species: Gallyls

Interest in monovalent Group 13 species has grown substantially, particularly in their capacity to replicate transformations often associated with transition metals. Although Aldridge and Goicoechea's groundbreaking work on anionic Al(I) species (aluminyls) inspired much of the subsequent research, analogous anions of boron (boryls), gallium (gallyls), and indium (indyls) were already known. Notably, Schmidbaur and co-workers provided the earliest description of an anionic gallyl species **X**,[6a] followed by work from Jones (Figure 3).[19] Later, Fedushkin, Schumann and co-workers[20] prepared related gallyl complexes **XI** using bulkier (amide) ligands (acenaphthenes), while Aldridge more recently introduced tridentate xanthene-based complexes **XII** and the first acyclic gallyl example **XIII**.[21] In contrast, indyl analogues remain scarce, with only two examples documented to date.[22]



X Schmidbaur (1999) Jones (2002)

XI Fedushkin and Schumann (2008)

XII Aldridge and Goicoechea (2018)

XIII Aldridge (2024)

Figure 3. Known examples of anionic gallium(I) carbene analogues (gallyls).

Although neutral gallium(I) species (N_2Ga:) are considered more stable than their aluminium(I) counterparts (N_2Al:), anionic gallyls ($[N_2Ga:]^-$) show a pronounced tendency toward Ga–Ga bond formation, ligand scrambling, and disproportionation.[13a, 23] These features have significantly limited the scope of gallyl chemistry relative to aluminyl systems.[21a, 24] Moreover, gallium's higher electronegativity and slightly larger atomic radius, compared to aluminium, impart distinctive bonding and reactivity profiles. In addition to these size and electronegativity differences, gallium(I) possesses a $[Ar]3d^{10}4s^2$ ground-state configuration, unlike aluminium's $3s^2$. Although gallium's 3d orbitals are typically considered core-like, their presence can affect overall orbital energies and polarizability in low-valent Ga(I) species, contributing to the distinct reactivity (for instance, Ga–Ga bonding) often observed in gallyls. Computational analyses reveal that these enhanced properties stem from a relatively narrow frontier molecular orbital (FMO) gap (approximately 3.5–4.5 eV), which promotes "umpolung" behaviour in aluminyls.[25] As a result, as gallium's electronic features differ from aluminium, this might enable nucleophilic reactivity distinct from aluminyls and the activation of small molecules via transformations otherwise deemed challenging.

Early examples of gallyl and indyl species appeared as charge-separated ion pairs that incorporate alkali metals for stability. Indeed, most syntheses rely on potassium-stabilized gallyls as the primary alkali-metal counterion (**X**–**XIII**, Figure 3).[6a, 19, 21, 26] As mentioned previously, chelating N–N'-donor frameworks can stabilize a wide range of low-valent species across the periodic table, with β-diketiminate ligands proving particularly effective for generating neutral aluminylenes (N_2Al:) and gallynes (N_2Ga:).[18a, 27] In the previous chapter, we demonstrated how BDI scaffolds stabilize aluminyl complexes derived from their neutral precursors.[24b, 28] However, isolating comparable gallyl complexes continues

to pose formidable synthetic challenges due to gallium's inherent structural and reactivity limitations.[23b] This chapter addresses those challenges by detailing the preparation of novel β-diketiminate-supported gallyls and examining their potential for bond activation pathways.

2.2 Objectives

Given the underexplored nature of anionic gallyl chemistry, the primary aim of this chapter is to develop new synthetic routes for accessing stable anionic gallium(I) carbene analogues under mild conditions, with a particular focus on avoiding gallium–gallium bond formation, an inherent challenge in electron-rich gallium-based systems. To achieve this, we utilize dianionic β-diketiminate (BDI) scaffolds that can effectively stabilise low-valent gallium centres while allowing to probe various aggregation states (ion pairs, dimeric assemblies) formed under different alkali metal ions (Li^+–Cs^+) and solvation environments.

Beyond the synthetic work, we also seek to compare these gallium(I) species to both their aluminyl counterparts and other gallium complexes discussed in the preceding chapter, paying special attention to bond activation at the electron-rich gallium(I) centre. In parallel, computational analyses will offer deeper insight into the electronic configuration and orbital interactions of these anionic gallyls, clarifying how they differ from analogous aluminyls and any other gallyl systems. Through this dual experimental/computational strategy, our overarching goal is to expand our understanding of the known reactivity and structural chemistry of Group 13 elements in electron-rich, low-valent anionic states, underscoring the potential of gallium for transition-metal-like bond activations.

2.3 Results and Discussion

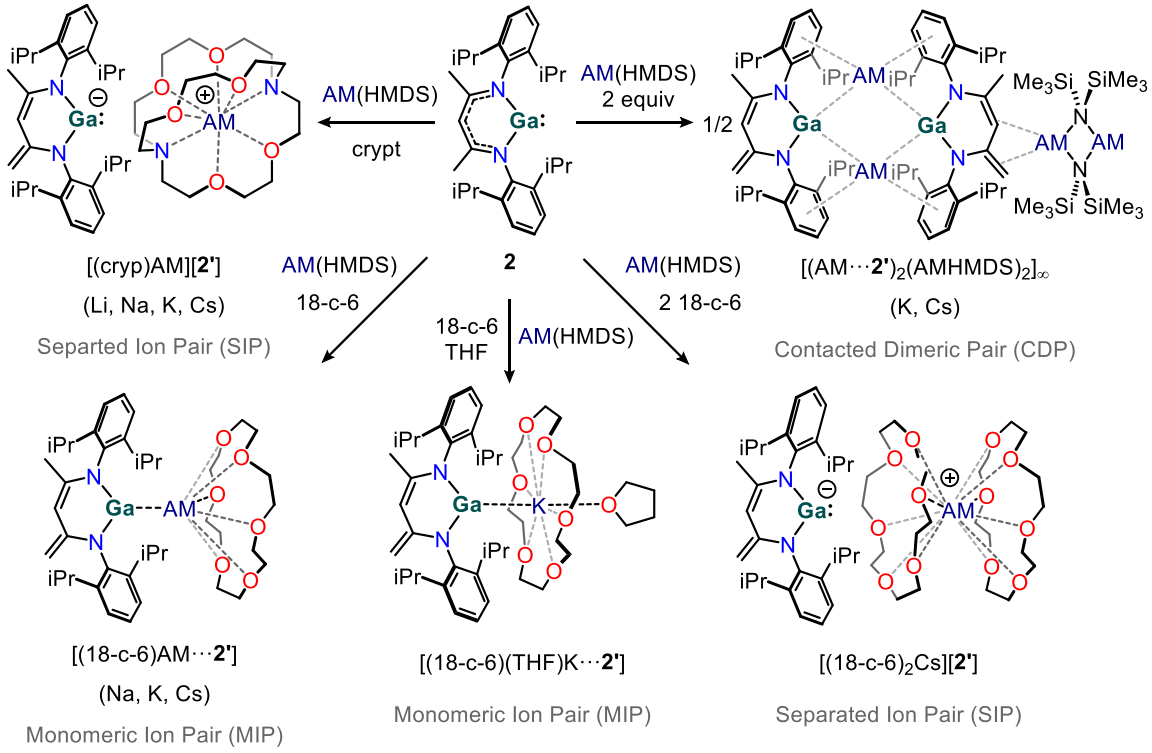
2.3.1 Synthesis of Alkali Metal Gallyls

Comparing the scarcity of known examples of anionic gallyls with the well-established aluminyl systems (*Chapter I*) reveals a significant gap in the field. Motivated by our success in isolating new aluminyl compounds, we sought to extend our understanding of anionic Group 13 chemistry by preparing gallium-based analogues. Consequently, we employed the same monoanionic β-diketiminate (BDI) ligand, $[^{Dipp}BDI]^-$, to obtain the neutral gallium(I) compound (^{Dipp}BDI)Ga (**2**) following a slightly modified procedure reported by Power and co-workers.[16a]

To convert the neutral gallium(I) species into its anionic counterparts, we adopted the same overall strategy used previously for aluminyl compounds. Under carefully tuned reaction conditions, different aggregation states were achieved, each potentially exhibiting distinct reactivity. Initial attempts to generate anionic gallyl species by directly reacting **2** with various alkali metal bis(trimethylsilyl)amides (AMHMDS, AM = Li, Na, K, Cs) at room temperature returned unreacted **2**, with no new NMR signals observed after 24 hours. However, upon heating **2** with either KHMDS or CsHMDS in a 1:2.1 ratio in aromatic solvents (benzene or toluene) at 323 K, selective deprotonation of a methyl group on the β-diketiminate backbone occurred. The resulting solids, isolated and characterised, were identified as contacted dimeric pairs (CDPs), $[(AM\cdots\mathbf{2'})_2(AMHMDS)_2]$ (AM = K, Cs), featuring additional coordination by dimeric $(AMHMDS)_2$ units (Scheme 1). Strong Ga···AM interactions and π-aryl contacts help stabilise these aggregates. Lowering the equivalents of AMHMDS below stoichiometric levels consistently afforded the same dimeric gallyl–AMHMDS complexes, though in lower yields, underscoring the strong affinity of gallium(I) anions for metal–ligand stabilisation compared to their lighter aluminyl counterparts. By contrast, reacting **2** with either LiHMDS or NaHMDS under the same conditions returned unreacted **2**, reflecting the higher basicity of KHMDS and CsHMDS under these conditions.

Reactions with MHMDS and 2.2.2-cryptand (crypt) in aromatic solvents at room temperature yielded well-defined “naked” gallyl anions $[\mathbf{2'}]^-$ as separated ion pairs (SIPs) [**2'**][AM(crypt)] (AM = Li, Na, K, Cs) at room temperature in toluene. by crypt minimises Ga···M interactions and prevents gallium–gallium bond formation. Replacing crypt with 18-crown-6 (18-c-6, 1.1 equiv) in benzene or toluene at room temperature, however, led to the isolation of distinct aggregates from the crypt

stabilised gallyls. For instance, the contacted monomeric ion pair (MIP) [(18-c-6)AM···**2'**] were obtained for Na^+, K^+ and Cs^+, typically precipitated as an amorphous solid upon addition of *n*-hexane, and [(18-c-6)(THF)K···**2'**] in the presence of THF. Efforts to prepare the Li^+ derivative were unsuccessful, even after employing alternative donors such as N,N,N′,N′-tetramethylethylenediamine), 1,2-dimethoxyethane, or diethyl ether. Moreover, increasing the equivalents of 18-crown-6 enabled modulation of the degree of ion pairing: introducing two equivalents of 18-crown-6 to the caesium derivative yielded the SIP species [**2'**][Cs(18-c-6)$_2$], akin to the crypt species, demonstrating that increasing the ligand saturation around the alkali metal effectively tunes the Ga···M separation.



Scheme 1. Synthesis of alkali metal derivatives of the novel anionic gallium(I) carbene analogue [**2'**]$^-$ (HMDS = bis(trimethylsilyl)amide).

Notably, these modifications to obtain anionic gallyl complexes (relative to analogous aluminyl species) underscore the differences in stability and reactivity of gallium-based systems. Indeed, our results contrast with earlier observations by Kretschmer and co-workers, who attempted to form similar gallyl species using organo potassium reagents, such as KCH(SiMe$_3$)$_2$, and instead isolated a dipotassium cyclopentagallane [R_5Ga_5]K_2 species at room temperature, resulting from gallium–gallium bond formation,[23b] whereas the same reagent yields stable

aluminyl dimers [(AM···Al)$_2$].[24b, 28a] Moreover, the stability of these new gallyl species contrasts sharply with the tendency of low-valent gallium systems to cluster or disproportionate,[29] and further diverges from aluminyl dimers, which react with aromatic solvents even at room temperature.[28a, 30]

Consequently, as with other bimetallic Group 13 systems, we employed ^{1}H, ^{11}B, ^{13}C, ^{19}F NMR spectroscopy, two-dimensional NMR experiments (COSY, HSQC, HMBC), single X-ray diffraction, elemental analysis, and computational methods, to characterise these gallium(I) species. Additionally, because of the various aggregation states and our interest in comparing these gallyl species with aluminyl analogues, we conducted ^{1}H *D*iffusion-*O*rdered *S*pectroscop*Y* (^{1}H DOSY) to investigate their solution behaviour. Intriguingly, we observed unconventional coordination modes of the monoanionic ^{Dipp}BDI ligand, and C–H activation reactivity with several organic substrates (including azobenzene and alkynes) afforded novel complexes, emphasizing the untapped potential of these anionic gallyl species.

2.3.2 Nuclear Magnetic Resonance (NMR) Spectroscopic Studies

NMR spectroscopy was employed to investigate the newly synthetised anionic gallium(I) species discussed in this chapter. Since electropositive alkali metals (Li^+, Na^+, K^+, Cs^+) can engage with the gallyl anion [**2'**]$^-$ forming various aggregation states in the presence or absence of donor ligands (2.2.2-cryptand, 18-crown-6), our primary goals were to study their stability in solution and clarify how alkali metal identity, donor ligands, and solvent effects influence their aggregation behaviour.

2.3.2.1 Contacted Dimeric Gallyl Pairs

Contacted dimeric pairs (CDPs) of the gallyl anion [**2'**]$^-$ were formed exclusively with K^+ and Cs^+ counterions, yielding bimetallic units [(AM···**2'**)$_2$]. In these assemblies, Ga···AM interactions partially stabilise the dimeric arrays, while the alkali metal further engages in AM$^+$···π-arene contacts with aromatic substituents on the BDI ligand framework, reinforcing the overall structures. Notably, these new gallyl CDPs exhibit extended coordination through AM$^+$··· β-diketiminate-backbone contacts, generating polymeric "(AM···**2'**)$_2$···(AMHMDS)" frameworks formulated as [(AM···**2'**)$_2$(AMHMDS)$_2$]$_\infty$ (AM = K, Cs, see Scheme 1).

Characterising these dimers in solution posed challenges due to poor solubility in aromatic solvents and the tendency for reprotonation of the BDI

backbone in neat THF, which regenerates neutral gallium(I) **2**. Consequently, a 4:1 benzene:THF mixture was used for NMR studies, enabling sufficient solubility and stability of $[(K\cdots\mathbf{2'})_2(KHMDS)_2]_\infty$ and $[(Cs\cdots\mathbf{2'})_2(CsHMDS)_2]_\infty$ despite their high reactivity.

The ^{1}H NMR spectra of these K- and Cs-based CDPs share analogous features, reflecting their similar structural motifs. In the potassium derivative (Figure 4), the γ-CH proton of the BDI backbone appears as a singlet at δ 5.18, while two septet signals at δ 4.05 and 3.96 (2H each, J = 6.9 Hz) correspond to the isopropyl CH groups. Notably, slightly broad singlets at δ 3.44 and 2.60 represent the newly formed methylene (CH_2=C) fragment arising from deprotonation of the BDI backbone, confirming the generation of the gallyl anion [**2'**]$^-$. A backbone methyl group is observed at δ 1.70, partially overlapping with the residual THF-d_8 peak, and the isopropyl methyl groups of the Dipp substituents appear as multiplets at δ 1.42 and 1.31. Finally, the HMDS unit resonates as a singlet at δ 0.22. In the caesium derivative, the γ-CH proton resonates at δ 5.08, and two septets at δ 3.98 and 3.87 are assigned to the isopropyl CH groups. A pair of broad doublets (δ 3.35, 2.51, J = 1.8 Hz) reflects the alkene CH_2=C group, again confirming backbone deprotonation. The BDI methyl group resonates at δ 1.65, while HMDS appears at δ 0.10. The close similarity of these ^{1}H NMR patterns underscore their analogous bonding environments, with slight chemical shift differences arising from the distinct radii and coordination behaviour of K^+ vs. Cs^+.

Both K and Cs CDPs display comparable ^{13}C signatures, consistent with their shared structural framework. In the potassium complex, the γ-CH carbon resonates at δ 100.4, the newly formed methylene (C=CH_2) appears at δ 71.4, and the HMDS carbons lie at δ 7.0. The caesium derivative shows minimal chemical shift variations, reflecting minor steric or electronic differences imparted by the larger Cs^+ cation. Moreover, a ^{133}Cs NMR experiment reveals a broad singlet at δ 60.9, in contrast to the δ 119.2 resonance of free CsHMDS,[31] indicating a distinct coordination environment for Cs in the gallyl dimer.

Collectively, the NMR data demonstrate that while K- and Cs-based dimeric gallyls share a closely related structural motif, subtle variations in chemical shifts highlight differences in alkali metal size and coordination. The successful detection of these dimers in solution, despite their limited solubility and propensity toward side reactions, confirms the formation of contacted dimeric gallyls stabilised by β-diketiminate ligands and alkali metal hexamethyldisilazides.

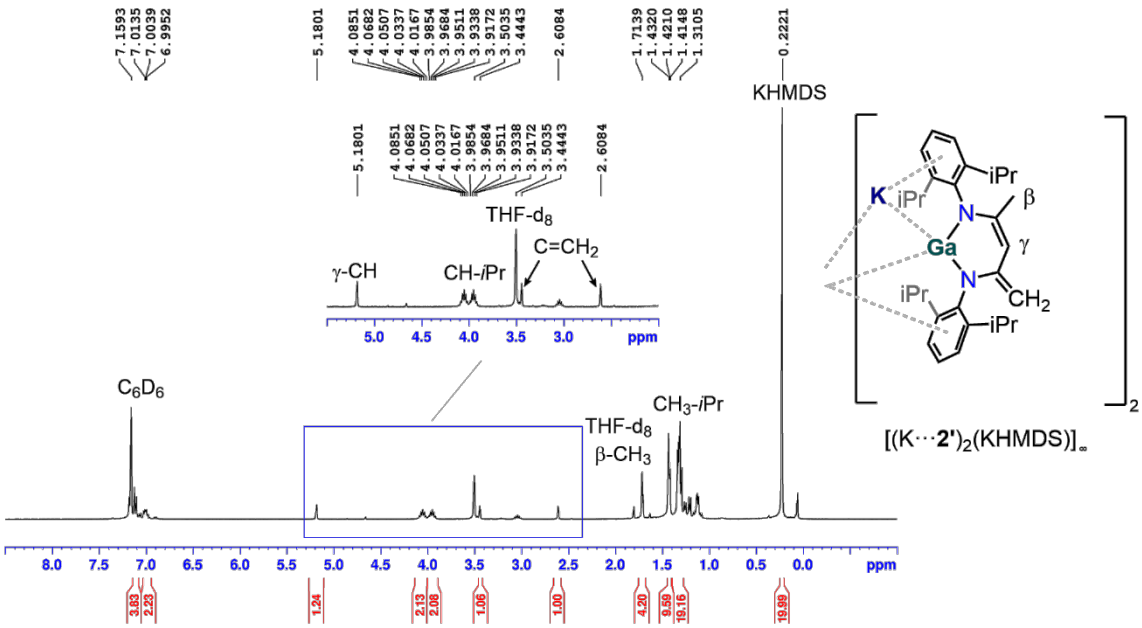


Figure 4. ^{1}H NMR (400 MHz, C_6D_6/THF-d_8, 298 K) of [(K···**2'**)$_2$(KHMDS)$_2$]$_\infty$.

Table 1. Selected ^{1}H and ^{13}C{^{1}H} NMR signals (ppm) in C_6D_6:THFd_8 (4:1) at 298 K of [(AM···**2'**)$_2$(AMHMDS)$_2$]$_\infty$ where AM = K or Cs.

Complex	γ-CH		C=CH$_2$		β-Me		AMHMDS	
	^{1}H	^{13}C	^{1}H	^{13}C	^{1}H	^{13}C	^{1}H	^{13}C
[(K···**2'**)$_2$(KHMDS)]$_\infty$	5.18	100.4	3.44 2.60	71.4	1.71	23.8	0.22	7.0
[(Cs···**2'**)$_2$(CsHMDS)]$_\infty$	5.08	100.7	3.35[a] 2.51[a]	72.0	1.65	23.8	0.09	6.9

[a] Doublet (J = 1.8 Hz).

2.3.2.2 Monomeric Gallyl Pairs

The 18-crown-6 gallyl MIPs proved generally more soluble than the dimeric gallyl complexes in aromatic solvents, thereby minimising the need for strongly donor solvents such as THF. An exception is [(18-c-6)K···**2'**], which exhibits lower solubility and required small amounts of THF-d_8 for characterisation. As with the analogous aluminyl MIPs from *Chapter I*, the three 18-crown-6 stabilised gallyl MIPs, [(18-c-6)AM···**2'**] (Na, K, Cs, see Scheme 1) display only minor differences in their ^{1}H and ^{13}C NMR spectra, with selected summarised in Table 2. In the ^{1}H spectra, aromatic resonances appear between δ 7.35 and 7.00, featuring typical splitting

patterns for the substituted phenyl rings. The γ-CH proton usually resonates near δ ~5.5 as a singlet. Two septet signals (δ 4.4–4.1, 2H each, *J* = 6–7 Hz) correspond to the isopropyl CH groups, while two doublets (δ 4.0–2.9, 1H each, *J* = 2.0 Hz) represent the methylene (CH_2=C) protons introduced by deprotonation of the β-diketiminate (BDI) backbone. A prominent resonance at δ ~2.8, integrating to 24 protons, is attributed to the coordinated 18-crown-6 ligand. The β-methyl group of the BDI framework is observed at δ 1.8–2.0 as a singlet, and the iPr methyl substituents typically appear as overlapping doublets with coupling constants around 6–7 Hz.

Comparisons of these 18-crown-6–supported gallyl MIPs with their aluminyl counterparts reveal interesting contrasts, particularly in the chemical shift of the γ-CH proton, which is highly sensitive to electronic changes in the BDI framework. In the neutral monovalent species **1** and **2**, this γ-CH group appears at δ ~5.19, whereas in the corresponding 18-crown-6 aluminyl and gallyl systems [(18-c-6)AM···**1'**] and [(18-c-6)AM···**2'**], it shifts to δ ~5.35 and 5.55, respectively. The greater deshielding observed in the gallyl MIPs aligns with gallium(I)'s [Ar]$3d^{10}4s^2$ electronic configuration, which can enable more extensive charge delocalization into the BDI ligand, in contrast to aluminium's absence of low-lying filled d orbitals. Consequently, the negative charge in the gallyl anion [**2'**]$^-$ is distributed not only at the metal centre but also across the ligand, reflected in the downfield-shifted ^{1}H resonances and implying extended electron delocalization.

By contrast, the THF-coordinated potassium species [(18-c-6)(THF)K···**2'**] exhibits a γ-CH shift at δ 5.36, more reminiscent of the 18-crown-6 aluminyl MIPs, suggesting that additional coordination at the potassium centre reduces electron density around the gallium site and the BDI backbone. This effect also influences the resonances of the 18-crown-6 ligand, which shift slightly upfield compared to the THF-free gallyl species.

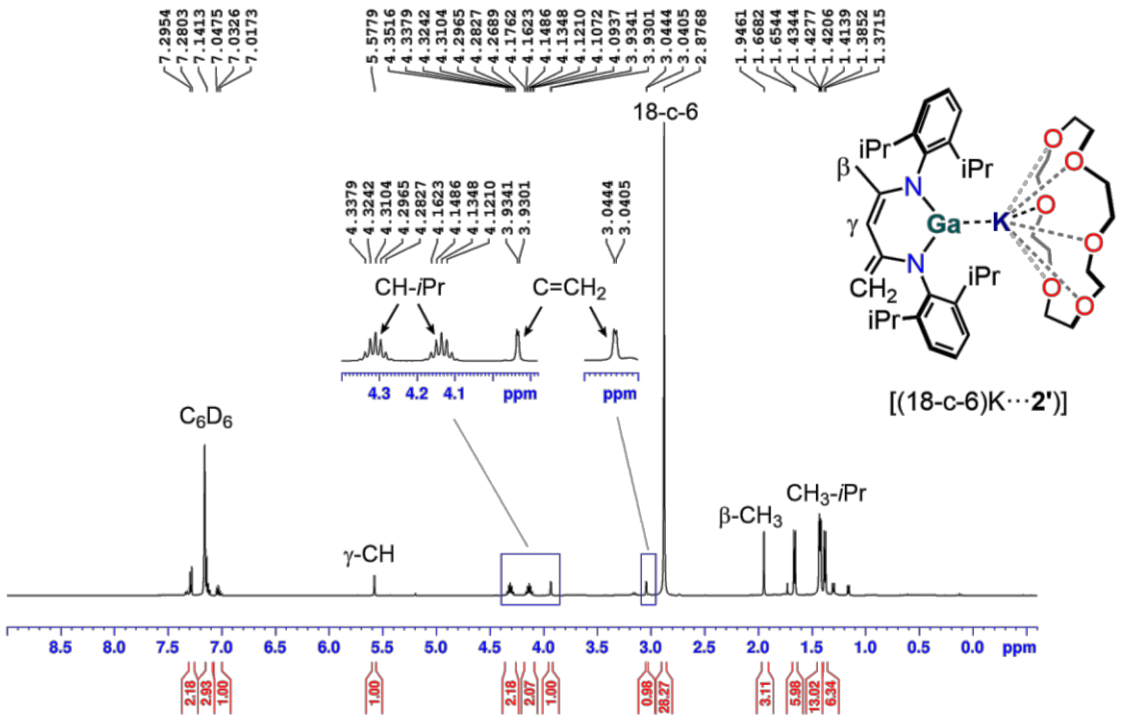


Figure 5. ^{1}H NMR (500 MHz, C_6D_6, 298 K) of [(18-c-6)K···**2'**)].

Table 2. Selected ^{1}H and ^{13}C{^{1}H} NMR signals (ppm) in C_6D_6 at 298 K of [(18-c-6)AM···**2'**] where AM = Na, K or Cs.

Complex	γ-CH		C=CH$_2$[a]		β-Me		18-c-6	
	^{1}H	^{13}C	^{1}H	^{13}C	^{1}H	^{13}C	^{1}H	^{13}C
[(18-c-6)Na···**2'**]	5.60	101.8	3.93 3.00	73.6	1.88	24.1	2.92	69.1
[(18-c-6)K···**2'**]	5.57	101.2	3.93 3.04	72.8	1.94	24.9	2.87	69.8
[(18-c-6)(THF)K···**2'**]	5.36		3.67 2.80		1.82		3.04	
[(18-c-6)Cs···**2'**]	5.51	100.9	3.81 2.94	71.7	1.95	24.9	2.98	69.8

[a] Doublet (J = 2 Hz).

2.3.2.3 Separated Gallyl Pairs

Separated ion pairs (SIPs), or "naked" gallyl anions, were accessed by using 2,2,2-cryptand (crypt) instead of 18-crown-6, yielding [(crypt)AM][**2'**] (AM = Li, Na, K,

Cs). These species could be characterised in neat THF-d_8 or in THF-d_8:C_6D_6 mixtures. Notably, replacing crypt with two equivalents of 18-crown-6 afforded an additional separated ion pair, [(18-c-6)$_2$AM][**2'**], wherein the caesium cation is fully encapsulated by two crown ether ligands.

Among the series, the lithium–crypt complex exhibited distinctive solution behaviour. As Li^+ is the smallest alkali metal tested, it is readily trapped by the macrocyclic cryptand. However, [(crypt)Li][**2'**] dissolved only in THF, necessitating NMR characterisation in THF-d_8. The ^{7}Li NMR spectrum (Figure 6) showed three resonances (δ 1.75, 0.52, −1.28), the most downfield corresponding to free LiHMDS. Simultaneously, broad ^{13}C NMR peaks (δ 71.8, 70.8, 57.6) reflect fluxional rearrangements within the cryptand cavity, likely due to mismatched sizes between Li^+ and the relatively large cryptand interior.[32] Also, the ^{1}H NMR signals confirm deprotonation of the β-diketiminate (BDI) backbone, with two doublets at δ 2.68 and 1.93, plus a γ-CH singlet at δ 4.52. Although this Li-crypt SIP shows somewhat shielded resonances compared to the monomeric ion pairs stabilised by 18-crown-6, direct comparisons are complicated by the distinct solvents and coordination equilibria.

For the remaining crypt-stabilised gallyl SIPs, [(crypt)AM][**2'**] (AM = Na, K, Cs), their reduced solubility in C_6D_6 necessitated small amounts of THF-d_8 (4:1 ratio) to achieve complete dissolution. The resulting ^{1}H NMR spectra resemble those of donor-free contacted dimeric pairs (CDPs) and 18-crown-6 monomeric ion pairs (MIPs). A singlet near δ 5.0 corresponds to the γ-CH group, while two septets at δ 4.3–4.0 reflect isopropyl CH signals. The cryptand resonates around δ ~3.1, 3.0, and 2.0, occasionally splitting into an apparent triplet (J = 4.6–4.8 Hz). Deprotonation of the BDI backbone is verified by two doublets (δ 3.6–3.2, 2.8–2.5); methyl groups from either the backbone's β-position or the isopropyl substituents appear at δ 1.8–1.3 as singlets or doublets, respectively (Figure 7).

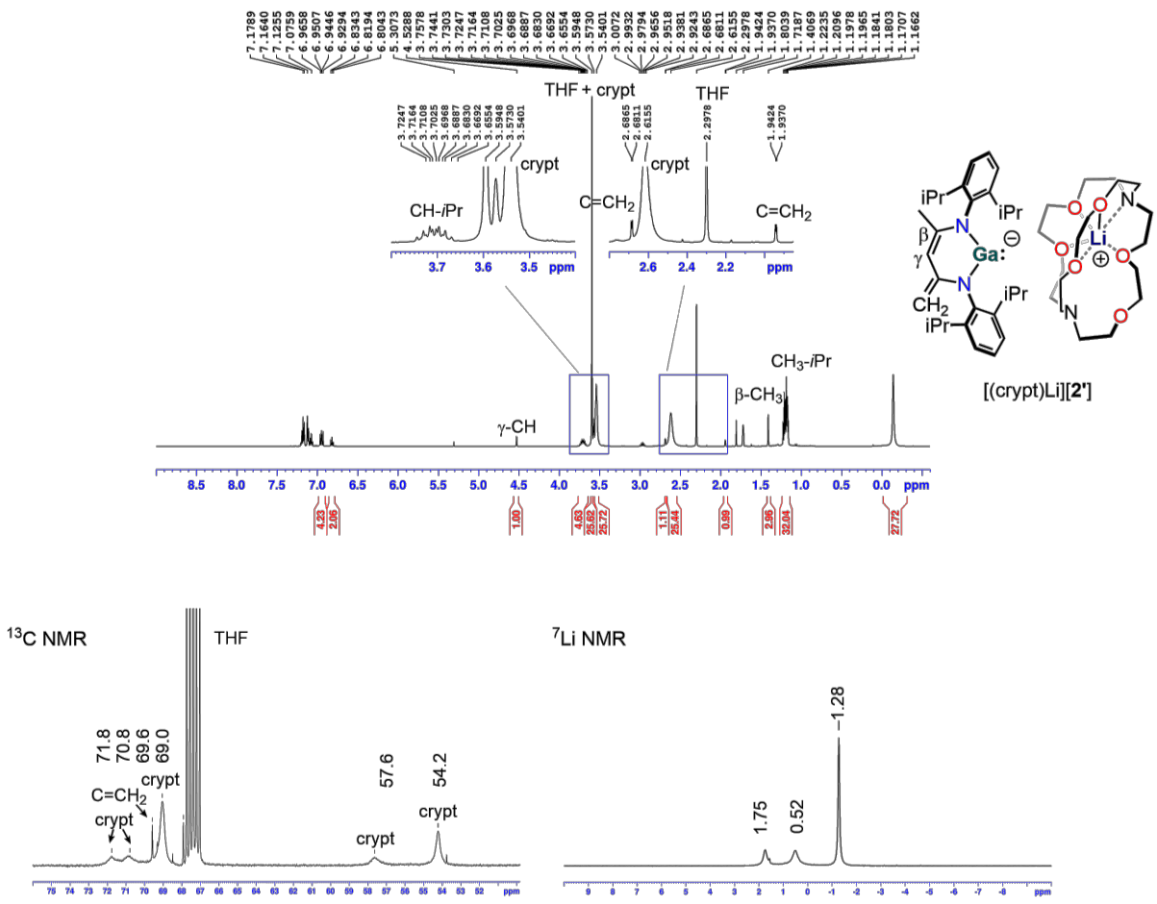


Figure 6. ^{1}H NMR (500 MHz) of [(crypt)Li][**2'**] (top), and selected sections (bottom) of the ^{13}C{^{1}H} NMR (125.6 MHz) and ^{7}Li NMR spectra (194.2 MHz) in THF-d_8 at 298 K.

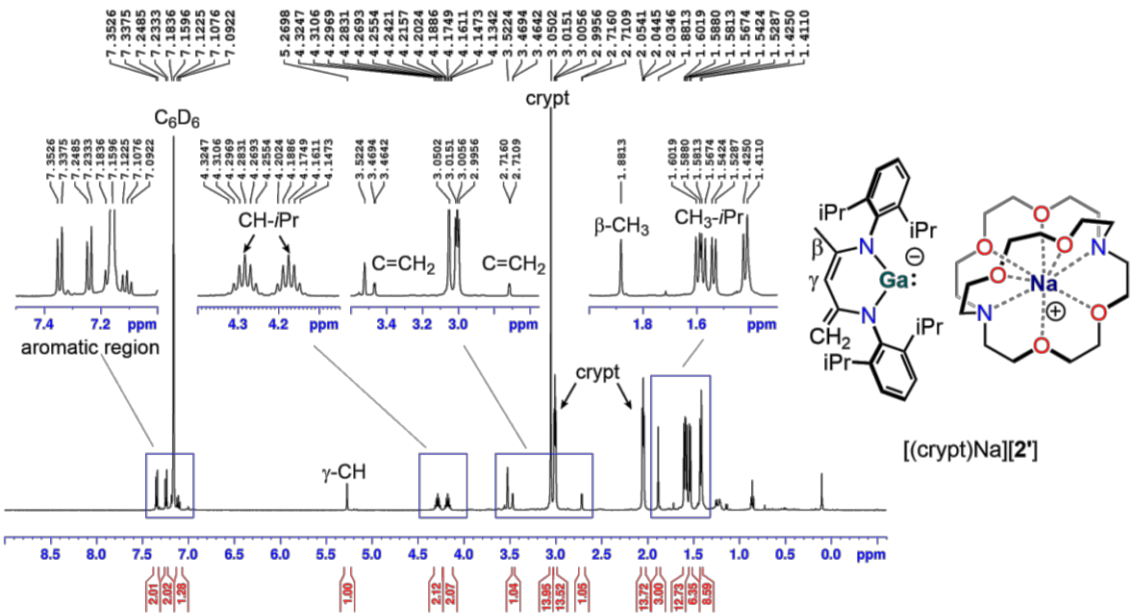


Figure 7. ^{1}H NMR (500 MHz, C_6D_6:THF-d_8, 298 K) of [(crypt)Na][**2'**].

The additional separated ion pair, [(18-c-6)$_2$Cs][**2'**], exhibits ^{1}H and ^{13}C patterns nearly identical to its crypt-based SIP analogue [(crypt)Cs][**2'**] , see Table 3. However, ^{133}Cs NMR experiments differentiate them. For instance, encapsulation of Cs^+ by crypt yields a broad resonance at δ 194.4, whereas coordination to two 18-crown-6 ligands shifts the ^{133}Cs signal to δ 15.6. This substantial difference highlights the strong influence of donor ligands on the ^{133}Cs environment, while the three-dimensional cryptand induces pronounced deshielding of caesium, the two-dimensional crown ethers lead to a comparatively upfield shift.

Although the analogous crypt-aluminyl SIPs, described in *Chapter I*, were typically characterised in fluorobenzene (C_6H_5F), parallels with crypt-gallyl SIPs indicate that once the alkali metal and gallium(I) anion are fully separated, ^{1}H and ^{13}C chemical shifts show only minor variations among these species. By contrast, contacted ion pairs exhibit more pronounced gallium···alkali metal interactions, resulting in distinct chemical shift patterns and divergent reactivity profiles for aluminyls and gallyls.

Table 3. Selected ^{1}H,^{13}C{^{1}H}, and ^{133}Cs{^{1}H} NMR signals (ppm) in (C_6D_6:THF) at 298 K of [(donor)AM][**2'**] where AM = Na, K or Cs and donor= crypt or (18-c-6)$_2$.

Complex	γ-CH		C=CH$_2$[a]		β-Me		
	^{1}H	^{13}C	^{1}H	^{13}C	^{1}H	^{13}C	^{133}Cs
[(crypt)Na][**2'**]	5.26	100.6	3.46 2.71	70.3	1.88	25.2	
[(crypt)K][**2'**]	5.25	100.6	3.45 2.69	70.3	1.86	25.2	
[(crypt)Cs][**2'**]	5.11	100.6	3.34 2.54	70.6	1.73	25.3	194.4
[(18-c-6)$_2$Cs][**2'**]	5.31	100.1	3.59 2.75	71.7	1.86	24.9	15.6

[a] Doublet (*J* = 2.5-2.6 Hz).

2.3.3 Diffusion Order SpectroscopY (DOSY) NMR Studies

^{1}H DOSY NMR spectroscopy was employed to investigate the aggregation states and dynamic behaviours of the anionic gallium(I) species in solution, providing valuable insights into metal–metal and metal–ligand interactions. By applying both an in-house external calibration method (OEC) and Stalke's established calibration curves (ECC),[33] we determined the molecular weights (MW) and diffusion

coefficients (D) of these species under various conditions (C_6D_6, THF-d_8, or C_6D_6:THF-d_8 mixtures). Stalke's ECC classification further distinguishes among compact spheres (CS), dissipated spheres and ellipsoids (DSE), and expanded discs (ED), based on the molecule's hydrodynamic behaviour, which is an approach suitable for these systems.

Additionally, the Stokes–Einstein equation[34] was used to estimate hydrodynamic diameters (D_{hyd}) for the diffusing species, enabling direct comparison to the crystallographic dimensions discussed in Section 2.3.4. This dual approach, combining DOSY-based MW estimation and hydrodynamic diameter analysis, clarifies whether the solution-phase species remain intact or undergo partial dissociation, while also gauging the extent of solvent coordination.

A core question for the contacted dimeric pairs $[(AM\cdots\mathbf{2'})_2(AMHMDS)_2]_\infty$ (AM = K, Cs), is whether the dimeric gallyl units persist in solution alongside the amide subunit $[(AMHMDS)_2]$. DOSY NMR analysis revealed two distinct diffusing species in C_6D_6:THF-d_8 for both the potassium and caesium derivatives, indicating that the gallyl dimers $[(AM\cdots\mathbf{2'})_2]$ and the amide $[(AMHMDS)_2]$ base persist as separate entities in solution.

For $[(K\cdots\mathbf{2'})_2(KHMDS)_2]_\infty$ (Figure 8), the dimeric $[(K\cdots\mathbf{2'})_2]$ showed ECC-CS and OEC MW estimates of 981 g/mol and 845 g/mol, respectively; within 7–14% of the calculated MW. In parallel, the amide base portion gave MWs of 490–572 g/mol (ECC–OEC), consistent with a THF-solvated $[(KHMDS)_2(THF)_2]$ species (calcd. 551 g/mol). These data confirm that $[(K\cdots\mathbf{2'})_2]$ persists in solution without dissociating into monomeric potassium gallyls, while $[(KHMDS)_2(THF)_2]$ remains independent. An analogous outcome was observed for $[(Cs\cdots\mathbf{2'})_2(CsHMDS)_2]_\infty$ showing two diffusing species. The caesium gallyl dimeric unit $[(Cs\cdots\mathbf{2'})_2]$ exhibited ECC and OEC MW estimates of 1067 and 986 g/mol, within 16–26% of its calculated MW (1239 g/mol). The amide unit was assigned an estimated MW (676–690 g/mol, ECC-OEC methods) consistent with a THF-solvated dimeric $[(CsHMDS)_2(THF)_2]$ unit. These DOSY data further indicate that the dimeric $[(Cs\cdots\mathbf{2'})_2]$ and $[(CsHMDS)_2(THF)_2]$ are the predominant units in solution, akin to what has been observe for the dimeric potassium gallyl analogue.

Hydrodynamic diameter analyses based on the Stokes–Einstein equation gave 16 Å for both dimers $[(K\cdots\mathbf{2'})_2]$ and $[(Cs\cdots\mathbf{2'})_2]$. These values are consistent with the dimensions derived from the X-ray crystal structures (16 Å for K and 17 Å for Cs), suggesting that the dimeric gallyl units remain intact in solution. Interestingly,

this solution behaviour differs from that reported for the dimeric aluminyl analogues [(AM···**1'**)$_2$] (AM = K, Cs), which partially dissociate in aromatic solvents.[24b, 28] Hence, the stronger gallium···alkali metal contacts allow these gallyl dimers to remain intact in solution, even in the presence of coordinating THF.

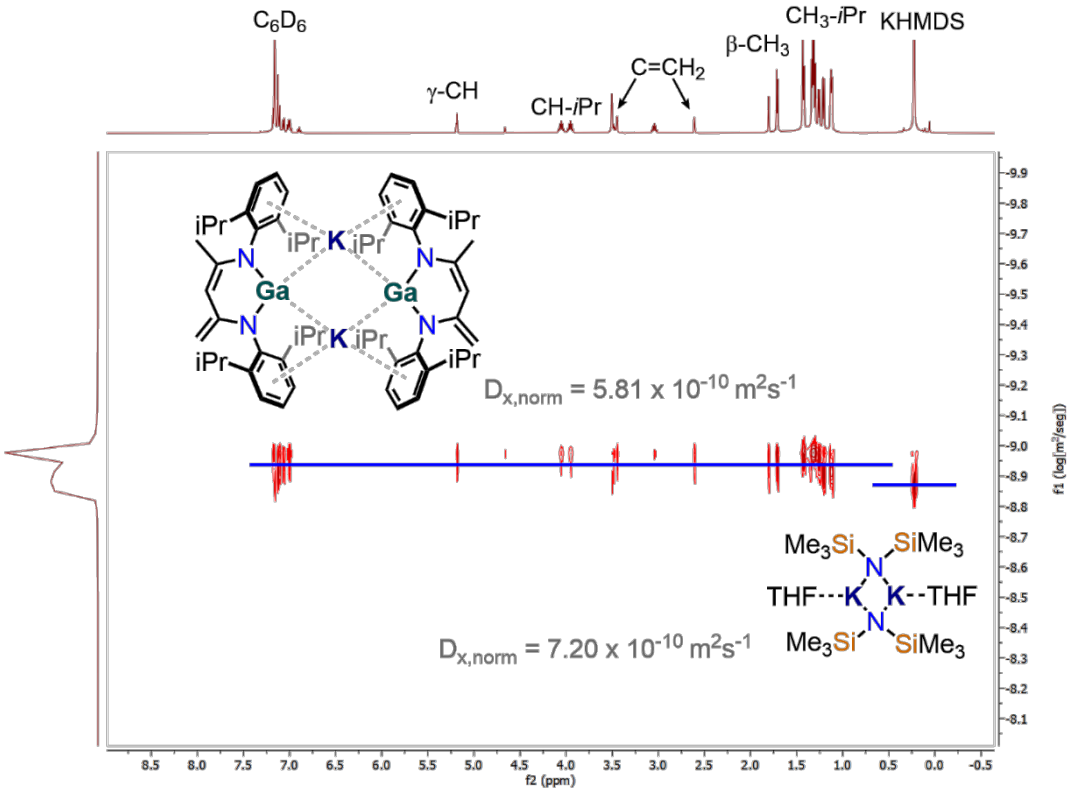


Figure 8. ^{1}H DOSY NMR 500 MHz (298 K) of [(K···**2'**)$_2$(KHMDS)$_2$]$_\infty$ in C_6D_6/THF-d_8.

DOSY analyses of the three 18-crown-6 monomeric gallyl species, [(18-c-6)AM···**2'**] (AM = Na, K, Cs), revealed only one diffusing species in C_6D_6 solution in each case (see Figure 9). Using Stalke's ECC-DSE approach, the estimated MW for [(18-c-6)Na···**2'**] was 665 g/mol (calcd. 774 g/mol), [(18-c-6)K···**2'**] 855 g/mol (calcd. 790 g/mol), and [(18-c-6)Cs···**2'**] 884 g/mol (calcd. 884 g/mol). These deviations (8–16%) are within acceptable limits for DOSY-based approximations. In addition, our OEC method returned similar MWs within deviations raging 19–30%, confirming their existence as single contacting entities through persistent gallium···alkali metal interactions in solution. Hydrodynamic diameter calculations for the 18-crown-6 MIPs corroborate dimensions of approximately 14–15 Å, matching the crystallographic dimensions of these derivatives (15 Å for Na, K, and Cs species). These findings mirror the MW observations, reinforcing that these gallyl retain contacted aggregation in solution.

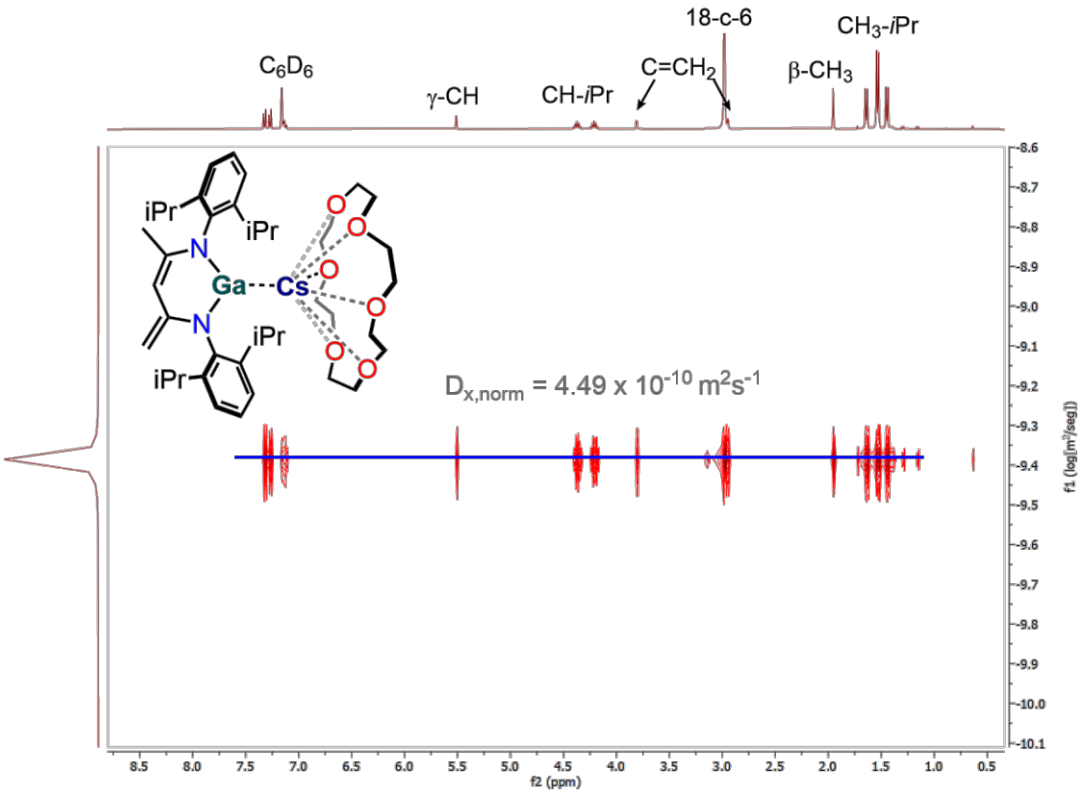


Figure 9. ^{1}H DOSY NMR 500 MHz (298 K) of [(18-c-6)Cs···**2'**] in C_6D_6.

For separated ion pairs [(crypt)AM][**2'**] (AM = Li, Na, K, Cs), the DOSY spectra suggest varying levels of interaction between the cationic and anionic units. Only one diffusing species was detected in neat THF-d_8 (Li) and C_6D_6/THF-d_8 (Na, K, Cs) solutions, with MWs determined by ECC-DSE at 770 g/mol (Li), 903 g/mol (Na), 1012 (K) g/mol, and 994 (Cs) g/mol, respectively. These values, within a 1–16% error margin, indicate that the $[AM(crypt)]^+$ and $[\mathbf{2'}]^-$ units interact in solution, likely forming contact ion pairs like those stabilized by 18-crown-6. The OEC results corroborate this interpretation, yielding MWs of 668 g/mol, 1157 g/mol, 1110 g/mol, and 1135 g/mol for Li, Na, K, and Cs SIPs within an 18–30% error margin. Hence, both methodologies converge on the suggestion that the [(crypt)AM][**2'**] species diffusing primarily as contacted pairs. The involvement of additional C_6D_6 and THF-d_8 solvent molecules in this association cannot be ruled out. In addition, the slightly larger error for the lithium SIP [(crypt)Li][**2'**] aligns with the smaller size and more dynamic nature of lithium compared to the other alkali metals within the crypt cavity.

Stokes–Einstein-derived diameters for these crypt-stabilized complexes (16–18 Å) mirror the crystallographic dimensions (17–18 Å), indicating that cryptand effectively encapsulates the alkali metal in solution while maintaining a contact or

close-ion-pair arrangement between crypt-cations and the gallyl anion, [(crypt)AM]$^{+}\cdots$[**2'**]$^{-}$. This consistent behaviour across different alkali metal derivatives underscores the stability of the gallium$\cdots$alkali metal interactions.

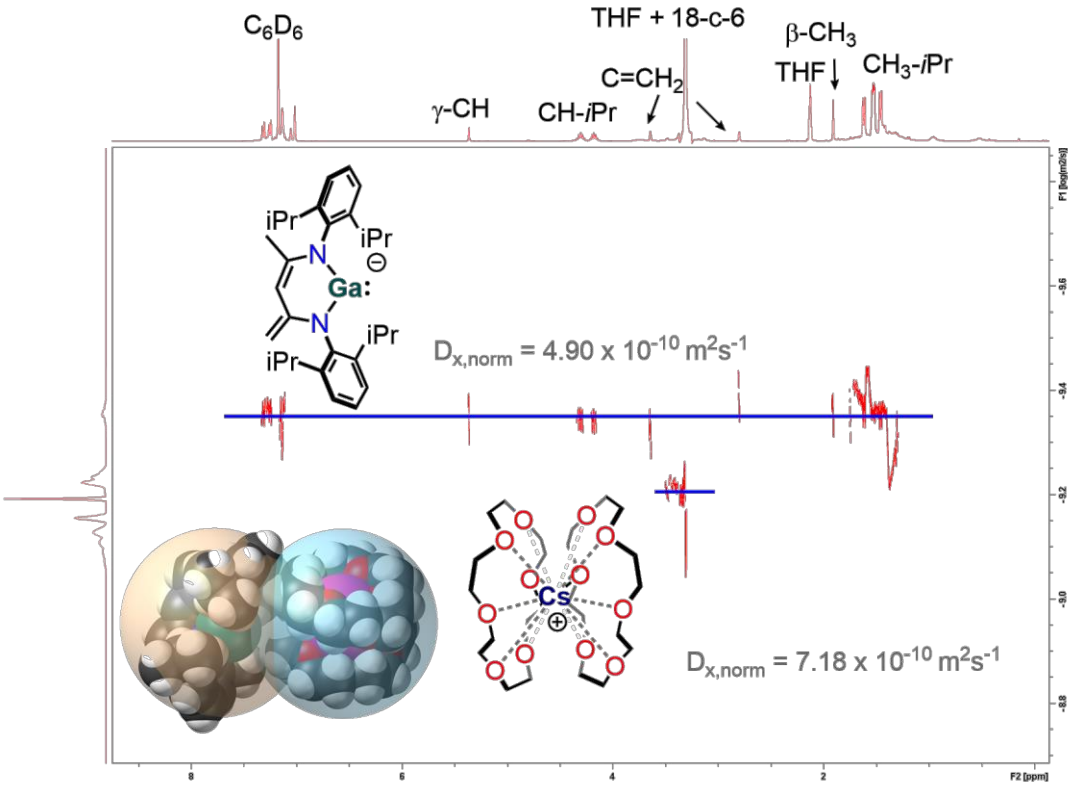


Figure 10. ^{1}H DOSY NMR 500 MHz of [(18-cr-6)Cs$\cdots$**2'**] in C_6D_6 at 298 K and their estimated molecular radius.

The only fully separated species found in solution is the SIP [(18-c-6)$_2$Cs][**2'**] (Figure 10), where caesium is encapsulated by two 18-crown-6 ligands, which showed two distinct species in solution, one assigned to [(18-c-6)$_2$Cs]$^{+}$ and the gallyl [**2'**]$^{-}$ unit. Both methodologies, EEC and OEC, suggest that this complex has two independent units in solution. The molecular weight estimate by ECC-DSE is 571 g/mol and OEC 557 g/mol for [(18-c-6)$_2$Cs]$^{+}$; the variations observed between the experimental and the calculated value fall within the range of 20%. With respect to the anionic unit, the ECC-DSE method suggests a molecular weight closer to the calculated (658 *vs* 486 g/mol) within a variation of 26%. OEC suggests a MW of 921 g/mol, which is higher than the calculated but not enough to indicate a persistent interaction. Notwithstanding, the interaction with solvent molecules with the separated species cannot be ruled out. In addition, the DOSY NMR-derived diameters of 12 Å for [(18-crown-6)$_2$Cs]$^{+}$ and 14 Å the gallyl anion [**2'**]$^{-}$, not only

confirms their crystallographic separation but also the absence of strong ion pairing in solution, consistent with the lack of gallium···caesium interactions.

2.3.4 Single-Crystal X-ray Structural Analysis

Throughout this research, multiple crystal structures were successfully obtained, reflecting the three principal aggregation states that gallyl species can adopt in the solid state: contacted dimers (CDPs) and separated (SIPs) or contacted monomeric pairs (MIPs). These structures offer vital information about metal–metal bonding and corroborate the solution-state behaviours detailed in Sections 2.3.2 and 2.3.3.

2.3.4.1 Crystalline Contacted Dimeric Gallyl Pairs

Single crystals of the contacted dimeric pairs, $[(K\cdots\mathbf{2'})_2(KMHMDS)_2]_\infty$ and $[(Cs\cdots\mathbf{2'})_2(CsMHMDS)_2]_\infty$, were grown by allowing saturated benzene solutions of each dimer to stand at 323 K for two days. The potassium-based complex crystallised in the monoclinic space group *C2/c*, while the caesium analogue adopted the triclinic space group *P–1*, with the asymmetric unit containing half of the complete dimeric motif in both cases. Additionally, each gallyl dimer is coordinated by a dimeric amide base, either $[KHMDS]_2$ or $[CsHMDS]_2$, resulting in polymeric, solvent-free networks $[(K\cdots\mathbf{2'})_2(KHMDS)_2]_\infty$ or $[(Cs\cdots\mathbf{2'})_2(CsHMDS)_2]_\infty$ (Figure 11 and Figure 12). Selected bond metrics for these dimeric assemblies are presented in Table 4 and Table 5.

In both polymeric structures, the gallyl $[\mathbf{2'}]^-$ units are linked by $K^+/Cs^+\cdots\pi$-(arene) interactions. For the potassium dimer, the mean AM···Ct (Ct = centroid of the aromatic ring) distances are 2.92 Å and 2.89 Å, whereas the caesium-based dimer exhibits slightly larger values of 3.25 Å and 3.28 Å, comparable to other alkali-metal complexes flanked by arene systems.[21a, 35] The Ga···K distance averages 3.47 Å, and Ga···Cs is 3.81 Å, slightly exceeding the sum of the covalent radii ($\sum_{cov}$(Ga,K) = 3.25 Å; $\sum_{cov}$(Ga,Cs) = 3.66 Å).[36] Nonetheless, these separations remain within typical van der Waals ranges.

Both dimers feature Ga–N bonds of 1.94–1.96 Å, longer than the 1.86–1.88 Å reported for analogous aluminyl species,[24b, 28] reflecting gallium's larger ionic/covalent radii. Correspondingly, the N–Ga–N' bite angle in $[K\cdots\mathbf{2'}]_2$ and $[Cs\cdots\mathbf{2'}]_2$ is 93.5°, smaller than the 95–96° values found in aluminyl analogues.[28b] In addition, the BDI backbone reveals a methylene CH_2=C groups with C–C bond

metrics in the range of 1.39–1.40 Å, indicative of partial double-bond character, and a methyl group (C–C bond 1.47–1.48 Å).

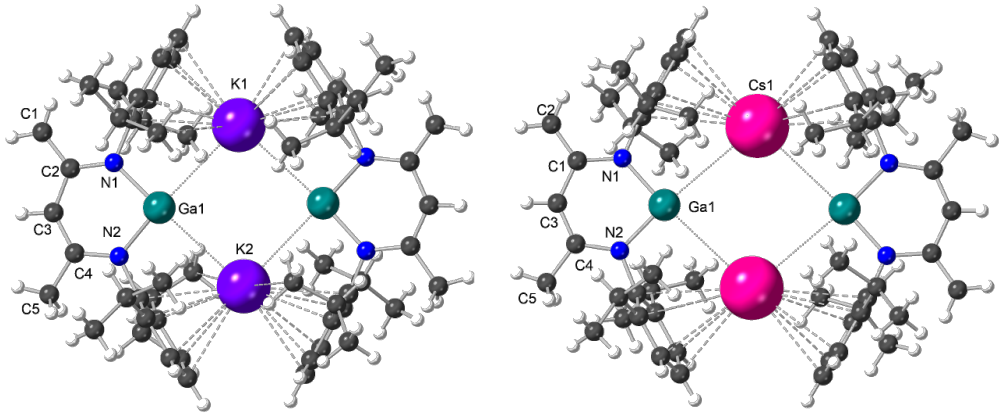


Figure 11. Molecular structure of [K···**2'**]$_2$ (left), and [Cs···**2'**]$_2$ (right) dimers.

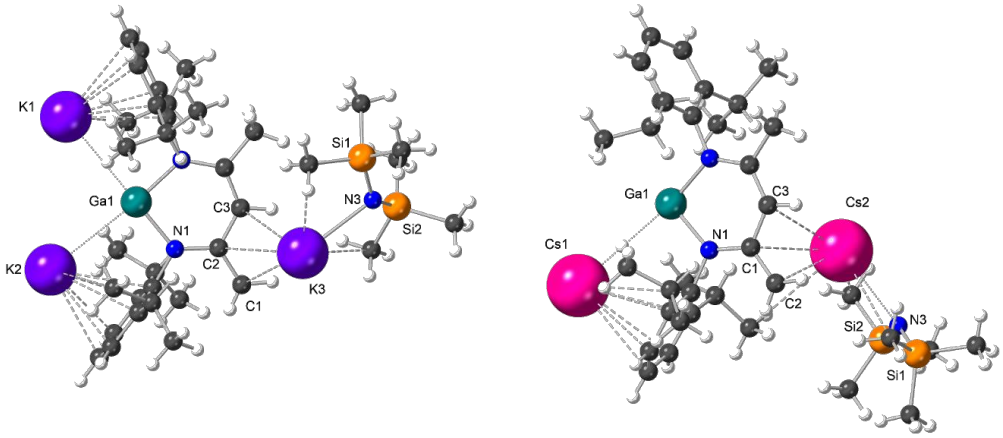


Figure 12. Molecular structure of [K···**2'**]$_2$(KHMDS)]$_\infty$(left), and [Cs···**2'**]$_2$(CsHMDS)]$_\infty$ (right) polymeric chain.

Table 4. Selected bond distances (Å) and angles (º) for [AM···**2'**]$_2$(AMHMDS)]$_\infty$(AM = K, Cs).

	K3	Cs2
C1–AM	3.340(2)	3.7266(19)
C2–AM	3.4890(15)	3.536(3)
C3–AM	3.2405(16)	3.835(2)
N3–AM	2.7718(15)	3.098(3)
N3–Si1	1.6721(16)	1.660(3)
N3–Si2	1.6674(16	1.664(3)

r_{cov}(Ga): 1.22 Å; r_{cov}(K): 2.03 Å; r_{cov}(Cs): 2.44 Å

Table 5. Selected bond distances (Å) and angles (º) for [AM···**2'**]$_2$ (AM = K, Cs).

	K	Cs
Ga–AM	3.4579(5)	3.8481(6)
	3.4778(5)	3.7860(6)
Ga–Ga	4.9561(7)	5.5397(8)
AM–AM	4.8662(6)	5.2531(8)
AM–Ct	2.92/2.89	3.25/3.28
N1–Ga1	1.9381(13)	1.9394(18)
N2–Ga1	1.9446(13)	1.960(2)
N1–C1	1.3886(19)	1.389(3)
C1–C2	1.394(2)	1.377(4)
C1–C3	1.435(2)	1.439(3)
C3–C4	1.385(2)	1.373(3)
C4–C5	1.477(2)	1.491(4)
C4–N2	1.3803(19)	1.376(3)
N1–Ga1–N2	93.57(6)	93.53(8)

r_{cov}(Ga): 1.22 Å; r_{cov}(K): 2.03 Å; r_{cov}(Cs): 2.44 Å
Ct = centroid defined by six-membered aromatic Dipp group

Notably, the methylene moiety on the BDI backbone adopts *cisoid*/*transoid* configurations in the two dimeric salts. In [K···**2'**]$_2$, the alkene (C2–C1) units of the coplanar BDI ligands occupy a *cisoid* arrangement, whereas in [Cs···**2'**]$_2$ is *transoid*. Moreover, each amide base molecule [KHMDS]$_2$ or [CsHMDS]$_2$ forms close contacts with the methylene moiety in the BDI backbone, with K···C contacts averaging 3.35 Å and Cs···C of 3.70 Å.

2.3.4.2 Crystalline Monomeric Gallyl Pairs

Single crystals of the monomeric ion pairs [(18-c-6)AM···**2'**] (AM = Na, K, Cs) were obtained by layering *n*-hexane onto saturated benzene solutions of each compound. In all three structures, the alkali metal cation is encapsulated by a single 18-crown-6 ether (Figure 13), which can adopt various conformations to accommodate and stabilize the metal centre. These encapsulated complexes display Ga···AM distances that scale with cationic radii, as detailed below. Selected bond metrics for these monomeric gallyls are presented in Table 6.

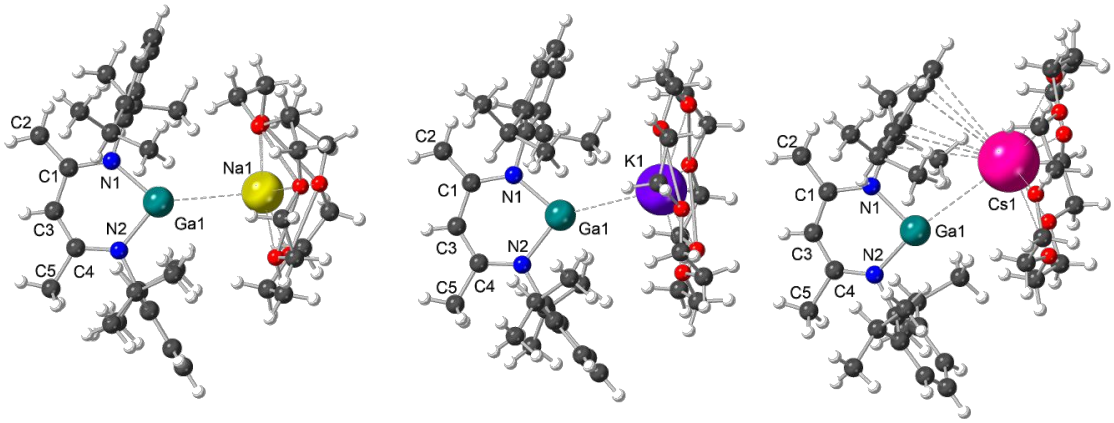


Figure 13. Molecular structure of [(18-c-6)Na···**2'**] (left), [(18-c-6)K···**2'**] (centre), and [(18-c-6)Cs···**2'**] (right).

In these MIPs [(18-c-6)AM···**2'**], the Ga···AM distances scale with the alkali metal cation's ionic radius, measuring approximately 3.33 Å (Na), 3.49 Å (K), and 3.71 Å (Cs). While these separations exceed the sums of the respective covalent radii ($\sum_{cov}$ of 2.88 Å for Na; 3.25 Å for K; and 3.66 Å for Cs), they remain indicative of robust (albeit non-covalent) gallium···alkali metal interactions. The difference from some earlier gallyl examples, such as those described by Yang and co-workers (Ga···Na of 2.97 Å),[26a] suggest that steric and electronic factors can modulate Ga···AM bond lengths. Notably, the shorter Ga···Cs gap here supports the notion of a stronger metal–gallium association. Additionally, an extra Cs···π(arene) contact of 3.55 Å is observed for the contacted caesium gallyl, mirroring interactions found in analogous caesium aluminyl complexes.[21a, 24b, 28, 35] Notably, when a coordinating solvent such as THF is introduced, as in [(18-c-6)(THF)K···**2'**], the structural motif remains largely unchanged (Figure 14). However, the THF molecule coordinates to the potassium cation weakening Ga···M bonding interaction from 3.49 Å in [(18-c-6)K···**2'**] to 3.70 Å in [(18-c-6)(THF)K···**2'**].

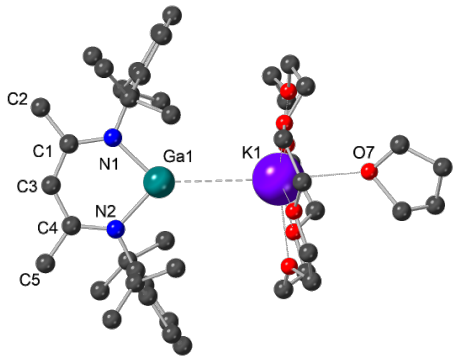


Figure 14. Molecular structure of [(18-c-6)(THF)K···**2'**].

The Ga–N distances (1.94–1.96 Å) are slightly longer than the 1.87 Å typically observed in aluminyl species,[21a, 24b, 28, 35] reflecting the naturally larger ionic/covalent radii of gallium. Moreover, the N–Ga–N angle (94.8–95.8°) is marginally more open compared to the 93–94° range in aluminyl analogues, aligning with gallium's higher coordination sphere demands. Examination of the β-diketiminate (BDI) backbone reveals a localized methylene (CH_2=C) group (C=C, 1.34–1.40 Å) and a single bond (1.47–1.54 Å) linking the methyl substituent to the BDI skeleton. These structural indicators confirm the successful deprotonation at the ligand backbone and the resultant partial double-bond character.

Interestingly, [(18-c-6)K···**2'**] crystallises in two polymorphic forms: one appears as orange prisms, showing an extended "dimeric" packing arrangement, while the other manifests as orange needles that enclose benzene solvent molecules, forming a "trimeric" assembly (Figure 15). It is important to note that "dimeric" and "trimeric" here describe how the monomeric units link or stack via weak K^+···(18-c-6) contacts and possible bridging in the crystal lattice, not a change in the underlying molecular species. Indeed, both polymorphs display identical NMR spectra in solution, indicating that these alternative packings arise from crystallisation conditions rather than any intrinsic difference in the gallyl core.

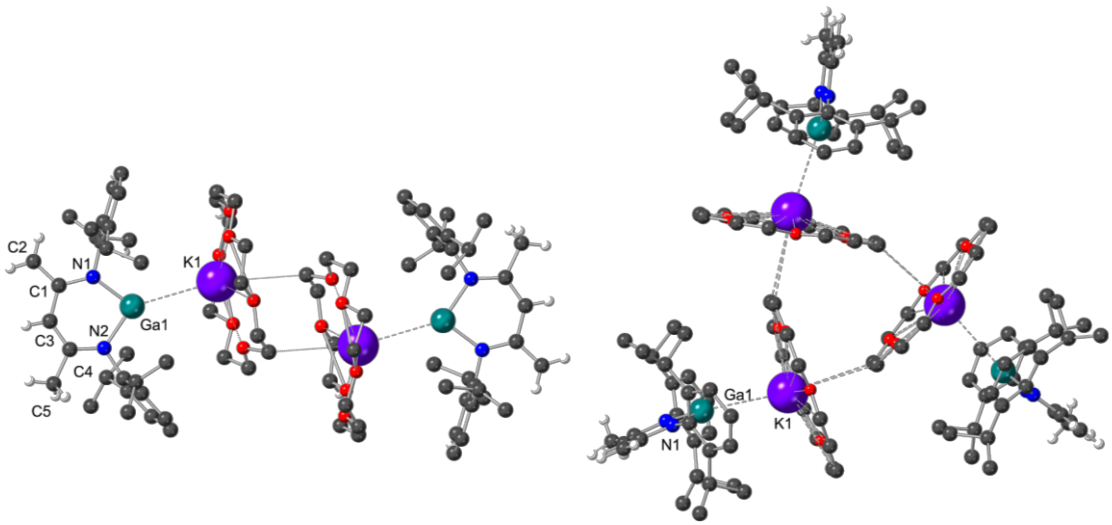


Figure 15. Molecular structure of two polymorph dimeric (left) and trimeric (right) packing arrangement of [(18-c-6)K···**2'**].

Table 6. Selected bond distances (Å) and angles (°) for [(18-c-6)AM···**2'**] (AM = Na, K, Cs).

	Na	K	Cs
Ga–AM	3.3372(16)	3.4900(5)	3.7076(17)
N1–Ga1	1.965(2)	1.9536(15)	1.971(11)
N2–Ga1	1.979(2)	1.9762(15)	1.979(12)
N1–C1	1.382(4)	1.386(2)	1.412(19)
C1–C2	1.363(4)	1.375(3)	1.41(2)
C1–C3	1.447(4)	1.451(3)	1.43(2)
C3–C4	1.354(4)	1.368(3)	1.363(18)
C4–C5	1.510(4)	1.496(3)	1.608(19)
C4–N2	1.374(3)	1.375(2)	1.313(17)
AM–Centroid			3.556
N1–Ga1–N2	92.16(9)	92.54(6)	91.7(4)

r_{cov} (Ga): 1.22 Å; r_{cov}(Na): 1.66 Å; r_{cov}(K): 2.03 Å; r_{cov}(Cs): 2.44 Å
For [(18-c-6)K···**2'**] crystal metrics are chosen from the dimeric polymorph.

2.3.4.3 Crystalline Separated Gallyl Pairs

Single-crystals of distinct separated ion pairs [(crypt)AM][**2'**] (AM = Li, K, Cs) and [(18-c-6)$_2$Cs][**2'**] were obtained from saturated solutions of each derivative in aromatic solvents, followed by layering with *n*-hexane. In these structures, the cationic and anionic components are fully separated, with the alkali metal either encapsulated by cryptand or, in the caesium derivative, by two molecules of 18-crown-6 (Figure 16 and Figure 17). Selected bond metrics for these gallyls are presented in Table 7.

Despite the three-dimensional nature of the cryptand, notable gallium···alkali metal separations are observed (5.77 Å for Li, 5.15 Å for K and 5.13 Å for Cs). Although these distances exceed the sums covalent radii for gallium and the respective alkali metals ($\sum_{cov}$ = 2.50 Å for Li, 2.88 Å for Na, and 3.68 Å for Cs), they nonetheless point to long-range electrostatic attractions. Intriguingly, the larger cations (K^+, Cs^+) display shorter Ga···M distances than might be anticipated, implying that the [**2'**]$^-$ anion engages an "open face" of the [(crypt)AM]$^+$ counterions, thereby minimizing metal–metal separations and stabilizing these discrete ion pairs. This finding contrasts with certain aluminyl examples from Mulvey and Coles, in which metal–metal interactions increase from Li^+ to Cs^+.[35] Here, the gallyl anion [**2'**]$^-$

appears to bind more strongly to heavier cations, challenging the common notion that lower charge density in larger cations leads to weaker electrostatic attraction.

The structure of [(crypt)Li][**2'**] exemplifies the fluxional nature observed in its NMR spectra (Section 2.3.2). In the solid state, lithium is only partially encapsulated by the cryptand, coordinating to a subset of its donor atoms (Figure 16). Consequently, the small Li^+ cation can "move" within the cryptand cavity in solution, in line with the multiple coordination environments revealed by its ^7Li NMR signals. By contrast, the K^+ and Cs^+ align more effectively with the cryptand, forming well-defined $[(cypt)K]^+$ or $[(cypt)Cs]^+$ cations.

To fully separate the gallyl anion from the alkali metal cation, a second equivalent of 18-crown-6 may be added, as in $[(18\text{-c-}6)_2Cs]$[**2'**]. In this arrangement, Cs^+ is entirely encapsulated by two 18-crown-6 ligands, producing a well-separated ion pair with no direct Ga···Cs contact (closest Ga···Cs separation >8 Å; Figure 17). This structural modification eliminates the Ga···M interaction, highlighting how ligand saturation around the metal modulates Ga···M bonding.

In all such separated gallyl ion pairs, the C–C distances within the BDI backbone (e.g., C1–C2, C4–C4) cluster near 1.40 Å, similar to those found in other monomeric cryptand- or crown-stabilised pairs. A detailed analysis of the full crystallographic data for all the gallyl species reveals average C–N and C–C bond lengths of 1.37 Å and 1.42 Å, respectively, across the N_2C_5 BDI skeleton, pointing to extended conjugation in [**2'**]$^-$ for diverse alkali metal derivatives (donor-free, cryptand-based, or 18-crown-6-stabilised). These observations reinforce that even at relatively long Ga···M distances, electrostatic interactions with the alkali metal support the delocalised negative charge in the gallyl anion.

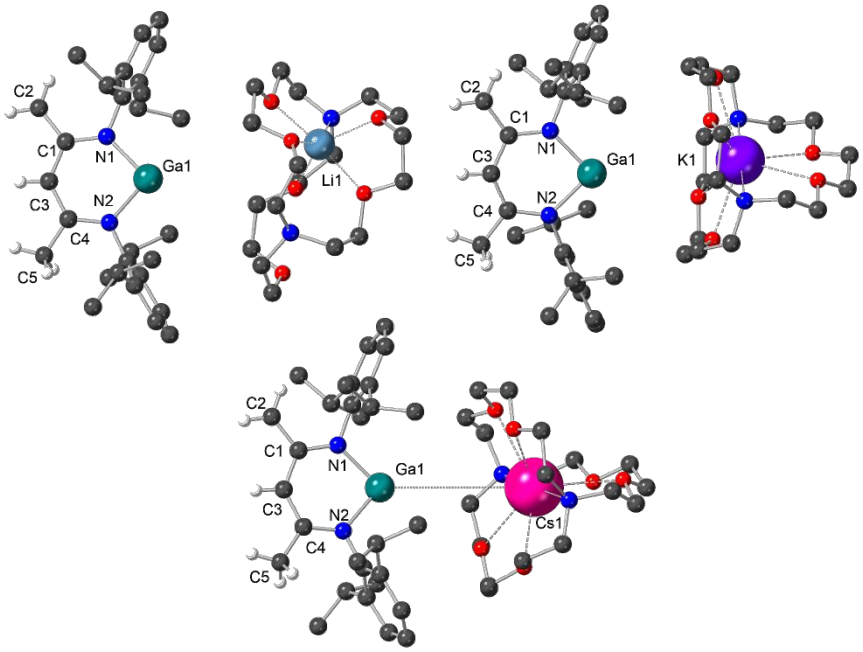


Figure 16. Molecular structure of [(crypt)Li][**2'**] (top left), [(crypt)K][**2'**] (top right), and [(crypt)Cs][**2'**] (bottom centre).

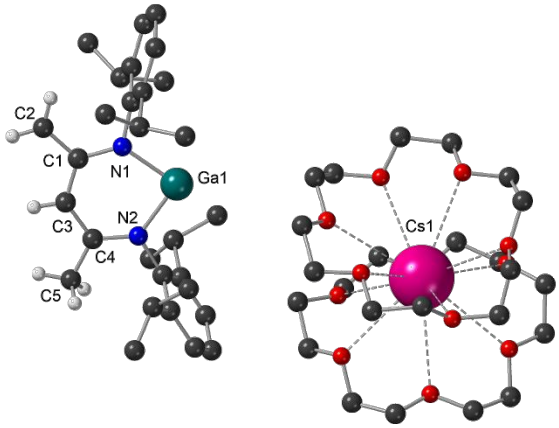


Figure 17. Molecular structure of [(18-c-6)$_2$Cs][**2'**].

Table 7. Selected bond distances (Å) and angles (º) for compounds [(crypt)AM][**2'**]

	Li	K	Cs
Ga–AM	5.769(2)	5.1539(17)	5.1288(11)
N1–Ga1	1.9846(10)	1.986(5)	2.000(4)
N2–Ga1	1.9863(9)	1.992(4)	1.995(7)
N1–C1	1.3800(12)	1.386(8)	1.378(9)
C1–C2	1.4234(16)	1.420(9)	1.426(10)
C1–C3	1.4201(16)	1.398(7)	1.406(10)
C3–C4	1.4021(16)	1.388(8)	1.392(8)
C4–C5	1.4555(16)	1.444(7)	1.460(12)
C4–N2	1.3769(12)	1.383(7)	1.368(10)
N1–Ga1–N2	91.47(3)	91.45(9)	91.3(3)

r_{cov}(Ga): 1.22 Å; r_{cov}(Li): 1.28 Å; r_{cov}(K): 2.03 Å; r_{cov}(Cs): 2.44 Å

Table 8. Selected bond distances (Å) and angles (º) for compounds [$(18\text{-c-}6)_2$Cs][**2'**]

	Cs
Ga–Cs	8.0128(14)
Cs–O	3.3579[a]
N1–Ga1	1.990(7)
N2–Ga1	2.003(8)
N1–C1	1.369(10)
C1–C2	1.424(13)
C1–C3	1.425(14)
C3–C4	1.402(14)
C4–C5	1.447(13)
C4–N2	1.364(11)
N1–Ga1–N2	90.4(3)

r_{cov}(Ga): 1.22 Å; r_{cov}(Cs): 2.44 Å; [a]Mean of the values

2.3.5 Computational Studies

Therefore, considering the different aggregates isolated and studied in this chapter, we initiated a collaboration with the group of Dr. Tobias Krämer (Trinity Collage Dublin), since his group is interested in study the electronic structure of inorganic systems. Hence, their theoretical studies aimed to elucidate the nature of the bimetallic interactions between the gallium electron rich centre and the different alkali metals.

2.3.5.1 Optimised Geometries

The initial crystal structures of each gallyl derivative were optimised in the gas phase to eliminate crystal-packing effects. These gas-phase-optimised structures typically exhibit shorter bond lengths than those measured crystallographically, reflecting the absence of intermolecular contacts present in the solid state. Overall, the computed geometries suggest smaller, more “idealised” frameworks than the experimental lattices. A comparison between the experimental and computed metrics is shown in Figure 18 for the gallyl anion [**2’**]$^-$ subtracted from the separated species [(crypt)Li][**2’**] which is comparable to [(18-c-6)$_2$Cs][**2’**] but of higher crystallographic quality.

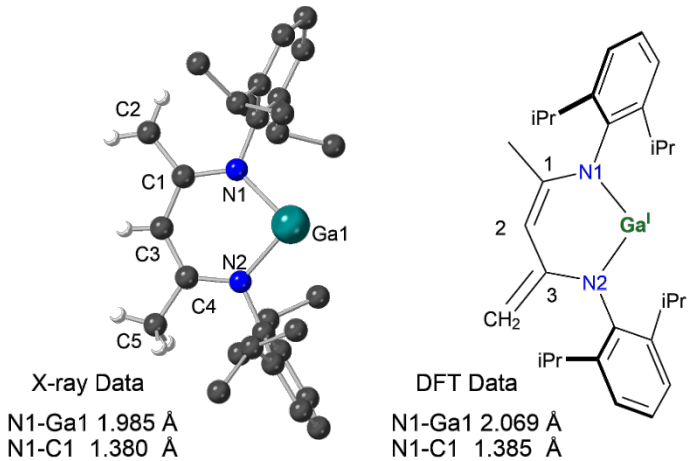


Figure 18. Comparison of selected experimental and calculated bond parameters (PBE/def2-TZVP/def2-SVPP).

2.3.5.2 Electronic Structure Analysis

2.3.5.2.1 Natural Bond Orbital (NBO) Analysis

NBO calculations were initially performed on the free anionic gallyl species [**2'**]$^-$. The natural population analysis (NPA) reveals that the negative charge is predominantly localized on the BDI ligand: N1 and N2 adopt charges of −0.90 and −0.94, respectively, while the gallium centre carries a partial positive charge of +0.72. As a result, the Ga–N bonds exhibit strong polarization toward the nitrogen atoms. Wilberg (Wiberg) bond indices for these Ga–N interactions (0.21 and 0.25) are well below unity, confirming a highly polar rather than purely covalent bond. Second-order perturbation analysis indicates comparable donations from each nitrogen lone pair into the gallium p orbital, alongside substantial donor–acceptor interactions across the ligand backbone, consistent with charge delocalization within the N_2C_5 BDI framework.

NBO analyses were extended to various aggregation states, including contacted dimeric pairs (CDPs), monomeric ion pairs (MIPs), and separated ion pairs (SIPs). For example, [(crypt)Li][**2'**] shows a slightly more positive gallium centre (+0.77) compared to the free anion, while the nitrogen centres become more negative (N1 = −0.98, N2 = −1.02). This shift suggests that electrostatic attraction from Li^+ slightly depletes negative charge on the BDI carbons, redirecting it to the nitrogen atoms. Wilberg bond indices for Ga–N in [(crypt)Li][**2'**] (0.15 and 0.18) are smaller still than in the free anion, reflecting greater polarity. Simultaneously, the Ga lone-pair occupancy decreases from 1.95 to 1.89 e^-, implying mild electron donation from gallium to the Li s orbital. In contrast, in [(crypt)K][**2'**], while the nitrogen charges remain similar to those in the Li-based complex, second-order perturbation analysis reveals a significantly larger Ga-lone-pair donation to the potassium s-orbital donation (6.27 kcal/mol for K vs. 0.11 kcal/mol for Li). This suggests a coulombic contact between Ga and K, despite the nominally separated arrangement not present for Li. The [(crypt)Cs][**2'**] species exhibits Ga-lone-pair Ga lone pair donation into Cs s-orbital weaker than that of the potassium derivative (4.38 vs. 6.27 kcal/mol) but higher than Li. These observations align with the lower electronegativity of caesium and electron affinity relative to potassium.

Moving on the monomeric 18-crown-6 ion pairs, [(18-c-6)AM···**2'**], comparisons with crypt ion pairs highlight an increased Ga-lone-pair donation to the alkali-metal s-orbital donation in [(18-c-6)Na···**2'**]. The Ga lone-pair occupancy drops

to 1.86 e^- (vs. 1.95 e^- in Li–SIPs), while the Na s-orbital occupancy rises (0.19 vs. 0.14 e^- for Li). Consequently, second-order perturbation analysis reveals a strong Ga–Na interaction (20.76 kcal/mol), consistent with the "contacted" nature of this structure. Substituting K for Na reduces the Ga-lone-pair donation to the K s-orbital donation by 5 kcal/mol in [(18-c-6)K···**2'**]. Furthermore, in the Cs species [(18-c-6)Cs···**2'**], the donation from Ga to Cs is slightly lower than to K (14.45 vs. 15.98 kcal/mol), aligned with the lower electron affinity of caesium. Another notable difference in the Cs system is that the N–Ga–N σ bond population is lower (1.76 vs. 1.91 e^- for K), matching the presence of Cs···π(arene) interactions in [(18-c-6)Cs···**2'**].

As observed crystallographically, introducing THF to coordinate potassium does not alter the overall structural motif of [(18-c-6)K···**2'**] but further modifies the bimetallic gallium···alkali metal interaction in [(18-c-6)(THF)K···**2'**]. In the latter, the Ga-lone-pair donation to K^+ rises to 20.11 kcal/mol^{-1} (vs. 15.98 without THF), presumably via an inductive effect from the additional donation of the O atom from THF to K^+. Accordingly, the partial charge of K^+ decreases to +0.78, while its s-orbital occupancy increases to 0.20 e^-, and the Ga lone-pair occupancy decreases slightly (1.84 e^-). Hence, the donation of O atoms aids the donation from the Ga lone pair into the s-orbital of potassium by an inductive-type effect.

A comparison of the two dimeric structures, [K···**2'**]$_2$ and [Cs···**2'**]$_2$, underscores degree of Ga-lone-pair to alkali-metal donation as the principal difference. Therefore, the donation from the lone pair of the gallium centres in the [K···**2'**]$_2$ is more than twice that the donation in [Cs···**2'**]$_2$ (18.54/18.51 kcal/mol for K and for Cs 8.36/8.14 kcal/mol). This is also reflected in the charges on the alkali metal centres (+0.78 K and +0.85 Cs), the occupancies of the gallium lone pair (1.78 and 1.84 e^- for K and Cs, respectively), and the alkali metal s-orbital population (0.20 for K and for Cs 0.13 e^-). Collectively, these data suggest stronger Ga–K interaction relative to Ga–Cs in the dimeric [AM···**2'**]$_2$ species.

2.3.5.2.2 Quantum Theory of Atoms in Molecules (QTAIM)

The Quantum Theory of Atoms in Molecules (QTAIM) provides a valuable framework for probing the nature of bonds in these synthesised gallyl systems. By analysing bond critical points (BCPs), energy densities, and bond ellipticities, QTAIM identifies the extent of gallium···alkali metal interactions and the bonding within the BDI ligand.

QTAIM analysis was first applied to the free anion [**2'**]$^-$ (Figure 19). The Ga–N bonds exhibit energies near zero, suggesting a closed-shell (ionic) character. Nonetheless, QTAIM identifies polar N–Ga bonds with the bond critical points (BCPs, ρ(r) = 0.081–0.089 e/a^3) and Laplacians ($\nabla^2\rho$(r) = 0.228–0.265 e/a$_0^5$), indicative of strong N→Ga covalent donation.[37] This stabilization is corroborated by second-order perturbation energies ($\Delta E^{(2)}$) of 5.7–7.5 kcal/mol. Within the N_2C_5 BDI backbone, the potential energy density dominates over the kinetic energy density, indicating a substantial covalent contribution for the C–N bonds. Examination of bond ellipticity reveals that roughly half of the C–X bonds (X = C or N) are best characterised as single, whereas the remainder appear closer to double bonds, consistent with partial charge delocalization across the ligand framework.

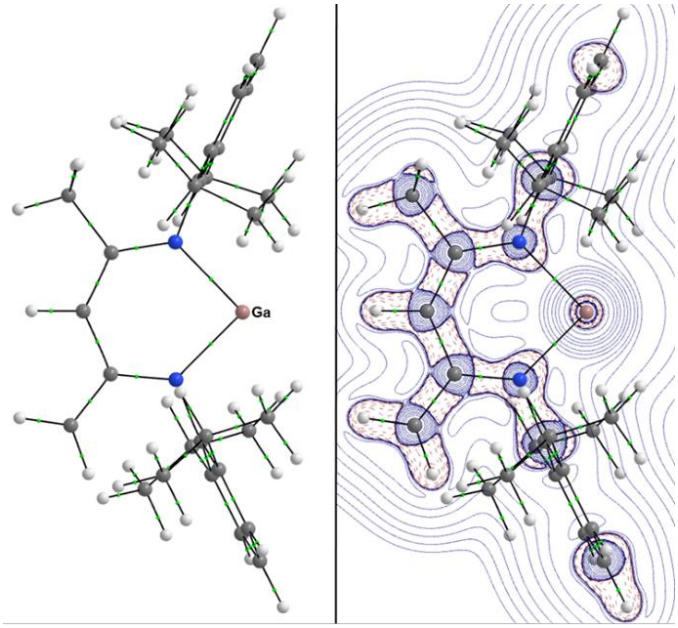


Figure 19. Molecular graph (left) and Laplacian $\nabla^2\rho$(r) of the electron density in the plane containing Ga, N1 and N2 (right) for [**2'**]$^-$ (PBE0D3BJ/def2-QZVP//PBE/def2-TZVP/def2-SVPP).

For the crypt-solvated gallyls ion pairs, [(crypt)AM][**2'**], weak electrostatic interactions are observed in the QTAIM analyses, with only [(crypt)Cs][**2'**] (Figure 20), exhibiting a discernible Ga···Cs weak interaction (BCP: $\rho(r)$ = 0.001 e/a^3, $\nabla^2\rho(r)$ = 0.003 e/a$_0^5$). Consequently, the bond topology of the anionic [**2'**]$^-$ fragment remain essentially unchanged from the free anion, reflecting the wide separation observed in their crystallographic structures.

By contrast, replacing crypt with 18-crown-6 strengthens the ionic Ga···M interactions in the monomeric ion pairs, [(18-c-6)AM···**2'**] (BCPs with $\rho(r)$ = 0.008–0.010 e/a_0^3 and $\nabla^2\rho(r)$ = 0.018–0.028 e/a_0^5), as seen in [(18-c-6)Na···**2'**] (Figure 21). The resulting bond critical points suggest an ionic interaction, underscoring the contacted arrangement seen experimentally. In addition, the decreasing second-order perturbation energies for crown-solvated species ($\Delta E^{(2)}$ = 20.8, 16.0 and 14.5 kcal/mol for Na, K, and Cs, respectively) reinforces weaker Ga→M donation down the group. Additionally, in [(18-c-6)Na···**2'**], an extra stabilising BCP arises with one ancillary aromatic group (Figure 22), consistent with the high π-binding propensity of Cs^+.[38]

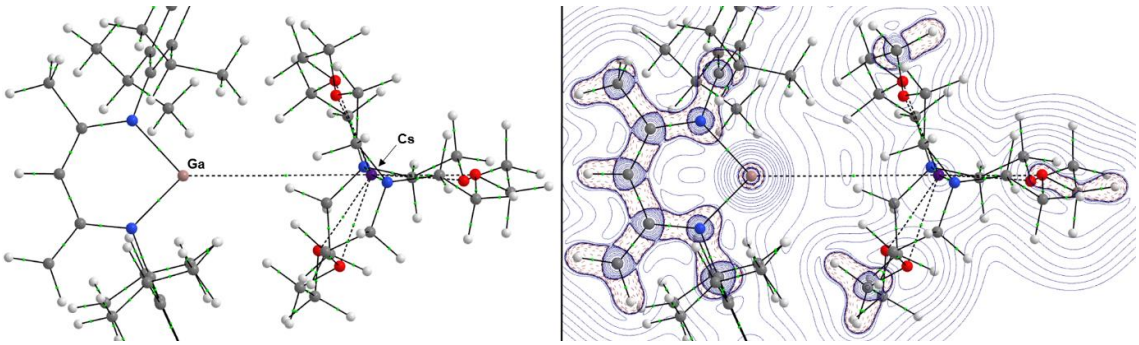


Figure 20. Molecular graph (left) and Laplacian $\nabla^2\rho$(r) of the electron density in the plane containing Ga, N1 and N2 (right) for [(crypt)Cs][**2'**] (PBE0D3BJ/def2-QZVP//PBE/def2-TZVP/def2-SVPP).

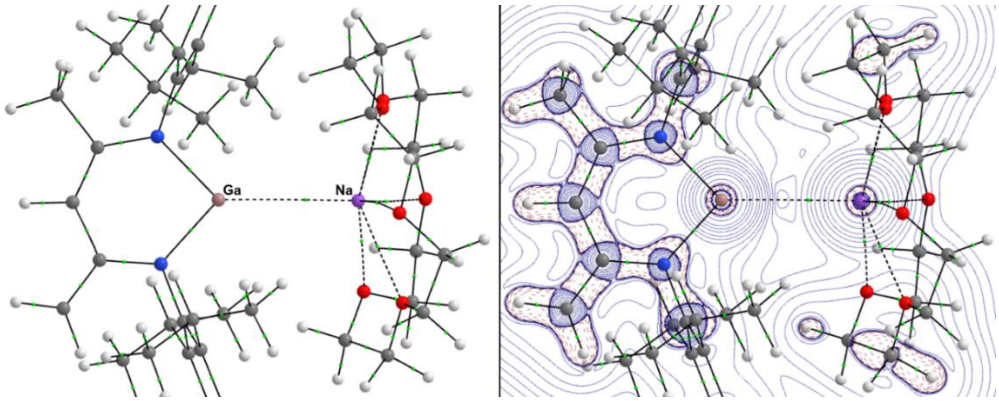


Figure 21. Molecular graph (left) and Laplacian $\nabla^2\rho$(r) of the electron density in the plane containing Ga, N1 and N2 (right) for [(18-c-6)Na···**2'**] (PBE0D3BJ/def2-QZVP//PBE/def2-TZVP/def2-SVPP).

In the dimeric species, [K···**2'**]$_2$ and [Cs···**2'**]$_2$, the Ga···M interactions show low-density BCPs ($\rho(r)$ = 0.008–0.009 e/a^3, $\nabla^2\rho(r)$ = 0.016–0.019 e/a_0^5), indicative of

ionic bonding. The dimeric assemblies are further stabilized by $M^+\cdots\pi$-arene BCPs with both aromatic groups. In addition, a weak Ga···Ga contact at 5.09 Å ($\rho(r)$ = 0.003 e/a^3, $\nabla^2\rho(r)$ = 0.004 e/a$_0^5$) in [K···**2'**]$_2$ (Figure 23) but absent in [K···**2'**]$_2$ due to a larger Ga···Ga spacing (5.71 Å). The polymerization of these dimers into extended [K···**2'**]$_2$···[AMHMDS]$_2$ chains reflects the increased electron density on the deprotonated β-diketiminate backbone, mirroring the M^+-induced polymerization also noted in analogous aluminyl systems.[28a]

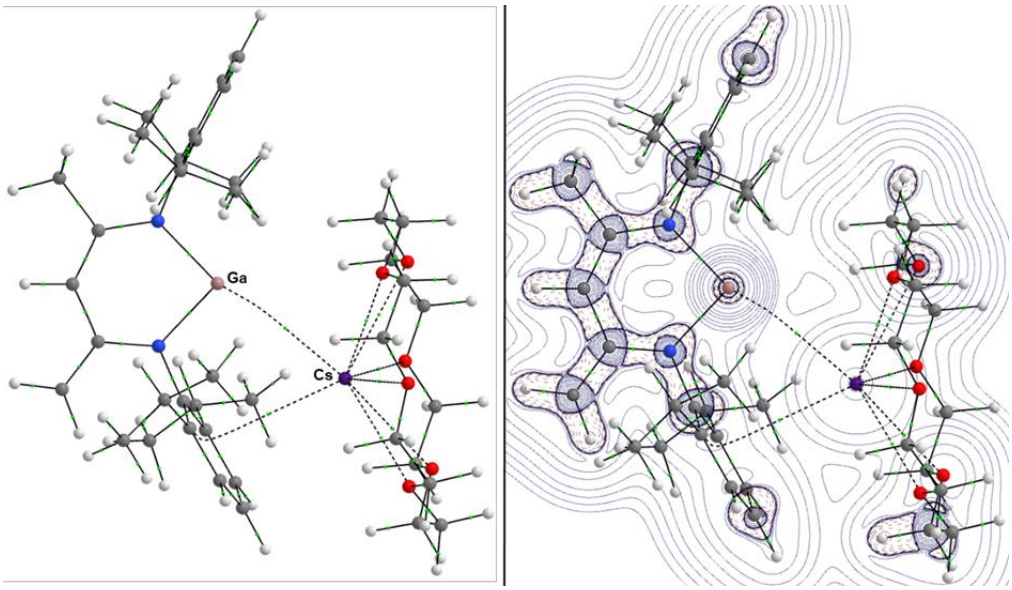


Figure 22. Molecular graph (left) and Laplacian $\nabla^2\rho$(r) of the electron density in the plane containing Ga, N1 and N2 (right) for [(18-c-6)Cs···**2'**] (PBE0D3BJ/def2-QZVP//PBE/def2-TZVP/def2-SVPP).

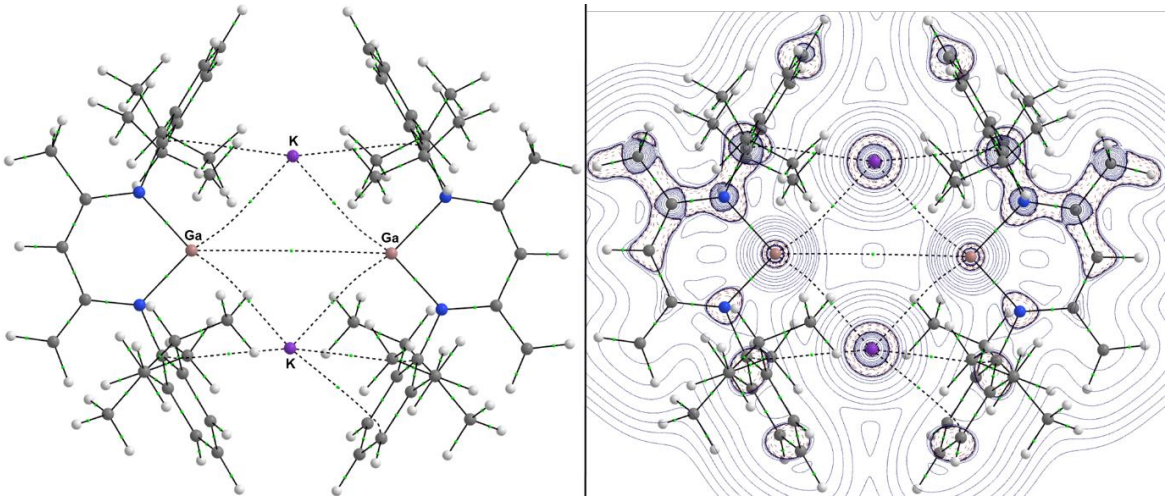


Figure 23. Molecular graph (left) and Laplacian $\nabla^2\rho(r)$ of the electron density in the plane containing Ga1, K1 and Ga2 (right) for [K···**2'**]$_2$ (PBE0D3BJ/def2-QZVP//PBE/def2-TZVP/def2-SVPP).

2.3.5.2.3 Non-Covalent Interaction (NCI) Analysis

Non-covalent interaction (NCI) plots offer additional insight into the weak electrostatic and van der Waals forces at play in these gallyl systems, complementing the QTAIM and NBO findings. By visualising regions of electron density, NCI analysis distinguishes long-range attractions (green surfaces for moderate interactions, blue for stronger ones) from repulsions (red surfaces), aiding the interpretation of diffuse metal–ligand contacts that shape overall stability.

In line with NBO and QTAIM data, crypt-solvated gallyls, [(crypt)AM][**2'**], show minimal electrostatic interactions, whereas crown-ligated species [(18-c-6)AM···**2'**] exhibit moderate, but also weak, van der Waals stabilisation. Although individually weak, these non-covalent attractions accumulate, also exhibit stabilizing the dimeric [K···**2'**]$_2$ and [Cs···**2'**]$_2$ assemblies (Figure 24). This observation aligns with the electrostatic forces identified as primary contributors to the contacted nature and robust persistence of these dimers in solution.

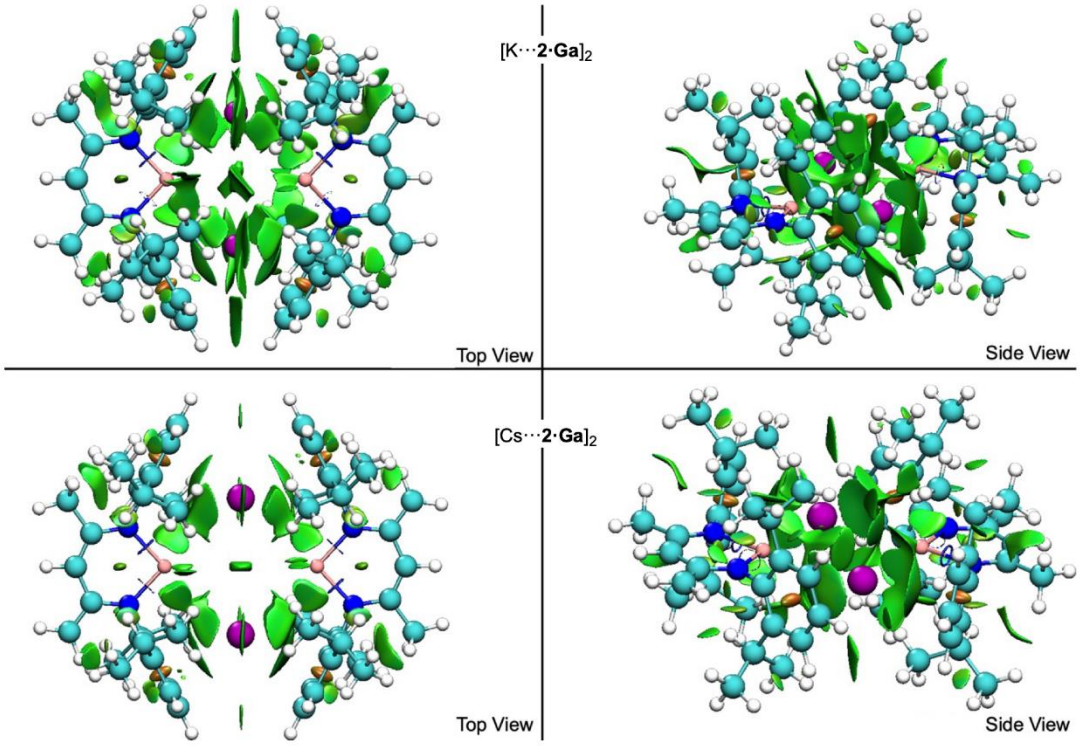


Figure 24. Non-covalent interaction (NCI) plots for [K···**2'**]$_2$ and [Cs···**2'**]$_2$.

2.3.5.2.4 Energy Decomposition Analysis (EDA)

An energy decomposition analysis (EDA) was performed to evaluate the interactions between the [**2'**]$^-$ anion and various cationic partners (Table 9). In most cases, gas-phase optimisations were used, but for [(18-c-6)(THF)K ⋯**2'**] periodic solid-state-type optimizations were required due to large discrepancies between gas phase optimised and experimentally measured bond lengths, particularly for Ga⋯Cs and K⋯O(THF). Analysis of monomeric ion pairs demonstrates that electrostatics constitutes the primary stabilizing factor, typically accounting for 60–70% of the total attractive interactions, with orbital (12–28%) and dispersion (2–15%) playing secondary roles. The Pauli repulsion term (12–17%) partially negates these stabilizing components but does not offset them completely, resulting in net attraction. Notably, in many contacted complexes, such as [(18-c-6)K(THF)⋯**2'**], the electrostatic and orbital contributions collectively yield a stronger gallium–alkali metal interaction than in separated pairs.

For the dimeric systems, [K⋯**2'**]$_2$ and [Cs⋯**2'**]$_2$, EDA indicates that electrostatics comprises roughly 70% of the AM$^+$⋯[**2'**]$^-$ interaction, with 28% from orbital contributions and 2% from dispersion, mirroring observations in analogous aluminyl species.[39] These factors produce significant stabilization energies (–350 kcal/mol for [K⋯**2'**]$_2$ and –328 kcal/mol for [Cs⋯**2'**], explaining their robust persistence even in coordinating solvents like THF.

Table 9. Energy decomposition analysis results for all non-dimeric complexes (PBE0D4/TZP, using an all-electron basis set). The structures are sorted from most to least stabilizing interaction energies (top to bottom). The values in rounded brackets are the percentage contribution of each component to the interaction energy. All energy values stated have units of kcal·mol^{-1}.

Structure	ΔE_{int}	ΔE_{elec}	ΔE_{pauli}	ΔE_{orb}	ΔE_{disp}
[(18-c-6)Na⋯**2'**]	-87.04	-76.85 (61%)	19.89 (16%)	-16.17 (13%)	-13.90 (11%)
[(18-c-6)K⋯**2'**]	-80.08	-71.73 (62%)	17.52 (15%)	-13.37 (12%)	-12.49 (11%)
[(18-c-6)(THF)K ⋯**2'**]	-78.79	-68.48 (61%)	17.01 (15%)	-14.58 (13%)	-12.74 (11%)
[(18-c-6)Cs⋯**2'**]	-78.64	-72.51 (61%)	20.51 (17%)	-16.34 (14%)	-10.27 (9%)
[(crypt)Li][**2'**]	-71.11	-59.80 (59%)	15.51 (15%)	-14.00 (14%)	-12.82 (13%)
[b][(18-c-6)(THF)K ⋯**2'**]	-68.98	-61.63 (61%)	16.10 (16%)	-11.96 (12%)	-11.49 (11%)

[(crypt)Cs][**2'**]	-68.16	-54.89 (61%)	11.04 (12%)	-10.85 (12%)	-13.46 (15%)
[(crypt)K][**2'**]	-68.11	-54.88 (62%)	10.84 (12%)	-10.95 (12%)	-12.13 (14%)
[(18-cr-6)$_2$Cs][**2'**]	-59.59	-49.99 (61%)	11.36 (14%)	-9.97 (12%)	-11.00 (13%)
[b][(18-c-6)$_2$Cs][**2'**]	-50.33	-42.20 (64%)	7.84 (12%)	-7.60 (12%)	-8.37 (13%)

[b]Energy decomposition analysis of solid-state optimized geometry.

2.3.5.2.5 Charge Delocalization and Frontier Orbital Analysis

DFT calculations indicate that the anionic gallyl species [**2'**]$^-$ adopts a highly polarised structure, with a substantial portion of the electron density residing on the deprotonated β-diketiminate (BDI) backbone. This conclusion is supported by both the QTAIM analysis, demonstrating robust N→Ga donation, and the molecular electrostatic potential (MEP) maps, which display pronounced negative potential over the ligand framework, in contrast to the more neutral distribution in **2** (Figure 25).

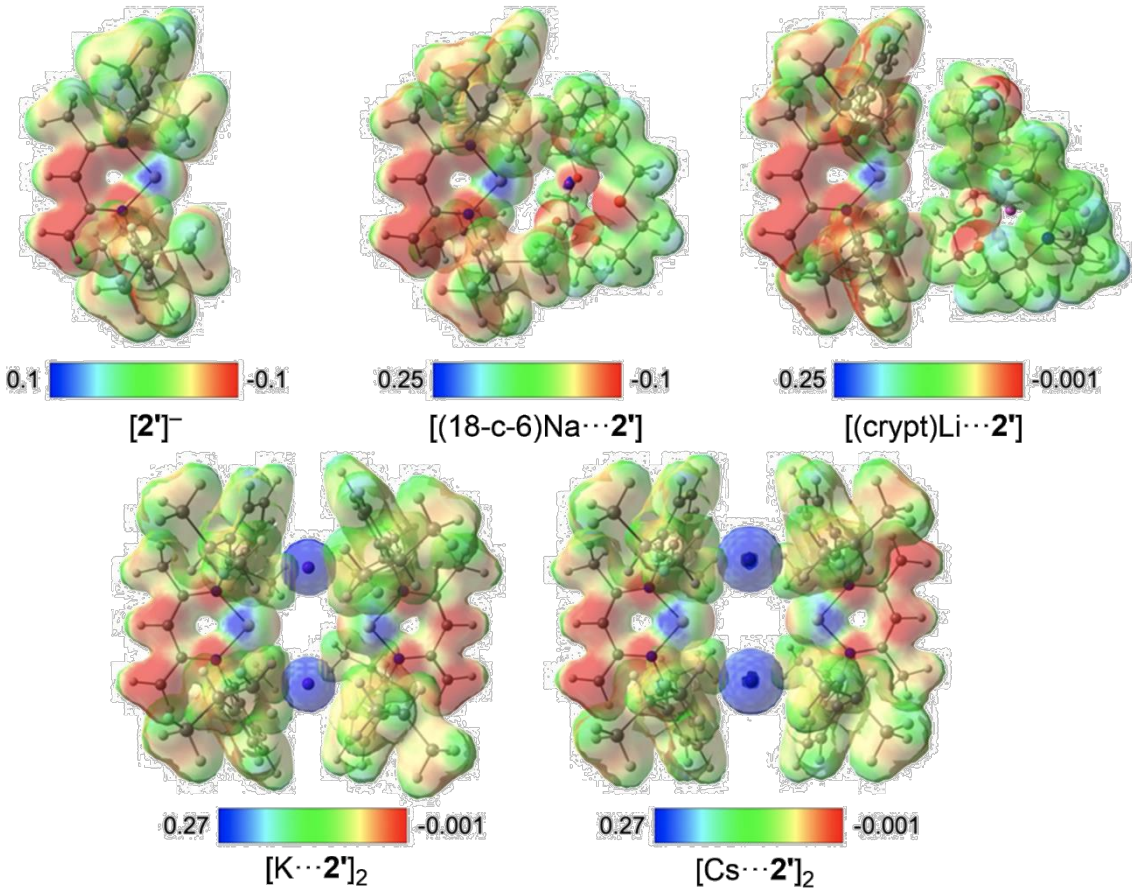


Figure 25. Molecular electrostatic maps for selected gallyls (isovalue = 0.025 a.u.).

The extensive delocalization of the negative charge across the N_2C_5 backbone, can be better visualized through the resonance structures depicted in Figure 26. These structures highlight the charge delocalization and tautomeric equilibrium within the BDI framework, distinguishing this class of gallyls systems.

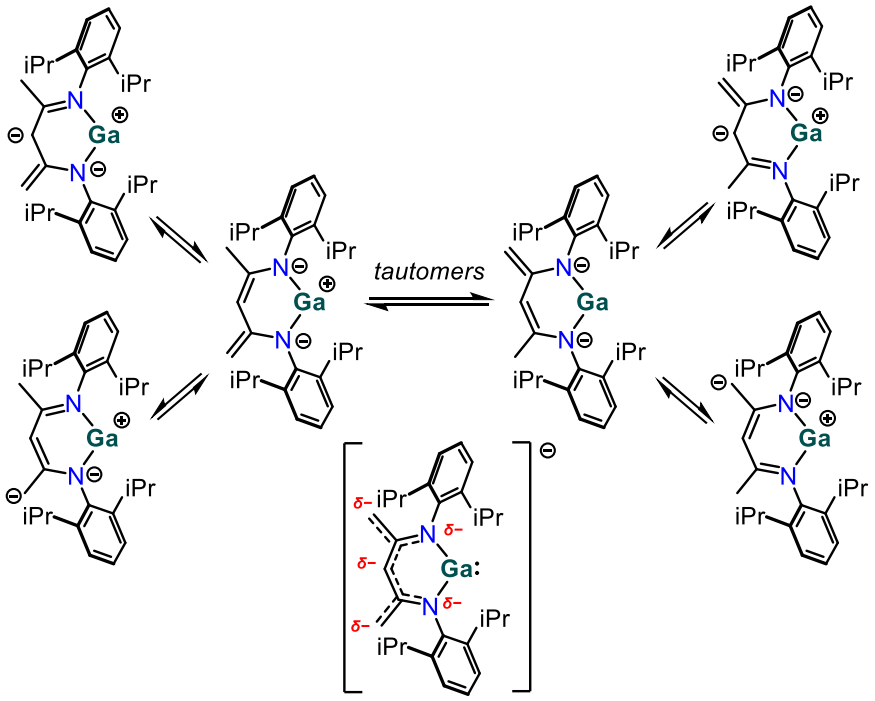
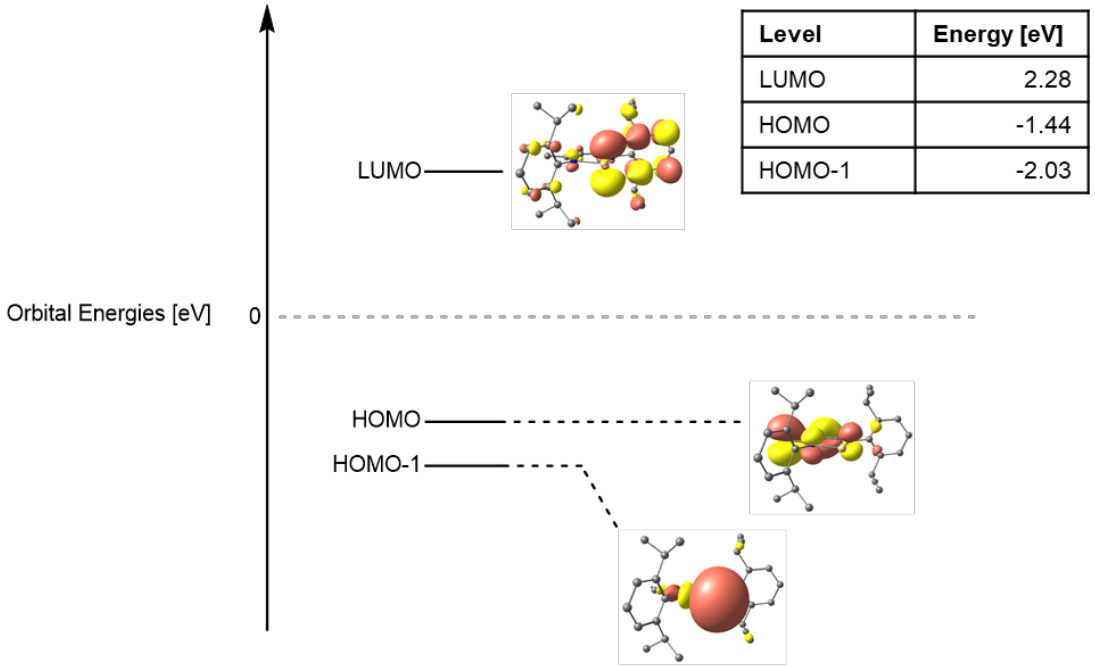


Figure 26. Representation of the resonance structures of the BDI backbone in the gallyl anion [**2'**]$^-$. The figure highlights the delocalization of the negative charge across the N_2C_5 backbone and the tautomeric equilibrium, as derived from NBO analysis.

Additionally, natural bond orbital (NBO) analyses reveal that the gallium centre maintains orbitals with dominant 4s (up to 93%) lone-pair character and a 4p acceptor orbital approaching 90% p-character within the gallyl anion [**2'**]$^-$. The overall charge distribution, when compared to neutral gallium species **2**, indicates that these anionic gallyls exhibit a more extensive negative charge region on the N^2C_5 ligand skeleton, a feature that enhances their stability and also provides a handle for potential new reactivity.

In [**2'**]$^-$ and its aggregates (cryptand- and 18-crown-6-solvated, or donor-free conditions), the HOMO is predominantly ligand-centred, underscoring the BDI

backbone's key role in electron delocalization as shown in the canonical Kohn-Sham frontier orbital analysis (Figure 27). Meanwhile, the lone pair on gallium typically occupies HOMO–1, with the LUMO featuring significant p-orbital character on gallium. Notably, these gallium-based orbitals exhibit very high s-character (up to 90–95%) for the lone pair, exceeding the 80–85% s-enrichment typical of aluminyl analogues.[35, 40] Despite this difference, the frontier orbital gap (4.1–4.5 eV) remains on par with that in aluminyls (3.4–4.1 eV),[25b] reinforcing the idea that these gallyls may engage in bond-activation pathways akin to their aluminium counterparts.



Level	Energy [eV]
LUMO	2.28
HOMO	-1.44
HOMO-1	-2.03

Figure 27. Canonical Kohn-Sham frontier MO diagram and orbitals for [**2'**]$^-$ (isovalue = 0.3 a.u.).

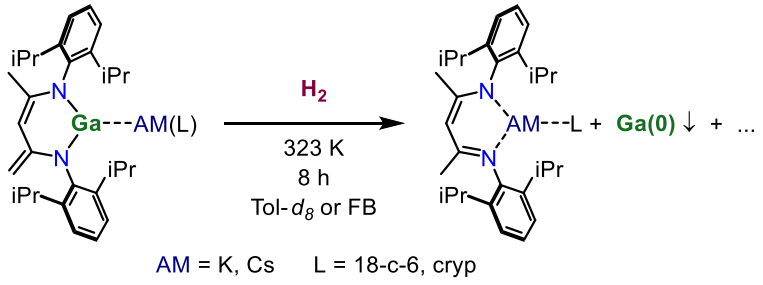
Combining the MEP visualizations with QTAIM and NBO data reveals that these novel gallyl species are highly polarised structures, characterised by extensive charge delocalization throughout the BDI ligand and a diffuse, s-rich gallium lone pair. These features not only enhance their stability but also underscore their potential to exhibit transition-metal-like reactivity, including potential small-molecule activation, paralleling the behaviours noted in heavier Group 13 and aluminyl analogues.

2.3.6 Small Molecule Reactivity

2.3.6.1 Oxidative Addition of H_2

Given the scarcity of anionic gallyl systems, and thus their limited reported applications, we investigated whether these new, charge-delocalized species could undergo oxidative addition of H_2. Such a transformation appeared plausible, as anionic gallyls might exhibit greater reactivity than their neutral counterparts, paralleling the mild conditions under which analogous aluminyl complexes activate H_2, as detailed in *Chapter I*. Moreover, a direct comparison of gallium- versus aluminium-based anionic reactivity was of particular interest to us.

A variety of alkali metal derivatives of the gallyl [**2'**]$^-$ were scrutinised for with H_2, including [(18-c-6)AM···**2'**] and [(crypt)AM][**2'**] species (AM = Li, Na, K, Cs). These reactivity trials were carried out under NMR scale condition in J. Young NMR tubes (typically ~15 µmol of each gallyl, 0.5 mL of an appropriate solvent, 1.5 bar of H_2 gas). The solvents benzene, toluene, and fluorobenzene were these gallyls are stable for long periods of time, were tested during these experiments. The addition of H_2 gas was done after freeze–pump–thaw cycles to degasify the gallyl solution, the solutions were pressurised with 1.5 bar of H_2. Then, the reaction mixture was monitored via ^{1}H NMR spectroscopy at room temperature or 323 K. No reaction was observed at room temperature. Upon heating the solutions to 323 K some reactivity was observed, however complicated reactions mixtures were obtained from which we could not detect the formation of gallium hydride products resulting from activation of H_2. Eventually, deposition of Ga(0) was observed and some of the new ^{1}H NMR signals corresponded to transmetalation products, BDI(AM-L), along with donor ligand resonances (AM = Li, Na, K, Cs; L = 18-c-6, crypt). This outcome echoes earlier findings by Kretschmer, during the formation of a cyclopentagallene $[R_5Ga_5]K_2$, they detected gallium to potassium exchange leading to BDI(K).[23b]



Scheme 2. Attempt of oxidative addition of H_2 with anionic gallyl systems.

X-ray diffraction analysis on the caesium-derived by-product, BDI(Cs), verified that the anionic $[BDI]^-$ ligand was not chelating to Cs^+ in a κ^2 fashion. Instead, the caesium centre was stabilized the donor cryptand or 18-crown-6 ether present in the reaction mixture, leaving the $[BDI]^-$ moiety as a free monoanionic ligand. This was an unprecedented result given the BDI ligands are well-stablished frameworks in coordination chemistry for their robust coordination and never seen as metal-free anionic species. Moreover, the $[BDI]^-$ entity was found to adopt either a *cisoid* or a *transoid* conformation (Figure 28), depending on the crystallisation solvent.

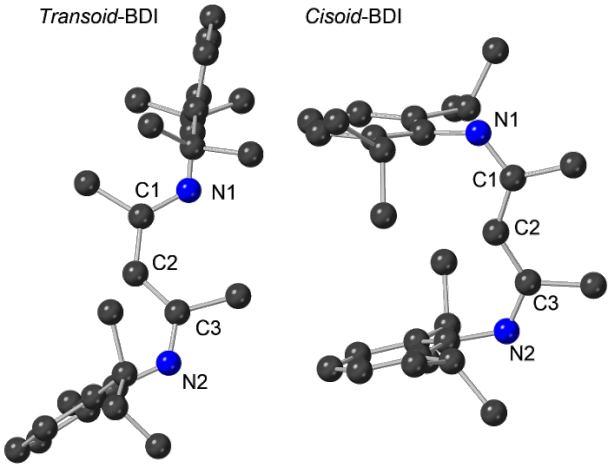


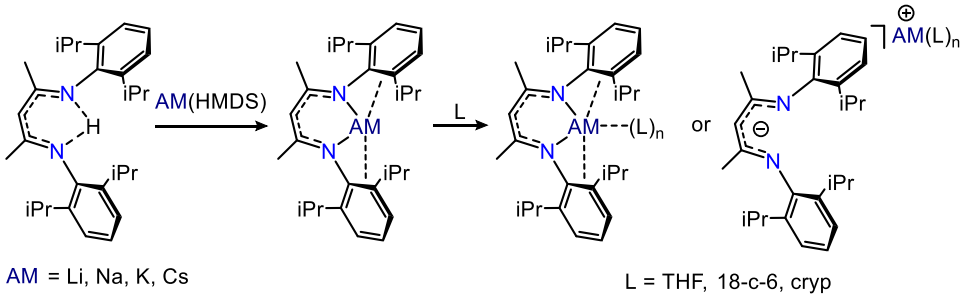
Figure 28. Molecular structure of *transoid* (left) and *cisoid* (right) isomeric forms of BDI^- anions. The Cs^+ cations were omitted for clarity.

2.3.6.2 Unbound β-diketiminate Ligand

To further investigate this unexpected transmetalation, we synthetised BDI(AM) salts (AM = Li, Na, K and Cs) directly by deprotonating the proligand BDI(H) with the appropriate alkali-metal amide base AMHMDS. The resultant monoanionic salts coordinate κ^2-N,N' to each alkali metal in non-coordinating solvents such as toluene, as evidenced by ^{1}H NMR spectra. In coordinating solvents (e.g., THF), however, the potassium and caesium species, BDI(K) and BDI(Cs), show broad signals consistent with fluxional ligand binding, mirroring the structures obtained crystallographically (Figure 28). By contrast, BDI(Li) and BDI(Na) species remain well-defined κ^2-N,N' BDI chelates under all tested conditions.

To sharpen the NMR signals for the BDI(K) and BDI(Cs) derivatives, exogenous donors (18-c-6 or cryptand) were added, encapsulating the cation and allowing clearer spectroscopic observation. Variable-temperature (VT) and DOSY

NMR experiments revealed that the *transoid* isomer of $[BDI]^-$ dominates in solution, while K^+ or Cs^+ forms a separate cationic unit with either cryptand or 18-crown-6 donor molecules (Scheme 3).



Scheme 3. Reactivity of the proligand BDI(H) with alkali metal hexamethyldisilazides AMHMDS to give BDI(AM), illustrating different coordination behaviours.

Remarkably, this fluxionality is only apparent for K and Cs (Figure 29). Li and Na form rigid BDI(AM) chelates, independent of solvent polarity or donor presence. Further experimental details can be found in Annexes II.[41]

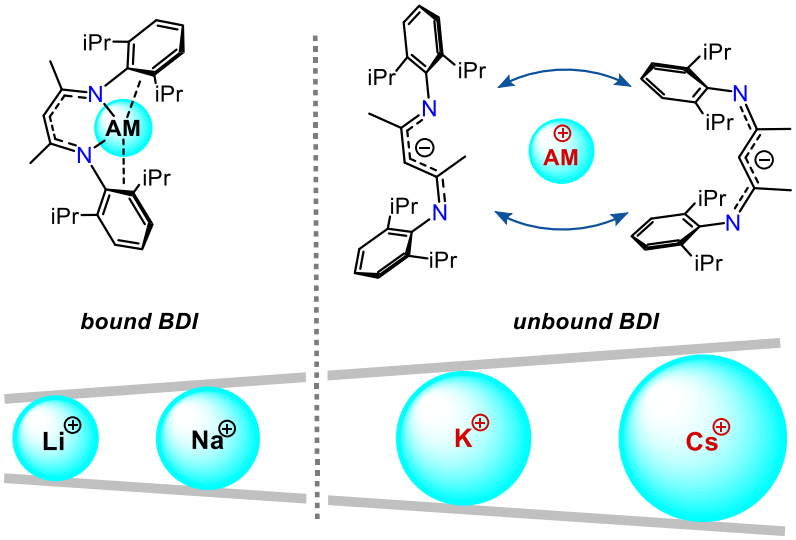
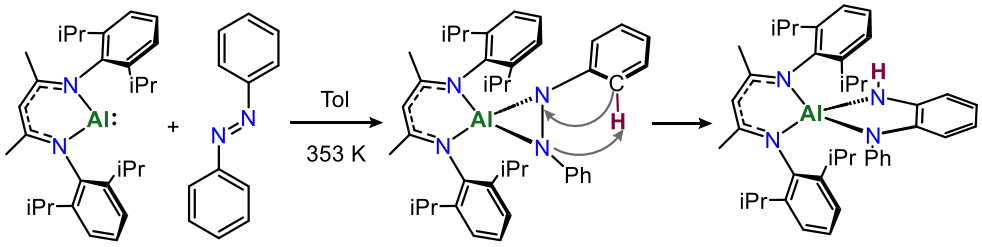


Figure 29. Summary of fluxional behaviour in BDI(AM) salts.

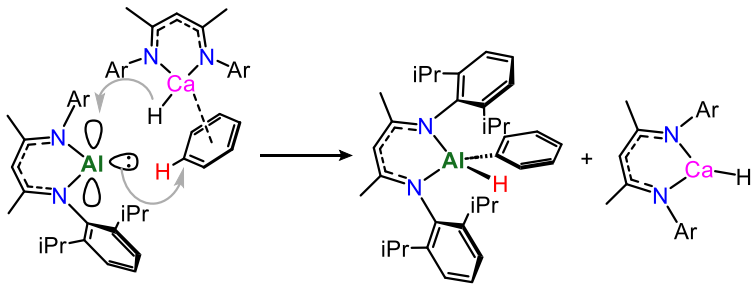
2.3.7 C−H Bond Reactivity

Following the unsuccessful attempts to activate H_2, we explored alternative pathways where anionic gallyl complexes might facilitate bond activations. The literature documents several cases where neutral monovalent aluminium(I) species (e.g., BDI(Al) or **1**) perform oxidative additions involving unsaturated bonds such as N=N (azobenzene),[18a] or even C–H activation in aromatics like benzene in their anionic forms.[28] Roesky, for instance, studied the reactivity of **1** employing unsaturated compounds such as acetylene[42] leading an aluminacyclopropene complex, [**1**(η^2-C_2H_2)], whereas using azobenzene[43] they obtained a five-member ring containing an N(H)-*o*-C_6H_4N(Ph) moiety indicating a rearrangement of azobenzene (Scheme 4).



Scheme 4. N=N bond activation of azobenzene with Al(I).

Similarly, Harder, achieved the C–H activation of benzene under mild conditions using a bimetallic low-valent aluminium/calcium system, underscoring transition-metal-like reactivity (Scheme 5).[44]



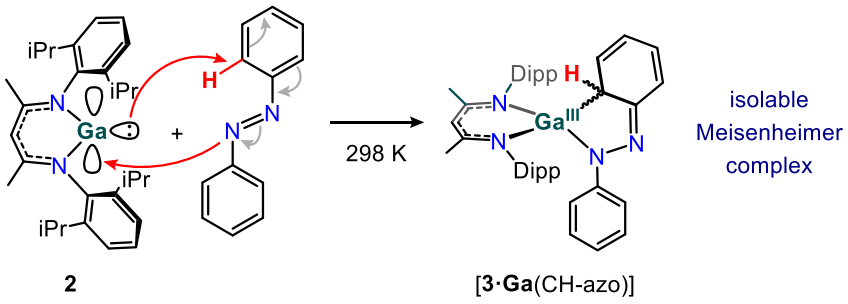
Scheme 5. C−H activation of benzene mediated by Al(I) and Ca(II) hydride species.

Given the parallels between aluminyl and gallyl anionic frameworks, we hypothesized that anionic gallyls might also induce C–H bond activation in unsaturated or aromatic substrates. This section details our attempts to achieve C–H activation, first using the neutral gallium(I) species **2**, then exploring how the anionic gallyl [**2'**]$^-$ derivatives compare.

2.3.7.1 C−H Activation of Azobenzene

Because the interaction of gallium(I) compounds with azobenzene remains unreported, we first examined the neutral monovalent species **2**. Equimolar amounts of **2** and azobenzene were combined in benzene within a J. Young ampoule and stirred at room temperature. Monitoring by ^{1}H NMR revealed complete consumption of both reagents. After reducing the solvent volume in vacuo and adding *n*-hexane, an orange solid precipitated. The isolated orange powder, following work-up, exhibited ^{1}H and ^{13}C NMR signals inconsistent with Roesky's earlier azobenzene-aluminium rearrangements (Scheme 4).[43] The ^{1}H NMR featured highly asymmetric shifts for the Dipp substituents (isopropyl CH and CH_3) and β-methyl groups, suggesting a strongly perturbed ligand environment around gallium. The γ-CH group of the BDI skeleton appeared as a single near δ 5.06, distinct from the typical shift in **2**. Additional broad signals, assigned to azobenzene moieties coordinating gallium, included a notable resonance at δ 2.70, implying partial loss of aromaticity in one phenyl ring.

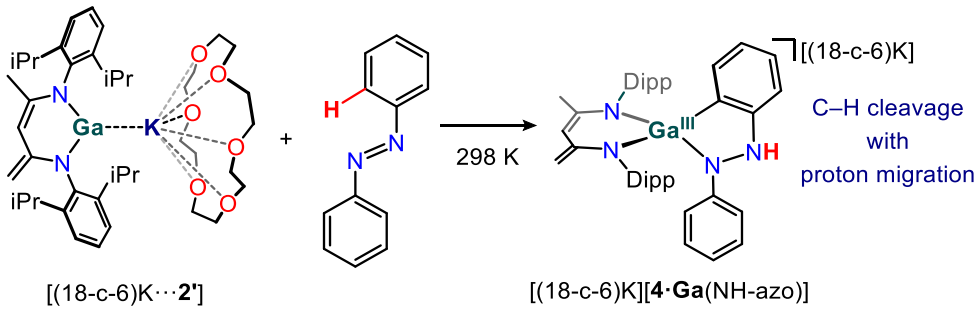
These data suggest a new gallium(III) complex, [**3**·**Ga**(CH-azo)] (Scheme 6), formed by two-electron transfer from the Ga(I) lone pair into the *ortho*-position of one azobenzene ring. This reorganization yields a "Meisenheimer-type" intermediate wherein gallium is formally oxidized from Ga(I) to Ga(III), forcing a ring rehybridization (sp^3 at the attacking *ortho*-carbon) and partial dearomatization. Such carbophilic reactivity echoes prior accounts of gallium-promoted ring reductions and Ga–C bond formation.[23b] Indeed, the system tolerates losing aromaticity in one phenyl ring when stabilized by the newly formed N=C bond and the electron density gained by the azo group.



Scheme 6. Proposed two-electron transfer from **2** to azobenzene forming a Meisenheimer-type gallium(III) complex [**3**·**Ga**(CH-azo)].

Building on this neutral-gallium route, we next tested [(18-c-6)K···**2'**] in a similar reaction with azobenzene. Mixing equimolar quantities in benzene at room temperature quickly produced a dark, oily mixture, prompting addition of 1.5 mL THF to yield a dark solution. Subsequent work-up (adding *n*-hexane, isolating the dark-purple solid) allowed characterisation in THF-d_8 (the product being insoluble in aromatic solvents). The ^{1}H NMR indicated the BDI backbone remained dianionic (i.e., methylene CH_2=C group persists). The γ-CH resonance shifted to δ 4.90 (from δ 5.27 in the parent anionic gallyl), means a new coordination environment at gallium. A singlet at δ 5.28 was assigned to azobenzene protons, indicative of an emerging NH group after *ortho*-activation and proton migration.

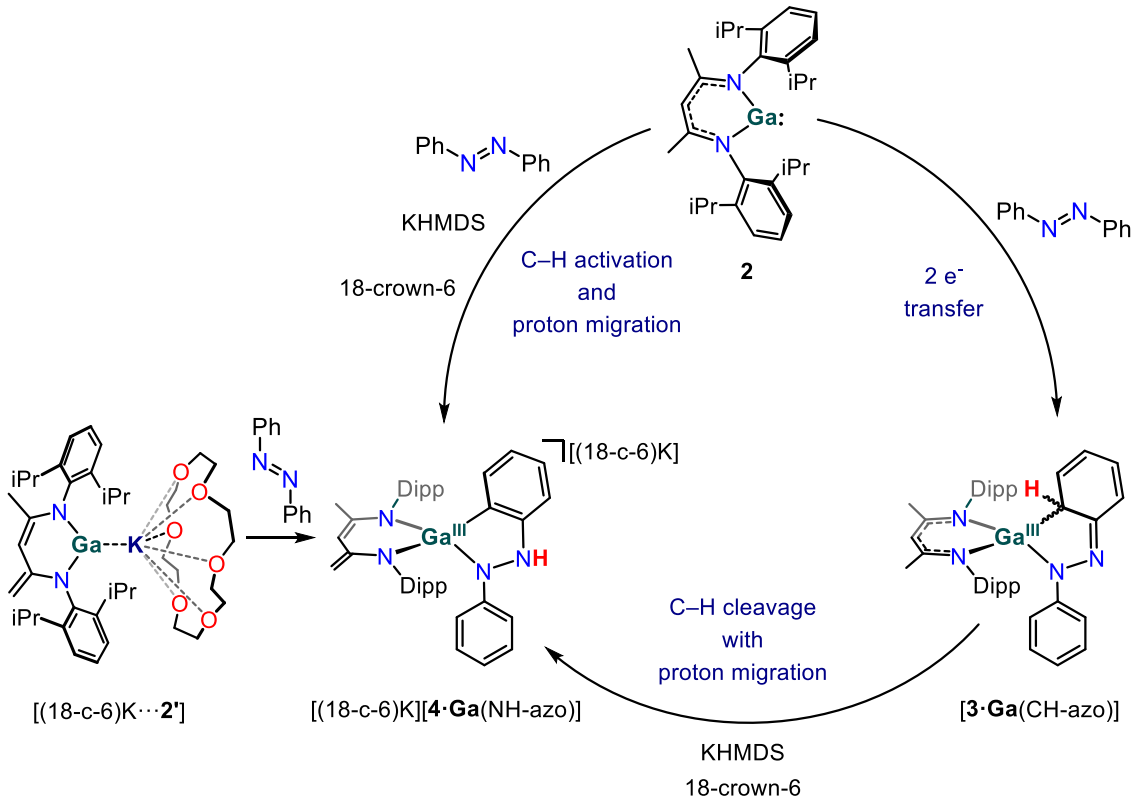
This data is consistent with the activates the *ortho*-position of azobenzene by the anionic gallyl centre in [(18-c-6)K···**2'**], in concert with a labile Ga···K interaction in THF, which favour the proton transfer from the ring to nitrogen forming a new NH group during the C–H activation process (Scheme 7). This product showcases how anionic gallium complexes can affect C–H functionalization, akin to the transition-metal-like behaviours documented in heavier main-group systems.[45]



[(18-c-6)K···**2'**] [(18-c-6)K][**4**·**Ga**(NH-azo)]

Scheme 7. Proposed H-migration and ortho-C–H activation of azobenzene by [(18-c-6)K···**2'**] to form [(18-c-6)K][**4**·**Ga**(CH-azo)].

Interestingly, the Meisenheimer-type gallium(III) species [**3**·**Ga**(CH-azo)], can be converted into the anionic azobenzene-gallyl complex, [(18-c-6)K][**4**·**Ga**(NH-azo)], by adding KHMDS and 18-crown-6. This step deprotonates the BDI backbone (forming the methylene CH_2=C moiety) while assisting the H-migration from ring C to an N site. Furthermore, reacting **2** with azobenzene in the presence of KHMDS and 18-crown-6 directly generates the C–H-activated species [(18-c-6)K][**4**·**Ga**(NH-azo)] (Scheme 8).



Scheme 8. Summary of azobenzene galliation with **2** and [(18-c-6)K···**2'**].

Both the Meisenheimer-type gallium(III) intermediate [**3**·**Ga**(CH-azo)] and the ortho-activated anionic azobenzene complex [(18-c-6)K][**4**·**Ga**(NH-azo)] afforded X-ray quality crystals. The pre-activated gallium(III) species crystallised in the triclinic space group *P–1*, existing as a racemic mixture of S/R-*ortho* stereoisomers around the ring-substituted carbon (Figure 30).

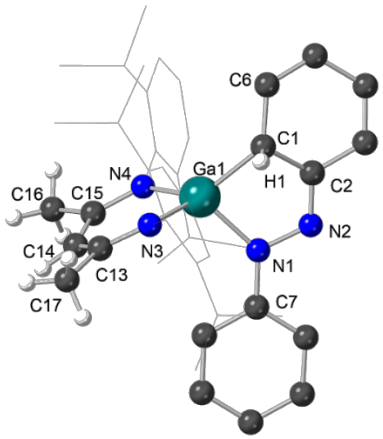


Figure 30. Molecular structure of *S-ortho*-[**3**·**Ga**(CH-azo)].

Selected crystallographic metrics for the *S-ortho*-[**3·Ga**(CH-azo)] species are given in Table 10. For this species, Ga–N bond lengths (average, 1.93 Å) are shorter than in **2**, consistent with partial oxidation from Ga(I) to Ga(III). The galliated-ring C1–C2 and C1–C6 distances hover near 1.50 Å, supporting sp^3 hybridization at the ortho carbon and dearomatisation of that ring. The slightly extended N=N length (1.38 Å) indicates partial electron transfer into gallium, forming a single N–N bond.

Table 10. Selected bond distances (Å) and angles (º) for *S-ortho*-[**3·Ga**(CH-azo)].

Ga1–N1	1.9217(10)	Ga1–N3	1.9301(9)
Ga1–C1	1.9963(11)	Ga1–N4	1.9371(8)
C1–H1	1.04(2)	N3–C13	1.3358(11)
C1–C2	1.5076(18)	C13–C17	1.5060(15)
C1–C6	1.466(4)	C13–C14	1.4000(12)
C2–N2	1.3015(13)	C14–C15	1.4001(13)
N1–N2	1.3776(11)	C15–C16	1.5071(14)
N1–C7	1.3905(13)	C15–N4	1.3336(12)
C1–Ga1–N1	85.8(15)	N3–Ga1–N4	97.02(3)

For [(18-c-6)K][**4·Ga**(NH-azo)], crystallising in P2/c (monoclinic), the structure comprises an ion pair, K^+ is coordinated by 18-crown-6 and a THF molecule, while Ga(III) binds the partially rearranged azobenzene ring (Figure 31). Selected crystallographic metrics for the *S-ortho*-[(18-c-6)K][**4·Ga**(NH-azo)] species are given in Table 11. The N–N, C–N, and N–Ga distances, emphasize the mixed single/double bond nature and rearomatisation of the activated ring. In addition, a new NH group is present in [(18-c-6)K][**4·Ga**(NH-azo)] resulting from the loss of the C–H at the ortho position of one of the aromatic rings of azobenzene and coordination of gallium. In addition, the Ga-moiety features a deprotonated BDI backbone, akin to what has been observed in the anionic gallyls systems, however, the methylene CH_2=C BDI skeleton is now stabilising a gallium(III) metal centre. Crystallographic data showing C–N and C–C bonds averaging ~1.39 Å and ~1.42 Å across the N_2C_5-backbone, further confirm this extended ligand conjugation in *S-ortho*-[(18-c-6)K][**4·Ga**(NH-azo)].

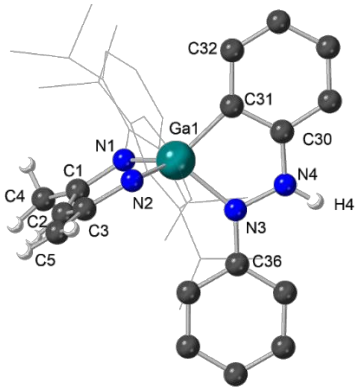


Figure 31. Molecular structure of [(18-c-6)K][**4**·**Ga**(CH-azo)].

Table 11. Selected bond distances (Å) and angles (°) for of ortho activated C−H bond of azobenzene, [(18-c-6)K][**4**·**Ga**(CH-azo)].

Ga1–N1	1.897(4)	Ga1–N3	1.961(5)
Ga1–N2	1.887(4)	Ga–C31	1.961(8)
N1–C1	1.393(7)	C31–C30	1.42(1)
C1–C4	1.439(9)	C31–C32	1.415(9)
C1–C2	1.395(7)	C30–N4	1.362(7)
C2–C3	1.406(7)	N4–H4	0.880(5)
C3–C5	1.417(9)	N4–N3	1.387(7)
C3–N2	1.398(7)	N3–C36	1.390(7)
N1–Ga1–N2	99.96(18)	C31–Ga1–N3	84.8(3)

2.4 Conclusions

In this chapter, we have established a new family of anionic gallium(I) carbene analogues, featuring extended charge delocalization and stabilised by a dianionic β-diketiminate (BDI) framework. We have elucidated their structural and electronic properties through X-ray crystallography, DOSY NMR, and computational analyses. The results show that electrostatic forces, aided by appropriate alkali metals and donor ligands, effectively maintain low-valent gallium(I) centres while preventing gallium–gallium bond formation, yielding a variety of aggregation states from discrete ion pairs to dimeric assemblies. Despite the failure to induce oxidative addition of H_2 under the investigated conditions, leading instead to transmetalation and free BDI-alkali-metal salts, these gallyl systems successfully activate a C–H bond in azobenzene, either by generating a Meisenheimer-like gallium(III) intermediate or by executing *ortho*-functionalisation and proton migration. These reactivities are distinct from any known aluminium(I) or gallium(I) systems, underscoring their capacity for transition-metal-like bond activation unusual in the main-group domain. Additionally, the isolation of a free anionic BDI ligand for the first time highlights the dynamic coordination and versatility with heavy alkali metals such as potassium and caesium. Collectively, these findings broaden our understanding of low-valent gallium chemistry, positioning these novel electron-rich gallium(I) carbene analogues as a versatile new platform poised for new reactivity in small-molecule activation and related bond activation pathways.

2.5 Experimental Methods

Herein a representative characterisation of the molecules is shown, further details are specified in the Annexes attached to this Thesis.

2.5.1 Materials

Experiments were conducted under a nitrogen inert atmosphere using either a glove box (MBraun, LabMaster SP) or standard Schlenk techniques. Benzene, n-hexane, and toluene were dried over sodium benzophenone and stored under a nitrogen atmosphere over a potassium mirror. Deuterated benzene (C_6D_6) and toluene (Tol-d_8) were dried with calcium hydride (CaH_2), distilled at low pressures (< 1 × 10^{-2} mbar), and similarly stored over a potassium mirror. THF-d_8 was sourced from Cambridge Isotopes or Merck and stored under nitrogen over 3 Å molecular sieves. Ga ingot (99.99%) and sodium bis(trimethylsilyl)amide (NaHMDS) (95%) were purchased from Alfa Aesar, stored in a glove box, and used as received. 4,7,13,16,21,24-hexaoxa-1,10-diazabicyclo[8.8.8]hexacosane (2.2.2-crypt, also abbreviated as crypt) was purchased from Merck, distilled, and stored in a glove box. 1,4,7,10,13,16-hexaoxacyclooctadecane (18-crown-6, also abbreviated as 18-c-6), bis(trimethylsilyl)amine HMDS(H), n-BuLi, and CsF were purchased from Merck and used as received. 2-((2,6-diisopropylphenl)imido)-2-penten-4-one BDI(H),[46] (BDI)Ga (**2**),[16a] LiHMDS,[47] KHMDS[47] and CsHMDS[31] were prepared according to previously reported procedures.

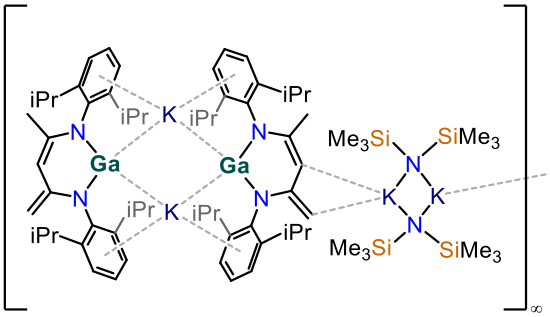
NMR experiments were conducted in J. Young tap NMR tubes prepared and sealed under a nitrogen atmosphere. Multinuclear NMR spectra were collected on either a Bruker AVIIIHD 400 nanobay (equipped with a 9.4 tesla magnet) or Bruker AVIII 500 (equipped with 11.7 tesla magnet and a Prodigy cryoprobe) spectrometer at 298 K unless otherwise stated. The non-deuterated solvents (fluorobenzene) were locked to an external standard sample of 10% fluorobenzene in C_6D_6. ^{7}Li and ^{133}Cs NMR data were referenced to external standard solutions of LiCl and $CsNO_3$ in D_2O (0.1 M). Assignments of NMR resonance signals in the ^{1}H and ^{13}C{^{1}H} NMR spectra were made with the help of two-dimensional NMR experiments (^{1}H,^{1}H-COSY, ^{1}H,^{13}C-HSQC, ^{1}H,^{13}C-HMBC). Chemical shifts (δ) are reported in ppm and referenced to residual solvent resonances. The coupling constants (*J*) were expressed in hertz. The signal multiplicities are denoted as s (singlet), d (doublet), sept (septet), m (multiplet), and br (broad).

CHN elemental microanalyses were performed at the elemental analysis services of the Metropolitan University of London using a Thermo Flash 2000 Elemental Analyser by manipulating and preparing the samples under an inert atmosphere of pure and dry nitrogen gas inside a glove box before analysis. This was followed by the immediate transfer of the sample to the analyzer to prevent environmental exposure. Both crystalline and bulk materials of the highly reactive and air-sensitive complexes were provided in sealed glass ampoules, ensuring complete protection from atmospheric conditions, and were analysed in several attempts. To aid the complete combustion of specific complex samples, V_2O_5 was also incorporated. Although both crystalline and bulk forms of the highly reactive, air-sensitive complexes were analysed multiple times, consistent results were challenging to obtain because of the inherent reactivity of these systems. This high reactivity, underscored by the small hydrolysis observed in both crystalline and bulk samples in solution by NMR spectroscopy, contributed to the challenges in obtaining meaningful elemental analysis data. Consequently, obtaining accurate elemental analysis data for such reactive complexes proved difficult, primarily because of sample decomposition and suboptimal combustion efficiency. Representative values of the organometallic species are presented in the characterisation data. Despite efforts to maintain the bulk purity of the compounds, some failed to meet the ± 0.4% accuracy criteria. The complications associated with CHN combustion analysis, especially for reactive organometallic species, are well-documented and understood in the literature.[48]

Infrared (IR) spectra were obtained using Nujol mulls between KBr discs inside a nitrogen glove box on a Bruker Alpha FT-IR spectrometer.

2.5.2 Synthesis and Characterisation

2.5.2.1 Synthesis and characterisation of $[(K\cdots\mathbf{2'})_2(KHMDS)_2]_\infty$



In J. Young's ampoule, (BDI)Ga **2** (212 mg, 0.435 mmol) and KHMDS (99 mg, 0.496 mmol) were combined. Benzene (3 mL) was then added, and the mixture was stirred at 50ºC for 2 days. The resulting brown-green suspension was filtered via a cannula. The solid residue was washed with *n*-hexane (2 x 5 mL) and dried under high vacuum (< 10^{-2} mbar) for 2 hours, yielding $[(K\cdots\mathbf{2'})_2(KHMDS)_2]_\infty$ as a dark yellow solid (50 mg, 0.034 mmol, 16%). Orange block-shaped crystals suitable of $[(K\cdots\mathbf{2'})_2(KHMDS)_2]_\infty$ for X-ray diffraction study were obtained by placing the reaction mixture in a hot water bath at 50ºC and allowing it to stand for 2 days.

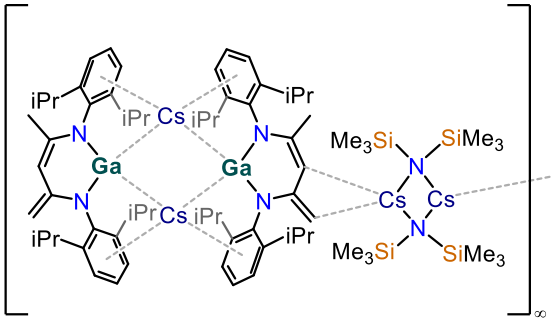
Note on NMR data: The NMR spectroscopic data of $[(K\cdots\mathbf{2'})_2(KHMDS)_2]_\infty$ in solution, obtained using ^{1}H, ^{13}C and DOSY, is consistent (identical), regardless of its physical form (dark yellow powder or orange block-shaped crystals of $[(K\cdots\mathbf{2'})_2(KHMDS)_2]_\infty$.

^{1}H NMR (400 MHz, 4:1 C_6D_6:THF-d_8, 298 K): δ 7.17-7.11 (m overlapped with residual solvent peak from C_6D_6, 4 H, Ar), 7.00 (m, 2 H, Ar), 5.18 (s, 1 H, γ-CH), 4.05 (sept, 2 H, *J* = 6.9 Hz, CH-^{i}Pr), 3.96 (sept, 2 H, *J* = 6.9 Hz, CH-^{i}Pr), 3.44 (s, 1 H, C=CH_2), 2.60 (s, 1 H, C=CH_2), 1.70 (s overlapped with residual solvent peak from THF-d_8, 3 H. β-Me), 1.42 (m, 6 H, Me-^{i}Pr), 1.31 (m, 18 H, Me-^{i}Pr), 0.22 (s, 18 H, $SiMe_3$).

^{13}C{^{1}H} NMR (125.6 MHz, 4:1 C_6D_6:THF-d_8, 298 K): *δ* 156.7 (C_q, *C*=CH_2), 150.7 (C_q, Ar), 148.9 (C_q, Ar), 147.3 (C_q, *C*-Me), 147.2 (C_q, Ar), 123.6 (CH, Ar), 123.2 (CH, Ar), 123.0 (CH, Ar), 122.6 (CH, Ar), 100.4 (*γ*-CH), 71.4 (C=*C*H_2), 28.0 (CH-^{i}Pr), 27.8 (CH-^{i}Pr), 26.2 (Me-^{i}Pr), 26.5 (Me-^{i}Pr), 25.4 (Me-^{i}Pr), 24.1 (Me-^{i}Pr), 23.8 (β-Me), 7.0 (Me, $SiMe_3$).

Elemental analysis found (calc.) for $C_{70}H_{166}Ga_2K_4N_6Si_4$: C 56.48 (57.99), H 7.50 (8.06), N 5.33 (5.80).

2.5.2.2 Synthesis and characterisation of $[(Cs\cdots 2')_2(CsHMDS)_2]_\infty$



In a J. Young's ampoule, (BDI)Ga **2** (225 mg, 0.462 mmol) and CsHMDS (187 mg, 0.637 mmol) were combined. Toluene (4 mL) was added, and the mixture was stirred at room temperature until a homogeneous solution formed (approximately 20 minutes). The yellow solution was then heated and maintained at 45ºC for 16 hours. Subsequent cooling resulted in a brown-green suspension, which was filtered via cannula. The solid was washed with *n*-hexane (2 x 3 mL) and dried under vacuum (< 10^{-2} mbar) for 2 hours, affording $[(Cs\cdots \mathbf{2'})_2(CsHMDS)_2]_\infty$as a yellow solid (80 mg, 0.088 mmol, 20%). For X-ray suitable crystals, this protocol was replicated, with the reaction mixture heated in a water bath at 45ºC, then allowed to cool gradually to room temperature over 2 days.

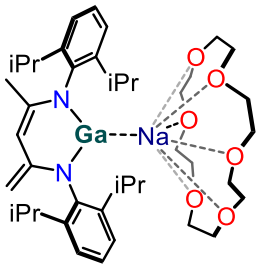
^{1}H NMR (400 MHz, 4:1 C_6D_6:THF-d_8, 298 K): δ 7.13 (d, 2 H, *J* = 7.6 Hz, Ar), 7.07 (d, 2 H, *J* = 7.6 Hz, Ar), 6.97 (m, 2 H, Ar), 5.08 (s, 1 H, γ-CH), 3.98 (sept, 2 H, *J* = 6.9 Hz, CH-^{i}Pr), 3.87 (sept, 2 H, *J* = 6.9 Hz, CH-^{i}Pr), 3.35 (d, 1 H, *J* = 1.8 Hz, C=CH_2), 2.51 (d, 1 H, *J* = 1.8 Hz, C=CH_2), 1.65 (s, 3 H. β-Me), 1.36 (d, 3 H, *J* = 6.9 Hz, Me-^{i}Pr), 1.31 (dd, 12 H, J_1 = 7.2 Hz, J_1 = 1.2 Hz, Me-^{i}Pr), 1.25 (d, 6 H, *J* = 6.9 Hz, Me-^{i}Pr), 0.09 (s, 18 H, $SiMe_3$).

^{13}C{^{1}H} NMR (100.6 MHz, 4:1 C_6D_6:THF-d_8, 298 K): *δ* 156.3 (C_q, *C*=CH_2), 151.5 (C_q, Ar), 149.8 (C_q, Ar), 148.7 (C_q, Ar),147.5 (C_q, Ar), 143.2 (*C*-Me), 123.7 (CH, Ar), 123.7 (CH, Ar), 123.5 (CH, Ar),122.9 (CH, Ar), 100.7 (*γ*-CH), 72.0 (C=*C*H_2), 28.0 (CH-^{i}Pr), 28.0 (CH-^{i}Pr), 26.1 (Me-^{i}Pr), 25.9 (Me-^{i}Pr), 25.2 (Me-^{i}Pr), 23.8 (β-Me), 6.9 ($SiMe_3$).

^{133}Cs{^{1}H} NMR (52.4 MHz, THF-d_8, 298 K): *δ* 60.9 (br s)

Elemental analysis found (calc.) for $C_{70}H_{116}Ga_2Cs_4N_6Si_4$: C 42.28 (46.07), H 5.47 (6.41), N 3.83 (4.60).

2.5.2.3 Synthesis and characterisation of [(18-c-6)Na···2']



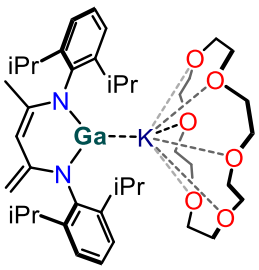
In a J. Young's ampoule, (BDI)Ga **2** (77 mg, 0.158 mmol), NaHMDS (50 mg, 0.273 mmol), and 18-c-6 (40 mg, 0.151 mmol) were combined and dissolved in benzene (2 mL). The mixture was stirred at room temperature. Progress of the reaction was monitored by ^{1}H NMR, and after 2 hours, the reaction was complete. The resulting yellow solution was filtered via cannula followed. Layering with *n*-hexane (5 mL) gave orange prism-shaped crystals after two days at room temperature. These crystals were dried under vacuum (< 10^{-2} mbar) for 1 hour, affording [(18-c-6)Na···**2'**] (40 mg, 0.052 mmol, 33%). These crystals were suitable for X-ray diffraction analysis.

^{1}H NMR (400 MHz, C_6D_6, 298 K): δ 7.29 (d, 2 H, *J* = 7.6 Hz, Ar), 7.13 (m overlapped with solvent peak, 3 H, Ar), 7.02 (t, 1 H, *J* = 7.2 Hz, Ar), 5.60 (s, 1 H, γ-CH), 4.28 (sept, 2 H, *J* = 6.9 Hz, CH-^{i}Pr), 4.11 (sept, 2 H, *J* = 6.9 Hz, CH-^{i}Pr), 3.93 (d, 1 H, *J* = 2 Hz, C=CH_2), 3.00 (d, 1 H, *J* = 2 Hz, C=CH_2), 2.92 (s, 24 H,18-c-6), 1.88 (s, 3 H, β-Me), 1.65 (d, 6 H, *J* = 6.9 Hz, Me-^{i}Pr), 1.39 (m, 18 H, Me-^{i}Pr).

^{13}C{^{1}H} NMR NMR (100.6 MHz, C_6D_6, 298 K): δ 156.6 (C_q, *C*=CH_2), 150.3 (C_q, Ar), 148.1 (C_q, Ar), 147.7 (C_q, Ar), 143.0 (*C*-Me), 124.0 (CH, Ar), 123.2 (CH, Ar), 122.6 (CH, Ar), 101.8 (*γ*-CH), 73.6 (C=*C*H_2), 69.1 (18-cr-6), 28.1 (CH-^{i}Pr), 28.1 (CH-^{i}Pr), 26.1 (Me-^{i}Pr), 25.9 (Me-^{i}Pr), 24.1 (β-Me).

Elemental analysis found (calc.) for $C_{41}H_{64}GaNaN_2O_6$: C 62.81 (63.65), H 8.50 (8.34), N 3.62 (3.62).

2.5.2.4 Synthesis and characterisation of [(18-c-6)K···2']



In a J. Young's ampoule, (BDI)Ga **2** (179 mg, 0.367 mmol), KHMDS (108 mg, 0.541 mmol), and 18-c-6 (100 mg, 0.378 mmol) were combined and dissolved in toluene (2 mL). The mixture was stirred at room temperature for 2 hours. Afterward, the resulting yellow suspension was filtered using a cannula. The isolated yellow solid was dried under a high vacuum (< 10^{-2} mbar) for 2 hours to afford [(18-c-6)K···**2'**] as a green-yellow solid (165 mg, 0.209 mmol, 57%). Crystals suitable for X-ray diffraction of [(18-c-6)K···**2'**] were achieved by slowly diffusing n-hexane (1 mL) into its benzene solution (0.5 mL). Under these conditions, two distinct crystallographic polymorphs of [(18-c-6)K···**2'**]

were isolated: one crystallised as orange prisms (dimer) and the other as orange needles (trimer).

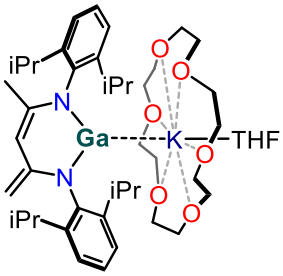
Note on NMR data: Regardless of the crystallized polymorph type, the ^{1}H, ^{13}C, and DOSY NMR data for [(18-c-6)K···**2'**] in solution were identical. The only discrepancy was observed with benzene, which was incorporated within the trimer polymorph as a solvent molecule, while the dimer existed in a solvent-free arrangement. For a comprehensive discussion, refer to Section 5.

^{1}H NMR (500 MHz, C_6D_6, 298 K): *δ* 7.29 (d, 2 H, *J* = 7.6 Hz, Ar), 7.14 (m overlapped with solvent peak, 3 H, Ar), 7.03 (t, 1 H, *J* = 7.5 Hz, Ar), 5.57 (s, 1 H, γ-CH), 4.31 (sept, 2 H, *J* = 6.9 Hz, CH-^{i}Pr), 4.13 (sept, 2 H, *J* = 6.9 Hz, CH-^{i}Pr), 3.93 (d, 1 H, *J* = 2.0 Hz, C=CH_2), 3.04 (d, 1 H, *J* = 2 Hz, C=CH_2), 2.87 (s, 24 H, 18-c-6), 1.94 (s, 3 H, β-Me), 1.66 (d, 6 H, *J* = 6.9 Hz, Me-^{i}Pr), 1.42 (d, 6 H, *J* = 6.7 Hz, Me-^{i}Pr), 1.42 (d, 6 H, *J* = 6.7 Hz, Me-^{i}Pr), 1.37 (d, 6 H, *J* = 6.9 Hz, Me-^{i}Pr).

^{13}C{^{1}H} NMR (125.6 MHz, C_6D_6, 298 K): *δ* 156.7 (C_q, *C*=CH_2), 150.4 (C_q, Ar), 150.0 (C_q, Ar), 148.0 (C_q, Ar), 147.6 (C_q, Ar), 143.0 (C_q, *C*-Me), 123.0 (CH, Ar), 122.9 (CH, Ar), 122.9 (CH, Ar), 122.4 (CH, Ar), 101.2 (*γ*-CH), 72.8 (C=*C*H_2), 69.8 (18-c-6), 28.1 (CH-^{i}Pr), 28.0 (CH-^{i}Pr), 26.4 (Me-^{i}Pr), 26.0 (Me-^{i}Pr), 24.9 (β-Me), 24.2 (Me-^{i}Pr).

Elemental analysis found (calc.) for $C_{41}H_{64}GaKN_2O_6$: C 60.86 (62.35), H 7.97 (8.17), N 3.40 (3.55).

2.5.2.5 Synthesis and characterisation of [(18-c-6)(THF)K···2']

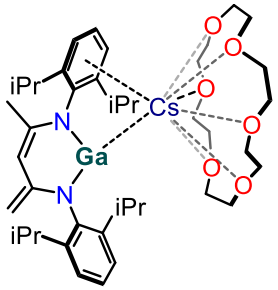


A J. Young's NMR tube was loaded with crystals of [(18-c-6)K···**2'**] (7 mg, 8.8 μmol). Upon dissolving these crystals in a 1:1 mixture of C_6D_6/THF-d_8 (0.5 mL), a yellow solution was obtained. After standing at room temperature for 12 hours, orange prism-shaped crystals of [(18-c-6)K···**2'**]·(THF) formed in nearly quantitative yield (5 mg, 5.8 μmol, 66%), which were dried under vacuum (< 10^{-2} mbar) for 2 hours and filtered. These crystals were suitable for X-ray diffraction analysis.

^{1}H NMR (500 MHz, THF-d_8, 298 K): *δ* 7.18-7.06 (m, 6 H, Ar overlapped with solvent peaks), 5.36 (s, 1 H, γ-CH), 4.16 (sept, 2 H, *J* = 7.0 Hz, CH-^{i}Pr), 4.04 (sept, 2 H, *J* = 6.9 Hz, CH-^{i}Pr), 3.67 (d, 1 H, *J* = 2.0 Hz, C=CH_2), 3.04 (24 H, 18-c-6), 2.80 (d, 1 H, *J* = 2 Hz, C=CH_2), 1.82 (s, 3 H, β-Me), 1.53 (d, 6 H, *J* = 6.9 Hz, Me-^{i}Pr), 1.33 (m, 12 H, *J* = 6.7 Hz, Me-^{i}Pr), 1.22 (d, 6 H, *J* = 6.7 Hz, Me-^{i}Pr).

Note on NMR data: Only ^{1}H NMR data was collected in THF-d_8 due to the limited solubility of the compound, hampering ^{13}C or DOSY characterization in solution.

2.5.2.6 Synthesis and characterisation of [(18-c-6)Cs···2']



In a J. Young's ampoule, (BDI)Ga **2** (156 mg, 0.320 mmol), CsHMDS (116 mg, 0.395 mmol), and 18-c-6 (85 mg, 0.322 mmol) were combined and dissolved in benzene (1.5 mL). The mixture was stirred at room temperature for 5 hours. The resulting yellow solution was then filtered via cannula and layered with *n*-hexane (5 mL). After two days, orange prism-shaped crystals formed. These crystals were dried under vacuum (< 10^{-2} mbar) for 1 hour, affording [(18-c-6)Cs···**2'**] (200 mg, 0.226 mmol, 71%). These were suitable for X-ray diffraction analysis.

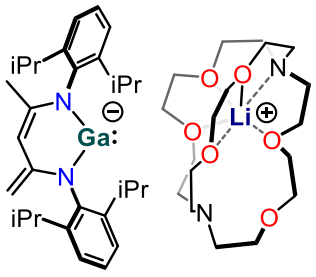
^{1}H NMR (400 MHz, C_6D_6, 298 K): δ 7.32 (d, 2 H, *J* = 7.5 Hz, Ar), 7.26 (d, 2 H, *J* = 7.5 Hz, Ar), 7.12 (m overlapped with solvent peak, 2 H, Ar), 5.51 (s, 1 H, γ-CH), 4.37 (sept, 2 H, *J* = 6.9 Hz, CH-^{i}Pr), 4.21 (sept, 2 H, *J* = 6.9 Hz, CH-^{i}Pr), 3.81 (d, 1 H, *J* = 2.0 Hz, C=CH_2), 2.98 (s, 24 H, 18-c-6), 2.94 (d, 1 H, *J* = 2.0 Hz, C=CH_2), 1.95 (s, 3 H, β-Me), 1.64 (d, 6 H, *J* = 6.9 Hz, Me-^{i}Pr), 1.53 (d, 12 H, *J* = 6.8 Hz, Me-^{i}Pr), 1.44 (d, 6 H, *J* = 6.9 Hz, Me-^{i}Pr).

^{13}C{^{1}H} NMR (100.5 MHz, C_6D_6, 298 K): δ 156.9 (C_q, *C*=CH_2), 151.8 (C_q, Ar), 149.6 (C_q, Ar), 148.7 (C_q, Ar),147.3 (C_q, Ar), 143.6 (*C*-Me), 123.6 (CH, Ar), 123.1 (CH, Ar), 122.6 (CH, Ar), 100.9 (*γ*-CH), 71.7 (C=*C*H_2), 69.8 (18-c-6), 28.2 (CH-^{i}Pr), 28.1 (CH-^{i}Pr), 26.6 (Me-^{i}Pr), 26.4 (Me-^{i}Pr), 25.8 (Me-^{i}Pr), 24.9 (β-Me), 24.1 (Me-^{i}Pr).

^{133}Cs{^{1}H} NMR (52.4 MHz, C_6D_6, 298 K): δ 31.1 (br s)

Elemental analysis found (calc.) for $C_{41}H_{64}GaCsN_2O_6$: C 53.96 (53.73), H 7.51 (7.30), N 2.12 (3.17).

2.5.2.7 Synthesis and characterisation of [(crypt)Li][2']



In a J. Young's ampoule, (BDI)Ga **2** (45 mg, 0.092 mmol), LiHMDS (15 mg, 0.089 mmol), and crypt (34 mg, 0.090 mmol) were combined and dissolved in toluene (1 mL). Vigorous stirring for 10 minutes yielded a pale-yellow solution alongside an orange oil. The solution was then decanted, isolating the orange oil, which upon drying under high vacuum resulted in [(crypt)Li][**2'**] as an oily compound (60 mg,

0.068 mmol, 74%). This material was taken up in 0.6 mL of THF-d_8 and verified as the desired product by ^{1}H, ^{7}Li and ^{13}C NMR analyses. Attempts to crystallise this compound from various solvent mixtures involving THF, hexane, benzene, toluene, and fluorobenzene were met with challenges. However, replicating the synthesis in benzene and allowing the oily compound to stand in benzene at room temperature for 7 days furnished a small crop of crystals suitable for X-ray analysis.

Due to the oily consistency of [(crypt)Li][**2'**] and the difficulties in crystallising it, conducting accurate elemental analyses was hampered, making it challenging to obtain precise compositional data. Nevertheless, the NMR and X-ray diffraction data supports the chemical identity of [(crypt)Li][**2'**].

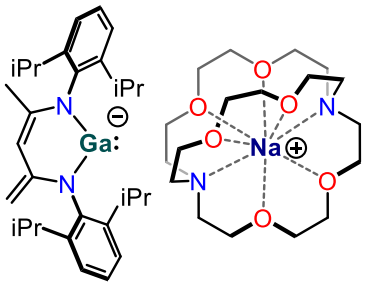
Note on NMR data: The NMR spectroscopic data of [(crypt)Li][**2**'] in solution, obtained using ^{1}H, ^{7}Li ^{13}C and DOSY, is consistent (identical), regardless of its physical form, either orange oil or orange prism-shaped crystals, of [(crypt)Li][**2'**]

^{1}H NMR (500 MHz, THF-d_8, 298 K): δ 6.95 (d, 2 H, J = 7.6 Hz, Ar), 6.93 (d, 2 H, J = 7.6 Hz, Ar), 6.81 (t, 2 H, J = 7.5 Hz, Ar), 4.52 (s, 1 H, γ-CH), 3.70 (m, 4 H, CH-^{i}Pr), 3.59 (s, 12 H, crypt), 3.54 (br s, 12 H, crypt), 2.68 (d, 1 H, J = 2.7 Hz, C=CH_2), 2.61 (br s, 12 H, crypt), 1.94 (d, 1 H, J = 2.7 Hz, C=CH_2), 1.40 (s, 3 H, β-Me), 1.18 (m, 24 H, Me-^{i}Pr).

^{13}C{^{1}H} NMR (125.6 MHz, THF-d_8, 298 K): δ 157.3 (C_q, *C*=CH_2), 151.0 (C_q, Ar), 147.6 (C_q, Ar),147.2 (C_q, Ar), 143.4 (*C*-Me), 142.6 (C_q, Ar), 122.8 (CH, Ar), 122.7 (CH, Ar), 122.6 (CH, Ar),122.4 (CH, Ar), 100.4 (*γ*-CH), 71.8 (br s, crypt), 70.8 (br s, crypt), 69.6 (C=*C*H_2), 69.0 (br s, crypt), 57.6 (br s, crypt), 54.2 (br s, crypt), 28.2 (CH-^{i}Pr), 28.1 (CH-^{i}Pr), 26.6 (Me-^{i}Pr), 26.6 (Me-^{i}Pr), 25.8 (Me-^{i}Pr), 24.2 (β-Me).

^{7}Li{^{1}H} NMR (194.2 MHz, THF-d_8, 298 K): δ 1.75 (s), 0.52 (s), 1.28 (s).

2.5.2.8 Synthesis and characterisation of [(crypt)Na][2']



In a J. Young's ampoule, (BDI)Ga **2** (76 mg, 0.156 mmol), NaHMDS (60 mg, 0.327 mmol), and crypt (56 mg, 0.149 mmol) were combined and dissolved in benzene (1.5 mL). After stirring vigorously for 10 minutes, a yellow solution accompanied by orange oil was observed. Tetrahydrofuran (0.6 mL) was then added, resulting in an orange solution. The solution volume was reduced until

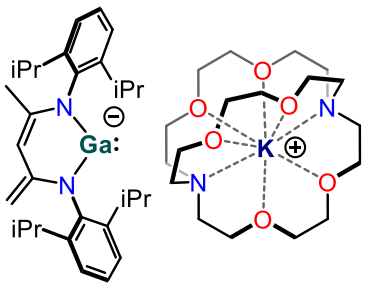
crystallization incipient crystallisation. Orange crystals of [(crypt)Na][**2'**] were subsequently isolated by filtration, dried under vacuum (< 10^{-2} mbar) for 2 hours and isolated (30 mg, 0.034 mmol, 22%). Suitable crystals for X-ray diffraction analysis were prepared by slowly diffusing *n*-hexane (1 mL) into a benzene solution (0.5 mL) containing [(crypt)Na][**2**].

^{1}H NMR (500 MHz, 4:1 C_6D_6:THF-d_8, 298 K): δ 7.34 (d, 2 H, J = 7.6 Hz, Ar), 7.24 (d, 2 H, J = 7.6 Hz, Ar), 7.16 (t overlapped with solvent peak, 1 H, Ar), 7.10 (t, 1 H, J = 7.5 Hz, Ar), 5.26 (s, 1 H, γ-CH), 4.28 (sept, 2 H, J = 6.9 Hz, CH-^{i}Pr), 4.17 (sept, 2 H, J = 6.9 Hz, CH-^{i}Pr), 3.46 (d, 1 H, J = 2.6 Hz, C=CH_2), 3.05 (s, 12 H, crypt), 3.00 (t, 12 H, J_1 = 4.8 Hz, crypt), 2.71 (d, 1 H, J = 2.6 Hz, C=CH_2), 2.04 (t, 12 H, J_1 = 4.8 Hz, crypt), 1.88 (s, 3 H, β-Me), 1.58 (m, 2 H, Me-^{i}Pr), 1.53 (d, 6 H, J = 6.9 Hz, Me-^{i}Pr), 1.41 (d, 6 H, J = 6.9 Hz, Me-^{i}Pr).

^{13}C{^{1}H} NMR (125.6 MHz, 4:1 C_6D_6:THF-d_8, 298 K): δ 157.4 (C_q, *C*=CH_2), 151.0 (C_q, Ar), 150.1 (C_q, Ar), 147.7 (C_q, Ar),147.1 (C_q, Ar), 143.2 (*C*-Me), 122.9 (CH, Ar), 122.8 (CH, Ar), 122.8 (CH, Ar),122.5 (CH, Ar), 100.6 (*γ*-CH), 70.3 (C=*C*H_2), 68.6 (crypt), 67.7 (crypt), 53.0 (crypt), 28.1 (CH-^{i}Pr), 28.1 (CH-^{i}Pr), 26.7 (Me-^{i}Pr), 26.7 (Me-^{i}Pr), 25.9 (Me-^{i}Pr), 25.2 (β-Me), 24.2 (Me-^{i}Pr).

Elemental analysis found (calc.) for $C_{47}H_{86}GaNaN_2O_6$: C 60.26 (63.01), H 8.81 (9.68), N 6.49 (6.25).

2.5.2.9 Synthesis and characterisation of [(crypt)K][2']



In a J. Young's ampoule, (BDI)Ga **2** (56 mg, 0.115 mmol), KHMDS (33 mg, 0.165 mmol), and 2,2,2-cryptand (40 mg, 0.106 mmol) were combined and dissolved in dry toluene (1 mL). After stirring vigorously for 10 minutes at room temperature, left-standing orange prism-shaped crystals were obtained after 2 hours. These crystals were filtered with a cannula and dried under vacuum (< 10^{-2} mbar) for 2 hours, affording [(crypt)K][**2'**] orange prism-shaped crystals (15 mg, 0.017 mmol, 15%). These crystals were suitable for X-ray diffraction analysis.

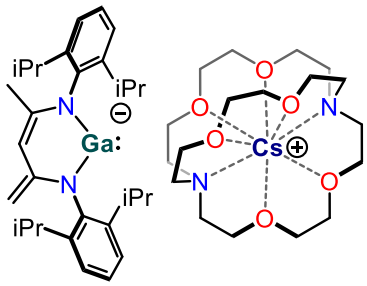
^{1}H NMR (500 MHz, 4:1 C_6D_6:THF-d_8, 298 K): δ 7.32 (d, 2 H, J = 7.6 Hz, Ar), 7.21 (d, 2 H, J = 7.6 Hz, Ar), 7.14 (t overlapped with C_6D_6 residual solvent peak, 1 H, J = 7.6 Hz, Ar), 7.08 (t, 1 H, J = 7.6 Hz, Ar), 5.25 (s, 1 H, γ-CH), 4.27 (sept, 2 H, J = 6.9 Hz, CH-^{i}Pr), 4.16 (sept, 2 H, J = 6.9 Hz, CH-^{i}Pr), 3.45 (d, 1 H, J = 2.6 Hz, C=CH_2), 3.07 (s, 12 H, crypt), 3.01 (t, 12 H, J = 4.6 Hz, crypt), 2.69 (d, 1 H, J = 2.6 Hz, C=CH_2),

2.03 (t, 12 H, *J* = 4.6 Hz, crypt), 1.86 (s, 3 H, β-Me), 1.57 (d, 6 H, *J* = 6.9 Hz, Me-^{i}Pr), 1.55 (d, 6 H, *J* = 6.9 Hz, Me-^{i}Pr), 1.51 (d, 6 H, *J* = 6.9 Hz, Me-^{i}Pr), 1.40 (d, 6 H, *J* = 6.9 Hz, Me-^{i}Pr).

^{13}C{^{1}H} NMR (125.6 MHz, 4:1 C_6D_6:THF-d_8, 298 K): *δ* 157.4 (C_q, *C*=CH_2), 151.1 (C_q, Ar), 150.3 (C_q, Ar), 147.7 (C_q, Ar),147.1 (C_q, Ar), 143.1 (C_q, *C*-Me), 122.9 (CH, Ar), 122.8 (CH, Ar), 122.8 (CH, Ar), 122.4 (CH, Ar), 100.6 (*γ*-CH), 70.5 (crypt), 70.3 (C=*C*H_2), 67.3 (crypt), 53.8 (crypt), 28.1 (CH-^{i}Pr), 28.1 (CH-^{i}Pr), 26.7 (Me-^{i}Pr), 26.6 (Me-^{i}Pr), 25.9 (Me-^{i}Pr), 25.2 (β-Me), 24.6 (Me-^{i}Pr).

Elemental analysis found (calc.) for $C_{47}H_{86}GaKN_4O_6$: C 58.23 (61.90), H 8.82 (9.50), N 6.04 (6.14).

2.5.2.10 Synthesis and characterisation of [(crypt)Cs][2']



In a J. Young's ampoule, (BDI)Ga **2** (64 mg, 0.131 mmol), CsHMDS (40 mg, 0.136 mmol), and 2,2,2-cryptand (50 mg, 0.133 mmol) were combined and dissolved in toluene (2 mL). The mixture was stirred at room temperature for 15 minutes. An *in situ* yellow crystalline solid was obtained. The solvent was removed by cannula. The yellow crystalline solid was dried under high vacuum (< 10^{-2} mbar) for 1 hour, affording [(crypt)Cs][**2'**] (92 mg, 0.092 mmol, 71%). The obtained crystals were suitable for X-ray diffraction analysis.

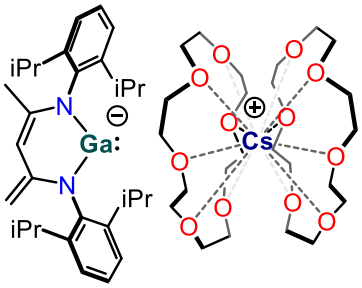
^{1}H NMR (500 MHz, 4:1 C_6D_6:THF-d_8, 298 K): *δ* 7.19 (d, 2 H, *J* = 7.5 Hz, Ar), 7.11 (d, 2 H, *J* = 7.5 Hz, Ar), 7.02 (t, 1 H, J_1 = 7.5 Hz, Ar), 6.98 (t, 1 H, *J* = 7.5 Hz, Ar), 5.11 (s, 1 H, γ-CH), 4.11 (sept, 2 H, *J* = 6.9 Hz, CH-^{i}Pr), 4.03 (sept, 2 H, *J* = 6.9 Hz, CH-^{i}Pr), 3.34 (d, 1 H, *J* = 2.5 Hz, C=CH_2), 3.16 (s, 12 H, crypt), 3.07 (t, 12 H, *J* = 4.6 Hz, crypt), 2.54 (d, 1 H, *J* = 2.5 Hz, C=CH_2), 2.14 (t, 12 H, *J* = 4.6 Hz, crypt), 1.73 (s, 3 H, β-Me), 1.44 (d, 6 H, *J* = 6.9 Hz, Me-^{i}Pr), 1.39 (d, 6 H, *J* = 6.9 Hz, Me-^{i}Pr), 1.37 (d, 6 H, *J* = 6.9 Hz, Me-^{i}Pr), 1.31 (d, 6 H, *J* = 6.9 Hz, Me-^{i}Pr).

^{13}C{^{1}H} NMR (125.6 MHz, 4:1 C_6D_6:THF-d_8, 298 K): *δ* 157.0 (C_q, *C*=CH_2), 151.2 (C_q, Ar), 150.2 (C_q, Ar), 147.9 (C_q, Ar),147.2 (C_q, Ar), 142.9 (*C*-Me), 122.9 (CH, Ar), 122.8 (CH, Ar), 122.7 (CH, Ar), 122.3 (CH, Ar), 100.6 (*γ*-CH), 70.6 (C=*C*H_2 and crypt, overlapped signals), 68.7 (crypt), 55.6 (crypt), 28.0 (CH-^{i}Pr), 26.4 (Me-^{i}Pr), 25.7 (Me-^{i}Pr), 25.3 (β-Me), 24.1 (Me-^{i}Pr).

^{133}Cs{^{1}H} NMR (52.4 MHz, 4:1 C_6D_6:THF-d_8, 298 K): δ 193.4 (br s).

Elemental analysis found (calc.) for $C_{47}H_{86}CsGaN_4O_6$: C 55.54 (56.12), H 7.83 (8.62), N 5.48 (5.57).

2.5.2.11 Synthesis and characterisation of [(18-c-6)$_2$Cs][2']



In a J. Young's ampoule, (BDI)Ga **2** (100 mg, 0.205 mmol), CsHMDS (66 mg, 0.225 mmol), and 18-c-6 (108 mg, 0.410 mmol) were weighed and dissolved in benzene (1.5 mL). The solution was mixed and allowed to stir at room temperature for a duration of 5 hours. Subsequently, the formed yellow suspension was processed through cannula filtration. The residual solid was then thoroughly washed with *n*-hexane (2 x 3 mL) and subjected to drying under vacuum (< 10^{-2} mbar) for a period of 2 hours, resulting with [(18-cr-6)$_2$Cs][**2'**] as a yellow solid (176 mg, 0.148 mmol, 72% yield). Crystals suitable for X-ray diffraction analysis were obtained by layering a solution of [(18-cr-6)$_2$Cs][**2'**] in benzene with *n*-hexane.

^{1}H NMR (400 MHz, Tol-*d*$_8$, 298 K): *δ* 7.26 (d, 2 H, *J* = 7.5 Hz, Ar), 7.20 (d, 2 H, *J* = 7.5 Hz; Ar), 7.08 (m overlapped with solvent peak, 2 H, Ar), 5.31 (s, 1 H, γ-CH), 4.25 (sept, 2 H, *J* = 6.7 Hz, CH-^{i}Pr), 4.13 (sept, 2 H, *J* = 6.8 Hz, CH-^{i}Pr), 3.59 (s, 1 H, C=CH_2), 3.26 (s, 48 H, 18-c-6), 2.75 (s, 1 H, C=CH_2), 1.86 (s, 3 H, β-Me), 1.56 (d, 6 H, *J* = 6.9 Hz, Me-^{i}Pr), 1.47 (m, 12 H, Me-^{i}Pr), 1.41 (d, 6 H, Me-^{i}Pr).

^{13}C{^{1}H} NMR (125.6 MHz, Tol-*d*$_8$, 298 K): *δ* 156.7 (C_q, *C*=CH_2), 151.7 (C_q, Ar), 149.7 (C_q, Ar), 148.5 (C_q, Ar),147.2 (C_q, Ar), 143.2 (β-*C*-Me), 123.3 (CH, Ar), 123.3 (CH, Ar), 122.9 (CH, Ar), 122.5 (CH, Ar), 101.0 (*γ*-CH), 71.7 (C=*C*H_2), 70.4 (18-c-6), 28.1 (CH-^{i}Pr), 28.1 (CH-^{i}Pr), 26.5 (Me-^{i}Pr), 26.4 (Me-^{i}Pr), 25.8 (Me-^{i}Pr), 24.9 (β-Me), 24.1 (Me-^{i}Pr).

^{133}Cs{^{1}H} NMR (52.4 MHz, Tol-*d*$_8$, 298 K): δ 15.6 (br s).

Elemental analysis found (calc.) for $C_{53}H_{88}CsGaN_2O_{12}$: C 54.64 (52.53), H 7.19 (7.32), N 2.21 (2.31).

2.6 References

[1] a) P. P. Power, *Nature* **2010**, *463*, 171-177; b) C. Weetman, S. Inoue, *ChemCatChem* **2018**, *10*, 4213-4228; c) R. D. Dewhurst, M.-A. Légaré, H. Braunschweig, *Commun. Chem.* **2020**, *3*, 131.

[2] M. He, C. Hu, R. Wei, X.-F. Wang, L. L. Liu, *Chem. Soc. Rev.* **2024**, *53*, 3896-3951.

[3] P. Schwerdtfeger, G. A. Heath, M. Dolg, M. A. Bennett, *J. Am. Chem. Soc.* **1992**, *114*, 7518-7527.

[4] G. Linti, H. Schnöckel, *Coord. Chem. Rev.* **2000**, *206-207*, 285-319.

[5] H. Schmidbaur, *Angew. Chem. Int. Ed.* **1985**, *24*, 893-904.

[6] a) E. S. Schmidt, A. Jockisch, H. Schmidbaur, *J. Am. Chem. Soc.* **1999**, *121*, 9758-9759; b) E. S. Schmidt, A. Schier, H. Schmidbaur, *J. Chem. Soc. Dalton Trans.* **2001**, 505-507.

[7] W. Uhl, *Angew. Chem. Int. Ed.* **1993**, *32*, 1386-1397.

[8] a) C. Dohmeier, C. Robl, M. Tacke, H. Schnöckel, *Angew. Chem. Int. Ed.* **1991**, *30*, 564-565; b) D. Loos, H. Schnöckel, *J. Organomet. Chem.* **1993**, *463*, 37-40; c) D. Loos, E. Baum, A. Ecker, H. Schnöckel, A. J. Downs, *Angew. Chem. Int. Ed.* **1997**, *36*, 860-862.

[9] M. C. Kuchta, J. B. Bonanno, G. Parkin, *J. Am. Chem. Soc.* **1996**, *118*, 10914-10915.

[10] a) C. Jones, P. C. Junk, J. A. Platts, A. Stasch, *J. Am. Chem. Soc.* **2006**, *128*, 2206-2207; b) G. Jin, C. Jones, P. C. Junk, A. Stasch, W. D. Woodul, *New J. Chem.* **2008**, *32*, 835-842; c) J. Overgaard, C. Jones, D. Dange, J. A. Platts, *Inorg. Chem.* **2011**, *50*, 8418-8426.

[11] X. Zheng, A. Heilmann, C. McManus, S. Aldridge, *Chem. Eur. J.* **2021**, *27*, 3159-3165.

[12] a) R. J. Wright, M. Brynda, J. C. Fettinger, A. R. Betzer, P. P. Power, *J. Am. Chem. Soc.* **2006**, *128*, 12498-12509; b) D. Dange, J. Li, C. Schenk, H. Schnöckel, C. Jones, *Inorg. Chem.* **2012**, *51*, 13050-13059.

[13] a) N. J. Hardman, R. J. Wright, A. D. Phillips, P. P. Power, *J. Am. Chem. Soc.* **2003**, *125*, 2667-2679; b) N. J. Hardman, R. J. Wright, A. D. Phillips, P. P. Power, *Angew. Chem. Int. Ed.* **2002**, *41*, 2842-2844.

[14] Z. Zhu, R. C. Fischer, B. D. Ellis, E. Rivard, W. A. Merrill, M. M. Olmstead, P. P. Power, J. D. Guo, S. Nagase, L. Pu, *Chem. Eur. J.* **2009**, *15*, 5263-5272.

[15] S. H. F. Schreiner, T. Rüffer, R. Kretschmer, *Nat. Synth.* **2025**, *4*, 67-74.

[16] a) N. J. Hardman, B. E. Eichler, P. P. Power, *Chem. Commun.* **2000**, 1991-1992; b) S. L. Choong, W. D. Woodul, A. Stasch, C. Schenk, C. Jones, *Aust. J. Chem.* **2011**, *64*, 1173-1176; c) T. Richter, S. Thum, O. P. E. Townrow, M. Wiesinger, J. Langer, S. Harder, *Z. Anorg. Allg. Chem.* **2024**, *650*, e202400044.

[17] P. J. Chirik, *Inorg. Chem.* **2011**, *50*, 9737-9740.

[18] a) M. Zhong, S. Sinhababu, H. W. Roesky, *Dalton Trans.* **2020**, *49*, 1351-1364; b) L. Zhu, R. Kinjo, *Chem. Soc. Rev.* **2023**, *52*, 5563-5606.

[19] R. J. Baker, R. D. Farley, C. Jones, M. Kloth, D. M. Murphy, *J. Chem. Soc. Dalton Trans.* **2002**, 3844-3850.

[20] I. L. Fedushkin, A. N. Lukoyanov, G. K. Fukin, S. Y. Ketkov, M. Hummert, H. Schumann, *Chem. Eur. J.* **2008**, *14*, 8465-8468.

[21] a) J. Hicks, P. Vasko, J. M. Goicoechea, S. Aldridge, *Nature* **2018**, *557*, 92-95; b) D. Sarkar, P. Vasko, T. Gluharev, L. P. Griffin, C. Bogle, J. Struijs, J. Tang, A. F. Roper, A. E. Crumpton, S. Aldridge, *Angew. Chem. Int. Ed.* **2024**, *63*, e202407427.

[22] R. J. Schwamm, M. D. Anker, M. Lein, M. P. Coles, C. M. Fitchett, *Angew. Chem. Int. Ed.* **2018**, *57*, 5885-5887.

[23] a) R. J. Baker, C. Jones, *Coord. Chem. Rev.* **2005**, *249*, 1857-1869; b) O. Kysliak, S. H. F. Schreiner, N. Grabicki, P. Liebing, F. Weigend, O. Dumele, R. Kretschmer, *Angew. Chem. Int. Ed.* **2022**, *61*, e202206963; c) A. Barthélemy, H. Scherer, H. Weller, I. Krossing, *Chem. Commun.* **2023**, *59*, 1353-1356; d) R. J. Wehmschulte, P. P. Power, *Angew. Chem. Int. Ed.* **1998**, *37*, 3152-3154; e) M. R. Lichtenthaler, F. Stahl, D. Kratzert, L. Heidinger, E. Schleicher, J. Hamann, D. Himmel, S. Weber, I. Krossing, *Nat. Commun.* **2015**, *6*, 8288; f) B. Twamley, P. P. Power, *Angew. Chem. Int. Ed.* **2000**, *39*, 3500-3503; g) W. Uhl, W. Hiller, M. Layh, W. Schwarz, *Angew. Chem. Int. Ed.* **1992**, *31*, 1364-1366; h) C. Bour, V. Gandon, *Coord. Chem. Rev.* **2014**, *279*, 43-57; i) J. T. Boronski, M. P. Stevens, B. van Ijzendoorn, A. C. Whitwood, J. M. Slattery, *Angew. Chem. Int. Ed.* **2021**, *60*, 1567-1572; j) N. Wiberg, T. Blank, M. Westerhausen, S. Schneiderbauer, H. Schnöckel, I. Krossing, A. Schnepf, *Eur. J. Inorg. Chem.* **2002**, *2002*, 351-356; k) M. Edwards, J. Hicks, C. McManus, J. M. Goicoechea, S. Aldridge, *Polyhedron* **2023**, *242*, 116520.

[24] a) R. J. Schwamm, M. D. Anker, M. Lein, M. P. Coles, *Angew. Chem. Int. Ed.* **2019**, *58*, 1489-1493; b) S. Grams, J. Mai, J. Langer, S. Harder, *Organometallics* **2022**, *41*, 2862-2867; c) D. Sarkar, P. Vasko, A. F. Roper, A. E. Crumpton, M. M. D. Roy, L. P. Griffin, C. Bogle, S. Aldridge, *J. Am. Chem. Soc.* **2024**, *146*, 11792-11800; d) G. Feng, K. L. Chan, Z. Lin, M. Yamashita, *J. Am. Chem. Soc.* **2022**, *144*, 22662-22668; e) R. J. Schwamm, M. P. Coles, M. S. Hill, M. F. Mahon, C. L. McMullin, N. A. Rajabi, A. S. S. Wilson, *Angew. Chem. Int. Ed.* **2020**, *59*, 3928-3932; f) R. J. Schwamm, M. S. Hill, H.-Y. Liu, M. F. Mahon, C. L. McMullin, N. A. Rajabi, *Chem. Eur. J.* **2021**, *27*, 14971-14980; g) K. Koshino, R. Kinjo, *J. Am. Chem. Soc.* **2020**, *142*, 9057-9062; h) C. Yan, R. Kinjo, *Angew. Chem. Int. Ed.* **2022**, *61*, e202211800; i) S. Kurumada, S. Takamori, M. Yamashita, *Nat. Chem.* **2020**, *12*, 36-39; j) M. J. Evans, M. D. Anker, M. P. Coles, *Inorg. Chem.* **2021**, *60*, 4772-4778.

[25] a) K. Hobson, C. J. Carmalt, C. Bakewell, *Chem. Sci.* **2020**, *11*, 6942-6956; b) J. Hicks, P. Vasko, J. M. Goicoechea, S. Aldridge, *Angew. Chem. Int. Ed.* **2021**, *60*, 1702-1713; c) M. P. Coles, M. J. Evans, *Chem. Commun.* **2023**, *59*, 503-519; d) M. D. Anker, M. Lein, M. P. Coles, *Chem. Sci.* **2019**, *10*, 1212-1218; e) D. Sorbelli, L. Belpassi, P. Belanzoni, *Inorg. Chem.* **2022**, *61*, 1704-1716; f) D. Sorbelli, L. Belpassi, P. Belanzoni, *Chem. Eur. J.* **2023**, *29*, e202203584.

[26] a) Y. Liu, S. Li, X.-J. Yang, Q.-S. Li, Y. Xie, H. F. Schaefer, B. Wu, *J. Organomet. Chem.* **2011**, *696*, 1450-1455; b) Y. Zhang, V. A. Dodonov, W. Chen, S. Zhang, P. W. Roesky, Y. Zhao, I. L. Fedushkin, X.-J. Yang, *Inorg. Chem.* **2023**, *62*, 6288-6296.

[27] Y. Liu, J. Li, X. Ma, Z. Yang, H. W. Roesky, *Coord. Chem. Rev.* **2018**, *374*, 387-415.

[28] a) S. Grams, J. Eyselein, J. Langer, C. Färber, S. Harder, *Angew. Chem. Int. Ed.* **2020**, *59*, 15982-15986; b) S. Grams, J. Mai, J. Langer, S. Harder, *Dalton Trans.* **2022**, *51*, 12476-12483.

[29] P. Dabringhaus, A. Barthélemy, I. Krossing, *Z. Anorg. Allg. Chem.* **2021**, *647*, 1660-1673.

[30] S. Grams, J. Mai, J. Langer, S. Harder, *Dalton Trans.* **2022**, *51*, 12476-12483.

[31] A. I. Ojeda-Amador, A. J. Martínez-Martínez, A. R. Kennedy, C. T. O'Hara, *Inorg. Chem.* **2016**, *55*, 5719-5728.

[32] a) J. M. Lehn, J. P. Sauvage, *J. Am. Chem. Soc.* **1975**, *97*, 6700-6707; b) A. D. Hamilton, in *Comprehensive Heterocyclic Chemistry* (Eds.: A. R. Katritzky, C. W. Rees), Pergamon, Oxford, **1984**, pp. 731-761.

[33] a) S. Bachmann, R. Neufeld, M. Dzemski, D. Stalke, *Chem. Eur. J.* **2016**, *22*, 8462-8465; b) A.-K. Kreyenschmidt, S. Bachmann, T. Niklas, D. Stalke, *ChemistrySelect.* **2017**, *2*, 6957-6960; c) R. Neufeld, D. Stalke, *Chem. Sci.* **2015**, *6*, 3354-3364.

[34] *CRC Handbook of Chemistry and Physics* (Ed.: W. M. Haynes), 97th Ed, CRC Press, Boca Raton, FL, **2016**, pp. 14-17.
[35] T. X. Gentner, M. J. Evans, A. R. Kennedy, S. E. Neale, C. L. McMullin, M. P. Coles, R. E. Mulvey, *Chem. Commun.* **2022**, *58*, 1390-1393.
[36] B. Cordero, V. Gómez, A. E. Platero-Prats, M. Revés, J. Echeverría, E. Cremades, F. Barragán, S. Alvarez, *Dalton Trans.* **2008**, 2832-2838.
[37] C. Lepetit, P. Fau, K. Fajerwerg, M. L. Kahn, B. Silvi, *Coord. Chem. Rev.* **2017**, *345*, 150-181.
[38] Z. Zhou, M. A. Petrukhina, *Coord. Chem. Rev.* **2023**, *486*, 215144.
[39] N. Villegas-Escobar, A. Toro-Labbé, H. F. Schaefer III, *Chem. Eur. J.* **2021**, *27*, 17369-17378.
[40] M. J. Evans, M. D. Anker, C. L. McMullin, S. E. Neale, M. P. Coles, *Angew. Chem. Int. Ed.* **2021**, *60*, 22289-22292.
[41] H. Videa, A. J. Martínez-Martínez, *Dalton Trans.* **2023**, *52*, 13058-13062.
[42] C. Cui, S. Köpke, R. Herbst-Irmer, H. W. Roesky, M. Noltemeyer, H.-G. Schmidt, B. Wrackmeyer, *J. Am. Chem. Soc.* **2001**, *123*, 9091-9098.
[43] H. Zhu, J. Chai, H. Fan, H. W. Roesky, U. N. Nehete, H.-G. Schmidt, M. Noltemeyer, *Eur. J. Inorg. Chem.* **2005**, *2005*, 2147-2150.
[44] S. Brand, H. Elsen, J. Langer, W. A. Donaubauer, F. Hampel, S. Harder, *Angew. Chem. Int. Ed.* **2018**, *57*, 14169-14173.
[45] T. X. Gentner, R. E. Mulvey, *Angew. Chem. Int. Ed.* **2021**, *60*, 9247-9262.
[46] X. He, Y. Yao, X. Luo, J. Zhang, Y. Liu, L. Zhang, Q. Wu, *Organometallics* **2003**, *22*, 4952-4957.
[47] M. F. Lappert, M. J. Slade, A. Singh, J. L. Atwood, R. D. Rogers, R. Shakir, *J. Am. Chem. Soc.* **1983**, *105*, 302-304.
[48] a) *Organometallics* **2016**, *35*, 3255-3256; b) A. C. Aiken, P. F. DeCarlo, J. L. Jimenez, *Anal. Chem.* **2007**, *79*, 8350-8358; c) R. E. H. Kuveke, L. Barwise, Y. van Ingen, K. Vashisth, N. Roberts, S. S. Chitnis, J. L. Dutton, C. D. Martin, R. L. Melen, *ACS Cent. Sci.* **2022**, *8*, 855-863.

CHAPTER III

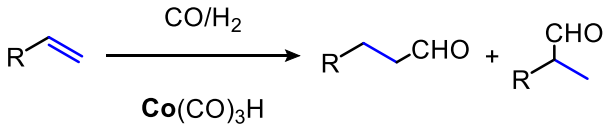
Synthesis, Characterisation and Reactivity of Bimetallic Ga−Rh Species: H_2 Activation and Catalytic Hydrogenation of Olefins

3.1 Introduction

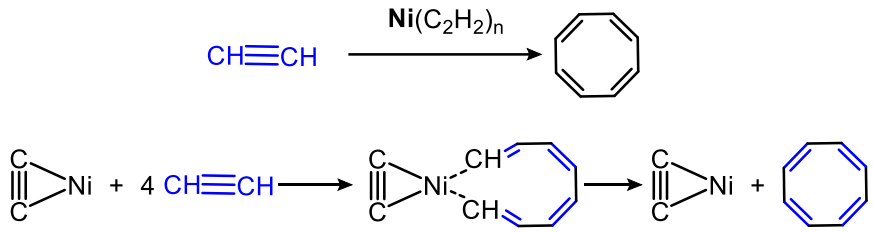
Transition metals have long served as indispensable catalysts in the synthesis of high-value organic compounds, enabling enhanced yields, selectivity, and atom/energy efficiency across a wide range of transformations. In both homogeneous and heterogeneous catalysis, the metal–ligand interface is central to controlling reactivity and selectivity, whether the metal centre is stabilised by ligands in solution or solid supports in bulk processes.

Historically, the earliest homogeneous catalytic systems featured relatively simple transition-metal fragments. In 1938, Roelen[1] pioneered cobalt(I) complexes for alkene hydroformylation (Scheme 1A), and not long after, Reppe[2] identified nickel homoleptic species as intermediates in acetylene cyclotetramerization (Scheme 1B). These breakthroughs laid the foundation for modern organometallic chemistry, showing that appropriate ligand design could endow metal centres with efficient bond-formation capabilities.

A) Roelen, 1938, *Alkene Hydroformylation*



B) Reppe, 1948, *Acetylene Cyclotetramerization*



Scheme 1. Early examples of single-site transition-metal catalysts for hydroformylation and cyclotetramerization.

Although numerous organometallic catalysts rely on metal–carbon bonds, ligands bearing heteroatoms, notably phosphorus or nitrogen, are equally critical. By adjusting stereo-electronic factors such as donor strength, steric bulk, and charge distribution, these “co-ligands” can profoundly alter a catalytic reaction profile. Researchers have thus explored a wide variety of ligand classes, from simple CO to

complex π systems and functionalised organic frameworks,[3] often categorised by electron-counting (X-, L-, Z-type), or orbital interactions (σ *versus* π), Figure 1.[4]

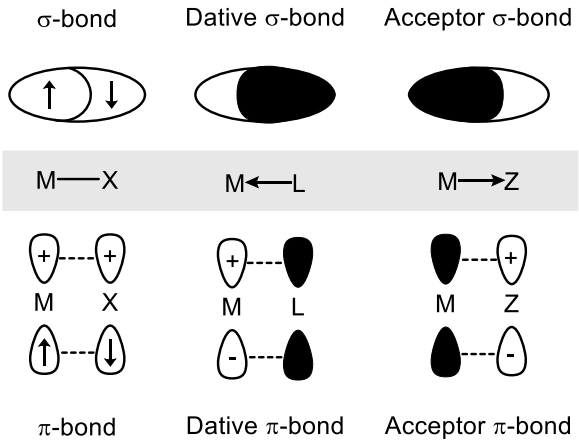


Figure 1. Examples of monofunctional ligating atoms.

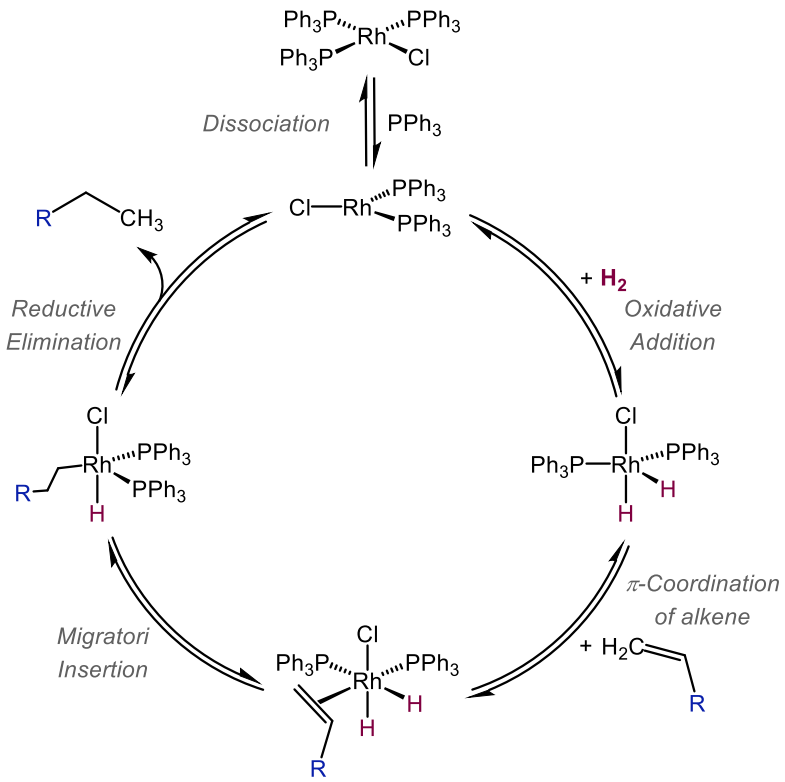
Focusing specifically on rhodium, this metal offers diverse oxidation states, ranging from Rh(0) to Rh(III), and coordination geometries (square planar, tetrahedral, octahedral), making it a powerful coordination test environment for ligand design. Following the foundational breakthroughs with phosphine complexes in hydroformylation and amine ligation for robust, potentially chiral catalysis, modern research has sought to expand rhodium's reactivity domain through unconventional ligands, namely carbenes and, as outlined in earlier chapters, main group carbene analogues. These latter species, especially from Group 13 (Al, Ga, In), bring amphoteric frontier orbitals (lone pair and empty p-orbital) reminiscent of classical CR_2 or NHC (N-heterocyclic) carbene ligands. As such, they have the potential to foster bimetallic metal–metal synergy, particularly in demanding scenarios like bond activation reactivity.

In this *Chapter*, we focus on the rhodium species, a metal offering diverse oxidation states and coordination geometries, making it a powerful platform for catalytic and coordination exploration within the scope of Group 13 low-valent metalloligands, particularly in the context of M(I) carbene analogues. With a well stablished ground floor on the chemistry of P-donor (phosphines), N-donor (amines) and C-donor (carbene) ligands, where key structural variations can significantly influence thermodynamics, kinetics, and, ultimately, catalytic performance, we will harness low-valent Group 13 M(I) states, Al(I), Ga(I) and In(I) species as carbene analogues, for accessing novel bimetallic or "metalloligand" frameworks that could

unlock reactivity beyond conventional single-metal transition metal scaffolds. By integrating this approach, we aim to demonstrate how Rh, historically dominated by amine-, phosphine- or carbene-based catalysis, can adopt new metalloligand ligand families to expand the frontier of transition-metal catalysis. Notably, such synergy could shed light on new modes of small-molecule activations (H_2, C–H, etc.) that challenge even well-established Rh chemistry, thus charting a new path toward bimetallic cooperation and more sophisticated bond-cleavage processes.

3.1.1 Amine and Phosphine Ligands in Rhodium Chemistry

Among the oldest and most impactful ligands in transition-metal catalysis are phosphines (PR_3). Their uses in rhodium chemistry dates back to Wilkinson's iconic [$RhCl(PPh_3)_3$], which demonstrated selective alkene hydrogenation under mild conditions, paving the way for numerous catalytic applications.[5] Since then, monodentate and chelating phosphines have proliferated in rhodium catalysis, enabling fine-tuning of electron density, steric environment, and coordination number for an array of transformations such as hydroformylation, hydrogenation, isomerization, and cross-coupling.[6]



Scheme 2. Schematic representation of Wilkinson's catalyst mechanism in the hydrogenation of olefins with molecular hydrogen.[7]

One key advantage of phosphines is the ease with which their electronic and steric properties can be manipulated by altering substituents on phosphorus (e.g., from PPh_3 to $P(p\text{-}Tol)_3$, PCy_3, or $P(OPh)_3$). Adjusting cone angles (in monodentate phosphines) or bite angles (in bidentate frameworks) can markedly influence reaction rates and product selectivity, Figure 2.[8] For instance, bulky phosphites ($P(OR)_3$) promote steric crowding at the rhodium centre, steering the formation of selected products, while electron-rich trialkyl phosphines can stabilise higher oxidation states or facilitate oxidative addition steps.[9]

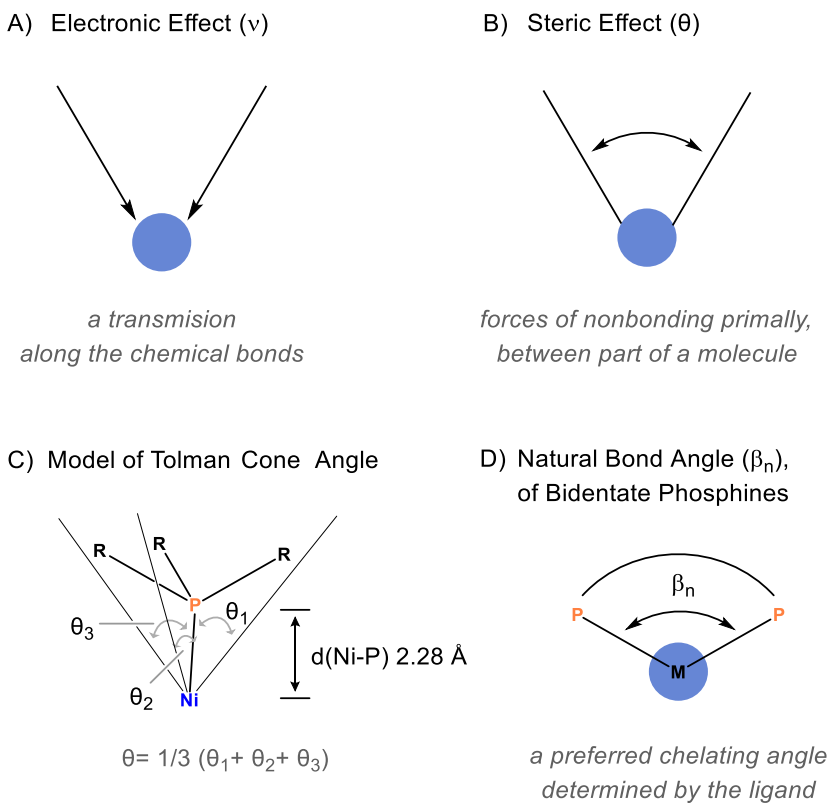


Figure 2. Schematic definition of A) electronic and B) steric effects. C) A Ni-PR_3 model to measure the Tolman cone angle and D) the natural bond angle in bidentate phosphines.

Industrial-scale hydroformylation represents a prime example of Rh–phosphine success, with the Shell High-Pressure and OXO processes relying on tailor-made rhodium–PR_3 (or diphosphine) complexes to convert alkenes into aldehydes.[1, 10] Phosphine ligands (Figure 3A) are also central to asymmetric hydrogenation, where chiral scaffolds like DIPAMP or BINAP impart enantioselectivity in reducing a broad spectrum of substrates (ketones, imines, alkenes).[11] A landmark example is Noyori's 1990 work employing chiral BINAP in

ruthenium and rhodium complexes to achieve highly enantioselective hydrogenation of olefins.[12] As the example were the cationic (*S*)-BINAP−Rh complex, is able to hydrogenate an (*Z*)-α-(benzamido)cinnamic acid or the methyl ester in ethanol to give the *R* hydrogenation product in 93−100% ee, Figure 3B.[13] This milestone set phosphine chemistry as a cornerstone of homogeneous catalysis, with rhodium often showcased as a pivotal metal centre for advanced transformations.

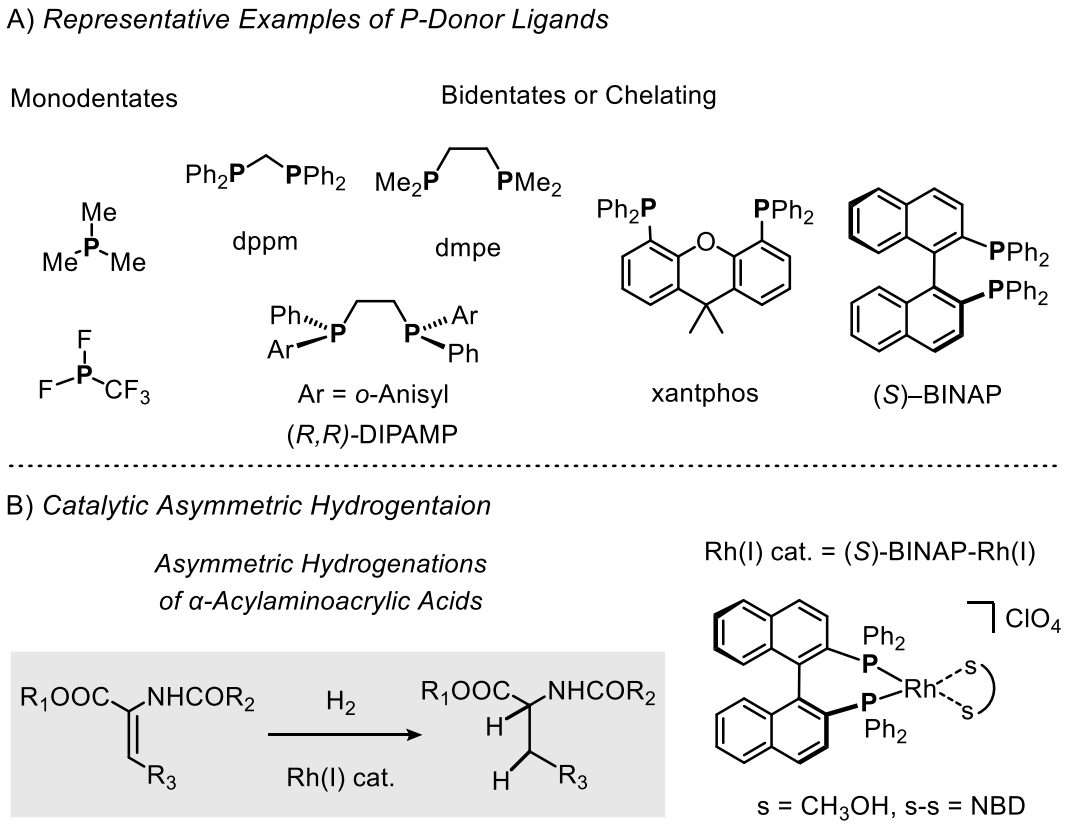
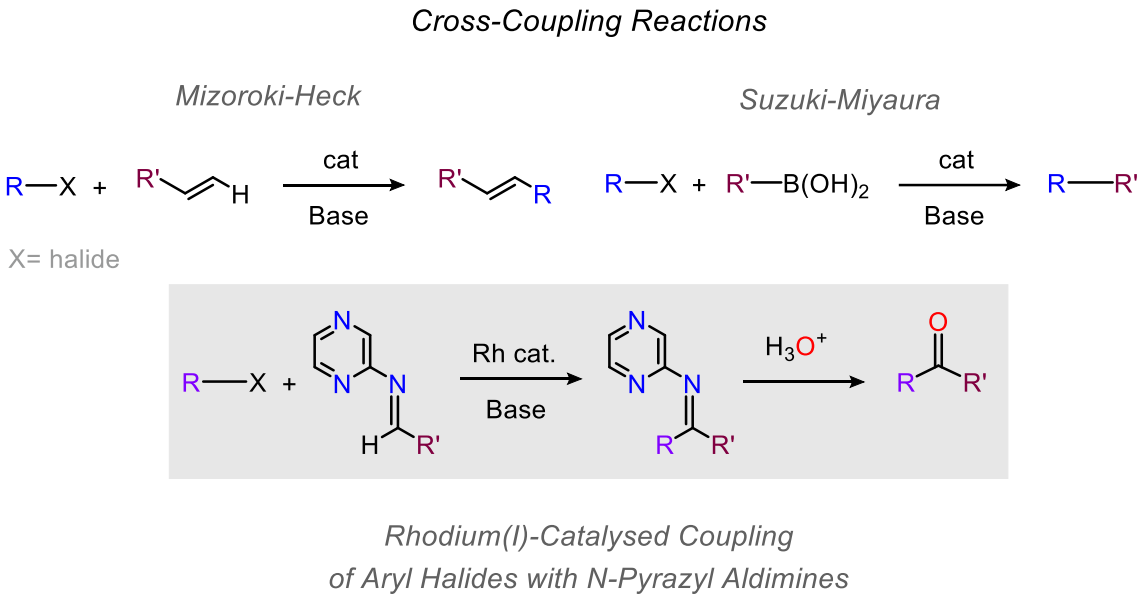


Figure 3. A) Representative P-donor ligands and B) a Rh-based catalyst exemplifying BINAP's chiral induction in hydrogenation reactions.

Beyond hydrogenation and hydroformylation, Rh–phosphine catalysts feature prominently in cross-coupling (Mizoroki-Heck, Suzuki) and C–H functionalisation steps, often sharing the stage with palladium or iridium complexes.[14] In these reactions, the phosphine ligands not only stabilise metal-centred intermediates but also facilitate oxidative addition or reductive elimination, depending on the catalytic cycle. Accordingly, the tuneable nature of phosphines, both steric and electronic, has led many to integrate them with other donor functionalities (e.g., amines or carbene moieties) in hybrid or multidentate frameworks, aiming for synergy across multiple binding sites.[15]



Scheme 3. Schematic representation of two of the most studied cross-coupling reactions and an applied example where Hartwig and co-workers employed a low-valent rhodium system as catalyst.[14a]

In parallel to phosphines, amine-based ligands (including simple amines, imines, and amidines) have proven equally vital for transition-metal stabilisation, especially for first- and second-row metals like rhodium.[16] Nitrogen-donor (N-donor) ligands can strongly influence the stability, electronic environment, and reactivity of the resulting metal complexes. By varying substituents on the nitrogen centre, one can tune the steric and electronic features, thus controlling both kinetics (reaction rates, barriers) and thermodynamics (overall stability). Moreover, the chelate effect arising from bidentate or polydentate N-donor ligands typically imparts greater stability than monodentate ligands, reducing ligand displacement by alternative substrates.[17] Beyond their practical robustness, often tolerant of air and moisture, many nitrogen-based ligands can be derived from biologically inspired frameworks, tapping into nature's vast library of chiral motifs.[18] Since numerous biochemical functions rely on chirality, harnessing chiral N-donor ligands has become a central strategy in enantioselective catalysis, enabling the transfer of chirality from a small amount of enantiopure catalyst to a much larger quantity of substrate.[17, 19]

One seminal illustration is given by Noyori and co-workers, who showed that ruthenium and iridium complexes bearing certain N-donor ligands can hydrogenate aromatic or acetylenic ketones to the corresponding alcohols under mild conditions, with 2-propanol serving as a hydrogen donor (Figure 4A and B).[20] Parallel work by

the groups of Grützmacher[18] and Lemaire[21] employed related rhodium complexes for asymmetric transfer hydrogenation of acetophenone (Figure 4C and D).

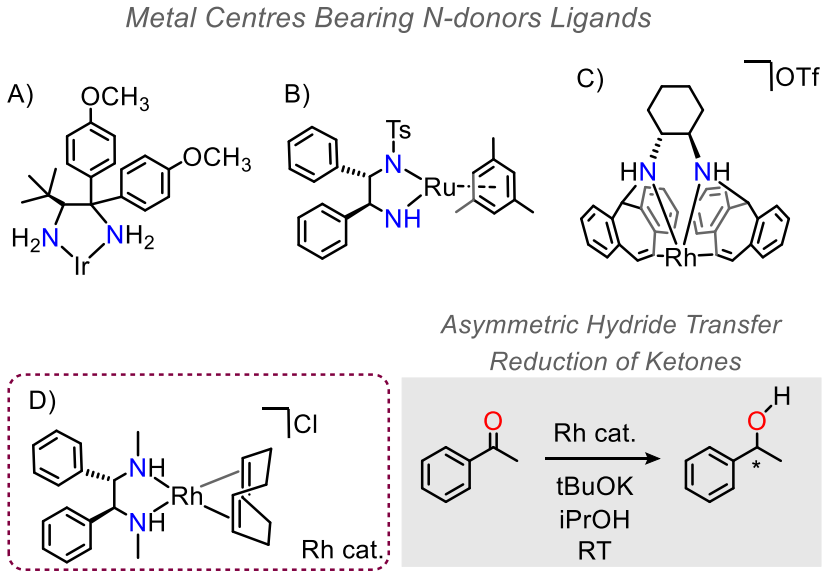


Figure 4. Representative examples of metal centres bearing N-donor ligands, including Ru, Ir, and Rh complexes, and a selected example of a rhodium complex employed in the asymmetric hydride transfer reduction of ketones.[21]

Although many transition metals form robust complexes with N-donor ligands, rhodium holds special prominence. Its chemistry is deeply investigated, thanks to its ability to coordinate an array of ligands spanning σ-donors (amines, phosphines) and π-acceptors (diolefins, carbene surrogates). Such versatility fosters multiple oxidations states and underpins rhodium's role in diverse catalytic processes, including hydrogenation, hydroformylation, and cross-coupling.[6a, 22] Progress in this field is further aided by a variety of rhodium precursors, which enable the formation of more tailor-made architectures.

Despite these advances, the use of amine-based ligands, particularly monodentate or chelating diamines that act primarily as σ-donors, remains less explored than other families of rhodium catalysts (e.g., phosphines). Early examples date to the 1970s, when Usón and Garralda prepared [Rh(olefin)(bis-amine)]$^+$ complexes incorporating 1,5-cyclooctadiene (COD) or 1,5-norbornadiene (NBD).[23] Yet these initial reports lacked in-depth structural data or comprehensive spectroscopic characterisation. Subsequent work introduced ligands such as ethylenediamine $H_2NCH_2CH_2NH_2$ and piperidines and found that bis(ammonia)-coordinated rhodium centres could form second-sphere complexes

with anions, crown ethers, or cyclodextrins. More recent studies examined bis(amino)borates,[24] triazacyclononanes,[25] and even chiral diamines like (-)-spatine,[26] or (+/-)-binaphtyl-$(NH_2)_2$.[22, 27] Nevertheless, complexes featuring both an olefin (COD/NBD) and bis(amine) ligands remain surprisingly underrepresented given the broad ligand repertoires established in rhodium chemistry, Figure 5.[23, 28] This gap is noteworthy because bis(amine) Rh(I) intermediates are often implicated in catalytic steps such as enantioselective transfer hydrogenation, hydrogenations, and aminations.[29]

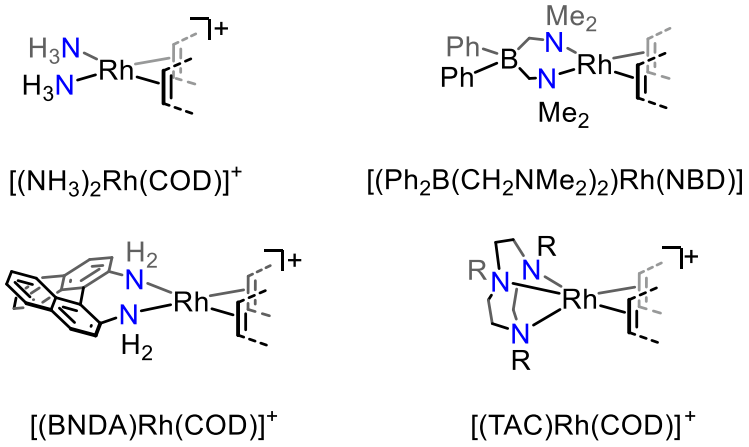


Figure 5. Selected examples of Rh(I) bis(olefin) complexes bearing diamine ligands.

Looking ahead, developing new N-donor frameworks for rhodium, or refining known diamine–Rh complexes, holds promise for addressing contemporary challenges in greener, more selective catalysis. By tapping into the interplay between Rh(I)'s inherent versatility and the fine-tuned properties of nitrogen ligands, researchers stand to uncover next-generation catalysts that could parallel or exceed established phosphine-based systems in both performance and scope.

3.1.2 Carbene Ligand in Rhodium Chemistry

Although amines and phosphines have each propelled major strides in rhodium(I) catalysis, carbene-based coordination often yields some of the most distinctive catalytic and synthetic transformations in rhodium chemistry.[30] Historically, Fischer carbenes, Figure 6A, bearing heteroatom substituents at the carbene carbon, were first reported in the late 1960s on chromium, tungsten, and

molybdenum,[31] but their scope soon expanded to a broader range of transition metals, including rhodium.[32] In parallel, Schrock carbenes, Figure 6B, defined by alkyl or alkenyl substituents, also found their way into Rh complexes (albeit less frequently in early stages).[33] Both classes illustrated how a carbene's dual role, serving as a strong σ-donor yet potential π-acceptor, can profoundly affect a metal's reactivity profile, enabling processes such as olefin metathesis,[34] C–H activation,[35] or cyclopropanation[36] under conditions milder than comparable phosphine-ligated catalysts.

In the Fischer-type realm, rhodium carbenes initially showcased unusual organometallic reactivity, such as insertion steps into M–H or M–C bonds,[37] and even small-molecule cleavage.[38] While less common than their chromium or tungsten counterparts, these early Rh–Fischer carbenes underscored the catalytic potential of a singlet carbene ligand to stabilise high-valent intermediates or facilitate multi-step processes (e.g., ring expansions, coupling reactions).[39] Meanwhile, in Schrock-type systems, the Rh–carbene centre sometimes promoted alkene functionalisation or cycloaddition pathways, leveraging the carbenic carbon with strong nucleophilic character for bond formation.[40]

A more recent and arguably more robust wave of Rh–carbene chemistry features N-heterocyclic carbene (NHC) ligands. NHCs are known for their substantial σ-donation (owing to the sp^2-hybridised lone pair on the carbene carbon) and relatively weak π-acceptance, endowing complexes with heightened thermal stability compared to classic P-donor systems, Figure 6C.[41] Notably, early work by Herrmann[42] and Glorius[43] demonstrated that Rh(I)–NHC catalysts excel in arene hydrogenation, where strong electron donation from the carbene stabilises the metal centre through oxidative and reductive sequences that might otherwise lead to catalyst degradation. More specialised asymmetric transformations have taken shape around chiral NHC frameworks (e.g., imidazolinium derivatives with a stereogenic backbone), which convey enantioselectivity with minimal ligand decomposition under harsh reaction conditions.[43-44]

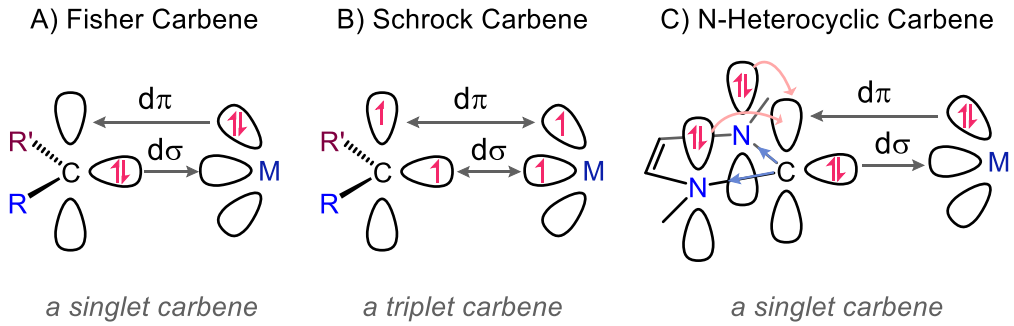


Figure 6. Schematic representation of the different types of carbenes: A) Fisher, B) Schrock and C) N-heterocyclic carbenes.

This catalytic diversity underscores how manipulating carbene substitution patterns (e.g., ring size, substituent bulk, backbone electronics) can systematically tune the push-pull capacity around rhodium, affecting not only redox steps but also substrate binding modes and transition-state energies. For instance, introducing bulky substituents on the NHC ring can modulate steric properties around the metal, steering selectivity in hydroformylation or cross-coupling, while varying the ring's electronic properties can shift the polarity at the M–C(carbene) bond, facilitating or hindering β-elimination or migratory insertion steps, Figure 7.

In hydrogenation of polar bonds (e.g., imine, aldehyde, or ketone functionalities), Rh–NHC(carbene) complexes can offer an alternative to classical phosphine-based catalysts, often benefiting from enhanced stability under strongly reducing conditions. This robustness extends to hydroformylation, where the strong σ-donation from NHCs can help stabilise formyl or acyl intermediates, influencing linear *vs*. branched aldehyde selectivity. Meanwhile, in cross-coupling reactions such as Mizoroki-Heck or Suzuki-Miyaura, Rh–carbene catalysts occasionally rival or complement palladium analogues, aided by the carbene's ability to facilitate oxidative addition or mediate ligand exchange cycles.[45]

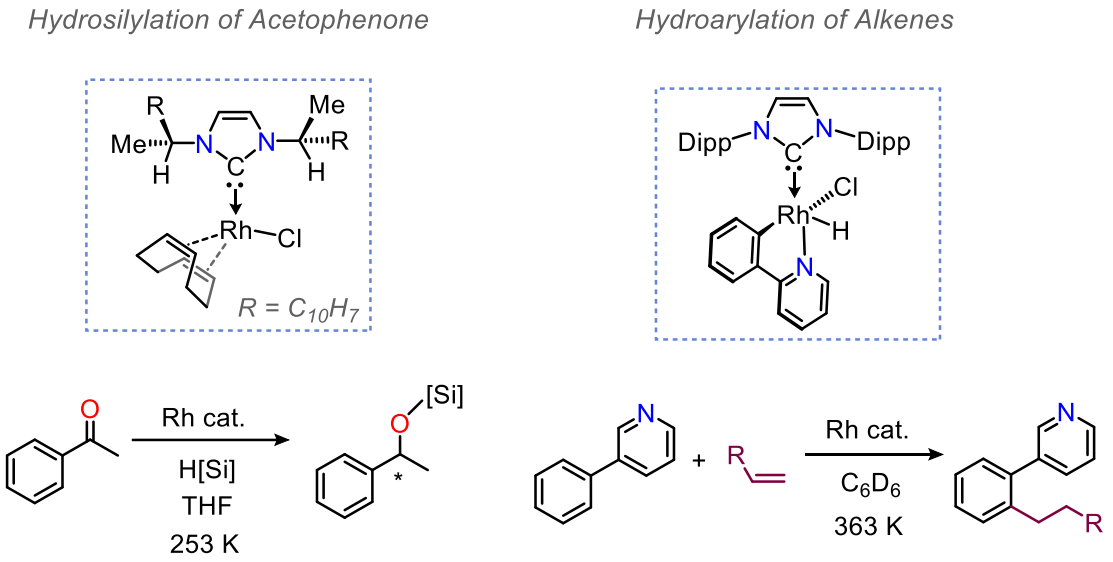


Figure 7. Representative examples of Rh-NHC complexes and catalytic applications in hydrosilylation reported by Herrman[42] and hydroarylation from Castarlenas.[45a]

Mechanistically, many Rh–carbene-mediated reactions involve key elementary steps, oxidative addition, 1,2-insertion into M–C or M–H bonds, or reductive elimination, where the carbene's dual donor/acceptor nature stabilises fleeting high-energy intermediates. Spectroscopic and computational studies highlight how strong σ-donation from the NHC can lower the activation barrier for bond cleavage or formation, while mild π-back bonding helps accommodate electron density on the carbene carbon at crucial points in the cycle. This synergy can reduce decomposition pathways often encountered with more labile ligands, yielding improved catalyst lifetimes

Beyond their demonstrated track record, carbene ligands, particularly NHCs, inspire parallels to main-group carbene analogues such as low-valent Group 13 species (Al(I), Ga(I), In(I)), which also feature a lone pair and an empty p-orbital. If these M(I) species indeed mimic the σ-donating and π-accepting capacities of conventional carbenes, Figure 8, then Rh–M(I) complexes might replicate or surpass the reactivity patterns observed in Rh–C(carbene) systems. Such bimetallic or metalloligand frameworks could break new ground in C–H functionalisation, hydrogenation, or small-molecule activation (e.g., H_2 cleavage) by uniting the amphoteric nature of Group 13 centres with rhodium's established catalytic versatility.

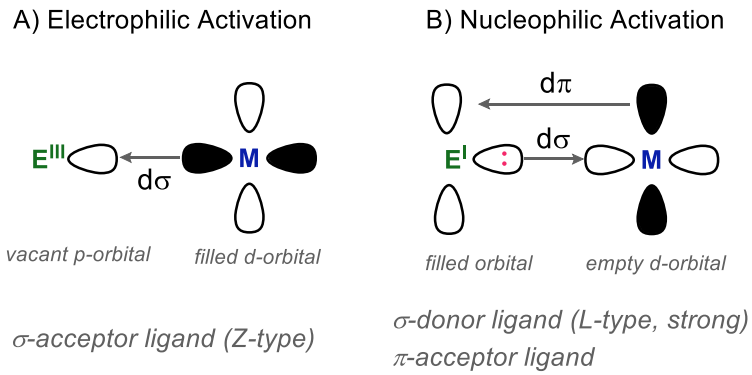


Figure 8. Dual electronic nature of Group 13 metalloligands.

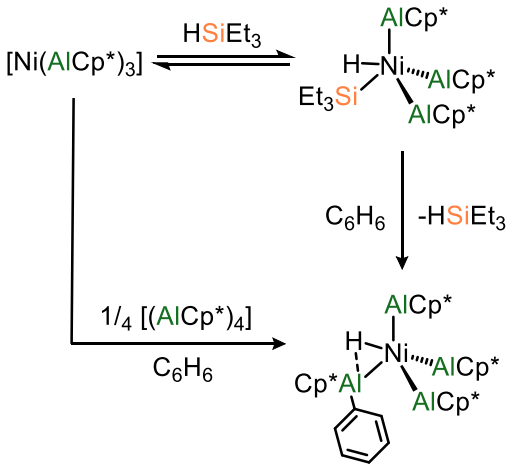
The mechanistic insights gleaned from Rh–carbene research, where selective bond formation and robust catalytic cycles hinge on carbene donation, serve as a vital template for exploring Group 13 “carbene-like” ligands. In upcoming sections, we will examine how these M(I) metalloligands might forge unprecedented Rh–M(I) interactions, leveraging the same conceptual underpinnings that have driven decades of success for classical Rh–carbene complexes. By combining the best of both worlds, NHC-like electronic profiles and rhodium’s multifaceted catalytic repertoire, we aim to expand the horizon of bond-activation processes achievable at metal–metal frameworks involving both a main group and a transition metal.

3.1.3 Group 13 M(I) Carbene Analogues as Metalloligands

While transition-metal complexes bearing a wide variety of ligands have been extensively explored, the advent of low-valent Group 13 organometallics, often denoted $E^{I}R$ (E = Al, Ga, In; R = alkyl, Cp*, BDI, amidinate, guanidinate), introduced an innovative avenue for coordination chemistry in the closing decades of the 20th century. These monovalent species derive their unique properties from a lone pair and an empty p-orbital on the Group 13 centre, granting them a combination of σ-donor and π-acceptor capabilities reminiscent of classical carbene (CR_2) or phosphine (PR_3) ligands. Consequently, they can act as X- or L-type metalloligands, forging metal–metal bonds that deviate significantly from those found in more conventional ligand systems.[46]

Most reported synthetic routes to such heterobimetallic complexes rely on ligand-displacement processes in organic solvents, often requiring thermal activation to dislodge existing ligands (e.g., COD, amines) in favour of the Group 13 metallylene. A representative example is provided by Fischer and co-workers, who

employed stoichiometric amounts of E^{I}Cp* (E = Al, Ga, In) to displace COD and bis(alkylamine) ligands from Pd or Ni precursors at elevated temperatures (~ 343 K).[47] Notably, when COD is displaced in a Ni precursor under aromatic solvent conditions, the resulting bimetallic system has been shown to activate a C–H bond directly from the benzene solvent, a striking demonstration of cooperative reactivity.



Scheme 4. Example of reactive bimetallic Al(I)–Ni intermediate, where the Al(I) metalloligand acts as directing ligand in C–H and Si–H bond activation.

For “precious” metals like rhodium and iridium, most low-valent Group 13 examples also feature E^{I}Cp* ligands. Building on these precedents, Lu and co-workers designed bimetallic Rh(III)–E(I) compounds, demonstrating that metal–metal cooperation between the two centres can drive challenging transformations.[48] Further extending rhodium-based chemistry, Shigeyoshi and Nakao synthetised a bimetallic Rh–Al system featuring low-valent aluminium generated in situ from an Al(III) species stabilised by a tripodal ligand; upon coordination to Rh, subsequent reduction with KC_8 yielded the targeted Al(I) complex, which proved effective in the C2-selective mono-alkylation of pyridine.[49] By contrast, only a single report so far documents an iridium-based system stabilised by low-valent Ga, employing a pincer ligand; in that instance, Ir(III) is formed via reduction of the Ga(III) precursor during complexation, suggesting further potential for metalloligand-induced redox events.[50]

These examples underscore how Group 13 carbene surrogates (E(I) species) can serve as powerful metalloligands for late transition metals, conferring unusual reactivity profiles such as C–H bond activation or cooperative redox processes. Their

amphoteric nature, combining lone-pair donation with p-orbital acceptance, echoes that of classical carbene or phosphine ligands, Figure 8, paving the way for bimetallic architectures with sophisticated electronic interplay. In the context of rhodium catalysis, harnessing these unique E(I) species promises to expand the synthetic landscape further, enabling strategies for small-molecule activation otherwise unattainable through conventional ligand platforms.

3.2 Objectives

Building upon the successful development of anionic gallium(I) carbene analogues from *Chapter II* and the broader interest in metal–metal cooperative reactivity, this chapter aspires to design, synthesise, and extensively characterise a new family of heterobimetallic Ga(I)–Rh(I) complexes. Specifically, we intend to combine low-valent gallium(I) species (β-diketiminate-based) with rhodium frameworks bearing amine and/or diolefin ligands, thereby forging ligated bimetallic assemblies that may facilitate small molecule activation, particularly H_2, and subsequent hydrogenation of unsaturated substrates under mild conditions using such bimetallic main-group-metal–transition-metal species.

To accomplish this, we first prepare a series of well-defined Rh(I)–diamine/olefin precursors suitable for ligand-exchange with gallium(I) carbene analogues, while comparing these novel heterobimetallic constructs to classical phosphine- or NHC-based rhodium systems. A thorough solution-state, gas-phase and single-crystal structural analysis of the resulting Ga(I)–Rh(I) species, employing techniques such as 1D/2D NMR spectroscopy, IR, mass spectrometry, and X-ray diffraction, will elucidate their electronic configurations and dynamic speciation behaviour. We will then investigate how Ga–Rh bonding and ancillary ligands (COD *vs.* NBD) dictate the formation of Rh(III)–dihydride, Rh–H_2 or Rh(III)–allyl intermediates upon exposure to H_2, thus revealing any equilibria or off-cycle species that govern partial versus complete hydrogenation. Furthermore, we will assess the catalytic performance of these *cis*-Ga(I)–Rh(I) complexes in hydrogenating selected di- and polyolefins, profiling both activity and selectivity (partial *vs.* complete hydrogenation). Finally, complementary computational (DFT) analyses will integrate experimental data and illuminate mechanistic pathways, rationalizing the observed reactivity and selectivity while highlighting potential cooperative roles of gallium(I) and rhodium in small-molecule activation. Through these objectives, *Chapter III* aims to extend the landscape of main-group–transition-metal synergy, introducing new bimetallic strategies for catalytic bond activation that harness the distinctive interplay of Group 13 and Group 9 metals.

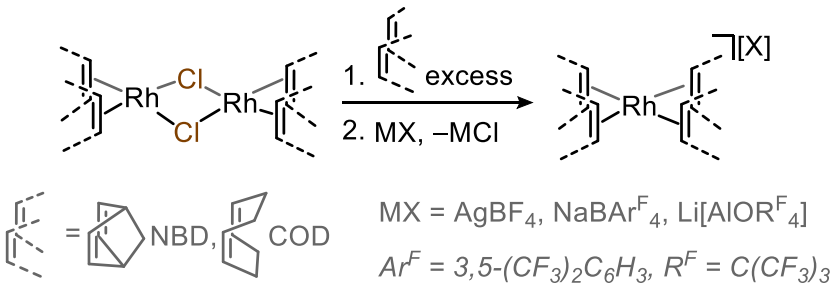
3.3 Synthesis of Ga(I)–Rh(I) Species form Rh(I) Amine/Olefin Precursors

3.3.1 Rh(I) Amine/Olefin Complexes: Precursors for M(I) Ligand-Exchange

A large body of work by Uson[23a, 23c], Green[51], Pertici[22] and Pannetier[52] has shown N-donor ligands to be efficient alternatives in asymmetric catalytic processes. However, there remain relatively few examples of ethylenediamine-based ligands with Rh(I). Seeking robust, σ-donating Rh–ligand frameworks lacking significant π-back-donation, we selected several ethylenediamine derivatives, including TMEDA, TMMDA, TEEDA, and DEEDA (Scheme 6). Each forms a chelate with 1,5-cyclooctadiene (COD) or 2,5-norbornadiene (NBD), known to stabilise Rh(I). Notably, TEEDA and DEEDA present stereogenic centres upon coordination to rhodium, hinting at potential asymmetric applications.

The first step involved preparing Rh(I) amine/olefin complexes via slightly modified literature methods starting from $RhCl_3$.[53] Chelating diolefins, COD or NBD, were used to obtain cationic bis(olefin) Rh units, $[Rh(\eta^2,\eta^2\text{−diolefine})_2]^+$, subsequently isolated as neutral salts incorporating $[BF_4]^-$, $[BAr^F{}_4]^-$, and $[AlOR^F{}_4]^-$ (where Ar^F = 3,5-$(CF_3)_2C_6H_3$ and R^F = $C(CF_3)_3$) to minimise undesired coordination from the counterion. These bis-olefin Rh(I) complexes, **[Rh(COD)$_2$]**[X] or **[Rh(NBD)$_2$]**[X] (X = $[BF_4]^-$, $[BAr^F{}_4]^-$, and $[AlOR^F{}_4]^-$), once isolated, were reacted with the selected diamino ligands to give cationic Rh(I)–diamine species (Scheme 5).

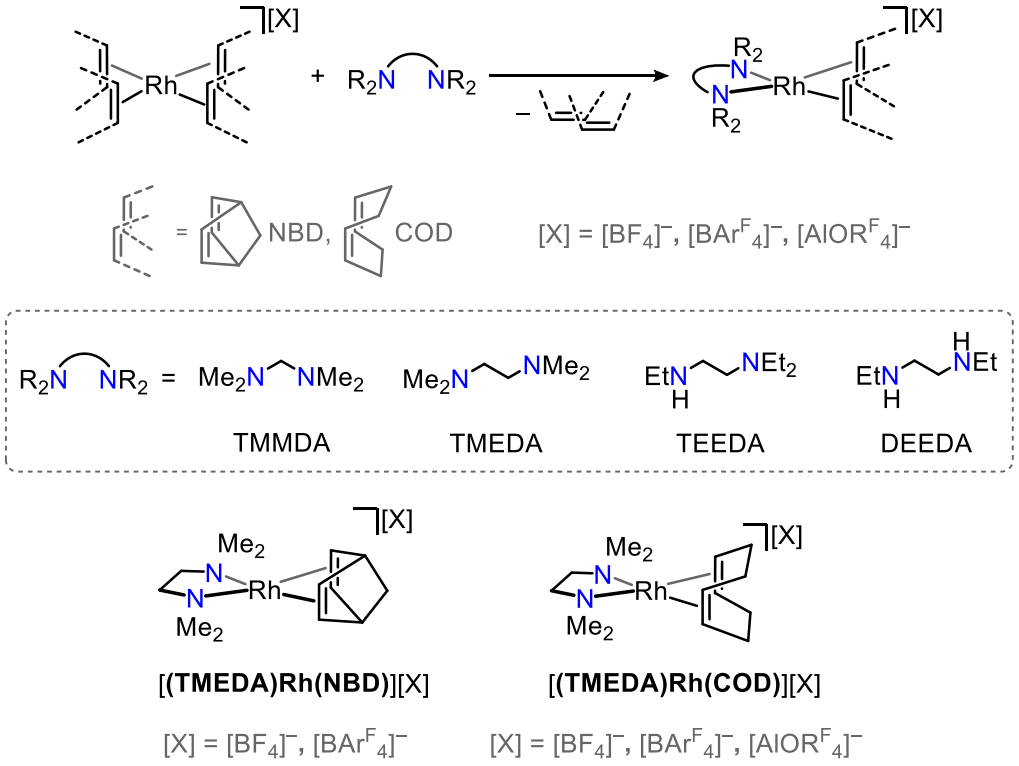
Preparation of bis-olefin Rh(I) complexes



Scheme 5. General synthetic protocol to obtain **[Rh(COD)$_2$]**[X] or **[Rh(NBD)$_2$]**[X] (X = $[BF_4]^-$, $[BAr^F{}_4]^-$, and $[AlOR^F{}_4]^-$).

A typical procedure involved dissolving **[Rh(COD)$_2$]**[X] or **[Rh(NBD)$_2$]**[X] (X = $[BF_4]^-$, $[BAr^F{}_4]^-$, and $[AlOR^F{}_4]^-$) in ~ 5 mL CH_2Cl_2, affording a reddish solution. Separately, a 1 mL CH_2Cl_2 solution of TMEDA, TMMDA, TEEDA, or DEEDA was prepared. Dropwise addition of the diamine solution to the Rh(I) solution elicited an

instant colour shift (from reddish to yellow). After stirring at room temperature for 1–3 h, partial solvent evaporation under reduced pressure preceded *n*-hexane addition to induce precipitation. In some cases, an ice bath aided crystallisation. The resulting yellow solids **[(κ²−diamino)Rh(η²,η²−COD)][X]** and **[(κ²−diamino)Rh(η²,η²−NBD)][X]** were collected by cannula filtration, washed with *n*-hexane, and dried under high vacuum for 2–3 h (< 10^{-2} mbar), Scheme 6.

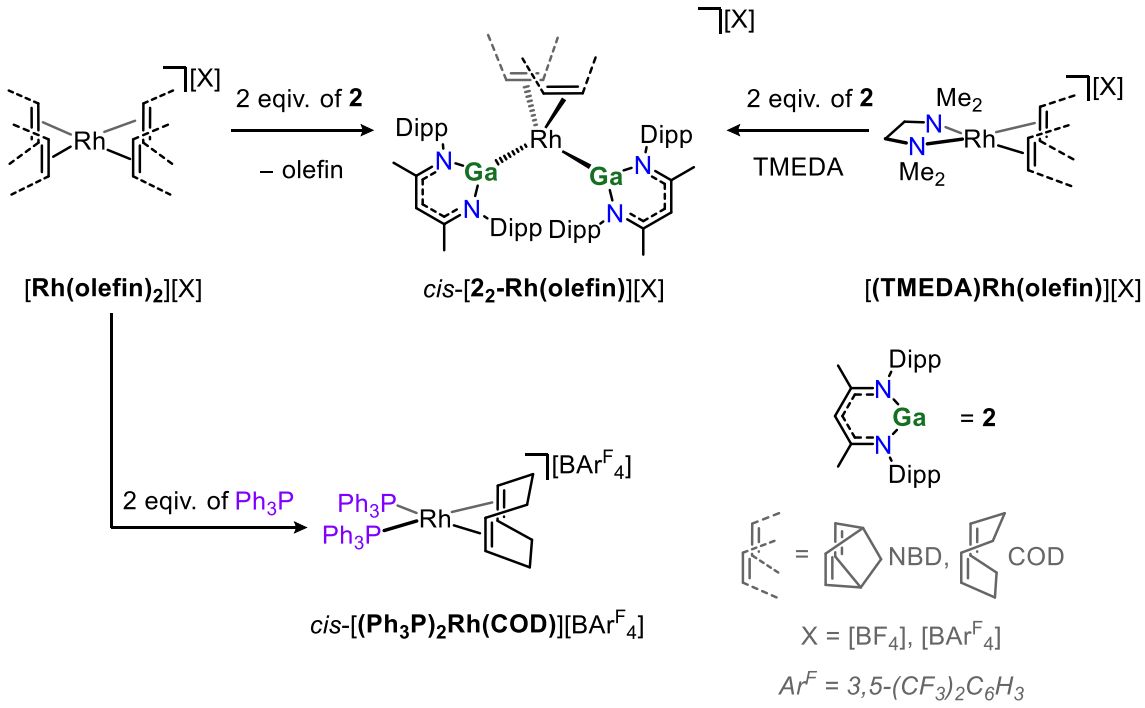


Scheme 6. Synthesis of complexes **[(κ²−diamino)Rh(η²,η²−COD)][X]** and **[(κ²−diamino)Rh(η²,η²−NBD)][X]** (X = $[BF_4]^-$, $[BAr^F_4]^-$, and $[AlOR^F_4]^-$).

Although this approach afforded a range of Rh(I)–diamino/olefin species, the TMEDA analogues were most relevant for subsequent Group 13 M(I) displacement. In prior reports, **[(TMEDA)Rh(COD)]**$^+$ and **[(TMEDA)Rh(NBD)]**$^+$ featuring $[ClO_4]^-$[23c] or $[Rh(COD)(Cl)_2]^-$[54] counterions, albeit lacking comprehensive characterisation beyond IR and elemental analyses. By contrast, our method delivers ion pairs bearing $[BF_4]^-$, $[BAr^F_4]^-$, and $[AlOR^F_4]^-$ anions alongside multinuclear NMR and solid-state data (Sections 3.3.3 and 3.3.4). Other ethylenediamine-derived Rh(I) complexes were also prepared during this research and are detailed in the *Annexes* of this Thesis.

3.3.2 Heterometallic Ga(I)–Rh(I) Olefin Species

Having successfully isolated the above Rh(I) bis(olefin) and Rh(I) diamine complexes, we next explored ligand-exchange with monovalent β-diketiminate aluminium(I) **1** and gallium(I) **2** species, each recognised as carbene analogues possessing a lone pair and an empty p-orbital. Because M(I) can act as an L-type metalloligand, akin to carbenes (CR_2) or phosphines (PR_3), we posited it might displace either the diamine or one of the olefin ligands to form bimetallic M(I)–Rh moieties. Notably, in this order, trials of either the bis(olefin) [**Rh(olefin)$_2$**][X] or the amino [**(TMEDA)Rh(olefin)**][X] (olefin = COD, NBD), with X = $[BF_4]^-$, $[BAr^F{}_4]^-$, and $[AlOR^F{}_4]^-$, using the β-diketiminate aluminium(I) species **1** as metalloligand, resulted in overly reactive mixtures, preventing clean isolation of a single product. Due to the laborious preparation of the $[AlOR^F{}_4]^-$ salt derivatives, the $[BF_4]^-$ and $[BAr^F{}_4]^-$ analogues were used during the scalable synthetic protocols. Conversely, the β-diketiminate gallium(I) complex **2** reliably displaced either one of the olefin ligands in the species [**Rh(COD)$_2$**][X] and [**Rh(NBD)$_2$**][X], or the amine TMEDA ligand in [**(TMEDA)Rh(COD)**][X] and [**(TMEDA)Rh(NBD)**][X], yielding the stable Ga–Rh frameworks *cis*-[**2$_2$−Rh(olefin)**][X] (Scheme 7).



Scheme 7. General synthetic protocol to obtain *cis*-[**2$_2$−Rh(olefin)**][X] and *cis*-[**(Ph$_3$P)$_2$Rh(COD)**][$BAr^F{}_4$].

In a typical experiment, [**(κ²−TMEDA)Rh(η²,η²−olefin)**][X] (olefin = COD or NBD; X = BAr^F_4 or BF_4) was dissolved in an aromatic solvent (often fluorobenzene, for better solubility and reduced side reactions). Then, two equivalents of **2** (the neutral carbene Ga(I) analogue) were added. The pale-yellow mixture gradually turned orange, signalling displacement of TMEDA by the β-diketiminate Ga(I) metalloligand. Aliquots of the reaction mixture were monitored via ^{1}H NMR to confirm complete transformation, revealing the free TMEDA signals alongside newly formed Ga–Rh species. Afterward, *n*-hexane was added to precipitate the corresponding product, sometimes aided by cooling. The orange solid was collected by cannula filtration, washed with hexane, and dried under high vacuum for several hours, yielding the heterometallic species *cis*-[**2₂−Rh(olefin)**][X] (Scheme 7). Yields were typically moderate to good (70–60%) depending on the specific olefin (COD or NBD) and the counterion $[BAr^F_4]^-$ or $[BF_4]^-$ as counterion. A parallel, shorter route omits isolation of the TMEDA–Rh step by directly combining the bis(olefin) species [**Rh(olefin)₂**][X], with **2** in fluorobenzene, though final yields are comparable (80–60%). Hence, this novel methodology allows the preparation of cationic species featuring two metal–metal Ga(I)–Rh(I) bonds within *cis*-[**2₂−Rh(olefin)**]$^+$, where both metals are stabilised in their low-oxidation state. Despite that the bimetallic bond between Ga−Rh is known in other bimetallic complexes,[46d, 48, 55] the exploration of their bimetallic chemistry and applications is underdeveloped. Notably, the final cationic fragment, *cis*-[**2₂−Rh(olefin)**]$^+$, consistently exhibited two direct Ga–Rh bonds, with each metal in a low-oxidation state, closely paralleling the NHC–Rh frameworks discussed in Section 3.1.2.

Interestingly, we also tested classical phosphine (triphenyl phosphine, PR_3) coordination under analogous conditions, targeting displacement of the diamine or an olefin from the same Rh(I) precursors, to give *cis*-[**(Ph₃P)₂Rh(olefin)**]$^+$ complexes (Scheme 7).[56] However, attempts using the same approach with a well-known NHC carbene, IPr (1,3-bis(2,6-diisopropylphenyl)imidazol-2-ylidene),[57] failed to give analogous NHC–Rh complexes, (ie. [**(NHC)₂Rh(olefin)**]$^+$). Under identical conditions, these trials led to *rapid decomposition* of either the diamino–Rh or the bis(olefin)–Rh precursors, highlighting the robust nature Ga(I)–Rh bonds relative to NHC–Rh linkages, and comparable to phosphines. In addition, we attempted to displace β-diketiminate Ga(I) metalloligand **2** in the *cis*-[**2₂−Rh(olefin)**][X], with aliphatic and aromatic phosphines PR_3 (R = Me, Ph) and phosphites $P(OR)_3$ (R = Et, Ph), recovering unreacted *cis*-[**2₂−Rh(olefin)**][X]. This unsuccessful ligand

displacement reactions together with failed NHC attempts, emphasises that the robust nature of Ga(I)–Rh bonds is not merely a matter of available coordination sites but also of Ga(I) carbene-like frontier orbital compatibility. It further highlights that Group 13 species can rival or surpass NHC carbene ligands in forming stable L-type complexes, a contrast to the more conventional phosphine PR_3 approach.

This novel synthetic strategy demonstrates that combining diamine-ligated Rh(I) frameworks creates suitable precursors for Ga(I) carbene analogues, specifically with the β-diketiminate gallium(I) **2**. Consequently, we assembled a library of cationic bimetallic Ga(I)–Rh(I) complexes featuring COD or NBD olefins, plus diverse counterions ($[BF_4]^-$, and $[BAr^F{}_4]^-$). We aim to investigate their reactivity toward small-molecule activation (H_2) and olefin functionalisation. Although attempts with Al(I) **1** proved overly reactive, gallium's relative stability in the +1 state of **2** allowed rational isolation of discrete Ga–Rh frameworks. In subsequent sections, we delve into their structural characterisation and reactivity assays, highlighting synergy at the main-group–transition-metal interface. The dual-metal arrangement in Ga(I)–Rh(I) of *cis*-[**2₂−Rh(olefin)**]$^+$ might open distinct reactive pathways or cooperative bond-activation processes, not accessible to single phosphine–ligated Rh(I) single-metal Rh(I) species *cis*-[**(Ph₃P)₂Rh(olefin)**]$^+$.

Overall, combining diamine-ligated Rh(I) with Ga(I) carbene surrogates (and contrasting stability with IPr NHC attempts) spotlights the unique metal–metal bonding that emerges when Group 13 low-valent species act as carbene-like L-type ligands. This underscores the potential for unprecedented transformations at Ga–Rh interfaces, adding yet another dimension to Rh(I) chemistry in the quest for innovative bond activation and catalysis.

3.3.3 Characterisation of Rh(I) Amine/Olefin and Heterometallic Ga(I)–Rh(I) Olefin Complexes

3.3.3.1 NMR Spectroscopy Studies of Rh(I) Amine/Olefin Complexes

The rhodium(I) complexes [**(κ²−TMEDA)Rh(η²,η²−COD)**][X] and [**(κ²−TMEDA)Rh(η²,η²−NBD)**][X], where X = BF_4, $BAr^F{}_4$, or $AlOR^F{}_4$, feature a four-coordinate Rh centre in a square-planar geometry typical of d^8 metal ions. In each complex, TMEDA provides a chelating N,N′-diamino environment, while the COD (1,5-cyclooctadiene) or NBD (2,5-norbornadiene) ligand completes the 16-electron Rh(I) configuration. Structurally, the cationic unit exhibits C_{2v} symmetry, reflecting a C_2 axis and vertical/horizontal mirror planes that interchange equivalent moieties.

An illustrative example is **[(TMEDA)Rh(NBD)]**$^{+}$ within the $[BAr^{F}_{4}]^{-}$ counterion, which in its ^{1}H NMR spectrum (CD_2Cl_2, 298 K) displays resonances at δ 3.94, 3.92, and 1.36 for the alkene NBD moiety. The two signals at δ 3.94 and 3.92 (each integrating to 4 protons total) originate from the olefinic protons from NBD, the slight chemical shift difference suggesting either subtle non-equivalence or diastereotopic protons on the bridging ring. The resonance at δ 1.36 (2 H) is assigned to the bridge CH–NBD, while a small upfield shift often corresponds to the bridgehead NBD–CH_2 environment. In ^{13}C NMR, the NBD ligand appears at δ 63.9, 63.4, and 52.6, each commonly displayed as doublets arising from $^{1}J_{C,Rh}$ or $^{n}J_{C,Rh}$ couplings. Specifically, the resonance at δ 63.9 correlates with CH_2–NBD, having a $^{3}J_{C,Rh}$ of ~ 6.7 Hz, whereas the alkene region at δ 63.4 couples directly ($^{1}J_{C,Rh}$ = 10.2 Hz). The bridge site near δ 52.6 experiences a smaller $^{2}J_{C,Rh}$ ~ 2.5 Hz. Determining all these coupling constants is somewhat atypical[58] but reflects the well-defined nature of this Rh–NBD system.

The TMEDA portion in **[(TMEDA)Rh(NBD)]**[BAr^{F}_{4}] appears in the ^{1}H NMR at δ 2.44 and 2.37, integrating to 4H (CH_2) and 12H (N–CH_3) respectively, consistent with two methyl substituents on each nitrogen. In the ^{13}C NMR, these arise near δ 60.8 (CH_2) and 48.5 (CH_3), generally as singlets (no resolvable Rh–C coupling for these distant carbons).

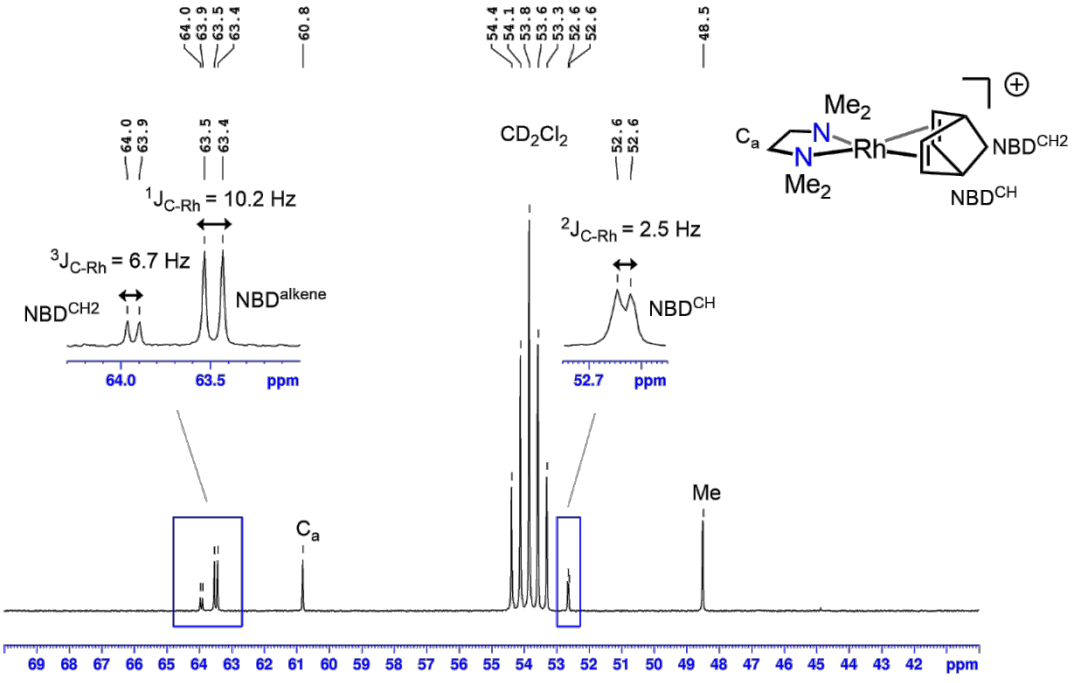


Figure 9. $^{13}C\{^{1}H\}$ (100.6 MHz, CD_2Cl_2 298 K) NMR spectrum of **[(TMEDA)Rh(NBD)]**[BAr^{F}_{4}].

For [**(TMEDA)Rh(COD)**][BAr^F_4], the ^{1}H NMR (CD_2Cl_2, 298 K) reveals three distinct signals integrating to 4 protons each. The most downfield signal at δ 3.92 corresponds to the alkene protons from COD, whereas resonances near δ 2.42 and 1.88 represent the aliphatic CH_2–COD groups, collectively incorporating 4 CH_2 units (each chemically equivalent by symmetry). The TMEDA portion again manifests as two sets of protons in the ^{1}H NMR, near δ 2.47 (methyl) and δ 2.44 (CH_2), integrating at 12 H and 4 H respectively, matching a N,N′-dimethyl substitution pattern. ^{13}C NMR signals emerge at δ 49.2 (CH_3) and δ 61.1 (CH_2). These typical chemical shifts reflect the chelation of TMEDA and overall square-planar arrangement around Rh(I). In the ^{13}C NMR, COD features two signals, a high chemical shift doublet at δ 84.4 (alkene carbon, with $^1J_{C,Rh}$ ~ 12.9 Hz) and a lower shift resonance at δ 30.2 for the methylene COD carbons.

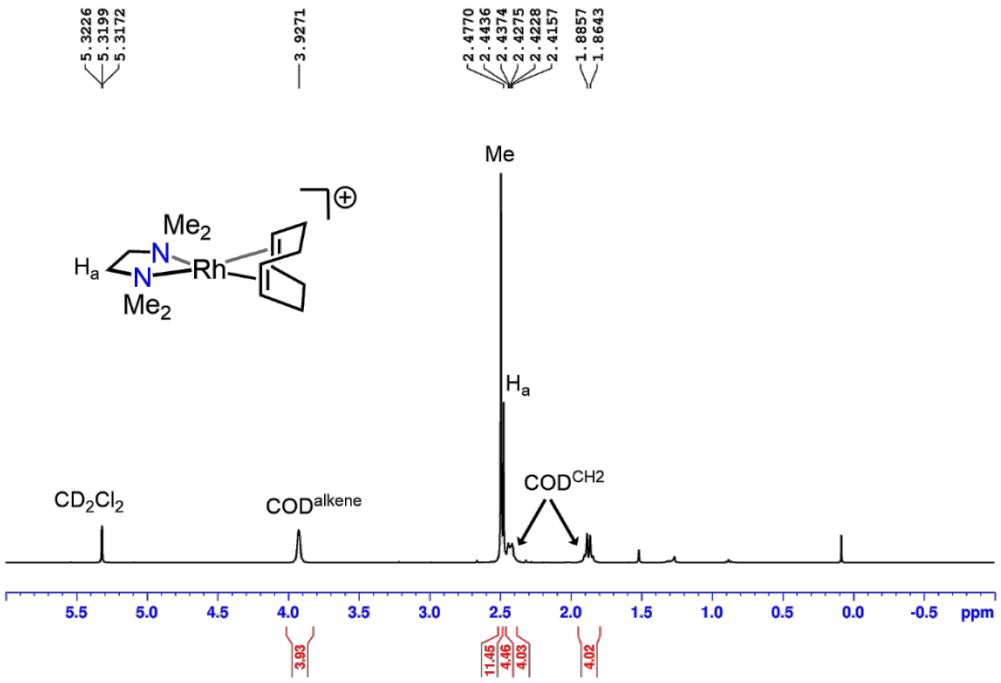


Figure 10. ^{1}H (400 MHz, CD_2Cl_2, 298 K) NMR spectrum of [**(TMEDA)Rh(NBD)**][BAr^F_4].

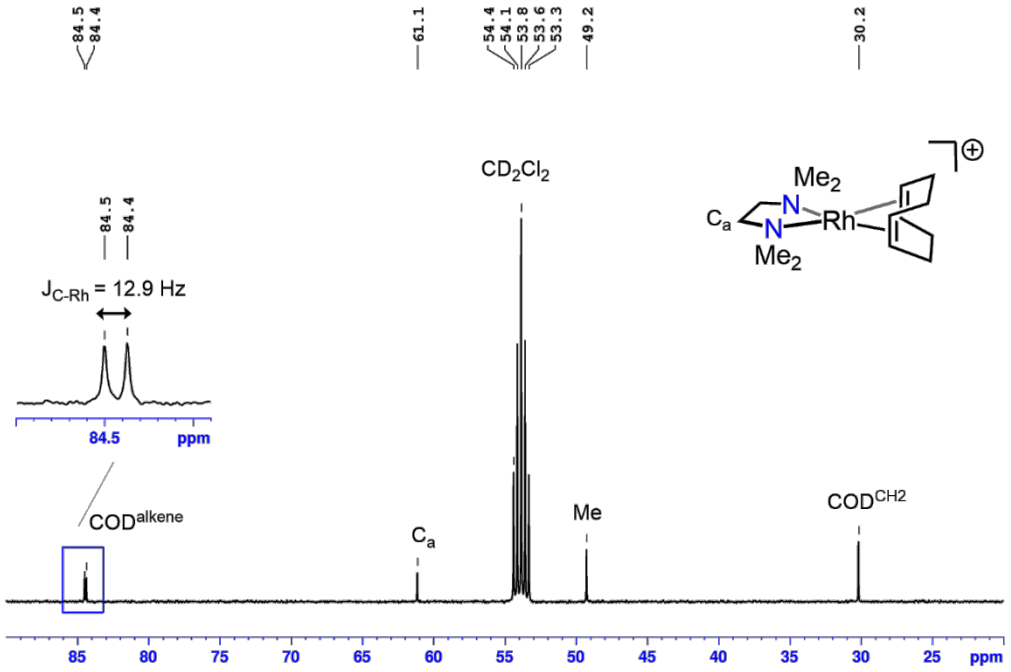


Figure 11. $^{13}C\{^{1}H\}$ (100.6 MHz, CD_2Cl_2, 298 K) NMR spectrum of **[(TMEDA)Rh(NBD)]**[BAr^F_4].

3.3.3.2 IR Spectroscopic Studies of Rh(I) Amine/Olefin Complexes

The complexes **[(κ²–TMEDA)Rh(η²,η²–COD)]**[X] and **[(κ²–TMEDA)Rh(η²,η²–NBD)]**[X], where X = BF_4, BAr^F_4, or $AlOR^F_4$, show similar IR spectra features. As shown in Table 1, the **[(TMEDA)Rh(COD)]**$^+$ cationic fragment consistently exhibits absorption bands in the 1420–530 cm^{-1} range corresponding to the COD ligand. Specifically, signals near 1410–1400 cm^{-1} and 1000–950 cm^{-1} are typically attributed to C–H bending or ring-deformation modes of the cyclooctadiene ring. Additional medium-intensity bands occur near 800–700 cm^{-1}, often arising from out-of-plane bending of alkene or CH_2 moieties.

Anions such as [BAr^F_4]$^-$ display their characteristic vibrations at ~ 1610, 1460, and 1010 cm^{-1}. These correspond to aromatic CF_3-substituent ring modes, which partially overlap with COD or TMEDA signals. In the [BF_4]$^-$ analogue, the [BF_4]$^-$ stretching modes typically appear around ~ 1080–1040 cm^{-1}, and the key metal–ligand vibrations also coincide with these bands, making explicit assignments more difficult to assess. By contrast, [$AlOR^F_4$]$^-$ anions produce strong absorptions in the 1300–1100 cm^{-1} region due to C–F stretches from the fluorinated $C(CF_3)_3$ groups.

Notably, a Rh–COD stretch is identifiable near ~ 580–560 cm^{-1} in both $[BAr^{F}_4]^-$ and $[AlOR^{F}_4]^-$ derivatives, whereas it is "silent" in the $[BF_4]^-$ salt. This band is typically attributed to the ν(Rh–alkene) vibrational mode or ring deformation influenced by metal–alkene coordination.[52]

Table 1. Selected IR data (cm^{-1}) for **[(TMEDA)Rh(COD)]**[X] species (X = BF_4, BAr^{F}_4, or $AlOR^{F}_4$).

Complex	BAr^{F}_4	BF_4	$Al\{OC(CF_3)_3\}_4$
ν(olefin)	1413, 998	1415, 1302	1415, 1354
	968, 947	1217, 1049	1278, 1163
	887, 838	999, 968	1099, 974
	802,771	950, 876	875, 831, 803
	510	520	773, 537
ν(BAr^{F}_4)	1610, 1464		
	1276, 1118		
	1013		
ν(Rh−COD)	579		560

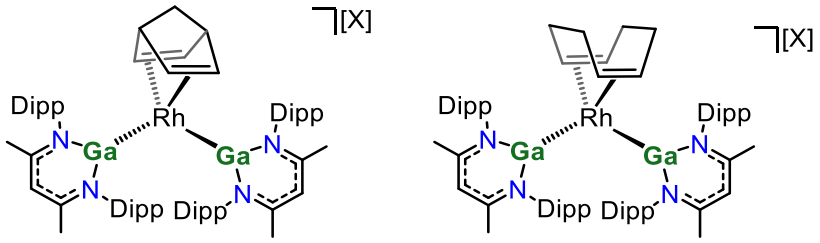
A similar pattern arises for the NBD derivatives, **[(TMEDA)Rh(NBD)]**[X] (X = BF_4, or BAr^{F}_4,). For these species, only a handful of bands can be definitively attributed to the NBD ligand at ~ 1415, 1308, 953, 804, and 521 cm^{-1}, while a Rh–NBD vibrational mode emerges near ~ 550–540 cm^{-1}. The rest of the $[BF_4]^-$ signals overlap with typical anionic stretching frequencies in the 1100–900 cm^{-1} region. When $[BAr^{F}_4]^-$ serves as the counterion, the anionic bands become more abundant, typically near 1610, 1465, 1275, 1118, and 1014 cm^{-1}, overshadowing or partially merging with some NBD modes. Nevertheless, one can still discern the NBD out-of-plane ring bends or CH_2 deformations near ~ 950–800 cm^{-1}.

3.3.3.3 NMR Spectroscopy Studies of Heterometallic Ga(I)–Rh(I) Olefin Complexes

Following the isolation of the new bimetallic Rh–Ga complexes, we employed NMR spectroscopy (^1H, $^{13}C\{^1H\}$, $^{11}B\{^1H\}$, $^{19}F\{^1H\}$, and $^{31}P\{^1H\}$) to investigate their stability, solution behaviour, and potential reactivity toward small molecules such as H_2, and the role of various non-coordinating anions. The data indicate that the **[2_2−Rh(olefin)]**$^+$ species remain intact under typical conditions, with no significant anion ($[BF_4]^-$, $BAr^{F}_4{}^-$, $AlOR^{F}_4{}^-$) influence on the cationic fragment. Accordingly, all

subsequent NMR references in this section focus on the $BAr^F_4^-$ derivatives as representative examples.

The new heterometallic complexes [**2₂−Rh(COD)**][X] and [**2₂−Rh(NBD)**][X] (X = $[BF_4]^-$ and $[BAr^F_4]^-$) each incorporate two β-diketiminate Ga(I) fragments, labelled with **2**, bound *cis* to a single Rh(I) centre. A COD or NBD ligand then completes the 16-electron coordination environment, forming a cationic species with two direct Ga–Rh bonds in a square-planar arrangement (Figure 12). Their NMR spectra confirm the stability of these complexes in CD_2Cl_2 at room temperature and allow full assignment of both the β-diketiminate Ga(I) metalloligand **2** and the coordinated olefin (COD or NBD).



cis-[**2₂-Rh(NBD)**][BF_4] *cis*-[**2₂-Rh(COD)**][BF_4]

cis-[**2₂-Rh(NBD)**][BAr^F_4] *cis*-[**2₂-Rh(COD)**][BAr^F_4]

Figure 12. Schematic representation of the heterometallic complexes *cis*-[**2₂−Rh(COD)**][X] and *cis*-[**2₂−Rh(NBD)**][X] (X = $[BF_4]^-$ and $[BAr^F_4]^-$). Dipp = 2,6-iPr-C_6H_3.

In the ^{1}H NMR spectrum, the Ga(I)–BDI backbone of the metalloligand **2** in *cis*-[**2₂−Rh(NBD)**][BAr^F_4] typically appears as a single resonance for the γ-CH at δ 5.57, integrating to two protons. Two distinct β-CH_3 signals at δ 1.76 and 1.73 (6H each) then correspond to the backbone methyl substituents. For the isopropyl substituents, the aromatic region (δ 7.44–7.14) integrates to ~ 12 protons, appearing as multiplets with coupling constants around 7.8–7.4 Hz, consistent with Dipp phenyl ring splitting. The isopropyl–CH protons emerge at δ 3.06, 2.63, and 2.52, each as septets integrating to either 2 or 4 protons, signifying slight asymmetry. Meanwhile, the CH_3–iPr signals populate δ 1.32, 1.24, 1.17, 1.08, 0.98, and 0.54. Notably, the signal at δ 0.54 is highly shielded, presumably due to ring-current effects from an adjacent aromatic ring in the second BDI–Ga(I) fragment. Subsequent X-ray crystallography (Section 3.3.4) confirms that one isopropyl methyl sits near the aromatic face of another BDI ring.

Turning to the NMR data corresponding to the NBD ligand in *cis*-[**2₂−Rh(NBD)**][BAr^F_4] , the alkene region displays two broad singlets at δ 4.56 and 3.08 (2 H each). The NBD–CH_2 resonates near δ 3.08 (2 H), partly overlapping with an isopropyl–CH signal. The NBD–CH bridging group is visible at δ 0.97. Figure 13 shows the ^{1}H NMR spectrum, highlighting the broad distribution of signals from the Dipp environment as well as the NBD peaks.

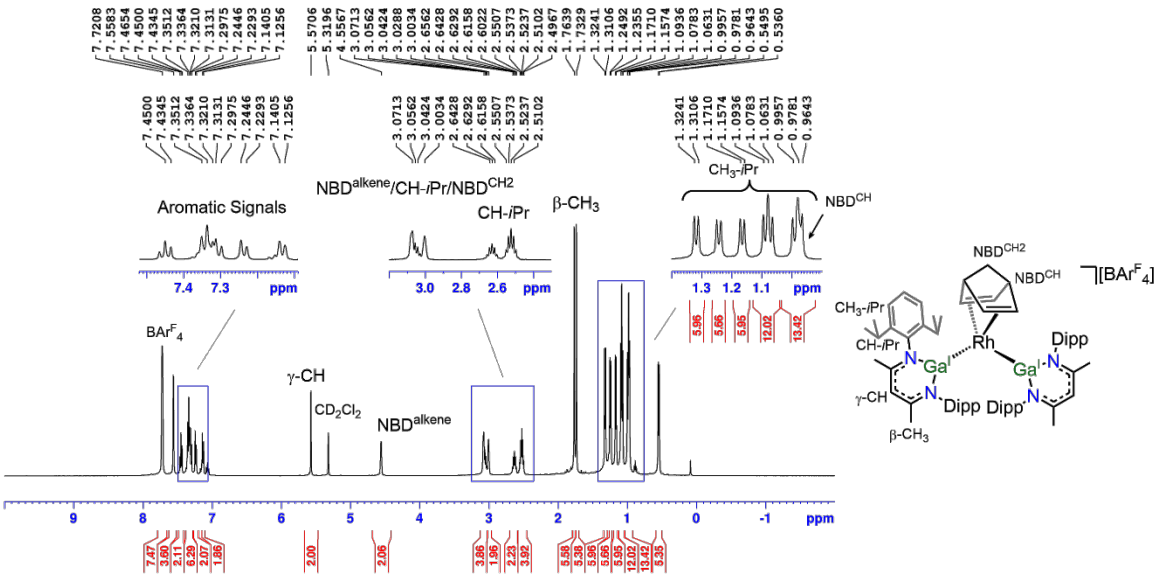


Figure 13. ^{1}H NMR (500 MHz, CD_2Cl_2, 298 K) spectrum of *cis*-[**2₂−Rh(NBD)**][BAr^F_4].

In the ^{13}C NMR of *cis*-[**2₂−Rh(NBD)**][BAr^F_4], the BDI backbone γ–CH carbon appears at δ 103.3, while the NBD carbons are found at δ 69.0, 68.2, 67.9, and 55.6. Of particular interest, the alkene carbons at δ 69.0 and 67.9 exhibit $^1J_{C,Rh}$ couplings of 7.4 and 6.7 Hz, respectively, akin to the earlier Rh(I) complexes in Section 3.3.1. The bridging CH_2 (~ δ 68.2) couples at the three-bond level ($^3J_{C,Rh}$ ~ 4.3 Hz), and the bridging CH resonates near δ 55.6 with a small $^2J_{C,Rh}$ ~ 1.5 Hz.

A comparable ^{1}H/^{13}C NMR pattern emerges for the COD derivative *cis*-[**2₂−Rh(COD)**][BAr^F_4]. The BDI γ–CH proton resonates as a single peak at δ 5.61 (2H), while the β–CH_3 groups appear at δ 1.76 and 1.73 (6 H each). The aromatic and iPr signals mirror those in the NBD complex, distributing across δ 7.44–7.10 (aromatic region) and δ 3.05–2.47 (CH–iPr septets) with coupling constants of ~ 6.7–6.8 Hz. Again, one of the CH_3–iPr shifts is quite shielded (δ 0.27), consistent with intramolecular aromatic face proximity observed crystallographically.

For the COD moiety in *cis*-[**2₂−Rh(COD)**][BAr^F_4], two alkene signals appear, a broad singlet at δ 5.13 (2 H) and a more complex resonance at δ 3.74 (2 H). The CH_2 portion splits into four multiplets spanning δ 1.64, 1.52, 0.96, and 0.67 (2 H each). Notably, δ 0.96 partially overlaps with an isopropyl–CH_3. In ^{13}C, the COD alkene carbons are observed at δ 83.4 and 82.1, each with $^1J_{C,Rh}$ couplings near 7.9 Hz.

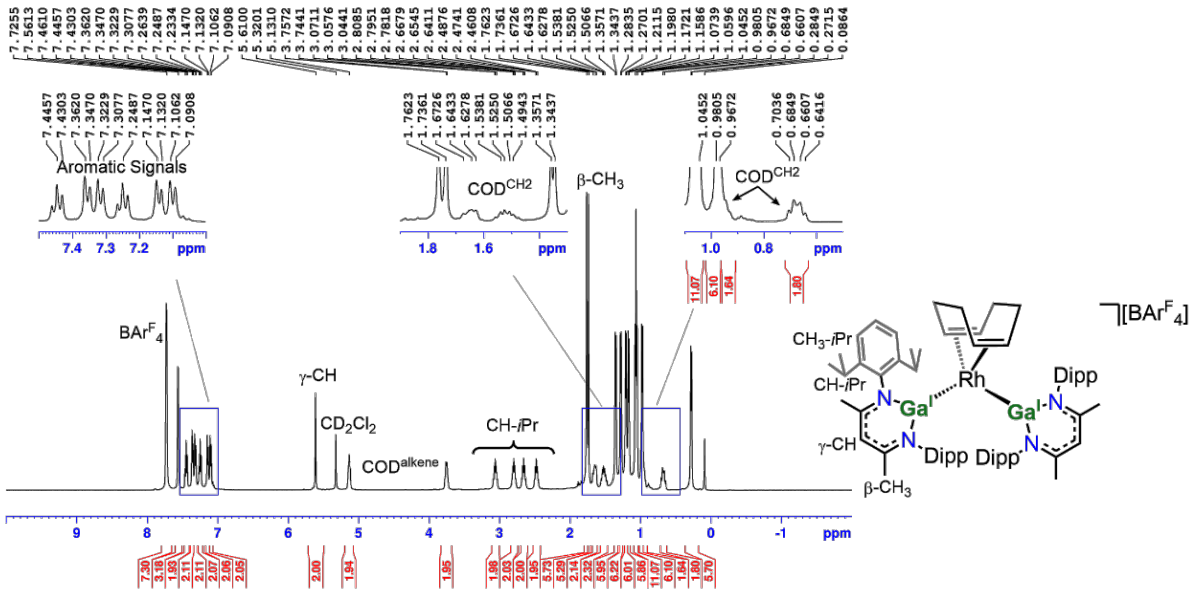


Figure 14. ^1H NMR (500 MHz, CD_2Cl_2, 298 K) spectrum of *cis*-[**2₂−Rh(COD)**][BAr^F_4].

3.3.4 Crystal Structures

3.3.4.1 Crystal Structures of Rh(I) Bis(Olefin) Complexes

Despite [**Rh(COD)₂**][BAr^F_4] and [**Rh(COD)₂**][$AlOR^F_4$] being widely recognised Rh(I) precursors,[53a, 53b] their solid-state structures remained unreported until this study. Fortunately, we succeeded in isolating suitable single crystals for X-ray diffraction via slow diffusion of *n*-hexane into a saturated CH_2Cl_2 solution. These complexes crystallised in monoclinic lattices, adopting space groups $P2_1/c$ for [**Rh(COD)₂**][BAr^F_4] and $P2_1/n$ for [**Rh(COD)₂**][$AlOR^F_4$]. In each asymmetric unit, one discrete cationic unit [**Rh(COD)₂**]$^+$, and the corresponding [BAr^F_4]$^-$ or [$AlOR^F_4$] anion are present.

As Figure 15 illustrates, the COD ligands bind through their π systems in a κ^2-η^2-C,C'-fashion, conferring a square-planar coordination environment about Rh(I) (typical of a d^8 configuration). Examination of Rh–C distances in **[Rh(COD)$_2$]**[BAr$^F{}_4$] spans ~ 2.22 Å, while in **[Rh(COD)$_2$]**[AlOR$^F{}_4$] they range 2.221–2.266 Å, in line with related trifluoromethanesulfonate-ligated Rh(I) bis(COD) analogues.[59] These values affirm the consistency of metal–alkene bonding across different non-coordinating anions, with no major distortion from ideal planar geometry.

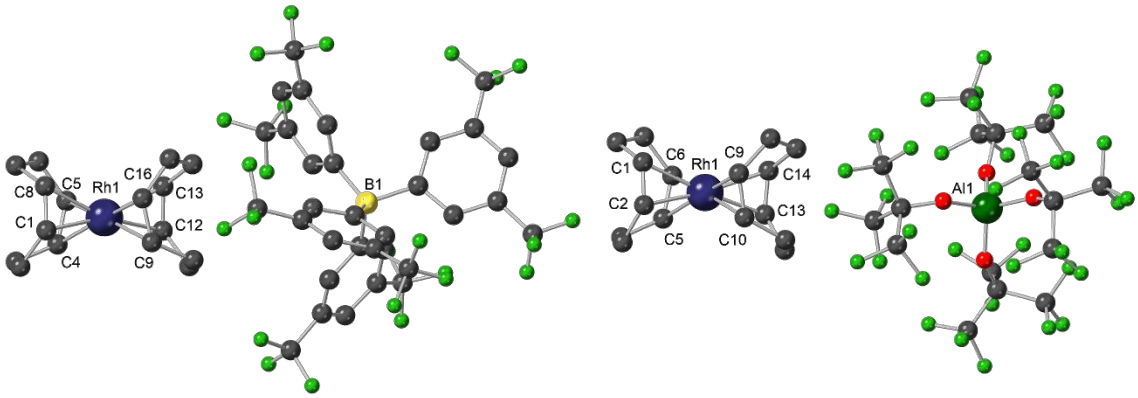


Figure 15. Molecular structures of **[Rh(COD)$_2$]**[BAr$^F{}_4$] (left) and **[Rh(COD)$_2$]**[AlOR$^F{}_4$] (right). Hydrogen atoms have been omitted for clarity.

Table 2 compiles selected bond lengths for the cationic moieties, highlighting Rh–C distances and (n,m) midpoints for each COD alkene group. The range of distances indicates slight variation in alkene coordination, often influenced by subtle differences in anion packing or intermolecular interactions. Nonetheless, all Rh–C bond lengths remain within typical COD-bound Rh(I) parameters,[59] supporting the C_{2V}-like symmetry suggested by the cationic arrangement.

Table 2. Selected bond lengths (Å) for **[Rh(COD)$_2$]**[BAr$^F{}_4$] and **[Rh(COD)$_2$]**[AlOR$^F{}_4$].

	[Rh(COD)$_2$][BAr$^F{}_4$]	**[Rh(COD)$_2$]**[AlOR$^F{}_4$]
Rh−C	C1 2.1186(18)	C1 2.266(4)
	C4 2.2396(17)	C2 2.223(4)
	C5 2.2255(17)	C5 2.244(4)
	C8 2.2415(18)	C6 2.231(4)
Rh−(n,m)	(C1,C8) 2.1202	(C1,C2) 2.137
	(C4,C5) 2.1233	(C5,C6) 2.219
	(C9,C16) 2.1303	(C9,C10) 2.130
	(C12,C13) 2.1268	(C13,C14) 2.123

(*n,m*) denote the midpoints between the olefinic moieties within the COD ligands

3.3.4.2 Crystal Structures of Rh(I) Amine/Olefin Complexes

Single crystals of [**(TMEDA)Rh(COD)**]$^+$ suitable for X-ray diffraction were isolated for each of the ion-pair variants, [BF_4]$^-$, [BAr^F_4]$^-$, and [$AlOR^F_4$]$^-$, via slow diffusion of *n*-hexane into their respective saturated solutions (benzene for the [BAr^F_4]$^-$ salt, dichloromethane for [BF_4]$^-$ and [$AlOR^F_4$]$^-$). Notably, crystals of [**(TMEDA)Rh(COD)**][BAr^F_4] and [**(TMEDA)Rh(COD)**][$AlOR^F_4$] each grew in monoclinic space groups (*P2₁/c* and *P2₁/n*, respectively), whereas [**(TMEDA)Rh(COD)**][BF_4] crystallised in an orthorhombic *Pna2₁*. Despite these different lattice settings, the cationic fragment [**(TMEDA)Rh(COD)**]$^+$ remains structurally analogous across all three salts.

In the [BF_4]$^-$ and [$AlOR^F_4$]$^-$ complexes, two domains of disorder appear in the final refined structures for both the COD and TMEDA ligands, preventing precise distance determinations for certain atoms. Nonetheless, the connectivity and overall geometry are unambiguously confirmed. Each asymmetric unit contains one cation–anion pair, except in [**(TMEDA)Rh(COD)**][BAr^F_4], whose crystal structure includes two independent ion pairs plus two co-crystallised C_6H_6 solvent molecules.

Figure 16 depicts the cationic portion in [**(TMEDA)Rh(COD)**][$AlOR^F_4$], [**(TMEDA)Rh(COD)**][BAr^F_4], and [**(TMEDA)Rh(COD)**][BF_4]. In every case, Rh(I) adopts a square-planar arrangement: COD coordinates via two η^2-C,C' units, while TMEDA contributes a κ^2-N,N' chelate. The [**(TMEDA)Rh(COD)**][BAr^F_4] salt, for instance, exhibits Rh1–(C1,C2) and Rh1–(C5,C6) midpoint distances of ∼ 2.02 Å, each well within expected ranges for Rh–alkene bonding.[60] Similarly, the N1–Rh1–N2 bite angle measures 82.14(11)°, and Rh–N distances of ∼ 2.171(3) Å mirror those observed in other five-membered diamine chelates on Rh(I).[54, 60b] A noteworthy structural feature common to all three cationic units is the presence of weak C–H···F interactions between the TMEDA methyl groups and the anion fluorine atoms, as illustrated in Figure 16. These C–H···F contacts presumably arise from electrostatic stabilisation within the crystal packing.

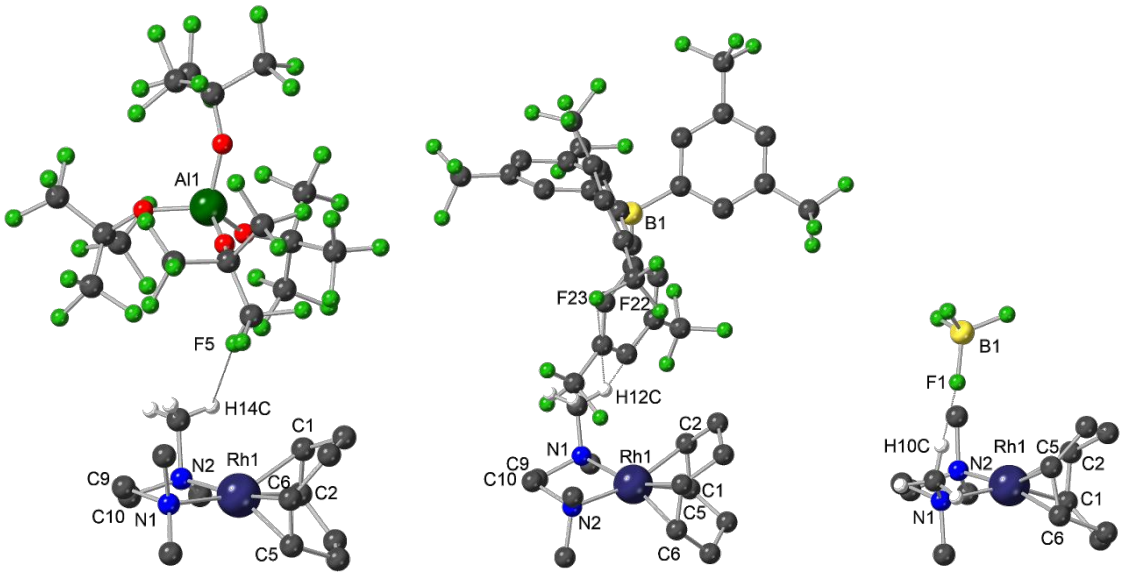


Figure 16. Molecular structure of [**(TMEDA)Rh(COD)**][AlOR$^{F}_{4}$] (left), [**(TMEDA)Rh(COD)**][BAr$^{F}_{4}$] (middle), and [**(TMEDA)Rh(COD)**][BF_4] (right). Hydrogen atoms are omitted for clarity with exception of those from the methyl groups interacting with the different counterions.

Table 3 summarises selected bond distances and angles for [**(TMEDA)Rh(COD)**][BAr$^{F}_{4}$]·C_6H_6. The Rh–C bonds typically fall between 2.13–2.15 Å, while the average Rh–N distance is about 2.17 Å. Collectively, these metrics confirm a d^8 Rh(I) centre adopting its characteristic 16-electron square-planar geometry, stabilized by COD π donation and TMEDA σ donation.

Table 3. Selected bond lenghts (Å) and angles (º) for [**(TMEDA)Rh(COD)**][BAr$^{F}_{4}$].

	[**(TMEDA)Rh(COD)**][BAr$^{F}_{4}$]·C_6H_6		
Rh−C	C1 2.131(3)	Rh−(n,m)	(C1,C2) 2.013
	C2 2.128(3)		(C5,C6) 2.022
	C5 2.146(3)	Rh−N	N1 2.171(3)
	C6 2.134(3)		N2 2.171(3)
N1−Rh1−N2	82.14(11)		

(*n,m*) denote the midpoints between the olefinic moieties within the COD ligands.

For the NBD derivative, only the $[BF_4]^-$ salt provided single crystals suitable for X-ray diffraction, obtained via slow diffusion of *n*-hexane into a saturated CH_2Cl_2 solution of [**(TMEDA)Rh(NBD)**][BF_4]. The crystalline lattice adopts an orthorhombic

Pnmna space group, featuring one ion-pair molecule per asymmetric unit. As in certain COD analogues, the cationic fragment exhibits two partially disordered domains; however, the resulting data quality is sufficiently high to precisely determine Rh–ligand distances.

Structurally, the **[(TMEDA)Rh(NBD)]**$^+$ cation parallels its COD-based counterparts, with the NBD ligand bound through two η^2–C,C' sites to produce a square-planar Rh(I) environment. The planarity arises from the Rh–(C1,C2) and Rh–(C5,C6) midpoints, along with the N1–Rh–N2 vector, forming a quasi-C_{2v} arrangement. Specifically, Rh1–(C1,C2) and Rh1–(C5,C6) measure 1.99 and 2.02 Å respectively, values in close agreement with **[(TMEDA)Rh(COD)]**[BAr^F_4] and other Rh(I) complexes known in the literature.[60] Likewise, the bite angle at N1–Rh–N2 is 82.84(12)°, mirroring the ~ 82° angles observed in five-membered chelating diamines.[54, 60b] Rh–N distances, at 2.147(3) and 2.141(4) Å, further reinforce this chelate motif, aligning with standard Rh–N metrics for σ-donating diamino ligands..

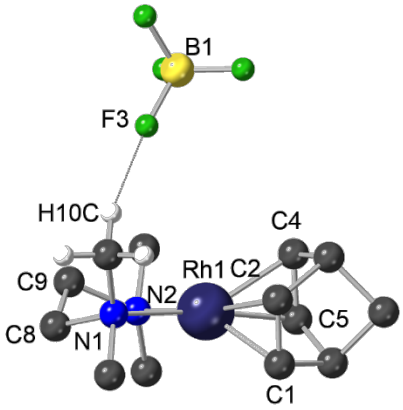


Figure 17. Molecular structure of **[(TMEDA)Rh(NBD)]**[BF_4]. Hydrogen atoms have been omitted for clarity with exception of those on the methyl group interacting with the $[BF_4]^-$ anion.

Table 4. Selected bond lengths (Å) and angles (°) for **[(TMEDA)Rh(NBD)]**[BF_4].

	[(TMEDA)Rh(NBD)][BF_4]		
Rh−C	C1 2.072(6)	Rh−(n,m)	(C1,C2) 1.985
	C2 2.133(6)		(C5,C6) 2.016
	C5 2.153(5)	Rh−N	N1 2.147(3)
	C6 2.113(4)		N2 2.141(4)
N1−Rh1−N2	82.84(12)		

(*n,m*) denote the midpoints between the olefinic moieties within the COD ligands.

As in the structure of [**(TMEDA)Rh(NBD)**][BAr^F_4], the [BF_4]$^-$ anion established a weak C–H···F contact with one Me group from the TMEDA amine ligand resulting from the crystal packing, as depicted in Figure 17. Overall, this structural data underscores that the cationic [**(TMEDA)Rh(NBD)**]$^+$ fragment adopts the same square-planar d^8 geometry, with the NBD ring substituting for COD but preserving the fundamental Rh–amino arrangement.

3.3.4.3 Crystal Structures of Heterometallic Ga(I)–Rh(I) Complexes

In tandem with the solution-based characterisation (Section 3.3.3.3), we pursued single-crystal X-ray diffraction studies to verify the proposed *cis* arrangement of the two Ga(I) metalloligands **2** around Rh(I) in these newly formed heterometallic systems, *cis*-[**2₂−Rh(COD)**][BAr^F_4] and *cis*-[**2₂−Rh(NBD)**][BAr^F_4]. The resulting structures provided direct evidence of the two-point Ga–Rh bonding motif, as well as the steric landscape introduced by the bulky β-diketiminate (BDI) substituents. Such data were crucial to interpreting the subtle features noted in the NMR spectra.

Slow diffusion of *n*-hexane into a saturated fluorobenzene solution of *cis*-[**2₂−Rh(NBD)**][BAr^F_4] generated monoclinic crystals in the $P2_1/n$ space group. Each asymmetric unit contains a *cis*-[**2₂−Rh(NBD)**]$^+$ cation, the [BAr^F_4]$^-$ counterion, and one co-crystallised C_6H_5F molecule. In the cationic *cis*-[**2₂−Rh(NBD)**]$^+$ moiety, Rh(I) binds the NBD ligand via a κ^2-η^2-C,C'-arrangement, while two β-diketiminate Ga(I) fragments **2** coordinate *cis* to the metal through their gallium centres, completing a square-planar environment (Figure 12).

Specifically, the centres of the NBD double bonds, (C59,C60) and (C62,C63), together with Ga1–Rh1–Ga2 define the planar geometry. Distances Rh1–(C59,C60) = 2.08 Å and Rh1–(C62,C63) 2.09 Å resemble typical Rh–diolefin metrics reported previously. The Ga–Rh bonds measure 2.4209(6) and 2.4294(6) Å, close to the 2.43 Å observed in analogous Rh–Ga complexes.[61] Moreover, the Ga1–Rh1–Ga2 angle is 95.811(17)°, consistent with a square-planar d^8 Rh(I) centre.

Moving to the Ga(I) metalloligands **2**, the Ga–N distances in each gallium fragment average ~ 1.97 Å, notably shorter than in free 2 (~ 2.05 Å). Simultaneously, angles such as N1–Ga1–N2 or N4–Ga2–N5 expand from about 87.5° (in free **2**) to ~ 93.2° upon coordination to Rh. These variations imply that the Rh–Ga interaction exerts a tightening effect on the Ga(I) scaffolds **2**, like the gallyl–cationic bridging

observed in *Chapter II*. This structural contraction further confirms the strength of Ga(I)–Rh(I) bonding in these heterometallic assemblies.

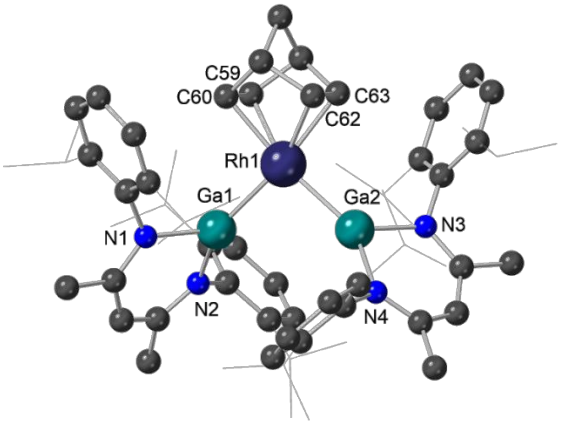


Figure 18. Molecular structure of *cis*-[**2₂−Rh(NBD)**][BAr^F_4]. Hydrogen atoms were omitted for clarity.

Table 5. Selected bond lengths (Å) and angles (º) for *cis*-[**2₂−Rh(NBD)**][BAr^F_4]·C_6H_5F

cis-[**2₂−Rh(NBD)**][BAr^F_4]·C_6H_5F			
Rh−C	C59 2.184(2)	Rh−(n,m)	(C59,C60) 2.0781
	C60 2.1968(19)		(C62,C63) 2.0893
	C62 2.1978(18)		
	C63 2.2040(19)		
Rh−Ga	Ga1 2.4209(6)	Ga1−N	N1 1.9777(15)
	Ga2 2.24294(6)		N2 1.9707(16)
		Ga2−N	N4 1.9749(16)
			N5 1.9715(15)
Ga1−Rh1−Ga2	95.811(17)	N1−Ga1−N2	93.23(6)
		N4−Ga2−N5	93.26(6)

An analogous procedure, *n*-hexane layered into a saturated fluorobenzene solution, afforded single crystals of *cis*-[**2₂−Rh(COD)**][BAr^F_4]. The resulting structure crystallises in a $P2_1/n$ monoclinic system, containing a *cis*-[**2₂−Rh(COD)**]$^+$ cation, a [BAr^F_4]$^-$ anion, and half molecule of *n*-hexane in the lattice. Similar to the NBD analogue, the Rh(I) centre is square-planar, now complexed to COD as a diolefin and by two *cis* Ga(I) metalloligands **2** (Figure 19).

Here, the midpoints (C1,C2) and (C5,C6) define the alkene coordination, with Rh1–(C1,C2) of 2.09 Å and Rh1–(C5,C6) of 2.09 Å, virtually identical to

cis-[**2₂−Rh(NBD)**][BAr^F_4]. Likewise, in *cis*-[**2₂−Rh(COD)**][BAr^F_4], Rh1–Ga1 and Rh1–Ga2 measure 2.4213(12) and 2.4245(5) Å, matching the ~ 2.42 Å value found in a related NBD congener, [Rh(η^2,η^2-NBD)(PCy_3)($GaCp^*$)$_2$][BAr^F_4].[55a] The Ga1–Rh1–Ga2 angle, 94.93(3)°, again confirms a square-planar arrangement. As with *cis*-[**2₂−Rh(NBD)**][BAr^F_4], the Ga(I)–N distances in the metalloligand **2** and Ga–N–Ga angles are slightly shifted from free **2**, indicating tighter bonding upon Rh attachment. The values observed are in the same range for both NBD and COD derivatives with shorter bond length distances (~ 1.97 Å *vs.* ~ 2.05 Å) and a bigger angle (92.9º *vs.* 87.5º).

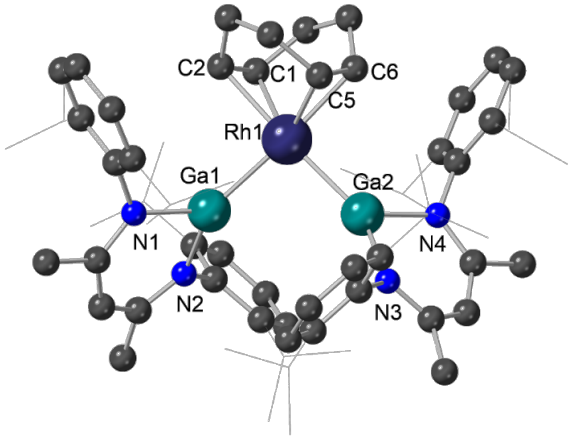


Figure 19. Molecular structure of *cis*-[**2₂−Rh(COD)**][BAr^F_4]. Hydrogen atoms were omitted for clarity.

Table 6. Selected bond lengths (Å) and angles (º) for *cis*-[**2₂−Rh(COD)**][BAr^F_4]·0.5 C_6H_{12}.

cis-[**2₂−Rh(COD)**][BAr^F_4]·0.5 C_6H_{12}			
Rh−C	C1 2.178(4)	Rh−(n,m)	(C1,C2) 2.097
	C2 2.240(3)		(C5,C6) 2.096
	C5 2.180(5)	Ga1−N	N1 1.975(3)
	C6 2.233(4)		N2 1.973(3)
Rh−Ga	Ga1 2.4213(12)	Ga2−N	N3 1.972(3)
	Ga2 2.4245(5)		N4 1.980(3)
Ga1−Rh1−Ga2	94.93(3)	N1−Ga1−N2	92.93(11)
		N3−Ga2−N4	92.74(10)

3.4 H_2 Activation and Hydrogenation of Olefins by Heterobimetallic Ga(I)–Rh(I) Species

Rhodium is widely recognized for its proficiency in dihydrogen (H_2) activation, with Rh(III)–dihydride intermediates playing pivotal roles in hydrogenation, hydrosilylation, and other transformations involving unsaturated substrates.[62] In heterobimetallic contexts, cooperativity between two distinct metals can further enhance or modulate overall reactivity, stabilizing reactive intermediates or enabling multi-site bond activation.[48] Stimulated by these insights and the promising combination of Rh(I) with Ga(I) observed in our *cis*-[**2_2−Rh(NBD)**][$BAr^F{}_4$] and *cis*-[**2_2-Rh(COD)**][$BAr^F{}_4$] complexes, we explored their behaviour under H_2. Specifically, we sought to evaluate their stability, detect potential hydride or dihydrogen species, and determine whether such complexes could function as catalysts for hydrogenation.

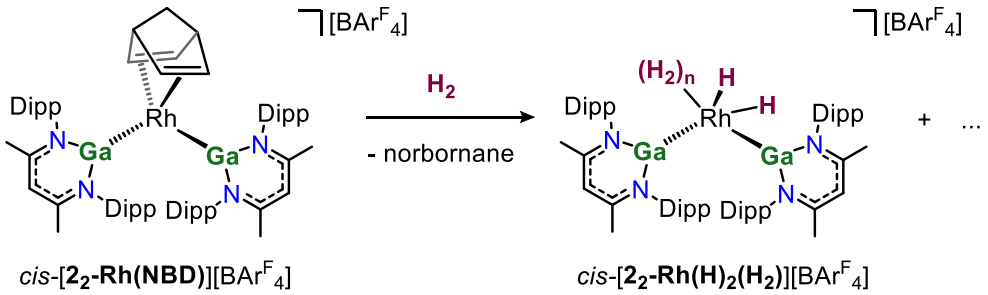
3.4.1 Speciation/Stability NMR Studies of *cis*-[2_2−Rh(NBD)][$BAr^F{}_4$] with H_2

To probe the fate of *cis*-[**2_2−Rh(NBD)**][$BAr^F{}_4$] and *cis*-[**2_2-Rh(COD)**][$BAr^F{}_4$], upon exposure to H_2, we performed in-situ NMR analyses in solution, focusing on the formation of Rh–H or Rh–(η^2–H_2) species. In a typical protocol, a J. Young NMR tube was charged with ~ 0.5 mL of dry CD_2Cl_2, in which freshly prepared *cis*-[**2_2−Rh(NBD)**][$BAr^F{}_4$] or *cis*-[**2_2-Rh(COD)**][$BAr^F{}_4$] were dissolved, yielding a pale orange–yellow solution. After freeze-pump-thaw degassing, 1.5 bar of H_2 was introduced at 298 K, whereupon the solution rapidly turned colourless, hinting at fast and substantial reactivity.

When *cis*-[**2_2−Rh(NBD)**][$BAr^F{}_4$] was treated with H_2, an *in-situ* ^{1}H NMR spectra indicated that norbornadiene (NBD) underwent complete hydrogenation to norbornane (NBA), concurrently generating multiple rhodium-based species, including dihydride and dihydrogen complexes, Rh–H or Rh–(H_2), hinting at the formation of the species of the type *cis*-[**2_2−Rh(H)$_2$(H_2)**][$BAr^F{}_4$] (Scheme 8). Ultimately, over-hydrogenation and subsequent decomposition took place (Rh mirrors), implying only transient stability for *cis*-[**2_2-Rh(NBD)**][$BAr^F{}_4$] under prolonged exposure to an H_2 atmosphere.

Figure 20 displays the NMR spectrum recorded 5 min after introducing 1.5 bar of H_2 gas. Two distinct hydride resonances can be distinguished, one at δ −15.88 and another at δ −15.12, each integrating for 2 H. The resonance at δ −15.88 exhibits a $^1J_{H,Rh}$ coupling constant of ~ 13 Hz and a T_1 relaxation time of

~ 780 ms, aligning well with other reported rhodium–hydride species.[63] Similarly, the second hydride peak (δ −15.12, $^1J_{H,Rh}$ ~ 22 Hz) gave a T_1 of ~ 630 ms, reinforcing its hydride identity despite the slightly larger coupling constant. The presence of both signals suggests coexisting dihydride species or isomeric Rh(III)–H_x forms. In contrast, the broad δ −9.30 resonance, integrating to 2 H yet exhibiting a notably short T_1 (~ 23 ms), indicates a Rh–dihydrogen (Rh–H_2) ligand still weakly bound to the rhodium(I) centre, consistent with other known rhodium dihydrogen complexes (Scheme 8).[64] The short T_1 relaxation time, is characteristic of Rh–(η^2–H_2) complexes, in which T_1 times can be an order of magnitude lower than conventional metal–hydride species. Although these observations confirm H_2 activation, the fate of *cis*-[**2_2−Rh(NBD)**]$^+$ is irreversible in with H_2, proceeding to full hydrogenation and decomposition overtime.



Scheme 8. Reactivity of [**2_2−Rh(NBD)**][$BAr^F{}_4$] with H_2 (1.5 bar, 5 min) to form dihydride and dihydrogen species leading to decomposition pathways.

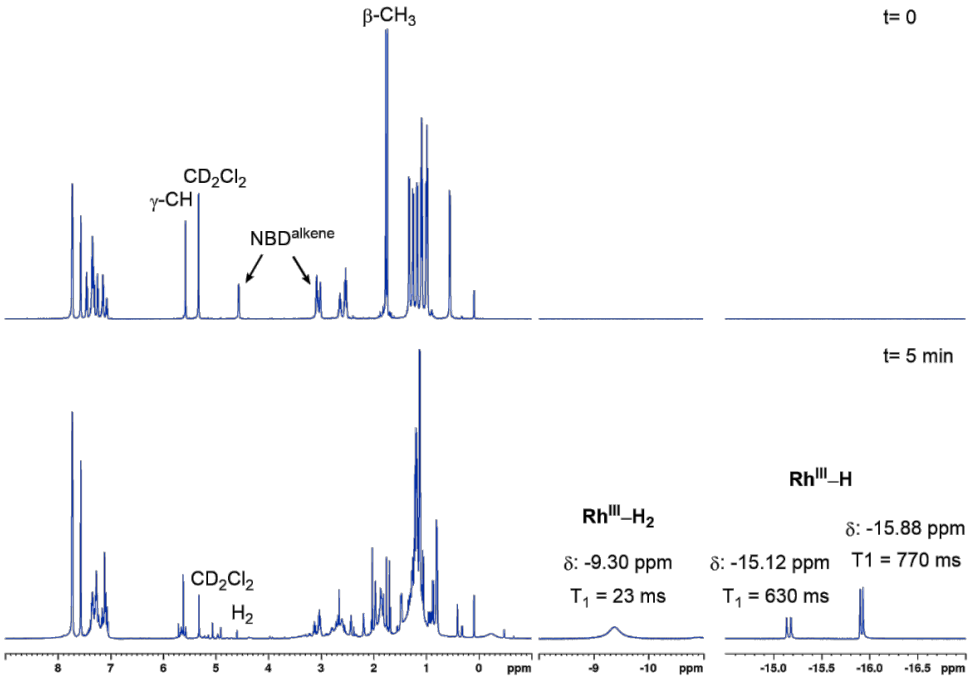
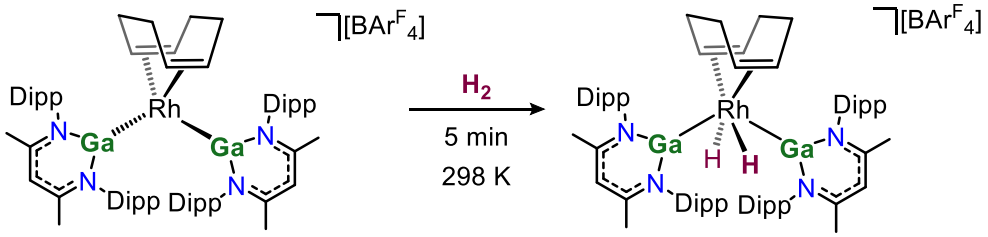


Figure 20. *In-situ* ^{1}H NMR (500 MHz, CD_2Cl_2, 298 K) monitoring of the reactivity of *cis*-[**2_2−Rh(NBD)**][$BAr^F{}_4$] with H_2 (top: t = 0; bottom: after 5 mins with 1.5 bar of H_2).

3.4.2 Speciation/Stability NMR Studies of *cis*-[2_2−Rh(COD)][$BAr^F{}_4$] with H_2

In contrast to *cis*-[**2_2−Rh(NBD)**][$BAr^F{}_4$], the species *cis*-[**2_2−Rh(COD)**][$BAr^F{}_4$] exhibits a simpler behaviour (Scheme 9). Under 1.5 bar H_2, ^{1}H NMR reveals the immediate formation of a single Rh–H species at δ −14.26, integrating for 2 H and appearing as a doublet with $^1J_{Rh,H}$ ~ 12 Hz, consistent with metal–hydride signals reported in the Rh(I)/Rh(III) literature.[63] A T_1 value of ~ 610 ms corroborates the hydride identity, indicating the *in-situ* generation of *cis*-[**2_2−Rh(COD)(H)$_2$**][$BAr^F{}_4$] (Figure 21). This outcome contrasts to *cis*-[**2_2−Rh(NBD)**][$BAr^F{}_4$] which fully hydrogenates NBD and eventually decomposes.



cis-[**2_2-Rh(COD)**][$BAr^F{}_4$] *cis*-[**2_2-Rh(COD)(H)$_2$**][$BAr^F{}_4$]

Scheme 9. Reactivity of *cis*-[**2_2−Rh(COD)**][$BAr^F{}_4$] with H_2 (1.5 bar, 5 min) to form the dihydride species *cis*-[**2_2−Rh(COD)(H)$_2$**][$BAr^F{}_4$].

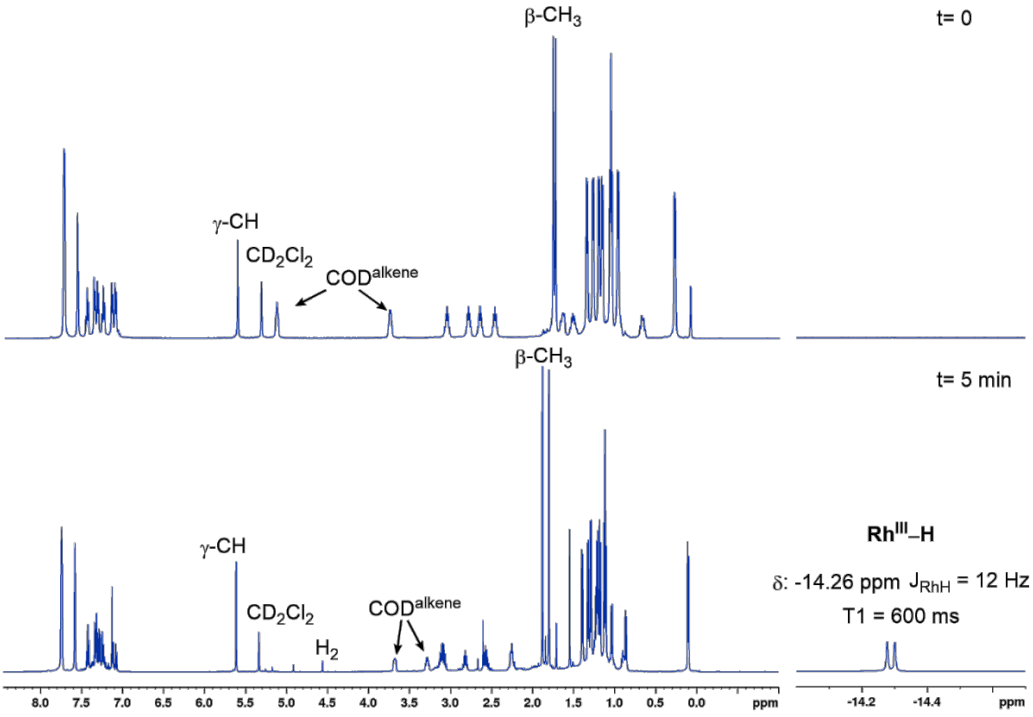


Figure 21. *In-situ* ^{1}H NMR (500 MHz, CD_2Cl_2, 298 K) monitoring of the reactivity of *cis*-[**2_2–Rh(COD)**][BAr^F_4] with H_2 (top: t = 0; bottom: after 5 mins with 1.5 bar of H_2).

Continuing our investigation into the Ga(I)–Rh(I) system's reactivity with H_2, we next examined the kinetic isotope effect (KIE) with *cis*-[**2_2−Rh(COD)**][BAr^F_4] by substituting H_2 for deuterium gas (D_2). The resulting ^{2}H NMR spectrum (Figure 22) revealed a single, symmetric set of deuteride resonances, corroborating that both incoming hydrides (or deuterides) occupy equivalent sites at the Rh(I) centre, a scenario consistent with a *cis*-addition of D_2 to give *cis*-[**2_2−Rh(COD)$(D)_2$**][BAr^F_4]. This observation supports a mechanism where H_2/D_2 binds or inserts in an identical, twofold fashion at Rh(I).

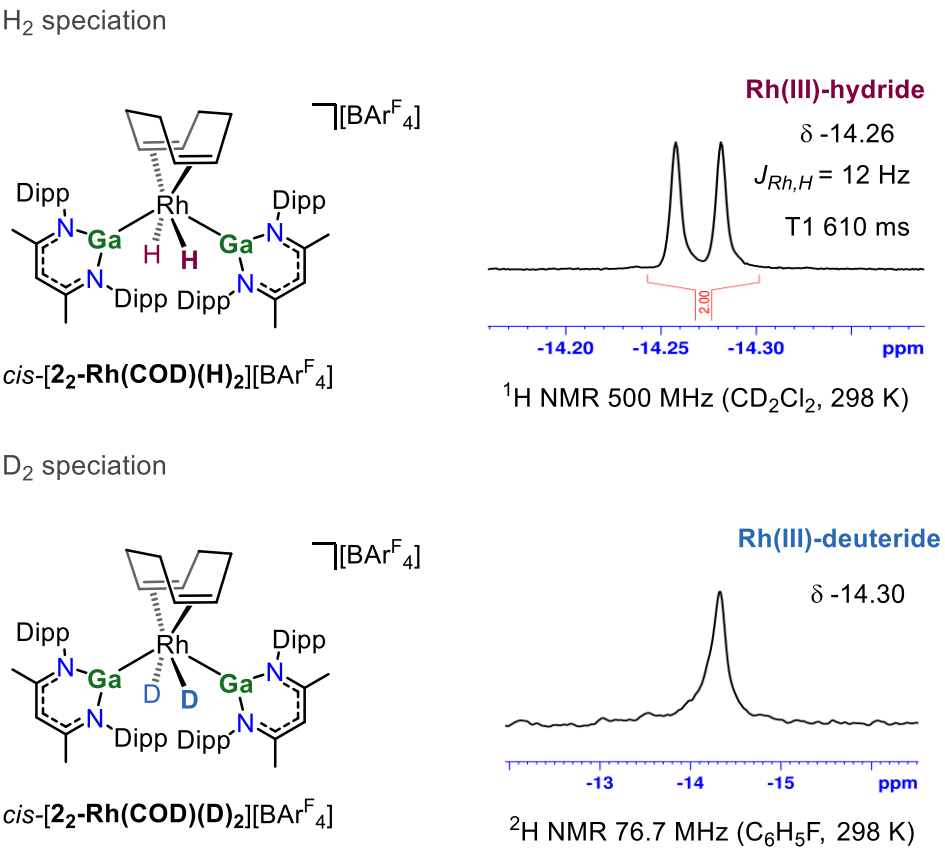


Figure 22. ^{1}H NMR spectra of *cis*-[**2_2−Rh(COD)$(H)_2$**][BAr^F_4] (top) and ^{2}H NMR spectrum of *cis*-[**2_2−Rh(COD)$(D)_2$**][BAr^F_4] (bottom).

Moreover, as illustrated in Figure 21 and Figure 22, only one dominant Rh–H species emerges in solution from the H_2 activation by *cis*-[**2_2−Rh(COD)**][BAr^F_4], implying that the two β-diketiminate Ga(I) metalloligands **2** remain intact and bound in a *cis* fashion to Rh(I) in *cis*-[**2_2−Rh(COD)$(H)_2$**][BAr^F_4]. With

an eye toward isolating this new dihydride as a possible mechanistic intermediate for catalytic applications, we opted to employ fluorobenzene (C_6H_5F) as the reaction medium on a larger scale, considering that the newly formed rhodium hydride complex, *cis*-[**2₂−Rh(COD)(H)₂**][BAr^F_4], displays notable longevity in C_6H_5F even after H_2 removal.

Hence, we loaded a J. Young ampoule with *cis*-[**2₂−Rh(COD)**][BAr^F_4] and ~ 1 mL of C_6H_5F. After freeze-pump-thaw degassing, we introduced 1.5 bar of H_2 gas, leading to a colourless solution upon stirring at room temperature for 5 minutes. Subsequently, H_2 was removed via additional freeze-pump-thaw cycles. We then added *n*-hexane at 0°C, generating a sand-yellow suspension, which was stirred for 15 minutes, allowed to settle, and filtered via cannula. The resulting yellow solid, washed with *n*-hexane and dried under vacuum, was confirmed by NMR to be *cis*-[**2₂−Rh(COD)(H)₂**][BAr^F_4]. This dihydride stands as the principal product when limited H_2 is applied.

For the dihydride product *cis*-[**2₂−RhCOD(H)₂**][BAr^F_4], the ^{1}H NMR resonances for the bulky β-diketiminate ligands **2** mirror those in the unhydrogenated *cis*-[**2₂−Rh(COD)**][BAr^F_4] species. Specifically, the aromatic Dipp substituents appear from δ 7.40 to 7.10, integrating to 12 H, in good agreement with two BDI ligands each bearing two diisopropylphenyl units. The backbone (γ-CH) protons of the β-diketiminate ligands **2** show a singlet near δ 5.59 (2 H total). Likewise, the methyl groups of the β-diketiminate backbones of **2** arise at δ 1.86 and 1.78 (6 H each). The iPr groups themselves display CH–iPr signals from δ 3.30 to 2.45 and CH_3–iPr resonances in the δ 1.50–0.80 region, plus an outlier peak at δ 0.08 (doublet, 6 H). This extremely upfield-shifted Me group presumably experiences ring-current shielding induced by a β-diketiminate Dipp of **2**. Turning to the COD portion, alkene protons are observed at δ 3.66 and 3.27, both broad singlets, shifted slightly upfield compared to the parent *cis*-[**2₂−Rh(COD)**]$^+$. The CH_2 resonances of COD occur at δ 2.23, 1.24, 1.01, and 0.88, though partial overlap with CH_3–iPr signals complicates a straightforward multiplicity assignment. Each peak, however, integrates consistently for 2 H. The Rh(I)–hydride environment in *cis*-[**2₂−Rh(COD)(H)₂**][BAr^F_4] is revealed by a single high-field signal at δ −14.26, a doublet with $^1J_{Rh,H}$ ~ 12 Hz, as noted in the *in-situ* experiments. This single Rh(I)–hydride resonance implies equivalent hydrides in a *cis* arrangement. A ^{1}H,^{1}H–NOE experiment further underscores their spatial proximity to both the COD alkene protons and the isopropyl substituents on the BDI ligand (Figure 23). Irradiation at δ −14.26 triggers distinct

enhancements in isopropyl–CH and CH–COD resonances, revealing the three-dimensional arrangement consistent with the C_{2v} geometry.

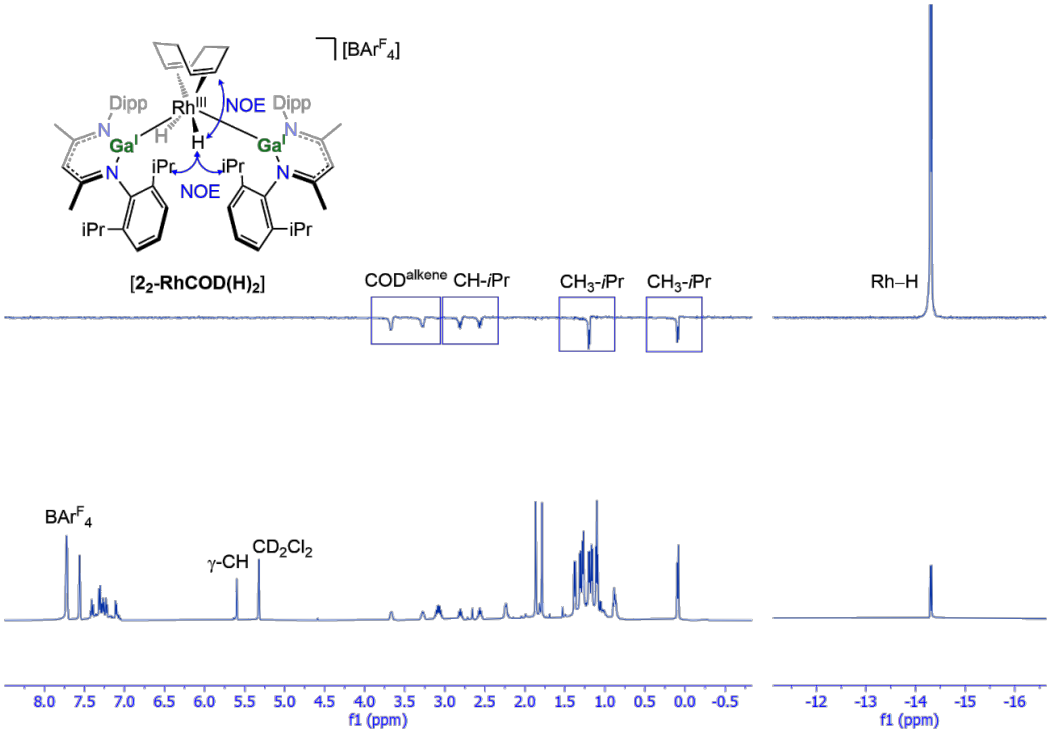
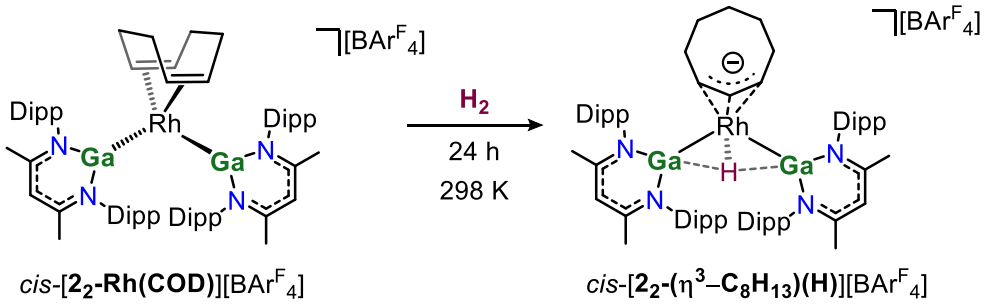


Figure 23. ^{1}H NOE NMR (500 MHz, CD_2Cl_2, 298 K) of *cis*-[**2₂−Rh(COD)(H)₂**][BAr^F_4] (top) with a selective gradient at –14.26 ppm *vs* ^{1}H NMR (500 MHz, CD_2Cl_2, 298 K) of *cis*-[**2₂−Rh(COD)(H)₂**][BAr^F_4] (bottom).

Remarkably, by carefully modulating the H_2 conditions, particularly the reaction time (1.5 bar of H_2, 24 hours), we can trap a partially hydrogenated COD moiety forming an allyl (η^3−C_8H_{13}) fragment co-ligated with a single Rh–H in *cis*-[**2₂−Rh(η^3−C_8H_{13})(H)**][BAr^F_4] (Scheme 10). Single crystals of *cis*-[**2₂−Rh(η^3−C_8H_{13})(H)**][BAr^F_4] reveal a Rh(III) centre still bound by two β-diketiminate ligands **2** but carrying only one hydride plus an η^3-allylic ligand.



cis-[**2₂-Rh(COD)**][BAr^F_4] *cis*-[**2₂-(η^3−C_8H_{13})(H)**][BAr^F_4]

Scheme 10. Reactivity of *cis*-[**2₂−Rh(COD)**][BAr^F_4] with H_2 (1.5 bar, 24 h) to form the allyl-dihydride species *cis*-[**2₂−Rh(η³−C₈H₁₃)(H)**][BAr^F_4].

This intermediate, *cis*-[**2₂−Rh(η³−C₈H₁₃)(H)**][BAr^F_4], when re-dissolved in CD_2Cl_2, spontaneously re-equilibrates with *cis*-[**2₂−Rh(COD)**][BAr^F_4] and *cis*-[**2₂−Rh(COD)(H)₂**][BAr^F_4] in a 1:1:2 ratio at 298 K (Figure 24). Minor free H_2 also emerges, indicative of back-and-forth hydrogen addition–elimination steps. Notably, such dynamic behaviour was confirmed across multiple independent syntheses, consistently reproducing the same NMR outcome. Thus, a delicate equilibrium governs the partial hydrogenation of the COD ligand, toggling between unchanged COD in *cis*-[**2₂−Rh(COD)**][BAr^F_4], an allylic (η^3−C_8H_{13}) moiety in *cis*-[**2₂−Rh(η³−C₈H₁₃)(H)**][BAr^F_4], and the final dihydride product *cis*-[**2₂−Rh(COD)(H)₂**][BAr^F_4]. These species can be undoubtedly identified in solution by their characteristic chemical shifts (see Table 7).

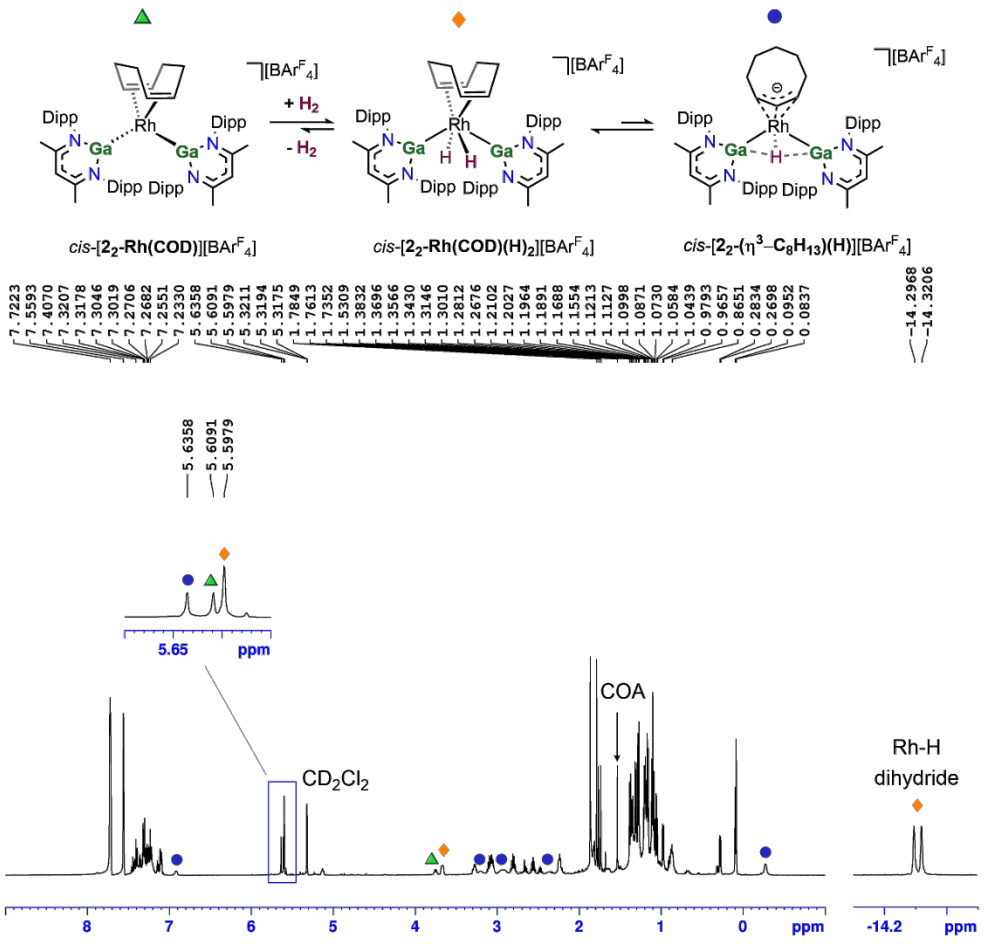


Figure 24. Top: Proposed equilibria with H_2 stemming from *cis*-[**2₂−Rh(COD)**][BAr^F_4], highlighting the presence of the allyl–hydride *cis*-[**2₂−Rh(η³−C₈H₁₃)(H)**][BAr^F_4] and

dihydride **2_2−Rh(COD)$(H)_2$**][$BAr^F{}_4$] species. Bottom: ^{1}H NMR (500 MHz, CD_2Cl_2, 298 K) showing the equilibrium stablished with isolated *cis*-**[2_2−Rh(η^3−C_8H_{13})(H)][$BAr^F{}_4$]** is placed in solution yielding a 1:1:2 mixture of **[2_2−Rh(η^3−C_8H_{13})(H)][$BAr^F{}_4$]**, **[2_2−Rh(COD)][$BAr^F{}_4$]** and **[2_2−Rh(COD)$(H)_2$][$BAr^F{}_4$]**.

Table 7. Selected ^{1}H and ^{13}C{^{1}H} NMR (CD_2Cl_2, 298 K) signals for the Ga(I)–Rh species.

Complex	[2_2−RhNBD]$^+$	[2_2−RhCOD]$^+$	[2_2−RhCOD$(H)_2$]$^+$	[2_2−Rh(η^3−C_8H_{13})(H)]$^+$
		^{1}H NMR (ppm)		
γ-CH	5.57	5.61	5.59	5.64 (br s)
[a]CH_3-*i*Pr	0.54	0.27	0.08	-0.59[b]
		^{13}C{^{1}H} NMR (ppm)		
γ-CH	103.3	103.6	102.4	-

[a] Shielded by the Dipp ring current. [b] Value found at 203 K.

These findings demonstrate the remarkable versatility of *cis*-[**2_2−Rh(COD)**][$BAr^F{}_4$] in H_2 activation by forming a stable dihydride *cis*-[**2_2−Rh(COD)$(H)_2$**][$BAr^F{}_4$] under moderated H_2 exposure, generating an allyl–hydride intermediate *cis*-[**2_2−Rh(η^3−C_8H_{13})(H)**][$BAr^F{}_4$] when partial COD hydrogenation is trapped, and re-equilibrating among these species in solution. This synergy between Ga(I) and Rh(I) likely underpins the robust reactivity and suitability for further catalytic applications of these Ga(I)–Rh(I) species.

To see whether lower temperatures might favour the allylic species in solution, we monitored a crystalline sample from *cis*-[**2_2−Rh(η^3−C_8H_{13})(H)**][$BAr^F{}_4$] by ^{1}H NMR from 298 down to 203 K (Figure 25). Even so, the ratios observed of the three complexes at this temperature remain unchanged for the observed at room temperature. At 298 K, the equilibrium mixture remains 1:1:2 *cis*-[**2_2−Rh(η^3−C_8H_{13})(H)**]$^+$:*cis*-[**2_2−Rh(COD)**]$^+$:*cis*-[**2_2−Rh(COD)$(H)_2$**]$^+$. Lowering the temperature to 253 K sharpens allyl resonances near δ 4.8 and 3.9, along with a broad monohydride at δ −7.9, yet the overall ratio of species remains effectively unchanged. Cooling further to 203 K likewise fails to displace the distribution, evidencing a strongly enthalpy- and entropy-balanced equilibrium.

Conversely, adding hydrogen abstractors such as 1,1-diphenylethylene (DPE) or 3,3-dimethyl-1-butene (TBE), failed to alter the mixture detectably, suggesting a robust equilibrium that is not easily perturbed by conventional hydrogen acceptors.

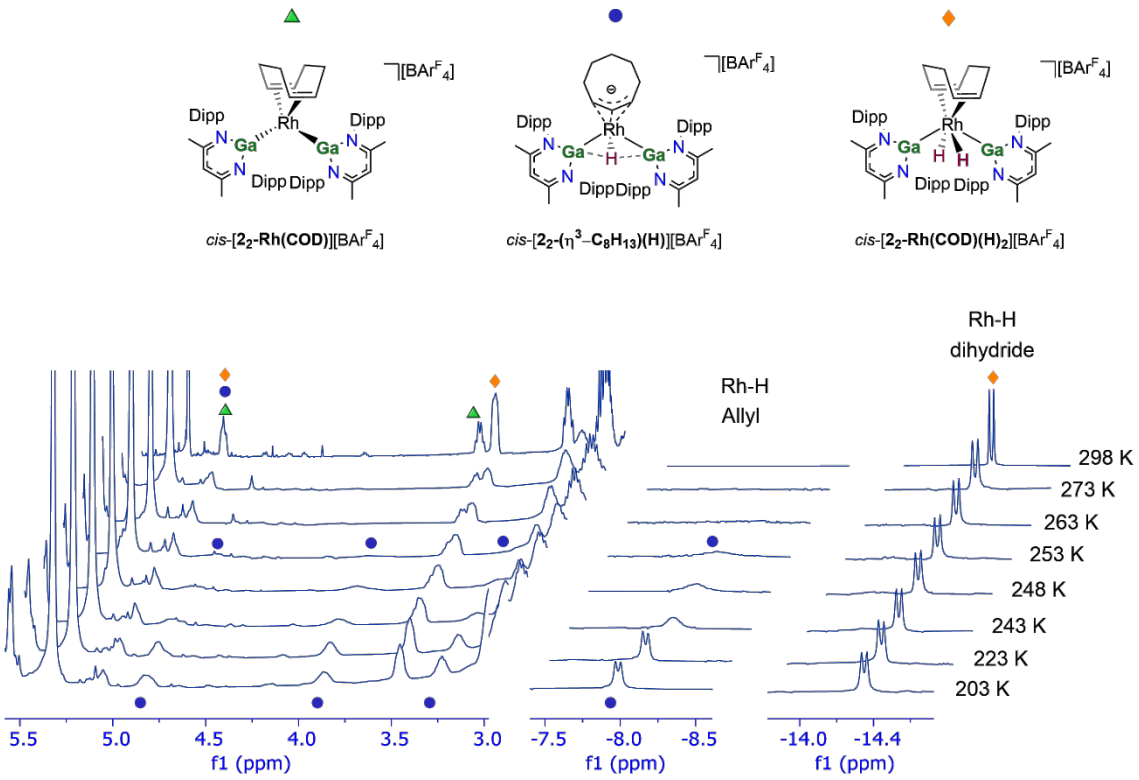


Figure 25. Stacked VT ^{1}H NMR (400 MHz, CD_2Cl_2) from 298–203 K of a crystalline of the allyl–hydride species *cis*-**[2₂−Rh(η³−C₈H₁₃)(H)][BArᶠ₄]**, re-equilibrating with *cis*-[**2₂−Rh(COD)(H)₂**][BAr^F_4] and *cis*-[**2₂−Rh(COD)**][BAr^F_4].

3.4.3 Speciation/Stability Crystallographic Studies with H_2

3.4.3.1 Molecular Structures of *cis*-[2₂−Rh(COD)(H)₂][BArᶠ₄]

Following our exploration of *cis*-[**2₂−Rh(COD)**][BAr^F_4] under dihydrogen, we succeeded in isolating two distinct crystalline species corresponding to partially and fully hydrogenated COD. First, crystals suitable for X-ray diffraction of *cis*-[**2₂−Rh(COD)(H)₂**][BAr^F_4] were obtained by slow diffusion of *n*-hexane into a solution of the dihydride at 262 K. The resulting structure crystallises in the monoclinic $P2_1/n$ space group, with an asymmetric unit composed of the cationic *cis*-[**2₂−Rh(COD)(H)₂**]$^+$ unit, a [BAr^F_4]$^-$ anion, and co-crystallised fluorobenzene (C_6H_5F) and *n*-hexane solvent molecules.

In *cis*-[**2₂−Rh(COD)(H)₂**]⁺, the rhodium centre adopts a pseudo-octahedral arrangement, characteristic of Rh(III). Unlike the nearly square-planar geometry observed in the Rh(I) species *cis*-[**2₂−Rh(COD)**]⁺, the presence of two hydrides demands an expanded coordination sphere. The COD ligand coordinates in a typical κ^2-η^2-C,C'-fashion, while the two β-diketiminate ligands **2** occupy positions twisted (out of the plane) with respect to the COD alkene groups, and two Rh–H bonds complete the octahedral coordination. Consequently, the Ga1–Rh1–Ga2 angle increases significantly to 126.5° in *cis*-[**2₂−Rh(COD)(H)₂**]⁺, exceeding the ~ 93.9° values in the original Rh(I) species *cis*-[**2₂−Rh(COD)**]⁺. This geometric change is also evident in slight elongations or adjustments of Ga–N and Rh–C bond distances (Table 8).

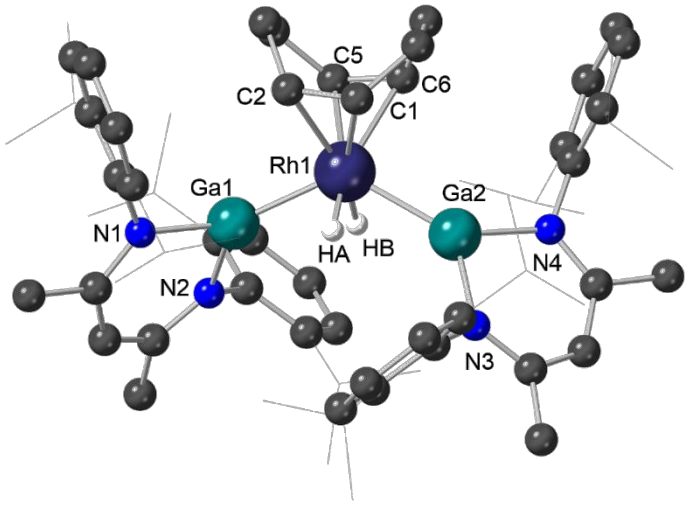


Figure 26. Molecular structure of the cationic fragment of *cis*-[**2₂−Rh(COD)(H)₂**][BAr^F_4]. Hydrogens atoms have been omitted for clarity.

As illustrated in Figure 26, the Rh–C distances to the COD alkene carbons (e.g., Rh1–C1, Rh1–C2) measure around 2.25–2.26 Å, each forming bond-midpoints (C1,C2) and (C5,C6) with Rh–(n,m) lengths of ~ 2.14 Å. The two hydrides, labelled HA and HB, appear at 1.42(5) and 1.52(5) Å from the metal centre, typical for rhodium–hydride linkages. Meanwhile, the Ga1–Rh1 and Ga2–Rh1 separations shorten slightly (2.36–2.37 Å) compared to the original Rh(I)–Ga(I) complexes, reflecting a stronger metal–metal bonding interplay in the higher coordination environment. Ga–N bond lengths remain around 1.95–1.96 Å, and the pseudo-octahedral hydride geometry is confirmed by an HA–Rh1–HB angle of 90(3)°.

Altogether, these metrics substantiate the formation of the Rh(III)–dihydride complex *cis*-[**2₂−Rh(COD)(H)₂**][BAr^F_4] bearing two Ga(I) metalloligands **2**. The transition from square-planar Rh(I) to pseudo-octahedral Rh(III) underscores the successful oxidative addition of H_2 at Rh, facilitated, or at least not precluded, by the presence of the Ga(I) metalloligands **2** in *cis*-[**2₂−Rh(COD)(H)₂**][BAr^F_4].

Table 8. Selected bond lenghts (Å) and angles (º) for *cis*-[**2₂−Rh(COD)(H)₂**][BAr^F_4].

cis-[**2₂−Rh(COD)(H)₂**][BAr^F_4]			
Rh−C	C1 2.252(5)	Rh–(n,m)	(C1,C2) 2.147
	C2 2.258(5)		(C5,C6) 2.144
	C5 2.252(5)	Rh–H	HA 1.42(5)
	C6 2.255(5)		HB 1.52(5)
Rh−Ga	Ga1 2.3633(6)	Ga1–N	N1 1.960(4)
	Ga2 2.3743(6)		N2 1.964(4)
		Ga2–N	N3 1.954(4)
HA–Rh1–HB	90(3)		N4 1.963(4)
Ga1–Rh1–Ga2	126.52(4)	N1–Ga1–N2	94.78(16)
		N3–Ga2–N4	94.31(15)

3.4.3.2 Molecular Structure of *cis*-[**2₂−Rh(η³−C₈H₁₃)(H)**][BAr^F_4]

Another intriguing species isolated from the H_2 reactivity studies is *cis*-[**2₂−Rh(η³−C₈H₁₃)(H)**][BAr^F_4] . Crystallisation was achieved by slow diffusion of *n*-hexane into a fluorobenzene solution of the complex under an H_2 atmosphere at room temperature. The crystals adopted a monoclinic system, $P2_1/n$, analogous to that observed for *cis*-[**2₂−Rh(COD)**][BAr^F_4]. Each asymmetric unit contained the cationic *cis*-[**2₂−Rh(η³−C₈H₁₃)(H)**]$^+$ (Figure 27), the anion [BAr^F_4]$^-$, and co-crystallised fluorobenzene (C_6H_5F) plus half a molecule of *n*-hexane.

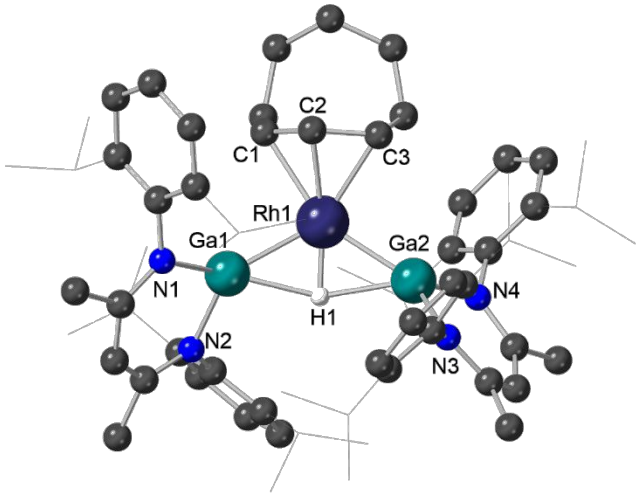


Figure 27. Molecular structure of the cationic fragment of *cis*-[**2₂−Rh(η³−C₈H₁₃)(H)**][BAr$^F_4$]. Hydrogens atoms have been omitted for clarity.

Examination of the *cis*-[**2₂−Rh(η³−C₈H₁₃)(H)**]$^+$ fragment reveals a partial hydrogenation of one COD double bond, forming an allylic moiety (η^3−C_8H_{13}). This outcome implies that, after initial H_2 coordination and ring insertion at Rh, one hydride migrates to an adjacent C=C bond, generating a η^3–allyl species. Notably, both Ga(I)–Rh bonds remain intact throughout, underscoring the robustness of the Ga–Rh interactions. Consequently, the allylic group serves as a mono-olefin chelating ligand in a η^3-C,C'-mode, while the second half of the ring remains unaffected.

Selected parameters are summarised in Table 9. The Ga1–Rh1–Ga2 angle of 117.94(4)° in *cis*-[**2₂−Rh(η³−C₈H₁₃)(H)**]$^+$ is considerably larger than that in the starting *cis*-[**2₂−Rh(COD)**]$^+$ (~ 94°), yet smaller than the 126.5° recorded for the fully dihydrogenated *cis*-[**2₂−Rh(COD)(H)₂**]$^+$. This intermediate angle corroborates an Rh(III) environment but in a five-ligand partial ring-hydrogenation regime, *cis*-[**2₂−Rh(η³−C₈H₁₃)(H)**]$^+$. A single rhodium–hydride (H1) at 1.602(7) Å sits adjacent to both Ga(I) centres, as indicated by the Ga1–H1 and Ga2–H1 distances (2.06–2.03 Å). Meanwhile, the allylic carbon atoms (C1, C2, C3) bond to Rh at 2.14–2.30 Å.

Table 9. Selected bond lengths (Å) and angles (°) for *cis*-[**2₂−Rh(η³−C₈H₁₃)(H)**][BAr^F_4].

cis-[**2₂−Rh(η³−C₈H₁₃)(H)**][BAr^F_4]·$C_9H_{12}F$			
Rh−C	C1 2.300(8)	Rh−H	H1 1.602(7)
	C2 2.141(8)	Ga1−H	H1 2.063(7)
	C3 2.264(9)	Ga2−H	H1 2.03(6)
Rh−Ga	Ga1 2.3317(7)	Ga1−N	N1 1.942(4)
	Ga2 2.3355(10)		N2 1.949(4)
		Ga2−N	N3 1.945(4)
			N4 1.952(4)
C1−C2−C3	63.2(5)	N1−Ga1−N2	95.44(16)
Ga1−Rh1−Ga2	117.94(4)	N3−Ga2−N4	95.11(17)

These metrics reinforce the notion that *cis*-[**2₂−Rh(η³−C₈H₁₃)(H)**]$^+$ forms *via* an intramolecular hydride shift after H_2 splitting in *cis*-[**2₂−Rh(COD)(H)₂**]$^+$, resulting in a stable allylic ligand plus a single hydride. Crucially, the double Ga(I)–Rh(I) linkage remains unaffected, highlighting how the bimetallic scaffold endures partial ring hydrogenation and rearrangements. The structure of *cis*-[**2₂−Rh(η³−C₈H₁₃)(H)**]$^+$, along with the dihydride counterpart *cis*-[**2₂−Rh(COD)(H)₂**]$^+$, exemplifies the multistep transformations accessible in this interesting heterometallic Ga(I)–Rh(I) system, confirming that these Ga(I)–Rh(I) complexes can navigate partial as well as complete hydrogenation pathways. In addition, the *cis*-[**2₂−Rh(η³−C₈H₁₃)(H)**]$^+$ structure underscores the flexible reactivity of Ga(I)–Rh(I) complexes upon H_2 treatment, capturing a key allylic intermediate *en route* to the fully hydrogenated dihydride state. Such multistep partial ring saturation, facilitated by main-group–transition-metal synergy, is a testament to the robustness and tunability of the heterobimetallic Ga(I)–Rh(I) framework.

3.4.4 Speciation/Stability Mass Spectroscopic Studies with H_2

A valuable complementary technique for characterising the Ga(I)–Rh(I) complexes *cis*-[**2₂−Rh(NBD)**][BAr^F_4] and *cis*-[**2₂−RhCOD**][BAr^F_4] under H_2 conditions is high-resolution electrospray ionization mass spectrometry (HRMS-ESI). Employing a quadruple time-of-flight instrument (QTOF HRMS-ESI) allows precise determination of molecular ion peaks, confirming both empirical formulae and isotopic patterns.

3.4.4.1 HRMS of *cis*-[**2₂−Rh(NBD)**][BAr^F_4] and *cis*-[**2₂−Rh(COD)**][BAr^F_4]

To evaluate the intactness of the as-synthesized bimetallic cations *cis*-[**2₂−Rh(NBD)**]$^+$ and *cis*-[**2₂−Rh(COD)**]$^+$, 1 mg of each [BAr^F_4]$^-$ compound was placed in a 1.5 mL glass vial under inert conditions, diluted with 1 mL fluorobenzene (C_6H_5F), and subsequently subjected to two further 1:2 dilutions prior to direct infusion.

For *cis*-[**2₂−Rh(NBD)**][BAr^F_4] the resulting spectrum displays three major cationic peaks. The most intense (100% intensity) at m/z = 1169.4733 corresponds to *cis*-[**2₂−Rh(NBD)**]$^+$ (calcd. m/z = 1169.4730), and its simulated isotopic distribution matches well with the experimental pattern, indicative of Rh/Ga presence (Figure 28, top). Two lower-intensity peaks at m/z = 419.3413 (~ 35%) and m/z = 613.3010 (~ 35%) were ascribed, respectively, to [$BDI(H)_2$]$^+$ (calcd. m/z = 419.3421) and [(BDI)Rh(NBD)(H)]$^+$ (calcd. m/z = 613.3023). Such species likely arise from partial ligand fragmentation or metal–ligand rearrangements under ESI conditions.

Likewise, *cis*-[**2₂−Rh(COD)**][BAr$^{F}_{4}$] exhibits three major peaks at m/z = 419.3419, 629.3322, and 1185.5029. The heaviest ion peak (1185.5029) coincides with *cis*-[**2₂−Rh(COD)**]$^{+}$ (calcd. m/z = 1185.5043), confirming the presence of the intact bimetallic cation. The remaining two signals again correspond to [BDI(H)$_2$]$^{+}$ (calcd. 419.3421) and [(BDI)Rh(NBD)(H)]$^{+}$ (calcd. 629.3336), Figure 28 (bottom).

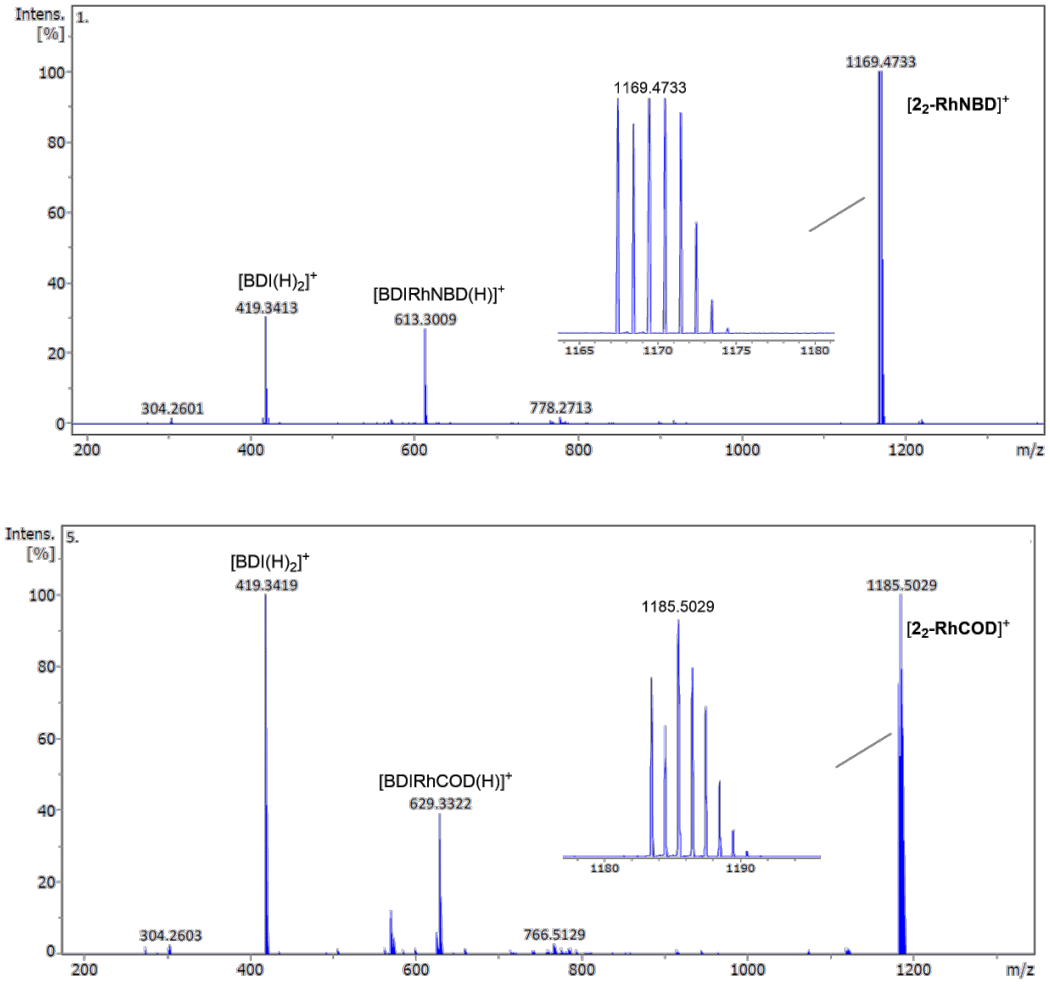


Figure 28. Overview of high-resolution positive-mode ESI-MS for crystalline *cis*-[**2₂−Rh(NBD)**][BAr$^{F}_{4}$] (top) and *cis*-[**2₂−Rh(COD)**][BAr$^{F}_{4}$] (bottom).

3.4.4.2 *In-Situ* Reaction Monitoring by HRMS of *cis*-[2_2−Rh(NBD)][BAr^F_4] and *cis*-[2_2−Rh(COD)][BAr^F_4] with H_2

With the dihydrogen activation experiments, we likewise pursued in-situ ESI-MS to detect potential Rh–H or Rh–(H_2) species. Hence, 3 mg of either *cis*-[**2_2−Rh(NBD)**][BAr^F_4] or *cis*-[**2_2−Rh(COD)**][BAr^F_4] was dissolved in 0.5 mL fluorobenzene (C_6H_5F) under inert conditions in an NMR tube (J. Young valve). After freeze-pump-thaw degassing, 1.5 bar H_2 was introduced, and the solution was stirred for ∼ 5 min at 298 K, yielding a near-colourless mixture. An aliquot (100 µL) was then transferred to a 1.5 mL vial containing 0.5 mL of C_6H_5F before immediate injection into QTOF HRMS-ESI (positive mode).

The *in-situ* reaction of *cis*-[**2_2−Rh(NBD)**][BAr^F_4] with H_2, despite forming hydrides in solution (as indicated by NMR), the HRMS spectrum showed no direct Rh(III)–hydride cation peaks. Instead, multiple adduct ions with alkali metals (Na^+, K^+) were present, e.g., [2_2−Rh(C_6H_5F)$(H)_n$Na]$^+$ or [2_2−Rh(C_6H_5F)$(H)_n$K]$^+$ (n = 2–3). Additionally, the [BDI$(H)_2$]$^+$ fragment reappears (m/z = 419.3437). The presence of these aggregates suggests that, under ESI conditions, the initially formed Rh–H species rearranges or fragments, possibly losing the direct H_2 adduct signature.

In contrast, the H_2-activated solution of *cis*-[**2_2−Rh(COD)**]$^+$ displays a prominent new peak at m/z = 1187.5254 (∼ 71% intensity), assigned to *cis*-[**2_2−Rh(COD)$(H)_2$**]$^+$ (calcd. m/z = 1187.5200). Its experimentally measured isotopic pattern aligns well with the theoretical distribution, attesting to a stable Rh(III)–dihydride. As before, the fragment ions [BDI$(H)_2$]$^+$ and [(BDI)Rh(COD)(H)]$^+$ arise at m/z = 419.3466 and 629.3343, respectively, with intensities of 100% and 54% (Figure 29, top).

When *cis*-[**2_2−Rh(COD)**][BAr^F_4] is treated with D_2 under the same conditions, an analogous peak emerges at m/z = 1189.5338 (∼ 70% intensity), matching *cis*-[**2_2−Rh(COD)$(D)_2$**]$^+$ (calcd. 1189.5357). Again, [BDI$(H)_2$]$^+$ and related fragments appear as secondary peaks, Figure 29 (bottom). This result, along with the NMR data, corroborates that the bimetallic cation tolerates partial or complete substitution of H by D while remaining structurally intact.

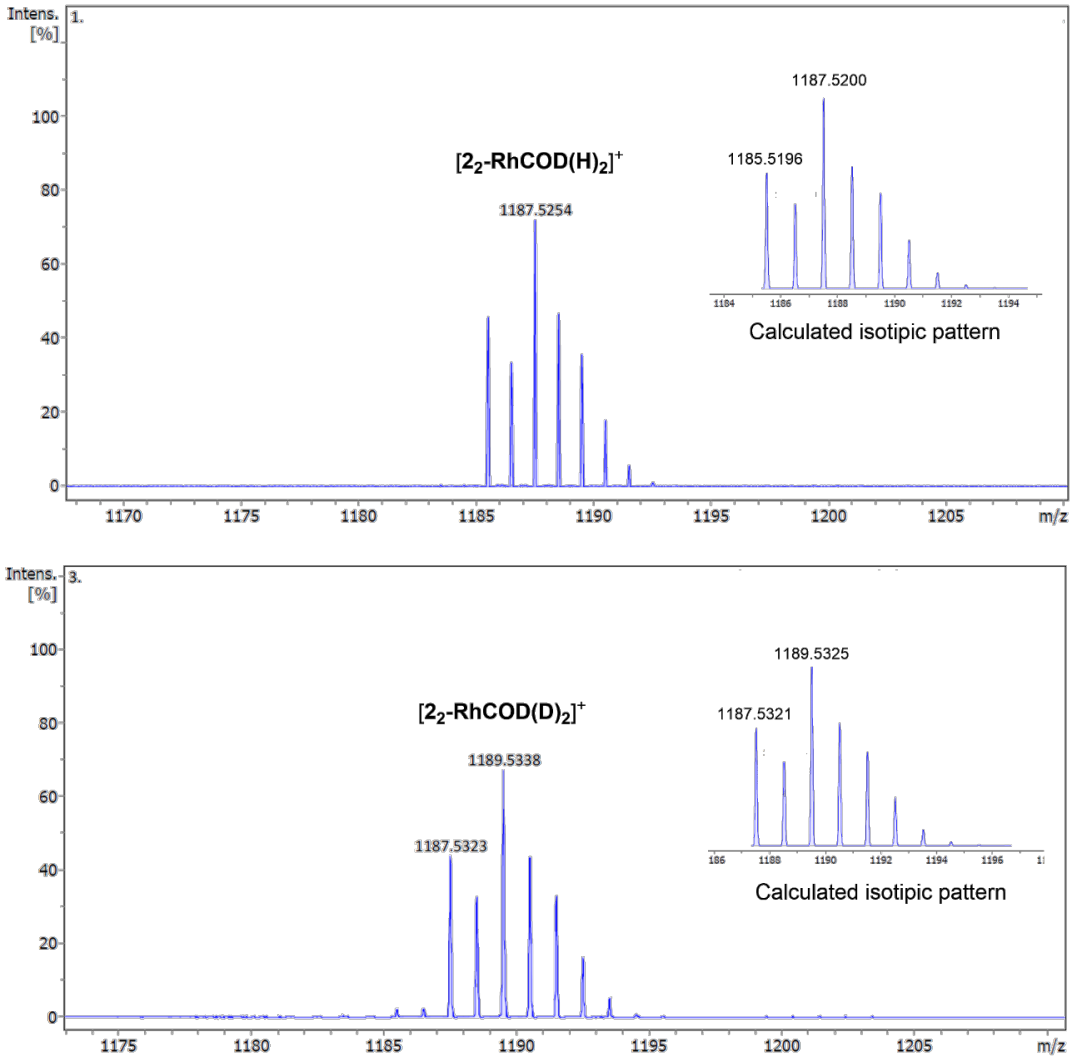


Figure 29. Positive-mode ESI-MS from *in-situ* H_2 (top) or D_2 (bottom) activation of *cis*-[**2₂−Rh(COD)**][BAr^F_4]. The dihydride or dideuteride cations are visible at m/z = 1187.5254 (H) and 1189.5338 (D).

Lastly, a fluorobenzene solution of the allylic intermediate *cis*-[**2₂−Rh(η³−C₈H₁₃)(H)**][BAr^F_4] likewise yields a major peak at m/z = 1187.5077 (~ 64% intensity), consistent with both the dihydride *cis*-[**2₂−Rh(COD)(H)₂**]⁺ and the allyl–hydride [**2₂−Rh(η³−C₈H₁₃)(H)**]⁺, since each shares the same stoichiometry. Minor traces of the original [**2₂−Rh(COD)**] are also detected, along with the usual BDI-based fragments. Hence, the allylic species is also partially or wholly converted under ESI conditions, reflecting the dynamic equilibrium observed by NMR.

Overall, our HRMS-ESI speciation studies with H_2 confirms that both Ga(I)–Rh(I) starting materials *cis*-[**2₂−Rh(NBD)**][BAr^F_4] and *cis*-[**2₂−RhCOD**][BAr^F_4] and their H_2-activated dihydride *cis*-[**2₂−Rh(COD)(H)₂**][BAr^F_4] or allylic *cis*-

[**2₂−Rh(η³−C₈H₁₃)(H)**][BAr$^F_4$] derivatives remain detectable in the gas phase, albeit accompanied by partial fragmentation or alkali-metal adduct formation. For the NBD system, direct observation of a dihydride cation is hampered by competing decomposition pathways under the ionization HRMS conditions. Conversely, the COD derivative cleanly generates a high-intensity *cis*-[**2₂−Rh(COD)(H)₂**]$^+$ peak and switching to D_2 reveals the analogous dideuteride *cis*-[**2₂−Rh(COD)(D)₂**]$^+$. These results underscore the robustness of the Ga(I)–Rh(I) framework, persisting through both solution- and gas-phase manipulations.

3.4.5 Catalytic Hydrogenation of Olefins by the Heterometallic Ga(I)–Rh(I) Species

Drawing on the speciation and stability studies of our bimetallic Ga(I)–Rh(I) complexes, their potential as hydrogenation catalysts for di- and polyolefins emerged. Indeed, *cis*-[**2₂−Rh(NBD)**][BAr$^F_4$] and *cis*-[**2₂−Rh(COD)**][BAr$^F_4$] were individually tested and monitored by NMR spectroscopy in hydrogenation reactions under mild conditions, aiming to assess selectivity, reaction times, and potential over-hydrogenation pathways.

The *cis*-[**2₂−Rh(NBD)**][BAr$^F_4$] species, as noted earlier, readily decomposes upon reacting with H_2, forming transient Rh(III)–hydride/dihydrogen intermediates that lack long-term stability. Nonetheless, these highly reactive intermediates effectively hydrogenate a range of polyolefins to the fully saturated alkane stage. In contrast, *cis*-[**2₂−Rh(COD)**][BAr$^F_4$] fosters a set of well-defined Rh–H species that exhibit partial hydrogenation in certain di- and polyolefins. Thus, selectivity arises particularly for non-conjugated π-systems, while substrates with conjugated double bonds undergo complete hydrogenation to the alkane product.

All catalytic runs employed fluorobenzene (C_6H_5F) as the solvent (due to excellent solubility for the Ga(I)–Rh(I) complexes and the minimal side reactivity with the solvent). Other aromatic solvents like benzene or toluene were unsuitable because *cis*-[**2₂−Rh(COD)**][BAr$^F_4$] and its analogues showed limited solubility therein. Likewise, CH_2Cl_2 or THF were avoided due to potential undesired reactivity (e.g., oxidative addition toward C–Cl and/or C–O bonds at CH_2Cl_2 or THF).[65] Catalyst loadings of 10, 5, and 3.5 mol% gave similar outcomes by ^{1}H NMR monitoring, so 3.5 mol% was chosen. Hydrogen pressures from 0.5 to 2.0 bar were also tested. We observed that below 1.5 bar, incomplete hydrogenation and partially

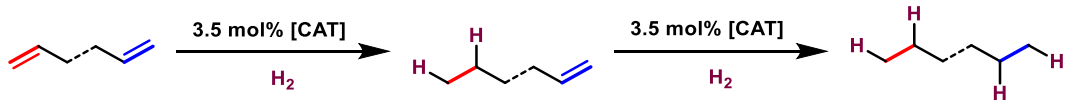
hydrogenated species persisted, whereas 2.0 bar enhanced either partial or full hydrogenation, depending on the substrate.

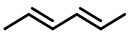
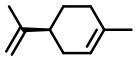
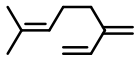
Thus, a typical run involved charging a J. Young NMR tube with 3.5 mol% *cis*-[**2₂−Rh(COD)**][BAr^F_4], and ~ 0.35 mL of fluorobenzene, followed by 0.065 mmol of the chosen polyolefin. After an initial ^1H NMR spectrum (t = 0), the sample was freeze-pump-thawed, then exposed to 2.0 bar of H_2. Subsequent ^1H NMR acquisitions (t = 5 min, 15 min, etc.) tracked substrate consumption and product formation. Where possible, known partial hydrogenation products were matched to reference ^1H NMR data, while more complex species (e.g., *R*–(+)–limonene, myrcene) were assigned by comparison to literature values.[66]

For 1,5-COD, roughly 60% conversion to the mono-alkene (COE = cyclooctene) was observed, with 10% cyclooctane (COA) and 30% unreacted COD at equilibrium (Table 10). Conversely, 1,3-COD (bearing a conjugated system) was fully hydrogenated to COA, reflecting how the Ga(I)–Rh(I) pre-catalyst, *cis*-[**2₂−Rh(COD)**][BAr^F_4], fosters complete hydrogenation of conjugated diene moieties. A similar pattern emerged for linear 2,4-hexadiene (conjugated), which was converted to *n*-hexane in 95% conversion (Table 10, entry 7). By contrast, more non-conjugated dienes tended to yield a significant proportion of partially hydrogenated alkene prior to further saturation, highlighting partial selectivity.

Extended tests of *cis*-[**2₂−Rh(COD)**][BAr^F_4], and H_2 used R–(+)–limonene and myrcene, revealing selective hydrogenation of external double bonds while internal or ring alkenes remained intact (Table 10, entries 8 and 9). For example, limonene gave 72% partially hydrogenated product (entry 8), and myrcene gave 46% partial hydrogenation (entry 9), consistent with a preference for less substituted (exocyclic or terminal) alkenes.

Table 10. Catalytic hydrogenation studies of poly-olefins.[a]



Entry	Substrate	Mono-alkene (%)	Alkane (%)
1		61	12
2		0	55
3		60	9
4		73	27
5		0	82
6		0	90
7		0	95
8	 R-(+)-limonele	72	28
9	 Myrcene	46	54

[a] All the experiments were carried out 298 K under continuous stirring with H_2 (2 bar) in fluorobenzene (C_6H_5F) and *cis*-[**2_2−Rh(COD)**][BAr^F_4] as pre-catalyst. The conversions (%) were obtained by referencing the integration of the ^{1}H NMR signals corresponding to the substrates and compounds with respect the those of BAr^F_4 which remained unchanged during the transformation and was used as internal standard.

Using 1,5-COD as a model substrate, repeated NMR sampling over 7 h traced substrate transformation for kinetic monitoring. After ~ 4 h, < 50% COD remained, ~ 40% cyclooctene formed, and ~ 10% cyclooctane was evident. By ~ 7 h, 60% cyclooctene was the maximum partial hydrogenation yield, with ~ 30% COD and ~ 10% cyclooctane (Figure 30). No signs of catalyst decomposition were observed throughout, and poisoning tests with Hg(0) or S(elemental) did not inhibit the reaction, implying a homogeneous mechanism.[67]

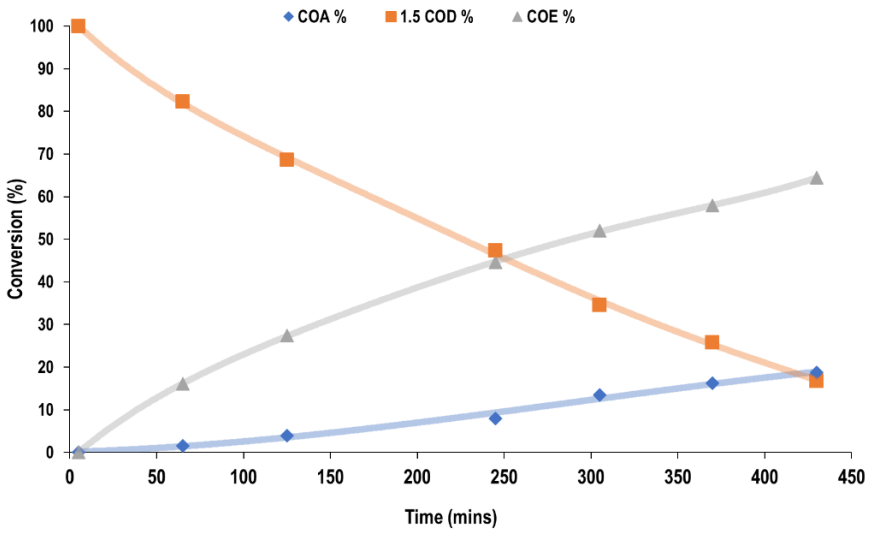
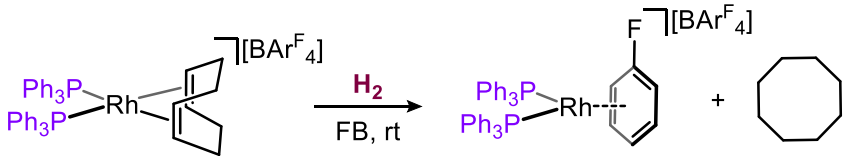


Figure 30. Time-resolved hydrogenation as monitored by ^{1}H NMR for the hydrogenation of 1,5-COD into COE and COA (%) using the pre-catalyst *cis*-[**2$_2$−Rh(COD)**][BAr$^F{}_4$] with H_2 gas (2 bar) at 298 K over a period of 7 hours. The conversions (%) were obtained by referencing the integration of the ^{1}H NMR signals corresponding to COD, COE and COA with respect to those of BAr$^F{}_4$ which remained unchanged during the transformation and was used as internal standard.

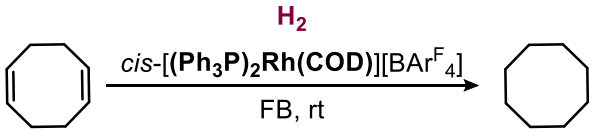
On the other hand, attempted NHC-bearing analogues proved unworkable, with [**Rh(olefin)$_2$**]$^+$ species decomposing in the presence of IPr or related carbenes. Meanwhile, a *cis*-[**(PPh$_3$)$_2$Rh(COD)**][BAr$^F{}_4$][56] was tested in these catalytic hydrogenation trials. Under H_2 in fluorobenzene, the *cis*-[**(PPh$_3$)$_2$Rh(COD)**][BAr$^F{}_4$] complex rapidly hydrogenates COD to COA and coordinates the solvent (η^6–C_6H_5F), Scheme 11A, forming an stable rhodium–arene adduct *cis*-[**(PPh$_3$)$_2$Rh(η^6–C$_6$H$_5$F)**][BAr$^F{}_4$] in solution as verified by NMR and X-ray crystallography. Using *cis*-[**Rh(COD)(PPh$_3$)$_2$**][BAr$^F{}_4$] as a hydrogenation pre-catalyst for 1,5-COD gave full hydrogenation to COA in timescales similar to *cis*-[**2$_2$−Rh(COD)**][BAr$^F{}_4$], but no partial selectivity towards the mono-olefin COE product was observed (Scheme 11B). This underscores that the Ga(I)–Rh(I) system *cis*-[**2$_2$−Rh(COD)**][BAr$^F{}_4$] can retain COD for a selective partial hydrogenation to COE, whereas phosphine-ligated Rh species *cis*-[**Rh(COD)(PPh$_3$)$_2$**][BAr$^F{}_4$] tends to fully hydrogenate COD to COA without selectivity for COE.

A) *Stability and Speciation Study*



cis-[**(Ph$_3$P)$_2$Rh(COD)**][BAr$^F_4$] *cis*-[**(Ph$_3$P)$_2$Rh(η^6-C$_6$H$_5$F)**][BAr$^F_4$]

B) *Hydrogenation Study of 1,5-COD Substrate*



Scheme 11. A) Speciation of *cis*-[**(Ph$_3$P)$_2$Rh(COD)**][BAr$^F_4$] with H_2 in fluorobenzene forming *cis*-[**(PPh$_3$)$_2$Rh(η^6–C$_6$H$_5$F)**][BAr$^F_4$]. B) Hydrogenation of 1,5-COD with *cis*-[**(Ph$_3$P)$_2$Rh(COD)**][BAr$^F_4$] yielding complete hydrogenation to cyclooctane (COA).

Hence, the bimetallic *cis*-[**2$_2$−Rh(COD)**][BAr$^F_4$] species emerges as a versatile pre-catalyst for selective partial hydrogenation of non-conjugated polyolefins, as well as complete hydrogenation of conjugated systems. Enhanced stability for mono-olefins, combined with the capacity to form stable Rh(III)–dihydride species *cis*-[**2$_2$−Rh(COD)(H)$_2$**]$^+$ or ephemeral allylic intermediates *cis*-[**2$_2$−Rh(η^3−C$_8$H$_{13}$)(H)**]$^+$, underscores the distinct reactivity profile conferred by main-group–transition-metal synergy.

3.4.6 Computational Mechanistic Insights

To elucidate a mechanistic rationale aligned with the experimental observations described above, Density Functional Theory (DFT) studies were undertaken in collaboration with Prof. Agustí Lledós at the Universitat Autònoma de Barcelona (UAB). Specifically, attention focused on how *cis*-[**2₂−Rh(COD)**][BAr^F_4] mediates H_2 activation and the subsequent hydrogenation of 1,5-COD *vs.* 1,3-COD, with emphasis on energetic barriers, key intermediates, and observed selectivity outcomes.

Initially, the *cis*-[**2₂−Rh(COD)**]$^+$ cation was optimized from the single-crystal X-ray coordinates for benchmarking, confirming a good match with experimental metrics. For instance, the Ga1–Rh1–Ga2 angle is 92.2° in the DFT model, compared to 94.9° measured crystallographically, suggesting a predominantly square-planar Rh(I) environment (Figure 31). This validated starting point then served as the computational reference for examining hydrogenation pathways on COD.

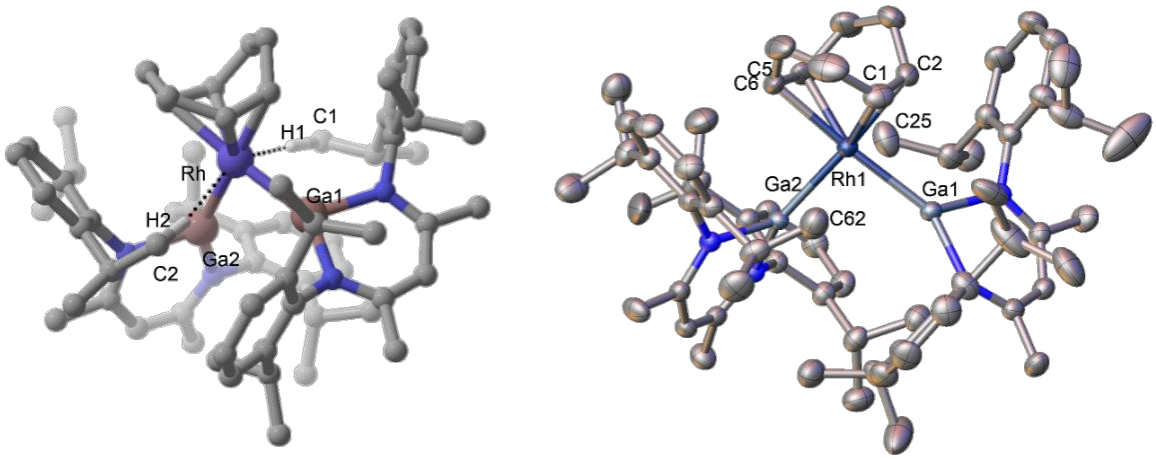


Figure 31. From left to right: Selected bond lengths (Å) and angles (º) of optimised structure of *cis*-[**2₂−Rh(COD)**]$^+$ Rh-Ga1 2.420, Rh-Ga2 2.433, Rh-H1 2.736, Rh-H2 2.683, Ga1-Rh-Ga2 92.2 and for the molecular structure from the same cation Rh1-Ga1 2.425 (2), Rh1-Ga2 2.421(3), Ga1-Rh1-Ga2 94.93(2).

From the DFT reaction profile, 1,5-COD activation proceeds via initial coordination of an H_2 molecule at the square-planar bimetallic fragment *cis*-[**2₂−Rh(COD)**]$^+$, homolysis of the H–H bond to give a dihydride Rh(III)–H species *cis*-

[**2₂−Rh(COD)(H)₂**]⁺, and subsequent stepwise transfer of hydrides onto the COD ligand (COD→COE). The highest energy transition state in this first partial hydrogenation step is ~ 20 kcal/mol (Figure 32), while the product (Rh(I)–COE) is energetically favourable at about −8.5 kcal/mol. A second H_2 addition can similarly proceed, culminating in full hydrogenation to cyclooctane (COE→COA). However, if unconverted COD remains in solution, the Rh(I)–COE intermediate can be displaced by fresh COD, effectively arresting the transformation at the partially hydrogenated stage. Thus, as the COD substrate concentration drops, the second hydrogenation step dominates, ultimately leading to COA.

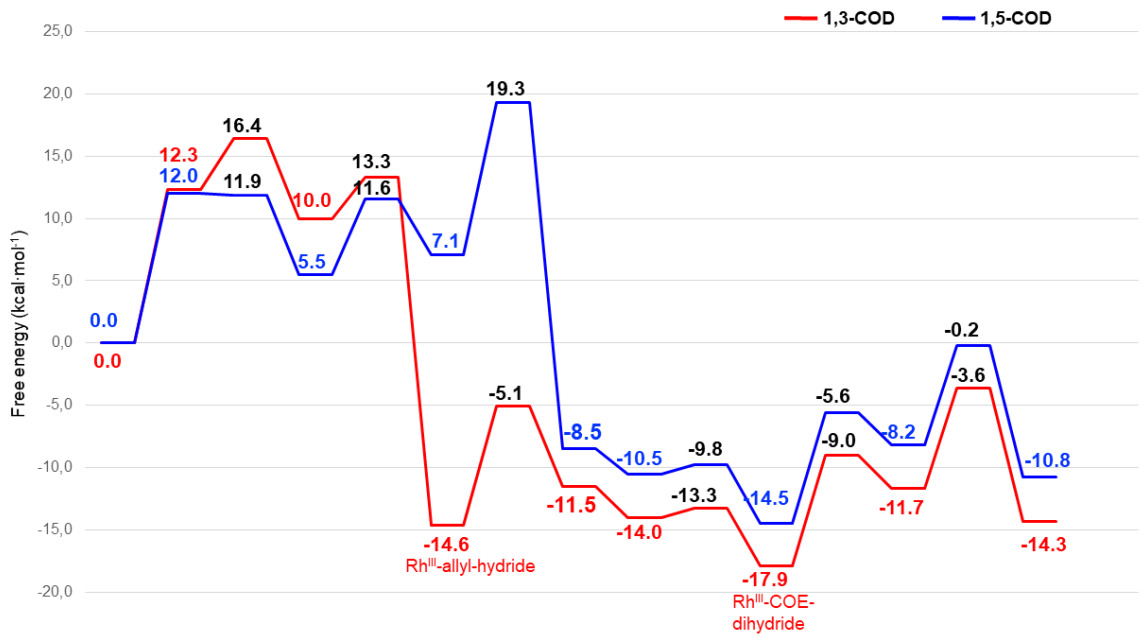


Figure 32. Schematic DFT energy comparison for 1,5-COD (red trace) *vs.* 1,3-COD (blue trace) hydrogenation steps via *cis*-[**2₂−Rh(COD)**]⁺.

By contrast, 1,3-COD (with a conjugated diene) exhibits a significantly lower-energy intermediate upon initial hydride transfer, forming a Rh–allyl species at ~ −14.6 kcal/mol, which stabilizes the pathway toward complete hydrogenation to COA. As a result, conjugated diene hydrogenation becomes more thermodynamically favoured, aligning with experimental observations that 1,3-COD is fully reduced to COA without observing the formation of COE, in contrast to 1,5-COD.

Interestingly, none of the X-ray-identified Rh(III)–dihydride *cis*-[**2₂–Rh(COD)(H)₂**]⁺ or allylic [**2₂–Rh(η³–C₈H₁₃)(H)**]⁺ structures appear directly along the minimal DFT hydrogenation pathway, being off-cycle species connected within the reaction pathway (Figure 33). Instead, as the computational model suggests, the on-cycle dihydride intermediate is only ~ 5.5 kcal/mol above reference but does not match the geometry or bond metrics of the isolated *cis*-[**2₂–Rh(COD)(H)₂**]⁺. Subsequent intramolecular rearrangements can transform the on-cycle dihydride into the off-cycle geometry observed crystallographically. This reconfiguration is estimated to have a small barrier of ~ 9.9 kcal/mol, delivering a lower-energy dihydride species consistent with the experimental *cis*-[**2₂–Rh(COD)(H)₂**]⁺. A similar scenario accounts for the allylic *cis*-[**2₂–Rh(η³–C₈H₁₃)(H)**]⁺ species, which could form off-cycle via hydride migration to generate an η³–allyl moiety.

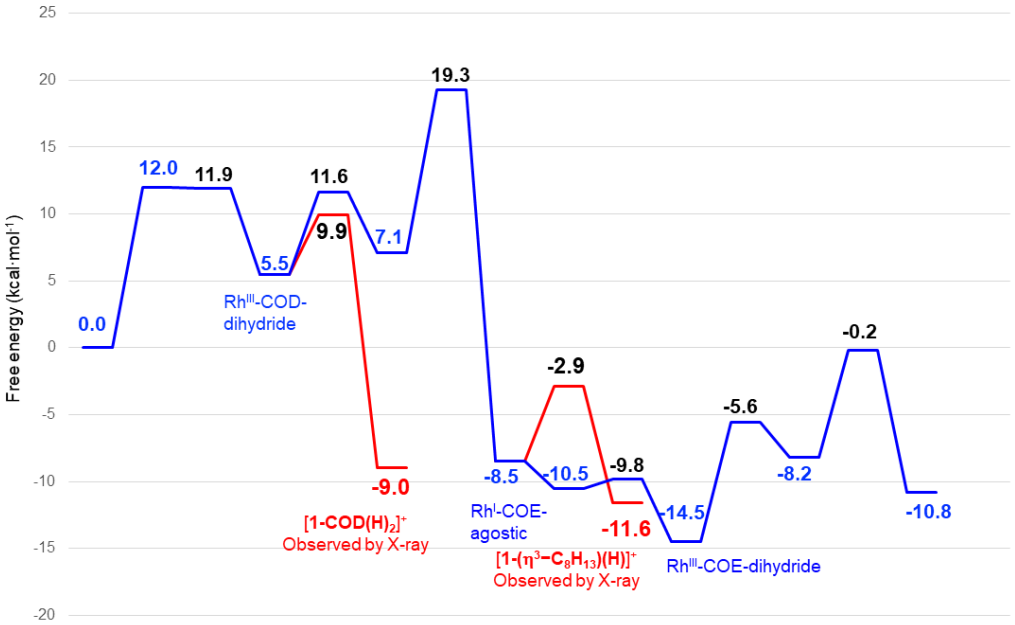


Figure 33. DFT-derived Gibbs free-energy profile for 1,5-COD hydrogenation, contrasted with the experimentally isolated *cis*-[**2₂–Rh(COD)(H)₂**]⁺ and *cis*-[**2₂–Rh(η³–C₈H₁₃)(H)**]⁺ states. The latter two are off-cycle but energetically more stable.

Finally, the bridging involvement of the two β-diketiminate ligands **2** in stabilising these rearranged dihydride *cis*-[**2₂–Rh(COD)(H)₂**]⁺ or allylic *cis*-[**2₂–Rh(η³–C₈H₁₃)(H)**]⁺ forms is non-trivial. The DFT data indicate additional

Ga···H interactions can lower the rearrangement barriers and favour the formation of off-cycle stable species. As illustrated in Figure 34, the hydride exchange or allyl formation steps are facilitated by Ga(I) Lewis-acid character through the Ga–Rh metal–metal interaction.

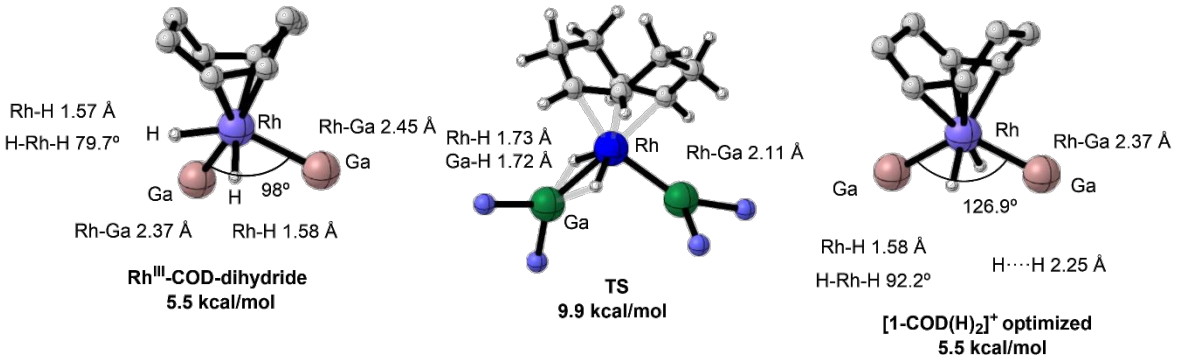


Figure 34. Proposed fluxional interconversion of the on-cycle dihydride to the off-cycle *cis*-[**2₂−Rh(COD)(H)₂**]$^+$ geometry, involving Ga···H contacts. Key optimized distances (Å) and angles (°) mirror those measured in X-ray data: Rh-Ga 2.3633(6)/2.3743(6), Rh-H 1.42(5)/1.51(5), Ga-Rh-Ga 126.53(2), H-Rh-H 90(3).

In summary, the DFT analysis supports a mechanism in which *cis*-[**2₂−Rh(COD)**]$^+$ initially activates H_2 to give the species *cis*-[**2₂−Rh(COD)(H)₂**]$^+$ which partially hydrogenates COD to COE, and cycles repeatedly if the concentration of COD is high enough. By contrast, 1,3-COD forms a stabilized allylic intermediate favouring full hydrogenation. The isolated hydride *cis*-[**2₂−Rh(COD)(H)₂**]$^+$ or allylic *cis*-[**2₂−Rh(η³−C₈H₁₃)(H)**]$^+$ complexes correspond to off-cycle conformations, accessible *via* small rearrangement barriers further stabilized by Ga(I)–Rh(I) interactions. This synergy between main-group gallium and transition-metal rhodium fosters unique selectivity and off-cycle states that rationalize the experimental hydrogenation outcomes.

3.5 Conclusions

In *Chapter III*, we introduced a new class of heterobimetallic systems combining β-diketiminate-supported Ga(I) carbene analogues and Rh(I) frameworks bearing diolefin/amine moieties. By tailoring the Rh precursor (COD or NBD) and exploiting *cis*-ligation of two Ga(I) "metalloligand" fragments, we assembled square-planar Rh(I) species that remain robust under inert conditions, enabling systematic exploration of their H_2-activation capabilities and catalytic reactivity. Detailed NMR and single-crystal X-ray diffraction studies revealed that exposure to H_2 transforms the original Rh(I)–Ga(I) complex into Rh(III)–hydride or Rh(III)–allyl intermediates, with the codified interplay between Ga(I) and Rh often stabilizing fleeting species *en route* to partial or full hydrogenation of coordinated olefins.

Critically, the NBD-based complex undergoes rapid NBD hydrogenation and subsequent decomposition, thereby hampering controlled hydrogenation. In contrast, the COD-based derivatives give rise to well-defined Rh(III)–dihydride complexes, including partially hydrogenated allyl intermediates that persist in solution or crystallize. These findings establish that Ga(I) remains intimately bonded to Rh throughout the hydrogenation events, shaping an unusual Ga(I)–Rh synergy wherein Ga(I)-carbene-ligand help stabilize hydride transfers at Rh. Additionally, time-resolved NMR experiments confirm that codirected partial hydrogenation is possible, with the outcome (mono-alkene *vs.* fully hydrogenated product) governed by the ratio of substrate, catalyst loading, and H_2 pressure. Comparative trials with phosphine-based Rh complexes, as well as attempts to incorporate classical NHC ligands, highlight the notable stability and distinct reactivity of the Ga(I)–Rh(I) platform, underscoring the potential for main-group–transition-metal cooperativity beyond that typically seen in conventional phosphine- or NHC-ligated systems.

Lastly, DFT studies provided mechanistic perspectives on how H_2 is cleaved and shuttled onto the diolefin, corroborating the experimental detection of hydride and allyl intermediates, yet also indicating that the "*off-cycle*" dihydride and allyl complexes isolated here lie in lower-energy minima than the "*on-cycle*" species along the computed catalytic pathway. Overall, these Ga(I)–Rh(I) complexes showcase an original form of bimetallic reactivity. By demonstrating partial hydrogenation selectivity, structural fluxionality, and high stability under mild conditions, this work paves a path for innovative dual-metal approaches to hydrogenation and small-

molecule activation, broadening both the chemistry of electron-rich Ga(I) and the toolkit for advanced main-group–transition-metal catalysis.

3.6 Experimental Methods

Herein a representative characterisation of the molecules is showing, further details are specified in the Annexes attached to this thesis.

3.6.1 Materials

All experiments were carried out under an inert atmosphere of nitrogen gas in a glove box (MBraun, Labmaster SP) or by using standard Schlenk techniques. *n*-Hexane was dried over Na/benzophenone and stored under an atmosphere of nitrogen gas over K mirror. Fluorobenzene (FB) was stirred over Al_2O_3 for two hours before stirring over CaH_2 overnight, vacuum distillation, and subsequent three-fold freeze-pump-thawing and stored under an atmosphere of nitrogen gas over 3Å molecular sieves. Dichloromethane (DCM, CH_2Cl_2) was stirred over CaH_2 overnight, vacuum distillation, and subsequent three-fold freeze-pump-thawing, then stored under atmosphere of nitrogen gas over molecular sieves (3 Å). Deuterated dichloromethane (CD_2Cl_2) was dried with CaH_2, distilled under low pressure (< 1 × 10^{-2} mbar) and stored under an atmosphere of nitrogen gas over molecular sieves (3 Å). 1,5-Cyclooctadiene (COD), cyclooctane (COA), 1,4-cyclohexadiene, cycloheptatriene, 1,3-cycloheptadiene, cycloheptene, cycloheptane, 2.4-hexadiene (mixture of isomers), 2-hexene (*cis/trans*), R-(+)-limonene and myrcene were purchased from Merck, stored in a fridge at 4°C, and used as received. 2,5-Norbornadiene (bicyclo[2.2.1]hepta-2,5-diene, NBD), *cis*-cyclooctene (COE), cyclohexene and cyclohexane were purchased from Alfa Aesar, stored in a fridge at 4°C, and used as received. *n*-Hexane was purchased from Scharlab and used as received. $[Rh(COD)_2][BAr^F{}_4]$,[53a] $[Rh(NBD)_2][BAr^F{}_4]$[53c] and BDIGa[68] were prepared according to reported procedures.

NMR experiments were conducted in J. Youngs tap NMR tubes prepared and sealed under nitrogen. Multinuclear NMR spectra were collected on either a Bruker AVIIIHD 400 nanobay (equipped with a 9.4 tesla magnet) or Bruker AVIII 500 (equipped with 11.7 tesla magnet and a Prodigy cryoprobe) spectrometer at 298 K unless otherwise stated. Non-deuterated solvent fluorobenzene was locked to standard external 10% fluorobenzene in C_6D_6 sample solution. Assignments of NMR resonance signals in the ^1H and $^{13}C\{^1H\}$ NMR spectra were made with the help of two-*d*imensional NMR experiments (^1H,^1H-COSY, ^1H,^{13}C-HSQC, ^1H,^{13}C-HMBC). ^1H 1D Selective Gradient NOE NMR experiment was performed irradiating at -14.26

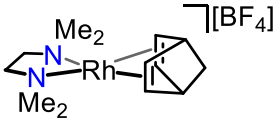
ppm in a mixing time of 500 ms. The ^{2}H NMR data were collected with either Bruker AVIIIHD 400 nanobay operating at 61.4 MHz or the Bruker AVIII 500 Prodigy cryoprobe operating at 76.1 MHz. The conventional inversion-recovery method (180°-τ-90°) was used to determine the longitudinal-relaxation T_1 times. Chemical shifts (δ) are reported in parts per million (ppm) and referenced the residual solvent resonances. Coupling constants (J) are given in Hertz (Hz). Signal multiplicities are abbreviated as follows: s (singlet), d (doublet), sept (septet), m (multiplet) and br (broad).

CHN elemental microanalysis were carried out at the elemental analysis services (strictly air sensitive procedures) using a ThermoFlash 2000 Elemental Analyzer from the Metropolitan University of London or a Perkin Elmer 2400 Series II CHNS/O Analyzer from the Central Scientific Services from CIQSO-University of Huelva. The CHN combustion analysis was performed on crystalline or microcrystalline materials. Representative values for the organometallic species are included in the characterization data. Despite efforts to maintain the bulk purity of the compounds, some compounds failed to meet the ± 0.4% accuracy criteria. These difficulties with CHN combustion analysis are well documented and understood.[69]

Electrospray ionization high resolution mass spectrometry (HRMS-ESI) was carried out using a Bruker Compact QToF. Typical acquisition parameters were used (sample flow rate: 3 μL min^{-1}, nebulizer gas pressure: 0.3 bar, drying gas: nitrogen at 200 K flowing at 3 L min^{-1}, capillary voltage: 3.5 kV, exit voltage: 0.5 kV). The spectrometer was calibrated using a mixture of sodium formates $[Na(NaCOOH)_n]Br$ (n = 1-22) in methanol. Samples were diluted to a concentration of *ca.* < 1 × 10^{-6} M in dry fluorobenzene under inert atmosphere of nitrogen gas using 1.5 mL glass vials capped with appropriate septum and then sampled by direct infusion using a 500 μL gas tight syringe.

3.6.2 Synthesis and Characterisation of Rhodium(I) Diamino Complexes

3.6.2.1 Synthesis and Characterisation of [(TMEDA)Rh(NBD)][BF_4]



One J. Young's ampoule was charged $[Rh(NBD)_2][BF_4]$ (50 mg, 0.134 mmol) and dissolved in CH_2Cl_2 (3 mL). Then, the amine *N,N,N′,N′*−tetramethylethylenediamine (TMEDA) (21 μL, 0.140 mmol) was added dropwise with vigorous stirring. The resulting yellow solution was allowed to stir for 3 hours at room temperature and *n*-hexane (15 mL) was added. The resulting yellow suspension was filtered via cannula. The solid was

washed with *n*-hexane (3 x 5 mL), and dried in vacuo (1 × 10^{-2} mbar, 45 min) to give [(**TMEDA)Rh(NBD)**][BF_4] as an yellow solid. Yield: 50 mg, 0.112 mmol, 84%. Crystals suitable for an X-ray diffraction study were obtained by slow diffusion of *n*-hexane (2 mL) into a solution of [(**TMEDA)Rh(NBD)**][BF_4] in CH_2Cl_2 (0.5 mL).

^{1}H NMR (400 MHz, CD_2Cl_2, 298 K): δ 3.94 (overlapped s, 2 H, CH_2 bridge NBD), 3.94 (m, 4 H, CH alkene NBD), 2.55 (s, 4 H, CH_2–TMEDA), 2.43 (s, 12 H, CH_3–TMEDA), 1.37 (s, 2 H, CH bridgehead NBD).

^{13}C{^{1}H} NMR (125.6 MHz, Tol-*d*$_8$, 298 K): δ 63.7 (d, J = 6.7 Hz, CH_2 bridgehead NBD), 63.1 (d, $J_{C\text{-}Rh}$ = 10.2 Hz, CH alkene-NBD), 60,8 (CH_2–TMEDA), 52.5 (d, J = 2.5 Hz C*H* bridge NBD), 48,5 (CH_3–TMEDA).

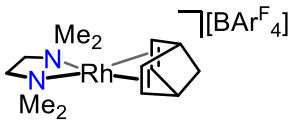
^{11}B{^{1}H} NMR (160.3 MHz, CD_2Cl_2, 298 K): δ −1.1 (s).

^{19}F{^{1}H} NMR (470.2 MHz, CD_2Cl_2, 298 K): δ -152.31 (s, ^{10}B), -152.37 (s, ^{11}B).

IR (KBr/Nujol, cm^{-1}): *v* 1415, 1308, 953, 804, 550, 521.

Elemental analysis found (calculated) for $C_{13}H_{24}BF_4N_2Rh$: C 39.10 (39.23), H 6.29 (6.08), N 7.07 (7.04).

3.6.2.2 Synthesis and Characterisation of [(TMEDA)Rh(NBD)][BAr$^F_4$]



One J. Young's ampoule was charged Rh(NBD)$_2$][BAr$^F_4$] (0.123 mg, 0.107 mmol) and dissolved in CH_2Cl_2 (3 mL). Then, the amine *N,N,N′,N′*−tetramethylethylenediamine (TMEDA) (18 µL, 0.120 mmol) was added dropwise with vigorous stirring. The resulting yellow solution was allowed to stir for 3 hours at room temperature and *n*-hexane (15 mL) was added. The resulting yellow suspension was filtered via cannula. The solid was washed with *n*-hexane (3 x 5 mL), and dried in vacuo (1 × 10^{-2} mbar, 45 min) to give [**(TMEDA)Rh(NBD)**][BAr$^F_4$] as an yellow solid. Yield: 28 mg, 0.071 mmol, 60%. Crystals suitable for an X-ray diffraction study were obtained by slow diffusion of *n*-hexane (2 mL) into a solution of [**(TMEDA)Rh(NBD)**][BAr$^F_4$] in CH_2Cl_2 (0.5 mL).

^{1}H NMR (400 MHz, CD_2Cl_2, 298 K): δ 7.69 (br s, 8 H, *ortho*–BAr$^F_4$), 7.57 (s, 4 H, *para*–BAr$^F_4$), 3.94 (m, 2 H, NBD), 3.92 (m, 4 H, CH=CH), 2.44 (s, 4 H,CH_2–TMEDA), 2.37 (d, 12 H, J = 0.8 Hz, CH_3–TMEDA), 1.36 (t, 2 H, J = 1.5 Hz, NBD).

^{13}C{^{1}H} NMR (125.6 MHz, Tol-*d*$_8$, 298 K): δ 162.2 (C_{ipso} BAr$^F_4$), 135.2 (*ortho*-BAr$^F_4$), 129.3 (q, $^2J_{C\text{-}F}$ =31.6 Hz, *meta*-BAr$^F_4$), 125.2 (*q*, $J_{C\text{-}F}$ = 272.4 Hz, overlapping CF_3 resonances, BAr$^F_4$), 117.8 (s, *para*-BAr$_4^F$), 63.9 (d, J = 10 Hz, CH_2 bridgehead NBD),

63.5 (d, $J_{C\text{-}Rh}$ = 10 Hz, CH alkene-NBD), 60,8 (CH_2–TMEDA), 52.6 (d, J = 10 Hz C*H* bridge NBD), 48,5 (CH_3–TMEDA).

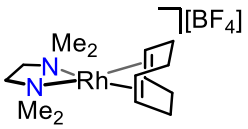
$^{11}B\{^1H\}$ NMR (160.3 MHz, CD_2Cl_2, 298 K): δ −6.6 (s).

$^{19}F\{^1H\}$ NMR (470.2 MHz, CD_2Cl_2, 298 K): δ −62.82 (s).

IR (KBr/Nujol, cm^{-1}): *v* 1783, 1610, 1465, 1376, 1275, 1118, 579.

Elemental analysis found (calculated) for $C_{45}H_{36}BF_{24}N_2Rh$: C 45.94 (46.02), H 2.89 (3.09), N 2.43 (2.39).

3.6.2.3 Synthesis and Characterisation of [(TMEDA)Rh(COD)][BF_4]



One J. Young's ampoule was charged with [$Rh(COD)_2$][BF_4] (120 mg, 0.296 mmol) and dissolved in dry CH_2Cl_2 (3 mL). Then, the amine *N,N,N′,N′*–tetramethylethylenediamine (TMEDA) (46 µL, 0.307 mmol) was added dropwise with vigorous stirring. The resulting yellow solution was allowed to stir for 6 hours at room temperature and *n*-hexane (15 mL) was added. The resulting yellow suspension was filtered via cannula. The solid was washed with *n*-hexane (2 x 5 mL), and dried in vacuo (1 × 10^{-2} mbar, 1 hour) to give [**(TMEDA)Rh(COD)**][BF_4] as an yellow solid. Yield: 114 mg, 0.275 mmol, 93%. Crystals suitable for an X-ray diffraction study were obtained by slow diffusion of *n*-hexane (2 mL) into a solution of [**(TMEDA)Rh(COD)**][BF_4] in CH_2Cl_2 (0.5 mL).

^1H NMR (400 MHz, CD_2Cl_2, 298 K): δ 3.95 (br s, 4 H, CH−alkene COD), 2.60(s, 4 H, CH_2−TMEDA), 2.58 (s, 12 H, CH_3−TMEDA), 2.46 (m, 4 H, COD), 1.86 (q, 4 H, J = 8.4 Hz, COD).

$^{13}C\{^1H\}$ NMR (100.6 MHz, CD_2Cl_2, 298 K): δ 83.9 (d, $J_{C\text{-}Rh}$ = 12.9 Hz, CH−alkene COD), 61.1 (CH_2−TMEDA), 49.1 (CH_3−TMEDA), 30.2 (COD).

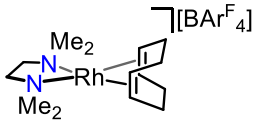
$^{11}B\{^1H\}$ NMR (128.3 MHz, CD_2Cl_2, 298 K): δ -1.15 (quintet, $J_{B\text{-}F}$ = 0.98 Hz).

$^{19}F\{^1H\}$ NMR (376.2 MHz, CD_2Cl_2, 298 K): δ -152.45 (br s, ^{10}B), -152.5 (m, ^{11}B).

IR (KBr/Nujol, cm^{-1}): *v* 2923, 2854, 2725, 1415, 1302, 1217, 1049, 999, 968, 950, 876, 819, 803, 776, 520.

Elemental analysis found (calculated) for $C_{14}H_{27}BF_4N_2Rh$: C 40.62 (40.61), H 6.61 (6.82), N 6.74 (6.77).

3.6.2.4 Synthesis and Characterisation of [(TMEDA)Rh(COD)][BAr$^F_4$]



One J. Young's ampoule was charged with [Rh(COD)$_2$][BAr$^F_4$] (197 mg, 0.167 mmol) and dissolved in dry CH_2Cl_2 (3 mL). Then, the amine *N,N,N′,N′*−tetramethylethylenediamine (TMEDA) (26 µL, 0.173 mmol) was added dropwise with vigorous stirring. The resulting yellow solution was allowed to stir for 5 hours at room temperature and *n*-hexane (15 mL) was added. The resulting yellow suspension was filtered via cannula. The solid was washed with *n*-hexane (2 x 5 mL), and dried in vacuo (1×10^{-2} mbar, 2 hours) to give **[(TMEDA)Rh(COD)]**[BAr$^F_4$] as an yellow solid. Yield: 114 mg, 0.096 mmol, 57%. Crystals suitable for an X-ray diffraction study were obtained by slow diffusion of *n*-hexane (2 mL) into a solution of **[(TMEDA)Rh(COD)]**[BAr$^F_4$] in benzene (0.5 mL).

^{1}H NMR (400 MHz, CD_2Cl_2, 298 K): δ 7.72 (t, 8 H, J = 2.36 Hz, *ortho*−Bar$_4^F$), 7.56 (s, 4 H, *para*−Bar$_4^F$), 3.92 (br s, 4 H, CH−alkene COD), 2.47 (s, 12 H, CH_3−TMEDA), 2.44 (s, 4 H, CH_2−TMEDA), 2.42 (m, 4 H, COD), 1.88 (m, 4 H, COD).

^{13}C{^{1}H} NMR (100.6 MHz, CD_2Cl_2, 298 K): δ 162.2 (q, J = 49.98 Hz, C_{ipso} BAr$^F_4$), 135.2 (*ortho*-BAr$^F_4$), 129.3 (qq, $^2J_{C\text{-}F}$ =34.9, $^4J_{C\text{-}F}$ = 2.7 Hz, *meta*-BAr$^F_4$), 125.0 (overlapped *q*, $J_{C\text{-}F}$ = 272.4 Hz, BAr$^F_4$), 117.9 (m, *para*-BAr$^F_4$), 84.4 (d, $J_{C\text{-}Rh}$ = 12.9 Hz, CH−alkene COD), 61.1 (CH_2−TMEDA), 49.2 (CH_3−TMEDA), 30.2 (COD).

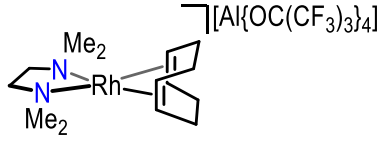
^{11}B{^{1}H} NMR (160.3 MHz, CD_2Cl_2, 298 K): δ -6.63 (s).

^{19}F{^{1}H} NMR (470.2 MHz, CD_2Cl_2, 298 K): δ -62.86 (s).

IR (KBr/Nujol, cm^{-1}): *v* 2919, 2725, 1610, 1464, 1413, 1376, 1276, 1118, 1013, 998, 968, 947, 887, 838, 802, 771, 579, 510.

Elemental analysis found (calculated) for $C_{46}H_{40}BF_{24}N_2Rh$: C 46.44 (46.41), H 3.31 (3.39), N 2.35 (2.35).

3.6.2.5 Synthesis and Characterisation of [(TMEDA)Rh(COD)][Al{OC(CF$_3$)$_3$}$_4$]



One J. Young's ampoule was charged with [Rh(COD)$_2$][Al{OC(CF$_3$)$_3$}$_4$] (214 mg, 0.166 mmol) and dissolved in dry CH_2Cl_2 (3 mL). Then, the amine *N,N,N′,N′*−tetramethylethylenediamine (TMEDA) (28 µL, 0.187mmol) was added dropwise with vigorous stirring. The resulting yellow solution was allowed to stir for 6 hours at room temperature and *n*-hexane (15 mL) was added. The resulting yellow suspension was filtered via cannula. The solid was washed with *n*-hexane (2 x 5 mL),

and dried in vacuo (1 × 10^{-2} mbar, 1 hour) to give [**(TMEDA)Rh(COD)**][Al{$OC(CF_3)_3$}$_4$] as an yellow solid. Yield: 120 mg, 0.093 mmol, 56%. Crystals suitable for an X-ray diffraction study were obtained by slow diffusion of *n*-hexane (2 mL) into a solution of [**(TMEDA)Rh(COD)**][Al{$OC(CF_3)_3$}$_4$] in CH_2Cl_2 (0.5 mL).

^{1}H NMR (400 MHz, CD_2Cl_2, 298 K): δ 3.95 (br s, 4 H, CH−alkene COD), 2.52 (overlapped s, 12 H, CH_3−TMEDA), 2.60 (overlapped s, 4 H, CH_2−TMEDA), 2.46 (v br s, 4 H, COD), 1.90 (m, 4 H, COD).

^{13}C{^{1}H} NMR (100.6 MHz, CD_2Cl_2, 298 K): δ 121.7 (overlapped *q*, J_{C-F} = 292.6 Hz, CF_3), 117.1 (Cq), 85.5 (d, J_{C-Rh} = 12.6 Hz, CH−alkene COD), 61.1 (CH_2−TMEDA), 49.2 (CH_3−TMEDA), 30.2 (COD).

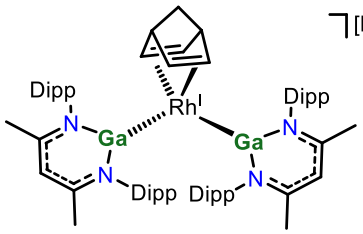
^{19}F{^{1}H} NMR (376.2 MHz, CD_2Cl_2, 298 K): δ -75.69.

IR (KBr/Nujol, cm^{-1}): *v* 1415, 1354, 1278, 1163, 1099, 974, 875, 831, 803, 773, 560.

Elemental analysis found (calculated) for $C_{30}H_{28}AlF_{36}N_2O_4Rh$: C 27.50 (27.84), H 2.04 (2.18), N 2.86 (2.16).

3.6.3 Synthesis and Characterisation of Heterometallic Ga(I)−Rh Olefin Complexes

3.6.3.1 Synthesis and characterisation of *cis*-[2_2−Rh(NBD)][BAr^F_4]



One J. Young's ampoule was charged with [Rh(NBD)$_2$][BAr^F_4] (150 mg, 0.130 mmol) and BDIGa (**2**) (190 mg, 0.390 mmol) and were dissolved in fluorobenzene (5 mL). Then, the mixture was left stirring for 2 h at room temperature. The resulting orange solution was filtered and layered with n-hexane (15 mL) to give red-orange needle-like crystals suitable for an X-ray diffraction study. The crystals were filtered, washed with n-hexane (3 mL), and dried in vacuo (1 × 10^{-2} mbar, 2 h) to give *cis*-[**2_2−Rh(NBD)**][BAr^F_4] as red-orange crystals. Yield: 180 mg, 0.089 mmol, 68%.

^{1}H NMR (500 MHz, CD_2Cl_2, 298 K): δ 7.72 (s, 8 H, *meta*-BAr^F_4), 7.56 (s, 4 H, *para*-BAr^F_4), 7.44 (t, 2 H, J_1 = 7.8 Hz, Ar), 7.32 (m, 6 H, Ar), 7.24 (d, 2 H, J = 7.6 Hz, Ar), 7.14 (t, 2 H, J = 7.4 Hz, Ar), 5.57 (s, 2 H, γ-CH), 4.56 (*br s*, 2 H, *alkene-NBD*), 3.08 (br s overlapped with the CH-^{i}Pr signal, 2 H, *alkene*-NBD), 3.06 (sept overlapped with the *alkene*-NBD signal, 2 H, CH-^{i}Pr), 3.01 (br s, 2 H, CH_2-NBD) 2.63 (sept, 2 H,

J = 6.8 Hz, CH-^{i}Pr), 2.52 (sept, 4 H, J = 6.8 Hz, CH-^{i}Pr), 1.76 (s, 6 H, β-Me), 1.73 (s, 6 H, β-Me), 1.32 (d, 6 H, J = 6.8 Hz, Me-^{i}Pr), 1.24 (d, 6 H, J = 6.9 Hz, Me-^{i}Pr), 1.17 (d, 6 H, J = 6.9 Hz, Me-^{i}Pr), 1.08 ("d", 12 H, J = 7.6 Hz, Me-^{i}Pr), 0.98 ("t" overlapped with CH-NBD signal, 12 H, J = 7.2 Hz, Me-^{i}Pr), 0.97 (overlapped with Me-^{i}Pr signal, 2 H, CH-NBD), 0.54 (d, 6 H, J = 6.8 Hz, Me-^{i}Pr).

^{13}C{^{1}H} NMR (125.6 MHz, CD_2Cl_2, 298 K): δ 168.8, 168.5, 162.2 (q, J = 49.95 Hz, C_{ipso} BAr^F_4), 145.7, 143.7, 143.6, 143.4, 141.7, 141.6, 135.2 (*ortho*-BAr^F_4), 129.2 (qq, $^{2}J_{C\text{-}F}$ =33.1, $^{4}J_{C\text{-}F}$ = 2.7 Hz, *meta*-BAr^F_4), 128.9, 128.4, 125.5, 125.3, 125.2 (*q*, $J_{C\text{-}F}$ = 272.5 Hz, BAr^F_4), 125.1, 124.9, 117.9 ("t", $^{4}J_{C\text{-}F}$ = 3.7 Hz, *para*-BAr^F_4), 103.3 (γ-CH), 69.0 (d, $J_{C\text{-}Rh}$ = 7.4 Hz, *alkene*-NBD), 68.2 (d, $J_{C\text{-}Rh}$ = 4.3 Hz, *CH*$_2$-NBD), 67.9 (d, $J_{C\text{-}Rh}$ = 6.7 Hz, *alkene*-NBD), 55.6 (d, $J_{C\text{-}Rh}$ = 1.5 Hz, bridge NBD), 30.3 (CH-^{i}Pr), 29.6 (CH-^{i}Pr), 28.8 (CH-^{i}Pr), 28.7 (CH-^{i}Pr), 27.5 (Me-^{i}Pr), 25.8 (Me-^{i}Pr), 25.1 (Me-^{i}Pr r), 24.6 (β-Me), 24.4 (Me, iPr), 24.3 (Me-^{i}Pr), 24.3 (Me-^{i}Pr), 24.3 (Me-^{i}Pr), 24.1 (β-Me), 23.5 (Me-^{i}Pr).

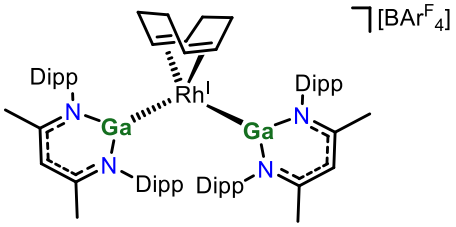
^{11}B{^{1}H} NMR (160.3 MHz, CD_2Cl_2, 298 K): δ −6.6 (s).

^{19}F{^{1}H} NMR (470.2 MHz, CD_2Cl_2, 298 K): δ −62.9 (s).

HRMS (ESI) m/z found (calculated) for $C_{65}H_{90}Ga_2N_4Rh$ $[M]^+$: 1169.4733 (1169.4730).

Elemental analysis found (calculated) for $C_{97}H_{102}BF_{24}Ga_2N_4Rh$: C 58.03 (57.31), H 4.95 (5.06), N 2.65 (2.76).

3.6.3.2 Synthesis and Characterisation of *cis*-[2$_2$−Rh(COD)][BAr$^F_4$]



One J. Young's ampoule was charged with [Rh(COD)$_2$][BAr$^F_4$] (319 mg, 0.270 mmol) and BDIGa (**2**) (144 mg, 0.759 mmol) and were dissolved in fluorobenzene (5 mL). Then, the mixture was left stirring for 5h at room temperature. The resulting red-orange solution was added *n*-hexane (15 mL). The resulting red-orange suspension was left stirred at 0°C 15 min and it was filtered via cannula. The solid was washed with *n*-hexane (2 x 5 mL), and dried in vacuo (1 × 10^{-2} mbar, 2 h) to give *cis*-[**2$_2$−Rh(COD)**][BAr$^F_4$] as a red-orange solid. Yield: 245 mg, 0.120 mmol, 77%. Crystals suitable for an X-ray diffraction study were obtained by slow diffusion of *n*-hexane (2 mL) into a solution of *cis*-[**2$_2$−Rh(COD)**][BAr$^F_4$] in FB (0.35 mL).

^{1}H NMR (500 MHz, CD_2Cl_2, 298 K): δ 7.72 (s, 8 H, *meta*-$BAr^F{}_4$), 7.56 (s, 4 H, *para*-$BAr^F{}_4$), 7.44 (t, 2 H, J_1 = 7.7 Hz, Ar), 7.35 (d, 2 H, J_1 = 7.5 Hz, Ar), 7.31 (d, 2 H, J_1 = 7.6 Hz, Ar), 7.24 (t, 2 H, J = 7.6 Hz, Ar), 7.14 (d, 2 H, J = 7.5 Hz, Ar), 7.10 (d, 2 H, J = 7.7 Hz, Ar), 5.61 (s, 2 H, γ-CH), 5.13 (*br s*, 2 H, *alkene*-COD), 3.74 (m, 2 H, *alkene*-COD), 3.05 (sept, 2 H, J = 6.8 Hz, CH-^{i}Pr), 2.79 (sept, 2 H, J = 6.7 Hz, CH-^{i}Pr), 2.65 (sept, 2 H, J = 6.7 Hz, CH-^{i}Pr), 2.47 (sept, 2 H, J = 6.8 Hz, CH-^{i}Pr), 1.76 (s, 6 H, β-Me), 1.73 (s, 6 H, β-Me), 1.64 (m, 2 H, COD), 1.52 (m, 2 H, COD), 1.35 (d, 6 H, J = 6.7 Hz, Me-^{i}Pr), 1.28 (d, 6 H, J = 6.7 Hz, Me-^{i}Pr), 1.20 (d, 6 H, J = 6.8 Hz, Me-^{i}Pr), 1.16 (d, 6 H, J = 6.8 Hz, Me-^{i}Pr), 1.05 (*pseudo* d, 12 H, J = 7.2 Hz, Me-^{i}Pr), 0.97 (d. 6 H, J = 6.7 Hz, Me-^{i}Pr), 0.94 (m, 2 H, overlapping COD), 0.67 (m, 2 H, COD), 0.27 (d, 6 H, J = 6.8 Hz, Me-^{i}Pr).

^{13}C{^{1}H} NMR (125.6 MHz, CD_2Cl_2, 298 K): δ 169.2, 168.7, 162.1 (q, J = 49.95 Hz, C_{ipso} $BAr^F{}_4$), 145.1, 143.7, 143.5, 143.3, 142.1, 141.4, 135.2 (*ortho*-$BAr^F{}_4$), 129.2 (qq, $^{2}J_{C\text{-}F}$ =34.6, $^{4}J_{C\text{-}F}$ = 3.0 Hz, *meta*-$BAr^F{}_4$), 129.0, 128.4, 125.4, 125.3, 125.1 (*q*, $J_{C\text{-}F}$ = 272 Hz, overlapping CF_3 resonances, $BAr^F{}_4$), 124.9, 124.8, 117.8 (q, $^{4}J_{C\text{-}F}$ = 3.7 Hz, *para*-$BAr^F{}_4$), 103.6 (γ-CH), 83.4 (d, $J_{C\text{-}Rh}$ = 7.9 Hz, *alkene*-COD), 82.1 (d, $J_{C\text{-}Rh}$ = 7.9 Hz, *alkene*-COD), 34.1 (COD), 31.1 (CH-^{i}Pr), 29.3 (CH-^{i}Pr), 28.9 (CH-^{i}Pr), 28.7 (CH-^{i}Pr), 27.9 (Me-^{i}Pr), 27.4 (COD), 26.3 (Me-^{i}Pr), 25.2 (Me-^{i}Pr), 24.7 (β-Me), 24.6 (β-Me), 24.5 (Me-^{i}Pr), 24.1 (Me-^{i}Pr), 24.0 (Me-^{i}Pr), 23.7 (Me-^{i}Pr), 23.0 (Me-^{i}Pr).

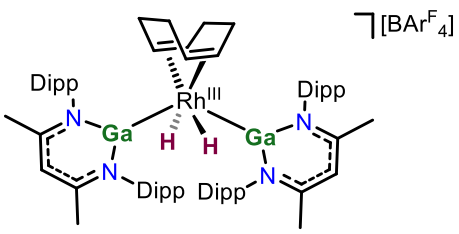
^{11}B{^{1}H} NMR (160.3 MHz, CD_2Cl_2, 298 K): δ −6.6 (s).

^{19}F{^{1}H} NMR (470.2 MHz, CD_2Cl_2, 298 K): δ −62.8 (s).

HRMS (ESI) m/z found (calculated) for $C_{66}H_{94}Ga_2N_4Rh$ $[M]^+$: 1185.5028 (1185.5043).

Elemental analysis found (calculated) for $C_{98}H_{106}BF_{24}Ga_2N_4Rh$: C 57.38 (57.44), H 5.35 (5.21), N 2.64 (2.73).

3.6.3.3 Synthesis and Characterisation of *cis*-[2₂−Rh(COD)(H)₂][BAr$^F_4$]



One J. Young's ampoule was charged with *cis*-[**2₂−Rh(COD)**][BAr$^F_4$] (150 mg, 0.073 mmol) were dissolved in fluorobenzene (1 mL). The orange solution was freeze-pump-thaw degassed three times before H_2 gas (1.5 bar) was added. The reaction mixture was allowed to stir for 5 min resulting in a light-yellow solution. Then, H_2 gas was completely removed by a three-fold freeze-pump-thawing cycle. To the resulting solution was *n*-hexane was added (8 mL). The resulting sand-yellow suspension was stirred at 0°C for 15 min. After this time, the suspension was filtered via cannula and the obtained solid was washed with *n*-hexane (2 x 3 mL), and dried in vacuo (1 × 10^{-2} mbar, 2 h) to give *cis*-[**2₂−Rh(COD)(H)₂**][BAr$^F_4$] as a sand-yellow solid. Yield: 80 mg, 0.039 mmol, 53%. Crystals suitable for an X-ray diffraction study were obtained by slow diffusion of *n*-hexane (2 mL) into a solution of *cis*-[**2₂−Rh(COD)(H)₂**][BAr$^F_4$] in fluorobenzene (0.35 mL) at -11ºC.

^{1}H NMR (500 MHz, CD_2Cl_2, 298 K): δ 7.72 (br s, 8 H, *meta*-BAr$^F_4$), 7.55 (s, 4 H, *para*-BAr$^F_4$), 7.40 (t, 2 H, J_1 = 7.7 Hz, Ar), 7.30 (d, 4 H, J_1 = 8.0 Hz, Ar), 7.27 (t, 2 H, J = 7.7 Hz, Ar), 7.22 (d, 2 H, J = 7.6 Hz, Ar), 7.10 (d, 2 H, J = 7.6 Hz, Ar), 5.59 (s, 2 H, γ-CH), 3.66 (*br s*, 2 H, *alkene*-COD), 3.27 (m, 2 H, *alkene*-COD), 3.07 (sept, 4 H, J = 7.3 Hz, CH-^{i}Pr), 2.80 (sept, 2 H, J = 6.8 Hz, CH-^{i}Pr), 2.56 (sept, 2 H, J = 6.7 Hz, CH-^{i}Pr), 2.23 (m, 2 H, COD), 1.86 (s, 6 H, β-Me), 1.78 (s, 6 H, β-Me), 1.37 (d, 6 H, J = 6.8 Hz, Me-^{i}Pr), 1.27 (d, 12 H, J = 6.8 Hz, Me-^{i}Pr), 1.19 (d, 6 H, J = 6.8 Hz, Me-^{i}Pr), 1.16 (d, 6 H, J = 6.8 Hz, Me-^{i}Pr), 1.10 (*pseudo* t, 12 H, J = 6.5 Hz, Me-^{i}Pr), 1.01 (m overlapped with residual *n*-hexane signal, 2 H, COD), 0.88 (m overlapped with residual *n*-hexane signal, 2 H, COD), 0.08 (d, 6 H, J = 6.4 Hz, Me-^{i}Pr), −14.26 (d, 2 H, J = 11.5 Hz, Rh−H_2, T_1 = 600 ms).

^{13}C{^{1}H} NMR (125.6 MHz, CD_2Cl_2, 298 K): δ 170.1, 170.0, 162.2 (q, J = 49.8 Hz, C_{ipso} BAr$^F_4$), 144.6, 144.2, 143.3, 142.9, 142.2, 140.9, 135.2 (*ortho*-BAr$^F_4$), 129.3 (qq, $^2J_{C-F}$ =31.7, $^4J_{C-F}$ = 2.7 Hz, *meta*-BAr$^F_4$), 129.2, 128.9, 125.7, 125.6, 125.3 (*q*, J_{C-F} = 272.4 Hz, overlapping CF_3 resonances, BAr$^F_4$), 124.8, 124.7, 117.9 (q, $^4J_{C-F}$ = 3.9 Hz, *para*-BAr$^F_4$), 102.4 (γ-CH), 76.7 (d, J_{C-Rh} = 5.7 Hz, *alkene*-COD), 75.5 (d, J_{C-Rh} = 6.0 Hz, *alkene*-COD), 39.3 (COD), 31.2 (CH-^{i}Pr), 30.7 (CH-^{i}Pr), 28.5 (CH-^{i}Pr), 28.3

(CH-^{i}Pr), 27.2 (Me-^{i}Pr), 26.0 (COD), 25.3 (Me-^{i}Pr), 24.9 (Me-^{i}Pr), 24.7 (β-Me), 24.6 (β-Me), 24.6 (Me-^{i}Pr), 24.6 (Me-^{i}Pr), 24.1 (Me-^{i}Pr), 23.6 (Me-^{i}Pr).

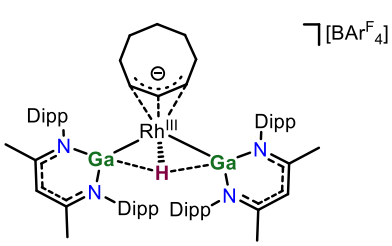
^{11}B{^{1}H} NMR (128.3 MHz, CD_2Cl_2, 298 K): δ −6.6 (s).

^{19}F{^{1}H} NMR (376.2 MHz, CD_2Cl_2, 298 K): δ −62.8 (s).

HRMS (ESI) m/z found (calculated) for $C_{66}H_{96}Ga_2N_4Rh$ $[M]^+$: 1187.5155 (1187.5200).

Elemental analysis found (calculated) for $C_{98}H_{108}BF_{24}Ga_2N_4Rh$: C 56.54 (57.39), H 5.00 (5.31), N 2.58 (2.73).

3.6.3.4 Synthesis and Characterisation of *cis*-[**2**$_2$−Rh(η^3−C_8H_{13})(H)][BAr^F_4]



One J. Young's ampoule was charged with *cis*-[**2**$_2$−**Rh(COD)**][BAr^F_4] (120 mg, 0.059 mmol) were dissolved in fluorobenzene (1 mL). The orange solution was freeze-pump-thaw degassed three times before H_2 gas (1.5 bar) was added. The reaction mixture was allowed to stir for five minutes resulting in a lighter yellow solution. Then, this yellow solution was filtered and layered with *n*-hexane (5 mL) to give suitable yellow block crystals of *cis*-[**2**$_2$−**Rh(η^3−C_8H_{13})(H)**][BAr^F_4] for an X-ray diffraction study. Yield: 50 mg, 0.039 mmol, 41%.

Note on X-ray diffraction and NMR data: Yellow block single crystals of [**2**$_2$−**Rh(η^3−C_8H_{13})(H)**][BAr^F_4] suitable for X-ray diffraction analyses, were obtained through the slow diffusion of *n*-hexane into an *in-situ* generated solution of the compound in fluorobenzene. Multiple independent syntheses and crystallisations consistently produced crystals of *cis*-[**2**$_2$−**Rh(η^3−C_8H_{13})(H)**][BAr^F_4] alone. Comprehensive crystal screenings were conducted for each independent synthesis and crystallization, demonstrating a consistent and reproducible synthetic and crystallization process. The NMR spectroscopic data for *cis*-[**2**$_2$−**Rh(η^3−C_8H_{13})(H)**][BAr^F_4] in CD_2Cl_2 solution, obtained by ^{1}H NMR spectroscopy, as well as that from HRMS-ESI spectrometry, were consistent (identical) for each synthesis and crystallization.

The ^{1}H NMR spectrum of isolated yellow block-shape crystals of *cis*-[**2**$_2$−**Rh(η^3−C_8H_{13})(H)**][BAr^F_4] in CD_2Cl_2 solution exhibits a 1:1:2 mixture of [**2**$_2$−**Rh(η^3−C_8H_{13})(H)**][BAr^F_4], [**2**$_2$−**Rh(COD)**][BAr^F_4] and [**2**$_2$−**Rh(COD)(H)**$_2$][BAr^F_4], respectively, along with trace amounts of H_2 generated as a result of this process in

solution. The dynamic equilibrium was also studied by ^{1}H NMR spectroscopy in the temperature range 298-203 K.

^{1}H NMR (500 MHz, CD_2Cl_2, 298 K) for [2_2−Rh(η^3−C_8H_{13})(H)][BAr^F_4]: δ 7.73 (8 H, *meta*-BAr^F_4), 7.56 (4 H, *para*-BAr^F_4), 7.48–6.92 (*several overlapped* m, 12 H, Ar), 5.64 (br s, 2 H, γ-CH), 3.20-2.38, 1.39-0.90 and –0.26 (*several overlapped* br s and m, 50 H, ^{i}Pr + β-Me + *CH_2−η^3−C_8H_{13}*); *hydride and CH−η^3−C_8H_{13} resonances not observed at this temperature*.

^{1}H NMR (400 MHz, CD_2Cl_2, 203 K) for [2_2−Rh(η^3−C_8H_{13})(H)][BAr^F_4]: δ 7.71 (8 H, *meta*-BAr^F_4), 7.53 (4 H, *para*-BAr^F_4), 7.48-6.70 (*several overlapped* m, 12 H, Ar), 5.54 (*overlapped* s, 2 H, γ-CH), 4.81 (v br s, 1 H, CH−η^3−C_8H_{13}), 3.80 (v br s, 2 H, CH−η^3−C_8H_{13}), 3.15-0.27 (*several overlapped* m, 38 H, ^{i}Pr + β-Me + CH_2-η^3−C_8H_{13}), −0.33 (br d, 6 H, J = 4.8 Hz, Me-^{i}Pr), −0.59 (br d, 6 H, J = 5.6 Hz, Me-^{i}Pr), –7.90 (br d, J = 13.9 Hz, Rh–H).

^{11}B{^{1}H} NMR (160.3 MHz, CD_2Cl_2, 298 K): δ −6.6 (s).

^{19}F{^{1}H} NMR (470.2 MHz, CD_2Cl_2, 298 K): δ −62.8 (s).

HRMS (ESI) m/z found (calculated) for $C_{66}H_{96}Ga_2N_4Rh$ $[M]^+$: 1187.5155 (1169.5200); for **$C_{66}H_{94}Ga_2N_4Rh$ $[M]^+$:** 1185.5146 (1185.5143).

3.7 References

[1] R. Franke, D. Selent, A. Börner, *Chem. Rev.* **2012**, *112*, 5675-5732.
[2] W. Reppe, O. Schlichting, K. Klager, T. Toepel, *Justus Liebigs Annalen der Chemie* **1948**, *560*, 1-92.
[3] J. Seitz, G. Maas, *Chem. Commun.* **2002**, 338-339.
[4] M. L. H. Green, *J. Organomet. Chem.* **1995**, *500*, 127-148.
[5] a) J. F. Young, J. A. Osborn, F. H. Jardine, G. Wilkinson, *Chem. Commun.* **1965**, 131-132; b) D. Evans, J. A. Osborn, G. Wilkinson, *J. Chem. Soc. A.* **1968**, 3133-3142; c) A. S. Hussey, Y. Takeuchi, *J. Am. Chem. Soc.* **1969**, *91*, 672-675; d) C. R. Landis, J. Halpern, *J. Am. Chem. Soc.* **1987**, *109*, 1746-1754; e) A. S. Hussey, Y. Takeuchi, *J. Org. Chem.* **1970**, *35*, 643-647; f) A. S. C. Chan, J. Halpern, *J. Am. Chem. Soc.* **1980**, *102*, 838-840.
[6] a) A. Togni, L. M. Venanzi, *Angew. Chem. Int. Ed.* **1994**, *33*, 497-526; b) T. R. Kégl, N. Pálinkás, L. Kollár, T. Kégl, *Molecules* **2018**, *23*, 3176-3187.
[7] A. J. Birch, D. H. Williamson, in *Organic Reactions*, **2011**, pp. 1-186.
[8] a) C. A. Tolman, W. C. Seidel, L. W. Gosser, *J. Am. Chem. Soc.* **1974**, *96*, 53-60; b) C. A. Tolman, *Chem. Rev.* **1977**, *77*, 313-348; c) J. Jover, J. Cirera, *Dalton Trans.* **2019**, *48*, 15036-15048; d) C. A. Tolman, *J. Am. Chem. Soc.* **1970**, *92*, 2956-2965; e) P. W. N. M. van Leeuwen, P. C. J. Kamer, J. N. H. Reek, **1999**, *71*, 1443-1452; f) C. P. Casey, G. T. Whiteker, *Israel J. Chem.* **1990**, *30*, 299-304; g) M. Kranenburg, Y. E. M. van der Burgt, P. C. J. Kamer, P. W. N. M. van Leeuwen, K. Goubitz, J. Fraanje, *Organometallics* **1995**, *14*, 3081-3089.
[9] a) R. R. Schrock, J. A. Osborn, *J. Am. Chem. Soc.* **1976**, *98*, 4450-4455; b) P. W. N. M. van Leeuwen, P. C. J. Kamer, *Catal. Sci. Technol.* **2018**, *8*, 26-113; c) G. M. Adams, A. S. Weller, *Coord. Chem. Rev.* **2018**, *355*, 150-172; d) J. J. Race, A. L. Burnage, T. M. Boyd, A. Heyam, A. J. Martínez-Martínez, S. A. Macgregor, A. S. Weller, *Chem. Sci.* **2021**, *12*, 8832-8843.
[10] a) G. G. Stanley, in *Kirk-Othmer Encyclopedia of Chemical Technology*, **2017**, pp. 1-19; b) M. Y. S. Ibrahim, J. A. Bennett, D. Mason, J. Rodgers, M. Abolhasani, *J. Catal.* **2022**, *409*, 105-117; c) R. Whyman, *Appl. Organomet. Chem.* **2001**, *15*, 315-316; d) G. Yagupsky, C. K. Brown, G. Wilkinson, *J. Chem. Soc. A.* **1970**, 1392-1401.
[11] W. S. Knowles, *Angew. Chem. Int. Ed.* **2002**, *41*, 1998-2007.
[12] R. Noyori, H. Takaya, *Acc. Chem. Res.* **1990**, *23*, 345-350.
[13] M. Kitamura, M. Tsukamoto, Y. Bessho, M. Yoshimura, U. Kobs, M. Widhalm, R. Noyori, *J. Am. Chem. Soc.* **2002**, *124*, 6649-6667.
[14] a) T. Ishiyama, J. Hartwig, *J. Am. Chem. Soc.* **2000**, *122*, 12043-12044; b) R. Martinez, F. Voica, J.-P. Genet, S. Darses, *Org. Lett.* **2007**, *9*, 3213-3216; c) M. Sakai, H. Hayashi, N. Miyaura, *Organometallics* **1997**, *16*, 4229-4231; d) E. M. Larin, J. Masson-Makdissi, Y. J. Jang, M. Lautens, *ACS Catal.* **2022**, *12*, 12744-12749; e) P. Schäfer, T. Palacin, M. Sidera, S. P. Fletcher, *Nat. Commun.* **2017**, *8*, 15762; f) D. Wang, M. Li, C. Shuang, Y. Liang, Y. Zhao, M. Wang, Z. Shi, *Nat. Commun.* **2022**, *13*, 2934; g) D. A. Colby, A. S. Tsai, R. G. Bergman, J. A. Ellman, *Acc. Chem. Res.* **2012**, *45*, 814-825.
[15] a) N. T. Coles, A. Sofie Abels, J. Leitl, R. Wolf, H. Grützmacher, C. Müller, *Coord. Chem. Rev.* **2021**, *433*, 213729; b) W. Matsuoka, Y. Harabuchi, S. Maeda, *ACS Catal.* **2023**, *13*, 5697-5711; c) K.-Y. Wang, J. Zhang, Y.-C. Hsu, H. Lin, Z. Han, J. Pang, Z. Yang, R.-R. Liang, W. Shi, H.-C. Zhou, *Chem. Rev.* **2023**, *123*, 5347-5420.
[16] R. G. Pearson, *J. Am. Chem. Soc.* **1963**, *85*, 3533-3539.
[17] R. H. Crabtree, in *The Organometallic Chemistry of the Transition Metals*, **2014**, pp. 1-39.

[18] P. Maire, F. Breher, H. Schönberg, H. Grützmacher, *Organometallics* **2005**, *24*, 3207-3218.
[19] R. Noyori, *Angew. Chem. Int. Ed.* **2002**, *41*, 2008-2022.
[20] T. Kégl, L. Kollár, in *Comprehensive Inorganic Chemistry II (Second Edition)* (Eds.: J. Reedijk, K. Poeppelmeier), Elsevier, Amsterdam, **2013**, pp. 271-308.
[21] M. Bernard, V. Guiral, F. Delbecq, F. Fache, P. Sautet, M. Lemaire, *J. Am. Chem. Soc.* **1998**, *120*, 1441-1446.
[22] P. Pertici, F. D'Arata, C. Rosini, *J. Organomet. Chem.* **1996**, *515*, 163-171.
[23] a) R. Uson, L. A. Oro, C. Claver, M. A. Garralda, *J. Organomet. Chem.* **1976**, *105*, 365-370; b) M. A. Garralda, L. Ibarlucea, *J. Organomet. Chem.* **1986**, *311*, 225-231; c) R. Usón, L. A. Oro, J. A. Cuchi, M. A. Garralda, *J. Organomet. Chem.* **1976**, *116*, C35-C37; d) R. Uson, L. A. Oro, M. A. Garralda, M. Carmen Claver, P. Lahuerta, *Trans. Met. Chem.* **1979**, *4*, 55-58.
[24] T. A. Betley, J. C. Peters, *Inorg. Chem.* **2002**, *41*, 6541-6543.
[25] a) A. L. Gott, P. C. McGowan, C. N. Temple, *Organometallics* **2008**, *27*, 2852-2860; b) H. Zhen, C. Wang, Y. Hu, T. C. Flood, *Organometallics* **1998**, *17*, 5397-5405; c) B. de Bruin, M. J. Boerakker, J. A. Brands, J. J. J. M. Donners, M. P. J. Donners, R. de Gelder, J. M. M. Smits, A. W. Gal, A. L. Spek, *Chem. Eur. J.* **1999**, *5*, 2921-2936; d) M. V. Baker, D. H. Brown, B. W. Skelton, A. H. White, *J. Chem. Soc. Dalton Trans.* **2000**, 4607-4616; e) A. L. Gott, P. C. McGowan, C. N. Temple, *Dalton Trans.* **2004**, 1841-1845.
[26] A. G. De Crisci, V. T. Annibale, G. K. Hamer, A. J. Lough, U. Fekl, *Dalton Trans.* **2010**, *39*, 2888-2902.
[27] a) M.-C. Melcher, T. Ivšić, C. Olagnon, C. Tenten, A. Lützen, D. Strand, *Chem. Eur. J.* **2018**, *24*, 2344-2348; b) M. D. Jones, F. A. Almeida Paz, J. E. Davies, B. F. G. Johnson, *Acta Crystallographica Section E* **2003**, *59*, m6-m7; c) F. Läng, F. Breher, D. Stein, H. Grützmacher, *Organometallics* **2005**, *24*, 2997-3007; d) M.-C. Melcher, B. Rolim Alves da Silva, T. Ivšić, D. Strand, *ACS Omega* **2018**, *3*, 3622-3630.
[28] a) M. A. Garralda, L. A. Oro, *Trans. Met. Chem.* **1980**, *5*, 65-73; b) W. A. Fordyce, G. A. Crosby, *Inorg. Chem.* **1982**, *21*, 1023-1026; c) D. J. A. De Waal, W. Robb, *Inorg. Chim. Acta* **1978**, *26*, 91-96.
[29] a) W. Zuo, A. J. Lough, Y. F. Li, R. H. Morris, *Science* **2013**, *342*, 1080-1083; b) A. Mikhailine, A. J. Lough, R. H. Morris, *J. Am. Chem. Soc.* **2009**, *131*, 1394-1395; c) P. O. Lagaditis, A. J. Lough, R. H. Morris, *J. Am. Chem. Soc.* **2011**, *133*, 9662-9665; d) R. Noyori, T. Ohkuma, *Angew. Chem. Int. Ed.* **2001**, *40*, 40-73; e) T. Ohkuma, H. Doucet, T. Pham, K. Mikami, T. Korenaga, M. Terada, R. Noyori, *J. Am. Chem. Soc.* **1998**, *120*, 1086-1087; f) T. Ohkuma, H. Ooka, S. Hashiguchi, T. Ikariya, R. Noyori, *J. Am. Chem. Soc.* **1995**, *117*, 2675-2676; g) P. J. Rayner, P. M. Richardson, S. B. Duckett, *Angew. Chem. Int. Ed.* **2020**, *59*, 2710-2714.
[30] a) Á. Vivancos, C. Segarra, M. Albrecht, *Chem. Rev.* **2018**, *118*, 9493-9586; b) D. Munz, *Organometallics* **2018**, *37*, 275-289; c) R. A. Moss, M. P. Doyle, in *Contemporary Carbene Chemistry*, Wiley, **2013**.
[31] M. Á. Fernández-Rodríguez, P. García-García, E. Aguilar, *Chem. Commun.* **2010**, *46*, 7670-7687.
[32] G. Zhou, Z. Guo, X. Shen, *Angew. Chem. Int. Ed.* **2023**, *62*, e202217189.
[33] R. R. Schrock, *Angew. Chem. Int. Ed.* **2006**, *45*, 3748-3759.
[34] R. R. Schrock, A. H. Hoveyda, *Angew. Chem. Int. Ed.* **2003**, *42*, 4592-4633.
[35] a) H. M. L. Davies, J. R. Manning, *Nature* **2008**, *451*, 417-424; b) Z. Ren, D. G. Musaev, H. M. L. Davies, *ACS Catal.* **2022**, *12*, 13446-13456; c) M. P. Doyle, R. Duffy, M. Ratnikov, L. Zhou, *Chem. Rev.* **2010**, *110*, 704-724; d) R. W. Kubiak, II, W. F. Tracy, J. S. Alford, H. M. L. Davies, *J. Org. Chem.* **2022**, *87*, 13517-13528.
[36] M. P. Doyle, D. C. Forbes, *Chem. Rev.* **1998**, *98*, 911-936.

[37] a) J. Barluenga, R. Vicente, L. A. López, E. Rubio, M. Tomás, C. Álvarez-Rúa, *J. Am. Chem. Soc.* **2004**, *126*, 470-471; b) J. Barluenga, R. Vicente, P. Barrio, L. A. López, M. Tomás, J. Borge, *J. Am. Chem. Soc.* **2004**, *126*, 14354-14355; c) J. Barluenga, R. Vicente, P. Barrio, L. A. López, M. Tomás, *J. Am. Chem. Soc.* **2004**, *126*, 5974-5975; d) E. Palomo, A. K. Sharma, Z. Wang, L. Jiang, F. Maseras, M. G. Suero, *J. Am. Chem. Soc.* **2023**, *145*, 4975-4981.

[38] a) K. H. Dötz, J. Stendel, Jr., *Chem. Rev.* **2009**, *109*, 3227-3274; b) I. Fernández, M. J. Mancheño, R. Vicente, L. A. López, M. A. Sierra, *Chem. Eur. J.* **2008**, *14*, 11222-11230.

[39] P. Soam, P. Kamboj, V. Tyagi, *Asian Journal of Organic Chemistry* **2022**, *11*, e202100570.

[40] A. Krüger, M. Albrecht, *Chem. Eur. J.* **2012**, *18*, 652-658.

[41] a) T. Dröge, F. Glorius, *Angew. Chem. Int. Ed.* **2010**, *49*, 6940-6952; b) M. N. Hopkinson, C. Richter, M. Schedler, F. Glorius, *Nature* **2014**, *510*, 485-496; c) D. Janssen-Müller, C. Schlepphorst, F. Glorius, *Chem. Soc. Rev.* **2017**, *46*, 4845-4854; d) H. V. Huynh, *Chem. Rev.* **2018**, *118*, 9457-9492; e) P. Bellotti, M. Koy, M. N. Hopkinson, F. Glorius, *Nat. Rev. Chem.* **2021**, *5*, 711-725; f) P. de Frémont, N. Marion, S. P. Nolan, *Coord. Chem. Rev.* **2009**, *253*, 862-892.

[42] W. A. Herrmann, L. J. Goossen, C. Köcher, G. R. J. Artus, *Angew. Chem. Int. Ed.* **1996**, *35*, 2805-2807.

[43] D. Zhao, L. Candish, D. Paul, F. Glorius, *ACS Catal.* **2016**, *6*, 5978-5988.

[44] a) M. Mauduit, H. Clavier, in *N-Heterocyclic Carbenes in Synthesis*, **2006**, pp. 183-222; b) F. Wang, L.-j. Liu, W. Wang, S. Li, M. Shi, *Coord. Chem. Rev.* **2012**, *256*, 804-853; c) K. Shimizu, M. Kushima, M. Seki, R. Yasue, K. Yoshida, *J. Org. Chem.* **2024**, *89*, 11811-11817.

[45] a) R. Azpíroz, A. Di Giuseppe, A. Urriolabeitia, V. Passarelli, V. Polo, J. J. Pérez-Torrente, L. A. Oro, R. Castarlenas, *ACS Catal.* **2019**, *9*, 9372-9386; b) P. A. Morton, A. L. Boyce, A. Pišpek, L. W. Stewart, D. J. Ward, B. E. Tegner, S. A. Macgregor, S. M. Mansell, *Organometallics* **2024**, *43*, 974-986; c) W. Gil, A. M. Trzeciak, J. J. Ziółkowski, *Organometallics* **2008**, *27*, 4131-4138; d) I. Özdemir, N. Gürbüz, T. Seçkin, B. Çetinkaya, *Appl. Organomet. Chem.* **2005**, *19*, 633-638; e) L. Yang, A. Krüger, A. Neels, M. Albrecht, *Organometallics* **2008**, *27*, 3161-3171; f) M. T. Zarka, M. Bortenschlager, K. Wurst, O. Nuyken, R. Weberskirch, *Organometallics* **2004**, *23*, 4817-4820; g) P. K. R. Panyam, B. Atwi, F. Ziegler, W. Frey, M. Nowakowski, M. Bauer, M. R. Buchmeiser, *Chem. Eur. J.* **2021**, *27*, 17220-17229.

[46] a) C. Gemel, T. Steinke, M. Cokoja, A. Kempter, R. A. Fischer, *Eur. J. Inorg. Chem.* **2004**, *2004*, 4161-4176; b) P. W. Roesky, *Dalton Trans.* **2009**, 1887-1893; c) S. González-Gallardo, T. Bollermann, R. A. Fischer, R. Murugavel, *Chem. Rev.* **2012**, *112*, 3136-3170; d) M. Asay, C. Jones, M. Driess, *Chem. Rev.* **2011**, *111*, 354-396; e) D. Vidovic, S. Aldridge, *Chem. Sci.* **2011**, *2*, 601-608; f) K. Nagata, T. Agou, N. Tokitoh, *Angew. Chem. Int. Ed.* **2014**, *53*, 3881-3884; g) G. Tan, T. Szilvási, S. Inoue, B. Blom, M. Driess, *J. Am. Chem. Soc.* **2014**, *136*, 9732-9742; h) D. Dange, C. P. Sindlinger, S. Aldridge, C. Jones, *Chem. Commun.* **2017**, *53*, 149-152; i) R. Murugavel, V. Chandrasekhar, *Angew. Chem. Int. Ed.* **1999**, *38*, 1211-1215.

[47] a) T. Steinke, C. Gemel, M. Cokoja, M. Winter, R. A. Fischer, *Angew. Chem. Int. Ed.* **2004**, *43*, 2299-2302; b) T. Steinke, C. Gemel, M. Winter, R. A. Fischer, *Angew. Chem. Int. Ed.* **2002**, *41*, 4761-4763.

[48] a) S. P. Desai, J. Ye, T. Islamoglu, O. K. Farha, C. C. Lu, *Organometallics* **2019**, *38*, 3466-3473; b) J. T. Moore, M. J. Dorantes, Z. Pengmei, T. M. Schwartz, J. Schaffner, S. L. Apps, C. A. Gaggioli, U. Das, L. Gagliardi, D. A. Blank, C. C. Lu, *Angew. Chem. Int. Ed.* **2022**, *61*, e202205575; c) S. P. Desai, J. Ye, J. Zheng, M. S. Ferrandon, T. E. Webber, A. E. Platero-Prats, J. Duan, P. Garcia-Holley, D. M. Camaioni, K. W. Chapman, M. Delferro, O. K. Farha, J. L. Fulton, L.

Gagliardi, J. A. Lercher, R. L. Penn, A. Stein, C. C. Lu, *J. Am. Chem. Soc.* **2018**, *140*, 15309-15318.
[49] N. Hara, T. Saito, K. Semba, N. Kuriakose, H. Zheng, S. Sakaki, Y. Nakao, *J. Am. Chem. Soc.* **2018**, *140*, 7070-7073.
[50] N. Saito, J. Takaya, N. Iwasawa, *Angew. Chem. Int. Ed.* **2019**, *58*, 9998-10002.
[51] M. Green, T. A. Kuc, *J. Chem. Soc. Dalton Trans.* **1972**, 832-839.
[52] a) B. Denise, G. Pannetier, *J. Organomet. Chem.* **1973**, *63*, 423-430; b) D. Brodzki, G. Pannetier, *J. Organomet. Chem.* **1973**, *63*, 431-440.
[53] a) B. Guzel, M. A. Omary, J. P. Fackler, A. Akgerman, *Inorg. Chim. Acta* **2001**, *325*, 45-50; b) A. L. Colebatch, A. I. McKay, N. A. Beattie, S. A. Macgregor, A. S. Weller, *Eur. J. Inorg. Chem.* **2017**, *2017*, 4533-4540; c) S. K. Furfari, B. E. Tegner, A. L. Burnage, L. R. Doyle, A. J. Bukvic, S. A. Macgregor, A. S. Weller, *Chem. Eur. J.* **2021**, *27*, 3177-3183.
[54] J. J. Kim, H. Alper, *Chem. Commun.* **2005**, 3059-3061.
[55] a) T. Cadenbach, C. Gemel, T. Bollermann, R. A. Fischer, *Inorg. Chem.* **2009**, *48*, 5021-5026; b) T. Cadenbach, C. Gemel, D. Zacher, R. A. Fischer, *Angew. Chem. Int. Ed.* **2008**, *47*, 3438-3441.
[56] J. Emerson-King, R. C. Knighton, M. R. Gyton, A. B. Chaplin, *Dalton Trans.* **2017**, *46*, 11645-11655.
[57] a) J. Huang, S. P. Nolan, *J. Am. Chem. Soc.* **1999**, *121*, 9889-9890; b) R. A. Kelly, G. A. Grasa, S. P. Nolan, D. J. Nelson, S. P. Nolan, in *Encyclopedia of Reagents for Organic Synthesis*, **2016**, pp. 1-3.
[58] P. Hermosilla, P. García-Orduña, F. J. Lahoz, V. Polo, M. A. Casado, *Organometallics* **2021**, *40*, 3720-3732.
[59] L. Dahlenburg, N. Osthoff, F. W. Heinemann, *Acta Crystallographica Section E* **2001**, *57*, m117-m118.
[60] a) R. G. Ball, N. C. Payne, *Inorg. Chem.* **1977**, *16*, 1187-1191; b) E. Anzuela, M. A. Garralda, R. Hernández, L. Ibarlucea, E. Pinilla, M. A. Monge, *Inorg. Chim. Acta* **1991**, *185*, 211-219; c) J. G. Leipoldt, S. S. Basson, G. J. Lamprecht, L. D. C. Bok, J. J. J. Schlebusch, *Inorg. Chim. Acta* **1980**, *40*, 43-46.
[61] S. P. Green, C. Jones, D. P. Mills, A. Stasch, *Organometallics* **2007**, *26*, 3424-3430.
[62] a) R. R. Schrock, J. A. Osborn, *J. Am. Chem. Soc.* **1976**, *98*, 2134-2143; b) A. Gómez-España, P. García-Orduña, F. J. Lahoz, I. Fernández, F. J. Fernández-Álvarez, *Organometallics* **2024**, *43*, 402-413; c) J. A. Osborn, F. H. Jardine, J. F. Young, G. Wilkinson, *J. Chem. Soc. A* **1966**, 1711-1732; d) P. C. Abhyankar, C. M. Thomas, *Angew. Chem. Int. Ed.* **2024**, *n/a*, e202416100.
[63] a) M. Findlater, K. M. Schultz, W. H. Bernskoetter, A. Cartwright-Sykes, D. M. Heinekey, M. Brookhart, *Inorg. Chem.* **2012**, *51*, 4672-4678; b) V. I. Bakhmutov, C. Bianchini, M. Peruzzini, F. Vizza, E. V. Vorontsov, *Inorg. Chem.* **2000**, *39*, 1655-1660.
[64] D. G. Gusev, A. B. Vymenits, V. I. Bakhmutov, *Inorg. Chem.* **1992**, *31*, 1-2.
[65] C. Helling, C. Ganesamoorthy, C. Wölper, S. Schulz, *Dalton Trans.* **2022**, *51*, 2050-2058.
[66] M. G. Speziali, F. C. C. Moura, P. A. Robles-Dutenhefner, M. H. Araujo, E. V. Gusevskaya, E. N. dos Santos, *J. Mol. Catal. A Chem.* **2005**, *239*, 10-14.
[67] a) J. A. Widegren, M. A. Bennett, R. G. Finke, *J. Am. Chem. Soc.* **2003**, *125*, 10301-10310; b) J. A. Widegren, R. G. Finke, *J. Mol. Catal. A Chem.* **2003**, *198*, 317-341; c) J. J. Stracke, R. G. Finke, *ACS Catal.* **2014**, *4*, 909-933; d) V. M. Chernyshev, A. V. Astakhov, I. E. Chikunov, R. V. Tyurin, D. B. Eremin, G. S. Ranny, V. N. Khrustalev, V. P. Ananikov, *ACS Catal.* **2019**, *9*, 2984-2995.
[68] N. J. Hardman, B. E. Eichler, P. P. Power, *Chem. Commun.* **2000**, 1991-1992.
[69] a) F. P. Gabbaï, P. J. Chirik, D. E. Fogg, K. Meyer, D. J. Mindiola, L. L. Schafer, S.-L. You, *Organometallics* **2016**, *35*, 3255-3256; b) A. C. Aiken, P. F. DeCarlo, J. L. Jimenez, *Anal. Chem.* **2007**, *79*, 8350-8358; c) R. E. H. Kuveke, L. Barwise,

Y. van Ingen, K. Vashisth, N. Roberts, S. S. Chitnis, J. L. Dutton, C. D. Martin, R. L. Melen, *ACS Cent. Sci.* **2022**, *8*, 855-863.

Publications

4.1 Introduction

In this section was included the scientific works published during the development of this *Doctoral Thesis*. Some of these results have been carried out in parallel with all the research date discussed in the last chapters.

Book Chapters:

The first scientific work was published in a book chapter based on the reactivity of organometallic species in confined spaces in solid/gas phases. Here, it was summarised most of the interesting cases observed under these conditions.

Therefore, this bibliographic work was published in *Monograph in Supramolecular Chemistry. Reactivity in Confined Spaces.*

Authors: Videa, H; Martínez-Martínez, A. J.*

Edited by: Lloyd, G. and Forgan, R. S.

Hardback ISBN: 978-1-78801-776-3

Year: 2021

DOI: 10.1039/9781788019705-00282

Journal Publications:

The first work published based on the first structural elucidation of β-diketiminate anions (BDI^-), known for strong coordination, in their unbound form within caesium complexes. β-Diketiminate caesium salts (BDICs) were synthesised, and upon the addition of Lewis donor ligands, free BDI^- anions and donor-solvated Cs^+ cations were observed. Notably, the liberated BDI^- anions exhibited an unprecedented dynamic cisoid–transoid exchange in solution.

Hence, these results were published in *Dalton Transactions* journal.

Authors: Videa, H; Martínez-Martínez, A. J.*

Citation: Dalton Trans., **2023**, *52*, 13058–13062

DOI: 10.1039/d3dt01592k

The second reported work was a collaboration of our group with Prof. Juan Cámpora, and Dr. Antonio Rodriguez-Delgado groups from *Instituto de Investigaciones Químicas, CSIC-Universidad de Sevilla*. Therefore, we report the synthesis of cationic 2,6-bisiminopyridine organoaluminium complexes, $[(BIP)AlR_2]^+$, as stable $BAr^F{}_4^-$ and PF_6^- salts, and their reversible single-electron reduction into well-defined paramagnetic species, $[(BIP^{\cdot})AlR_2]$. Four redox couples, $[(BIP)AlR_2]^{+/0}$, have been fully characterised through structural, spectroscopic, electrochemical and computational techniques.

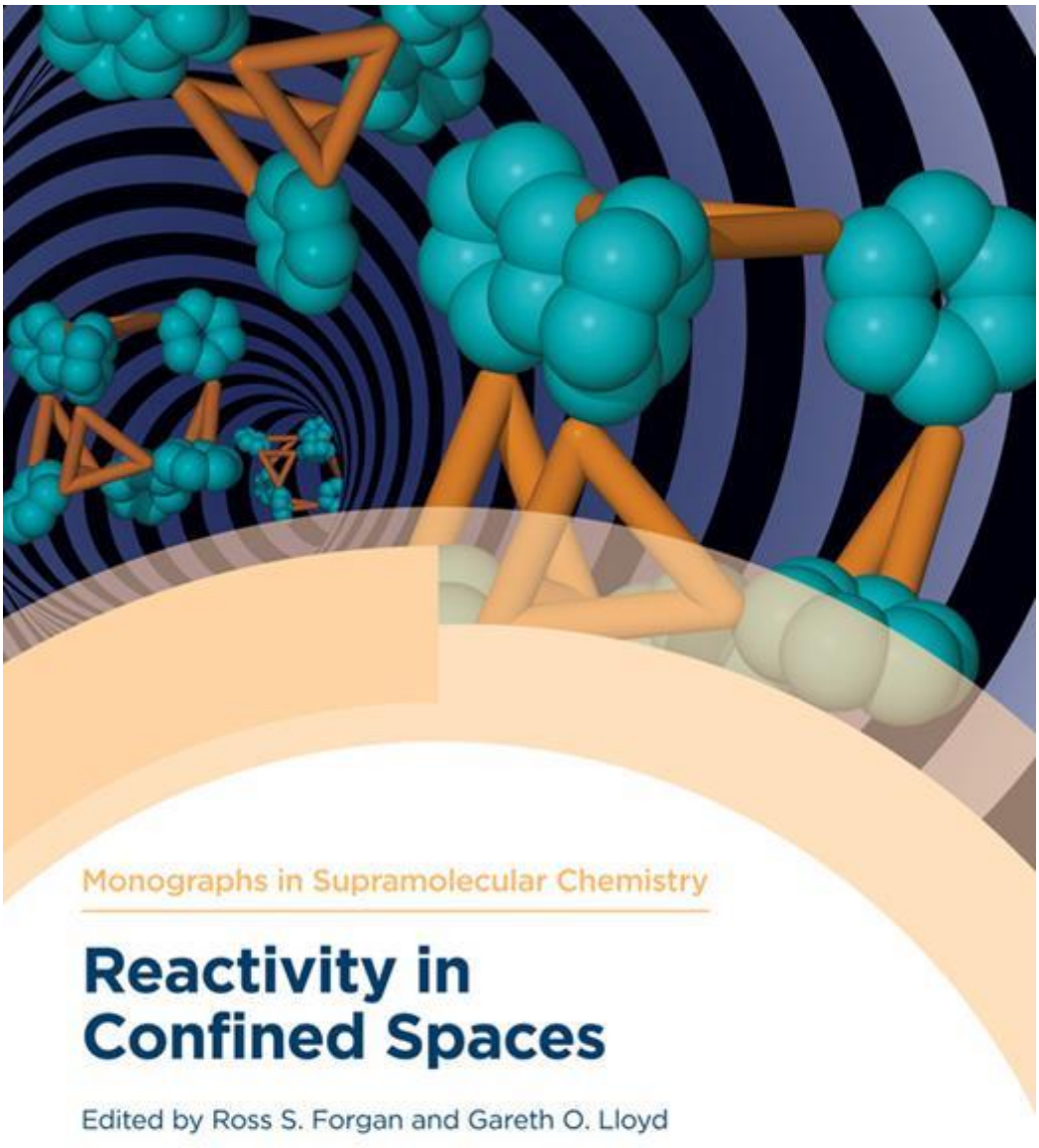
These results were published in *Inorganic Chemistry* journal.

Authors: Delgado-Collado, J. M., Videa, H., Serrano-Laguna, P. J., Fuentes, M. A., Álvarez, E., Diaz Quintana, A., Martinez-Martinez, A. J., Rodriguez-Delgado, A., and Cámpora J.

Citation: Inorg. Chem. **2024**, *63*, 19156−19166

DOI: 10.1021/acs.inorgchem.4c02664

4.2 Chapter 9: Solid/Gas Reactivity of Organometallic Species in Confined Spaces



CHAPTER 9

Solid/Gas Reactivity of Organometallic Species in Confined Spaces

HELLEN VIDEA AND ANTONIO J. MARTÍNEZ-MARTÍNEZ*

CIQSO-Centre for Research in Sustainable Chemistry and Department of Chemistry, University of Huelva, Campus El Carmen, ES-21007 Huelva, Spain
*Email: antonio.martinez@ciqso.uhu.es

9.1 Introduction

Catalysis is key to advancing sustainable and green protocols in synthetic chemistry.[1] The use of catalysts has the advantage, over stoichiometric methodologies, of allowing bond activation reactions, otherwise difficult, and shortening multistep synthetic protocols. In this context, organometallic chemistry has been long recognised for enabling bond breaking/forming reactions that are often unprecedented with organic chemistry. This remarkable capacity of organometallic chemistry for new chemical reactivity makes transition and main group metals indispensable for the production of feedstock chemicals, in both stoichiometric and catalytic transformations. For example, stoichiometric alkyl lithium reagents are widely used in the large-scale chemical manufacturing[2] and transition metals in catalytic transformations.[3] Three fundamental aspects have driven advances in organometallic chemistry and catalysis: ligand design, manipulation of oxidation states and electronic excitation. The application of supramolecular concepts to catalysis and organometallic chemistry, supramolecular catalysis[4] and supramolecular organometallic chemistry[5] is an emerging tool for improving selectivity,

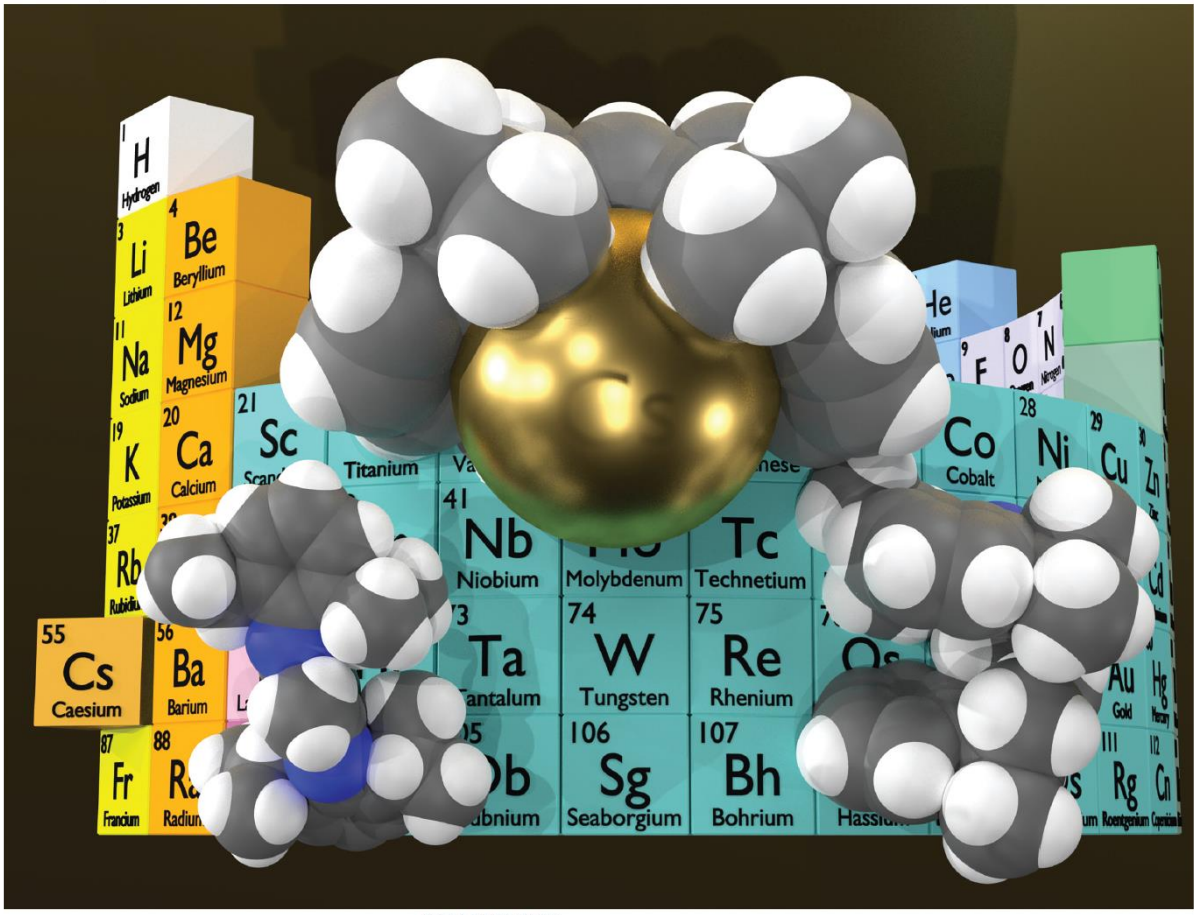
Monographs in Supramolecular Chemistry No. 31
Reactivity in Confined Spaces
Edited by Gareth Lloyd and Ross S. Forgan
© The Royal Society of Chemistry 2021
Published by the Royal Society of Chemistry, www.rsc.org

4.3 Revealing unbound β-diketiminate anions: structural dynamics from caesium complexes

Volume 52
Number 37
7 October 2023
Pages 13013-13438

Dalton Transactions

An international journal of inorganic chemistry
rsc.li/dalton



ISSN 1477-9226

ROYAL SOCIETY OF CHEMISTRY

COMMUNICATION
Hellen Videa and Antonio J. Martínez-Martínez
Revealing unbound β-diketiminate anions: structural dynamics from caesium complexes

Dalton Transactions

ROYAL SOCIETY OF CHEMISTRY

COMMUNICATION

View Article Online
View Journal | View Issue

Check for updates

Cite this: *Dalton Trans.*, 2023, **52**, 13058

Received 25th May 2023,
Accepted 15th June 2023

DOI: 10.1039/d3dt01592k

rsc.li/dalton

Revealing unbound β-diketiminate anions: structural dynamics from caesium complexes†‡

Hellen Videa and Antonio J. Martínez-Martínez *

This study reports the first structural elucidation of β-diketiminate anions (BDI$^-$), known for strong coordination, in their unbound form within caesium complexes. β-Diketiminate caesium salts (BDICs) were synthesised, and upon the addition of Lewis donor ligands, free BDI$^-$ anions and donor-solvated Cs$^+$ cations were observed. Notably, the liberated BDI$^-$ anions exhibited an unprecedented dynamic *cisoid–transoid* exchange in solution.

Monoanionic β-diketiminate (BDI) ligands,[1] commonly referred to as NacNac ligands, are an important class of ligands with diverse applications in multiple chemical fields.[2] Characterised by two ketiminate moieties linked by a 1,3-carbon chain, these ligands can be readily obtained *via* the deprotonation of β-diketimines (Fig. 1A).[3] BDI ligands are known for their ability to stabilise a broad array of metal ions from the s,[4] p,[5] d[6] and f-blocks[7] in diverse oxidation states by forming strong coordination complexes. Moreover, they have been shown to enhance catalytic activity, selectivity, and stability in several processes, including olefin polymerisation[8] and copolymerization,[9] transfer hydrogenation,[10] and cross-coupling reactions.[11] BDI ligands have demonstrated potential in developing unique main group species[12] with unconventional electronic and stereochemical properties that enable novel reactivity and catalysis.[13] They have also been used in material science for crafting novel metal–organic frameworks (MOFs),[14] biomedical chemistry for developing new metal-based therapeutics,[15] and biochemistry for modelling metalloenzymes.[16]

While BDI ligands commonly form stable and robust chelating complexes by donating two nitrogen atoms as κ^2-*N*,*N*′-ligands **I** (Fig. 1B),[17] examples of alternative coordination modes involving partial ligand dissociation have also been observed, **II–V**.[18] Recent studies have underscored the importance of the dissociation properties of BDI ligands in catalysis and bond activation chemistry. For instance, BDI dissociation has been shown to boost catalytic activities in lactide polymerisation with $(BDI)_2ZrCl_2$ species,[19] trigger C–F activation in hemilabile (BDI)Co(I) complexes,[18d,20] and promote unusual ligand rearrangements during N_2 activation in low-valent $[(BDI)Ca(I)]_2$ species.[21] Thus, understanding the dissociation and free anionic forms of BDI ligands is pivotal for gaining a deeper insight into their chemistry. However, despite their widespread use, examples of free BDI$^-$ anions have remained elusive.

In this study, we explored the free-form structures of BDI$^-$ exhibiting *cisoid–transoid* dynamic behaviour in solution, using various spectroscopic and crystallographic techniques. We report novel examples of unbound ^{Dipp}BDI$^-$ $[(DippNCMe)_2CH]^-$ anions (Dipp = 2,6-$iPr_2C_6H_3$) and examine them in their "*naked*" state, free from metal-ion binding interactions. To achieve this, we selected heavy and soft alkali metal caesium (Cs), the Lewis donor solvent THF, and strongly coordinating secondary ligands such as 18-crown-6 and [2.2.2]

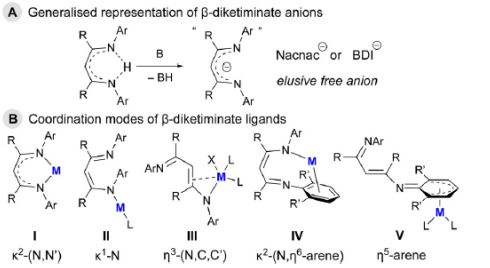


Fig. 1 (A) Generalised representation of β-diketiminate (BDI) anions. (B) Known coordination modes of BDI ligands.

CIQSO – Centre for Research in Sustainable Chemistry and Department of Chemistry, University of Huelva, Campus El Carmen, Huelva ES-21007, Spain. E-mail: antonio.martinez@ciqso.uhu.es

†Dedicated to Professor Robert E. Mulvey for his unwavering guidance and mentorship.

‡Electronic supplementary information (ESI) available: Experimental procedures, characterisation data, selected figures, computational and crystallographic details. CCDC 2256945–2256948. For ESI and crystallographic data in CIF or other electronic format see DOI: https://doi.org/10.1039/d3dt01592k

This journal is © The Royal Society of Chemistry 2023

cryptand. The selection of Cs was motivated by its larger ionic radius and higher polarisability, typically leading to weaker ligand interactions than lighter alkali metals, a behaviour discussed extensively in the context of alkali metal mediation in organometallic chemistry.[22] Our work represents the first identification of BDI^- anions without metal-ion binding, offering valuable insights into their properties.

Deprotonation of the β-diketimine proligand ^{Dipp}BDI(H) by caesium bis(trimethylsilyl)amide CsHMDS[23] occurred quantitatively within 1 h at room temperature (Fig. 2A), as evidenced by ^{1}H NMR spectroscopy. The resulting caesium salt (BDI)Cs was isolated in 45% yield. Crystals of $[(BDI)Cs]_\infty$ **1**, obtained by the slow diffusion of freshly distilled *n*-hexane into a toluene solution of the complex, confirmed the formation of a solvent-free complex (Fig. 2B). The BDI ligand chelates the Cs^+ metal ion (Cs–N 2.972(2) and 2.941(2) Å) in **1**, resembling lighter alkali metal κ^2-*N*,*N*′-derivatives (Li,[24] Na,[25] and K[7d]). Cs coordination is further facilitated by internal Cs···π(η^2-arene) (3.334(2)–3.765(3) Å) contacts, along with additional Cs···π(η^6-arene) (3.35 Å) and Cs···Me (3.828(2) Å) interactions with neighbouring molecules, leading to a zigzag polymeric structure. NMR data of **1**, obtained in Tol-d_8 solution at room temperature, revealed a symmetric C_{2v} BDI skeleton with characteristic resonance signals at δ 4.75 and 1.86 ppm for the backbone γ-CH and Me groups in the ^{1}H NMR spectrum (δ range 4.67–5.10 and 1.75–2.15 ppm, respectively, for Li,[26,24b] Na[25] and K[27]). Diffusion-Ordered NMR Spectroscopy (DOSY) revealed polymer monomerization through the coordination of toluene molecules, leading to $[(BDI)Cs(toluene)_n]$ **1·(toluene)$_n$** monomeric aggregates in Tol-d_8 solution.

When the stronger coordinating solvent THF-d_8 was used, the ^{1}H NMR spectrum of **1** exhibited a noticeable broadening at room temperature. The γ-CH and Me groups resonated as singlets at δ 4.23 and 1.54 ppm, respectively. This suggests that BDI chelates Cs^+, accompanied by further THF coordination. This resulted in monomers identified as $[(BDI)Cs(THF)_n]$ **1·(THF)$_n$**, supported by DOSY NMR studies, resembling the observed behaviour of **1·(toluene)$_n$**. As the temperature decreased, resonance signals of **1·(THF)$_n$** sharpened, with the γ-CH and Me signal appearing at δ 4.21 and 1.52 ppm at 258 K, respectively. Similar to **1·(toluene)$_n$**, the NMR data for **1·(THF)$_n$** in the 333–258 K temperature range reveal a symmetrical BDI array. Interestingly, the ^{1}H NMR spectrum of **1·(THF)$_n$** displayed two additional sets of broad resonances at room temperature, which narrowed into two sets of signals in a 10 : 1 ratio at 258 K (40% relative to that of **1**). Each new set of signals consisted of two distinct Dipp, one γ-CH, and two Me environments, indicating two new asymmetrical BDI species in solution. The significantly shielded γ-CH groups for both species (δ 3.55 ppm, overlapped) suggested discoordination of the BDI ligand (δ 3.80 ppm for γ-CH in related κ^1-(*N*, arene) BDI examples).[18e] Also, the two distinct Me groups resonate at δ 2.51/1.22 and δ 2.16/1.22 for the major and minor BDI species, respectively (note that two Me signals are overlapped), reflecting asymmetric BDI skeletons. We hypothesised that the partial ionisation of **1** in THF-d_8 would lead to the formation of two distinct separated ion pairs (SIPs) of the type $[Cs]^+[BDI]^-$, comprising two types of unbound asymmetrical $[BDI]^-$ anions and free THF-solvated $[(THF)_nCs]^+$ cations. Excitingly, ^{1}H NMR titrations of **1** in THF-d_8 with increasing amounts of the bulkier and strongly coordinating crown ether 18-crown-6 (18-cr-6, 0–2 equiv.) or encapsulating [2.2.2]cryptand (crypt, 0–1 equiv.) exclusively produced these two new asymmetric BDI species in the same ratio as THF-d_8, accompanied by the presence of either $[(18\text{-cr-}6)_2Cs]^+$ or $[(crypt)Cs]^+$ cations. This observation showed, for the first time, the complete dissociation of the BDI ligand, generating SIP species $[(donor)Cs]^+[BDI]^-$ in solution. We attempted kinetic studies to study the pathways and factors governing BDI ligand dissociation; however, our efforts were hindered by the overlapping of NMR signals and the small amount of one of the free BDI^- anionic species in the studied temperature range.

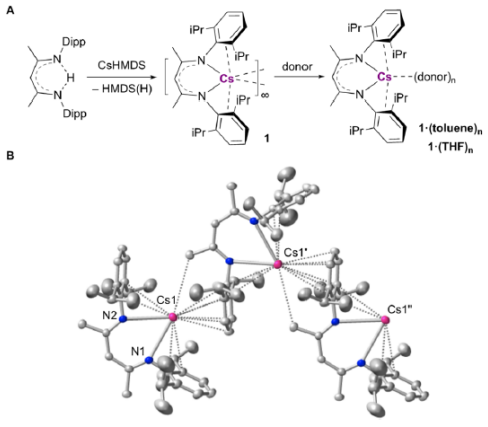


Fig. 2 (A) Synthesis of $[(BDI)Cs]_\infty$ **1**. (B) Crystal structure of **1** showing a section of the polymeric zigzag array *via* Cs···π(arene) and Cs···Me contacts.

To gain a better understanding of these new BDI species, we synthesised and isolated the corresponding SIP species, $[(18\text{-cr-}6)_2Cs]^+[(BDI)]^-$ **2** and $[(crypt)Cs]^+[(BDI)]^-$ **3** (Fig. 3A). The addition of 18-cr-6 (2 equiv.) and crypt (1 equiv.) to **1** in toluene yielded **2** and **3** as yellow powders in isolated yields of 40 and 54%, respectively. Crystallisation from *n*-hexane/toluene allowed us to obtain crystals of **2a** and **3a**. X-ray diffraction analysis confirmed their arrangements as solvent-separated ion-pairs (Fig. 3B and C). In **2a**, the Cs^+ ion is fully solvated by two molecules of 18-cr-6, whereas in **3a**, Cs^+ is fully entrapped by a crypt molecule. Remarkably, the BDI^- anion remains unbound and adopts a *transoid* conformation (indicated by the relative position of the Me backbone groups). Intriguingly, crystals of a second isomeric form, **2b**, featuring a *ciscoid* conformation of the BDI^- anion, were obtained by crystallising **2** in a mixture of *n*-hexane/THF (Fig. 3C). The metrics

This journal is © The Royal Society of Chemistry 2023

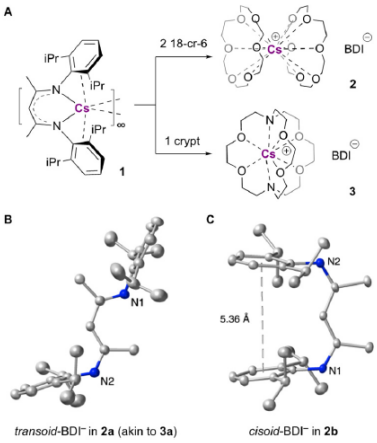


Fig. 3 (A) Synthesis of $[(18\text{-cr-}6)_2Cs]^+[(BDI)]^-$ 2 and $[(crypt)Cs]^+[(BDI)]^-$ 3. (B) and (C) Crystal structures of 2a and 2b showing the *transoid* and *cisoid* isomeric forms of BDI^- anions. 2a and 3a exhibit identical *transoid* BDI arrays. The Cs cations were omitted for clarity.

of the cation $[(18\text{-cr-}6)_2Cs]^+$ are similar to those in **2a**. Both the *transoid*-BDI^- and *cisoid*-BDI^- anions in structures **2a**, **2b** and **3a** present average C–N and C–C bond lengths that lie between those of single and double bonds (1.309(4)–1.326(5) and 1.408(4)–1.427(7) Å, respectively), indicative of charge delocalisation across the BDI backbone. A noteworthy feature of **2b** is the BDI^- anions staggered yet eclipsed arrangement of the two aromatic Dipp groups, which are separated by a distance of 5.63 Å.

The reproducibility of multiple independent crystallisations from isolated powders **2** and **3**, yielding *transoid*-BDI^- anions within the structures of **2a** and **3a** and *cisoid*-BDI^- in **2b**, underscores the dynamic nature of free BDI^- anions and their sensitivity to the surrounding environment. This anion sensitivity to environmental conditions is also reflected in the crystal packing effects observed in the structures of **2a**, **2b**, and **3a**. Weak noncovalent $Cs^+\cdots$Me and $Cs^+\cdots\pi$(arene) interactions between the ancillary Dipp aromatic groups of the BDI^- anions and the $[(18\text{-cr-}6)_2Cs]^+$ or $[(crypt)Cs]^+$ cations are evident in structures **2a** and **3a**, where the BDI^- anion adopts a *transoid* arrangement. The absence of these weak interactions in the structure of **2b** promotes a highly compact *cisoid*-BDI^- conformation that compensates for the lack of noncovalent anion–cation interactions. Taken together, these unique BDI^- anion conformations, which are shaped by the presence or absence of weak ionic and noncovalent interactions, highlights the influence of the Cs^+ cations and coordinating ligands on the BDI^- anions.

NMR experiments conducted on small samples of crystals of **2a**, **2b**, and **3a**, or powders **2** and **3**, revealed identical NMR data (^1H and ^{13}C), except for the signals corresponding to the different cations $[(18\text{-cr-}6)_2Cs]^+$ and $[(crypt)Cs]^+$. This finding suggests the rapid interconversion of *cisoid* and *transoid* BDI^- species, following the equilibrium $[(donor)Cs]^+[transoid\text{-}BDI]^- \rightleftarrows [(donor)Cs]^+[cisoid\text{-}BDI]^-$. The absence of any correlation or trend in the ^{133}Cs NMR chemical shifts for the various Cs–BDI complexes indicates that Cs^+ cations are affected by the dynamic nature of the BDI^- anions. Furthermore, 2D chemical exchange ^1H–^1H EXSY NMR experiments on the 18-cr-6 and crypt SIP $[(donor)_nCs]^+[(BDI)]^-$ species confirmed this dynamic process (Fig. 4A), which likely involves bond rotations in the BDI backbone chain. DFT calculations considering THF solvent effects (Fig. 4B) demonstrated that the *transoid* conformation C, characterised in the crystal structures of **2a** and **3a**, is more stable than the *cisoid* conformation E found in **2b**, by 2.6 kcal mol^{-1}. These calculations also suggest that rotations within the BDI^- anion backbone around the C–C and C–N bonds involve almost energetically equivalent *cisoid* and *transoid* rotamers A ⇄ E. Particularly, the unbound chelating conformation A was found to be less stable by 5.2 kcal mol^{-1} when compared to the *transoid* conformation C. Furthermore, DOSY NMR studies support the existence of the SIP species $[(donor)_nCs]^+[(BDI)]^-$, indicating weak noncovalent electrostatic interactions between pairs $[(donor)_nCs]^+\cdots[BDI]^-$. This state suggests high anion polarisation of BDI^- species in solution, requiring electrostatic contact with electropositive $[(donor)_nCs]^+$ cations for stabilisation, similar to the crystal packing effects observed for the *transoid* isomer in the solid-state structures of **2a** and **3a**. Collectively, these findings suggest that the *transoid* arrangement predominates in solu-

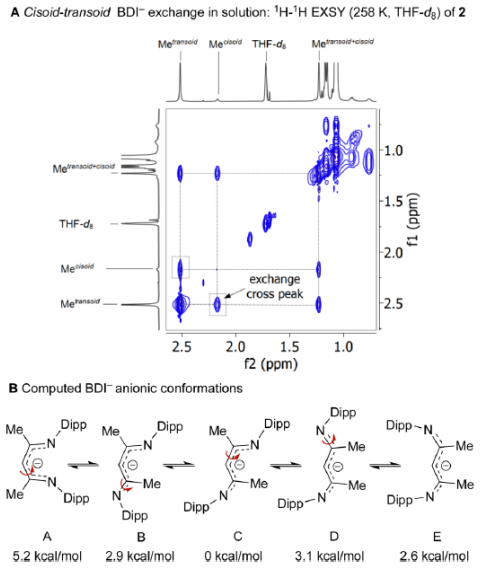


Fig. 4 (A) EXSY NMR study showing *cisoid*–*transoid* exchange between BDI^- anions in 2 in THF-d_8 solution. (B) Conformers of BDI^- anions computed through backbone rotations (Gibbs free energies in THF at 298 K).

This journal is © The Royal Society of Chemistry 2023

tion, emphasising the dynamic behaviour and sensitivity of BDI^- anions to the surrounding ionic environment.

Conclusions

In conclusion, we successfully synthesised and characterised a series of BDI complexes with Cs cations. These complexes dissociate to form solvent-separated ion-pairs with free, unbound BDI^- anions in the presence of coordinating ligands such as THF, 18-cr-6, and crypt. This study provides valuable insights into the structural and dynamic features of unbound BDI^- anions in *cisoid* and *transoid* conformations, and their weak interactions with counterions in solution and in solid form. Notably, the presence of Cs^+ cations enables weak interactions and dynamic *cisoid–transoid* BDI^- exchange in solution, thus challenging the conventional view of BDI ligands as predominantly bound entities to metal ions. These findings have important implications for the design and utilisation of new BDI ligands in coordination chemistry, catalysis, and related areas, encouraging further studies of unbound BDI^- anions within other soft metal systems.

Conflicts of interest

There are no conflicts to declare.

Acknowledgements

The authors acknowledge financial support from the Spanish Ministry of Science and Innovation (PID2019-108292RA-I00, EUR2020-112189), FEDER, the Andalusian Government (P20-00373), the University of Huelva (UHU-202043), and the Spanish Research State Agency AEI for a Ramón y Cajal Research Contract (RYC-2017-21783). We thank Prof. F. J. Blas for his valuable assistance with the computational studies. Funding for open access charge: Universidad de Huelva/CBUA.

References

1 (*a*) S. G. McGeachin, *Can. J. Chem.*, 1968, **46**, 1903–1912; (*b*) J. E. Parks and R. H. Holm, *Inorg. Chem.*, 1968, 7, 1408–1416.
2 (*a*) L. Bourget-Merle, M. F. Lappert and J. R. Severn, *Chem. Rev.*, 2002, **102**, 3031–3066; (*b*) S. Hohloch, B. M. Kriegel, R. G. Bergman and J. Arnold, *Dalton Trans.*, 2016, **45**, 15725–15745; (*c*) R. L. Webster, *Dalton Trans.*, 2017, **46**, 4483–4498.
3 D. J. Mindiola, P. L. Holland and T. H. Warren, in *Inorg. Synth*, ed. T. B. Rauchfuss, John Wiley & Sons, Inc., 2010, vol. 35, pp. 1–55.
4 S. P. Sarish, S. Nembenna, S. Nagendran and H. W. Roesky, *Acc. Chem. Res.*, 2011, **44**, 157–170.
5 M. Asay, C. Jones and M. Driess, *Chem. Rev.*, 2011, **111**, 354–396.
6 C. Chen, S. M. Bellows and P. L. Holland, *Dalton Trans.*, 2015, **44**, 16654–16670.
7 (*a*) S. V. Klementyeva, M. Y. Afonin, A. S. Bogomyakov, M. T. Gamer, P. W. Roesky and S. N. Konchenko, *Eur. J. Inorg. Chem.*, 2016, **2016**, 3666–3672; (*b*) W. Mao, L. Xiang and Y. Chen, *Coord. Chem. Rev.*, 2017, **346**, 77–90; (*c*) M. A. Boreen, C. A. Gould, C. H. Booth, S. Hohloch and J. Arnold, *Dalton Trans.*, 2020, **49**, 7938–7944; (*d*) O. A. Mironova, T. S. Sukhikh, S. N. Konchenko and N. A. Pushkarevsky, *Inorg. Chem.*, 2022, **61**, 15484–15498.
8 (*a*) D. Liu, C. Yao, R. Wang, M. Wang, Z. Wang, C. Wu, F. Lin, S. Li, X. Wan and D. Cui, *Angew. Chem., Int. Ed.*, 2015, **54**, 5205–5209; (*b*) F. Lin, Z. Liu, M. Wang, B. Liu, S. Li and D. Cui, *Angew. Chem., Int. Ed.*, 2020, **59**, 4324–4328.
9 S.-F. Yuan, Y. Yan, G. A. Solan, Y. Ma and W.-H. Sun, *Coord. Chem. Rev.*, 2020, **411**, 213254.
10 M. Espinal-Viguri, S. E. Neale, N. T. Coles, S. A. Macgregor and R. L. Webster, *J. Am. Chem. Soc.*, 2019, **141**, 572–582.
11 (*a*) A. Bakhoda, O. E. Okoromoba, C. Greene, M. R. Boroujeni, J. A. Bertke and T. H. Warren, *J. Am. Chem. Soc.*, 2020, **142**, 18483–18490; (*b*) R. Li, X. Yang and H. Ping, *Catal. Sci. Technol.*, 2022, **12**, 4281–4287.
12 (*a*) S. P. Green, C. Jones and A. Stasch, *Science*, 2007, **318**, 1754–1757; (*b*) M. Zhong, S. Sinhababu and H. W. Roesky, *Dalton Trans.*, 2020, **49**, 1351–1364; (*c*) C. Färber, P. Stegner, U. Zenneck, C. Knüpfer, G. Bendt, S. Schulz and S. Harder, *Nat. Commun.*, 2022, **13**, 3210.
13 (*a*) M. Arrowsmith, M. S. Hill, G. Kociok-Köhn, D. J. MacDougall and M. F. Mahon, *Angew. Chem., Int. Ed.*, 2012, **51**, 2098–2100; (*b*) T. Chu, I. Korobkov and G. I. Nikonov, *J. Am. Chem. Soc.*, 2014, **136**, 9195–9202; (*c*) M. D. Anker, M. S. Hill, J. P. Lowe and M. F. Mahon, *Angew. Chem., Int. Ed.*, 2015, **54**, 10009–10011; (*d*) L. Davin, R. McLellan, A. R. Kennedy and E. Hevia, *Chem. Commun.*, 2017, **53**, 11650–11653; (*e*) H. Bauer, M. Alonso, C. Färber, H. Elsen, J. Pahl, A. Causero, G. Ballmann, F. De Proft and S. Harder, *Nat. Catal.*, 2018, **1**, 40–47; (*f*) T. N. Hooper, M. Garçon, A. J. P. White and M. R. Crimmin, *Chem. Sci.*, 2018, **9**, 5435–5440; (*g*) M. Magre, B. Maity, A. Falconnet, L. Cavallo and M. Rueping, *Angew. Chem., Int. Ed.*, 2019, **58**, 7025–7029; (*h*) R. M. Gauld, J. R. Lynch, A. R. Kennedy, J. Barker, J. Reid and R. E. Mulvey, *Inorg. Chem.*, 2021, **60**, 6057–6064.
14 N. C. Thacker, Z. Lin, T. Zhang, J. C. Gilhula, C. W. Abney and W. Lin, *J. Am. Chem. Soc.*, 2016, **138**, 3501–3509.
15 J. M. Hope, J. J. Wilson and S. J. Lippard, *Dalton Trans.*, 2013, **42**, 3176–3180.
16 D. J. E. Spencer, N. W. Aboelella, A. M. Reynolds, P. L. Holland and W. B. Tolman, *J. Am. Chem. Soc.*, 2002, **124**, 2108–2109.
17 C. Camp and J. Arnold, *Dalton Trans.*, 2016, **45**, 14462–14498.

This journal is © The Royal Society of Chemistry 2023

18 (*a*) R. J. Wright, P. P. Power, B. L. Scott and J. L. Kiplinger, *Organometallics*, 2004, **23**, 4801–4803; (*b*) W. H. Bernskoetter, E. Lobkovsky and P. J. Chirik, *Organometallics*, 2005, **24**, 6250–6259; (*c*) N. Carrera, N. Savjani, J. Simpson, D. L. Hughes and M. Bochmann, *Dalton Trans.*, 2011, **40**, 1016–1019; (*d*) T. R. Dugan, X. Sun, E. V. Rybak-Akimova, O. Olatunji-Ojo, T. R. Cundari and P. L. Holland, *J. Am. Chem. Soc.*, 2011, **133**, 12418–12421; (*e*) A. J. Wooles, W. Lewis, A. J. Blake and S. T. Liddle, *Organometallics*, 2013, **32**, 5058–5070.
19 (*a*) I. El-Zoghbi, S. Latreche and F. Schaper, *Organometallics*, 2010, **29**, 1551–1559; (*b*) I. El-Zoghbi, T. J. J. Whitehorne and F. Schaper, *Dalton Trans.*, 2013, **42**, 9376–9387.
20 M. H. Al-Afyouni, E. Suturina, S. Pathak, M. Atanasov, E. Bill, D. E. DeRosha, W. W. Brennessel, F. Neese and P. L. Holland, *J. Am. Chem. Soc.*, 2015, **137**, 10689–10699.
21 B. Rösch, T. X. Gentner, J. Langer, C. Färber, J. Eyselein, L. Zhao, C. Ding, G. Frenking and S. Harder, *Science*, 2021, **371**, 1125–1128.
22 T. X. Gentner and R. E. Mulvey, *Angew. Chem., Int. Ed.*, 2021, **60**, 9247–9262.
23 A. I. Ojeda-Amador, A. J. Martínez-Martínez, A. R. Kennedy and C. T. O'Hara, *Inorg. Chem.*, 2016, **55**, 5719–5728.
24 (*a*) B. A. Jazdzewski, P. L. Holland, M. Pink, V. G. Young, D. J. E. Spencer and W. B. Tolman, *Inorg. Chem.*, 2001, **40**, 6097–6107; (*b*) M. Stender, R. J. Wright, B. E. Eichler, J. Prust, M. M. Olmstead, H. W. Roesky and P. P. Power, *J. Chem. Soc., Dalton Trans.*, 2001, 3465–3469; (*c*) N. Burford, M. D'Eon, P. J. Ragogna, R. McDonald and M. J. Ferguson, *Inorg. Chem.*, 2004, **43**, 734–738; (*d*) P. Jutzi, K. Leszczyńska, A. Mix, B. Neumann, W. W. Schoeller and H.-G. Stammler, *Organometallics*, 2009, **28**, 1985–1987; (*e*) R. M. Gauld, J. R. Lynch, A. R. Kennedy, J. Barker, J. Reid and R. E. Mulvey, *Inorg. Chem.*, 2021, **60**, 6057–6064.
25 B. Rösch, T. X. Gentner, J. Eyselein, J. Langer, H. Elsen and S. Harder, *Nature*, 2021, **592**, 717–721.
26 B. Qian, D. L. Ward and M. R. Smith, *Organometallics*, 1998, **17**, 3070–3076.
27 W. Clegg, E. K. Cope, A. J. Edwards and F. S. Mair, *Inorg. Chem.*, 1998, **37**, 2317–2319.

This journal is © The Royal Society of Chemistry 2023

4.4 Reversible Redox Ligand-Centered Reactivity in 2,6-Bisiminopyridine Aluminum Systems

Inorganic Chemistry

Open Access

This article is licensed under CC-BY 4.0

pubs.acs.org/IC

Article

Reversible Redox Ligand-Centered Reactivity in 2,6-Bisiminopyridine Aluminum Systems

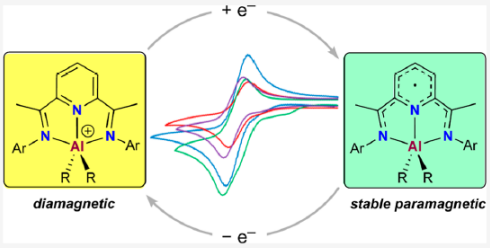
Juan Manuel Delgado-Collado,[§] Hellen Videa,[§] Pablo J. Serrano-Laguna,[§] M. Ángeles Fuentes, Eleuterio Álvarez, Antonio Díaz Quintana, Antonio J. Martínez-Martínez,* Antonio Rodríguez-Delgado,* and Juan Cámpora*

Cite This: *Inorg. Chem.* 2024, 63, 19156−19166

Read Online

ACCESS | Metrics & More | Article Recommendations | Supporting Information

ABSTRACT: We report the synthesis of cationic 2,6-bisiminopyridine organoaluminum complexes, $[(BIP)AlR_2]^+$, as stable $BAr^F{}_4^-$ or PF_6^- salts, and their reversible single-electron reduction into well-defined paramagnetic species, $[(BIP^{\cdot})AlR_2]$. Four redox couples, $[(BIP)AlR_2]^{+/0}$, have been fully characterized through structural, spectroscopic, electrochemical and computational techniques.



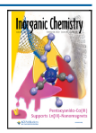
■ INTRODUCTION

Replacing costly or scarce chemical elements with more abundant alternatives is essential for advancing sustainable technologies.[1] This task is particularly challenging for catalysts based on noble metals since these facilitate various bond formation/cleavage reactions through facile and reversible two-electron redox processes—a capability not easily replicated by more abundant metals.[2,3] While many artificial catalysts rely on these scarce precious metals, living organisms employ enzymes containing "base" metals like Fe or Cu and, frequently, main-group elements like Zn or Mg that lack inherent redox capabilities.[4] In these biological systems, the organic ligand framework is crucial for enabling electron, proton, or even complex molecular fragment transfers in a highly selective fashion.

Recent advances have demonstrated that base-metal catalysts can be significantly enhanced by "metal−ligand" cooperative effects, where ligands actively complement the metal by accepting or releasing electrons, protons, and/or functional units,[5,6] thereby mimicking enzyme-like behavior. This includes the redox "non-innocence" phenomenon, whereby ligands mediate electron transfers independently from the metal,[7] thus enhancing the versatility of catalysts in precious-metal-free transformations across a wide variety of substrates, including CO_2.[8] Particularly interesting are the 2,6-bis(imino)pyridine (BIP) ligands,[9] whose ability to reversibly take up to four electrons can impart "nobility" to base metals such as Co or Fe.[10,11] These BIP ligands enable such base metal complexes to catalyze reactions typically reserved for precious metals like C−C couplings,[12] hydrogenations,[13] hydrosilylations[14] or hydroborations.[15]

Building on the initial work on the interaction of [(BIP)Fe] systems with AlR_3 reagents reported by Gambarotta,[16] and some of us,[17] which led to the discovery of unusual paramagnetic organoaluminum $[(BIP^{\cdot})AlR_2]$ species, we have now devised their rational synthesis and unveiled their uniqueness to undergo reversible redox processes. Despite the established reactivity and applications in catalysis of some main-group metal $[(BIP)MX_n]$ complexes,[8,18,19] including Berben's systems with "AlH",[20] "AlCl"[21] and "$AlCl_2$"[22] fragments, a straightforward approach to reversibly manipulate reduced "Al^{2+}"-like species has remained elusive. Herein, we present a simple method for reversible ligand-centered reduction of aluminum species without significant structural alterations. We report the synthesis of cationic organoaluminum complexes $[(BIP)AlR_2]^+$, $\mathbf{1}^+$, and their reversible single-electron reduction to well-defined and isolable paramagnetic $[(BIP^{\cdot})AlR_2]$, **2** (Scheme 1). Our study expands the understanding of BIP redox capabilities with main-group metals and showcases reversible redox organoaluminum pairs $[(BIP)AlR_2]^{+/0}$, illustrating their potential for redox-mediated reactivity.

Received: June 27, 2024
Revised: September 18, 2024
Accepted: September 24, 2024
Published: October 4, 2024

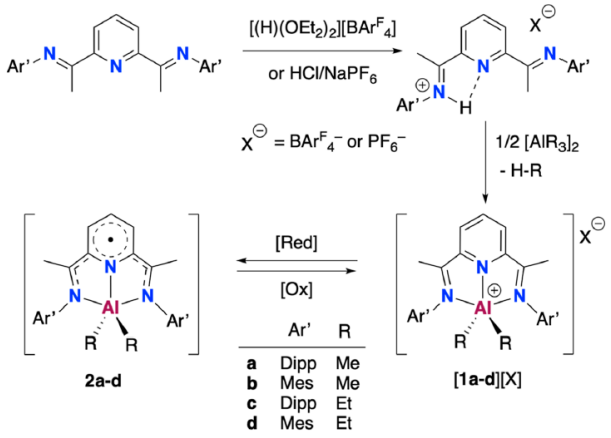


ACS Publications

© 2024 The Authors. Published by American Chemical Society

https://doi.org/10.1021/acs.inorgchem.4c02664
Inorg. Chem. 2024, 63, 19156−19166

Scheme 1. Syntheses of Cationic Aluminum Complexes $[(^{Ar'}BIP)AlR_2]^+$ 1$^+$ as $BAr^F{}_4^-$ or PF_6^- Salts and Reversible Redox Transformation to Paramagnetic Derivatives $[(^{Ar'}BIP^{\bullet})AlR_2]$ 2



Dipp = 2,6-iPr$_2$C$_6$H$_3$, Mes = 2,4,6-Me$_3$C$_6$H$_2$, Ar^F = 3,5-(CF$_3$)$_2$C$_6$H$_3$

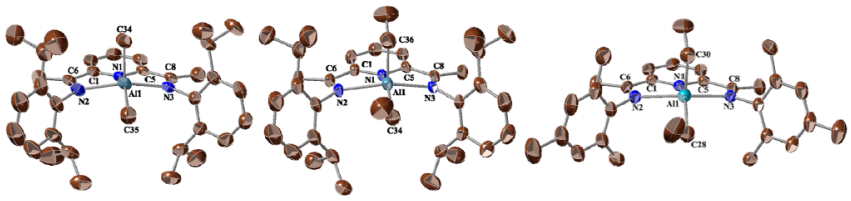


Figure 1. Crystal structures of [**1a**][$BAr^F{}_4$] (left), [**1c**][PF_6] (center) and [**1d**][$BAr^F{}_4$] (right), showing only the cationic organometallic units. All hydrogen atoms have been omitted for clarity. Selected bond lengths (Å) and angles (deg), approximately symmetrical bonds are given as averages: **1a**$^+$: Al1−N1, 2.011(4); Al−N(im), 2.152(3); C═N, 1.283(4); NC−C(Py), 1.492(4); N1−C, 1.339(4); Al1−C34, 1.959(5); Al1−C35, 1.945(5); N2−Al1−N(3), 144.32(15); N2−Al1−C35, 142.5(2). **1c**$^+$: Al1−N1, 1.997(3), Al1−N(im), 2.169(2); Al−C, 1.970(3); C═N, 1.281(3); NC−C(Py), 1.483(3); N1−C, 1.342(3); N2−Al1−N3, 144.51(12); N1−Al1−C, 114.8(2)-**1d**$^+$: Al1−N1, 2.019(2); Al−N(im), 2.177(1); Al−C, 1.972(2); C═N, 1.283(2); 1.484(2); N1−C, 1.344(2); N2−Al1−N3, 148.23(8); N1−Al1−C, 137.18(12).

■ RESULTS AND DISCUSSION

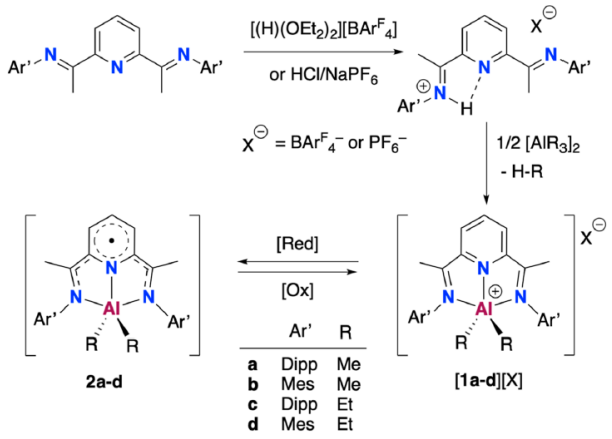
We synthesized the conjugated acids for the BIP ligands, [$^{Ar'}$BIP(H)][$BAr^F{}_4$] (Scheme 1), which previously proved to be ideal precursors for accessing cationic alkyl metal complexes such as [($^{Ar'}$BIP)MnR][$BAr^F{}_4$][23] or [($^{Ar'}$BIP)ZnR][$BAr^F{}_4$].[24] Reacting equimolar amounts of these pro-ligand salts with alkyl reagents $AlMe_3$ or $AlEt_3$ led to the formation of the $BAr^F{}_4^-$ salts of the organoaluminum cations $[(^{Ar'}BIP)AlR_2]^+$ as orange-yellow crystalline solids in excellent yields of 90−95%. This selectivity was confirmed by NMR spectroscopy, which showed a single Al−R cleavage in each case. Additionally, we synthesized the PF_6^- salts of selected examples obtaining [**1a**][PF_6] and [**1c**][PF_6], in 91% and 87% yields, respectively. A related analog, [(^{Dipp}BIP)$AlEt_2$][$Al(OC_4F_9)_4$], similar to [**1c**][$BAr^F{}_4$], was recently prepared by transmetalation from a low valent "[(^{Dipp}BIP)Ga]$^+$" precursor;[18] however, only a few crystals of this compound could be isolated, contrasting with the straightforward robustness of our method.

These cationic complexes were fully characterized, including by NMR spectroscopy (see Supporting Information for full details). Their ^{1}H NMR spectra show distinct, sharp signals for the BIP ligand with a characteristic resonance in the range δ 2.45−2.62 for the Me−C═N group. Additionally, these spectra display a single set of resonances for the Al-bound alkyl groups at $\delta \approx -0.91$ for $AlMe_2$ and $\delta \approx -0.05$ CH_2 and 0.12 CH_3 for $AlEt_2$, indicating chemical equivalency of both Me and Et groups.

The crystal structures of [**1a**][$BAr^F{}_4$], [**1c**][PF_6], and [**1d**][$BAr^F{}_4$] (Figure 1) reveal pentacoordinate Al centers, robustly coordinated by the BIP ligands in a slightly distorted square pyramidal configuration. The three N donor atoms from the tripodal BIP ligand and one C-alkyl atom form the base of the pyramid, while the second alkyl group occupies the apex. The Al atom is displaced by ca. 0.6 Å above the mean coordination plane formed by the BIP ligand, approaching the geometric center of the pyramid. The intraligand C═N, (Py)C−C(N) and αC−N(Py) bond lengths (ca. 1.28, 1.48 and 1.36 Å, respectively) are similar to those observed in

https://doi.org/10.1021/acs.inorgchem.4c02664
Inorg. Chem. 2024, 63, 19156−19166

Scheme 1. Syntheses of Cationic Aluminum Complexes $[(^{Ar'}BIP)AlR_2]^+$ 1^+ as $BAr^F{}_4^-$ or PF_6^- Salts and Reversible Redox Transformation to Paramagnetic Derivatives $[(^{Ar'}BIP^{\cdot})AlR_2]$ 2



Dipp = 2,6-$iPr_2C_6H_3$, Mes = 2,4,6-$Me_3C_6H_2$, Ar^F = 3,5-$(CF_3)_2C_6H_3$

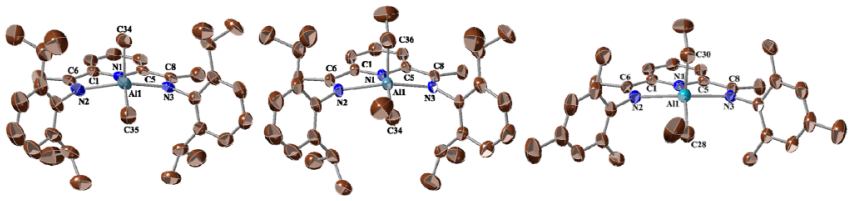


Figure 1. Crystal structures of [**1a**][$BAr^F{}_4$] (left), [**1c**][PF_6] (center) and [**1d**][$BAr^F{}_4$] (right), showing only the cationic organometallic units. All hydrogen atoms have been omitted for clarity. Selected bond lengths (Å) and angles (deg), approximately symmetrical bonds are given as averages: **1a**$^+$: Al1−N1, 2.011(4); Al−N(im), 2.152(3); C=N, 1.283(4); NC−C(Py), 1.492(4); N1−C, 1.339(4); Al1−C34, 1.959(5); Al1−C35, 1.945(5); N2−Al1−N(3), 144.32(15); N2−Al1−C35, 142.5(2). **1c**$^+$: Al1−N1, 1.997(3), Al1−N(im), 2.169(2); Al−C, 1.970(3); C=N, 1.281(3); NC−C(Py), 1.483(3); N1−C, 1.342(3); N2−Al1−N3, 144.51(12); N1−Al1−C, 114.8(2)-**1d**$^+$: Al1−N1, 2.019(2); Al−N(im), 2.177(1); Al−C, 1.972(2); C=N, 1.283(2); 1.484(2); N1−C, 1.344(2); N2−Al1−N3, 148.23(8); N1−Al1−C, 137.18(12).

■ RESULTS AND DISCUSSION

We synthesized the conjugated acids for the BIP ligands, [$^{Ar'}$BIP(H)][$BAr^F{}_4$] (Scheme 1), which previously proved to be ideal precursors for accessing cationic alkyl metal complexes such as [($^{Ar'}$BIP)MnR][$BAr^F{}_4$][23] or [($^{Ar'}$BIP)ZnR][$BAr^F{}_4$].[24] Reacting equimolar amounts of these pro-ligand salts with alkyl reagents $AlMe_3$ or $AlEt_3$ led to the formation of the $BAr^F{}_4^-$ salts of the organoaluminum cations $[(^{Ar'}BIP)AlR_2]^+$ as orange-yellow crystalline solids in excellent yields of 90−95%. This selectivity was confirmed by NMR spectroscopy, which showed a single Al−R cleavage in each case. Additionally, we synthesized the PF_6^- salts of selected examples obtaining [**1a**][PF_6] and [**1c**][PF_6], in 91% and 87% yields, respectively. A related analog, [(^{Dipp}BIP)$AlEt_2$][$Al(OC_4F_9)_4$], similar to [**1c**][$BAr^F{}_4$], was recently prepared by transmetalation from a low valent "[(^{Dipp}BIP)Ga]$^+$" precursor;[18] however, only a few crystals of this compound could be isolated, contrasting with the straightforward robustness of our method.

These cationic complexes were fully characterized, including by NMR spectroscopy (see Supporting Information for full details). Their ^{1}H NMR spectra show distinct, sharp signals for the BIP ligand with a characteristic resonance in the range δ 2.45−2.62 for the Me−C=N group. Additionally, these spectra display a single set of resonances for the Al-bound alkyl groups at $\delta \approx -0.91$ for $AlMe_2$ and $\delta \approx -0.05$ CH_2 and 0.12 CH_3 for $AlEt_2$, indicating chemical equivalency of both Me and Et groups.

The crystal structures of [**1a**][$BAr^F{}_4$], [**1c**][PF_6], and [**1d**][$BAr^F{}_4$] (Figure 1) reveal pentacoordinate Al centers, robustly coordinated by the BIP ligands in a slightly distorted square pyramidal configuration. The three N donor atoms from the tripodal BIP ligand and one C-alkyl atom form the base of the pyramid, while the second alkyl group occupies the apex. The Al atom is displaced by ca. 0.6 Å above the mean coordination plane formed by the BIP ligand, approaching the geometric center of the pyramid. The intraligand C=N, (Py)C−C(N) and αC−N(Py) bond lengths (ca. 1.28, 1.48 and 1.36 Å, respectively) are similar to those observed in

https://doi.org/10.1021/acs.inorgchem.4c02664
Inorg. Chem. 2024, 63, 19156−19166

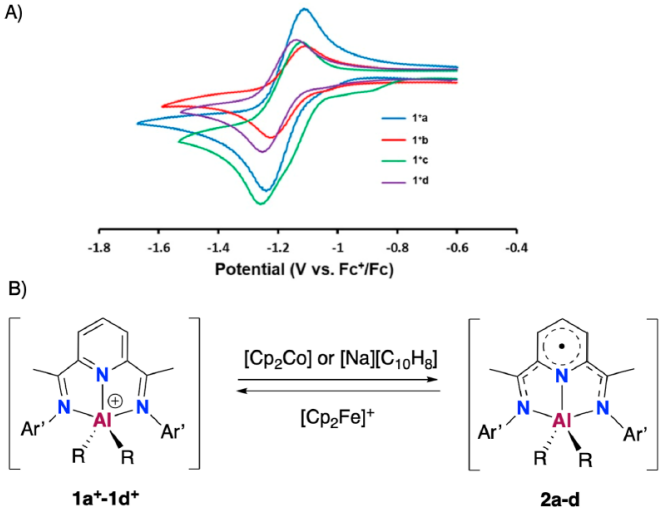


Figure 2. (A) CV traces for cationic complexes $\mathbf{1}^+$ (as $BAr^F_4{}^-$ salts) showing a single reduction event ($E^{o\prime}$ vs $Fc^{+/0}$, dichloromethane, 100 mV·s^{-1}, [TBA][PF_6]). (B) Reversible redox reactions involving the paramagnetic electroneutral derivatives [($^{Ar'}$BIP·)AlR_2] **2**.

unperturbed BIP ligands.[9c,25] The Al–N(Py) bond lengths are notably short (ca. 2.00 Å) compared to the relatively longer Al–N(imine) bonds (ca. 2.17 Å), presumably due to the steric hindrance of the bulky Ar groups. Although the solid-state structures of the cationic units $\mathbf{1}^+$ exhibit two distinct alkyl groups, this distinction is not observed in the solution NMR spectra, suggesting positional exchange between the apical and basal alkyl groups. This dynamic behavior evinces an intramolecular swinging motion with a low energy barrier, similar to the positional exchange processes observed in solution for analogous dialkyl complexes [(BIP)FeR_2][26] and [(BIP)ZnR_2].[27]

The derivatives [**1**][BAr^F_4] demonstrate remarkable stability, despite the typical high reactivity and hydrolytic sensitivity associated with organoaluminum compounds. They do not react with weak protic reagents such as common alcohols or traces of water, likely due to the reduced Lewis acidity of the coordinatively crowded Al centers. Solutions of complexes [**1**][BAr^F_4] in dichloromethane remained stable for days under a normal air atmosphere as long as these were kept in closed NMR tubes. No degradation was detected by NMR spectroscopy for over 2 days. Encouraged by their chemical stability in solution, we further explored their redox properties using cyclic voltammetry (CV), as illustrated in Figure 2A. Each [(^{Ar}BIP)-AlR_2][BAr^F_4] complex, [**1**][BAr^F_4], undergoes a single reversible reduction event within diffusion-controlled processes (Figures S21, S24, S27 and S30). The redox potentials exhibit slight variations depending on the Ar' substituents on the BIP ligands (Dipp: $\mathbf{1a}^+$ and $\mathbf{1c}^+$ with $E^{o\prime}$ = −1.17 V; Mes $\mathbf{1b}^+$ and $\mathbf{1d}^+$ with $E^{o\prime}$ = −1.19 V). In addition, the effect of the alkyl groups, "$AlMe_2$" or "$AlEt_2$", on their redox potentials is negligible, suggesting overall that the redox process is predominantly ligand-centered, involving the conjugated pyridine and imino moieties.

Interestingly, the presence of the AlR_2 unit appears to significantly stabilize the reduced forms, contributing to the reversibility of the redox process. In contrast, the CV study of the protonated salt of the ligand, [^{Dipp}BIP(H)][BAr^F_4] shows an irreversible reduction at a somewhat more positive potential ($E_p \approx -1.07$ V, Figure S31), highlighting the lower chemical stability of the resulting free radical [^{Dipp}BIP(H)·]. Additionally, when conducted in THF, the irreversible reduction of the free ^{Dipp}BIP ligand occurs at $E_p \approx -2.55$ V. The significant cathodic shift of the latter CV trace compared to [^{Dipp}BIP-(H)]$^+$ and the similar cationic species $\mathbf{1}^+$ is attributed to the absence of electrostatic compensation provided by the positive charge.

The reversibility and moderate reduction potentials of around −1.2 V for the cationic species $\mathbf{1a}^+$–$\mathbf{1d}^+$ suggested that a mild single-electron reductant such as cobaltocene, $CoCp_2$, could effectively reduce cations $\mathbf{1}^+$ ([Cp_2Co]$^{+/0}$, $E^{o\prime}$ = −1.33 V vs $Fc^{+/0}$ in dichloromethane).[28] In situ monitoring of the reaction of complexes [**1**][BAr^F_4] with one equivalent of Cp_2Co by ^{1}H NMR spectroscopy, in either CD_2Cl_2 or Tol-d_8, revealed complete disappearance of the resonances of $\mathbf{1a}^+$-$\mathbf{1d}^+$ within 20 min (see Supporting Information for further details). The resulting dark red-purple solutions exhibited only signals attributed to [Cp_2Co][BAr^F_4], suggesting the formation of paramagnetic aluminum species. Subsequently, adding one equivalent of ferrocenium hexafluorophosphate [Fc][PF_6] as an oxidant to these mixtures immediately restored the ^{1}H NMR signals of the diamagnetic cations $\mathbf{1}^+$. The restored spectra appeared somewhat broad and displayed slightly shifted resonances for the species $\mathbf{1}^+$, more pronounced for the $\mathbf{1c}^+$/**2c** redox pair (Figures S15–S18), likely due to minor variations in the system, such as ion pairing and exchange effects involving [BAr^F_4]$^-$ and [PF_6]$^-$ counterions, or the presence of residual paramagnetic species. These in situ reversible redox reactions are essentially quantitative as

https://doi.org/10.1021/acs.inorgchem.4c02664
Inorg. Chem. 2024, 63, 19156−19166

concluded from comparing the signal intensities with the residual solvent peaks. This encouraged us to isolate the corresponding paramagnetic organoaluminum species for detailed structural analyses.

Scaling up these NMR-monitored reductions with $[Cp_2Co]$ enabled us to isolate and fully characterize the reduced species, namely $[(^{Ar'}BIP^{\cdot})AlR_2]$ **2a**–**2d** (Figure 2A). Specifically, **2a** and **2c** were prepared in dichloromethane where the byproduct $[Cp_2Co][BAr^F_4]$ crystallized upon cooling to −36 °C, as confirmed by X-ray diffraction (see Supporting Information for full details). The $BAr^F_4{}^-$ salt of cobalticinium was removed by filtration, and precipitation with *n*-hexane allowed the isolation of **2a** and **2c**. Similarly, **2b** and **2d**, more soluble in aromatic solvents, were prepared in toluene, and the insoluble cobalticinium salt was filtered out, facilitating the isolation of **2b** and **2d**. Although complexes **2** were isolated as analytically pure red-purple solids in good to excellent yields (59–71%), this was challenging due to the high solubility of the $[Cp_2Co][BAr^F_4]$ salt. To overcome this, we replaced the cobaltocene reductant with the readily available reductant sodium naphthalene $[Na][C_{10}H_8]$ and replaced the $[BAr^F_4]^-$ anion with $[PF_6]^-$ to reduce the solubility issues and simplify product isolation. The reduction of $[\mathbf{1c}][PF_6]$ with freshly titrated $[Na][C_{10}H_8]$ in THF produced **2c** along with volatile naphthalene. The insolubility of $NaPF_6$ in *n*-hexane facilitated the isolation of **2c** in almost quantitative yield (88%, Figure 2B). In contrast, although using $[Cp_2Co][BF_4]$ as the reductant led to the formation of red-purple solutions, complex reaction mixtures were obtained, likely due to the incompatibility of the $[BF_4]^-$ anion with the reduced species **2**, leading to decomposition.

We successfully grew crystals of the new reduced species **2b** by cooling a saturated solution in toluene at −36 °C, which yielded crystals suitable for X-ray diffraction analysis (Figure 3). The key structural metrics of **2b** are consistent with those

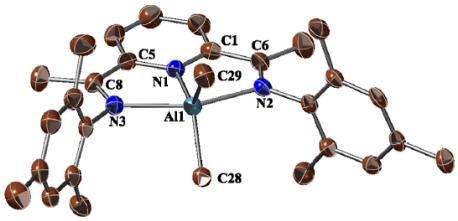


Figure 3. Crystal structure of **2b**. All hydrogen atoms have been omitted for clarity Thermal ellipsoids plot at 50% probability. Selected bond lengths (Å) and angles (deg): Al1–N1, 1.927(3); Al1–N2, 2.166(3); Al1–N3, 2.148(3); C6–N2, 1.304(5); C8–N3, 1.308(4); C1–C6, 1.439(6); C5–C8, 1.446(6); C1–N1, 1.381(5); C5–N1, 1.373(4); N1–Al–C29, 123.25(13); N2–Al1–N3, 153.21(10); C28–Al1–C29, 113.79(15).

previously reported for the analogs **2a**[16] and **2c**,[17] except for the variations in the aromatic substituents on the BIP ligands. The reduction from $\mathbf{1}^+$ to **2** is characterized by significant changes in bond lengths within the BIP ligand. For instance, considering averages for the three structures reported for each type of complex,[29] the imino C=N bond and α–C–N lengthen from 1.283(6) and 1.342(6) Å, respectively, in $\mathbf{1}^+$ to 1.313(6) and 1.373(7) Å, respectively, in **2** while the corresponding C(Py)–C(N) bonds at the pyridine ring shorten from 1.486(6) in $\mathbf{1}^+$ to 1.439(7) Å in **2**. These changes are consistent with the effects expected for a single-electron reduction of the BIP ligand.[9c,30]

Notably, the central Al–N(Py) bond in complexes **2**, averaging ca. 1.92 Å, is substantially shorter than in their oxidized counterparts $\mathbf{1}^+$ (average ca. 2.01 Å). However, the Al–N(imine) bond lengths remain similar between the oxidized and reduced complexes, averaging ca. 2.17 Å in both $\mathbf{1}^+$ and **2**. The geometry around the Al center also reflects changes due to the reduction of the systems. In particular, in the neutral methyl derivatives **2a** and **2b**, the Al atom is coplanar with the N3 donor set of the BIP ligand, aligning with a trigonal bipyramidal geometry as depicted in Figure 3. Conversely, in the slightly more hindered ethyl derivative **2c**,[17] the Al center deviates from the N3 plane, adopting a square-pyramidal geometry, similar to that observed in its cationic counterpart $\mathbf{1c}^+$.

The characterization of the paramagnetic species **2a**–**d** was completed with their IR and solution X-band electronic paramagnetic resonance (EPR) spectra. It is worth noting that their IR spectra lack the prominent band at ∼1600 cm^{-1}, characteristic of the C=N stretch of the BIP ligand. This is consistent with the reduced π-bond character of the BIP skeleton. The EPR spectra of **2b**–**d**, along with the previously characterized **2a**[16] (Figure 4) exhibit a signal at $g \approx 2.00$,

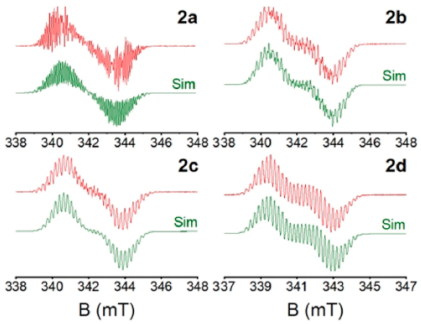


Figure 4. Experimental (top) and simulated (bottom) X-band EPR signals of **2a**–**d** in dichloromethane at 293 K.

indicative of a ligand-centered radical. In addition, the EPR spectra displayed a singular complex pattern for complexes **2** due to hyperfine couplings with the ^{27}Al ($I = 3/2$) and ^{15}N ($I = 1$) atoms from the pyridine and imine functions, along with several hydrogen ($I = 1/2$) nuclei. The values of these coupling constants, shown in Table 1, were determined by fitting the simulated signal shape to the experimental data. Our EPR results are in good agreement with those previously reported for **2a**,[16] underscoring their similar electronic structures. Our data confirm that the unpaired electron is more strongly coupled with the pyridine ^{15}N and the ^{27}Al nuclei, which suggests a significant contribution of the Al orbitals to the molecular SOMO, thereby modulating the radical-like nature and chemical stability of the paramagnetic species **2**. The hyperfine coupling constant to the ^1H atom at the pyridine's position 4 is remarkably large, which indicates a significant localization of the unpaired electron at this position. The

https://doi.org/10.1021/acs.inorgchem.4c02664
Inorg. Chem. 2024, 63, 19156–19166

Table 1. Main Isotropic g and Hyperfine Constants (A) for Complexes 2[a]

compound	2a	2b	2c	2d
ligand/R	^{Dipp}BIP/Me	^{Mes}BIP/Me	^{Dipp}BIP/Et	^{Mes}BIP/Et
g	2.0063	2.0049	2.0042	2.0063
A^{Al}	14.83	16.43	15.30	15.25
A^{Npy}	14.87	12.16	12.32	14.42
A^{Nim} (2)	4.99	2.99	5.18	4.94
A^{H4}	16.04	14.47	13.28	17.50
$A^{H3,3'}$(2)	2.57	5.13	2.16	5.02
A^{CH3} (6)	4.99	6.82	6.55	7.45
Fit RMSD	0.065	0.043	0.039	0.097

[a]10^{-3} M (toluene, 298 K). Number of equivalent nuclei shown in parentheses. For full listings of A values, see Supporting Information (Tables S1−S4).

couplings to other ^{1}H nuclei within the BIP ligands are smaller, and contributions from the Al-bonded methyl (Me) or ethyl (Et) groups are negligible (see Tables S1−S4). This pattern accounts for the observed high reactivity previously observed at the C4 position of the pyridine ring, although reactivity at the C3 position often competes.[31]

DFT calculations using the M06-L functional were performed to deepen our understanding of the redox behavior of the $[(^{Ar'}BIP)AlR_2]^{+/0}$ **1**$^+$/**2** pairs in conjunction with the $[Cp_2Fe]^{+/0}$ and $[Cp_2Co]^{+/0}$ redox reagents.[32] The crystal geometries for complexes **1**$^+$ and **2** were optimized at the M06-L/SV(P) level, using the CPCM solvation model in dichloromethane. A set of critical bond distances, including the C=N and C−C bonds in the BIP ligand, and the Al−N bonds, as well as the geometric τ_5 index,[33] calculated from the N(imine)−Al−N′(imine) and the largest N(Py)−Al−C angles, were used to assess the coordination geometries (see Supporting Information, Table S7). These calculations replicated the experimental crystal structures of the couples **1**$^+$/**2**, within an average deviation <1% between experimental and calculated bond lengths. The τ_5 value for the computed geometries showed consistent results with experimental data, indicating near-zero values for square-pyramidal (SQP) structures of **1**$^+$ and **2b** species and approximately 0.5 for **2a** and **2b**, indicating trigonal-bipyramidal (TBP) geometries for the latter. The τ_5 index for an ideal trigonal-bipyramid is 1, but the nonlinearity along the main N2−Al−N3 axis decreases the geometry index to an intermediate value. For **1c**$^+$ and **2d**, for which no experimental X-ray data is available, our calculations predicted SQP geometries ($\tau_5 \approx 0$). The vibrational M06-L/SV(P) calculations also predict a significant intensity loss of the ν(C=N) stretch band, and a shift to lower frequencies (ca. 100 cm^{-1}) on going from **1a**−**d**$^+$ to **2a**−**d**, explaining the difficulty of assigning this band in the IR spectra of the reduced species.

Single-point energy corrections at the M06-L/SVPD level provided accurate enough values of the free energy changes for the reversible redox reactions **1a**−**d**$^+$ ↔ **2a**−**d**, thereby allowing precise computation of their ΔE^o potentials vs the ferrocene (Fc) or cobaltocene (*Cc*) redox couples. As a benchmark, the calculated potentials for the $[Fc]^{+/0}$ vs $[Cc]^{+/0}$ couples dichloromethane was −1.36 V, closely aligned with the experimental −1.33 V.[28] The calculated reduction potentials for the **1**$^+$/**2** couples vs. were within the experimental range of −1.15 to −1.20 V vs $Fc^{+/0}$ (Table 2), and confirming their ability to oxidize *Cc*.

Table 2. Experimental and Calculated Reduction Potentials (V) vs (Fc^+/Fc)

redox pair	$\Delta E^{o\prime}$ Exptal[a]	ΔE^o Calcd[b]
Cc^+/Cc^{ref}	−1.33	−1.36
1a$^+$/**2a**	−1.17	−1.20
1b$^+$/**2b**	−1.19	−1.12
1c$^+$/**2c**	−1.17	−1.11
1d$^+$/**2d**	−1.19	−1.16

[a]vs Fc^+/Fc, in CH_2Cl_2, 293 K. [TBA][PF_6] background electrolyte. [b]M06-L,CPCM-CH_2Cl_2/SVPD//SV(P).

Additionally, we computed the EPR parameters for paramagnetic complexes **2**. While EPR parameters for **2a** were initially approximated using the BP86 or B3LYP functionals,[16] the *meta*-GGA functional BW6D95 paired with the EPR-II and def2-TZVP (for Al) basis sets yielded slightly more consistent results across complexes **2a**−**d**. A full description of the computational methodology and comparative results are collected in the Supporting Information (Tables S10−S13).

■ CONCLUSIONS

In this study, we have established a general methodology for synthesizing reduced aluminum paramagnetic species [(BIP·)-AlR_2] through the chemical reduction of their isostructural cations $[(BIP)AlR_2]^+$ using mild one-electron redox reagents, like $[Cp_2Co]$. The organoaluminum precursors $[(BIP)AlR_2]^+$ were conveniently synthesized as stable $BAr^F{}_4^-$ or PF_6^- salts by the reaction of the conjugate acids of BIP ligands, with commercial aluminum reagents, $AlMe_3$ and $AlEt_3$. Furthermore, we demonstrated the reversibility of the redox process involving the $[(BIP)AlR_2]^{+/0}$ couples, both electrochemically via voltammetry and chemically with $[Cc]$ and $[Fc]^+$ reagents. The redox processes linking the diamagnetic $[(BIP)AlR_2]^+$ and paramagnetic $[(BIP\cdot)AlR_2]$ species were characterized in detail using a suite of spectroscopic, crystallographic, electrochemical, and computational methods to confirm their mild exchange potentials and redox reversibility. These findings significantly advance our understanding of BIP ligand redox capabilities with main-group metals, particularly with Earth-abundant aluminum, paving the way for future studies into their reactivity and potential applications in redox catalysis.

■ EXPERIMENTAL SECTION

Most compounds presented in this work are highly sensitive to oxygen and moisture. Therefore, inert atmosphere Schlenk techniques and a N_2-filled glovebox were routinely used in manipulations and procedures. All solvents (dichloromethane, toluene, *N*-hexane, tetrahydrofuran and diethyl ether) were rigorously degassed, dried, and distilled immediately prior to use. Instrumentation and procedures, NMR, IR and EPR spectra of new compounds, elemental analysis (EA), X-ray diffraction studies, electrochemistry and computational details are included in the Supporting Information.

Solutions of HCl (2 M in diethyl ether) and $NaPF_6$ were supplied by Thermo Scientific, stored in a glovebox and employed as received. Aluminum trialkyls ($AlMe_3$, pure and 2 M in toluene and $AlEt_3$ 1.0 M in hexane) were purchased from Sigma-Aldrich and used as received. The protonated tetraarylborate salts $[H^{DippBIP}][BAr^F{}_4]$ and $[H^{Mes}BIP][BAr^F{}_4]$ where ^{Dipp}BIP is 2,6-[2,6-^{i}Pr$_2$C$_6$H$_3$N=C(Me)]$_2$-C_5H_3N, ^{Mes}BIP is 2,6-[2,4,6-Me$_3$C$_6$H$_2$N=C(Me)]$_2$-C_5H_3N, and $Ar^F{}_4$ is (3,5-(CF$_3$)$_2$C$_6$H$_3$) respectively, were prepared according to our own reported methodology.[25] Bis(cyclopentadienyl)cobalt (Cp_2Co, where Cp=C_5H_5) in powder form, purchased from Alfa Aesar was stored at −30 °C within a glovebox and used without further purification. Ferrocenium hexafluorophosphate ($[Cp_2Fe][PF_6]$ with Cp=C_5H_5,

https://doi.org/10.1021/acs.inorgchem.4c02664
Inorg. Chem. 2024, 63, 19156−19166

abbreviated as [Fc][PF_6]), sourced from Merck, was also stored in a glovebox and used as received.

Synthesis of [^{Dipp}BIPH][Cl]. A 2 M solution in Et_2O of HCl (206.0 μL, 0.412 mmol) was added dropwise to stirred suspension of ^{Dipp}BIP (198.1 mg, 0.412 mmol) in Et_2O (20 mL) at −30 °C. The resulting pale-yellow solution was stirred for 30 min at room temperature. Then, the solvent was evaporated under vacuum, isolating a pale-yellow solid residue that corresponded to [^{Dipp}BIPH][Cl] (204.4 mg; 96%). **^{1}H NMR** (C_6D_6, 25 °C, 400 MHz): δ 1.13 (d, $^3J_{HH}$ = 6.9 Hz, 12H, CHM*e*Me), 1.22 (d, $^3J_{HH}$ = 6.9 Hz, 12H, CHMe*Me*), 2.27 (s, 6H, *Me*(CN)), 2.91 (sept, $^3J_{HH}$ = 7.0 Hz, 4H, *CH*MeMe), 7.15 (m, 6H, CH_{N-Ar}), 7.43 (br s, 1H, 4-CH_{py}), 8.66 (d, $^3J_{HH}$ = 7.9 Hz, 2H, 3-CH_{py}). **^{13}C{^{1}H} NMR** (C_6D_6, 25 °C, 100 MHz): δ 17.57 (*Me*−CN), 23.02 (CHM*e*Me), 23.67 (CHM*e*Me), 28.96 (*CH*MeMe), 123.78 (3,5-CH_{py}), 125.43 (*m*-CH_{N-Ar}), 136.91 (*o*-C_{N-Ar}), 137.76 (4-CH_{py}), 144.46 (*i*-CH_{N-Ar}), 154.05 (2-CH_{py}), 168.97 (Me−CN). *The signal attributed to p-CH_{N-Ar} was not-observed.* **EA for $C_{33}H_{44}ClN_3$** (found vs calculated, crystalline sample): C 76.42 (76.49), H 8.28 (8.56), N 8.29 (8.11).

Synthesis of [^{Dipp}BIPH][PF_6]. In a nitrogen-filled glovebox, 53.7 mg (0.320 mmol) of $NaPF_6$ are slowly added to a pale-yellow solution of [^{Dipp}BIPH][Cl] (150 mg, 0.290 mmol), dissolved in 20 mL of THF, cooled to −30 °C. The solution instantly changed to orange. After 1 h stirring at room temperature, the solvent and volatiles were removed at reduced pressure. The solid residue was extracted in dichloromethane, filtered and dried again. The NMR spectra of the isolated orange solid corresponded exclusively to compound [^{Dipp}BIPH][PF_6] (163.6 mg, 90%). **^{1}H NMR** (CD_2Cl_2, 25 °C, 400 MHz): δ 1.14 (d, $^3J_{HH}$ = 6.9 Hz, 12H, CHM*e*Me), 1.19 (d, $^3J_{HH}$ = 7.0 Hz, 12H, CHM*e*Me), 2.45 [s, 6H, *Me*(CN)], 2.70 (sept, $^3J_{HH}$ = 7.1 Hz 4H, *CH*MeMe), 7.25 (br s, 6H, CH_{N-Ar}) 8.46 (br s, 1H, 4-CH_{py}), 8.65 (br s, 2H, 3-CH_{py}). **^{19}F{^{1}H} NMR** (CD_2Cl_2, 25 °C, 376 MHz): δ −72.91 (d, J_{FP} = 718.0 Hz, [PF_6]$^-$). **^{31}P{^{1}H} NMR** (CD_2Cl_2, 25 °C, 162 MHz): δ −144.56 (sept, J_{PF} = 716.0 Hz, [PF_6]$^-$). **^{13}C{^{1}H} NMR** (CD_2Cl_2, 25 °C, 100 MHz): δ 17.39 (*Me*−CN), 22.87 (CHM*e*Me), 23.58 (CHM*e*Me), 29.07 (*CH*MeMe), 124.12 (3,5-CH_{py}), 127.54 (*m*-CH_{N-Ar}), 128.91 (*p*-CH_{N-Ar}), 138.07 (*o*-C_{N-Ar}), 143.79 (4-CH_{py}), *not observed* (*i*-CH_{N-Ar}), *not observed* (2-CH_{py}), 168.50 (Me−CN). **EA for $C_{33}H_{44}PF_6N_3$** (found vs calculated, crystalline sample): C 63.12 (63.15), H 7.31 (7.07), N 6.83 (6.69).

Synthesis of [Al(Me)$_2$(^{Dipp}BIP)][PF_6] ([1a][PF_6]). A 5 mL CH_2Cl_2 cold (−25 °C) colorless solution of $AlMe_3$ (32 μL, 0.313 mmol) was slowly added to another orange CH_2Cl_2 solution (15 mL) of [^{Dipp}BIPH][PF_6] (178.5 mg; 0.285 mmol) at the same temperature, immediately changing to a yellow-brown. The mixture was stirred vigorously for 10 min, and then, the solvent and volatiles were removed under vacuum. The solid residue was washed with hexane (3 × 5 mL). Finally, the product was filtered and dried at reduced pressure, obtaining a yellow-brown powdery solid (177.2 mg, 91%) that corresponded to complex [**1a**][PF_6]. **^{1}H NMR** (CD_2Cl_2, 25 °C, 300 MHz): δ −0.92 (s, 6H, $AlMe_2$), 1.09 (d, $^3J_{HH}$ = 7.0 Hz, 12H, CHM*e*Me), 1.23 (d, $^3J_{HH}$ = 6.9 Hz, 12H, CHM*e*Me), 2.57(sept, $^3J_{HH}$ = 6.9 Hz, 4H, *CH*MeMe), 2.59 (s, 6H, *Me*(CN)), 7.30 (d, $^3J_{HH}$ = 7.3 Hz, 4H, *m*-CH_{N-Ar}), 7.38 (t, $^3J_{HH}$ = 7.4 Hz, 2H, *p*-CH_{N-Ar}), 8.68 (d, $^3J_{HH}$ = 7.9 Hz, 2H, 3-CH_{py}), 8.95 (t, $^3J_{HH}$ = 8.1 Hz, 1H, 4-CH_{py}). **^{19}F{^{1}H} NMR** (CD_2Cl_2, 25 °C, 376 MHz): δ −72.80 (d, J_{FP} = 718.0 Hz, [PF_6]$^-$). **^{31}P{^{1}H} NMR** (CD_2Cl_2, 25 °C, 162 MHz): δ −144.55 (sept, J_{PF} = 716.0 Hz, [PF_6]$^-$). **^{13}C{^{1}H} NMR** (CD_2Cl_2, 25 °C, 100 MHz): δ −7.93 ($AlMe_2$), 19.27 (*Me*−CN), 24.15 (CHM*e*Me), 25.15 (CHM*e*Me), 29.16 (CHMeMe), 125.14 (*m*-CH_{N-Ar}), 128.70 (3,5-CH_{py}), 129.35 (*p*-CH_{N-Ar}), 139.35 (*o*-C_{N-Ar}), 140.25 (*i*-C_{N-Ar}), 147.73 (4-CH_{py}), 148.07 (2-CH_{py}), 171.10 (Me−CN). IR (KBr/Nujol, cm-1): ν 1600 (Intense, C=N stretch). **EA for $C_{35}H_{49}AlPF_6N_3$** (found vs calculated, crystalline sample): C 61.46 (61.48), H 7.48 (7.22), N 6.21 (6.15).

Synthesis of [Al(Me)$_2$(^{Dipp}BIP)][BAr^F_4] ([1a][BAr^F_4]). A dichloromethane (5 mL) solution of trimethyl aluminum ($AlMe_3$, 11.6 μL, 0.121 mmol) was added via pipette to another CH_2Cl_2 solution (15 mL) of [(^{Dipp}BIPH)][BAr^F_4] (142.5 mg; 0.101 mmol) both at −25 °C, observing an instantaneous change from orange to yellow-green. The reaction mixture was magnetically stirred for 16 h. Then, the solvent and volatiles were removed at vacuo, isolating a solid which upon washing with hexane (3 × 5 mL), filtration and drying allow obtaining a yellow-green powdery solid (131.6 mg, 93%) that corresponded with ([**1a**][BAr^F_4]). Recrystallization in a cold (−35 °C) CH_2Cl_2: hexane (5:1) solution produced yellow cubic crystals suitable for X-ray diffraction studies. **^{1}H NMR** (CD_2Cl_2, 25 °C, 400 MHz): δ −0.91 (s, 6H, $AlMe_2$), 1.08 (d, $^3J_{HH}$ = 6.9 Hz, 12H, CHM*e*Me), 1.22 (d, $^3J_{HH}$ = 6.9 Hz, 12H, CHM*e*Me), 2.51 (sept, $^3J_{HH}$ = 6.9 Hz, 4H, *CH*MeMe), 2.55 (s, 6H, *Me*(CN)), 7.31 (d, $^3J_{HH}$ = 7.3 Hz, 4H, *m*-CH_{N-Ar}), 7.40 (t, $^3J_{HH}$ = 7.4 Hz, 2H, *p*-CH_{N-Ar}), 7.55 (s, 4H, *p*-CH_{Ar} BAr^F_4), 7.72 (br s, 8H, *o*-CH_{Ar} BAr^F_4), 8.45 (d, $^3J_{HH}$ = 7.9 Hz, 2H, 3-CH_{py}), 8.68 (d, $^3J_{HH}$ = 8.0 Hz, 1H, 4-CH_{py}). **^{19}F{^{1}H} NMR** (CD_2Cl_2, 25 °C, 376 MHz): δ −62.87 (s, BAr^F_4). **^{11}B{^{1}H} NMR** (CD_2Cl_2, 25 °C, 128 MHz): δ −6.61 (s, BAr^F_4). **^{13}C{^{1}H} NMR** (CD_2Cl_2, 25 °C, 100 MHz): δ −7.80 ($AlMe_2$), 19.22 (*Me*−CN), 24.09 (CHM*e*Me), 25.01 (CHM*e*Me), 29.33 (CHMeMe), 117.90 (*p*-CH_{Ar} BAr^F_4), 123.64 (*m*-CH_{N-Ar}), 125.33 (CF_3 BAr^F_4), 126.35 (3,5-CH_{py}), 128.35 (*p*-CH_{N-Ar}), 129.23 (q, $^2J_{CF}$ = 33 Hz, *C*-CF_3 BAr^F_4), 135.21 (*o*-CH_{Ar} BAr^F_4), 138.95 (*o*-C_{N-Ar}), 139.81 (*i*-C_{N-Ar}), 147.16 (4-CH_{py}), 147.94 (2-CH_{py}), 162.11 (q, $^1J_{CB}$ = 50 Hz, *i*-C_{Ar} BAr^F_4), 170.12 (Me−CN). **EA for $C_{67}H_{61}AlBF_{24}N_3$** (found vs calculated, crystalline sample): C 57.42 (57.40), H 4.51 (4.39), N 2.85 (3.00).

Synthesis of (^{Dipp}BIP•)AlMe$_2$ (2a). A J. Young's ampule was loaded with 200 mg (0.142 mmol) of [**1a**][BAr^F_4] and 27 mg (0.142 mmol) of Cp_2Co. The solids were combined with 3 mL of dry dichloromethane to form a dark purple suspension. This mixture was stirred vigorously at room temperature and progress was monitored via ^{1}H NMR analysis of aliquots. After 4 h, the resonances attributed to [**1a**][BAr^F_4] disappeared. The mixture was then filtered through a cannula into a Schlenk tube and cooled to −36 °C. After 16 h, single crystals of [Cp_2Co][BAr^F_4] suitable for X-ray crystallography were harvested. This crystalline material was filtered to give a dark purple solution. The resulting dark purple solution was concentrated to 1 mL, and the addition of 20 mL of anhydrous *n*-hexane precipitated a purple solid. This product was isolated by cannula filtration and dried under high vacuum (<10^{-2} mbar), affording (^{Dipp}BIP•)AlMe$_2$ (**2a**) as a dark purple solid (Yield: 46 mg, 0.084 mmol, 59%.), according to its EA and its EPR spectrum, which can be checked in the Supporting Information. Single crystals suitable for X-ray diffraction analysis were obtained by cooling a toluene solution of **2a** at −36 °C for 24 h. The X-ray crystal structure of (^{Dipp}BIP•)AlMe$_2$ (**2a**) obtained in this study is consistent with the structure earlier reported by Gambarotta.[2] This confirmation reinforces the reproducibility of the crystalline structure under the described synthesis conditions.

Note on ^{1}H NMR Data: *The absence of ^{1}H NMR resonances for (^{Dipp}BIP•)AlMe$_2$ (**2a**) is attributable to the paramagnetic nature of the compound.* **EA for $C_{35}H_{49}AlN_3$** (found vs calculated, crystalline sample): C 78.08 (78.03), H 9.30 (9.17), N 7.99 (7.80). **IR (KBr/Nujol, cm^{-1})**: ν 1644, 1607, 1587 (medium intensity, C=C Py and C=N imine). *The bands observed at 1644 cm^{-1} for the C=C stretch is characteristic of the dearomatized pyridine ring.*

Synthesis of [Al(Me)$_2$(^{Mes}BIP)][BAr^F_4] ([1b][BAr^F_4]). To 148 mg (0.118 mmol) of [(^{Mes}BIPH)][BAr^F_4] in 15 mL of CH_2Cl_2 at −25 °C was added 13.5 μL (0.142 mmol) of $AlMe_3$ in 5 mL of CH_2Cl_2 via syringe. Then, the same experimental protocol used for the preparation of [**1a**][BAr^F_4] was applied to the synthesis of [**1b**][BAr^F_4], isolating a brown solid (150.8 mg, 95%) which according to the NMR spectra corresponded to the expected compound [**1b**][BAr^F_4]. Recrystallization attempts did not afford suitable crystals for X-ray diffraction studies. **^{1}H NMR** (CD_2Cl_2, 25 °C, 400 MHz): δ −0.91 (s, 6H, $AlMe_2$), 2.01 (s, 12H, *o*-*Me*$_{N-Ar}$), 2.36 (s, 6H, *p*-*Me*$_{N-Ar}$), 2.47 (s, 6H, *Me*−CN), 7.01 (s, 4H, *m*-CH_{N-Ar}), 7.59 (s, 4H, *p*-CH_{Ar} BAr^F_4), 7.76, (br s, 8H, *o*-CH_{Ar} BAr^F_4), 8.48 (d, $^3J_{HH}$ = 8.0 Hz, 2H, 3-CH_{py}), 8.73 (d, $^3J_{HH}$ = 7.8 Hz, 1H, 4-CH_{py}). **^{19}F{^{1}H} NMR** (CD_2Cl_2, 25 °C, 376 MHz): δ −62.82 (s, BAr^F_4). **^{11}B{^{1}H} NMR** (CD_2Cl_2, 25 °C, 128 MHz): δ −6.61 (s, BAr^F_4). **^{13}C{^{1}H} NMR** (CD_2Cl_2, 25 °C, 100 MHz): δ −9.67 ($AlMe_2$), 14.29,

https://doi.org/10.1021/acs.inorgchem.4c02664
Inorg. Chem. 2024, 63, 19156−19166

17.19 (*Me*−CN), 18.37 (*o*-*Me*$_{N-Ar}$), 20.87 (*p*-*Me*$_{N-Ar}$), 117.90 (*p*-CH_{Ar} BAr^F_4), 123.64 (CF_3 BAr^F_4), 128.10 (3,5-CH_{Py}), 128.53 (*p*-C_{N-Ar}), 129.28 (q, $^2J_{CF}$ = 33 Hz, *C*-CF_3 BAr^F_4), 130.36 (*m*-CH_{N-Ar}), 135.25 (*o*-CH_{Ar} BAr^F_4), 137.87 (*o*-C_{N-Ar}), 138.95 (*i*-C_{N-Ar}), 147.50 (4-CH_{Py}), 149.14 (2-CH_{Py}), 162.10 (q, $^1J_{CB}$ = 50 Hz, *i*-C_{Ar} BAr^F_4), 169.22 (Me−CN). **EA for** $C_{61}H_{49}AlBF_{24}N_3$ (found vs calculated, bulk sample): C 55.65 (55.60), H 4.04 (3.75), N 3.22 (3.19).

Synthesis of (^{Mes}BIP·)AlMe$_2$ (2b). A J. Young's ampule was charged with 233 mg (0.177 mmol) of [**1b**][BAr^F_4] and 33 mg (0.177 mmol) of Cp_2Co. The solids were combined with 3 mL of anhydrous toluene, forming a dark red suspension. This mixture was stirred vigorously at room temperature and progress was monitored via ^{1}H NMR analysis of aliquots. After 4 h, the resonances attributed to [**1b**][BAr^F_4]disappeared. After this time, the reaction mixture was filtered into a Schlenk tube via cannula to remove the salt [Cp_2Co][BAr^F_4] precipitated. Then, dry *n*-hexane was added dropwise to the resulting solution to point of incipient crystallization. The Schlenk tube was then stored at −36 °C overnight. The resultant solid was isolated via cannula filtration, dried under high vacuum (<10^{-2} mbar), yielding (^{Mes}BIP·)AlMe$_2$ (**2b**) as a dark red solid. Yield: 57 mg, 0.125 mmol, 71%. Suitable plate-shaped single crystals of **2b** for X-ray diffraction analysis were obtained by layering a toluene solution (1 mL) of the compound with *n*-hexane (2 mL) and progressively cooling down the mixture to 0 °C for 4 h and then from 0 °C to −36 °C overnight. Note on ^{1}H NMR data: *The absence of ^{1}H NMR resonances for (^{Mes}BIP·)AlMe$_2$ (**2b**) is attributable to the paramagnetic nature of the compound.* **EA for** $C_{29}H_{37}AlN_3$ (found vs calculated, bulk sample): C 76.63 (76.62), H 8.30 (8.20), N 9.01 (9.24). **IR (KBr/Nujol, cm^{-1}):** ν 1640, 1609, 1557 (medium to weak intensity, C=C Py and C=N imine). *The band observed at 1640 cm^{-1} for the C=C stretch is characteristic of the dearomatized pyridine ring.* The **EPR** of **2b** spectrum is available in the Supporting Information.

Synthesis of [Al(Et)$_2$(^{Dipp}BIP)][BAr^F_4] [1c][BAr^F_4]. The synthesis of [**1c**][BAr^F_4] was carried out following a similar experimental protocol than that applied for the preparation of [**1a**][BAr^F_4]. To 120.0 mg (0.089 mmol) of [(^{Dipp}BIP)]$^+$[BAr^F_4]$^-$ in 15 mL of CH_2Cl_2 at −25 °C was added 106.8 μL (0.107 mmol) of $AlEt_3$ 106.8 μL (0.107 mmol, 1 M in *n*-hexane). An orange powdery solid (114.5 mg, 90%) was isolated which according to the NMR spectra corresponded solely to compound [**1c**][BAr^F_4]. **^{1}H NMR** (CD_2Cl_2, 25 °C, 300 MHz): δ −0.05 (q, $^3J_{HH}$ = 8.0 Hz, 4H, Al(CH_2CH_3)$_2$), 0.11 (t, $^3J_{HH}$ = 7.0 Hz 6H, Al(CH_2CH_3)$_2$), 1.09 (d, $^3J_{HH}$ = 6.9 Hz, 12H, CH*Me*Me), 1.26 (d, $^3J_{HH}$ = 6.8 Hz, 12H, CHMe*Me*), 2.49 (sept, $^3J_{HH}$ = 6.5 Hz, 4H, *CH*MeMe), 2.57 (s, 6H, *Me*(CN)), 7.32 (d, $^3J_{HH}$ = 7.7 Hz, 4H, *m*-CH_{N-Ar}), 7.42 (t, $^3J_{HH}$ = 7.7 Hz, 2H, *p*-CH_{N-Ar}), 7.56 (s, 4H, *p*-CH_{Ar} BAr^F_4), 7.73 (br s, 8H, *o*-CH_{Ar} BAr^F_4), 8.47 (d, $^3J_{HH}$ = 8.0 Hz, 2H, 3-CH_{py}), 8.65 (d, $^3J_{HH}$ = 8.0 Hz, 1H, 4-CH_{py}). **^{19}F{^{1}H} NMR** (CD_2Cl_2, 25 °C, 376 MHz): δ −62.82 (s, BAr^F_4). **^{11}B{^{1}H} NMR** (CD_2Cl_2, 25 °C, 128 MHz): δ −6.59 (s, BAr^F_4). **^{13}C{^{1}H} NMR** (CD_2Cl_2, 25 °C, 100 MHz): δ −1.29 (Al(CH_2CH_3)$_2$), 8.10 (Al(CH_2CH_3)$_2$), 19.20 (*Me*−CN), 23.92 (CHMe*Me*), 25.11 (CH*Me*Me), 29.31 (CHMeMe), 117.91 (*p*-CH_{Ar} BAr^F_4), 123.66 (*m*-CH_{N-Ar}), 125.34 (CF_3 BAr^F_4), 126.36 (3,5-CH_{Py}), 127.99 (*p*-CH_{N-Ar}), 129.30 (q, $^2J_{CF}$ = 30 Hz, *C*-CF_3 BAr^F_4), 135.23 (*o*-CH_{Ar} BAr^F_4), 139.55 (*o*-C_{N-Ar}), 139.85 (*i*-C_{N-Ar}), 146.77 (4-CH_{Py}), 147.72 (2-CH_{Py}), 162.21 (q, $^1J_{CB}$ = 50 Hz, *i*-C_{Ar} BAr^F_4), 170.41 (Me−CN). **EA for** $C_{69}H_{65}AlBF_{24}N_3$ (found vs calculated, bulk sample): C 57.88 (57.95), H 4.21(4.58), N 3.16(2.94).

Synthesis of [Al(Et)$_2$(^{Dipp}BIP)][PF_6] ([1c][PF_6]). An orange solution of [^{Dipp}BIPH][PF_6] (130.2 mg; 0.208 mmol) in 15 mL of CH_2Cl_2 was reacted with another of $AlEt_3$ 1 M in hexane (208 μL, 0.208 mmol) at −30 °C. The resultant solution immediately changed to a yellow-brown color and this was kept under magnetic stirring for 10 min. The solvent and volatiles were then removed under vacuum, isolating a crude orange solid. This residue was washed with hexane (3 × 5 mL), filtered and evaporated to dryness, producing a yellow-brown powdery solid corresponding with [**1c**][PF_6] (128.3 mg, 87%). Then, this was dissolved in 1 mL of CH_2Cl_2 and subsequently 0.1 mL of hexane. The resulting solution was stored at −30 °C and after 72 h, a yellow cubic microcrystalline solid appeared that was suitable for X-ray diffraction studies. **^{1}H NMR** (CD_2Cl_2, 25 °C, 300 MHz): δ −0.06 (q, $^3J_{HH}$ = 8.3 Hz, 4H, Al(CH_2CH_3)$_2$), 0.13 (t, $^3J_{HH}$ = 7.9 Hz 6H, Al(CH_2CH_3)$_2$), 1.12 (d, $^3J_{HH}$ = 6.9 Hz, 12H, CH*Me*Me), 1.28 (d, $^3J_{HH}$ = 6.9 Hz, 12H, CHMe*Me*), 2.55 (sept, $^3J_{HH}$ = 6.5 Hz, 4H, *CH*MeMe), 2.62 (s, 6H, *Me*(CN)), 7.32 (d, $^3J_{HH}$ = 7.7 Hz, 4H, *m*-CH_{N-Ar}), 7.41 (t, $^3J_{HH}$ = 7.7 Hz, 2H, *p*-CH_{N-Ar}), 8.69 (d, $^3J_{HH}$ = 8.0 Hz, 2H, 3-CH_{py}), 8.92 (t, $^3J_{HH}$ = 8.0 Hz, 1H, 4-CH_{py}). **^{19}F{^{1}H} NMR** (CD_2Cl_2, 25 °C, 376 MHz): δ −72.96 (d, J_{FP} = 710.0 Hz, [PF_6]$^-$). **^{31}P{^{1}H} NMR** (CD_2Cl_2, 25 °C, 162 MHz): δ −144.54 (sept, J_{PF} = 712.0 Hz, [PF_6]$^-$). **^{13}C{^{1}H} NMR** (CD_2Cl_2, 25 °C, 100 MHz): δ −1.40 (Al(CH_2CH_3)$_2$), 8.14 (Al(CH_2CH_3)$_2$), 19.19 (*Me*−CN), 23.91 (CHMe*Me*), 25.20 (CH*Me*Me), 29.12 (CHMeMe), 125.10 (*m*-CH_{N-Ar}), 128.73 (3,5-CH_{Py}), 128.89 (*p*-CH_{N-Ar}),, 139.87 (*o*-C_{N-Ar}), 140.18 (*i*-C_{N-Ar}), 147.47 (4-CH_{Py}), 147.67 (2-CH_{Py}), 171.33 (Me−CN). **EA for** $C_{37}H_{53}AlPF_6N_3$ (found vs calculated, bulk sample): C 62.44 (62.43), H 7.50 (7.51), N 5.92 (5.90). **IR (KBr/Nujol, cm^{-1}):** ν 1597 (C=N, BIP).

Synthesis of (^{Dipp}BIP·)AlEt$_2$ (2c). ***Route A.*** A J. Young's ampule was loaded with 397 mg (0.277 mmol) of [**1c**][BAr^F_4] and 54 mg (0.282 mmol) of Cp_2Co. The solids were combined with 3 mL of anhydrous dichloromethane, giving a dark red suspension. This mixture was stirred vigorously at room temperature and progress was monitored via ^{1}H NMR analysis of aliquots. After 4 h, the resonances attributed to [**1c**][BAr^F_4] disappeared. Subsequent cooling of the mixture to −36 °C initiated the precipitation of [Cp_2Co][BAr^F_4]. After 2 h at this temperature, the cold mixture was filtered and the filtrate was dried under vacuum (<10^{-2} mbar) to yield (^{Dipp}BIP·)-AlEt$_3$ (**2c**) as a dark golden/brown solid. Yield: 81 mg, 0.142 mmol, 51%. Crystallization was attempted with several solvent mixtures but not achieved. Note on ^{1}H NMR data: *The absence of ^{1}H NMR resonances for (^{Dipp}BIP·)AlEt$_2$ (**2c**) is attributable to the paramagnetic nature of the compound.* **IR (KBr/Nujol, cm^{-1}):** ν 1643, 1607, 1584 (medium to weak intensity, C=C Py and C=N imine). *The band observed at 1643 cm^{-1} for the C=C stretch is characteristic of the dearomatized pyridine ring.*

Synthesis of 2c. ***Route B.*** Compound [**1c**][PF_6] (82.2 mg; 0.115 mmol) was dissolved in 10 mL of THF and cooled to −30 °C. Then, 131 μL of a solution of sodium-naphthalene (0.88 M in THF, 0.115 mmol) was added at the same temperature. The orange solution turned brown immediately, being stirred for 30 min at room temperature. Then, the solvent and volatiles were dried under vacuum. The solid residue was then extracted in hexane (3 × 5 mL), filtered and brought to dryness, yielding 57.6 mg (88%) of a brown solid corresponding to complex **2c**. Although the synthesis and full characterization of **2c** has already been reported by us,[17] this route provide pure samples as the corresponding **EA for** $C_{37}H_{53}AlN_3$ (found vs calculated): C 78.48 (78.40), H 9.66 (9.48), N 7.30 (7.41) and **EPR spectrum** (see Supporting Information) confirmed.

Synthesis of [Al(Et)$_2$(^{Mes}BIP)][BAr^F_4] ([1d][BAr^F_4]). The same experimental protocol employed for the preparation of ([**1a**][BAr^F_4]) was used for the synthesis of ([**1d**][BAr^F_4]). To 252.0 mg (0.200 mmol) of [(^{Mes}BIPH)][BAr^F_4], 239.8 μL (0.240 mmol) of $AlEt_3$ (1 M in hexane) was added via pipet, both at approximately −25 °C. An orange solid that according to the NMR spectra corresponded to [**1d**][BAr^F_4]. was isolated (250.2 mg, 93%). Then, this was dissolved in a CH_2Cl_2/hexane (4:1) mixture and stored at −35 °C. An orange crystalline solid suitable for X-ray diffraction studies was obtained within 48 h. **^{1}H NMR** (CD_2Cl_2, 25 °C, 300 MHz): δ −0.05 (q, $^3J_{HH}$ = 8.4 Hz, 4H, Al(CH_2CH_3)$_2$), 0.25 (t, $^3J_{HH}$ = 7.9 Hz 6H, Al(CH_2CH_3)$_2$), 2.01 (s, 12H, *o*-*Me*$_{N-Ar}$), 2.32 (s, 6H, *p*-*Me*$_{N-Ar}$), 2.45 (s, 6H, *Me*−CN), 7.02 (s, 4H, *m*-CH_{N-Ar}), 7.55 (s, 4H, *p*-CH_{Ar} BAr^F_4), 7.73, (br s, 8H, *o*-CH_{Ar} BAr^F_4), 8.45 (d, $^3J_{HH}$ = 7.7 Hz, 2H, 3-CH_{py}), 8.68 (d, $^3J_{HH}$ = 7.8 Hz, 1H, 4-CH_{py}).**^{19}F{^{1}H} NMR** (CD_2Cl_2, 25 °C, 376 MHz): δ −62.85 (s, BAr^F_4).**^{11}B{^{1}H} NMR** (CD_2Cl_2, 25 °C, 128 MHz): δ −6.61 (s, BAr^F_4). **^{13}C{^{1}H} NMR** (CD_2Cl_2, 25 °C, 100 MHz): δ −0.51 (Al(CH_2CH_3)$_2$), 8.23 (Al(CH_2CH_3)$_2$), 17.26 (*Me*−CN), 18.22 (*o*-*Me*$_{N-Ar}$), 20.88 (*p*-*Me*$_{N-Ar}$), 117.91 (*p*-CH_{Ar} BAr^F_4), 123.66 (CF_3 BAr^F_4), 126.36 (3,5-CH_{Py}), 127.87 (*p*-C_{N-Ar}), 129.30 (q, $^2J_{CF}$ = 33 Hz, *C*-CF_3 BAr^F_4), 130.37 (*m*-CH_{N-Ar}), 135.22

https://doi.org/10.1021/acs.inorgchem.4c02664
Inorg. Chem. 2024, 63, 19156−19166

(o-CH_{Ar} $BAr^F{}_4$), 137.99 (o-C_{N-Ar}), 140.04 (i-C_{N-Ar}), 146.98 (4-CH_{Py}), 148.44 (2-CH_{Py}), 162.20 (q, $^1J_{CB}$ = 50 Hz, i-C_{Ar} $BAr^F{}_4$), 170.02 (Me−CN). **IR (KBr/Nujol, cm^{-1}):** ν 1599 (intense, C=N, ^{Mes}BIP); 1276, 1125, 887 (B−C for $[BAr^F{}_4]^-$). **EA for $C_{63}H_{53}AlBF_{24}N_3$** (found vs calculated, bulk sample): C 56.36 (56.22), H 4.16 (3.97), N 3.22 (3.12).

Synthesis of (^{Mes}BIP·)AlEt$_2$ (2d). A J. Young's ampule was loaded with 325 mg (0.241 mmol) of **[1d][BAr$^F{}_4$]** and 46 mg (0.241 mmol) of Cp_2Co. The solids were combined with 3 mL of anhydrous toluene, giving a dark red suspension. This mixture was stirred vigorously at room temperature and progress was monitored via ^{1}H NMR analysis of aliquots. After 4 h, the resonances attributed to **[1d][BAr$^F{}_4$]** disappeared. Subsequent cooling of the mixture to −36 °C initiated the precipitation of $[Cp_2Co][BAr^F{}_4]$. The reaction mixture was then filtered into a Schlenk tube via cannula, to which dried n-hexane was added until incipient crystallization occurred, and subsequently stored at −36 °C overnight. The next day, a brown/red solid was collected, isolated by cannula filtration, and dried under vacuum (<10^{-2} mbar) to yield (^{Mes}BIP·)AlEt$_2$ **(2d)** as a red/brown solid. Yield: 70 mg, 0.145 mmol, 60%. Despite the appearance of incipient crystallization, the procedure did not yield single crystals suitable for X-ray diffraction analysis. **Note on ^{1}H NMR data:** *The absence of ^{1}H NMR resonances for (^{Mes}BIP·)AlEt$_2$ (2d) is attributable to the paramagnetic nature of the compound.* **EA for $C_{31}H_{41}AlN_3$** (found vs calculated, bulk sample): C 77.33 (77.14), H 8.87 (8.56), N 8.69 (8.71). **IR (KBr/Nujol, cm^{-1}):** ν 1641, 1528 (medium to weak intensity, C=C Py and C=N imine). *The band observed at 1641 cm^{-1} for the C=C stretch is characteristic of the dearomatized pyridine ring.* The **EPR** of **2d** spectrum is available in the Supporting Information.

Redox in Situ NMR Monitoring. General Procedure. Initial Setup. A J. Young tap NMR tube was loaded with 10 mg of the chosen aluminum complex [$^{Ar'}$**BIP**AlR$_2$][**BAr$^F{}_4$**], (**1a$^+$_d$^+$**, where Ar'= Dipp and Mes and R = Me and Et). Solvents were chosen based on their ability to dissolve the reactants and products, as well as their compatibility with NMR spectroscopy. Depending on the starting complex, either 0.5 mL of CD_2Cl_2 (for complexes with L = ^{Dipp}BIP) or Tol-d_8 (for complexes with L = ^{Mes}BIP) was added. The redox reaction was then in situ monitored via ^{1}H NMR spectroscopy, with continuous monitoring being crucial for determining the exact point of reaction completion and observing the dynamic changes during the redox processes. The temperature was maintained at room temperature to facilitate the redox reactions without additional thermal input.

Reduction Step. Before the addition of the reductant, a ^{1}H NMR experiment was acquired for each aluminum complex **1a$^+$−d$^+$** to establish a baseline. An equimolar quantity of Cp_2Co was then added to the corresponding aluminum complex solution. The solution was mixed using a bespoke NMR tube rotor at room temperature, with the progress and completion of the reduction monitored by ^{1}H NMR analyses. After 20 min, the reduction of all aluminum complexes was confirmed by the disappearance of ^{1}H NMR resonances for **1a$^+$−d$^+$** attributable to the paramagnetic NMR-silence nature of the reduced compound [($^{Ar'}$**BIP**·)AlR$_2$] **(2a−d)** with the only signals being those of $[Cp_2Co][BAr^F{}_4]$.

Oxidation Step. Following the reduction of each aluminum complex to the corresponding **2a−d**, species, an equimolar amount of $[Fc][PF_6]$ was added. The mixture was then mixed and monitored by ^{1}H NMR analyses. After 20 min, the oxidation of the aluminum species was evidenced by the reappearance of ^{1}H NMR resonances for the species **1a$^+$−d$^+$** along with resonances attributable to Fc and species $[Cp_2Co]^+$.

Notes on Alternative Reducing and Oxidizing Agents. Further experiments tested the redox behavior using Ferrocene (Fc) and Cp_2Co as alternative reducing agents, with only Cp_2Co successfully reducing the aluminum complexes **1a$^+$−d$^+$**. Attempts to oxidize the **2a−d** species with $[Fc][BF_4]$ failed. THF-d_8 was also trialed as a solvent; however, it led to degradation of the reduced aluminum species, resulting in complex reaction mixtures.

Single-Crystal X-ray Analysis. A summary of the crystallographic data and the structure refinement results for compounds **[1a][BAr$^F{}_4$]**, **[1c][PF$_6$]**, **[1d][BAr$^F{}_4$]**, **[Cp$_2$Co][BAr$^F{}_4$]** and **2b** is given in Tables S1−S5 in the Supporting Information. Crystals of a suitable size for X-ray diffraction analysis were coated with dry perfluoropolyether and mounted on glass fibers and fixed in a cold nitrogen stream (T = 193 K) to the goniometer head. Data collection was carried out on a Bruker-AXS, D8 QUEST ECO, PHOTON II area detector diffractometer, using monochromatic radiation λ(Mo K_α) = 0.71073 Å, by means of ω and φ scans with a width of 0.50°. The data were reduced (SAINT[34]) and corrected for absorption effects by the multiscan method (SADABS[35]). The structures were solved by intrinsic phasing modification of direct methods (SHELXT[36]) and refined against all F^2 data by full-matrix least-squares techniques (SHELXL-2018/3[37]) minimizing $w[F_o^2 - F_c^2]^2$. All non-hydrogen atoms were refined anisotropically. The hydrogen atoms were included from calculated positions and refined riding on their respective carbon atoms with isotropic displacement parameters. In general, the $-CF_3$ groups of $BAr^F{}_4$ in **[1a][BAr$^F{}_4$]** present positional disorder, so five of them were modeled as two components of the disorder with their respective occupancy coefficients. Therefore, it was also necessary to use some geometric restraints (SADI, SIMU) during the structure refinement to ensure a sensible geometry. In the asymmetric unit of **[1c][PF$_6$]**, a crystallizing THF molecule that did not need to be modeled is shown next to the salt complex. A search for solvent-accessible voids for structure **[1a][BAr$^F{}_4$]** using SQUEEZE[38] showed two volumes of potential solvents of 190 Å^3 for each (52 electron count), whose solvent content could not be identified or refined with the most severe restrictions, but due to the volume and the electrons present, it would match a very disordered n-hexane molecule. While a search for solvent-accessible voids for the **[1c][PF$_6$]** structure using SQUEEZE showed a single potential solvent volume of 292 Å3 (70 electron count), whose solvent content could not be identified or refined under the most severe constraints, but due to the volume and electrons present, it would match one and a half molecules of very disordered n-hexane. The corresponding CIF data represent SQUEEZE treated structures with the solvent molecules handling as a diffuse contribution to the overall scattering, without specific atom position and excluded from the structural model. The SQUEEZE results were appended to the CIF. Crystallizing compounds **[1a][BAr$^F{}_4$]** and **[1c][PF$_6$]** is challenging due to their instability, and they appear somewhat twinned, exhibiting at least four additional minority domains. Refining these structures using HKLF 5 and BASF did not yield improved results. Consequently, due to the imperfections in the crystals and the presence of some disorder, as previously discussed and resolved, all the R-values are somewhat elevated. Single-crystal X-ray diffraction data for **[Cp$_2$Co][BAr$^F{}_4$]** and **2b** were obtained under a nitrogen gas stream using an Oxford Cryostream 800 unit[39] at the specified temperature with a Bruker D8 Quest Eco diffractometer equipped with a Photon II 7 detector (Mo, λ = 0.71073 Å). The raw frame data was reduced using APEX3. Structures were resolved using SHELXT and refined using full-matrix least-squares refinement on all F^2 data using the SHELXL[40] interface within GUI OLEX2.[41] Unless stated otherwise, all non-hydrogen atoms were refined anisotropically, while hydrogen atoms were geometrically placed and allowed to ride on their parent atoms. Disorder was addressed by implementing a split-site model and restraining geometries and displacement parameters. In several structures some of the CF_3 groups on the $BAr^F{}_4^-$ anion was disordered and modeled over two main domains, and restrained to maintain sensible geometries. Distances and angles were calculated using the full covariance matrix. The corresponding crystallographic data were deposited with the Cambridge Crystallographic Data Centre as supplementary publications. CCDC 2337930 (**[1a][BAr$^F{}_4$]**), 2337931 (**[1c][PF$_6$]**), 2334613 (**[1d][BAr$^F{}_4$]**) 2326416 **[Cp$_2$Co][BAr$^F{}_4$]** and 2326417 for **2b** contain the supplementary crystallographic data for this paper. The data can be obtained free of charge via: https://www.ccdc.cam.ac.uk/structures/.

https://doi.org/10.1021/acs.inorgchem.4c02664
Inorg. Chem. 2024, 63, 19156−19166

■ ASSOCIATED CONTENT

Supporting Information

The Supporting Information is available free of charge at https://pubs.acs.org/doi/10.1021/acs.inorgchem.4c02664.

Instrumentation description, characterization data including NMR, IR and EPR spectra, EA, crystallographic files (CIF), cyclic voltammetry (CV), and computational data (PDF)

Accession Codes

Accession Codes. CCDC 2337930, 2337931, 2334613, 2326416 and 2326417 contain the supplementary crystallographic data for this paper. This data can be obtained free of charge via www.ccdc.cam.ac.uk/data_request/cif or by emailing data_request@ccdc.cam.ac.uk or by contacting the Cambridge Crystallographic Data Centre 12, Union Road, Cambridge CB2 IEZ, UK; fax +44 1223 336033.

■ AUTHOR INFORMATION

Corresponding Authors

Antonio J. Martínez-Martínez − *CIQSO-Center for Research in Sustainable Chemistry and Department of Chemistry, CSIC-Associated Unit, University of Huelva, Huelva 21007, Spain;* orcid.org/0000-0002-0684-1244; Email: antonio.martinez@dqcm.uhu.es

Antonio Rodríguez-Delgado − *Instituto de Investigaciones Químicas, CSIC-Universidad de Sevilla, Sevilla 41092, Spain;* orcid.org/0000-0002-2207-9149; Email: arodriguez@us.es

Juan Cámpora − *Instituto de Investigaciones Químicas, CSIC-Universidad de Sevilla, Sevilla 41092, Spain;* orcid.org/0000-0001-7305-1296; Email: campora@iiq.csic.es

Authors

Juan Manuel Delgado-Collado − *Instituto de Investigaciones Químicas, CSIC-Universidad de Sevilla, Sevilla 41092, Spain;* orcid.org/0009-0006-2000-9303

Hellen Videa − *CIQSO-Center for Research in Sustainable Chemistry and Department of Chemistry, CSIC-Associated Unit, University of Huelva, Huelva 21007, Spain;* orcid.org/0000-0002-8171-9804

Pablo J. Serrano-Laguna − *CIQSO-Center for Research in Sustainable Chemistry and Department of Chemistry, CSIC-Associated Unit, University of Huelva, Huelva 21007, Spain;* orcid.org/0000-0003-0567-5587

M. Ángeles Fuentes − *CIQSO-Center for Research in Sustainable Chemistry and Department of Chemistry, CSIC-Associated Unit, University of Huelva, Huelva 21007, Spain;* orcid.org/0000-0003-4546-3984

Eleuterio Álvarez − *Instituto de Investigaciones Químicas, CSIC-Universidad de Sevilla, Sevilla 41092, Spain;* orcid.org/0000-0002-8378-8459

Antonio Díaz Quintana − *Instituto de Investigaciones Químicas, CSIC-Universidad de Sevilla, Sevilla 41092, Spain;* orcid.org/0000-0001-8973-8009

Complete contact information is available at: https://pubs.acs.org/10.1021/acs.inorgchem.4c02664

Author Contributions

[§]J.M.D.-C., H.V., and P.J.S.-L. authors contributed equally. The manuscript was written through contributions of all authors. All authors have given approval to the final version of the manuscript.

Notes

The authors declare no competing financial interest.

■ ACKNOWLEDGMENTS

The authors acknowledge the financial support by the Ministerio de Ciencia e Innovación MICIN/AEI/10.13039/501100011033 (grants PID2021-128392NB-100 for J.C., PID2019-108292RA-I00 and PID2022-142270OB-I00 for A.J.M.-M.) and MICIN/NextGenerationEU/PRTR (CNS2022-136087 for A.J.M.-M), the Thematic Network "OASIS" RED2022-134074-T, the ERDF/EU, the Junta de Andalucía (grant P20_00104 for J.C. and P20_00373 for A.J.M.-M.) and the University of Huelva (UHU-202043 and EPIT1442023 for A.J.M.-M.). A.J.M.-M. also thanks the Spanish Research State Agency AEI for a Ramón y Cajal research (RYC-2017-21783).

■ REFERENCES

(1) 5th Chemical Sciences and Society Summit (CS3) 2013 Whitepaper: Efficient Utilization of Elements. 2013, https://www.acs.org/content/dam/acsorg/greenchemistry/industriainnovation/cs3-whitepaper2013.pdf. (b) Hunt, A. Element Recovery and Sustainability. In *Green Chemistry*; Clark, J. H., Ed.; RSC Publishing: Cambridge,CB4 0WF, UK, 2013; p 270. (c) Hunt, A. J.; Matharu, A. S.; King, A. H.; Clark, J. H. The importance of elemental sustainability and critical element recovery. *Green Chem.* **2015**, *17*, 1949−1950. (d) Rhodes, C. J. Endangered elements, critical raw materials and conflict minerals. *Sci. Prog.* **2019**, *102*, 304−350.

(2) (a) Wheelhouse, K. M. P.; Webster, R. L.; Beutner, G. L. Advances and Applications in Catalysis with Earth-Abundant Metals. *Organometallics* **2023**, *42*, 1677−1679. (b) Fürstner, A. Iron Catalysis in Organic Synthesis: A Critical Assessment of What It Takes To Make This Base Metal a Multitasking Champion. *ACS Central Sci.* **2016**, *2*, 778−789. (c) Chirik, P. J.; Morris, R. Getting Down to Earth: The Renaissance of Catalysis with Abundant Metals. *Acc. Chem. Res.* **2015**, *48*, 2495. (d) Bullock, M. *Catalysis without Precious Metals*; Wiley-VCH, 2010. (e) Phapale, V. B.; Cárdenas, D. J. Nickel-catalysed Negishi cross-coupling reactions: scope and mechanisms. *Chem. Soc. Rev.* **2009**, *38*, 1598−1607.

(3) Holland, P. L. Distinctive Reaction Pathways at Base Metals in High-Spin Organometallic Catalysts. *Acc. Chem. Res.* **2015**, *48*, 1696−1702.

(4) Bullock, R. M.; Chen, J. G.; Gagliardi, L.; Chirik, P. J.; Farha, O. K.; Hendon, C. H.; Jones, C. W.; Keith, J. A.; Klosin, J.; Minteer, S. D.; et al. Using nature's blueprint to expand catalysis with Earth-abundant metals. *Science* **2020**, *369*, No. eabc3183.

(5) (a) Khusnutdinova, J. R.; Milstein, D. Metal−Ligand Cooperation. *Angew. Chem., Int. Ed.* **2015**, *54*, 12236−12273. (b) Wodrich, M. D.; Hu, X. Natural inspirations for metal-ligand cooperative catalysis. *Nat. Rev. Chem* **2017**, *2*, 0099−107. (c) Baumgardner, D. F.; Parks, W. E.; Gilbertson, J. D. Harnessing the active site triad: merging hemilability, proton responsivity, and ligand-based redox-activity. *Dalton Trans.* **2020**, *49*, 960−965. (d) Elsby, M. R.; Baker, R. T. Strategies and mechanisms of metal−ligand cooperativity in first-row transition metal complex catalysts. *Chem. Soc. Rev.* **2020**, *49*, 8933−8987.

(6) (a) Sterle, M.; Huš, M.; Lozinšek, M.; Zega, A.; Cotman, A. E. Hydrogen-Bonding Ability of Noyori−Ikariya Catalysts Enables Stereoselective Access to CF3-Substituted syn-1,2-Diols via Dynamic Kinetic Resolution. *ACS Catal.* **2023**, *13*, 6242−6248. (b) Lan, S.; Huang, H.; Liu, W.; Xu, C.; Lei, X.; Dong, W.; Liu, J.; Yang, S.; Cotman, A. E.; Zhang, Q.; et al. Asymmetric Transfer Hydrogenation of Cyclobutenediones. *J. Am. Chem. Soc.* **2024**, *146*, 4942−4957.

(7) (a) Luca, O. R.; Crabtree, R. H. Redox-active ligands in catalysis. *Chem. Soc. Rev.* **2013**, *42*, 1440−1459. (b) Blanchard, S.; Derat, E.; Desage-El Murr, M.; Fensterbank, L.; Malacria, M.; Mouriès-Mansuy, V. Non-Innocent Ligands: New Opportunities in Iron Catalysis. *Eur.*

J. Inorg. Chem. **2012**, *2012*, 376−389. (c) Chacon-Teran, M. A.; Findlater, M. Redox-Active BIAN-Based Iron Complexes in Catalysis. *Eur. J. Inorg. Chem.* **2022**, *2022*, No. e202200363. (d) Swatiputra, A. A.; Mukherjee, D.; Dinda, S.; Roy, S.; Pramanik, K.; Ganguly, S. Electron transfer catalysis mediated by 3d complexes of redox non-innocent ligands possessing an azo function: a perspective. *Dalton Trans.* **2023**, *52*, 15627−15646. (e) Protchenko, A. V.; Dange, D.; Harmer, J. R.; Tang, C. Y.; Schwarz, A. D.; Kelly, M. J.; Phillips, N.; Tirfoin, R.; Birjkumar, K. H.; Jones, C.; Kaltsoyannis, N.; Mountford, P.; et al. Stable GaX_2, InX_2 and TlX_2 radicals. *Nat. Chem.* **2014**, *6*, 315−319. (f) Regenauer, N. I.; Wadepohl, H.; Roşca, D. A. Metal−Ligand Cooperativity in Iron Dinitrogen Complexes: Proton-Coupled Electron Transfer Disproportionation and an Anionic $Fe(0)N_2$ Hydride. *Inorg. Chem.* **2022**, *61* (19), 7426−7435.

(8) (a) Berben, L. A. Catalysis by Aluminum (III) Complexes of Non-Innocent Ligands. *Chem.—Eur. J.* **2015**, *21*, 2734−2742. (b) Parsons, L. W. T.; Berben, L. A. Metallated dihydropyridinates: prospects in hydride transfer and (electro)catalysis. *Chem. Sci.* **2023**, *14*, 8234−8248. (c) Carr, C. R.; Vesto, J. I.; Xing, X.; Fettinger, J. C.; Berben, L. A. Aluminum-Ligand Cooperative O−H Bond Activation Initiates Catalytic Transfer Hydrogenation. *ChemCatChem* **2022**, *14* (13), 202101869. (d) Gahlaut, P. S.; Yadal, K.; Gautam, D.; Jana, B. Recent Development in the Syntheses of Aluminum Complexes Based on Redox-Active Ligands. *J. Organomet. Chem.* **2022**, *963*, 122298.

(9) (a) Cámpora, J.; Rodríguez-Delgado, A.; Palma, P. σ-Organometallic Chemistry With 2,6-Bis(imino) pyridine Ligands: New Pathways to Innovative Pincer Architectures. In *Pincer Compounds: Chemistry and Applications*; Morales-Morales; Ed.; Wiley: Amsterdam, 2018; pp 539−586. (b) Zhu, D.; Thapa, I.; Korobkov, I.; Gambarotta, S.; Budzelaar, P. H. M. Redox-Active Ligands and Organic Radical Chemistry. *Inorg. Chem.* **2011**, *50*, 9879−9887. (c) Römelt, C.; Weyhermüller, T.; Wieghardt, K. Structural characteristics of redox-active pyridine-1,6-diimine complexes: Electronic structures and ligand oxidation levels. *Coord. Chem. Rev.* **2019**, *380*, 287−317.

(10) (a) Flisak, Z.; Sun, W.-H. Progression of Diiminopyridines: From Single Application to Catalytic Versatility. *ACS Catal.* **2015**, *5*, 4713−4724. (b) Small, B. L. Discovery and Development of Pyridine-bis(imine) and Related Catalysts for Olefin Polymerization and Oligomerization. *Acc. Chem. Res.* **2015**, *48*, 2599−2611.

(11) Chirik, P. J.; Wieghardt, K. Radical Ligands Confer Nobility on Base-Metal Catalysts. *Science* **2010**, *327*, 794−795.

(12) Chirik, P. J. Carbon−Carbon Bond Formation in a Weak Ligand Field: Leveraging Open-Shell First-Row Transition-Metal Catalysts. *Angew. Chem., Int. Ed.* **2017**, *56*, 5170−5181.

(13) Chirik, P. J. Iron- and Cobalt-Catalyzed Alkene Hydrogenation: Catalysis with Both Redox-Active and Strong Field Ligands. *Acc. Chem. Res.* **2015**, *48*, 1687−1695.

(14) (a) de Almeida, L. D.; Wang, H. L.; Junge, K.; Cui, X. J.; Beller, M. Recent Advances in Catalytic Hydrosilylations: Developments beyond Traditional Platinum Catalysts. *Angew. Chem., Int. Ed.* **2021**, *60*, 550−565. (b) Royo, B. Recent advances in catalytic hydrosilylation of carbonyl groups mediated by well-defined first-row late transition metals. In *Advances in Organometallic Chemistry*; Pérez, P. J., Ed.; Academic Press, 2019; Vol. *72*, pp 59−102.

(15) Obligacion, J. V.; Neely, J. M.; Yazdani, A. N.; Pappas, I.; Chirik, P. J. Cobalt Catalyzed Z-Selective Hydroboration of Terminal Alkynes and Elucidation of the Origin of Selectivity. *J. Am. Chem. Soc.* **2015**, *137*, 5855−5858.

(16) Scott, J.; Gambarotta, S.; Korobkov, I.; Knijnenburg, Q.; de Bruin, B.; Budzelaar, P. H. M. Formation of a Paramagnetic Al Complex and Extrusion of Fe during the Reaction of (Diiminepyridine)Fe with AlR_3 (R = Me, Et). *J. Am. Chem. Soc.* **2005**, *127*, 17204−17206.

(17) Cartes, M. A.; Rodríguez-Delgado, A.; Palma, P.; Álvarez, E.; Cámpora, J. Sequential Reduction and Alkyl Exchange Reactions of Bis(imino)pyridine Dialkyliron(II) with Trimethylaluminum. *Organometallics* **2014**, *33*, 1834−1839.

(18) Dabringhaus, P.; Heizmann, T.; Krossing, I. Activation of the GaI Cation for Bond Activation: from Oxidative Additions into C−Cl and H−P Bonds to Reversible Insertion into P4. *Chem.—Eur. J.* **2023**, *29*, No. e202302212.

(19) See, for example: (a) Dawkins, M. J. C.; Simonov, A. N.; Jones, C. 2,6-Diiminopyridine complexes of group 2 metals: synthesis, characterisation and redox behaviour. *Dalton Trans.* **2020**, *49*, 6627−6634. (b) Chu, T.; Belding, L.; Poddutoori, P. K.; van der Est, A.; Dudding, T.; Korobkov, I.; Nikonov, G. I. Unique molecular geometries of reduced 4- and 5-coordinate zinc complexes stabilised by diiminopyridine ligand. *Dalton Trans.* **2016**, *45*, 13440−13448. (c) Chu, T.; Belding, L.; van der Est, A.; Dudding, T.; Korobkov, I.; Nikonov, G. I. A Coordination Compound of Ge0 Stabilized by a Diiminopyridine Ligand. *Angew. Chem., Int. Ed.* **2014**, *53*, 2711−2715.

(20) Myers, T. W.; Berben, L. A. Aluminum−Ligand Cooperative N−H Bond Activation and an Example of Dehydrogenative Coupling. *J. Am. Chem. Soc.* **2013**, *135*, 9988−9990.

(21) Thompson, E. J.; Myers, T. W.; Berben, L. A. Synthesis of Square-Planar Aluminum(III) Complexes. *Angew. Chem., Int. Ed.* **2014**, *53*, 14132−14134.

(22) Myers, T. W.; Sherbow, T. J.; Fettinger, J. C.; Berben, L. A. Synthesis and characterization of bis(imino)pyridine complexes of divalent Mg and Zn. *Dalton Trans.* **2016**, *45*, 5989−5998.

(23) Pérez, C. M.; Rodríguez-Delgado, A.; Palma, P.; Álvarez, E.; Gutiérrez-Puebla, E.; Cámpora, J. Neutral and Cationic Alkylmanganese(II) Complexes Containing 2,6-Bisiminopyridine Ligands. *Chem.—Eur. J.* **2010**, *16*, 13834−13842.

(24) Sandoval, J. J.; Álvarez, E.; Palma, P.; Rodríguez-Delgado, A.; Cámpora, J. Neutral Bis(imino)-1,4-dihydropyridinate and Cationic Bis(imino)pyridine σ-Alkylzinc(II) Complexes as Hydride Exchange Systems: Classic Organometallic Chemistry Meets Ligand-Centered, Biomimetic Reactivity. *Organometallics* **2018**, *37*, 1734−1744.

(25) (a) Knijnenburg, Q.; Gambarotta, S.; Budzelaar, P. H. M. Ligand-centred reactivity in diiminepyridine complexes. *Dalton Trans.* **2006**, 5442−5448. (b) Budzelaar, P. H. M.; de Bruin, B.; Gal, A. W.; Wieghardt, K.; van Lenthe, J. H. Metal-to-Ligand Electron Transfer in Diiminopyridine Complexes of Mn−Zn. A Theoretical Study. *Inorg. Chem.* **2001**, *40*, 4649−4655.

(26) Cámpora, J.; Naz, A. M.; Palma, P.; Álvarez, E.; Reyes, M. L. 2,6-Diiminopyridine Iron(II) Dialkyl Complexes. Interaction with Aluminum Alkyls and Ethylene Polymerization Catalysis. *Organometallics* **2005**, *24*, 4878−4881.

(27) Sandoval, J. J.; Palma, P.; Álvarez, E.; Rodríguez-Delgado, A.; Cámpora, J. Dibenzyl and diallyl 2,6-bisiminopyridinezinc(ii) complexes: selective alkyl migration to the pyridine ring leads to remarkably stable dihydropyridinates. *Chem. Commun.* **2013**, *49*, 6791−6793.

(28) Connelly, N. G.; Geiger, W. E. Chemical Redox Agents for Organometallic Chemistry. *Chem. Rev.* **1996**, *96*, 877−910.

(29) For complexes **2**, in addition to **2b** we used literature data for **2a** and **2c** (see refs 16 and 17, respectively).

(30) The NC-C(Py), C=N and αC−N(Py) bond distances for $\mathbf{1}^+$ and **2** can be used to calculate the corresponding Δgeometry parameters, which correlate with the reduction state of the BIP ligand (see ref 9c). Theoretically calculated (DFT-based) values of Δf or the neutral and singly reduced BIP ligands are 0.184 and 0.120, respectively. The average Δf or $\mathbf{1}^+$ and 2 are 0.17 ± 0.05 and 0.10 ± 0.06, respectively (error intervals taken $\approx 3\sigma$), respectively.

(31) (a) Budzelaar, P. H. M. Radical Chemistry of Iminepyridine Ligands. *Eur. J. Inorg. Chem.* **2012**, *2012*, 530−534. (b) Sherbow, T. J.; Parsons, L. W. T.; Phan, N. A.; Fettinger, J. C.; Berben, L. A. Ligand Conjugation Directs the Formation of a 1,3-Dihydropyridinate Regioisomer. *Inorg. Chem.* **2020**, *59*, 17614−17619.

(32) Toma, M.; Kuvek, T.; Vrček, V. Ionization Energy and Reduction Potential in Ferrocene Derivatives: Comparison of Hybrid and Pure DFT Functionals. *J. Phys. Chem. A* **2020**, *124*, 8029−8039.

(33) Blackman, A. G.; Schenk, E. B.; Jelley, R. E.; Krenske, E. H.; Gahan, L. R. Five-coordinate transition metal complexes and the value of τ5: observations and caveats. *Dalton Trans.* **2020**, *49*, 14798−14806.

https://doi.org/10.1021/acs.inorgchem.4c02664
Inorg. Chem. 2024, 63, 19156−19166

(34) *Bruker, SAINT+*; Bruker AXS Inc.: Madison, Wisconsin, USA, 2007.
(35) Sheldrick, G. M. *SADABS, Programs Scaling Absorpt. Correct. Area Detect. Data*; University of Göttingen: Göttingen, Germany, 1997.
(36) Sheldrick, G. SHELXT - Integrated space-group and crystal-structure determination. *Acta Crystallogr., Sect. A* **2015**, *71*, 3−8.
(37) Sheldrick, G. Crystal structure refinement with SHELXL. *Acta Crystallogr., Sect. C: Struct. Chem.* **2015**, *71*, 3−8.
(38) van der Sluis, P.; Spek, A. L. BYPASS: an effective method for the refinement of crystal structures containing disordered solvent regions. *Acta Crystallogr., Sect. A* **1990**, *46*, 194−201.
(39) Cosier, J.; Glazer, A. M. A nitrogen-gas-stream cryostat for general X-ray diffraction studies. *J. Appl. Crystallogr.* **1986**, *19*, 105−107.
(40) Sheldrick, G. A short history of SHELX. *Acta Crystallogr., Sect. A* **2008**, *64*, 112−122.
(41) Dolomanov, O. V.; Bourhis, L. J.; Gildea, R. J.; Howard, J. A. K.; Puschmann, H. OLEX2: a complete structure solution, refinement and analysis program. *J. Appl. Crystallogr.* **2009**, *42*, 339−341.

https://doi.org/10.1021/acs.inorgchem.4c02664
Inorg. Chem. 2024, 63, 19156−19166

Conclusiones

Conclusiones

Esta Tesis Doctoral demuestra que los complejos de aluminio(I) y galio(I) en bajo estado de valencia, tradicionalmente considerados meras curiosidades sintéticas en la química de los elementos de los grupos principales, pueden exhibir una reactividad muy similar a la de los metales de transición en procesos como la activación de H_2 y la activación selectiva de enlaces C–H. Al integrar estas especies del Grupo 13 ricas en electrones, en sistemas bimetálicos junto con metales alcalinos (Li^+, Na^+, K^+, Cs^+) o con el metal de transición Rh(I), pone de manifiesto cómo las interacciones metal–metal pueden reproducir o incluso mejorar la reactividad típica de especies de metales del bloque d. A continuación, se resumen las conclusiones principales:

- **Desarrollo y Caracterización de Nuevos Sistemas de Al(I) y Ga(I)**

  Se ha aislado y estudiado una familia extensa de compuestos en bajo estado de oxidación de metales del Grupo 13, que abarca tanto aniones aluminilo $[Al(I)]^-$ como gallilo $[Ga(I)]^-$, soportados sobre ligandos β-dicetiminatos dianiónicos. Mediante modificaciones sistemáticas en los cationes alcalinos (Li^+ a Cs^+) o en los ligandos dadores (éteres corona, criptandos), es posible controlar de forma precisa sus estados de agregación (desde especies diméricas y monoméricas hasta pares iónicos "libres" o "*naked*"). Estudios avanzados de RMN (incluyendo estudios de difusión en disolución, DOSY), difracción de rayos X y cálculos DFT demuestran que la cooperación de tipo metal–metal (Al(I)–metal alcalino o Ga(I)–metal alcalino) desempeña un papel determinante en la estructura, la distribución electrónica y la reactividad de estos sistemas.

- **Sistemas Aluminilo: Activación de H_2 y Control del Estado de Agregación**

  En la serie de aluminilos desarrollados en esta Tesis Doctoral, los complejos diméricos Al(I)–metal alcalino pueden romper el enlace H–H bajo condiciones suaves. Por otro lado, los aniones aluminilo $[Al(I)]^-$ no activan H_2 a menos que se introduzcan iones Cs^+ "libres", lo que facilita la ruptura del enlace H–H. Este hallazgo sugiere una nueva forma de activar el H_2 de forma sinérgica, de forma que el centro Al(I) nucleofílico y el catión alcalino colaboran para disminuir la barrera energética asociada a la fragmentación del H_2. Los cálculos DFT apuntan a una vía de activación de tipo S_N2, donde la solvatación dinámica de los aniones aluminilo $[Al(I)]^-$ por cationes alcalinos (en especial Cs^+) estabiliza los estados de

transición durante de activación del H_2. Así, estos sistemas aluminilo bimetálicos representan especies novedosas para de activación de enlaces.

- **Sistemas Galilo: Activación C–H**

  En el caso de galio(I), se obtuvieron nuevos compuestos de tipo galilo $[Ga(I)]^-$ estabilizados con ligandos β-dicetiminatos, los cuales mostraron propiedades estructurales y electrónicas distintas a las de los aluminilos desarrollados en el *Capítulo I*. Si bien no se logró la activación de H_2 bajo condiciones comparables, estos galilos sí son capaces de participar en la activación selectiva de enlaces C–H en sustratos aromáticos como azobenceno, demostrando la capacidad del Ga(I) para oxidarse a Ga(III), de forma muy similar a lo que ocurre en los procesos de adición oxidante en metales de transición. Por tanto, los sistemas galilo exhiben un gran potencial para la activación de enlaces E–H (E = C, heteroátomo), debido a su analogía con los carbenos derivados de los metales del Grupo 13.

- **Sistemas Heterometálicos de Ga(I)–Rh(I): Activación de H_2 e Hidrogenación Catalítica de Olefinas**

  La coordinación del compuesto monovalente de Ga(I) como metaloligando a complejos de Rh(I) condujo a la formación de sistemas heterometálicos del tipo Ga_2Rh capaces de activar selectivamente H_2 y de hidrogenar (ya sea de forma parcial o total) olefinas no conjugadas y conjugadas. A diferencia de los catalizadores basados en Rh–fosfina o Rh–NHC, los complejos Ga(I)–Rh(I) muestran una alta estabilidad y dan lugar a intermedios, como Rh(III)–hidruro o Rh(III)–alilo, durante el proceso de hidrogenación de olefinas. Los cálculos DFT demuestran que los metaloligandos de Ga(I) fomentan modos bimetálicos inusuales para romper el H_2 y en la hidrogenación de olefinas, al tiempo que reducen las barreras energéticas de reacción. Indicando la relevancia de la cooperación metal–metal entre metales de los grupos principales y metales de transición en procesos catalíticos.

- **Relevancia y Perspectivas Futuras**

  En conjunto, los resultados de esta Tesis Doctoral demuetran que los compuestos de Al(I) y Ga(I) en bajo estado de oxidación pueden dar lugar a reactividades tradicionalmente asociadas a metales de transición, ya sea en la ruptura de enlaces H–H, C–H o en la hidrogenación cooperativa junto con metales del bloque d. Mediante el control de las interacciones metal–metal (ya sea con

metales alcalinos o de transición) se logra modular de forma precisa la reactividad de estos compuestos que son análogos a los carbenos, pero con metales del Grupo 13. De este modo, esta Tesis Doctoral no solo amplía las fronteras de la química de los compuestos de baja valencia, sino que también sienta bases sólidas para futuros desarrollos de estos compuestos en catálisis y activación de enlaces E–H, resaltando el papel esencial de la cooperación bimetálica, en particular, cuando combinamos metales de los grupos principales con metales alcalinos o con otros metales de transición a través de interacciones metal–metal.

Conclusions

Conclusions

This *Doctoral Dissertation* shows that low-valent aluminium(I) and gallium(I) complexes, traditionally viewed as main-group curiosities, can achieve transition-metal-like reactivity in challenging H_2 bond activation and selective C–H transformations. By integrating these electron-rich Group 13 species into bimetallic frameworks, either with alkali metals (Li^+, Na^+, K^+, Cs^+) or Rh(I) transition-metal centers, the present work demonstrates how fine-tuning metal–metal interactions can unlock reactivities typically reserved for d-block metals. Key conclusions and findings are summarised below.

- **Development and Characterization of Novel Anionic Al(I) and Ga(I) Systems**

  A broad family of low-valent Group 13 complexes was developed, spanning both anionic aluminyl $[Al(I)]^-$ and gallyl $[Ga(I)]^-$ frameworks stabilised by dianionic β-diketiminate ligands. By systematically varying alkali-metal cations (Li^+ to Cs^+) and donor ligands (crown ethers, cryptands), we precisely controlled aggregation states (dimeric, monomeric, "*naked*"). Advanced NMR (including DOSY), X-ray diffraction, and DFT analyses revealed the decisive influence of metal–metal cooperativity on structure, electron distribution, and reactivity.

- **Aluminyl Systems: H_2 Cleavage and Aggreation**

  In the aluminyl series, dimeric Al(I)–alkali-metal complexes efficiently cleaved H_2 under mild conditions, whereas monomeric "*naked*" aluminyl required "free" Cs^+ to achieve dihydrogen activation. This underscores a synergistic mechanism wherein the nucleophilic Al(I) centre and alkali-metal cation collectively lower barriers for H–H bond cleavage. DFT results supported an S_N2-type path for H_2 addition, highlighting how fluxional alkali-metal solvation stabilises transition states. These advances broaden the scope of electron-rich aluminium(I) species as novel bond-activation tools in main-group chemistry.

- **Gallyl Systems: C–H Activation**

  Shifting to gallium, a series of β-diketiminate-supported Ga(I) carbene analogues displayed robust yet contrasting reactivity. Unlike aluminyls, H_2 activation was not observed under analogous conditions, yet C–H functionalisation in azobenzene succeeded. This indicates distinct redox pathways wherein Ga(I) transitions to Ga(III) states in a manner reminiscent of transition metals. Their structural

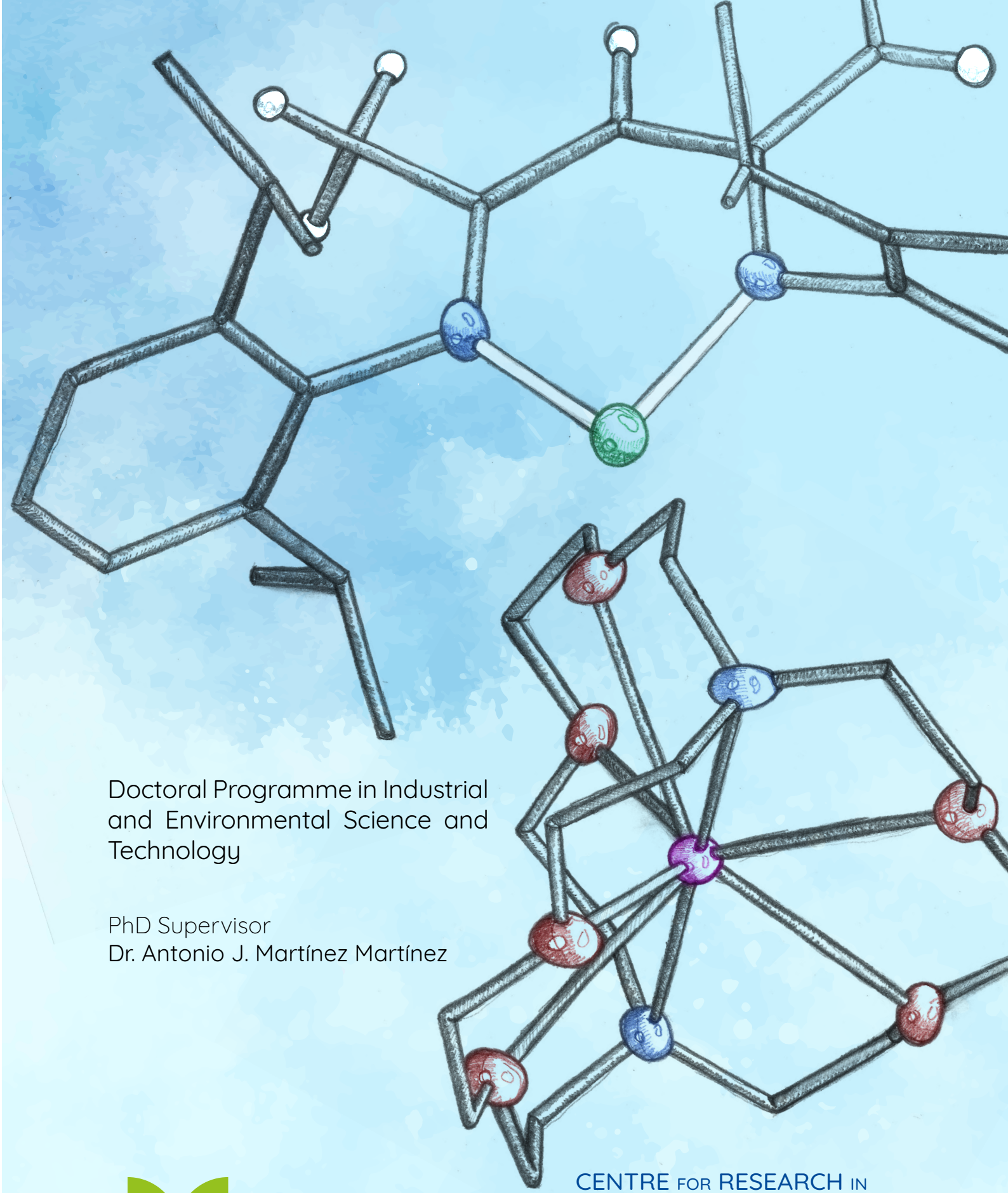
durability and redox agility emphasize the potential of anionic gallyls as complementary or alternative systems to classical Group 13 compounds.

- **Ga(I)–Rh(I) Heterometallic Systems: H_2 Activation and Catalytic Hydrogenation of Olefins**

  The coordination of Ga(I) to Rh(I) afforded robust heterometallic Ga_2Rh complexes capable of selective H_2 activation and controlled hydrogenation (partial or complete) of non-conjugated/conjugated olefins. In contrast to Rh–phosphine/NHC catalysts, the Ga(I)–Rh(I) platform formed stable, well-characterised Rh(III)–hydride or allyl intermediates. DFT simulations confirmed that Ga(I) metalloligands enable unusual bimetallic modes of H_2 cleavage and lower energy barriers for selective hydrogenation steps, demonstrating the power of main-group–transition-metal cooperative catalysis.

- **Significance and Outlook**

  Collectively, these findings reaffirm that low-valent Group 13 species can transcend their conventional boundaries, mimicking transition-metal-like reactivity through H–H bond cleavage, C–H functionalisation, and cooperative hydrogenation in tandem with d-block metals. By tuning alkali-metal or transition-metal centers, the chemistry of Al(I) and Ga(I) carbene surrogates can be finely modulated, unlocking pathways typically dominated by heavier metals. This dissertation thus lays a firm foundation for future exploration in bond-activation catalysis, enhancing the synthetic toolbox of main-group and transition-metal chemistry alike.



Doctoral Programme in Industrial and Environmental Science and Technology

PhD Supervisor
Dr. Antonio J. Martínez Martínez

CIQSO

CENTRE FOR RESEARCH IN SUSTAINABLE CHEMISTRY

CENTRO DE INVESTIGACIÓN EN QUÍMICA SOSTENIBLE